Mechanical resonators for liquid viscosity and mass density sensing

Martin Heinisch

▶ **To cite this version:**

Martin Heinisch. Mechanical resonators for liquid viscosity and mass density sensing. Electronics. Université de Bordeaux; Johannes-Kepler-Universität (Linz, Autriche), 2015. English. NNT : 2015BORD0116 . tel-01240432

HAL Id: tel-01240432
https://theses.hal.science/tel-01240432

Submitted on 9 Dec 2015

HAL is a multi-disciplinary open access archive for the deposit and dissemination of scientific research documents, whether they are published or not. The documents may come from teaching and research institutions in France or abroad, or from public or private research centers.

L'archive ouverte pluridisciplinaire **HAL**, est destinée au dépôt et à la diffusion de documents scientifiques de niveau recherche, publiés ou non, émanant des établissements d'enseignement et de recherche français ou étrangers, des laboratoires publics ou privés.

THÈSE

Présentée à

L'UNIVERSITE DE BORDEAUX

ÉCOLE DOCTORALE DE SCIENCES PHYSIQUES ET DE L'INGÉNIEUR

par **Martin HEINISCH**

POUR OBTENIR LE GRADE DE

DOCTEUR

SPÉCIALITÉ : ÉLECTRONIQUE

****

RESONATEURS MECANIQUES POUR LA MESURE DE LA MASSE VOLUMIQUE ET DE LA VISCOSITE DE LIQUIDE

****

Soutenue le : 25 septembre 2015 à LINZ (Autriche)

Cotutelle avec Johannes Kepler Universitat, Linz, Autriche

Devant la commission d'examen composée de :

M. Liviu NICU…….	Directeur de Recherche CNRS, LAAS
M. Stephen HEINRICH	Professeur à Marquette University, USA
M^{me}. Isabelle DUFOUR……..	Professeur à l'Université de Bordeaux
M. Bernhard JAKOBY	Professeur à JKU, Autriche

JOHANNES KEPLER
UNIVERSITÄT LINZ | JKU

TNF

Technisch-Naturwissenschaftliche
Fakultät

Mechanical Resonators for Liquid Viscosity and Mass Density Sensing

DISSERTATION

zur Erlangung des akademischen Grades

Doktor der technischen Wissenschaften

im Doktoratsstudium der

Technischen Wissenschaften

im Rahmen eines

International Joint Doctorate

zwischen der Johannes Kepler Universität Linz und der Université de Bordeaux

Eingereicht von:
Dipl.-Ing. Martin Heinisch

Angefertigt am:
Institut für Mikroelektronik und Mikrosensorik
Laboratoire IMS, Université de Bordeaux, Frankreich

Beurteilung:
Univ.-Prof. Dipl.-Ing. Dr. Bernhard Jakoby (Betreuung JKU)
Professeur Isabelle Dufour (Betreuung Université de Bordeaux)

Linz, August 2015

Résumé

Cette thèse synthétise les approches théoriques et expérimentales faites dans le cadre de travaux récents de l'auteur sur l'utilisation de résonateurs mécaniques pour la détermination simultanée de la viscosité et de la masse volumique de liquides. Ces travaux ont été réalisés entre 2010 et 2015 dans le cadre d'une thèse en cotutelle entre l'Institut de Microélectronique et des Microcapteurs de l'Université Johannes Kepler à Linz en Autriche et le Laboratoire de l'Intégration du Matériau au Système de l'Université de Bordeaux en France. Dans des études précédentes effectuées sur ce sujet par les groupes des deux laboratoires, le concept de l'utilisation de résonateurs mécaniques actionnés et mesurés électriquement pour la détermination de la viscosité et de la masse volumique de liquide avait été établi et validé. Ces travaux antérieurs ont montré que la fréquence de résonance et le facteur de qualité de résonateurs immergés dépendent à la fois de la viscosité et de la masse volumique du fluide environnant.

La viscosité et la masse volumique sont des quantités importantes décrivant le comportement physique d'un liquide. Une fois déterminées, ces quantités peuvent être utilisées pour tirer des conclusions sur l'état et la qualité du liquide examiné. A titre d'exemple voici quelques applications de ce type de mesures : le contrôle de la capacité lubrifiante des huiles et leur vieillissement, le contrôle de la qualité des encres d'impression ou la caractérisation des solutions d'ADN ... L'utilisation de capteurs pour mesurer la viscosité et la masse volumique de liquides à la place d'instruments conventionnels de laboratoire présente de nombreux avantages. Sans avoir un caractère exhaustif, les avantages peuvent être regroupés en trois catégories :

1. Quantité d'échantillons faibles : Dans les applications biologiques ou médicales, la quantité de liquide disponible peut être très faible. Pour les viscosimètres et

rhéomètres classiques, quelques millilitres de liquides sont généralement nécessaires. Dans la littérature, il a été spécifié qu'il faut moins d'un nanolitre de liquide pour la mesure de la viscosité de liquides à l'aide d'une micropoutre telle que celles utilisées dans les microscopes à force atomique (AFM).

2. Principe de mesure en ligne ou appareils portables : Dans de nombreux procédés de production de liquides industriels, quel que soit le domaine d'application (boisson, médical, huile, peinture, produit chimique, industrie de l'environnement, etc.) les liquides doivent généralement être analysés dans un laboratoire spécialisé. Ceci a généralement une répercussion à la fois sur le coût et sur la durée de production. Pour surmonter ce coût et surtout les inconvénients liés à la durée d'obtention de la mesure, il est important d'utiliser des principes et des appareils portables permettant des mesures en ligne. Dans certains cas, par exemple pour le contrôle d'un processus dans une chambre de réaction, cela est même quasiment indispensable.

3. Extension de la gamme de fréquence étudiée : D'un point de vue rhéologique, ces dispositifs résonants permettent d'effectuer des mesures à des fréquences supérieures à 100 Hz, qui est généralement la fréquence maximale de mesure dans les rhéomètres conventionnels.

Au cours des deux dernières décennies, de nombreux principes ont été rapportés dans la littérature. Les différentes approches peuvent se distinguer par exemple par leur structure mécanique, par la technologie de fabrication, par les matériaux utilisés ainsi que par l'actionnement et les principes de mesure. Les structures mécaniques utilisées peuvent être par exemple encastrées à une seule extrémité (poutre), à deux extrémités (ponts), ou être des structures de type diapasons, membranes vibrantes ou des plaques rigides oscillantes. En ce qui concerne la technologie et les matériaux, il existe des dispositifs à base de silicium ou de quartz mais aussi à base de feuilles de polymère recouvertes de cuivre, ou en PZT sérigraphié ou utilisant des fils en tungstène.

Les dispositifs à base de quartz fonctionnant en cisaillement (balance à quartz, QCM), qui sont fréquemment utilisés en rhéologie, fonctionnent à des fréquences de l'ordre du MegaHertz. Des fréquences de fonctionnement inférieures pourraient devenir intéressantes pour les caractérisations de liquides complexes tels que les émulsions. Ainsi, il existe un besoin entre les fréquences opératives des rhéomètres classiques et celles des dispositifs à quartz et donc pour la gamme de fréquence entre 100 Hz et 100 kHz environ. L'objectif de cette thèse est de cibler cette gamme de fréquence, ce qui implique des dimensions de dispositifs allant environ du millimètre au centimètre.

Dans cette thèse, l'interaction des résonateurs mécaniques, actionnés et mesurés électriquement, avec des liquides visqueux a été étudiée en vue de la mesure de la viscosité et de la masse volumique des liquides. Ces capteurs peuvent en outre être utilisés pour des mesures en ligne, in situ et sont des dispositifs portables fonctionnant à des fréquences allant d'environ 100 Hz à 100 kHz. Cette gamme de fréquence n'est pas encore couverte par les instruments standards, mais représente une gamme de fréquences intéressante d'un point de vue rhéologique. Une vaste étude de la littérature du domaine a montré que de nombreuses approches pour cette problématique ont déjà été publiées avant cette thèse. A l'issu de cette étude bibliographique il a semblé intéressant d'étudier la possibilité de mesurer simultanément la viscosité et la masse volumique avec un seul appareil, d'avoir des géométries et des matériaux optimums pour une précision élevée, de connaitre les stabilités requises pour la fréquence de résonance et le facteur de qualité pour une précision donnée pour la viscosité et pour la masse volumique. Pour répondre à ces exigences, les réponses en fréquence de résonateurs mécaniques immergés, interagissant avec des échantillons liquides ont été étudiées.

Une grande partie du travail de thèse a été basée sur une approche expérimentale. Cependant, une étude théorique approfondie a été menée impliquant des connaissances en mécanique des structures, mécaniques des fluides ainsi qu'en électrodynamique. Ceci a conduit à une modélisation des effets physiques et des résultats observés. Un modèle

généralisé reliant la fréquence de résonance et le facteur de qualité d'un résonateur mécanique immergé à la masse volumique et à la viscosité du liquide a pu être formulé. Ce modèle a permis d'estimer la sensibilité parasite du résonateur mécanique à la grandeur d'influence qu'est la température. Neuf résonateurs ont été fabriqués et successivement étudiés, permettant d'améliorer non seulement les aspects manipulation, mais de façon plus importante la précision des mesures. Les principales conclusions et les connaissances acquises par les approches mentionnées ci-dessus sont :

1. La possibilité de mesurer à la fois la masse volumique et la viscosité a été montrée pour plusieurs types de résonateurs. Si la matrice de sensibilité est inversible, ou en d'autres termes, si les sensibilités de la fréquence de résonance et du facteur de qualité vis-à-vis de la viscosité et de la masse volumique sont différentes, la viscosité et la masse volumique peuvent être déterminée avec un seul dispositif. En général, cela est le cas pour les résonateurs dont les interactions fluide-structure ne donnent pas uniquement des ondes de cisaillement.

2. Un enjeu important pour la stabilité et la précision des mesures est l'encastrement de la structure vibrante. Il a été montré que des dispositifs encastrés sur une seule zone donnent une stabilité beaucoup plus élevée de leur fréquence de résonance que les dispositifs doublement encastrés. Cela peut être illustré en considérant par exemple la différence entre les instruments à base d'une anche ou les instruments à cordes. Ces derniers doivent être fréquemment réglés, alors que la fréquence de résonance de la première catégorie d'instrument ne change pas de manière significative. En outre, les dispositifs doublement encastrés sont sujets à diverses contraintes mécaniques, qui sont induites par exemple par des variations thermiques ou simplement à cause du fait que l'on touche le boîtier du résonateur lors de la manipulation de celui-ci.

3. Il a été montré que les diapasons sont des types de résonateurs bien adaptés pour la mesure de la viscosité et de la masse volumique de liquides. En raison de leur conception symétrique, la dépendance de la fréquence de résonance aux

conditions d'encastrement est faible. Cela devient particulièrement important pour les appareils portables.

4. L'étude pour le choix des matériaux constituant les résonateurs a montré que le tungstène donne les meilleurs résultats pour les résonateurs excités par la force de Lorentz. Dans le cas de résonateurs en forme de 'U' réalisés avec un fil de tungstène, les plus faibles sensibilités à la grandeur d'influence qu'est la température ont été obtenues. En fait, dans le cas où les sensibilités aux grandeurs d'influence deviennent trop importantes, les résonateurs compensés en température représentent une alternative intéressante.

5. Viser une précision de 1% pour la viscosité et 1 mg / cm^3 pour la masse volumique implique des stabilités relatives de l'ordre de 10^{-5} pour la fréquence de résonance et 10^{-3} pour le facteur de qualité.

6. Le fait de viser les précisions mentionnées ci-dessus pour la viscosité et la masse volumique nécessite une précision de mesure de la température d'au moins 0,5°C pour les diapasons en acier étudiés.

7. L'utilisation de diapasons en acier a montré qu'avec des résonateurs mécaniques il est possible d'obtenir une précision de 1% sur la mesure de la viscosité et de 0,01% sur la mesure de la masse volumique (c'est à dire une précision de 0,1 mg / cm^3 pour des liquides aqueux). Ceci est du même ordre que les précisions des instruments de laboratoires commerciaux.

Preface

The present PhD thesis was written in the course of an International Joint Doctorate program of the Johannes Kepler University Linz, Austria and the University of Bordeaux, France and is based on six journal publications as well as 31 conference proceedings papers published between 2010 and 2015 as first author. The intention of this thesis was to review these results in a compact manner and to present them in a single manuscript. For better readability, theory, figures and verbatim text passages taken from these publications are not highlighted (for example through indentation and italic text style). However, special reference styles are used to clearly point out the origin of the passages in the thesis. References to first and co-authored publications are indicated by [MHxxxNo] where 'xxx' stands for an abbreviation designating the type of publication and 'No' is the numbering for the particular publication type. The reference keys and the according publication are given in the list of publications in the beginning of this thesis. References to other works are cited by using numbers, i.e. [No], the list for these references can be found at the end of the manuscript. Studies close to submission for publication are cited by 'work in progress'.

Acknowledgement

Now, that my PhD studies at the Johannes Kepler University Linz and the Université de Bordeaux are coming to an end and after completing this manuscript, I can honestly embrace this period as the greatest and most instructive time of my life. I was honored with the unique opportunity of following an international joint doctorate program and the possibility to teach students in class. Therefore, I am greatly indebted to the people who provided me with the inimitable chance for this work, who supported me in a professional, technical but also in a very personal way. Their support during all the ups and downs I experienced in this important time of my professional and personal career is very much appreciated.

First and foremost, I want to thank my supervisor Prof. Bernhard Jakoby, not only for offering me this PhD position, but also for enabling excellent writing conditions for this thesis at his institute. At all times he was amenable to any of my requests and endeavoring to guarantee the basic requirements for reliable research, trust, freedom and self-responsibility. Also, I am very much obliged to my co-supervisor Prof. Isabelle Dufour, for arranging the joint doctorate program, her tireless support of any concerns at all times and her warm hospitality in Bordeaux. This program facilitated the essential part of the extraordinary research possibilities I was provided with for my thesis. I profited from the experience of two laboratories and was given the opportunity to spend several research stays in Bordeaux, where I was allowed to work undistracted and very much focused, which was necessary to accomplish the major milestones in this thesis. Furthermore, I want to thank Prof. Steven Heinrich for our very enriching discussions and his exceedingly precise review of my thesis. I am also indebted to Liviu Nicu for his offer to review the thesis and to attend my defense.

I very much appreciated the working atmosphere and collaboration with my colleagues at both institutes. In particular, I am very grateful to Thomas Voglhuber-Brunnmaier for his altruistic support, his indefatigable patience during numerous discussions and all his enriching inputs for this thesis. He always finds a way for breaking down complex problems into their constituent parts, while solving them clearly and precisely. With his pioneer spirit, Erwin Reichel did not only lay a significant foundation for this work but paved the way for proceeding investigations in the field of resonant viscosity and mass density sensors. Special thanks go to Johann Katzenmayer and Bernhard Mayrhofer for their excellent assistance. Without their interest and passion for work, the required measurement setups and resulting measurement accuracies would not have been possible. Furthermore, I would like to emphasize the pleasant cooperation with Etienne Lemaire and Damien Thuau's helpfulness and cordiality.

While writing my thesis I also experienced situations during which I especially relied on the support of my family and friends. I am deeply grateful to my parents Elisabeth and Ernst, to my brother Florian, his partner Eva and to my sister Julia, her husband Manuel and my goddaughter Eloisa. Also, I am very much obliged to my close friends Christoph Goniva, Christoph Kloss, Florian König and Hubert Mitterhofer. With their open ears, hearts and doors they represent the most valuable part during this important period of my life.

Kurzfassung

Die vorliegende Dissertation fasst die rezenten Forschungsergebnisse des Verfassers im Bereich mechanischer Resonatoren für Viskositäts- und Dichtesensorik zusammen, welche zwischen 2010 und 2015 im Rahmen eines international joint doctorate programs am Institut für Mikroelektronik und Mikrosensorik der Johannes Kepler Universität Linz, sowie am Laboratoire de l'Intégration du Matériau au Système der Université de Bordeaux erreicht wurden. In den Vorarbeiten von Arbeitsgruppen beider Institute wurden bereits Konzepte für elektrisch angeregte und ausgelesene mechanische Resonatoren zur Bestimmung von Viskosität und Dichte von Flüssigkeiten erarbeitet und umgesetzt. Hierbei konnte gezeigt werden, dass die Resonanzfrequenz und Güte eingetauchter Resonatoren abhängig sind von Viskosität und Dichte der jeweiligen Flüssigkeiten. Die dabei untersuchten Konzepte beinhalteten strukturierte Polymerfolien, nass-chemisch geätzte Neusilberbleche, mikromechanisch hergestellte Siliziumstrukturen, sowie siebgedruckte PZT Resonatoren.

Die Motivation zur Untersuchung und Entwicklung solcher miniaturisierter Resonatoren resultiert unter anderem aus deren Anwendbarkeit für Inline-, Insitu- und Handgeräte für Labor- bzw. industrielle Anwendungen. Besonders für Letztere sind Robustheit, Langzeitstabilität und Zuverlässigkeit, aber auch präzise Messergebnisse Grundvoraussetzung. Um den Anforderungen der Ergebnisse und Erkenntnisse der zuvor genannten Arbeiten gerecht zu werden, wurden folgende Ziele für diese Dissertation definiert. Erstens, die Entwicklung robuster, langzeitstabiler Messaufbauten zur Erreichung präziser Messergebnisse, wodurch eine geringe Temperaturquerempfindichkeit als weitere Bedingung aufgestellt wurde. Zweitens sollte untersucht werden ob und mit welcher Genauigkeit sowohl Viskosität als auch Dichte mit einem einzigen Instrument gemessen werden können. Drittens, sollte einerseits das Verhalten verschiedener Viskositäts- und Dichtesensoren modelliert bzw. deren Vergleich ermöglicht werden. Basierend auf einer vorwiegend experimentellen Herangehensweise und unter Miteinbeziehung der zugrundeliegenden Theorien von Strömungs- und Strukturmechanik sowie der Elektrodynamik, konnten die o.g. Anforderungen erfüllt werden.

Mit der schrittweisen Entwicklung und Untersuchung von insgesamt neun verschiedenen Sensorkonzepten konnte gezeigt werden, dass besonders einfach eingespannte Strukturen, wie U-Draht und Stimmgabelresonatoren am besten dafür geeignet sind, um Langzeitstabilität, hohe Messgenauigkeit und geringe Temperaturquerempfindlichkeit zu erzielen. Für Letzteres führte die Verwendung von Wolfram als Resonatormaterial zu den besten Ergebnissen. Mit Stimmgabelsensoren konnten Genauigkeiten im Bereich von 1 % für Viskosität und 0.01 % für Dichte erreicht werden. Die Verwendung von speziell gemischten Flüssigkeiten mit konstanten Dichten, aber verschiedenen Viskositäten und umgekehrt, ermöglichte getrennte, experimentelle Untersuchungen der Empfindlichkeiten auf Viskosität und Dichte. Für die Berechnung der im Rahmen dieser Experimente benötigten Flüssigkeitsmengen zur Erreichung einer gewissen Viskosität und Dichte bei einer bestimmten Temperatur, wurden Modelle sowohl für Einzelflüssigkeiten als auch für binäre und ternäre Flüssigkeitsmischungen erarbeitet. Diese Modelle sowie entsprechende Mischungsanleitungen wurden auf der Internetplattform www.rheo-logic.info zur Verfügung gestellt. Durch Verwendung solcher Flüssigkeitsserien konnte für die untersuchten Sensoren gezeigt werden, dass die Empfindlichkeiten der Güte auf Viskosität und Dichte ähnlich sind, wohingegen die Empfindlichkeit der Resonanzfrequenz auf Dichte mindestens zehn mal höher ist als auf Viskosität. Diese Erkenntnis belegt, dass beide Größen mit einem einzigen Sensor gemessen werden können. Des Weiteren wurde ein generalisiertes Modell entwickelt, welches nicht nur die Funktionsweise der Sensoren unter Berücksichtigung von deren Temperaturquerempfindlichkeiten vollständig beschreibt, sondern auch den Vergleich unterschiedlicher Sensordesigns ermöglicht. Dass für die Kalibrierung die Ergebnisse von Messungen in nur drei Flüssigkeiten ausreichend sind und dass damit bereits hohe Modellgenauigkeiten für verschiedene Sensordesigns erreicht wurden, sind weitere Vorteile dieses generalisierten Modells.

Abstract

This thesis summarizes the author's recent work on the topic of mechanical resonators for liquid viscosity and mass density sensing, which were achieved between 2010 and 2015 in the course of an international joint doctorate program performed at the Institute for Microelectronics and Microsensors at the Johannes Kepler University Linz, Austria and the Laboratoire de l'Intégration du Matériau au Système in Bordeaux, France. In previous studies performed by work groups of both laboratories, the concept of using electrically actuated and read-out mechanical resonators for the determination of liquids' viscosities and mass densities has been established and elaborated. These works showed that the resonance frequencies and quality factors of immersed resonators are affected by the liquids' viscosities and mass densities, respectively. The investigated concepts included devices using structured polymer or wet-etched new silver sheets as well as micro-machined silicon and screen-printed PZT resonators.

The motivation for investigating and developing such miniaturized resonators was formed, amongst others, by their capability for in-line, in-situ and handheld-devices for laboratory as well as for industrial applications. Especially for the latter, physical robustness, long-term stability and reliability, as well as accurate measurement results are basic requirements. To satisfy these requirements and considering the results and insights of earlier works, the objectives of this thesis were first, implementing robust measuring setups featuring long-term stability and high measurement accuracy, where the latter furthermore requires low cross-sensitivity to temperature. Second, investigating the capability of measuring both, a liquid's mass density and viscosity with a single device as well as providing an estimate of achievable measurement accuracies for both quantities. And third, enabling the modeling of the performance of different viscosity and mass density sensors on the one side and their comparison on the other side. These three specifications were accomplished by following mainly experimental approaches and investigations but also by elaborating the underlying theory of hydrodynamics, structural mechanics, and electrodynamics.

The investigation of nine different, successively developed sensor concepts showed that especially singly clamped device approaches such as vibrating U-shaped wires or tuning fork sensors are best suited for obtaining long-term stability, high measurement accuracy, and low cross-sensitivity to temperature. For the latter, the usage of tungsten as resonator's material yielded the best results. With tuning fork sensors, accuracies in the order of 1 % in viscosity and 0.01 % in mass density could be achieved. Using specially developed liquid mixtures with constant mass densities but varying viscosities and vice versa, allowed for a separate experimental investigation of the devices' sensitivities to viscosity and mass density. To prescribe the necessary amounts of liquids for obtaining a certain viscosity and mass density at a given temperature, models for single liquids as well as binary and ternary liquid mixtures were elaborated. These models and associated mixture prescriptions can be accessed via the platform www.rheo-logic.info. By using such liquid series it was shown for the investigated sensors that the sensitivities of the quality factor to viscosity and mass density are similar but that the sensitivities of the resonance frequency are typically at least ten times higher to mass density than to viscosity. This finding proves that both, viscosity and mass density can be measured while using a single device. Furthermore, a generalized model was developed which not only describes completely the sensors' performances considering their cross-sensitivity to temperature but also enables the comparison of different sensor designs. The circumstances, that the measurement results in only three liquids are sufficient for the models calibration and that high modeling accuracies for different sensor designs could therefore be achieved, are further highlights of this generalized model.

Résumé

Cette thèse synthétise les travaux récents de l'auteur sur l'utilisation de résonateurs mécaniques pour la détermination simultanée de la viscosité et de la masse volumique de liquides. Ces travaux ont été réalisés entre 2010 et 2015 dans le cadre d'une thèse en cotutelle entre l'Institut de Microélectronique et des Microcapteurs de l'Université Johannes Kepler à Linz en Autriche et le Laboratoire de l'Intégration du Matériau au Système de l'Université de Bordeaux en France. Dans des études précédentes effectuées sur ce sujet par les groupes des deux laboratoires, le concept de l'utilisation de résonateurs mécaniques actionnés et mesurés électriquement pour la détermination de la viscosité et de la masse volumique de liquide avait été établi et validé. Ces travaux antérieurs ont montré que la fréquence de résonance et le facteur de qualité de résonateurs immergés dépendent à la fois de la viscosité et de la masse volumique du fluide environnant.

L'intérêt d'utiliser de tels microcapteurs résonants vient du fait qu'il est possible de les utiliser in-situ, notamment pour des applications industrielles. Pour ce type d'applications, il est important que les capteurs aient entre autre une bonne résistance physique, une bonne stabilité à long terme, une bonne fiabilité, ainsi qu'une bonne précision de mesure. Pour satisfaire ces exigences et compte tenu des résultats des travaux antérieurs, les objectifs principaux de cette thèse étaient (1) la mise en œuvre de configurations de mesure robustes offrant une bonne stabilité à long terme et une bonne précision de mesure, ce qui nécessite une faible sensibilité à la température, (2) la mesure simultanée de la viscosité et de la masse volumique avec un seul capteur et (3) la modélisation et la comparaison des performances des différents dispositifs mis au point et testés. Ces trois objectifs ont été atteints en combinant des approches expérimentales et théoriques (hydrodynamique, mécanique du solide et électrodynamique).

Au cours de cette thèse, neuf types de capteurs résonants ont été conçus, fabriqués et étudiés. Cette étude a permis de montrer que les structures en forme de U et les diapasons sont les mieux adaptés pour l'obtention d'une bonne stabilité à long terme, d'une précision de mesure élevée et d'une faible sensibilité parasite à la température. Pour les diapasons, l'utilisation de tungstène comme matériau a donné les meilleurs résultats : des précisions de l'ordre de 1 % pour la viscosité et de 0,01 % pour la masse volumique ont été obtenues. Pour étudier séparément l'effet de la viscosité et de la masse volumique, des séries de liquides ayant différentes viscosités mais une masse volumique constante et vice-versa sont nécessaires. De telles séries de liquides peuvent être obtenues en utilisant des mélanges de liquides connus. Afin de déterminer la quantité requise de chaque liquide constituant le mélange pour obtenir une certaine viscosité et une certaine masse volumique à une température donnée, des modèles de calcul de la masse volumique et de la viscosité de mélanges binaires ou ternaires de liquides ont été élaborés. Ces modèles et les proportions pour les mélanges sont accessibles via la plate-forme www.rheo-logic.info. En utilisant ces mélanges de liquides, il a été montré pour les capteurs testés que le facteur de qualité avait des sensibilités comparables vis-à-vis de la viscosité et de la masse volumique, alors que la fréquence de résonance est au moins dix fois plus sensible à la masse volumique qu'à la viscosité. Néanmoins, les deux quantités dépendent à la fois de la viscosité et de la masse volumique et permettent la détermination simultanée de la viscosité et de la masse volumique des liquides avec un seul appareil. En outre, un modèle généralisé a été formulé qui permet de relier les fréquences de résonance et les facteurs de qualité de tout résonateur mécanique aux masses volumiques et aux viscosités des liquides. L'avantage de ce modèle est qu'il ne nécessite au préalable que des mesures dans trois liquides afin de déterminer les caractéristiques du capteur, à savoir ses sensibilités vis-à-vis de la viscosité et de la masse volumique.

Contents

List of symbols xi

List of publications xv

1 Introduction 1
- 1.1 Viscosimetry and rheometry . . . 1
- 1.2 Motivation for using mechanical resonators . . . 2
- 1.3 Working principle of resonant viscosity and mass density sensors . . . 3
  - 1.3.1 Modeling approaches . . . 3
  - 1.3.2 Liquid series for experimental characterization of the resonator . . . 4
- 1.4 Notation of absolute and relative deviations . . . 5
- 1.5 Temperature dependence of viscosity and mass density . . . 5
  - 1.5.1 Normalized illustration . . . 5
  - 1.5.2 Temperature dependence of viscosity . . . 6
  - 1.5.3 Temperature dependence of mass density . . . 8
- 1.6 Viscosity and mass density of binary mixtures . . . 9
  - 1.6.1 Existing models for viscosity and mass density of binary liquid mixtures . . . 12
  - 1.6.2 New models for viscosity . . . 13
  - 1.6.3 New models for mass density . . . 16
- 1.7 Viscosity and mass density of ternary mixtures . . . 17
  - 1.7.1 Bézier triangle . . . 18
  - 1.7.2 Temperature dependent control points . . . 18
  - 1.7.3 Mixture dependent temperature coefficients . . . 19
- 1.8 Governing equations for oscillating fluid-structure interaction . . . 21
  - 1.8.1 Conservation of mass . . . 21
  - 1.8.2 Equation of motion . . . 22
  - 1.8.3 Stress tensor for Newtonian, compressible liquids . . . 22
  - 1.8.4 Equation of motion in liquids (Navier-Stokes) . . . 22
  - 1.8.5 Strain, stress and the differential equation of motion of elastic solids . . . 23
  - 1.8.6 Relation for stress and strain in isotropic elastic materials . . . 24
  - 1.8.7 Equation of motion for solids and approximated oscillatory fluid motion . . . 24
- 1.9 Lumped element approach . . . 25

2 Theory and modeling 29
- 2.1 Fluid dynamics . . . 29
  - 2.1.1 Forces on oscillating objects . . . 29
  - 2.1.2 In-plane oscillating plate . . . 29
  - 2.1.3 Rotating oscillating cylinders or tubes . . . 30
  - 2.1.4 Oscillating sphere . . . 32
  - 2.1.5 Transversally oscillating cylinder . . . 32
  - 2.1.6 Transversally oscillating rectangular beam . . . 33
- 2.2 Mechanical resonators . . . 33
  - 2.2.1 Transverse vibrations of prismatic beams . . . 33
  - 2.2.2 Torsional vibrations . . . 37
  - 2.2.3 Theory of vibrating plates and membranes . . . 39
  - 2.2.4 Frequency tuning . . . 39

2.3 Temperature dependence of the resonance frequency . . . 41
2.3.1 Singly clamped beams . . . 41
2.3.2 Young's modulus as a function of the melting point . . . 41
2.3.3 Correlation of the thermal expansion and melting point . . . 42
2.3.4 Strings . . . 43
2.4 Vibrating structures described by second order systems . . . 43
2.4.1 Effective mass m_i . . . 44
2.4.2 Effective stiffness k_i . . . 44
2.4.3 Effective damping c_i . . . 45
2.4.4 Lumped force $F_{\mathrm{ex},i}$ . . . 45
2.4.5 Lumped element oscillator . . . 45
2.5 Identification of second order systems . . . 48
2.5.1 Extraction of the second order system . . . 48
2.5.2 Evaluation of f_r and Q from free oscillations . . . 50
2.5.3 Evaluation of f_r and Q from the frequency response obtained by spectrum analysis of forced oscillations . . . 51
2.6 Recording the frequency response . . . 55
2.6.1 Investigated bandwidth . . . 55
2.6.2 Frequency sweep speed and prevention from non-linear deflections . . . 57
2.7 Liquid loaded resonator (LLR) . . . 58
2.7.1 Equations for resonance frequency and quality factor . . . 58
2.7.2 Inverse model . . . 59
2.8 Application of the generalized equations . . . 60
2.8.1 Relative sensitivity . . . 60
2.8.2 Estimation of required accuracies for f_r and Q . . . 61
2.8.3 Error propagation . . . 62
2.9 Higher mode excitation . . . 63
2.10 Cross-sensitivity to temperature . . . 63
2.11 Theoretical study on the frequency dependence of $m(\omega)$ and $c(\omega)$ . . . 66
2.11.1 Examples of liquid loaded resonators . . . 66
2.11.2 Estimation of the change of $m(\omega)$ and $c(\omega)$ in the investigated frequency range 66
2.11.3 Estimation of systematic errors of η and ρ resulting from second order fit . . . 67

3 Device concepts and approaches 69
3.1 Lorentz force driven resonators (LFDRs) . . . 69
3.2 Principle of one conductor and two conductors LFDRs . . . 70
3.3 Measurable output voltage V_out . . . 71
3.4 Offset voltage and cross-talk . . . 72
3.4.1 One conductor LFDR (U-wire) . . . 72
3.4.2 Two conductors LFDRs . . . 78
3.4.3 Single versus double coil setup (torsional resonator) . . . 81
3.5 Magnetic circuitry . . . 81
3.5.1 Effect of magnetic flux density on the motion-induced voltage . . . 81
3.5.2 Halbach array for straight structures . . . 82
3.5.3 Magnet assemblies for non-straight structures (U-shaped wire) . . . 82
3.6 Reluctance actuation and electromagnetic pickups . . . 83

4 Sensors 85
4.1 Double membrane sensor . . . 86
4.1.1 Sensor principle . . . 86
4.1.2 Fabrication . . . 87
4.1.3 Results . . . 87
4.2 Suspended platelet . . . 89

4.3 Single plate resonator . . . 89
4.4 Wire viscometer . . . 91
4.5 U-shaped wire sensor . . . 92
4.6 U-tube density sensor . . . 94
4.7 Spring viscometer . . . 95
4.8 Torsional resonator . . . 97
4.9 Tuning fork . . . 99
4.9.1 Measurements . . . 99
4.10 Examples of resonant sensors for fluid properties from literature . . . 102
4.10.1 Microacoustic devices . . . 103
4.10.2 MEMS devices . . . 103

5 Summary, conclusions and outlook **107**
5.1 Theoretical approach and insights . . . 108
5.2 Experimental approach and insights . . . 109
5.3 Outlook . . . 111
5.3.1 Works in progress . . . 111
5.3.2 Future research . . . 114

Bibliography **117**

Journal Publications **137**

Curriculum vitae **191**

Eidesstattliche Erklärung **193**

List of symbols

Notation	Description
x, X	scalar quantities (x might be replaced by another symbol)
$\boldsymbol{x}$	vector
$\boldsymbol{X}$	matrix
x, y, z	components of a cartesian coordinate system
r, φ, z	components of a cylindrical coordinate system
$\hat{\cdot}$	amplitude of a quantity
$\underline{\cdot}$	complex quantity
$\cdot^{\mathrm{T}}$	transpose of a matrix or a vector
$\cdot_{x,y,z}$	x-, y- or z-component of a vectorial quantitiy
$\partial/\partial\cdot$	partial derivative
$D/D\cdot$	substantial derivative
$\otimes$	tensor product
∇	Nabla operator
∇_{s}	symmetric gradient operator
diag	diagonal matrix
det	determinant
H_1^2	first order, second kind Hankel function
H_2^2	second order, second kind Hankel function
J_1	first kind, first order Bessel function
K_0	zeroth order, second kind modified Bessel function
K_1	first order, second kind modified Bessel function
Re	Reynolds number
Γ	Hydrodynamic function

Symbol	Description	Unit
A	area (of a cross section)	m^2
B	magnetic flux density	T
C	capacitance	F
C	constant, factor	a.u.
c	damping constant	$\mathrm{N}\cdot\mathrm{s/m}$
$\boldsymbol{c}$	forth rank elasticity tensor	$\mathrm{N/m}^2$
e	Euler's number, base of the natural logarithm	
E	Young's modulus	N/m^2
F	force	N
f	force per unit length	N/m
f	force density	$\mathrm{N/m}^3$
f	frequency	Hz
f_r	resonance frequency	Hz
G	shear modulus	Pa
H	magnetic field strength	A/m
I	electric current	A/m
I_y	second moment of area about the y-axis	m^4
I_p	polar moment of area	m^4
$\boldsymbol{I}$	identity matrix	
j	imaginary number $\mathrm{j}^2 = -1$	
k	spring stiffness	N/m
L	length	m
L	inductance	H
M	mutual inductance	H
m	mass	kg
N	normal force	N
$N_{\delta l,r}$	number of bandwidths	
$\boldsymbol{n}$	normal vector of length one	
p	pressure	Pa
Q	quality factor	
r_c	covering ratio	
R	radius	m
R	resistance	Ω
S	strain	
S	sensitivity	
T	(normal) stress	Pa
$\boldsymbol{T}$	stress tensor	Pa
T	temperature	K
t	time variable	s
u	deflection	m
v	velocity	m/s
V	volume	m^3
V	voltage	V
w	mass fraction	
w	width	m
x	mole fraction	
Y	admittance	S

Symbol	Description	Unit
γ	shear angle	
$\Delta\cdot$	absolute change of a quantity	a.u.
$\Delta^{\mathrm{r}}\cdot$	relative change or deviation of a quantity	
δ	damping constant	s^{-1}
δ	penetration depth	m
ε	strain	
ε_0	electric field constant	$\mathrm{A\,s\,/\,(V\,m)}$
η	dynamic viscoisty	Pa·s
ϑ	temperature	°C
λ	eigenvalue	a.u.
λ	volume viscosity	Pa·s
μ_0	magnetic field constant	$\mathrm{V\,s\,/\,(A\,m)}$
ρ	mass density	$\mathrm{kg/m^3}$
σ	tensile (normal) stresses	Pa
τ	time constant	s
τ	shear stress	Pa
φ	volume fraction	
φ_0	initial phase angle of transient oscillation	rad
$\varphi_{\mathrm{ex},0}$	initial phase angle of excitation force	rad
φ_{u}	phase angle between excitation force and deflection	rad
φ_{v}	phase angle between excitation force and velocity	rad
ϕ	magnetic flux	Wb
ψ	linked magnetic flux	Wb
ω	angular frequency	rad/s
ω_0	undamped angular eigenfrequency	rad/s
$\omega_{0,\delta}$	damped angular eigenfrequency	rad/s
ω_{r}	angular resonance frequency	rad/s

List of publications

Bookchapters

Co-authored Bookchapters

[MHbcc1] [1] E. K. Reichel, M. Heinisch, B. Jakoby, Chapter 17, fluid property sensors in, resonant mems: Principles, modeling, implementation, and applications, Wiley, Editors: O. Brand, I. Dufour, S. Heinrich, F. Josse, J.G. Korvnik and O. Tabata (2015) 427–446

Journal Publications

First author (given in the Appendix)

[MHj1] [2] M. Heinisch, T. Voglhuber-Brunnmaier, E. Reichel, I. Dufour, B. Jakoby, Electromagnetically driven torsional resonators for viscosity and mass density sensing applications, Sensors and Actuators A: Physical

[MHj2] [3] M. Heinisch, T. Voglhuber-Brunnmaier, E. Reichel, I. Dufour, B. Jakoby, Application of resonant steel tuning forks with circular and rectangular cross sections for precise mass density and viscosity measurements, Sensors and Actuators A: Physical 226 (2015) 163–174

[MHj3] [4] M. Heinisch, T. Voglhuber-Brunnmaier, E. K. Reichel, I. Dufour, B. Jakoby, Reduced order models for resonant viscosity and mass density sensors, Sens. Actuators A: Physical 220 (2014) 76–84

[MHj4] [5] M. Heinisch, E. K. Reichel, I. Dufour, B. Jakoby, A u-shaped wire for viscosity and mass density sensing, Sens. Actuators A: Phys. 214 (2014) 245–251

[MHj5] [6] M. Heinisch, E. K. Reichel, I. Dufour, B. Jakoby, Tunable resonators in the low khz range for viscosity sensing, Sensors and Actuators A: Physical 186 (2012) 111–117. doi:http://dx.doi.org/10.1016/j.sna.2012.03.009

[MHj6] [7] M. Heinisch, E. K. Reichel, I. Dufour, B. Jakoby, A resonating rheometer using two polymer membranes for measuring liquid viscosity and mass density, Sensors and Actuators A: Physical 172 (1) (2011) 82–87. doi:10.1016/j.sna.2011.02.031

Co-authored Journal Publications

[MHjc1] [8] A. Abdallah, E. K. Reichel, T. Voglhuber-Brunmaier, M. Heinisch, S. Clara, B. Jakoby, Symmetric mechanical plate resonators for fluid sensing, Sensors and Actuators A: Physical

[MHjc2] [9] A. Abdallah, M. Heinisch, B. Jakoby, Measurement error estimation and quality factor improvement of an electrodynamic-acoustic resonator sensor for viscosity measurement, Sensors and Actuators A: Physical 199 (2013) 318–324

[MHjc3] [10] E. Lemaire, M. Heinisch, B. Caillard, B. Jakoby, I. Dufour, Comparison and experimental validation of two potential resonant viscosity sensors in the kilohertz range, Measurement Science and Technology 24 (8) (2013) 084005

[MHjc4] [11] T. Voglhuber-Brunnmaier, M. Heinisch, E. K. Reichel, B. Weiss, B. Jakoby, Derivation of reduced order models from complex flow fields determined by semi-numeric spectral domain models, Sensors and Actuators A: Physical 202 (2013) 44–51

[MHjc5] [12] B. Weiss, M. Heinisch, E. Reichel, B. Jakoby, Driving modes and material stability of a double membrane rheometer and density sensor, J. Sens. Sens. Syst. 2 (2013) 19–26

[MHjc6] [13] T. Lederer, Thomas, M. Heinisch, W. Hilber, B. Jakoby, Electromagnetically actuated membrane-based micropumps with integrated magnetic yoke, Journal of microelectronics and electronic packaging 6 (4) (2009) 205–210

Papers in Conference Proceedings

First author

[MHc1] [14] M. Heinisch, T. Voglhuber-Brunnmaier, E. K. Reichel, I. Dufour, B. Jakoby, Separate experimental investigation of the influence of liquids' mass densities and viscosities on the frequency response of resonant sensors using designated liquid series, Proc. IEEE Sensors 2015, Accepted Manuscript

[MHc2] [15] M. Heinisch, T. Voglhuber-Brunnmaier, E. K. Reichel, A. Abdallah, S. Clara, I. Dufour, B. Jakoby, U-shaped wire based resonators for mass density and viscosity sensing, Proc. IEEE Sensors 2015, Accepted Manuscript

[MHc3] [16] M. Heinisch, T. Voglhuber-Brunnmaier, E. Reichel, I. Dufour, B. Jakoby, Introduction of a general model for the resonance parameters of fluid sensors and validation with recent sensor setups, in: IEEE Sensors 2014, 2014, pp. 4–pages

[MHc4] [17] M. Heinisch, E. Reichel, T. Voglhuber-Brunnmaier, I. Dufour, B. Jakoby, Investigation of higher mode excitation of resonant mass density and viscosity sensors, in: IEEE Sensors 2014, 2014, pp. 4–pages

[MHc5] [18] M. Heinisch, A. O. Niedermayer, I. Dufour, B. Jakoby, Concept studies of torsional resonators for viscosity and mass density sensing applications, Procedia Engineering 87 (2014) 1198–1201

[MHc6] [19] M. Heinisch, A. Abdallah, I. Dufour, B. Jakoby, Resonant steel tuning forks for precise inline viscosity and mass density measurements in harsh environments, Procedia Engineering 87 (2014) 1139–1142

[MHc7] [20] M. Heinisch, S. Clara, I. Dufour, B. Jakoby, A spiral spring resonator for mass density and viscosity measurements, Procedia Engineering 87 (2014) 1143–1146

[MHc8] [21] M. Heinisch, E. K. Reichel, I. Dufour, B. Jakoby, Modeling and experimental investigation of resonant viscosity and mass density sensors considering their cross-sensitivity to temperature, Procedia Engineering 87 (2014) 472–475

[MHc9] [22] M. Heinisch, T. Voglhuber-Brunnmaier, I. Dufour, B. Jakoby, Validity of describing resonant viscosity and mass density sensors by linear 2nd order resonators, Proc. Eurosensors XXVIII (2014)

[MHc10] [23] M. Heinisch, T. Voglhuber-Brunnmaier, E. K. Reichel, S. Clara, A. Abdallah, B. Jakoby, Concept study on an electrodynamically driven and read-out torsional oscillator, Proceedings Microelectronic Systems Symposium (2014)

[MHc11] [24] M. Heinisch, T. Voglhuber-Brunnmaier, E. K. Reichel, B. Jakoby, Modeling approaches for electrodynamically driven viscosity and mass density sensors operated in the khz range and experimental verifications, in: SENSORS, 2013 IEEE, IEEE, 2013, pp. 1–4

[MHc12] [25] M. Heinisch, T. Voglhuber-Brunnmaier, E. K. Reichel, B. Jakoby, Experimental and theoretical evaluation of the achievable accuracies of resonating viscosity and mass density sensors, in: SENSORS, 2013 IEEE, IEEE, 2013, pp. 1–4

[MHc13] [26] M. Heinisch, E. K. Reichel, T. Voglhuber-Brunnmaier, B. Jakoby, Characterization and calibration of u-shaped mass density and viscosity sensors by an analytical modeling approach, The 17th International Conference on Solid-State Sensors, Actuators and Microsystems (2013) 1448 –1 1451

[MHc14] [27] M. Heinisch, E. K. Reichel, T. Voglhuber-Brunnmaier, B. Jakoby, U-shaped, wire-based oscillators for rheological applications bridging the gap between 100 hz and 100 khz, The 17th International Conference on Solid-State Sensors, Actuators and Microsystems

[MHc15] [28] M. Heinisch, E. Reichel, T. Voglhuber-Brunnmaier, W. Hortschitz, M. Stifter, J. Schalko, E. Lemaire, I. Dufour, B. Jakoby, Wire based and micromachined u-shaped cantilever devices for viscosity and mass density sensing for measurements in a frequency range of 100 hz to 100 khz, in: 10th International Workshop on Nanomechanical Cantilever Sensors, 2013, pp. 2–pages

[MHc16] [29] M. Heinisch, E. K. Reichel, B. Jakoby, U-shaped wire based resonators for viscosity and mass density sensing, Proc. of. SENSOR 2013 OPTO 2013 IRS2 2013

[MHc17] [30] M. Heinisch, E. Lemaire, B. Caillard, I. Dufour, B. Jakoby, A study of wire-based resonators for viscosity sensing, Proceedings Microfluidics 2012

[MHc18] [31] M. Heinisch, E. K. Reichel, T. Voglhuber-Brunnmaier, B. Jakoby, Miniaturized viscosity and mass density sensors combined in a measuring cell for handheld applications, in: Proceedings of the IEEE Sensors conference 2012, 2012

[MHc19] [32] M. Heinisch, A. Abdallah, B. Jakoby, The effect of temperature on resonant viscosity sensors, Procedia Engineering 47 (2012) 786–790

[MHc20] [33] M. Heinisch, A. Abdallah, E. K. Reichel, B. Weiss, B. Jakoby, Concepts for lorentz force driven resonators for inline and handheld viscosimetry, Proceedings of the 13th Mechatronics Forum International Conference (2012) 632 – 638

[MHc21] [34] M. Heinisch, T. Voglhuber-Brunnmaier, A. Abdallah, B. Jakoby, Application of resonant sensors for magnetic flux density measurements, Proceedings I2MTC conference

[MHc22] [35] M. Heinisch, E. K. Reichel, I. Dufour, B. Jakoby, Tunable miniaturized viscosity sensors operating in the khz-range, in: Proceedings of the IEEE Sensors conference 2011, 2011

[MHc23] [36] M. Heinisch, E. K. Reichel, I. Dufour, B. Jakoby, Miniaturized resonating viscometers facilitating measurements at tunable frequencies in the low khz-range, in: Proc. Eurosensors, 2011

[MHc24] [37] M. Heinisch, E. K. Reichel, B. Jakoby, A suspended plate in-plane resonator for rheological measurements at tunable frequencies, in: Proc. Sensor + Test, 2011, pp. 61– 66

[MHc25] [38] M. Heinisch, E. K. Reichel, B. Jakoby, A study on tunable resonators for rheological measurements, in: Proc. SPIE, Vol. 8066, 2011. doi:10.1117/12.887103

[MHc26] [39] M. Heinisch, E. K. Reichel, B. Jakoby, A feasibility study on tunable resonators for rheological measurements, in: Proceedings GMe Forum, 2011, pp. 85–89

[MHc27] [40] M. Heinisch, E. K. Reichel, B. Jakoby, On the modelling of resonant fluid sensors, Springer LNCS (2011) 25–32

[MHc28] [41] M. Heinisch, E. K. Reichel, B. Jakoby, A comprehensive study and optimization of nozzle-diffuser valves for reciprocating micropumps, Proceedings of the 2nd European Conference on Microfluidics

[MHc29] [42] M. Heinisch, T. Voglhuber-Brunnmaier, A. Niedermayer, B. Jakoby, E. K. Reichel, Double membrane sensors for liquid viscosity and mass density facilitating measurements in a large frequency range, in: Sensors, 2010 IEEE, IEEE, 2010, pp. 1750–1753

[MHc30] [43] M. Heinisch, E. Reichel, T. Voglhuber-Brunnmaier, B. Jakoby, A double membrane sensor for liquid viscosity facilitating measurements in a large frequency range, Procedia Engineering 5 (2010) 1458–1461

[MHc31] [44] M. Heinisch, E. K. Reichel, B. Jakoby, Electromagnetically actuated valveless micropump in polymer-technology, The 12th Mechatronics Forum Biennial International Conference Proceedings Book 2/2 (2010) 360 – 367

Co-authored Conference Proceedings

[MHcc1] [45] A. Abdallah, E. Reichel, S. Clara, M. Heinisch, B. Jakoby, Tuning fork based electrodynamically actuated resonating-plate viscosity sensor, in: Proceedings Microelectronics System Symposium, Vienna, 2014

[MHcc2] [46] A. Abdallah, E. Reichel, M. Heinisch, S. Clara, B. Jakoby, Symmetric plate resonators for viscosity and density measurement, Procedia Engineering 87 (2014) 36–39

[MHcc3] [47] A. Abdallah, E. K. Reichel, M. Heinisch, B. Jakoby, T. Voglhuber-Brunnmaier, Parallel plates shear-wave transducers for the characterization of viscous and viscoelastic fluids, SENSORS, 2014 IEEE (2014) 245–248

[MHcc4] [48] E. Reichel, A. Abdallah, T. Voglhuber-Brunnmaier, M. Heinisch, B. Jakoby, Parallel plate resonators for shear-wave rheometry of viscoelastic fluids, German Rheological Society (Eds.): AERC

[MHcc5] [49] E. K. Reichel, M. Heinisch, B. Jakoby, T. Voglhuber-Brunnmaier, Efficient numerical modeling of oscillatory fluid-structure interaction, sensors 9 10

[MHcc6] [50] T. Voglhuber-Brunnmaier, M. Heinisch, A. O. Niedermayer, A. Abdallah, R. Beigelbeck, B. Jakoby, Optimal parameter estimation method for different types of resonant liquid sensors, Procedia Engineering 87 (2014) 1581–1584

[MHcc7] [51] E. K. Reichel, M. Heinisch, B. Jakoby, Droplet mixing and liquid property tracking using an electrodynamic plate resonator, in: SENSORS, 2013 IEEE, IEEE, 2013, pp. 1–4

[MHcc8] [52] E. K. Reichel, M. Heinisch, B. Jakoby, Resonator sensors for rheological properties-theory and devices

[MHcc9] [53] E. K. Reichel, M. Heinisch, A. Vananroye, J. Vermant, B. Jakoby, Rheometry using shear-wave resonators, Belgian Group of Rheology (Eds.): AERC 2013, Series Annual European Rheology Conference (2013) 73

[MHcc10] [54] E. K. Reichel, M. Heinisch, J. Vermant, C. E. A. Kirschhock, B. Jakoby, Acoustic streaming in sessile droplets driven by in-plane actuation, Proc. of the Nanomechanical Sensing Workshop (2013) 2

[MHcc11] [55] A. Abdallah, M. Heinisch, B. Jakoby, Viscosity measurement cell utilizing electrodynamic-acoustic resonator sensors: Design considerations and issues, Procedia Engineering 47 (2012) 160–164

[MHcc12] [56] A. Abdallah, M. Heinisch, F. Lucklum, A. O. Niedermayer, B. Jakoby, A viscosity sensor utilizing electrodynamic-acoustic resonators, Informationstagung Mikroelektronik12 OVE (64) (2012) 103

[MHcc13] [57] A. Abdallah, M. Heinisch, F. Lucklum, A. O. Niedermayer, B. Jakoby, A viscosity measurement unit utilizing an electrodynamic-acoustic resonator, The 13th Mechatronics Forum International Conference Proceedings 2 (2012) 621

[MHcc14] [58] A. Abdallah, F. Lucklum, M. Heinisch, A. Niedermayer, B. Jakoby, Viscosity measurement cell utilizing electrodynamic-acoustic resonator sensors: Issues and improvements, Proceedings I2MTC conference 2012

[MHcc15] [59] E. Lemaire, M. Heinisch, B. Caillard, B. Jakoby, I. Dufour, Fluid characterization using a vibrating microstructure - the future (micro)rheology?, The 13th Mechatronics Forum International Conference Proceedings

[MHcc16] [60] E. K. Reichel, M. Heinisch, B. Jakoby, J. Vermant, C. Kirschhock, Modeling and data analysis of a multimode resonator sensor loaded with viscous and viscoelastic fluids, in: Sensors, 2012 IEEE, IEEE, 2012, pp. 1–4

[MHcc17] [61] T. Voglhuber-Brunnmaier, M. Heinisch, E. Reichel, B. Weiss, B. Jakoby, Complete semi-numeric model of a double membrane liquid sensor for density and viscosity measurements, Procedia Engineering 47 (2012) 598–602

[MHcc18] [62] E. K. Reichel, M. Heinisch, B. Jakoby, J. Vermant, C. E. Kirschhock, Viscoelasticity sensor with resonance tuning and low-cost interface, Procedia Engineering 25 (2011) 623–626

[MHcc19] [63] B. Weiss, M. Heinisch, B. Jakoby, E. K. Reichel, Density sensitive driving mode of a double membrane viscometer, in: Sensors, 2011 IEEE, IEEE, 2011, pp. 1538–1541

[MHcc20] [64] B. Weiss, M. Heinisch, E. Reichel, B. Jakoby, Driving modes and material stability of a vibrating polyethylene membrane viscosity sensor, Procedia Engineering 25 (2011) 176–179

[MHcc21] [65] T. Lederer, M. Heinisch, W. Hilber, B. Jakoby, Electromagnetic membrane-pump with an integrated magnetic yoke, in: Sensors, 2009 IEEE, IEEE, 2009, pp. 532–537

[MHcc22] [66] L. Lederer, M. Heinisch, W. Hilber, B. Jakoby, Electromagnetic membrane-pumps with integrated mangetic yoke, Proc. Internationales Forum für Mechatronik

Work in progress

[MHwp1] [67] M. Heinisch, Lorentz force driven and read out glass tubes for mass density measurements, Work in Progress

[MHwp2] [68] M. Heinisch, Experimental investigation of the validity of existing models for viscously damped mechanical resonators with rectangular cross-sections, Work in Progress

[MHwp3] [69] M. Heinisch, Optimal aspect ratios of mechanical resonators with rectangular cross-sections for precise viscosity and mass density measurements, Work in Progress

[MHwp4] [70] M. Heinisch, Scaling of resonant viscosity and mass density sensors using resonant tuning forks as example, Work in Progress

[MHwp5] [71] M. Heinisch, Higher mode excitation of resonant viscosity and mass density sensors, Work in Progress

[MHwp6] [72] M. Heinisch, Cross-sensitivity of resonant viscosity and mass density sensors to temperature, Work in Progress

[MHwp7] [73] M. Heinisch, Theoretical and experimental investigation of u-shaped wire based resonators for mass density and viscosity sensing, Work in Progress

[MHwp8] [74] M. Heinisch, A falling ball viscosimeter using differential transformers for precise position measurements, Work in progress

[MHwp9] [75] M. Heinisch, A handheld capillary viscosimeter using pressure – velocity measurements in a convential syringe, Work in progress

[MHwp10] [76] M. Heinisch, Investigation of temperature models for the viscosity and mass densitity of liquids, Work in Progress

[MHwp11] [77] M. Heinisch, Modeling of the viscosity and mass densitity of binary liquid mixtures, considering their temperature dependence, Work in Progress

[MHwp12] [78] M. Heinisch, Modeling of the viscosity and mass densitity of ternary liquid mixtures, considering their temperature dependence, Work in Progress

[MHwp13] [79] M. Heinisch, Viscosity and mass densitity of the ternary liquid mixture acetone – ethanol – isopropanol in a temperature range from 5°C to 45°C, Work in Progress

[MHwp14] [80] M. Heinisch, Viscosity and mass densitity of the ternary liquid mixture ethanol – glycerol – water in a temperature range from 5°C to 45°C, Work in Progress

Chapter 1

Introduction

1.1 Viscosimetry and rheometry

The dynamic viscosity η describes the proportionality between shear stress τ and shear rate $\partial\gamma/\partial t$ in a fluid where γ is the shear angle and t is the time variable. For so-called Newtonian liquids this proportionality factor remains constant independently of shear-rate or stress. In general (amongst others), however, it is temperature (T) and pressure (p) dependent i.e. [81],

$$\tau = \eta(T, p, \ldots)\frac{\partial\gamma}{\partial t}. \tag{1.1}$$

The dots indicate, that the viscosity might also depend on other quantities such as, e.g., time which considers aging or evaporation of solvents in a liquid mixture. In this thesis, the temperature dependence of viscosity and associated models describing the latter is discussed in Sec. 1.5.2 and the intrinsic temperature dependence of mechanical resonators used for viscosity and mass density measurements is described in Sec. 2.10. The pressure dependence however, of both, the liquid and the mechanical resonator is not considered in this thesis but have to be investigated in future research.

Generally expressed, the mass density is the quotient of an infinitesimal mass dm contained in an infinitesimal volume dV i.e.,

$$\rho(T, p, \ldots) = \frac{\mathrm{d}m}{\mathrm{d}V} \tag{1.2}$$

and is also temperature and pressure dependent. The temperature dependence of the mass density is described in Sec. 1.5.3 and as most liquids might be considered incompressible, the pressure dependence is neglected.

In this thesis mechanical resonators are used for viscosity and mass density measurements. It will be shown in Sec. 2.8.1, that these devices are sensitive to both, viscosity and mass density. Thus, in any case, both quantities, viscosity and mass density have always to be taken into account and determined, even if only for one of both quantities a measurement result has to be given.

The variety of viscosity measurement principles is relatively large. Extensive overviews are given in [82–84] and are not discussed in detail here. An overview of sensor principles published in the literature and principles which were elaborated in the course of this thesis will be given Sec. 4. In general, the means of measuring a liquid's viscosity can be divided in four basic categories of viscometers:

1. Falling or rolling objects viscosimeters
2. Capillary viscometers
3. Rotational viscometers
4. Oscillatory viscometers

In the course of this thesis, a feasibility study of a falling ball viscosimeter was performed, where the position (over time) of a falling steel ball can be precisely measured over the whole falling length using differential transformers [MHwp8]. Furthermore, a conceptual study for a handheld capillary viscosimeter has been conducted using a conventional syringe with which pressure – velocity measurements are performed [MHwp9]. These studies will be discussed and published elsewhere.

The category of viscosity and mass density measurement principles investigated in this thesis, are mechanical resonators which are fully immersed into the sample liquid. This complete immersion of the measurement device allows in-line viscosity and mass density measurements. Furthermore, due to their capability of miniaturized devices designs, such mechanical resonators are applicable for handheld applications.

1.2 Motivation for using mechanical resonators

Viscosity and mass density are important quantities describing the physical behavior of a liquid. Once determined, these quantities can be used to draw conclusions about the condition and the quality of the examined liquid. Examples for the latter are the monitoring of the lubricating capacity of oils and their aging [85] or the condition of printing inks [86] or the characterization of DNA solutions [87], just to name a few examples. The need for using viscosity and mass density sensors instead of conventional laboratory instruments may have many reasons but generally – without claiming completeness – can be split up in three categories:

1. **Low sample quantities:** In biological or medical applications the amount of available sample liquid can be very low. For conventional viscosimeters and rheometers usually, some milliliters of the sample liquids are required. In [88] the amount necessary for a resonant Atomic Force Microscope (AFM) cantilever used for viscosity measurement is specified with 1 nL and lower.

2. **In-line or handheld devices:** In many industrial liquid production processes, regardless of the field, be beverage, medical, oil, painting, chemical or environmental industry et cetera, the liquids usually have to be analyzed in a particular laboratory. This is often a necessary process which manifests not only in production costs but can become rather time consuming. To overcome this cost and especially time related drawbacks, in-line or handheld devices become beneficial and become even indispensable if a process e.g. in a reaction chamber has to be monitored. When aiming at handheld devices, the capability for miniaturized devices becomes especially advantageous.

3. **Extension of investigated frequency range**: From a rheological point of view, these resonating devices are beneficial to allow measurements for frequencies higher than 100 Hz, which is usually the limit for conventional rheometers.

During the last two decades, a large amount of different principles was reported [89, 90]. The variety of different approaches can, for example, be distinguished by their fundamental mechanical structure, the manufacturing technology, the used materials as well as actuation and read-out principles. The mechanical structures comprise amongst others, singly clamped beams [91], doubly clamped beams [92], tuning forks [93], vibrating membranes [94, 95], and oscillating platelets [96], [MHjc2]. Concerning technology and materials, silicon and quartz crystal [97,98] based devices but also concepts using copper coated polymer sheets [99], [MHj6], screen printed PZT cantilevers [100] or tungsten wires [101–105] [MHj5] were also reported, just to name some examples. As for comparison of different sensor concepts working principle and theory has to be thoroughly explained first, a comprehensive overview of resonant viscosity and mass density sensors is not performed at this place but will be given in Sec. 4.10.

In comparison with well established shear oscillating quartz crystals which are usually operated in the Megahertz range, lower operational frequencies might become important when investigating complex liquids such as emulsions, see [106]. That is, between the frequency range of conventional rheometers and the mentioned quartz crystal devices is a gap of 100 Hz to 100 kHz, approximately. Thus, this frequency is the aimed range for this thesis and implies device dimensions in the millimeter to the centimeter range.

calibration effort, such closed form models which were derived for a particular resonator design, hardly allow comparison with other mechanical resonator designs.

Besides the simplicity of the generalized model given in Fig. 1.1 and its general applicability, a further big advantage is that measurements in three calibration liquids only are necessary to identify the model's coefficients and thus, the sensor's characteristics at a fixed temperature. This simple procedure can be done as follows: From the measurements in the (at least) three liquids, f_r and Q are evaluated which then allows evaluating the six coefficients in the equations of the generalized model. For resonant sensors whose identified model slightly deviates from the measurements, the model still can be used to approximately describe the sensor's characteristics and allows comparison with other principles which were identified with this generalized, reduced order model. For this calibration the liquids can be randomly chosen and do not have to suit viscosity or mass density series respectively, as it is depicted in Fig. 1.1. However, if the response to viscosity or to mass density has to be investigated experimentally, it is a big advantage to have a series of test liquids, where only either η or ρ changes.

1.3.2 Liquid series for experimental characterization of the resonator

In this thesis, liquid series with constant mass densities but varying viscosities are called 'viscosity series', whereas the term 'mass density series' is used for liquid series with constant viscosities but varying mass densities. For the viscosity series, used to get the measurement data depicted in Fig. 1.1, solutions of acetone and isopropanol have been mixed. The values for η and ρ for the associated solutions, characterized with an Anton Paar SVM 3000 at 25 °C are depicted and listed in Fig. 1.2. There, it is shown that the obtained soultions yield viscosities from approximately 0.2 mPa·s to 2 mPa·s for mass densities of roughly 0.78 g/cm^3. However a clear trend in the mass densities can be observed. An interesting result is the fact that the mass densities of the mixed solutions can get lower than both unmixed mass densities. As these relatively small deviations in mass density can be observed in the f_r and Q measurements, see Sec. 4.9 and [MHj2], more precise viscosity and mass density series might become necessary to presume constant viscosities or mass densities, respectivley. This task might be difficult to solve using binary mixtures only as it is even not sufficient that both liquids do have the same mass density or viscosity, respectively. Ternary liquid mixtures might help to overcome this imperfection of liquid series. With an appropriate model for ternary liquid mixtures, the mixing ratio necessary to obtain viscosity and mass density series can be calculated. Such models, also considering the influence of the temperature dependence of η and ρ, can hardly be found in literature. For this reason a comparison of existing temperature models [MHwp10], binary mixture models [MHwp11] as well as ternary mixture models [MHwp12] have been performed and based on the insights obtained

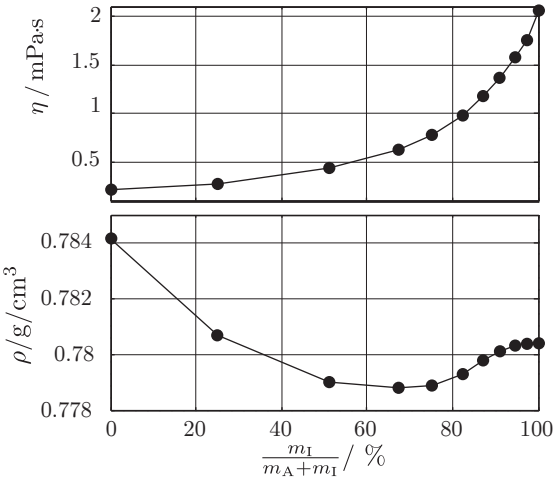

$\frac{m_\mathrm{I}}{m_\mathrm{A}+m_\mathrm{I}}$ / %	η/mPa · s	ρ/(g/cm^3)
0	0.2069	0.7841
25	0.2743	0.7807
51	0.4334	0.7790
67	0.6271	0.7788
75	0.7755	0.7789
83	0.9803	0.7793
87	1.1727	0.7798
91	1.3673	0.7801
95	1.5764	0.7803
97	1.7516	0.7804
100	2.0543	0.7804

Figure 1.2: Acetone-isopropanol solution at 25 °C. m_A: mass acetone, m_I: mass isopropanol. Note the scale of the density axis: the variation of density is small ($\approx 7 \cdot 10^{-3}$), however, a clear trend can be observed.

by this survey new improved models have been elaborated and are briefly discussed in the following sections.

As not only the modeling of ternary liquid mixtures considering the temperature dependence of η and ρ but as also experimental results are still not sufficiently reported, two ternary liquid mixtures, acetone – ethanol – isopropanol [MHwp13] and ethanol – glycerol – water [MHwp14], consisting of 96 liquid mixtures each, were measured at 14 temperatures ranging from 5 °C to 45 °C in 2.5 °C steps, using an Anton Paar SVM 3000 together with an XSample 361. To provide an easy access for the temperature dependence of viscosity and mass density of liquids, as well as the viscosities and mass densities of binary and ternary liquid mixtures in dependence of their mixing ratio and temperature, a website has been set up where these quantities can be looked up online. This website can be accessed via `www.rheo-logic.info`.

1.4 Notation of absolute and relative deviations

In this thesis absolute and relative deviations or changes of a quantity x in respect to the quantity x_0 are noted using

$$\Delta x = x - x_0 \qquad \text{and} \qquad \Delta^{\mathrm{r}} x = \frac{x - x_0}{x_0}. \tag{1.3}$$

In the following sections models for the temperature dependence of η and ρ as well as for binary and ternary liquid mixtures will be discussed. For evaluating and comparing these models among each other, two quantities are defined serving as figures of merit. These quantities are noted using the symbols $\overline{\Delta}_x$ and $\widehat{\Delta}_x$ and are explained in the following giving the according formulae. In prose, $\overline{\Delta}_x$ is the 'mean value of mean absolute values of the relative error' of a quantity x and $\widehat{\Delta}_x$ is the 'mean value of maximum absolute value of relative error' of a quantity x.

The quantities $\overline{\Delta}_x$ and $\widehat{\Delta}_x$ are explained for the example, of evaluating the accuracy of a temperature model for viscsosity: It is assumed that the viscosity of N liquids denoted by $j \in [1, \ldots, N]$ was experimentally determined at M temperatures which are denoted by $i \in [1, \ldots, M]$. The latter may vary from liquid to liquid. In a first step, the absolute values of the relative deviations of modeled values $\eta_{\mathrm{mod},j}(T_i)$ from measured values $\eta_j(T_i)$ at temperatures T_i

$$|\Delta^{\mathrm{r}} \eta_j(T_i)| = \left| \frac{\eta_{\mathrm{mod},j}(T_i) - \eta_j(T_i)}{\eta_j(T_i)} \right| \tag{1.4}$$

are evaluated. In a second step the mean and the maximum value of the latter, i.e.

$$\overline{\Delta^{\mathrm{r}}} \eta_{j,\mathrm{T}} = \frac{1}{M} \sum_{i=1}^{M} |\Delta^{\mathrm{r}} \eta_j(T_i)| \qquad \text{and} \qquad \widehat{\Delta^{\mathrm{r}}} \eta_{j,\mathrm{T}} = \max(|\Delta^{\mathrm{r}} \eta_j(T_i)|) \tag{1.5}$$

are calculated. Finally, for giving two quantities describing the accuracy of the temperature model for viscosity, the mean values of the latter are calculated using

$$\overline{\Delta} \eta_{\mathrm{T}} = \frac{1}{N} \sum_{j=1}^{N} \overline{\Delta^{\mathrm{r}}} \eta_{j,\mathrm{T}} \qquad \text{and} \qquad \widehat{\Delta} \eta_{\mathrm{T}} = \frac{1}{N} \sum_{j=1}^{N} \widehat{\Delta^{\mathrm{r}}} \eta_{j,\mathrm{T}}. \tag{1.6}$$

1.5 Temperature dependence of viscosity and mass density

1.5.1 Normalized illustration

Using data for viscosity and mass density at different temperatures for liquids, collected from [107–139] the change of viscosity and mass density is illustrated by normalizing η, ρ and T in respect to their highest values, i.e.,

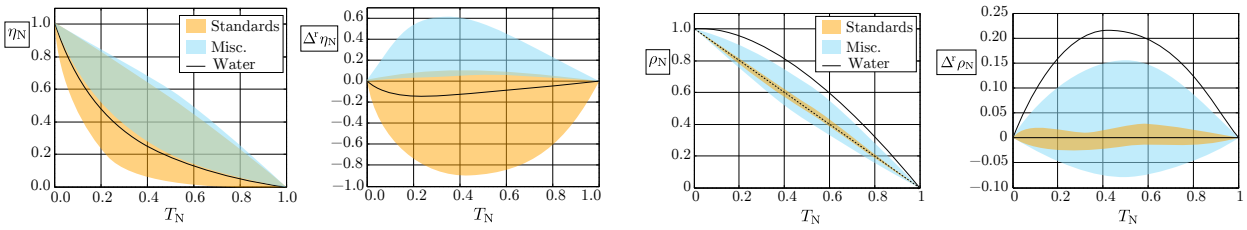

(a) Temperature dependence of viscosity

(b) Temperature dependence of mass density

Figure 1.3: Illustration of possible temperature dependencies for viscosity and mass density. For both quantities negative as well as positive deviations from a linear relation are obtained. The three categories plotted there, include viscosity and mass density standards from Cannon Instruments company consisting of silicone oils, miscellaneous liquids and water.

$$\eta_N(T) = \frac{\eta(T_{max}) - \eta(T)}{\eta(T_{max}) - \eta(T_{min})}, \quad \rho_N(T) = \frac{\rho(T_{max}) - \rho(T)}{\rho(T_{max}) - \rho(T_{min})} \quad \text{and} \quad T_N(T) = \frac{T_{max} - T}{T_{max} - T_{min}}. \tag{1.7}$$

In general, $\eta(T_{max}) < \eta(T_{min})$ and $\rho(T_{max}) < \rho(T_{min})$. The collected data comprises 130 independent measurement series for viscosity and mass density in a certain temperature range for 35 different liquids in total. The normalized values for these liquids as well as the relative deviations from a linear, normalized relation

$$\Delta^r\eta_N = \frac{\eta_N - x_{lin}}{x_{lin}}, \quad \text{and} \quad \Delta^r\rho_N = \frac{\rho_N - x_{lin}}{x_{lin}} \quad \text{where} \quad x_{lin} = 1 - T_N \tag{1.8}$$

are shown in Fig. 1.3. There, the shaded areas show the range and shape of possible temperature dependencies for the investigated liquids which are distinguished in three categories: Viscosity and mass density standards from Cannon Instruments company consisting of silicone oils, miscellaneous liquids and water. This evaluation for both quantities, clearly shows the non-linear dependence of η and ρ on T. This nonlinearity becomes more distinctive, the higher the difference $T_{max} - T_{min}$. Usually, the temperature dependency of η is considered using exponential functions whereas for ρ polynomial functions are used.

1.5.2 Temperature dependence of viscosity

Two constants equations from literature

Most models for the temperature dependence of viscosity are based on Arrhenius' equation [140]

$$k = A\,e^{\frac{-E}{RT}} \tag{1.9}$$

which expresses the temperature dependence of a chemical reaction relating the dependence of the rate constant k to absolute temperature T, where R is the universal gas constant, E is the activation energy and A is a factor depending on the order of the reaction. In relation to Arrhenius' equation, the according models for the temperature dependence of viscosity found in literature read in the order of the following references [141], [83, 142] and [143]

$$\eta = Ae^{\frac{E_V}{RT}}, \qquad \eta = Ae^{\frac{B}{T}}, \qquad \text{and} \qquad \ln\eta = A + \frac{B}{T}. \tag{1.10}$$

The second equation is also known as the Andrade equation which is expressed logarithmically in the third equation. Note that for simplicity and keeping the number of used coefficients short, two equal letters might not express the same physical quantity and thus, might also have different units.
Further empirical two constant equations in the order of citation [81] (Macosko), [83, 144] (Viswanath) and [141] (Brancker) are

$$\eta = A\mathrm{e}^{B\,T}, \qquad \eta = A\,T^{B}, \qquad \text{and} \qquad \eta = \frac{A}{1-\frac{B}{T}} \tag{1.11}$$

where the last equation is also discussed in [145]. A comparison of these two constants temperature models for viscosity is given in Fig. 1.4(a), which clearly shows, that models deduced from the Arrhenius equation yield the best results for the liquids investigated here.

Three constants equations from literature

Introducing a third factor for modeling the viscosity's temperature dependence, significantly improves the modeling accuracy. Frequently used models are physically or empirically motivated models from Vogel et al. where

$$\eta = A\,\mathrm{e}^{\frac{B}{T-C}} \tag{1.12}$$

is known as the Vogel–Tammann–Fulcher (VTF) equation [146] whereas the Vogel–Fulcher–Tammann (VFT) equation [147] reads:

$$\eta = A\,T^{0.5}\,\mathrm{e}^{\frac{B}{T-C}}. \tag{1.13}$$

In [83, 144] Viswanath uses a similar equation using 10 as the basis instead of Euler's number for the exponential function. The given equation is

$$\log_{10}\eta = A + \frac{B}{C-T}. \tag{1.14}$$

A further three constants equation but with and additional quadratic term in the denominator of the exponential function's argument is given in [83, 148] (Girifalco) and reads:

$$\ln\eta = A + \frac{B}{T} + \frac{C}{T^2}. \tag{1.15}$$

A rational function for the viscosity's temperature dependence using three coefficients [83,149] (Thorpe) is:

$$\eta = \frac{A}{1 + B\,\vartheta + C\,\vartheta^2} \tag{1.16}$$

where in this case ϑ is the temperature in °C.

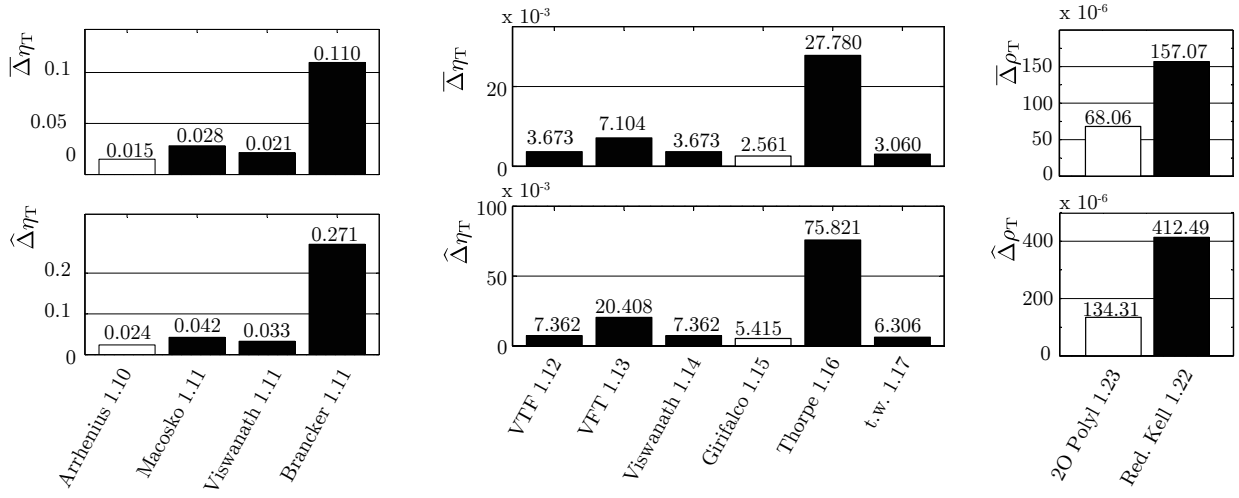

(a) 2 coeffs for $\eta(T)$ (b) 3 coeffs for $\eta(T)$ (c) 3 coeffs for $\rho(T)$

Figure 1.4: Comparison of two and tree constants mopdels for the temperature dependence of η and ρ. The best models are highlighted for the particular cases. The numbers indicate the according equations.

Further three constants equations

Except for the rational function, Eq. 1.16, the previously mentioned three constant equations yield all good modeling accuracies, see Fig. 1.4(b). However, considering the temperature dependence in the denominator of a rational expression, as it is the case in Eqs. 1.12 to 1.14, may yield singularities. Furthermore, knowing the coefficients from Eq. 1.15 does not allow an (intuitive) estimation of the liquid's viscosity. To overcome these drawbacks a further three constants model was elaborated in the course of this thesis, reading

$$\eta = \eta_0 \, \mathrm{e}^{b_1 \, (T - T_\mathrm{m}) + b_2 \, (T - T_\mathrm{m})^2} \tag{1.17}$$

where η_0, b_1 and b_2 are fitting parameters and T_m is a temperature in the range of investigated temperature range, e.g. the mean value of investigated temperatures. The knowledge of the parameter η_0 gives intuitive insights of the particular liquid's viscosity. For comparison reasons, and for examining if the usage of T_m changes the modeling accuracy,

$$\eta = A \, \mathrm{e}^{B\,T + C\,T^2} \tag{1.18}$$

was also investigated. This comparison showed that no higher modeling accuracy is achieved when using T_m, however comparing η_0 and A substantiated the intuitive character of η_0. The minimum value, median and maximum value for the viscosity of all 236 examined liquids at 25 °C were obtained for acetone [122], 1,4-Dioxane [124] and S30 000 from Cannon Instruments yiedling $[0.307 \cdot 10^{-3}, 1.069 \cdot 10^{-3}, 71 \cdot 10^{3}]$ Pa·s. The according values for η_0 are $[0.307 \cdot 10^{-3}, 1.17 \cdot 10^{-3}, 6\,272.13]$ Pa·s, whereas the corresponding values for A are $[8.08 \cdot 10^{8}, 287.2, 8.02 \cdot 10^{28}]$ Pa·s, respectively. This example substantiates, that compared with Eq. 1.18, Eq. 1.17 is advantageous, as η_0 gives the order of magnitude for viscosity which is not the case for the fitted values for A.

Multi constants equations

In the literature, models with more than three constants can be found and read in the order of citations [150–152]

$$\ln\eta = A + \frac{B}{T} + C\,T + D\,T^2, \quad \log_{10}\eta = A + \frac{B}{T} + C\,T + D\,T^2, \quad \text{and} \quad \eta = A + B\,\vartheta + C\,\vartheta^2 + D\,\vartheta^3 + E\,\vartheta^4 \tag{1.19}$$

but were not further investigated, as for many reported liquids, η is not given for a sufficient number of temperatures.

1.5.3 Temperature dependence of mass density

Common models

In [153] (Kell) the temperature dependence of the mass density of water is modeled using a seven coefficients rational function

$$\rho = \frac{a_0 + a_1\,\vartheta + a_2\,\vartheta^2 + a_3\,\vartheta^3 + a_4\,\vartheta^4 + a_5\,\vartheta^5}{1 + b\,\vartheta} \tag{1.20}$$

which can also be expressed as

$$\rho = \frac{\sum_{i=0}^{N} a_i\,\vartheta^i}{1 + b\,\vartheta} \qquad \text{or} \qquad \rho = \sum_{i=0}^{N_A} A_i\,\vartheta^i + \frac{B}{1 + C\,\vartheta}. \tag{1.21}$$

Limiting the amount of constants to three this equation reads

$$\rho = A + \frac{B}{1 + C\,\vartheta}. \tag{1.22}$$

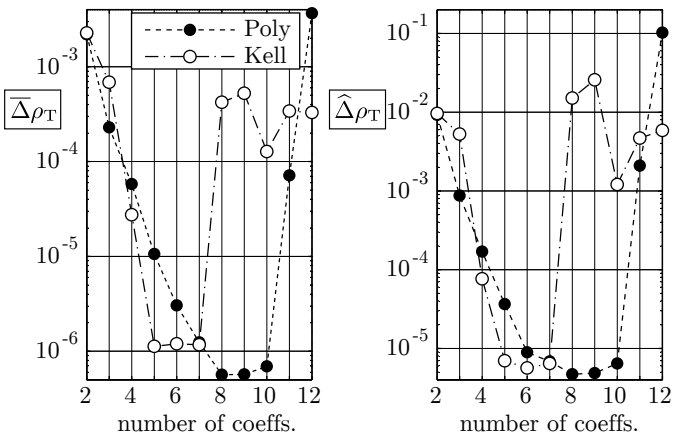

Figure 1.5: Comparison of modeling accuracy for Kell's model, Eq. 1.21 and a regular polynomial in dependence of the number of used coefficients. For three constants models, the polynomial function yields better results.

All variants of this model suffer from the same drawbacks of possible singularities and unintuitive model parameters, as already discussed for viscosity models Eqs. 1.12 to 1.14. Thus second order polynomials reading

$$\rho = \rho_0 + r_1\,(T - T_\mathrm{m}) + r_2\,(T - T_\mathrm{m})^2 \qquad \text{or} \qquad \rho = \rho_0 + \rho_1 \frac{T - T_\mathrm{m}}{T_\mathrm{m}} + \rho_2 \frac{(T - T_\mathrm{m})^2}{T_\mathrm{m}^2} \tag{1.23}$$

have been investigated, where $\rho_1 = r_1\,T_\mathrm{m}$ and $\rho_2 = r_2\,T_\mathrm{m}^2$. Both models yield the same modeling accuracy, however the second expression might be preferred as all coefficients have the same unit as ρ. The usage of second order polynomials is also quite common for modeling a liquid's mass density's temperature dependence, see e.g., in [146]. A comparison between the three constants model given in Eq. 1.22 and the second order polynomial is given in Fig. 1.4(c). For the investigated liquids, the second order polynomial model yielded more accurate results.

The temperature dependence of the mass density of water is extensively reported and thoroughly investigated, see e.g. [154, 155]. For the case of water it was possible to study the effect of the used numbers of model parameters on the modeling accuracy, see Fig. 1.5. There, the evaluation of obtained modeling accuracy versus used number of coefficients is shown for Kell's model, Eq. 1.21 and a polynomial function. Again, for three coefficients models, the second order polynomial also yields better results than Eq. 1.22.

1.6 Viscosity and mass density of binary mixtures

In 1887 Arrhenius proposed the following expression for the viscosity η of a binary mixture [156, 157]:

$$\ln \eta = x_1 \ln \eta_1 + x_2 \ln \eta_2 \tag{1.24}$$

where η_i is the viscositiy of the unmixed liquid i and x_i is the molar fraction in the mixture where $x_1 = 1 - x_2$.

Assuming no interaction between the mixed components, the ideal relation for the mass density ρ of a binary liquid mixture can be calculated considering the total mass of the mixture $m = m_1 + m_2$ and assuming that the volume of the mixture is the sum of the single components' volumes, i.e. $V = V_1 + V_2$. Thus, the ideal relation reads

$$\rho = \varphi_1\,\rho_1 + \varphi_2\,\rho_2 \tag{1.25}$$

where φ_i is the volume fraction of component i in the mixture.

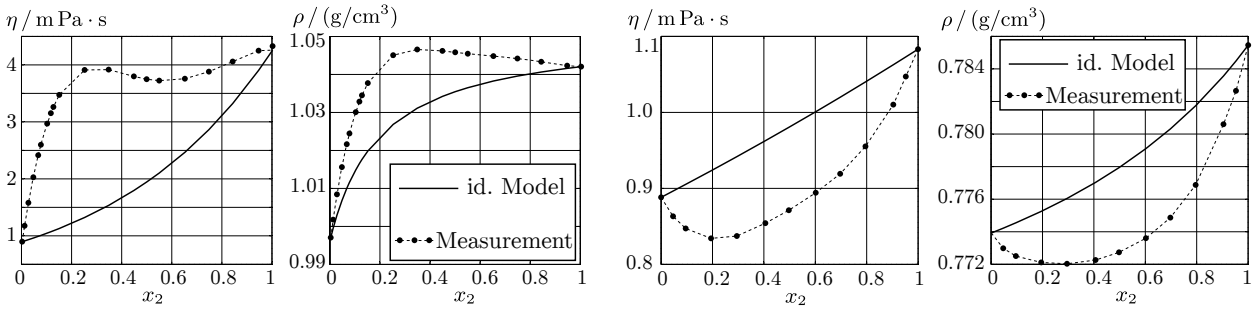

(a) Water (1) + 1-vinyl-2-pyrrolidinone (2), [112]

(b) Cyclohexane (1) + ethanol (2), [139]

Figure 1.6: Examples of liquid mixtures at 25 °C: The viscosity and mass density of the mixture can get higher or lower than the viscosities and mass densities of the unmixed liquids.

These ideal models for η and ρ were applied to 100 binary mixtures reported in [107–139] . For the associated liquid mixtures it was found that $\overline{\Delta}_\eta = 0.17$, $\widehat{\Delta}_\eta = 12.32$, $\overline{\Delta}_\rho = 0.0038$, and $\widehat{\Delta}_\rho = 0.0557$. The evaluation showed that the highest deviation for both ideal models were obtained for aqueous mixtures. These deviations can have many reasons. For some liquid mixtures the minimum or the maximum viscosity of the mixture can be lower or higher than both, η_1 and η_2. Such behavior can also be obtained for mixture's mass densities and can not be described by equations such as the ideal models for η and ρ, Eqs. 1.24 and 1.25. Examples for liquid mixtures which can not be described by these ideal equations are shown in Fig. 1.6. As furthermore the errors of the ideal equations can get relatively high, these equations have been tried to be improved in many publications. In the following, a short overview of such models is given and associated modeling accuracies are provided. This evaluation shows that these frequently used models are still incommensurate, especially when it comes to the influence of the temperature T on the liquid mixture's η and ρ. To overcome these drawbacks new models for binary and ternary liquid mixtures were elaborated based on the insights of the temperature models for η and ρ.

Fractions of mixtures

Liquid mixtures are mostly specified by their mole fractions x_i, volume fractions φ_i or mass fractions w_i. Their definitions are:

$$x_i = \frac{n_i}{\sum\limits_j n_j} \qquad \varphi_i = \frac{V_i}{\sum\limits_j V_j} \qquad \text{and} \qquad w_i = \frac{m_i}{\sum\limits_j m_j} \tag{1.26}$$

where n_i is the amount of moles of constituent i, V_i is the volume of constituent i and m_i is the mass of constituent i. For all three quantities, the relation

$$\xi_i = 1 - \sum_{\substack{j \\ j \neq i}} \xi_j$$

applies, where ξ stands either for x, φ or w. For given x_i or φ_i, w_i can be calculated using

$$w_i = x_i \frac{M_i}{\sum\limits_j x_j\, M_j} = \varphi_i \frac{\rho_i}{\sum\limits_j \varphi_j\, \rho_j}, \tag{1.27}$$

where M_i is the molar Mass of constituent i. For given w_i the relation for x_i or φ_i reads:

$$\varphi_i = \frac{1}{\rho_i} \frac{w_i}{\sum\limits_j \frac{w_j}{\rho_j}} \qquad \text{and} \qquad x_i = \frac{1}{M_i} \frac{w_i}{\sum\limits_j \frac{w_j}{M_j}}. \tag{1.28}$$

Modifications of the ideal equations

The measured values of the mixtures' η and ρ may significantly deviate from the ideal models Eqs. 1.24 and 1.25 and thus in many papers, the deviations for η and ρ are evaluated for different mixture concentrations at various temperatures T in tabulated form. To correct the ideal equations, the models are usually complemented by (empiric) correction functions, i.e. Eqs. 1.24 and 1.25 are extended to the form

$$\ln \eta = x_1 \ln \eta_1 + x_2 \ln \eta_2 + f_\eta \tag{1.29}$$

$$\rho = \varphi_1 \rho_1 + \varphi_2 \rho_2 + f_\rho \tag{1.30}$$

where f_η and f_ρ are correction functions depending on the mixing ratio.

For the part containing the ideal equation of mass density (which is valid if both components do not interact) modifications using other mixing fractions can be found: In [158] Cheng uses

$$\rho = w_1 \rho_1 + w_2 \rho_2 \tag{1.31}$$

to model the density of a glycerol water mixture. Jouyban uses two different versions for the ideal model for ρ. In [159] he uses

$$\ln \rho = \varphi_1 \ln \rho_1 + \varphi_2 \ln \rho_2 + f_\rho \tag{1.32}$$

(f_ρ will be discussed in Sec. 1.6.1), whereas in [160] the equation reads

$$\ln \rho = x_1 \ln \rho_1 + x_2 \ln \rho_2 + f_\rho. \tag{1.33}$$

As these equations deviate from the ideal model for ρ, Eqs. 1.31 to 1.33 have empiric character and suggest the investigation of all possible variants of Eqs. 1.24 and 1.25 which are given in Fig. 1.7(a). The variants of the ideal equations were applied to data of 100 liquid mixtures collected from [107–139] and the evaluation of $\overline{\Delta}\eta$ and $\overline{\Delta}\rho$ is depicted in Figs. 1.7(b) and 1.7(c). There, it can be observed, that Eqs. 1.24 and 1.25 yield the best results and thus variants of these equations are not necessary. Deviations of these ideal equations and measured values however, have to be corrected with appropriate (empiric) correction functions.

$X \in \{\eta, \rho\}$

1. $X = x_1 X_1 + x_2 X_2$
2. $X = \varphi_1 X_1 + \varphi_2 X_2$
3. $X = w_1 X_1 + w_2 X_2$
4. $\ln X = x_1 \ln X_1 + x_2 \ln X_2$
5. $\ln X = \varphi_1 \ln X_1 + \varphi_2 \ln X_2$
6. $\ln X = w_1 \ln X_1 + w_2 \ln X_2$

(a) Variants of the ideal equations

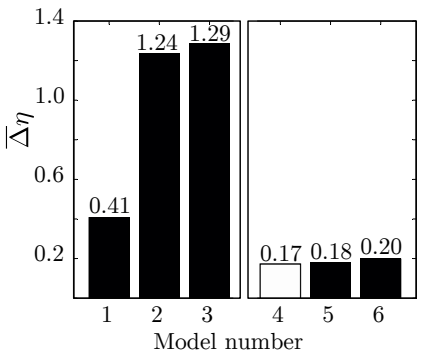

(b) Viscosity

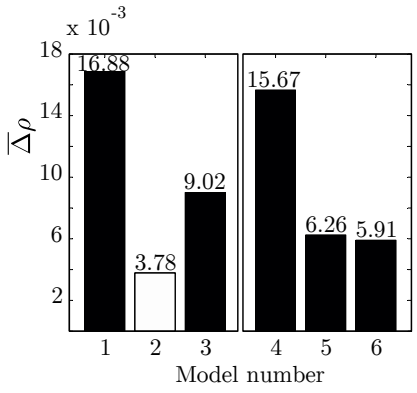

(c) Mass density

Figure 1.7: Evaluation of modifications of the ideal equations for η and ρ: Eqs. 1.24 and 1.25 yield the best results.

1.6.1 Existing models for viscosity and mass density of binary liquid mixtures

Viscosity models for binary liquid mixtures

Overviews of different models for η of a binary liquid mixture can be found in [83, 161–163] and are summarized in the following.

- **Grunberg-Nissan equation**

  In [157] Eq. 1.24 is extended by the term $x_1\,x_2\,d$, i.e., the equation for the logarithm of η reads:

  $$\ln\eta = x_1\ln\eta_1 + x_2\ln\eta_2 + x_1\,x_2\,d \tag{1.34}$$

  where in [157] d is explained as a characteristic constant of the system, whereas in [83] it is explained as an interaction coefficient which is dependent on temperature but independent of composition.

- **Acree and Jouyban-Acree Model**

  In [164] Acree gives an expression corresponding to

  $$\begin{aligned}\ln\eta = {} & x_1\ln\eta_1(T) + x_2\ln\eta_2(T) + A_0\,x_1\,x_2 \\ & + A_1\,x_1\,x_2\,(x_1 - x_2) + A_2\,x_1\,x_2\,(x_1 - x_2)^2\end{aligned} \tag{1.35}$$

  which is a further expansion of the Grunberg-Nissan equation, Eq. 1.34. In [165] Jouyban devides the factors A_i by the temperature yielding

  $$\begin{aligned}\ln\eta = {} & x_1\ln\eta_1(T) + x_2\ln\eta_2(T) + A_0\frac{x_1\,x_2}{T} \\ & + A_1\frac{x_1\,x_2\,(x_1 - x_2)}{T} + A_2\frac{x_1\,x_2\,(x_1 - x_2)^2}{T}.\end{aligned} \tag{1.36}$$

  In [159] Jouyban introduced a similar version of this equation for modeling a binary mixture's mass density and in [160] he gave a generalized version of this model, stated to be valid for viscosity, mass density and molar volume.

  Both models, the Acree equation and the Jouyban-Acree equation have been applied to measurement data of 100 liquid mixtures found in [107–139]. For both cases, the model parameters were fitted using a standard linear least square fitting procedure, see e.g., [166]. According to the evaluations of $\overline{\Delta}\eta$, the Jouyban-Acree model does not give an improvement in modeling accuracy but even yields worse results. For the evaluated liquids, $\overline{\Delta}\eta = 19.07\cdot10^{-3}$ for the Acree equation and $\overline{\Delta}\eta = 19.12\cdot10^{-3}$ for the Jouyban-Acree equation, respectively.

- **Further models**

  In the literature further models for liquid mixtures' viscosity can be found. However, as (amongst others) the influence of the temperature on the mixtures' viscosities is not sufficiently modeled in these equations, these models are not further investigated here.

Mass density models for binary liquid mixtures

The models for the mass density of binary liquid mixtures, which consider the influence of temperature, are empiric equations developed by Jouyban and Acree as well as empiric polynomial functions and are listed below. In the following equations A_i, A_{ij}, B_i and C_i are modeling coefficients.

- **Jouyban-Acree model**

  In [159] the logarithmic expression for a binary liquid's mixture considering the mixture's temperature is

$$\ln \rho = \varphi_1 \ln \rho_1(T) + \varphi_2 \ln \rho_2(T) + \varphi_1 \varphi_2 \sum_{i=0}^{2} A_i \frac{(\varphi_1 - \varphi_2)^i}{T} \tag{1.37}$$

  wheras in [160] the relation reads

$$\ln \rho = x_1 \ln \rho_1(T) + x_2 \ln \rho_2(T) + x_1 x_2 \sum_{j=0}^{2} A_j \frac{(x_1 - x_2)^i}{T}. \tag{1.38}$$

Polynomial functions for a binary liquid mixture's mass density are

- **Lee** [167]

$$\rho = \sum_{i=0}^{2} A_i w_2^i + B_i w_2^i T + C_i w_2^i T^2 \tag{1.39}$$

- **Jiménez** [168]

$$\rho = \sum_{i=1}^{3} \sum_{j=1}^{3} A_{i\,j}\, x^{i-1} (T - T_0)^{j-1} \tag{1.40}$$

- **Tovar relation** [169]

$$\frac{1}{\rho} = \sum_{i=1}^{5} \sum_{j=1}^{3} A_{i\,j}\, 10^{1-j}\, x^{i-1} (T - T_0)^{j-1} \tag{1.41}$$

  where the benefit of the usage of the term 10^{1-j} is not evident.

1.6.2 New models for viscosity

Representation of polynomial correction functions

The unmixed liquid's temperature dependencies are accurately modeled using Eq. 1.17, i.e.,

$$\eta_1(T) = \eta_{0,1}\, \mathrm{e}^{b_{1,1}\, T^* + b_{2,1}\, T^{*2}} \qquad \text{and} \qquad \eta_2(T) = \eta_{0,2}\, \mathrm{e}^{b_{1,2}\, T^* + b_{2,2}\, T^{*2}} \tag{1.42}$$

where $T^* = T - T_\mathrm{m}$. That is, the temperature dependent viscosity of the mixture $\eta(x_1, x_2, T)$ is sufficiently modeled for $\eta(x_1 = 1, x_2 = 0, T)$ and $\eta(x_1 = 0, x_2 = 1, T)$, respectively using the above expressions. For this reason, functions $f_\eta(x_1, x_2)$ where $f_\eta(1, 0) = f_\eta(0, 1) = 0$ might be good candidates for modeling the liquid mixtures in dependence of x_1 and x_2. Such functions can be implemented using polynomials. In the Acree model, Eq. 1.35, the term $A_0\, x_1\, x_2 + A_1\, x_1\, x_2\, (x_1 - x_2) + A_2\, x_1\, x_2\, (x_1 - x_2)^2$ is already a polynomial with this behavior. Polynomials of this type were also already used in [170] and [171] reading

$$Z_N = x_1\, x_2 \sum_{j=1}^{N} A_j (x_1 - x_2)^{j-1} \tag{1.43}$$

in general form, where $x_1,\, x_2 \in [0 \ldots 1]$ and $x_1 = 1 - x_2$. Note that compared with the expression used in Eq. 1.35 the numbering of coefficients A_i starts at 1 instead of 0.

For $N = 3$ using the relations

$$Y_1 = \frac{1}{4}(A_1 + A_2 + A_3) \tag{1.44}$$

$$Y_2 = \frac{1}{3}(A_1 - A_3) \tag{1.45}$$

$$Y_3 = \frac{1}{4}(A_3 + A_1 - A_2) \tag{1.46}$$

the previous polynomial representation can be written as

$$F_3 = Y_1\, x_1^3\, x_2 + Y_2\, x_1^2\, x_2^2 + Y_3\, x_1\, x_2^3 \tag{1.47}$$

wich is an explizit Bézier polynomial which is a polynomial function expressed in the Bernstein polynomial basis, which in turn using $x_1 = 1 - x_2$ and

$$p_1 = 4\, Y_1 \tag{1.48}$$

$$p_2 = -12\, Y_1 + 6\, Y_2 \tag{1.49}$$

$$p_3 = 12\, Y_1 - 12\, Y_2 + 4\, Y_3 \tag{1.50}$$

$$p_4 = -4\, Y_1 + 6\, Y_2 4\, Y_3 \tag{1.51}$$

can be written as 4-th order polynomial reading

$$P_4 = p_4\, x_2^4 + p_3\, x_2^3 + p_2\, x_2^2 + p_1\, x_2. \tag{1.52}$$

In Fig. 1.8 the relations between these three types of polynomial functions for $N = 2, 3, 5$ are given and the effect of higher N used for approximating experimental data is illustrated. There furthermore, the control points for the explicit Bézier functions are depicted as well.

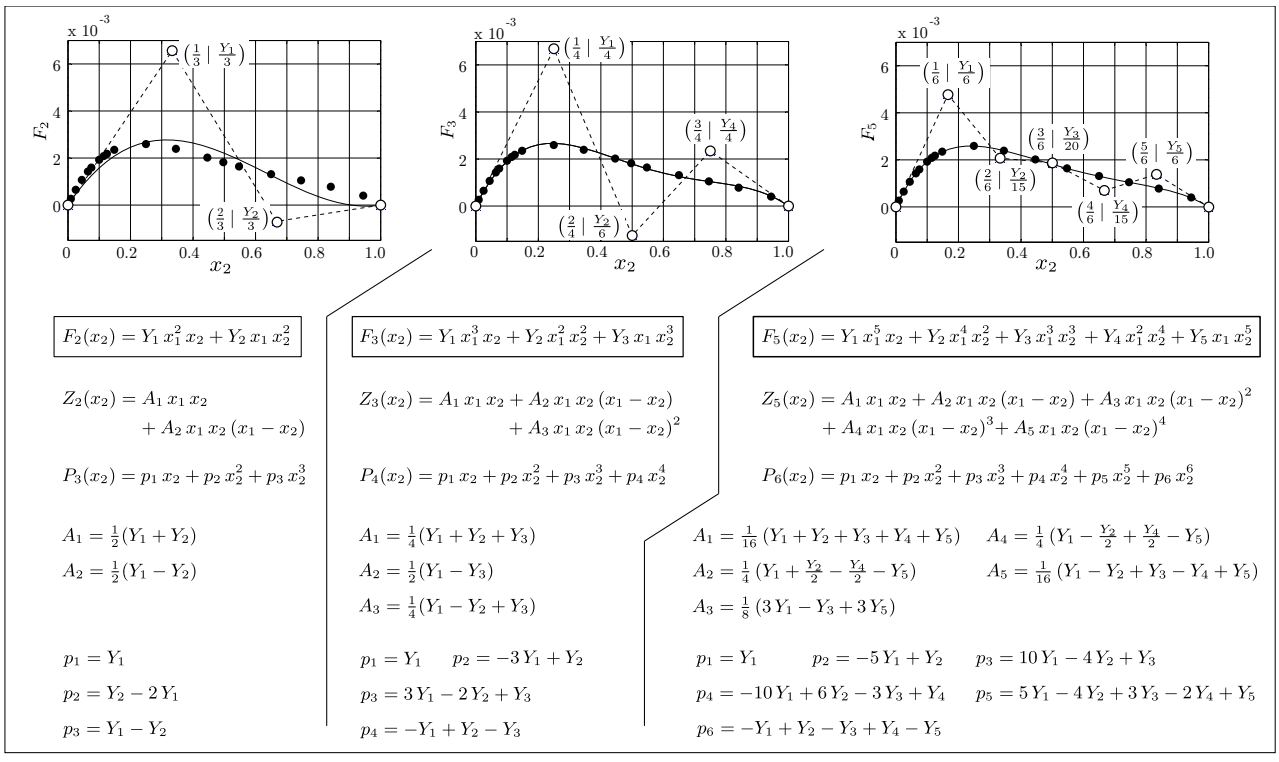

Figure 1.8: Correction functions

Nine coefficients model

Considering that the viscosities' temperature dependencies are modeled using three constant equations, the Acree and the Jouyban-Acree models, Eqs. 1.35 and 1.36 require nine coefficients in total, which have to be determined by an appropriate fitting procedure. For comparison reason a further nine coefficient model reading

$$\eta = \eta_0 \, \mathrm{e}^{b_{11}\, x_1\, T + b_{21}\, x_1^2\, T^2} \, \mathrm{e}^{b_{21}\, x_2\, T + b_{22}\, x_2^2\, T^2} \tag{1.53}$$

where η_0 is calculated using

$$\eta_0 = \eta_0(1,0)^{x_1}\, \eta_0(0,1)^{x_2} + Y_1\, x_1^3\, x_2 + Y_2\, x_1^2\, x_2^2 + Y_3\, x_1\, x_2^3 \tag{1.54}$$

was elaborated. This model yields more accurate results than both, the Acree and the Jouyban-Acree model, see Fig. 1.9(a) for the data of the 100 liquid mixtures from [107–139].

Fifteen coefficients models

- **Acree model with temperature dependent coefficients**

  Applying the Acree- (and the Jouyban-Acree-) model to the 100 liquid mixtures showed that the Acree-model yields acceptable accuracies for a single temperature but not, if the temperature behavior of the binary liquid mixture also has to be modeled. For this reason, besides the modeling of the temperature dependency of the unmixed liquids, the coefficients A_i were separately determined for the available temperatures. Plotting the three coefficients over temperature showed a clear dependency of the modeling parameters, which suggested to model this dependence by second order polynomials to keep the number of modeling coefficients low. Thus, the such obtained model reads:

$$\begin{aligned} \ln \eta = & x_1 \ln \eta_1(T) + x_2 \ln \eta_2(T) + A_1(T)\, x_1\, x_2 \\ & + A_2(T)\, x_1\, x_2\, (x_1 - x_2) + A_3(T)\, x_1\, x_2\, (x_1 - x_2)^2 \end{aligned} \tag{1.55}$$

  with

$$A_i(T) = A_{i0} + A_{i1}\, T + A_{i2}\, T^2. \tag{1.56}$$

- **Temperature model with mixture dependent coefficients**

  The form as well as the good modeling accuracy of the three constant equation of the viscosity's temperature dependence of Eq. 1.17 ($\eta(T) = \eta_0^{b_1\, T^* + b_2\, T^{*2}}$, $\overline{\Delta}\eta \approx 3 \cdot 10^{-3}$ and $\widehat{\Delta}\eta \approx 6 \cdot 10^{-3}$, suggested to extend this model for liquid mixtures. The approach was to express the parameters of the temperature model η_0, b_1 and b_2 as a function of the molar fractions x_1 and x_2, i.e.,

$$\eta = \eta_0(x_1,\, x_2) \, \mathrm{e}^{b_1(x_1,\, x_2)\, T^* + b_2(x_1,\, x_2)\, T^{*2}} \tag{1.57}$$

  where for $\eta_0(x_1,\, x_2)$, $b_1(x_1,\, x_2)$, and $b_2(x_1,\, x_2)$

$$\eta_0(x_1,\, x_2) = \eta_0(1,\, 0)^{x_1}\, \eta_0(0,\, 1)^{x_2} + Y_1\, x_1^5\, x_2 + Y_2\, x_1^4\, x_2^2 + Y_3\, x_1^3\, x_2^3 + Y_4\, x_1^2\, x_2^4 + Y_5\, x_1\, x_2^5 \tag{1.58}$$

  as well as

$$b_i(x_1,\, x_2) = b_i(1,\, 0)) + x_2\, b_i(0,\, 1)) + B_{1i}\, x_1^2\, x_2 + B_{2i}\, x_1\, x_2^2 \tag{1.59}$$

  was defined. This model yielded the best results for all investigated binary liquid mixtures, see Fig. 1.9(a).

Third order polynomial

As the usage of polynomials yielded good results for the previous models, the question of modeling a binary liquid's viscosity considering the temperature dependence by using polynomials only arose. Thus a third order polynomial for the mixture dependence as well as a third order polynomial for the temperature dependence of the mixture coefficients, i.e.,

$$\eta = A_0(T) + A_1(T)\, x_2 + A_2\, x_2^2 + A_3\, x_2^3 \tag{1.60}$$

where

$$A_i(T) = A_{i0} + A_{i1}\, T + A_{i2}\, T^2 + A_{i3}\, T^3 \tag{1.61}$$

was assumed, yielding a 16 coefficients model. The application of the 100 binary liquid mixtures showed, that both 15 coefficient model yielded better results than this pure polynomial function, see Fig. 1.9(a).

1.6.3 New models for mass density

Motivated by the good modeling accuracy by considering mixture dependent coefficients of the temperature model for the viscosity, the same approach was chosen for the mass density of a binary liquid mixture, i.e.,

$$\rho = \rho_0(\varphi_1, \varphi_2) + r_1(\varphi_1, \varphi_2)\, T^* + r_2(\varphi_1, \varphi_2)\, T^{*2} \tag{1.62}$$

Note, as the volume fractions φ_i themselves are temperature dependent as well, they are calculated from $\rho_{0,i} = r_{1,i}\, T^* + r_{2,i}\, T^{*2}$ and w_i. Using this modeling approach the usage of different order polynomials for the temperature coefficients was investigated yielding 9, 12 and 15 coefficients models. The polynomial functions for the mixture dependent temperature model coefficients are

- **Nine coefficients model**

$$\begin{aligned} \rho_0 &= \rho_0(1,0) + R_1\, \varphi_1^2\, \varphi_2 + R_2\, \varphi_1\, \varphi_2^2 + \rho_0(0,1) \\ r_1 &= r_1(1,0)\, \varphi_1 + B_1\, \varphi_1\, \varphi_2 + r_1(0,1)\, \varphi_2 \\ r_2 &= r_2(1,0)\, \varphi_1 + r_2(0,1)\, \varphi_2 \end{aligned} \tag{1.63}$$

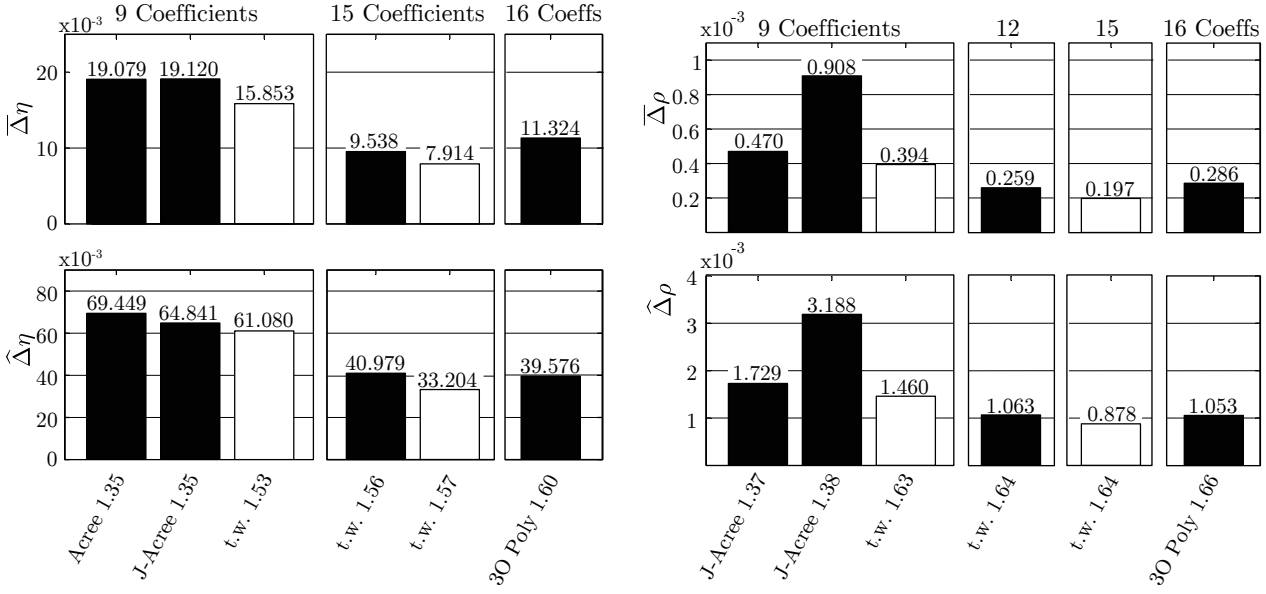

(a) Viscosity

(b) Mass density

Figure 1.9: Evaluation of the investigated models

- **Twelve coefficients model**

$$\begin{aligned} \rho_0 &= \rho_0(1,0) + R_1\,\varphi_1^3\,\varphi_2 + R_2\,\varphi_1^2\,\varphi_2^2 + R_3\,\varphi_1\,\varphi_2^3 + \rho_0(0,1) \\ r_1 &= r_1(1,0)\,\varphi_1 + B_{11}\,\varphi_1^2\,\varphi_2 + B_{12}\,\varphi_1\,\varphi_2^2 + r_1(0,1)\,\varphi_2 \\ r_2 &= r_2(1,0)\,\varphi_1 + B_2\,\varphi_1\,\varphi_2 + r_2(0,1)\,\varphi_2 \end{aligned} \tag{1.64}$$

- **Fifteen coefficients model**

$$\begin{aligned} \rho_0 &= \rho_0(1,0) + R_1\,\varphi_1^4\,\varphi_2 + R_2\,\varphi_1^3\,\varphi_2^2 + R_3\,\varphi_1^2\,\varphi_2^3 + R_4\,\varphi_1\,\varphi_2^4 + \rho_0(0,1) \\ r_1 &= r_1(1,0)\,\varphi_1 + B_{11}\,\varphi_1^3\,\varphi_2 + B_{12}\,\varphi_1^2\,\varphi_2^2 + B_{13}\,\varphi_1\,\varphi_2^3 + r_1(0,1)\,\varphi_2 \\ r_2 &= r_2(1,0)\,\varphi_1 + B_{21}\,\varphi_1^2\,\varphi_2 + B_{22}\,\varphi_1\,\varphi_2^2 + r_2(0,1)\,\varphi_2 \end{aligned} \tag{1.65}$$

A comparison of both Jouyban-Acree models Eqs. 1.37 and 1.38, the nine, twelve and fifteen coefficients model using the approach of mixture dependent temperature model coefficients Eq. 1.62 as well as a pure 16 coefficients polynomial function in the form of Eq. 1.60 for the mass density i.e.,

$$\rho = A_0(T) + A_1(T)\,\varphi_2 + A_2\,\varphi_2^2 + A_3\,\varphi_2^3 \tag{1.66}$$

where

$$A_i(T) = A_{i0} + A_{i1}\,T + A_{i2}\,T^2 + A_{i3}\,T^3 \tag{1.67}$$

is given in Fig. 1.9. Figure 1.10 shows modeled mass density and viscosity in comparison with measured results, taking the mixture of water and 1-vinyl-2-pyrrolidinone as example. This mixture was already shown and compared with the ideal models in Fig. 1.6(a) at 25 °C.

1.7 Viscosity and mass density of ternary mixtures

Approaches for modeling the viscosity of ternary liquid mixtures are given in [172, 173]. However, in these models, the temperature dependence of the liquid mixture's viscosity is not sufficiently considered.

For modeling a ternary liquid's mixture viscosity and mass density and the influence of temperature on the latter, two basic approaches – a model with temperature dependent control points and a model with

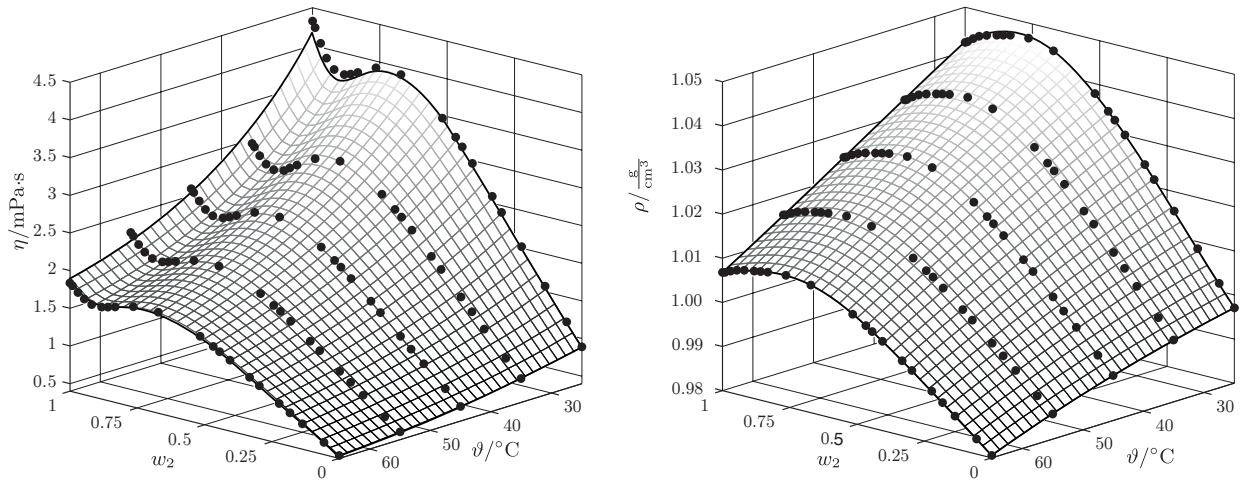

(a) Viscosity

(b) Mass density

Figure 1.10: Water (1) + 1-vinyl-2-pyrrolidinone (2), [112] as function of w_2 and ϑ

mixture dependent temperature coefficients – are investigated. In both cases correcting or interpolating functions are necessary to complete the ideal equations,

$$\eta(x_1, x_2, x_3, T) = \eta_1^{x_1}(T)\,\eta_2^{x_2}(T)\,\eta_3^{x_3}(T) \tag{1.68}$$

and

$$\rho(\varphi_1, \varphi_2, \varphi_3, T) = \varphi_1\,\rho_1(T) + \varphi_2\,\rho_2(T) + \varphi_3\,\rho_3(T) \tag{1.69}$$

for achieving sufficient modeling accuracy. As three-components mixture fractions satisfy the equation $\xi_1 = 1 - \xi_2 - \xi_3$, (where ξ_i is either x_i or φ_i) Bézier triangles are a good candidate for such correcting functions.

1.7.1 Bézier triangle

A Bézier triangle S_n of order n can be expressed as

$$S_n = (\alpha\,x_1 + \beta\,x_2 + \gamma\,x_3)^n \tag{1.70}$$

where $x_1 = 1 - x_2 - x_3$. Products of α, β and γ (and their powers) form the control points which will be replaced by P_j in the following. The control points at $x_1 = 1$, $x_2 = 1$ or $x_3 = 1$ are set to zero for both approaches (temperature dependent control points and mixture dependent temperature coefficients), i.e., $\alpha^n = \beta^n = \gamma^n = 0$ as there, no mixing takes place ant the temperature dependent viscosities and mass densities are calculated using Eqs. 1.17 and 1.23. In the following, the usage of Bézier triangles for $n = 2, \ldots, 5$ are investigated. The equations for the first two, i.e., square ($n = 2$) and cubic ($n = 3$) Bézier rectangles, respectively read:

$$\begin{aligned} S_2 &= 2\,P_{121}\,x_1\,x_2 + 2\,P_{131}\,x_1\,x_3 + 2\,P_{231}\,x_2\,x_3 && (1.71)\\ S_3 &= 3\,P_{121}\,x_1^2\,x_2 + 3\,P_{122}\,x_1\,x_2^2 + 3\,P_{131}\,x_1^2\,x_3 \\ &\quad +3\,P_{132}\,x_1\,x_3^2 + 3\,P_{231}\,x_2^2\,x_3 + 3\,P_{232}\,x_2\,x_3^2 + 6\,P_{1231}\,x_1\,x_2\,x_3 \\ S_n &= \ldots && (1.72) \end{aligned}$$

The usage of the Bézier triangles of different orders is illustrated for the case of the mass density model with temperature dependent control points in the following section.

1.7.2 Temperature dependent control points

In this modeling approach, the ternary liquid mixtures' viscosity and mass density are calculated transferring the ideal equations for binary mixtures Eqs. 1.24 and 1.25 to the case of ternary mixtures which are completed by additive functions $\Delta\eta$ and $\Delta\rho$, i.e.,

$$\eta(x_1, x_2, x_3, T) = \eta_1^{x_1}(T)\,\eta_2^{x_2}(T)\,\eta_3^{x_3}(T) + \Delta\eta(x_1, x_2, x_3, T) \tag{1.73}$$

and

$$\rho(\varphi_1, \varphi_2, \varphi_3, T) = \varphi_1\,\rho_1(T) + \varphi_2\,\rho_2(T) + \varphi_3\,\rho_3(T) + \Delta\rho(\varphi_1, \varphi_2, \varphi_3, T). \tag{1.74}$$

Viscosity model

With the knowledge of the temperature coefficients of the unmixed liquids' viscosities

$$\eta_1(T) = \eta_{01}\,\mathrm{e}^{b_{11}\,T^* + b_{21}\,T^{*2}}, \qquad \eta_2(T) = \eta_{02}\,\mathrm{e}^{b_{12}\,T^* + b_{22}\,T^{*2}}, \qquad \text{and} \qquad \eta_3(T) = \eta_{03}\,\mathrm{e}^{b_{13}\,T^* + b_{23}\,T^{*2}} \tag{1.75}$$

in a first step, the deviations

$$\Delta\eta(x_{1d}, x_{2d}, x_{3d}, T_i) = \eta(x_{1d}, x_{2d}, x_{3d}, T_i) - \eta_\mathrm{c}(x_{1d}, x_{2d}, x_{3d}, T_i) \tag{1.76}$$

from the measured values $\eta(x_{1d}, x_{2d}, x_{3d}, T_i)$ at discrete, measured mixture fractions x_{1d}, x_{2d}, and x_{3d} at temperatures T_i, where

$$\eta_\mathrm{c}(T_i) = \eta_1(T_i)^{x_{1\mathrm{d}}}\,\eta_2(T_i)^{x_{2\mathrm{d}}}\,\eta_3(T_i)^{x_{3\mathrm{d}}} \tag{1.77}$$

are calculated. These deviations are fit using Bézier triangles $S_{\eta n}$ for every temperature T_i yielding control points $P_j(T_i)$. The temperature dependence of these coefficients is then fit using a second order polynomial, i.e.

$$P_j(T) = P_{j0} + P_{j1}\,T + P_{j2}\,T^2 \tag{1.78}$$

yielding $3\,(\frac{(n+1)\,(n+2)}{2} - 3)$ coefficients for the correction function and thus, $9 + 3\,(\frac{(n+1)\,(n+2)}{2} - 3)$ coefficients in total for the temperature dependent mixture coefficients model.

With the knowledge of these coefficients the viscosity of a ternary liquid mixture $\eta(x_1, x_2, x_3, T)$ is calculated as follows, see also Fig. 1.11: First, using Eqs. 1.68 and 1.75 the first term in Eq. 1.73 is calculated. Second, the temperature dependent control points $P_j(T)$ using Eq. 1.78 are determined. Third, the second term in Eq. 1.73, i.e. $\Delta\eta(x_1, x_2, x_3, T)$ using these control points is evaluated. An illustrated explanation of this procedure for the case of an ethanol + 2-butanone + 2,2,4-trimethylpentane mixture [174] is given. For the mixture's mass density the fitting procedure is identical.

Mass density model

Analogous to the viscosity model, the mass density model for ternary liquid mixtures using temperature dependent mixtures coefficients, the deviations

$$\Delta\rho(T_i) = \rho(T_i) - \rho_\mathrm{c}(T_i) \qquad \text{with} \qquad \rho_\mathrm{c}(T_i) = \rho_1(T_i)\,x_{1\mathrm{d}} + \rho_2(T_i)\,x_{2\mathrm{d}} + \rho_3(T_i)\,x_{3\mathrm{d}} \tag{1.79}$$

are evaluated which subsequently are used to fit a fit Bézier triangle at all temperatures T_i yielding again coefficients $P_i(T_i)$ which in turn are used to fit the second order polynomial of the form of Eq. 1.78.

1.7.3 Mixture dependent temperature coefficients

Viscosity model

For the mixture dependent temperature coefficients model, the coefficients η_0, b_1 and b_2 of Eq. 1.17 are expressed in dependence of the mixing fractions x_1, x_2 and x_3, i.e.,

$$\eta(x_1, x_2, x_3, T) = \eta_0(x_1, x_2, x_3)\,\mathrm{e}^{b_1(x_1,x_2,x_3)\,T^* + b_2(x_1,x_2,x_3)\,T^{*2}} \tag{1.80}$$

For every experimentally determined mixture at discrete mixing fractions $x_{1\mathrm{d}}$, $x_{2\mathrm{d}}$ and $x_{3\mathrm{d}}$ the coefficients η_0, b_1 and b_2 are determined by a linear, least square algorithm, yielding temperature coefficients $\eta_{0\mathrm{d}}$, $b_{1\mathrm{d}}$ and $b_{2\mathrm{d}}$ at these discrete mixing fractions.

In a first step, parameters

$$\begin{aligned} \eta_{0\mathrm{c}} &= \eta_{01}^{x_1}\,\eta_{02}^{x_2}\,\eta_{03}^{x_3} \\ b_{1\mathrm{c}} &= b_{11}\,x_1 + b_{12}\,x_2 + b_{13}\,x_3 \\ b_{2\mathrm{c}} &= b_{21}\,x_1 + b_{22}\,x_2 + b_{23}\,x_3 \end{aligned} \tag{1.81}$$

are defined yielding a first approximate solution for the liquid mixture. With this functions, the deviations

$$\Delta\eta_{0\mathrm{d}} = \eta_{0\mathrm{d}} - \eta_{0\mathrm{c}}(x_{1\mathrm{d}}, x_{2\mathrm{d}}, x_{3\mathrm{d}}), \quad \Delta b_{1\mathrm{d}} = b_{1\mathrm{d}} - b_{1\mathrm{c}}(x_{1\mathrm{d}}, x_{2\mathrm{d}}, x_{3\mathrm{d}}), \quad \text{and} \quad \Delta b_{2\mathrm{d}} = b_{2\mathrm{d}} - b_{2\mathrm{c}}(x_{1\mathrm{d}}, x_{2\mathrm{d}}, x_{3\mathrm{d}}) \tag{1.82}$$

are calculated which then are approximated by Bézier triangles $S_{\eta n}$, $S_{\mathrm{b}_1 n}$ and $S_{\mathrm{b}_2 n}$ of order n. With the fitted Bézier triangles, the mixture dependent temperature coefficients from Eq. 1.80 are calculated as follows:

$$\begin{aligned} \eta_0(x_1, x_2, x_3) &= \eta_{0\mathrm{c}} + S_{\eta n} \\ b_1(x_1, x_2, x_3) &= b_{1\mathrm{c}} + S_{\mathrm{b}_1 n} \\ b_2(x_1, x_2, x_3) &= b_{2\mathrm{c}} + S_{\mathrm{b}_2 n}. \end{aligned} \tag{1.83}$$

- Comparison of measured data (•) and the results from ideal equations ▨ at 25 °C, i.e.

$$\eta_{\mathrm{id}}(x_1, x_2, x_3, T) = \eta_1^{x_1}(T)\,\eta_2^{x_2}(T)\,\eta_3^{x_3}(T)$$

where

$$\eta_1(T) = \eta_{01}\,\mathrm{e}^{b_{11}\,T^* + b_{21}\,T^{*2}}, \qquad \eta_2(T) = \eta_{02}\,\mathrm{e}^{b_{12}\,T^* + b_{22}\,T^{*2}}, \qquad \text{and} \qquad \eta_3(T) = \eta_{03}\,\mathrm{e}^{b_{13}\,T^* + b_{23}\,T^{*2}}$$

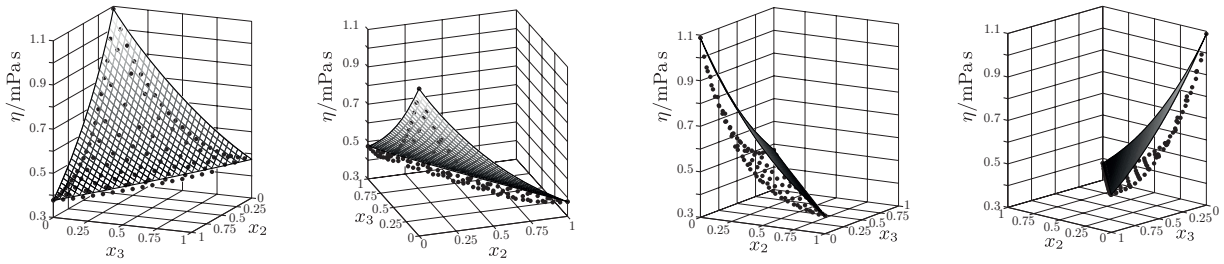

- Deviation $\Delta\eta$ between (ideally) modeled and measured data

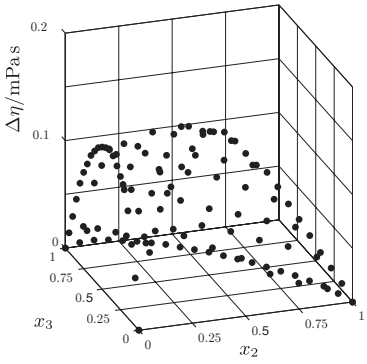

- Distribution of control points for Bézier triangles $S_2, S_3, S_4,$ and, S_5.

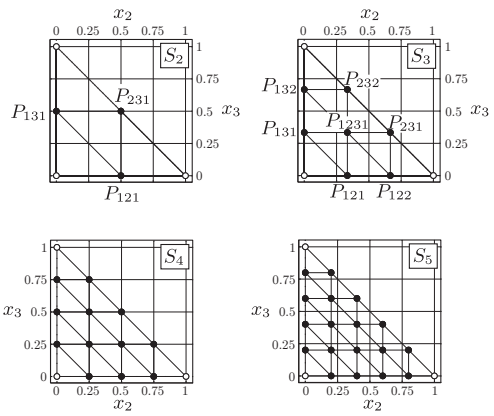

- Bézier trianlge S_5 with control points

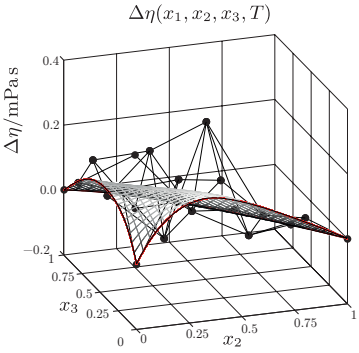

- The control points are determined for at least three temperatures. Their temperature dependence is modeled using a second order polynomial, i.e,

$$P_j(T) = P_{j0} + P_{j1}\,T + P_{j2}\,T^2$$

- Comparison between modeld and measured data $\eta(x_1, x_2, x_3, T) = \eta_1^{x_1}(T)\,\eta_2^{x_2}(T)\,\eta_3^{x_3}(T) + \Delta\eta(x_1, x_2, x_3, T)$

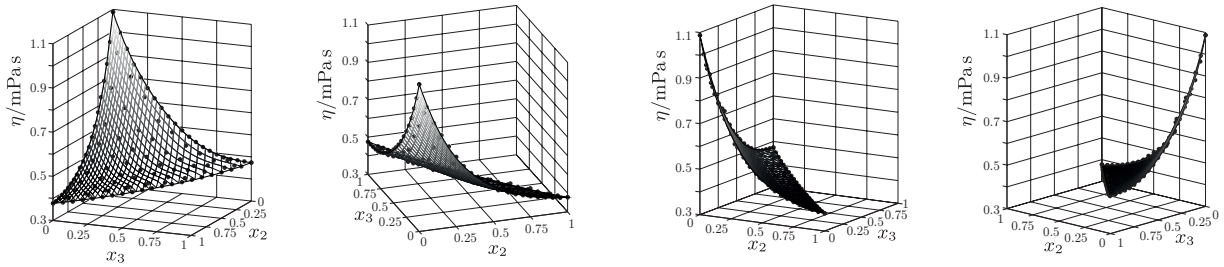

Figure 1.11: Illustrative explanation for the modeling approach with temperature dependent control points

Mass density model

The structure of the mass density model with mixture dependent temperature coefficients

$$\rho(\varphi_1, \varphi_2, \varphi_3, T) = \rho_0(\varphi_1, \varphi_2, \varphi_3) + r_1(\varphi_1, \varphi_2, \varphi_3)\,T^* + r_2(\varphi_1, \varphi_2, \varphi_3)\,T^{*2} \tag{1.84}$$

is analogous to the viscosity model, i.e. at all discrete mixing fractions $x_{1\mathrm{d}}$, $x_{2\mathrm{d}}$ and $x_{3\mathrm{d}}$, parameters ρ_0, r_1 and r_2 from the temperature model for a liquid's mass density Eq. 1.23, are fit. With the knowledge of the mass densities' temperature dependences of the unmixed liquids

$$\rho_1(T) = \rho_{01} + r_{11}\,T^* + r_{21}\,T^{*2}, \quad \rho_2(T) = \rho_{02} + r_{12}\,T^* + r_{22}\,T^{*2}, \quad \text{and} \quad \rho_3(T) = \rho_{03} + r_{13}\,T^* + r_{23}\,T^{*2}, \tag{1.85}$$

and the calculable mixture dependent parameters

$$\begin{aligned} \rho_{0\mathrm{c}} &= \rho_{01}\,\varphi_1 + \rho_{02}\,\varphi_2 + \rho_{03}\,\varphi_3 \\ r_{1\mathrm{c}} &= r_{11}\,\varphi_1 + r_{12}\,\varphi_2 + r_{13}\,\varphi_3 \\ r_{2\mathrm{c}} &= r_{21}\,\varphi_1 + r_{22}\,\varphi_2 + r_{23}\,\varphi_3 \end{aligned} \tag{1.86}$$

the deviations

$$\Delta\rho_{0\mathrm{d}} = \rho_{0\mathrm{d}} - \rho_{0\mathrm{c}}(\varphi_{1\mathrm{d}}, \varphi_{2\mathrm{d}}, \varphi_{3\mathrm{d}}), \quad \Delta r_{1\mathrm{d}} = r_{1\mathrm{d}} - r_{1\mathrm{c}}(\varphi_{1\mathrm{d}}, \varphi_{2\mathrm{d}}, \varphi_{3\mathrm{d}}), \quad \text{and} \quad \Delta r_{2\mathrm{d}} = r_{2\mathrm{d}} - r_{2\mathrm{c}}(\varphi_{1\mathrm{d}}, \varphi_{2\mathrm{d}}, \varphi_{3\mathrm{d}}) \tag{1.87}$$

are fit with Bézier triangles $S_{\rho n}$, $S_{\mathrm{r}_1 n}$ and $S_{\mathrm{r}_2 n}$ of order n. With the calculable parameters and these correction functions, the parameters of the mixture dependent temperature model for mass density read:

$$\begin{aligned} \rho_0(x_1, x_2, x_3) &= \rho_{0\mathrm{c}} + S_{\rho n} \\ r_1(x_1, x_2, x_3) &= r_{1\mathrm{c}} + S_{\mathrm{r}_1 n} \\ r_2(x_1, x_2, x_3) &= r_{2\mathrm{c}} + S_{\mathrm{r}_2 n}. \end{aligned} \tag{1.88}$$

For both, the binary as well as the ternary liquid mixture models, the number of measurements has to be at least as high as the number of modeling coefficients. That is, using a 15 coefficients model for binary mixtures, at least five liquid mixtures at three different temperatures have to be available. A fifth order Bézier triangle for the case of the temperature dependent control points model for ternary mixtures has 63 coefficients, and thus requires at least 21 mixtures measured at three temperatures. However, more measurements are generally of interest, to ensure that the modeled behavior is valid. In the literature research performed for this study, mainly measurement results at three temperatures for binary mixtures and measurement results at two temperatures for ternary mixtures were found. The latter does not give sufficient temperature points for using the introduced models and thus, a significant comparison of different modeling approaches or and investigation effect of number of coefficients on modeling accuracy can not be performed yet. For the measurements performed in [MHwp13] and [MHwp14] to investigate ternary liquid mixtures, 98 mixtures were prepared which were then measured between 5 °C and 45 °C in 2.5 °C steps yielding 1666 measurements for one ternary mixture. To allow an easy fitting procedure of the model parameters, the presented models have been elaborated such, to allow the applicability of linear least square fitting algorithms.

1.8 Governing equations for oscillating fluid-structure interaction

In Sec. 1.3, the working principle of resonant viscosity and mass density sensors has already been briefly explained. There, it was explained that a mechanical resonator interacts with the sample liquid. To describe the fluid mechanical modeling approach for such sensors, in the following, the governing equations of the fluid motion of oscillating fluid-structure interaction are presented and in Fig. 1.12 a summary of this derivation is given.

1.8.1 Conservation of mass

The law of conservation of mass [175] reads

$$\frac{\partial \rho}{\partial t} + \nabla \cdot (\rho\, \boldsymbol{v}) = 0, \tag{1.89}$$

where ρ is the medium's mass density, t is the time variable, $\boldsymbol{v}$ the velocity and *nabla*$\cdot$ denotes the divergence operator.

1.8.2 Equation of motion

The Cauchyian equation of motion which is valid for all continua [176] in Lagrangian (or convective) form using Eulerian specification [177, 178] of the flow field reads

$$\rho \frac{\mathrm{D}\boldsymbol{v}}{\mathrm{D}t} = \boldsymbol{f} + \nabla \cdot \boldsymbol{T} \qquad \text{or} \qquad \rho \frac{\partial \boldsymbol{v}}{\partial t} + \rho\,(\boldsymbol{v} \cdot \nabla)\boldsymbol{v} = \boldsymbol{f} + \nabla \cdot \boldsymbol{T} \tag{1.90}$$

respectively. $\boldsymbol{f}$ is the volumetric force density considering e.g., gravitational or Coriolis forces and $\boldsymbol{T}$ is the stress tensor. Replacing the substantial derivative $\mathrm{D}(.)/\mathrm{D} = \partial(.)/\partial t + \boldsymbol{v} \cdot \nabla(.)$. Substituting the velocity vector by the deformation vector using $\boldsymbol{v} = \partial \boldsymbol{u}/\partial t = \dot{\boldsymbol{u}}$, the equation of motion for acoustic waves in liquids

$$\rho\,\ddot{\boldsymbol{u}} + \rho\,(\dot{\boldsymbol{u}} \cdot \nabla)\dot{\boldsymbol{u}} = \boldsymbol{f} + \nabla \cdot \boldsymbol{T} \qquad \text{and solids [179]} \qquad \rho\,\ddot{\boldsymbol{u}} = \boldsymbol{f} + \nabla \cdot \boldsymbol{T}, \tag{1.91}$$

can be formulated.

1.8.3 Stress tensor for Newtonian, compressible liquids

The stress tensor $\boldsymbol{T}$ for a Newtonian, i.e. linear viscous fluid [175] can be written using the tensor (or dyadic) product $\otimes$ as follows [180]:

$$\boldsymbol{T} = -p\,\boldsymbol{I} + \eta(\nabla \otimes \boldsymbol{v} + [\nabla \otimes \boldsymbol{v}]^{\mathrm{T}}) + \lambda(\nabla \cdot \boldsymbol{v}) \cdot \boldsymbol{I}. \tag{1.92}$$

1.8.4 Equation of motion in liquids (Navier-Stokes)

Using

$$\nabla \cdot \boldsymbol{I}(.) = \nabla(.), \quad \nabla \cdot (\nabla \otimes (.)) = \Delta(.), \quad \nabla \cdot [\nabla \otimes (.)]^{\mathrm{T}} = \nabla(\nabla \cdot (.)), \quad \text{and} \quad \nabla \cdot (\nabla \cdot (.)) \cdot \boldsymbol{I} = \nabla(\nabla \cdot (.)) \tag{1.93}$$

it follows for the equation of motion of a Newtonian fluid, see also [181]

$$\rho \frac{\partial \boldsymbol{v}}{\partial t} + \rho\,(\boldsymbol{v} \cdot \nabla)\boldsymbol{v} = \boldsymbol{f} - \nabla p + \eta\,\Delta \boldsymbol{v} + (\eta + \lambda)\nabla(\nabla \cdot \boldsymbol{v}). \tag{1.94}$$

$\boldsymbol{f}$ is usually not relevant for resonant liquid sensors, i.e., $\boldsymbol{f} = 0$. The pressure in the fluid can be expressed as [182]

$$p = p_0 - \frac{1}{\zeta}\nabla \cdot \boldsymbol{u} \qquad \text{and thus} \qquad \nabla p = -\frac{1}{\zeta}\nabla(\nabla \cdot \boldsymbol{u}) \tag{1.95}$$

for $\nabla p_0 = 0$, where ζ is the adiabatic compressibility coefficient.

Neglecting the convective term

The nonlinear, convective term $(\boldsymbol{v} \cdot \nabla)\boldsymbol{v}$ can be neglected in case of oscillatory fluid motion [180,183–185] if $\frac{2\pi}{\alpha}\hat{u}_{\max} \ll 1$, where α is the wave-length of the highest spectral component in the oscillation of the liquid and $\hat{u}_{\max}$ is the maximum amplitude of the oscillation. Strictly speaking, only the deformation in direction of the propagating wave is relevant. For shear waves, the convective term is negligible in any case. Through this simplification and the neglect of internal forces, the equation of motion for liquids obtains the same form as for acoustic waves in solids. Using these simplifications and the relation for the pressure gradient, the linearized Navier-Stokes equation for Newtonian, compressible liquids can be formulated [180]

$$\rho\ddot{\boldsymbol{u}} = \frac{1}{\zeta}\nabla(\nabla \cdot \boldsymbol{u}) + \eta\,\Delta\dot{\boldsymbol{u}} + (\eta + \lambda)\nabla(\nabla \cdot \dot{\boldsymbol{u}}) \qquad \Leftrightarrow \qquad \rho\,\ddot{\boldsymbol{u}} = \nabla \cdot \boldsymbol{T} \tag{1.96}$$

Incompressible liquids

Incompressibility can be assumed if the maximum fluid velocity $v_{\max}$ is much smaller than its velocity of sound c, i.e. $v_{\max} \ll c$. A further (similar) means of judging the applicability of incompressibility is Mach's Number $Ma = \frac{v}{c}$, where v is the local flow velocity and c is the fluid's speed of sound. For $Ma < 1$ incompressibility can be assumed [186]. Thus the law of mass conservation and the stress tensor for incompressible viscous fluids simplify to [177, 178]

$$\nabla \cdot \boldsymbol{u} = 0 \tag{1.97}$$

and

$$\boldsymbol{T} = -p\,\boldsymbol{I} + \eta(\nabla \otimes \boldsymbol{v} + [\nabla \otimes \boldsymbol{v}]^{\mathrm{T}}). \tag{1.98}$$

Thus considering $\nabla p_0 = 0$ the equation of motion for incompressible flow reads:

$$\rho\ddot{\boldsymbol{u}} = \eta\,\Delta\dot{\boldsymbol{u}} \qquad \Leftrightarrow \qquad \rho\,\ddot{\boldsymbol{u}} = \nabla \cdot \boldsymbol{T}. \tag{1.99}$$

1.8.5 Strain, stress and the differential equation of motion of elastic solids

Strain tensor

Since the strain tensor is symmetric by definition [187], the theoretically nine independent components reduce to six independent components and thus, the components in the strain tensor can be specified by one subscript rather than two. Using this abbreviated notation, the strain tensor can also be be written as a six-element column vector (also known as Voigt notation) rather than a nine-element symmetric square matrix [179]

$$\boldsymbol{S} = \begin{bmatrix} \varepsilon_{xx} & \varepsilon_{xy} & \varepsilon_{xz} \\ \varepsilon_{xy} & \varepsilon_{yy} & \varepsilon_{yz} \\ \varepsilon_{xz} & \varepsilon_{yz} & \varepsilon_{zz} \end{bmatrix} = \begin{bmatrix} S_1 & \frac{1}{2}S_6 & \frac{1}{2}S_5 \\ \frac{1}{2}S_6 & S_2 & \frac{1}{2}S_4 \\ \frac{1}{2}S_5 & \frac{1}{2}S_4 & S_3 \end{bmatrix} \quad \Leftrightarrow \quad \boldsymbol{S} = [S_1, \ldots, S_6]^{\mathrm{T}}. \tag{1.100}$$

This abbreviated notation and the usage of the factors $\frac{1}{2}$ allows simple notation for the relation of strain and displacement

$$\boldsymbol{S} = \nabla_{\mathrm{s}}\,\boldsymbol{u} \tag{1.101}$$

where in this notation, ∇_{s} is the symmetric gradient operator in matrix notation and reads [179]

$$\nabla_{\mathrm{s}} = \begin{bmatrix} \frac{\partial}{\partial x} & 0 & 0 \\ 0 & \frac{\partial}{\partial y} & 0 \\ 0 & 0 & \frac{\partial}{\partial z} \\ 0 & \frac{\partial}{\partial z} & \frac{\partial}{\partial y} \\ \frac{\partial}{\partial z} & 0 & \frac{\partial}{\partial x} \\ \frac{\partial}{\partial y} & \frac{\partial}{\partial x} & 0 \end{bmatrix}, \quad \nabla_{\mathrm{s}} = \begin{bmatrix} \frac{\partial}{\partial r} & 0 & 0 \\ \frac{1}{r} & \frac{1}{r}\frac{\partial}{\partial \varphi} & 0 \\ 0 & 0 & \frac{\partial}{\partial z} \\ 0 & \frac{\partial}{\partial z} & \frac{1}{r}\frac{\partial}{\partial \varphi} \\ \frac{\partial}{\partial z} & 0 & \frac{\partial}{\partial r} \\ \frac{1}{r}\frac{\partial}{\partial \varphi} & \frac{\partial}{\partial r} - \frac{1}{r} & 0 \end{bmatrix}, \quad \text{and} \quad \nabla_{\mathrm{s}} = \begin{bmatrix} \frac{\partial}{\partial r} & 0 & 0 \\ \frac{1}{r} & \frac{1}{r}\frac{\partial}{\partial \vartheta} & 0 \\ \frac{1}{r} & \frac{\cot\vartheta}{r} & \frac{1}{r\sin\vartheta}\frac{\partial}{\partial \varphi} \\ 0 & \frac{1}{r\sin\vartheta}\frac{\partial}{\partial \varphi} & \frac{1}{r}\frac{\partial}{\partial \vartheta} - \frac{\cot\vartheta}{r} \\ \frac{1}{r\sin\vartheta}\frac{\partial}{\partial \varphi} & 0 & \frac{\partial}{\partial r} - \frac{1}{r} \\ \frac{1}{r}\frac{\partial}{\partial \vartheta} & \frac{\partial}{\partial r} - \frac{1}{r} & 0 \end{bmatrix}, \tag{1.102}$$

respectively, for cartesian (x, y, z), cylindrical (r, φ, z) and spherical (r, ϑ, φ) coordinates. Note, that in Voigt notation the strain-displacement relation could also be written as $\boldsymbol{S} = \nabla_{\mathrm{s}} \cdot \boldsymbol{u}$. However this could be misleading as $\nabla\cdot$ is usually used to express the divergence operator.

Stress tensor

The stress tensor, in general, is unsymmetric when body torques are present which is e.g. the case for media with permanent electric and magnetic polarization, i.e. ferroelectric or ferromagnetic materials. However as even for strongly polarized materials the body torques have negligibly small importance in linear vibration theory, they can be neglected and the stress tensor becomes symmetric [188]. This

assumption is valid for non-ferroelectric and non-ferromagnetic materials in any case and thus the symmetric stress tensor in matrix and abbreviated vector notation reads

$$\boldsymbol{T} = \begin{bmatrix} \sigma_{xx} & \sigma_{xy} & \sigma_{xz} \\ \sigma_{xy} & \sigma_{yy} & \sigma_{yz} \\ \sigma_{xz} & \sigma_{yz} & \sigma_{zz} \end{bmatrix} = \begin{bmatrix} T_1 & T_6 & T_5 \\ T_6 & T_2 & T_4 \\ T_5 & T_4 & T_3 \end{bmatrix} \quad \Leftrightarrow \quad \boldsymbol{T} = [T_1, \ldots, T_6]^{\mathrm{T}}. \tag{1.103}$$

Using the abbreviated, six-element-vector notation for the divergence-of-stress operator [179] reads

$$\nabla\cdot = \begin{bmatrix} \frac{\partial}{\partial x} & 0 & 0 & 0 & \frac{\partial}{\partial z} & \frac{\partial}{\partial y} \\ 0 & \frac{\partial}{\partial y} & 0 & \frac{\partial}{\partial z} & 0 & \frac{\partial}{\partial x} \\ 0 & 0 & \frac{\partial}{\partial z} & \frac{\partial}{\partial y} & \frac{\partial}{\partial x} & 0 \end{bmatrix}, \quad \nabla\cdot = \begin{bmatrix} \frac{\partial}{\partial r} + \frac{1}{r} & -\frac{1}{r} & 0 & 0 & \frac{\partial}{\partial z} & \frac{1}{r}\frac{\partial}{\partial \varphi} \\ 0 & \frac{1}{r}\frac{\partial}{\partial \varphi} & 0 & \frac{\partial}{\partial z} & 0 & \frac{\partial}{\partial r} + \frac{2}{r} \\ 0 & 0 & \frac{\partial}{\partial z} & \frac{1}{r}\frac{\partial}{\partial \varphi} & \frac{\partial}{\partial r} + \frac{1}{r} & 0 \end{bmatrix}, \tag{1.104}$$

and

$$\nabla\cdot = \begin{bmatrix} \frac{2}{r} + \frac{\partial}{\partial r} & -\frac{1}{r} & -\frac{1}{r} & 0 & \frac{1}{r\sin\vartheta}\frac{\partial}{\partial \varphi} & \frac{\cot\vartheta}{r} + \frac{1}{r}\frac{\partial}{\partial \vartheta} \\ 0 & \frac{\cot\vartheta}{r} + \frac{1}{r}\frac{\partial}{\partial \vartheta} & -\frac{\cot\vartheta}{r} & \frac{1}{r\sin\vartheta}\frac{\partial}{\partial \varphi} & 0 & \frac{3}{r} + \frac{\partial}{\partial r} \\ 0 & 0 & \frac{1}{r\sin\vartheta}\frac{\partial}{\partial \varphi} & \frac{2\cot\vartheta}{r} + \frac{1}{r}\frac{\partial}{\partial \vartheta} & \frac{3}{r} + \frac{\partial}{\partial r} & 0 \end{bmatrix}, \tag{1.105}$$

for cartesian, cylindrical and spherical coordinates, respectively

1.8.6 Relation for stress and strain in isotropic elastic materials

Using the abbreviated vector notation for the tensors $\boldsymbol{S}$ and $\boldsymbol{T}$ and using the forth rank elasticity tensor $\boldsymbol{c}$, Hooke's law for an arbitrary linear elastic material can be expresses as [179, 189]

$$\boldsymbol{T} = \boldsymbol{c} : \boldsymbol{S} \tag{1.106}$$

and using Eq. 1.101 it follows

$$\boldsymbol{T} = \boldsymbol{c} : \nabla_{\mathrm{s}}\, \boldsymbol{u} \tag{1.107}$$

where the elasticity tensor for an isotropic elastic material can be given by [179]

$$\boldsymbol{c} = \begin{bmatrix} c_{11} & c_{12} & c_{12} & 0 & 0 & 0 \\ c_{12} & c_{11} & c_{12} & 0 & 0 & 0 \\ c_{12} & c_{12} & c_{11} & 0 & 0 & 0 \\ 0 & 0 & 0 & c_{44} & 0 & 0 \\ 0 & 0 & 0 & 0 & c_{44} & 0 \\ 0 & 0 & 0 & 0 & 0 & c_{44} \end{bmatrix} \qquad \text{where} \qquad c_{44} = \frac{1}{2}(c_{11} - c_{12}). \tag{1.108}$$

Note that in Voigt notation, Eq. 1.106 could also be written using $(\cdot)$, i.e., $\boldsymbol{T} = \boldsymbol{c} \cdot \boldsymbol{S}$.

1.8.7 Equation of motion for solids and approximated oscillatory fluid motion

Substituting the relation for the stress tensor Eq. 1.106 in the equation of motion for acoustic waves in solids, Eq. 1.91 yields

$$\rho\, \ddot{\boldsymbol{u}} = \nabla\cdot (\boldsymbol{c} : \nabla_{\mathrm{s}}\, \boldsymbol{u}) \qquad \text{or} \qquad -\rho\, \omega^2 \underline{\boldsymbol{u}} = \nabla\cdot (\boldsymbol{c} : \nabla_{\mathrm{s}}\, \underline{\boldsymbol{u}}), \tag{1.109}$$

respectively, where $\underline{\cdot}$ denotes complex notation. These expressions are also valid for oscillatory liquid motion, if the volumetric force density and the convective term are neglected. For the components in the stiffness tensor it follows

$$c_{11} = \frac{E(1-\nu)}{(1+\nu)(1-2\nu)}, \qquad c_{12} = \frac{E\,\nu}{(1+\nu)(1-2\nu)}, \qquad \text{and} \qquad c_{44} = \frac{E}{2(1+\nu)} \tag{1.110}$$

for linear elastic solids with Young's modulus E and Poisson's ratio ν,

$$c_{11} = \mathrm{j}\omega(\lambda + 2\eta) + \frac{1}{\zeta}, \qquad c_{12} = \mathrm{j}\omega\lambda + \frac{1}{\zeta}, \qquad \text{and} \qquad c_{44} = \mathrm{j}\omega\eta \tag{1.111}$$

■ Cauchian equation of motion (EOM), valid for all continua

$$\rho \frac{\mathrm{D}\boldsymbol{v}}{\mathrm{D}t} = \boldsymbol{f} + \nabla \cdot \boldsymbol{T}$$

Substantial derivative

$$\frac{\mathrm{D}(.)}{\mathrm{D}} = \partial(.)\partial t + \boldsymbol{v} \cdot \nabla(.)$$

$$\boldsymbol{v} = \dot{\boldsymbol{u}}$$

EOM for acoustic waves in solids

$$\rho\, \ddot{\boldsymbol{u}} = \boldsymbol{f} + \nabla \cdot \boldsymbol{T}$$

EOM for liquids

$$\rho\, \ddot{\boldsymbol{u}} + \rho\, (\dot{\boldsymbol{u}} \cdot \nabla)\dot{\boldsymbol{u}} = \boldsymbol{f} + \nabla \cdot \boldsymbol{T}$$

$\boldsymbol{f}$ ... volumetric force density (e.g. gravitational forces)

■ Stress tensor for Newtonian liquids

$$\boldsymbol{T} = -p\, \boldsymbol{I} + \eta(\nabla \otimes \boldsymbol{v} + [\nabla \otimes \boldsymbol{v}]^{\mathrm{T}}) + \lambda(\nabla \cdot \boldsymbol{v}) \cdot \boldsymbol{I}$$

incompressible fluids: $\nabla \cdot \boldsymbol{u} = 0 \quad \Rightarrow \quad \boldsymbol{T} = -p\, \boldsymbol{I} + \eta(\nabla \otimes \boldsymbol{v} + [\nabla \otimes \boldsymbol{v}]^{\mathrm{T}})$

pressure in the liquid

$$p = p_0 - \frac{1}{\zeta} \nabla \cdot \boldsymbol{u}$$

tensor product

$$\boldsymbol{a} \otimes \boldsymbol{b} = \boldsymbol{a}\, \boldsymbol{b}^{\mathrm{T}} = \begin{bmatrix} a_x \\ a_y \\ a_z \end{bmatrix} [b_x\, b_y\, b_z] = \begin{bmatrix} a_x\, b_x & a_x\, b_y & a_x\, b_z \\ a_y\, b_x & a_y\, b_y & a_y\, b_z \\ a_z\, b_x & a_z\, b_y & a_z\, b_z \end{bmatrix}$$

λ ... volume viscosity

ζ ... adiabatic compressibility coefficient

■ Navier-Stokes equation (EOM for a Newtonian liquid)

$$\rho \frac{\partial \boldsymbol{v}}{\partial t} + \rho\, (\boldsymbol{v} \cdot \nabla)\boldsymbol{v} = \boldsymbol{f} - \nabla p + \eta\, \Delta \boldsymbol{v} + (\eta + \lambda)\nabla(\nabla \cdot \boldsymbol{v})$$

■ Linearized Navier-Stokes equation (neglect of the convective term $(\boldsymbol{v} \cdot \nabla)\boldsymbol{v} = 0$)

Neglects:

$$\boldsymbol{f} = 0$$
$$\nabla p_0 = 0$$
$$(\boldsymbol{v} \cdot \nabla)\boldsymbol{v} = 0$$

$$\rho \ddot{\boldsymbol{u}} = \frac{1}{\zeta} \nabla(\nabla \cdot \boldsymbol{u}) + \eta\, \Delta \dot{\boldsymbol{u}} + (\eta + \lambda)\nabla(\nabla \cdot \dot{\boldsymbol{u}}) \qquad \Leftrightarrow \qquad \rho\, \ddot{\boldsymbol{u}} = \nabla \cdot \boldsymbol{T}$$

Incompressible liquids ($\nabla \cdot \boldsymbol{u} = 0$):

$$\rho \ddot{\boldsymbol{u}} = \eta\, \Delta \dot{\boldsymbol{u}} \qquad \Leftrightarrow \qquad \rho\, \ddot{\boldsymbol{u}} = \nabla \cdot \boldsymbol{T}$$

■ Relation between stress and strain tensor in Voigt notation

$$\boldsymbol{T} = \boldsymbol{c} : \boldsymbol{S}$$
$$\boldsymbol{S} = \nabla_{\mathrm{s}}\, \boldsymbol{u} \quad \Rightarrow \quad \boldsymbol{T} = \boldsymbol{c} : \nabla_{\mathrm{s}}\, \boldsymbol{u} \quad \Rightarrow \quad \rho\, \ddot{\boldsymbol{u}} = \nabla \cdot (\boldsymbol{c} : \nabla_{\mathrm{s}} \boldsymbol{u}) \quad \circ\!\!-\!\!\bullet \quad -\rho\, \omega^2 \underline{\boldsymbol{u}} = \nabla \cdot (\boldsymbol{c} : \nabla_{\mathrm{s}} \underline{\boldsymbol{u}})$$

∇_{s} ... symmetric gradient operator

Note: Relation for viscoelastic materials

$$\boldsymbol{T}(t) = \boldsymbol{c} : \boldsymbol{S}(t) + \boldsymbol{d} : \dot{\boldsymbol{S}}(t)$$
$$\dot{\boldsymbol{S}}(t) = \boldsymbol{d}^{-1} : \boldsymbol{T}(t) + \boldsymbol{c}^{-1} : \dot{\boldsymbol{T}}(t)$$

■ Elasticity tensor for iostropic, elastic materials

$$\boldsymbol{c} = \begin{bmatrix} c_{11} & c_{12} & c_{12} & 0 & 0 & 0 \\ c_{12} & c_{11} & c_{12} & 0 & 0 & 0 \\ c_{12} & c_{12} & c_{11} & 0 & 0 & 0 \\ 0 & 0 & 0 & c_{44} & 0 & 0 \\ 0 & 0 & 0 & 0 & c_{44} & 0 \\ 0 & 0 & 0 & 0 & 0 & c_{44} \end{bmatrix}$$

$$c_{44} = \frac{1}{2}(c_{11} - c_{12})$$

- Compressible liquids

$$c_{11} = \mathrm{j}\omega(\lambda + 2\eta) + \frac{1}{\zeta}, \qquad c_{12} = \mathrm{j}\omega\lambda + \frac{1}{\zeta}, \qquad \text{and} \qquad c_{44} = \mathrm{j}\omega\eta$$

- Incompressible liquids

$$c_{11} = \mathrm{j}\omega 2\eta, \qquad c_{12} = 0, \qquad \text{and} \qquad c_{44} = \mathrm{j}\omega\eta$$

Figure 1.12: Summary of the governing equations for oscillatory fluid motion

for compressible liquids [84], [MHbcc1] and

$$c_{11} = \mathrm{j}\omega 2\eta, \qquad c_{12} = 0, \qquad \text{and} \qquad c_{44} = \mathrm{j}\omega\eta \tag{1.112}$$

for incompressible liquids, respectively.

The derivation of the governing equations for oscillating fluid-structure interaction is summarized in Fig. 1.12.

1.9 Lumped element approach

A linear, mechanical oscillator with lumped mass m_0, damping coefficient c_0 and spring constant k_0, being immersed in a liquid and oscillating in the latter as it was depicted in Fig. 1.1 is considered. The time dependent equation of motion for the displacement u upon forced actuation with an excitation

force F_{ex} and accounting for the influence of the liquid on the oscillation with a fluid related force F_{F} is

$$m_0 \frac{\mathrm{d}^2 u(t)}{\mathrm{d}t^2} + c_0 \frac{\mathrm{d}u(t)}{\mathrm{d}t} + k_0\, u(t) = F_{\mathrm{ex}}(t) - F_{\mathrm{F}}(t). \tag{1.113}$$

A harmonic excitation force with angular frequency ω and time dependence $\mathrm{e}^{\mathrm{j}\,\omega\, t}$ where $\mathrm{j}^2 = -1$ is furthermore assumed. Thus, the equation of motion using the steady state velocity of the oscillation in the frequency domain $\underline{v}(\omega) = \mathrm{j}\,\omega\,\underline{u}(\omega)$ reads

$$\left(c_0 + \mathrm{j}\left(\omega\, m_0 - \frac{k_0}{\omega}\right)\right) \underline{v}(\omega) = \underline{F}_{\mathrm{ex}}(\omega) - \underline{F}_{\mathrm{F}}(\omega). \tag{1.114}$$

The force $\underline{F}_{\mathrm{F}}$ induced by the fluid can be represented by a complex valued function of ω in the frequency domain. As the interaction will have a linear character for small vibration amplitudes it will be proportional to the velocity such that it can be expressed as

$$\underline{F}_{\mathrm{F}}(\omega) = \underline{Z}_{\mathrm{F}}(\omega)\, \underline{v}(\omega) \tag{1.115}$$

where the symbol $\underline{Z}_{\mathrm{F}}$ was used for the proportionality factor as it resembles an acoustic impedance. $\underline{Z}_{\mathrm{F}}(\omega)$ can be split in a real and imaginary part, $Z_{\mathrm{F},\Re}$ and $Z_{\mathrm{F},\Im}$, respectively. The interaction with the fluid leads to an added mass (due to fluid mass moved in unison with the vibration) and to a damping due to viscous losses and radiated acoustic waves. The latter effect will lead to a real part of $\underline{Z}_{\mathrm{F}}(\omega)$ while the mass entrainment corresponds to the imaginary part. This motivates to write the real part as

$$Z_{\mathrm{F},\Re} = c_{\mathrm{f}} \tag{1.116}$$

and the imaginary part as

$$Z_{\mathrm{F},\Im} = \omega\, m_{\mathrm{f}}, \tag{1.117}$$

where c_{f} represents the additional damping and m_{f} represents the added mass. If additional lumped mass were actually added to the lumped mass m_0 of the mechanical oscillator, m_{f} would represent this added mass. However, as it represents the fluid interaction of a distributed resonator, the terms m_{f} and c_{f} will, in general, be frequency dependent. Thus the fluid forces in the frequency domain can be written as

$$\underline{F}_{\mathrm{F}}(\omega) = (c_{\mathrm{f}}(\omega) + \mathrm{j}\,\omega\, m_{\mathrm{f}}(\omega))\, \underline{v}(\omega). \tag{1.118}$$

Just as the parameters of the lumped mass model (m_0, c_0, k_0), the frequency dependence of $m_{\mathrm{f}}(\omega)$ and $c_{\mathrm{f}}(\omega)$ can be moderate, though, such that, if ω is close to the resonance frequencies, the values can be approximated by their values at the resonance frequency. Introducing the above relation Eq. 1.118 in Eq. 1.114, the following spectral transfer function is obtained

$$\frac{\underline{v}}{\underline{F}_{\mathrm{ex}}} = \frac{1}{c_0 + c_{\mathrm{f}}(\omega) + j\left(\omega\,(m_0 + m_{\mathrm{f}}(\omega)) - \dfrac{k_0}{\omega}\right)}. \tag{1.119}$$

This frequency response can be compared to the standardized response of a second order system

$$\underline{H}_2(\omega) = \frac{A}{1 + j\, Q\left(\dfrac{\omega}{\omega_0} - \dfrac{\omega_0}{\omega}\right)} \tag{1.120}$$

where ω_0 represents the resonance frequency and Q the quality factor. Neglecting the frequency dependence of $\underline{Z}_{\mathrm{F}}$ near resonance, the resonance frequency and the Q-factor of our model system can be readily identified. The resonance frequency is defined as the frequency where the above transfer function Eq. 1.119 becomes real-valued which yields an implicit equation for ω_0:

$$\omega_0\,(m_0 + m_{\mathrm{f}}(\omega)) = \frac{k_0}{\omega_0}. \tag{1.121}$$

This equation could, e.g. be solved iteratively using the approximation $m_\mathrm{f}(\omega) \approx m_\mathrm{f}(\omega_{00})$ as a starting value for $m_\mathrm{f}(\omega)$ where $\omega_{00} = \sqrt{k_0/m_0}$ is the resonance eigenfrequency for the unloaded resonator. For weak frequency dependence of $m_\mathrm{f}(\omega)$ or small resonance frequency shifts, this first approximation may already be considered as sufficiently accurate. With this simple approximation it is found that

$$\omega_0 \approx \omega_{01} = \sqrt{\frac{k_0}{m_0 + m_\mathrm{f}(\omega_{00})}} \tag{1.122}$$

which represents the decrease of resonance frequency associated with the added mass as expected. ω_{01} is the approximated value for ω_0 after the first iteration. Similarly, for Q we find

$$Q \approx Q_1 = \frac{1}{\omega_0} \cdot \frac{k_0}{c_0 + c_\mathrm{f}(\omega_{00})}. \tag{1.123}$$

The exact values for ω_0 and Q are

$$\omega_0 = \sqrt{\frac{k_0}{m_0 + m_\mathrm{f}(\omega_0)}} \quad \text{and} \quad Q = \frac{1}{\omega_0} \cdot \frac{k_0}{c_0 + c_\mathrm{f}(\omega_0)} \tag{1.124}$$

yielding an implicit equation for ω_0.

Chapter 2

Theory and modeling

2.1 Fluid dynamics

2.1.1 Forces on oscillating objects

Using the equation of motion Eq. 1.109 for calculating $\underline{\boldsymbol{u}}$ and the relation for the stress tensor Eq. 1.106 introduced in Sec. 1.8.2, i.e.,

$$-\rho\,\omega^2\underline{\boldsymbol{u}} = \nabla\cdot(\boldsymbol{c}:\nabla_{\mathrm{s}}\,\underline{\boldsymbol{u}}) \qquad \text{and} \qquad \boldsymbol{T} = \boldsymbol{c}:\nabla_{\mathrm{s}}\,\boldsymbol{u}$$

the force on an oscillating object

$$\boldsymbol{F} = \int_V \boldsymbol{f}dV = \int_V \nabla\cdot\boldsymbol{T}dV = \int_A \boldsymbol{T}\cdot\boldsymbol{n}\,\mathrm{d}A \tag{2.1}$$

can be calculated, if a solution for $\underline{\boldsymbol{u}}$ is known.

2.1.2 In-plane oscillating plate

In the following, an oscillating plate with a given oscillation amplitude is assumed. It is considered that a translatory in-plane oscillating plate (with lateral extensions much larger than its thickness) yields only shear displacement in the liquid. Furthermore it is assumed, that the direction of motion of this plate coincides with the x-Axis of a cartesian coordinate system, i.e., $\underline{\boldsymbol{u}} = (\underline{u}_x, 0, 0)^{\mathrm{T}}$, c.f. Fig. 2.1. Thus the only non-vanishing component of the stress tensor (in Voigt-notation) is given by

$$T_{xz} = T_5 = \mathrm{j}\,\omega\,\eta\frac{\partial\underline{u}_x}{\partial z} \tag{2.2}$$

and the equation of motion of this one-dimensional problem is thus

$$-\rho\,\omega^2\underline{u}_x = c_{44}\frac{\partial^2\underline{u}_x}{\partial z} \qquad \text{with} \qquad c_{44} = \mathrm{j}\omega\eta. \tag{2.3}$$

Solving this equation for u_x yields an attenuated shear wave propagating in the surface normal direction (i.e., z-direction)

$$\underline{u}_x(z,t) = \hat{u}_x\,e^{-\frac{z}{\delta}}\,e^{-\mathrm{j}\left(\frac{z}{\delta}-\omega\,t\right)}, \tag{2.4}$$

where

$$\delta = \sqrt{\frac{2\,\eta}{\rho\,\omega}} \tag{2.5}$$

is the so-called penetration depth [84, 190], or decay length [97]. Resubstitution of $\underline{u}_x$ in the relation for the stress tensor, Eq. 2.2, substituting $z = 0$ to account for the liquid solid interface and applying Eq. 2.1 yields [MHc24]

$$\underline{F}_{\mathrm{p}} = \underline{u}_x\,A_{\mathrm{p}}\,(1-\mathrm{j})\sqrt{\frac{\eta\,\rho\,\omega^3}{2}} \tag{2.6}$$

for the fluid force which is induced into the liquid by the oscillating plate and thus acting on the latter. A_{p} is the surface of the plate and might be determined by a data fit. Comparison of coefficients of the latter and Eq. 1.118

$$\underline{F}_{\mathrm{F}}(\omega) = (c_{\mathrm{f}}(\omega) + \mathrm{j}\,\omega\,m_{\mathrm{f}}(\omega))\,\underline{v}(\omega)$$

yields for the additional effective fluid mass and damping parameter in case of the in-plane oscillating plate

$$m_{\mathrm{f,p}}(\omega) = \sqrt{\frac{\eta\,\rho}{2\,\omega}} A_{\mathrm{p}} \qquad \text{and} \qquad c_{\mathrm{f,p}}(\omega) = \sqrt{\frac{\eta\,\rho\,\omega}{2}} A_{\mathrm{p}}. \tag{2.7}$$

2.1.3 Rotating oscillating cylinders or tubes

Considering harmonically oscillating cylindrical objects in a viscous fluid with their axis coinciding with the axis of a cylindrical coordinate system and assuming liquid displacement only in φ-direction, i.e. $\underline{\boldsymbol{u}} = (u_r, u_\varphi, u_z)^{\mathrm{T}}$, where $u_r = u_z = 0$, only one component in the stress tensor [179]

$$\underline{T}_{r\varphi} = c_{44}\left(\frac{\partial \underline{u}_\varphi}{\partial r} - \frac{\underline{u}_\varphi}{r}\right) \qquad \text{where} \qquad c_{44} = \mathrm{j}\omega\eta \tag{2.8}$$

remains and using δ, Eq. 2.5, the equation of motion of this rotationally symmetric problem reads

$$\mathrm{j}\frac{2}{\delta^2}\underline{u}_\varphi = \frac{\partial^2 \underline{u}_\varphi}{\partial r^2} + \frac{1}{r}\frac{\partial \underline{u}_\varphi}{\partial r} - \frac{\underline{u}_\varphi}{r^2}. \tag{2.9}$$

The solution of this equation is

$$\underline{u}_\varphi(r) = A\,\mathrm{H}_1^1\left((1-\mathrm{j})\frac{r}{\delta}\right) + B\,\mathrm{H}_1^2\left((1-\mathrm{j})\frac{r}{\delta}\right) \tag{2.10}$$

where H_ν^i denotes Hankel's function of order ν and i-th kind. A and B have to be determined considering the boundary conditions.

Solid cylinder (rod)

For a solid cylinder with radius r_{c}, oscillating in a liquid with rotational displacement amplitude $\hat{u}_\varphi$ it follows for the displacement profile (outside of the cylinder), considering the boundary conditions for an outward propagating shear wave $\underline{u}_\varphi(r = r_{\mathrm{c}}) = \hat{u}_\varphi$ and $\underline{u}_\varphi(r \to \infty) = 0$

$$\underline{u}_\varphi(r) = \hat{u}_\varphi \frac{\mathrm{H}_1^2\left((1-\mathrm{j})\frac{r}{\delta}\right)}{\mathrm{H}_1^2\left((1-\mathrm{j})\frac{r_{\mathrm{c}}}{\delta}\right)}\,. \tag{2.11}$$

Taking into account that the radius of the cylinder r_{c} is constant, the relation for the force, Eq. 2.1, can be written as

$$\underline{F}_{\mathrm{r,t}} = T_{r\varphi}(r_{\mathrm{c}})\,n\,A_{\mathrm{c}} \tag{2.12}$$

where $n = 1$ in case of a solid cylinder (rod) and $n = -1$ for a tube. Note that instead of a torque, the tangential force acting on the cylinder is expressed here, to allow the comparison of rotational with transversal motions. Thus, using the Reynolds number

$$\mathrm{Re} = \frac{\rho\,\omega\,r_{\mathrm{c}}^2}{\eta} \tag{2.13}$$

and considering Eq. 2.5 for substituting δ it follows for the total tangential force F_{c} acting on the solid cylinder

$$\underline{F}_{\mathrm{r}} = (1-\mathrm{j})A_{\mathrm{c}}\sqrt{\frac{\rho\,\eta\,\omega^3}{2}}\left(-\mathrm{j}\frac{\mathrm{H}_2^2\left(\sqrt{-\mathrm{j}\,\mathrm{Re}}\right)}{\mathrm{H}_1^2\left(\sqrt{-\mathrm{j}\,\mathrm{Re}}\right)}\right) = \underline{F}_{\mathrm{p}}\left(-\mathrm{j}\frac{\mathrm{H}_2^2\left(\sqrt{-\mathrm{j}\,\mathrm{Re}}\right)}{\mathrm{H}_1^2\left(\sqrt{-\mathrm{j}\,\mathrm{Re}}\right)}\right) \tag{2.14}$$

assuming that the effective surface of the cylinder equals the effective surface of the plate, i.e., $A_{\mathrm{c}} = A_{\mathrm{p}}$ and that the amplitude of deflections of the plate and cylinder are equal, i.e., $\hat{u}_{\mathrm{p}} = \hat{u}_\varphi$.

Hollow cylinder (tube)

For a rotationally oscillating hollow cylinder (tube) filled with a liquid, the boundary conditions are $\underline{u}_\varphi(r = r_\mathrm{c}) = \hat{u}_\varphi$ and $\underline{u}_\varphi(r = 0) = 0$ and thus it follows for the displacement profile inside the cylinder:

$$u(r) = \hat{u}_\varphi \frac{\mathrm{J}_1\left((1-\mathrm{j})\frac{r}{\delta}\right)}{\mathrm{J}_1\left((1-\mathrm{j})\frac{r_\mathrm{c}}{\delta}\right)}\,, \tag{2.15}$$

where J_1 is the first kind, first order Bessel function. It follows for the force F_t acting on the tube

$$\underline{F}_\mathrm{t} = (1-\mathrm{j})A_\mathrm{c}\sqrt{\frac{\rho\eta\omega^3}{2}}\left(\mathrm{j}\frac{\mathrm{J}_2\left(\sqrt{-\mathrm{j}\,\mathrm{Re}}\right)}{\mathrm{J}_1\left(\sqrt{-\mathrm{j}\,\mathrm{Re}}\right)}\right) = \underline{F}_\mathrm{p}\left(\mathrm{j}\frac{\mathrm{J}_2\left(\sqrt{-\mathrm{j}\,\mathrm{Re}}\right)}{\mathrm{J}_1\left(\sqrt{-\mathrm{j}\,\mathrm{Re}}\right)}\right) \tag{2.16}$$

where again, it was assumed that the effective surfaces of the tube and the plate are identical.

Approximation of torsional shear waves by planar shear waves

A comparison of the relative deviations $\Delta^\mathrm{r}_\mathrm{pr}$ and $\Delta^\mathrm{r}_\mathrm{pt}$ of the solutions for the forces acting on the plate or the cylinder and the tube, respectively over Re are depicted in Fig. 2.1. Considering the cylinder's and tube's radii of $r_\mathrm{c} = 5\,\mathrm{mm}$ (c.f., [MHj1]) and the penetration depth of aqueous liquids at 1 kHz $\delta \approx 18\mu\mathrm{m}$, it follows $\mathrm{Re} = 157 \cdot 10^3$ and thus $\Delta^\mathrm{r}_\mathrm{pr} \approx \Delta^\mathrm{r}_\mathrm{pt} = 3.8 \cdot 10^{-3}$. As the solutions for the oscillating cylinders become quite unintuitive, this result suggests and substantiates the applicability and the validity of using the approximated solution of in-plane plate oscillations rather than the solution of torsionally oscillating cylinders for the case of millimeter-sized devices.

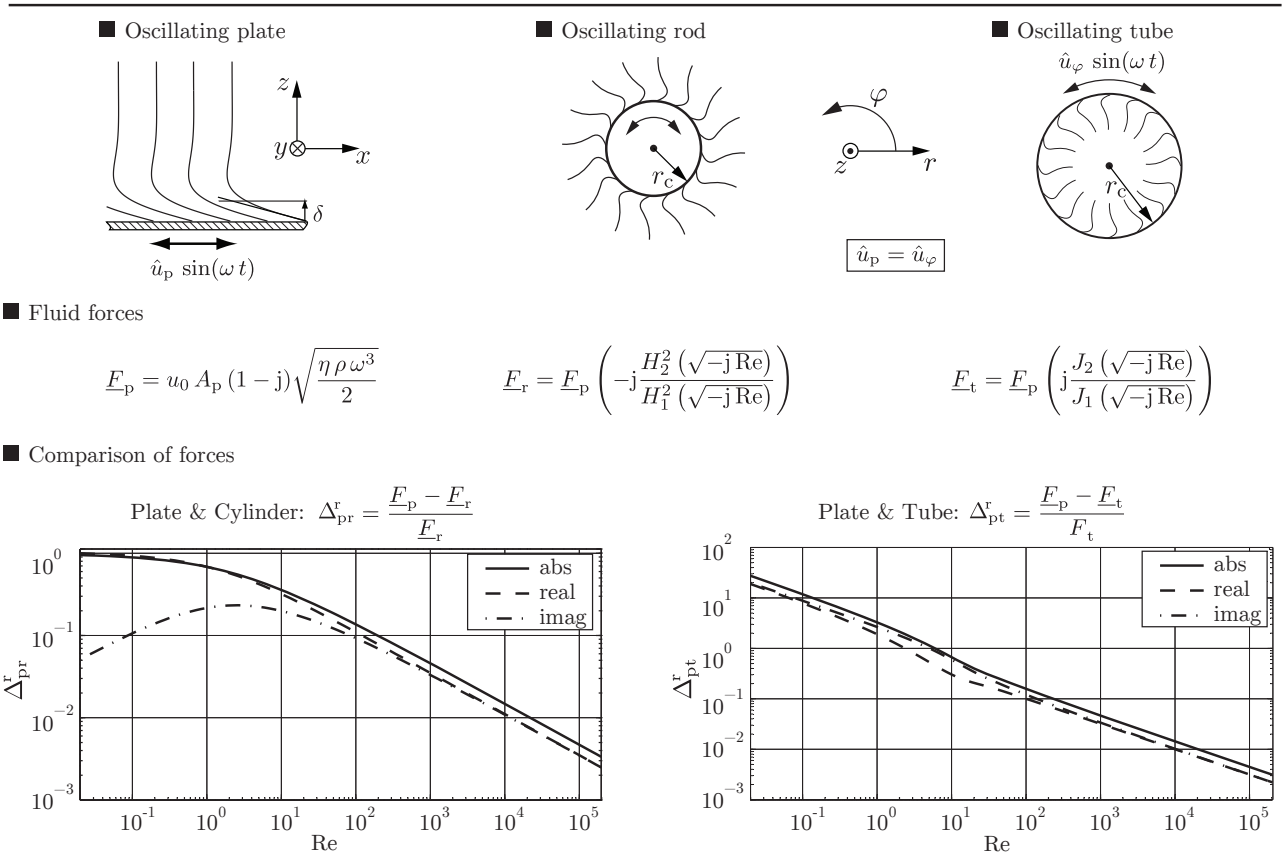

Figure 2.1: Comparison of the solutions for the fluid forces F_r, F_t and F_p acting on an oscillating solid cylinder (rod), a hollow cylinder (tube) with the liquid inside and an in-plane oscillating plate, respectively. For all three cases, the same surface interacting with the liquid is considered. In case of the solution for the cylinder and tube, Hankel and Bessel functions are obtained which make an intuitive interpretation of the obtained equations difficult. For high Reynolds numbers, i.e. for high ratios of the cylinders radius r_c and the penetration depth δ, the difference between both solutions is negligibly small.

2.1.4 Oscillating sphere

The fluid forces acting on a rigid sphere with radius r_s, oscillating with velocity $v(t)$ in one direction is [178]

$$\begin{aligned} F_\tau &= 6\,\pi\,\eta\,r_\mathrm{s}\left(1+\frac{r_\mathrm{s}}{\delta}\right)v(t) \\ &\quad +3\,\pi\,r_\mathrm{s}^2\sqrt{\frac{2\,\eta\,\rho}{\omega}}\left(1+\frac{2\,r_\mathrm{s}}{9\,\delta}\right)\frac{\partial v(t)}{\partial t}. \end{aligned} \tag{2.17}$$

Substituting the penetration depth δ, Eq. 2.5, in Eq. 2.17, transformation to the frequency domain and comparison of coefficients with Eq. 1.118 yields

$$\begin{aligned} m_{\mathrm{f,\,s}}(\omega) &= 3\,\pi\,r_\mathrm{s}^2\left(\sqrt{\frac{2\,\eta\,\rho}{\omega}}+\frac{2\,r_\mathrm{s}}{9}\,\rho\right) \quad \text{and} \\ c_{\mathrm{f,\,s}}(\omega) &= 6\,\pi\,r_\mathrm{s}\left(\eta+r_\mathrm{s}\sqrt{\frac{\omega\,\eta\,\rho}{2}}\right) \end{aligned} \tag{2.18}$$

for the fluid loading related additional mass and damping parameter in case of an oscillating sphere.

2.1.5 Transversally oscillating cylinder

The fluid force per unit length $\underline{F}'_\mathrm{c}$ on an oscillating cylinder with radius r_c, is e.g. given in [191–193] and reads:

$$\underline{F}'_\mathrm{c}(\omega) = -\pi\,\rho\,\omega^2\,r_\mathrm{c}^2\,\underline{\Gamma}_\mathrm{cyl}\,\underline{u}(\omega) \tag{2.19}$$

with

$$\underline{\Gamma}_\mathrm{cyl} = 1+\frac{4\,\mathrm{K}_1\left(\sqrt{\mathrm{j}\,\mathrm{Re}}\right)}{\sqrt{\mathrm{j}\,\mathrm{Re}}\,\mathrm{K}_0\left(\sqrt{\mathrm{j}\,\mathrm{Re}}\right)} \tag{2.20}$$

where the same expression, i.e. $\mathrm{Re}=\frac{\rho\,\omega\,r_\mathrm{c}^2}{\eta}$ as in Eq. 2.13 for the Reynold's number is used. K_0 and K_1 are zeroth and first order modified Bessel functions of second kind and $\underline{\Gamma}_\mathrm{cyl}$ is the so-called hydrodynamic function.

To allow evaluating the real and imaginary part of Eq. 2.19, necessary for calculating added mass $m_\mathrm{f,c}$ and damping parameter $c_\mathrm{f,c}$ for the oscillating cylinder, a second order series expansion of $\underline{\Gamma}_\mathrm{cyl}$ at $\mathrm{Re}\to\infty$ is performed, yielding

$$\underline{\Gamma}_\mathrm{cyl} \approx \underline{\Gamma}_\mathrm{cyl,T} = 1+\frac{4}{\sqrt{2\,\mathrm{Re}}}-\mathrm{j}\left(\frac{4}{\sqrt{2\,\mathrm{Re}}}+\frac{2}{\mathrm{Re}}\right) \tag{2.21}$$

where the subscript 'T' denotes the solution obtained by a Taylor series expansion. The relative deviations of real and imaginary parts $\Delta^\mathrm{r}\,\underline{\Gamma}_{\mathrm{cyl},\Re}$ and $\Delta^\mathrm{r}\,\underline{\Gamma}_{\mathrm{cyl},\Im}$ as well as of the absolute value $\Delta^\mathrm{r}\left|\underline{\Gamma}_\mathrm{cyl}\right|$of the approximated hydrodynamic function Eq. 2.21 and the exact solution Eq. 2.20 are depicted in Fig. 2.2. This comparison shows that for Reynolds numbers larger than 10, the deviation of the Taylor series approximated solution is less than 1 %.

Substituting the approximated solution of the hydrodynamic function, Eq. 2.21 in Eq. 2.19 and comparison of coefficients with the equation of the fluid forces F_F, Eq. 1.118, yields

$$\begin{aligned} m_{\mathrm{f,c}}(\omega) &\approx \pi\,r_\mathrm{c}^2\left(\rho+\frac{4}{\sqrt{2}\,r_\mathrm{c}}\sqrt{\frac{\eta\,\rho}{\omega}}\right)l_\mathrm{c} \quad \text{and} \\ c_{\mathrm{f,c}}(\omega) &\approx \left(2\,\pi\,\eta+\frac{4\,\pi}{\sqrt{2}}\,r_\mathrm{c}\sqrt{\omega\,\eta\,\rho}\right)l_\mathrm{c} \end{aligned} \tag{2.22}$$

for the added mass and damping parameters in case of the oscillating cylinder, where l_c is the length of the cylinder.

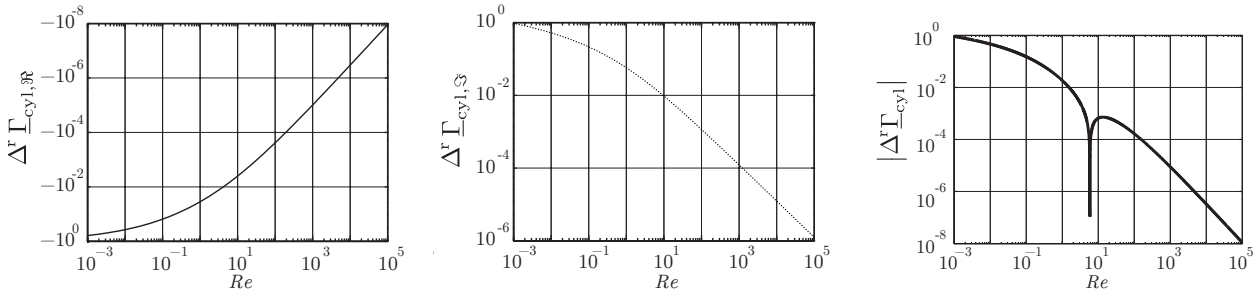

(a) Real part (b) Imaginary part (c) Absolute value

Figure 2.2: Relative deviations of the real part, the imaginary part and the imaginary value of the approximated hydrodynamic function Eq. 2.21 from the exact solution Eq. 2.20.

2.1.6 Transversally oscillating rectangular beam

In [192] Tuck et al. found that the hydrodynamic function for a circular cylinder and an infinitely thin rectangular beam are similar, i.e., the relative deviation between both functions never exceed $15 \cdot 10^{-2}$ for a range of Reynolds numbers from 10^{-1} to 10^3. In [193] Sader calculated a correction function $\Omega(\omega)$ relating the hydrodynamic functions of a rectangular and circular beam, i.e.,

$$\Gamma_{\mathrm{rect}}(\omega) = \Omega(\omega)\Gamma_{\mathrm{circ}}(\omega). \tag{2.23}$$

$\Omega(\omega)$ was calculated for the case of incompressible fluids and an infinitely thin beam oscillating in out-of-plane direction. Figure 2.3 shows a comparison between the hydrodynamic functions of a circular and a rectangular beam $\Gamma_{\mathrm{circ}}(\omega)$ and $\Gamma_{\mathrm{rect}}(\omega)$, the correction function $\Omega(\omega)$ versus Reynolds number Re as well as the relative deviations

$$|\Re(\Delta^r\Gamma)| = \left|\frac{\Re(\Gamma_{\mathrm{rect}}) - \Re(\Gamma_{\mathrm{circ}})}{\Re(\Gamma_{\mathrm{rect}})}\right|, \quad |\Im(\Delta^r\Gamma)| = \left|\frac{\Im(\Gamma_{\mathrm{rect}}) - \Im(\Gamma_{\mathrm{circ}})}{\Im(\Gamma_{\mathrm{rect}})}\right| \quad \text{and} \quad |\Delta^r\Gamma| = \left|\frac{|\Gamma_{\mathrm{rect}}| - |\Gamma_{\mathrm{circ}}|}{|\Gamma_{\mathrm{rect}}|}\right| \tag{2.24}$$

of real parts, imaginary parts and absolute values between circular and rectangular hydrodynamic functions.

In Fig. 2.3(a), a difference between both hydrodynamic functions can hardly be observed in the used display format. Fig. 2.3(b) shows real and imaginary part as well as absolute values of the correction function $\Omega(\omega)$ and in Fig. 2.3(c) it can be observed that the relative deviation $|\Delta^r\Gamma|$ between Γ_{rect} and Γ_{circ} is smaller than 0.15 in the investigated range of Reynolds numbers $\mathrm{Re} = 10^{-6} \ldots 10^4$. In contrast to this approach, where incompressible liquids were considered, Weiss et al. investigated in [194] the influence of the liquid's compressibility for an infinitely thin beam.

2.2 Mechanical resonators

According to an extended literature review which will be presented in Sec. 4.10, mechanical resonators used for viscosity and mass density sensing can be categorized in vibrating beams and membranes. Cantilever, U-shaped cantilever [87,195], [MHj4] and tuning fork [196,197], [MHj2] devices for example, can be represented by singly clamped beams whereas bridges and suspended plates can be interpreted as doubly clamped beams. In the following, the governing equations for transversally oscillating beams, rotationally oscillating resonators and a brief introduction for oscillating membranes is given.

2.2.1 Transverse vibrations of prismatic beams

Figure 2.4 shows the derivation of the Timoshenko and the Euler-Bernoulli beam and is intended to be self-explanatory. Further information can be found in fundamental textbooks for structural mechanics such as [198–201]. In this figure, the difference between Euler-Bernoulli and Timoshenko beam theory

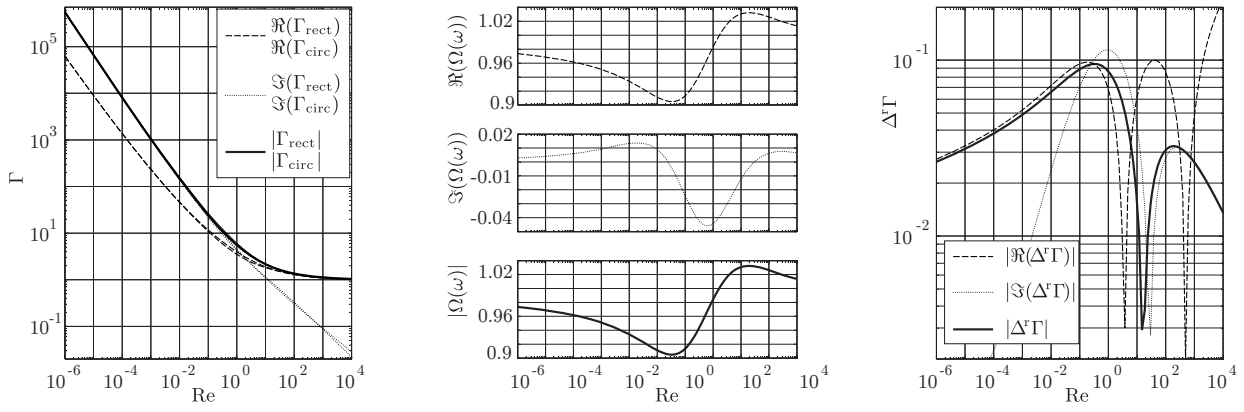

(a) Comparison of Γ_{rect} and Γ_{circ} (b) Correction function $\Omega(\omega)$ (c) Deviation of Γ_{rect} from Γ_{circ}

Figure 2.3: Illustration of the difference between the hydrodynamic functions Γ_{circ} and Γ_{rect} versus Reynolds number Re: a) A difference between Γ_{circ} and Γ_{rect} can hardly be observed. b) Real part, imaginary part and absolute values of the correction function $\Omega(\omega)$. c) Relative deviation of real part, imaginary part and absolute values of Γ_{rect} from Γ_{circ}.

is highlighted. The latter considers also displacement due to a finite shear modulus as well as the effect of the moment of inertia, which are neglected in classical Euler-Bernoulli beam theory. In [202, 203] a study on cantilevers immersed in liquid media using Timoshenko beam theory (i.e., considering shear deflection and rotatory moment of inertia) is presented. In Fig. 2.4 indices x and z for the deflection (u_x, u_z) are used to distinguish between deflection in x- and in z-direction which is necessary for deriving the governing equations. In the following however u only will be used to express the deflection in z-direction.

Considering a homogeneous, isotropic prismatic beam as it is depicted in 2.4, the general equation of motion for the deflection $u(x,t)$ in z-direction reads [204]:

$$E\,I_y\frac{\partial^4 u}{\partial x^4} - N\frac{\partial^2 u}{\partial x^2} + \rho\,A\frac{\partial^2 u}{\partial t^2} + c_0'\frac{\partial u}{\partial t} - \rho\,I_y\left(1+\frac{E\,A}{G\,A_{\text{s}}}\right)\frac{\partial^4 u}{\partial x^2\,\partial t^2} + \rho^2\frac{I_y\,A}{G\,A_{\text{s}}}\frac{\partial^4 u}{\partial t^4} = f \tag{2.25}$$

E: Young's modulus, I_y: second moment of area about the y-Axis, N: normal force within the beam, ρ beam's mass density, A cross-section of the beam (constant), c_0': damping parameter per unit length, G: shear modulus, $A_{\text{s}} = \kappa\,A$, where κ is a correction factor, which considers, that the shear stresses are not constant over the beam's cross secion (in z-direction), i.e. $\frac{\partial\tau(z)}{\partial z} \neq 0$, f: force per unit length resulting from the distributed load $q(x)$, c.f., Fig. 2.4.

The particular terms in the last equation are forces per unit length (f_i) in z-direction and are explained in the following:

- $E\,I_y\frac{\partial^4 u}{\partial x^4}$: f_i due to bending stiffness $E\,I_y$ where $I_y = \int_A z^2\,\mathrm{d}A$ and $I_y = \frac{w\,h^3}{12}$ for a rectangular beam with width w and thickness h as well as $I_y = \pi\frac{r^4}{4}$ for a circular beam with radius r
- $-N\frac{\partial^2 u}{\partial x^2}$: f_i due to normal stresses in the beam
- $\rho\,A\frac{\partial^2 u}{\partial t^2}$: f_i considering the translational inertia of the beam
- $c_0'\frac{\partial u}{\partial t}$: f_i considering (internal and external) damping
- $-\rho\,I_y\left(1+\frac{E\,A}{G\,A_{\text{s}}}\right)\frac{\partial^4 u}{\partial x^2\,t^2} + \rho^2\frac{I_y\,A}{G\,A_{\text{s}}}\frac{\partial^4 u}{\partial t^4}$: f_i considering the effect of shear displacement and rotational inertia

■ Resulting forces and moments due to positive deformation in x- and z-direction

3D view of deformed beam

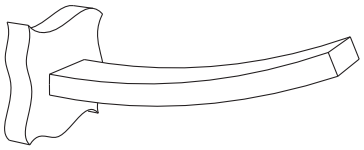

undeformed beam

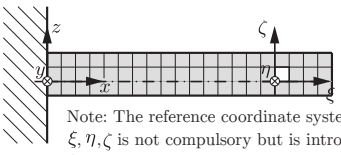

Note: The reference coordinate system ξ, η, ζ is not compulsory but is introduced for easier comprehansion.

deformed beam

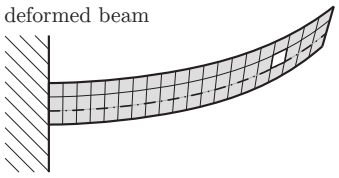

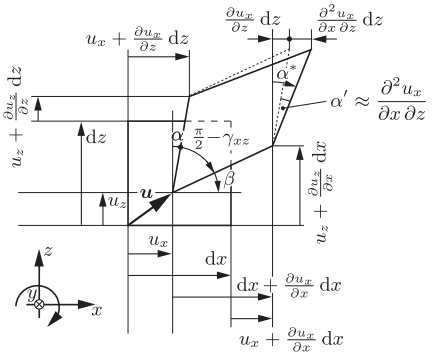

$$\sigma_x = E\,\varepsilon_x \qquad \tau_{xz} = G\,\gamma_{xz}$$

$$\varepsilon_x = \frac{\partial u_x}{\partial x}$$

$$\gamma_{xz} = \alpha + \beta$$

$$\alpha, \beta \ll \;\Rightarrow\; \begin{matrix}\tan\alpha, \beta = \alpha, \beta \\ \sin\alpha, \beta = \alpha, \beta \\ \cos\alpha, \beta = 1\end{matrix}$$

$$\varepsilon_x(\zeta) = \underbrace{\varepsilon_x(\zeta = 0)}_{0} + \frac{\partial \varepsilon_x}{\partial z}\,\mathrm{d}z$$

$$\approx \frac{\partial^2 u_x}{\partial x \partial z}\,\zeta$$

$$\sigma_x(\zeta) = E\,\frac{\partial^2 u_x}{\partial x \partial z}\,\zeta$$

$$\alpha \approx \tan\alpha = \frac{\frac{\partial u_x}{\partial z}\,\mathrm{d}z}{\mathrm{d}z + \frac{\partial u_x}{\partial z}} \approx \frac{\partial u_x}{\partial z}$$

$$\beta \approx \tan\beta = \frac{\frac{\partial u_z}{\partial x}\,\mathrm{d}x}{\mathrm{d}x + \frac{\partial u_x}{\partial x}} \approx \frac{\partial u_z}{\partial x}$$

$$\gamma_{xz} = \frac{\partial u_x}{\partial z} + \frac{\partial u_z}{\partial x}$$

$$\tau_{xz} = G\left(\frac{\partial u_x}{\partial z} + \frac{\partial u_z}{\partial x}\right)$$

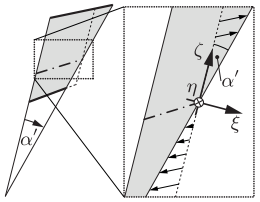

$$M_y = \int_A \zeta\,\sigma_x(\zeta)\,\mathrm{d}A$$

$$M_y = E\,\frac{\partial^2 u_x}{\partial x \partial z}\,\underbrace{\int_A \zeta^2\,\mathrm{d}A}_{I_y}$$

$$\boxed{M_y = E\,I_y\,\frac{\partial^2 u_x}{\partial x \partial z}}$$

$$F_\tau = \int_A \tau_{xz}\,\mathrm{d}A$$

Correction factor. Considers that $\frac{\partial \tau(\zeta)}{\partial \zeta} \neq 0$

$$F_\tau = \kappa\,G\,A\left(\frac{\partial u_x}{\partial z} + \frac{\partial u_z}{\partial x}\right)$$

$$\boxed{F_\tau = G\,A_\mathrm{s}\left(\frac{\partial u_x}{\partial z} + \frac{\partial u_z}{\partial x}\right)}$$

■ Deformation due to (distributed) load in z-direction

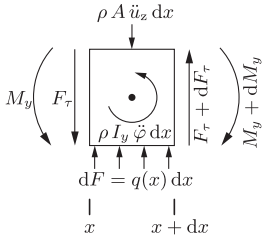

Equilibrium of forces:

$$\rho\,A\,\frac{\partial^2 u_z}{\partial t^2} = \frac{\mathrm{d}F_\tau}{\mathrm{d}x} + q$$

$$\boxed{\rho\,A\,\frac{\partial^2 u_z}{\partial t^2} - \frac{\partial}{\partial x}\left[G\,A_\mathrm{s}\left(\frac{\partial u_z}{\partial x} + \frac{\partial u_\mathrm{x}}{\partial z}\right)\right] = q(x)}$$

Moment equilibrium:

$$\rho\,I_y\,\frac{\partial^2 \varphi}{\partial t^2} = \frac{\mathrm{d}M_y}{\mathrm{d}x} - F_\tau$$

$$\boxed{\rho\,I_y\,\frac{\partial^2 \varphi}{\partial t^2} - \frac{\partial}{\partial x}\left(E\,I_y\,\frac{\partial^2 u_\mathrm{x}}{\partial x \partial z}\right) + G\,A_\mathrm{s}\left(\frac{\partial u_z}{\partial x} + \frac{\partial u_\mathrm{x}}{\partial z}\right) = 0}$$

■ For a constant cross section, these equations can be express as one single equation which reads:

Timoshenko beam

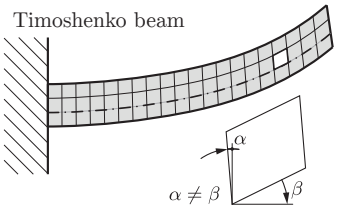

$$\boxed{E\,I_y\,\frac{\partial^4 u_z}{\partial x^4} + \rho\,A\,\frac{\partial^2 u_z}{\partial t^2} - \rho\,I_y\left(1 + \frac{E\,A}{G\,A_\mathrm{s}}\right)\frac{\partial^4 u_z}{\partial x^2 \partial t^2} + \rho^2\,\frac{I_y\,A}{G\,A_\mathrm{s}}\,\frac{\partial^4 u_z}{\partial t^4} = q(x) - \frac{E\,I_y}{G\,A_\mathrm{s}}\,\frac{\partial^2 q(x)}{\partial x^2} + \frac{\rho\,I_y}{G\,A_\mathrm{s}}\,\frac{\partial q(x)}{\partial t^2}}$$

■ For the case, that the beam is rigid against shear, it follows $G\,A_\mathrm{s} \to \infty$ and thus $\frac{\partial u_x}{\partial z} = -\frac{\partial u_z}{\partial x}$

and neglecting the moment of inertia per unit length, i.e. $\rho\,I_y \to 0$ yields

Euler-Bernoulli beam

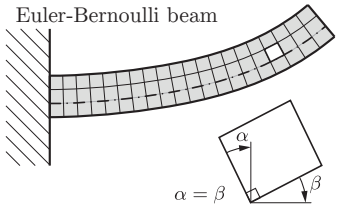

$$\boxed{E\,I_y\,\frac{\partial^4 u_z}{\partial x^4} + \rho\,A\,\frac{\partial^2 u_z}{\partial t^2} = q(x)}$$

$$\boxed{M_y = -E\,I_y\,\frac{\partial^2 u_z}{\partial x^2}}$$

$$\boxed{\frac{\mathrm{d}M_y}{\mathrm{d}x} = -E\,I_y\,\frac{\partial^3 u_z}{\partial x^3} = F_\tau}$$

$$\boxed{\frac{\mathrm{d}F_\tau}{\mathrm{d}t} = -E\,I_y\,\frac{\partial^4 u_z}{\partial x^4} = \rho\,A\,\frac{\partial^2 u_z}{\partial t^2} - q(x)}$$

Figure 2.4: Derivation of Timoshenko and Euler Bernoulli beam. In the first part internal moments about the y-axis and shear forces due to the deformation of the beam are derived. With these results, in the second part, a set of two equations of motion is obtained for a distributed load. In the third part, considering a constant cross-section, the Timoshenko beam equation is derived and neglecting shear and rotational inertia, in the last part yields the Euler-Bernoulli equation.

Dominating bending stiffness (Euler-Bernoulli-Beam)

Considering a time dependence $\mathrm{e}^{\mathrm{j}\,\omega\,t}$, with $\mathrm{j}^2 = -1$, angular frequency ω and time variable t, the equation of motion for transverse free vibrations of a beam with dominating bending stiffness $E\,I_y$ and its solution using complex notation for the deflection $\underline{u}$ read

$$\frac{\partial^4 \underline{u}}{\partial x^4} - \omega^2 \frac{\rho\,A}{E\,I_y}\,\underline{u} = 0 \tag{2.26}$$

and

$$\underline{u}(x) = C_1 \sin\frac{\lambda_i}{L}\,x + C_2 \cos\frac{\lambda_i}{L}\,x + C_3 \sinh\frac{\lambda_i}{L}\,x + C_4 \cosh\frac{\lambda_i}{L}\,x. \tag{2.27}$$

Where L is the length of the beam and λ_i is the eigenvalue of the i-th vibrational mode. The constants C_j have to be determined by taking the boundary conditions into account which can be expressed by considering the amplitude of the deflection $\underline{u}(\mathrm{x})$, the slope of the amplitude of the deflection $\frac{\partial \underline{u}(x)}{\partial x}$, the bending moment about the y-axis $M_y(x)$, the shear force $F_\tau(x)$ and the shear force per unit length $f_\tau(x)$ acting on the beam with which the higher order derivatives for $\underline{u}(x)$ can be expressed as follows, c.f. Fig. 2.4:

$$\frac{\partial^2 \underline{u}(x)}{\partial x^2} = -\frac{M_y(x)}{E\,I_y}, \qquad \frac{\partial^3 \underline{u}(x)}{\partial x^3} = -\frac{F_\tau(x)}{E\,I_y} \qquad \text{and} \qquad \frac{\partial^4 \underline{u}(x)}{\partial x^4} = \frac{f_\tau(x)}{E\,I_y}. \tag{2.28}$$

Most prominent examples of micro-resonators are resonating cantilevers and bridges see Sec. 4.10.2, which can be described by singly and doubly clamped beams, respectively. For calculating the natural frequencies and the mode shapes of undamped, free oscillations of these devices the boundary conditions for the singly clamped beam

$$\underline{u}(0) = 0, \quad \left.\frac{\partial \underline{u}(x)}{\partial x}\right|_{x=0} = 0, \quad \left.\frac{\partial^2 \underline{u}(x)}{\partial x^2}\right|_{x=L} = 0, \quad \left.\frac{\partial^3 \underline{u}(x)}{\partial x^3}\right|_{x=L} = 0 \tag{2.29}$$

and the doubly clamped beam

$$\underline{u}(0) = 0, \quad \left.\frac{\partial \underline{u}(x)}{\partial x}\right|_{x=0} = 0, \quad \underline{u}(L) = 0, \quad \left.\frac{\partial \underline{u}(x)}{\partial x}\right|_{x=L} = 0 \tag{2.30}$$

are considered. For both cases, the first two boundary conditions yield $C_3 = -C_1$ and $C_4 = -C_2$. Substituting these relations in Eq. 2.27 and calculating the third and fourth boundary conditions with the obtained equation for $\underline{u}(x)$ yields two equations which can be written in Matrix notation

$$\boldsymbol{A}(\lambda) \cdot \begin{bmatrix} C_1 \\ C_2 \end{bmatrix} = 0. \tag{2.31}$$

Claiming $\det(\boldsymbol{A}) = 0$ yields transcendental equations for the infinite number of eigenvalues λ_i, with which the angular eigenfrequencies $w_{0,i}$ of the i–th mode of undamped, free oscillations can be calculated. It follows that

$$\omega_{0,i} = \frac{\lambda_i^2}{L^2}\sqrt{\frac{E\,I_y}{\rho\,A}}. \tag{2.32}$$

For calculating the mode shape function of the i-th mode for the singly and doubly clamped beam, considering $C_3 = -C_1$ and $C_4 = -C_2$ in Eq. 2.27 and dividing the latter by C_2 yields

$$\widetilde{U}_i(\xi) = \cos\lambda_i\xi + \cosh\lambda_i\xi + \widetilde{C}_i\,(\sin\lambda_i\xi + \sinh\lambda_i\xi) \qquad \text{with} \qquad \xi = \frac{x}{L} \tag{2.33}$$

Where $\widetilde{.}$ is used to express ta quantity used for the mode shape function. The coefficient $\widetilde{C}_i$ is calculated solving

$$\boldsymbol{A}(\lambda_i) \cdot \begin{bmatrix} \widetilde{C}_i \\ 1 \end{bmatrix} = 0. \tag{2.34}$$

For both, the singly and the doubly clamped beam, the equations from which λ_i and $\widetilde{C}_i$ can be calculated as well as their values for the first modes and evaluated mode shapes are shown in Tab. 2.1.

Dominating normal stresses (string)

The equation of motion in the frequency domain for free, transversal oscillations of a beam with dominant tensile (normal) forces N and its solution read

$$\frac{\partial^2 \underline{u}(x)}{\partial x^2} + \frac{\omega^2}{a^2}\underline{u}(x) = 0 \qquad \text{with} \qquad a = \sqrt{\frac{N}{\rho\, A}} \tag{2.35}$$

and

$$\underline{u}(x) = C_1 \sin\frac{\omega\, x}{a} + C_2 \cos\frac{\omega\, x}{a}. \tag{2.36}$$

Taking the boundary conditions $\underline{u}(0) = 0$ and $\underline{u}(L) = 0$ into account,

$$\omega_{0,i} = \frac{i\,\pi}{L}\sqrt{\frac{N}{\rho\, A}} \tag{2.37}$$

and

$$\widetilde{U}_i(\xi) = \sin i\,\pi\,\xi \tag{2.38}$$

are found for the natural angular frequencies and the mode shape function. The mode shapes of the first three modes are depicted in Tab. 2.1.

2.2.2 Torsional vibrations

A common principle of a torsional resonator [205], [MHj1] is depicted in Tab. 2.1. There, a solid mass is supported by two torsional springs. Due to the device's symmetry, only one half of the torsional resonator is considered. The partial differential equation describing the twisting of the flexible bar reads

$$\frac{\partial T}{\partial x} - \rho\, I_\mathrm{p}\frac{\partial^2 \varphi}{\partial t^2} = 0 \qquad \text{with} \qquad T = G\, I_\mathrm{p}\frac{\partial \varphi}{\partial x} \tag{2.39}$$

where φ is the twisting angle, G is the shear modulus, and $I_\mathrm{p} = \int_A r^2\,\mathrm{d}A = \int_A (y^2+z^2)\,\mathrm{d}A = I_y + I_z$ [199] is the polar moment of area and is $I_\mathrm{p} = \pi\frac{R^4}{2}$ for a torsional cylinder with radius R. Equation 2.39 is transformed to the frequency domain

$$\frac{\partial^2 \underline{\varphi}}{\partial x^2} + \frac{\omega^2}{b^2}\underline{\varphi} = 0 \qquad \text{where} \qquad b = \sqrt{\frac{G}{\rho}} \tag{2.40}$$

which is the same form as Eq. 2.35 and thus

$$\underline{\varphi}(x) = C_1 \sin\frac{\omega\, x}{b} + C_2 \cos\frac{\omega\, x}{b}. \tag{2.41}$$

Considering the twisting angle and the expression for the internal torque in Eq. 2.39 and the torque resulting from the moment of inertia of the solid mass, the boundary conditions can be expressed as

$$\underline{\varphi}(0) = 0 \qquad \text{and} \qquad \left.\frac{\partial \underline{\varphi}}{\partial x}\right|_{x=L} = \frac{J}{G\, I_\mathrm{p}}\omega^2\, \underline{\varphi}(L) \tag{2.42}$$

where J is the moment of inertia of the mass attached at the singly clamped, torsional beam's end. By solving the boundary conditions, the transcendental equation

$$\cot(\lambda) = \frac{1}{\beta}\lambda \qquad \text{with} \qquad \beta = \frac{I_\mathrm{p}\,\rho\, L}{J} \tag{2.43}$$

for the eigenvalues is found. The eigenvalues depend on β and thus can not be given for a general case. With the solutions for λ_i the eigenfrequencies of free torsional vibrations

$$\omega_{0,i} = \frac{\lambda_i}{L}\sqrt{\frac{G}{\rho}} \tag{2.44}$$

and the mode shape functions

$$\widetilde{\Phi}_i(\xi) = \sin\lambda_i\,\xi \tag{2.45}$$

can be calculated.

Device	Mode shape	$\widetilde{C}_i$	Eigenvalues	Eigenfrequencies
Singly clamped beam 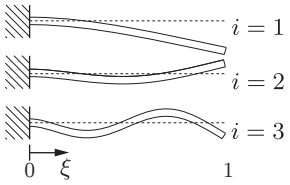	$\widetilde{U}_i(\xi) = \cos\lambda_i\xi + \cosh\lambda_i\xi + \widetilde{C}_i\,(\sin\lambda_i\xi + \sinh\lambda_i\xi)$	$\widetilde{C}_i = \dfrac{\sin\lambda_i - \sinh\lambda_i}{\cos\lambda_i - \cosh\lambda_i}$ $\widetilde{C}_1$=−0.734 095 513 759 $\widetilde{C}_2$=−1.018 467 318 759 $\widetilde{C}_3$=−0.999 224 496 517	$\lambda_i = \operatorname{acos}\dfrac{-1^i}{\cosh\lambda_i} + (i-1)\,\pi$ λ_1=1.875 104 068 712 λ_2=4.694 091 132 974 λ_3=7.854 757 438 237	$\omega_{0,i} = \dfrac{\lambda_i^2}{L^2}\sqrt{\dfrac{E\,I}{\rho\,A}}$
Doubly clamped beam 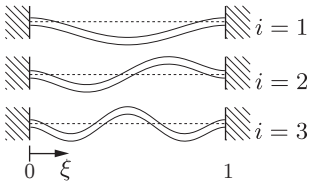		$\widetilde{C}_i = \dfrac{\cos\lambda_i - \cosh\lambda_i}{\sin\lambda_i - \sinh\lambda_i}$ $\widetilde{C}_1$=−0.982 502 214 576 $\widetilde{C}_2$=−1.000 777 311 907 $\widetilde{C}_3$=−0.999 966 450 125	$\lambda_i = \operatorname{acos}\dfrac{-1^i}{\cosh\lambda_i} + i\,\pi$ λ_1=4.730 040 744 863 λ_2=7.853 204 624 096 λ_3=10.995 607 838 002	
Streched wire 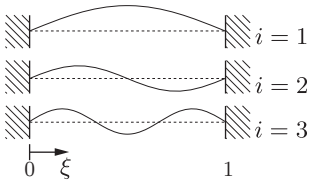	$\widetilde{U}_i(\xi) = \sin\lambda_i\,\xi$	—	$\lambda_i = i\,\pi$	$\omega_{0,i} = \dfrac{i\,\pi}{L}\sqrt{\dfrac{N}{\rho\,A}}$
Torsional resonator 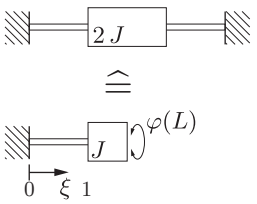	$\widetilde{\Phi}_i(\xi) = \sin\lambda_i\,\xi$	—	$\lambda_i = \operatorname{acot}\dfrac{\lambda_i}{\beta} + (i-1)\,\pi$ The eigenvalues λ_1,λ_2 and λ_3 are depicted over β below.	$\omega_{0,i} = \dfrac{\lambda_i}{L}\sqrt{\dfrac{G}{\rho}}$
	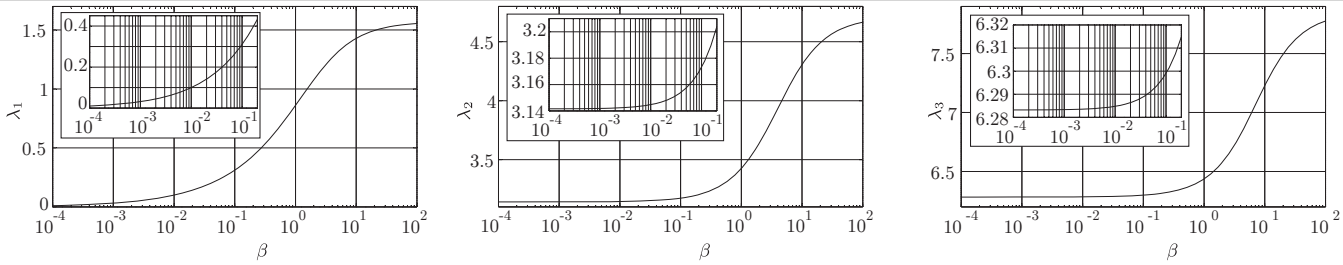			

Table 2.1: Overview of fundamental resonators

2.2.3 Theory of vibrating plates and membranes

Similar to the beams, plates show resonant modes which can be used for fluid sensing applications. The differential equation obtained from the Kirchhoff plate theory [206] is given by

$$\rho h \frac{\partial^2 u}{\partial t^2} + D\left(\frac{\partial^4 u}{\partial x^4} + 2\frac{\partial^4 u}{\partial x^2 \partial y^2} + \frac{\partial^4 u}{\partial y^4}\right) = f^{\mathrm{A}}(x, y, t) \tag{2.46}$$

The quantities D and f^{A} denote the bending stiffness $D = Eh^3/(12(1-\nu^2))$ and the transverse loading force per unit area, respectively. Poisson's ratio is denoted by ν. For a rectangular plate the resonance frequencies are determined by

$$f_{i,j} = \frac{\lambda_{i,j}^2}{2\pi a^2}\sqrt{\frac{D}{\rho h}}\,, \tag{2.47}$$

where a denotes the length of the plate and $\lambda_{i,j}^2$ the dimensionless frequency parameter for a given (i/j)-mode (i.e., i/j denote the number of antinodes in x/y-direction). This parameter is tabulated for different boundary conditions (free, pinned, clamped) and length to width ratios of the plate e.g., in [207]. The implementation of tensile forces into Eq. 2.46 is complex and is shown e.g, in [208]. However, the influence of moderate tensile forces on the resonance frequency can be approximated by

$$g_{i,j} = \sqrt{\left(f_{i,j}^2 + \frac{N_x B_i}{4\rho h a^2} + \frac{N_y B_j}{4\rho h b^2}\right)}\,. \tag{2.48}$$

The dimensionless coefficients B_i and B_j are functions of the boundary conditions applied at the length a and b and can be found in [207] and [209].

For dominant tensile stresses or negligible bending stiffness, the plate theory can be substituted by the theory of membranes, which is the two-dimensional analogon of the string. The resonance frequency for a tensile stress N per unit length at the edges is given by

$$f_{i,j} = \frac{\lambda_{i,j}}{2}\sqrt{\left(\frac{N}{\rho h a b}\right)} \tag{2.49}$$

with [207]

$$\lambda_{i,j} = \sqrt{i^2\frac{b}{a} + j^2\frac{a}{b}}. \tag{2.50}$$

2.2.4 Frequency tuning

Higher modes

The operation of resonators at several modes allows measuring at different discrete frequencies without any modifications of the device. The ratio between the resonance frequencies of higher and fundamental modes depends on the type of resonator. For singly clamped beams for example, the ratio between second and first resonance frequency is 6.27 which was also approximately achieved by measurements with tuning forks [MHj2] and U-shaped wires [MHj4].

The ratio of higher and the fundamental resonance frequency is only dependent of the particular eigenvalues λ_i for a given type of resonator. For the examples discussed before, we get

$$\left.\frac{\omega_{0,i}}{\omega_{0,1}}\right|_{\text{beam}} = \frac{\lambda_i^2}{\lambda_1^2}, \qquad \left.\frac{\omega_{0,i}}{\omega_{0,1}}\right|_{\text{string}} = i, \qquad \text{and} \qquad \left.\frac{\omega_{0,i}}{\omega_{0,1}}\right|_{\text{tors.}} = \frac{\lambda_i}{\lambda_1} \tag{2.51}$$

for the singly and doubly clamped beam, the stretched string and the torsional resonator, respectively.

Scaling

By changing the dimensions of the resonator, e.g. the length of a stretched string or the thickness of a singly clamped beam, the resonance frequency can be adjusted. In the following, an overview of the effect of changing the particular resonator's length L, its diameter R, height h, width w on its resonance frequencies (of any but the same resonant mode i) is given where applicable. For this, the particular dimension is normalized to 1.

The resonance frequency of the torsional resonator strongly depends on β, given in Eq. 2.43, which influences the solution for λ, which can not be expressed analytically. Assuming that the inertia of the torsional resonator is mainly affected by the mass which is supported by the torsional springs, the torsional resonator can be considered as a lumped element resonator with a lumped mass supported by a lumped torsional spring, see also [MHj1] and thus, the first resonance frequency of the torsional resonator can be expressed as:

$$\omega_0 = \sqrt{\frac{G\,\pi}{J\,L}} R^2. \tag{2.52}$$

For beams, strings and torsional resonators it follows:

- **Change in length**

$$\left.\frac{\omega_{0,i}(L)}{\omega_{0,i}(1)}\right|_{\text{beam}} = \frac{1}{L^2}, \qquad \left.\frac{\omega_{0,i}(L)}{\omega_{0,i}(1)}\right|_{\text{string}} = \frac{1}{L}, \qquad \left.\frac{\omega_{0}(L)}{\omega_{0}(1)}\right|_{\text{tors.}} = \frac{1}{\sqrt{L}} \tag{2.53}$$

- **Change in radius** for circular cross-sectioned structures

$$\left.\frac{\omega_{0,i}(R)}{\omega_{0,i}(1)}\right|_{\text{beam}} = R, \qquad \left.\frac{\omega_{0,i}(R)}{\omega_{0,i}(1)}\right|_{\text{string}} = \frac{1}{R}, \qquad \left.\frac{\omega_{0}(R)}{\omega_{0}(1)}\right|_{\text{tors.}} = R^2 \tag{2.54}$$

- **Change in height** for rectangular cross-sectioned structures

$$\left.\frac{\omega_{0,i}(h)}{\omega_{0,i}(1)}\right|_{\text{beam}} = h, \qquad \left.\frac{\omega_{0,i}(h)}{\omega_{0,i}(1)}\right|_{\text{string}} = \frac{1}{\sqrt{h}} \tag{2.55}$$

- **Change in width** for rectangular cross-sectioned structures

$$\left.\frac{\omega_{0,i}(w)}{\omega_{0,i}(1)}\right|_{\text{beam}} = 1, \qquad \left.\frac{\omega_{0,i}(w)}{\omega_{0,i}(1)}\right|_{\text{string}} = \frac{1}{\sqrt{w}} \tag{2.56}$$

Miniaturization – total scaling

To estimate the influence of miniaturizing a resonator, it is assumed that every dimension is miniaturized by the same factor. Thus, it follows for the resonance frequency change, modifying each dimension by the same scaling factor $\widetilde{L}$

$$\left.\frac{\omega_{0,i}(\widetilde{L})}{\omega_{0,i}(1)}\right|_{\text{beam}} = \frac{1}{\widetilde{L}}, \qquad \left.\frac{\omega_{0,i}(\widetilde{L})}{\omega_{0,i}(1)}\right|_{\text{string}} = \frac{1}{\widetilde{L}^2}, \qquad \text{and} \qquad \left.\frac{\omega_{0,i}(\widetilde{L})}{\omega_{0,i}(1)}\right|_{\text{tors.}} = \frac{1}{\widetilde{L}}. \tag{2.57}$$

Stress variation

For changing the resonance frequency of a doubly clamped structure without changing its geometry, the tensile stresses in the structure can be changed. The ratio of the resonance frequency of a doubly clamped beam with dominant normal stresses, Eq. 2.37, and the resonance frequency of a beam with no normal stresses, Eq. 2.32, is

$$\frac{\omega_0(N)}{\omega_{0,\text{beam}}} = \frac{L\,i\,\pi}{\lambda_i^2}\sqrt{\frac{N}{\rho\,A}}. \tag{2.58}$$

In [210, 211] frequencies from 2000 Hz to 2300 Hz, approximately were achieved for a doubly clamped titanium beam and in [MHj5] resonance frequencies between 820 Hz to 4040 Hz were obtained for a 3 cm long, 100 µm thick tungsten wire by changing the normal stresses in the wire. Tungsten features relatively high yield stresses of approximately 600 MPa [212] and a relatively high mass density of 19.25 g/cm^3 [213, 214]. With high strength steel alloys an even higher frequency range could be obtained as they feature yield stresses up to 1.6 GPa [215] and a mass density of 7.8 g/cm^3 [216]. However, tuning the resonance frequency by stretching the resonator by a factor higher than 10 is hardly possible with common materials and aspect ratios applicable for reasonable sensor designs.

2.3 Temperature dependence of the resonance frequency

The equations for the resonance frequency of singly and doubly clamped beams (with dominant bending stiffness) are identical, c.f., Eq. 2.32. The theory of the resonance frequency's temperature dependence discussed in Secs.2.3.1 – 2.3.3 is only valid if free elongation capability is guaranteed. This however, is usually only the case for singly but not for doubly clamped beams. For the latter, the theory of the resonance frequency's temperature dependence of strings discussed in Sec. 2.3.4 can be applied.

2.3.1 Singly clamped beams

The temperature dependent angular eigenfrequency of mode i can be given by

$$\omega_{0,i}(T) = C_i \frac{D(T)}{L(T)^2} \sqrt{\frac{E(T)}{\rho(T)}} \tag{2.59}$$

where C_i is a factor of the i-th resonant mode and D can either be the radius R of the circular beam or the thickness h of a rectangular beam. For small variances, the change of the resonance frequency $\Delta\omega_{0,i}$ affected by the thermally induced changes ΔD, ΔL, ΔE and $\Delta\rho$ can be approximatively calculated using the relation

$$\frac{\Delta\omega_{0,i}}{\omega_{0,i}} \approx \frac{\Delta E}{2E} + \frac{\Delta D}{D} - 2\frac{\Delta L}{L} - \frac{\Delta\rho}{2\rho}. \tag{2.60}$$

Assuming the applicability of linear thermal expansion $\Delta L \approx \alpha\, L\, \Delta T$ it follows

$$\frac{\Delta D}{D} = \frac{\Delta L}{L} \approx \alpha \Delta T \tag{2.61}$$

and with $\rho = m/V$ and $\Delta V/V = 3\,\alpha\,\Delta T$ it follows for the relative change of mass density

$$\frac{\Delta\rho}{\rho} \approx -3\,\alpha\,\Delta T \tag{2.62}$$

Thus, the equation for the thermally induced relative change of the i-th resonance frequency reads

$$\frac{\Delta\omega_{0,i}}{\omega_{0,i}} \approx \frac{\Delta E}{2\,E} + \frac{1}{2}\,\alpha\,\Delta T. \tag{2.63}$$

2.3.2 Young's modulus as a function of the melting point

In [217], the Young's modulus temperature dependency is given by

$$E(T) \approx E_0(1 - \kappa\frac{T}{T_\mathrm{M}}), \tag{2.64}$$

where E_0 is the Young's modulus at $T = 0\,\mathrm{K}$ and T_M is the melting point. For metals $\kappa = 0.5$ whereas it is $\kappa = 0.3$ for crystals. From this relation it follows for the relative change of the Young's modulus with respect to the change of temperature

$$\left.\frac{\Delta E}{E}\right|_T = \frac{\Delta T}{(T - T_\mathrm{M}/\kappa)} \tag{2.65}$$

which is substituted in Eq. 2.63 and thus, it follows that

$$\frac{\Delta\omega_{0,i}}{\omega_{0,i}} \approx \frac{1}{2}\left(\frac{1}{T - T_\mathrm{M}/\kappa} + \alpha\right)\Delta T \tag{2.66}$$

For plain carbon steel (AISI-SAE 1020) with $\vartheta_\mathrm{M} = 1515\,^\circ\mathrm{C}$, $\alpha = 10.8 \cdot 10^{-6}$ [154] and tungsten $\vartheta_\mathrm{M} = 3420\,^\circ\mathrm{C}$, $\alpha = 4.2 \cdot 10^{-6}$ [214] it follows

$$\left.\frac{\Delta f}{f_\mathrm{r}}\right|_\mathrm{steel} \approx -147 \cdot 10^{-6}\Delta T \qquad \text{and} \qquad \left.\frac{\Delta f}{f_\mathrm{r}}\right|_\mathrm{tungsten} \approx -68 \cdot 10^{-6}\Delta T. \tag{2.67}$$

2.3.3 Correlation of the thermal expansion and melting point

As a rule of thumb, the linear thermal expansion coefficient α is smaller, the higher the melting point T_M, which seems to be valid for metals with a melting point higher than 1500 °C, see Fig. 2.5. There, α is plotted versus the melting point ϑ_M in °C for pure metals and for alloys given in [154] with melting points higher than 500 °C. The regression curve depicted there reads

$$\alpha^*(T_\mathrm{M}) = \frac{0.014}{233.756\,\mathrm{K} + T_\mathrm{M}}. \tag{2.68}$$

Substituting this relation in Eq. 2.66 yields an equation giving a rough estimation of the resonance frequency's dependence to temperature for metals at 25 °C:

$$\frac{\Delta\omega_{0,i}}{\omega_{0,i}} \approx \frac{1}{2}\left(\frac{1}{298.15\,\mathrm{K} - 2\,T_\mathrm{M}} + \frac{0.014}{233.756\,\mathrm{K} + T_\mathrm{M}}\right)\Delta T. \tag{2.69}$$

Using the above values for melting points it follows for plain carbon steel and tungsten

$$\left.\frac{\Delta f}{f_\mathrm{r}}\right|_\mathrm{steel} \approx -149 \cdot 10^{-6}\Delta T \qquad \text{and} \qquad \left.\frac{\Delta f}{f_\mathrm{r}}\right|_\mathrm{tungsten} \approx -69 \cdot 10^{-6}\Delta T \tag{2.70}$$

which is in relatively good accordance with measured values obtained for a steel tuning fork ($\Delta f_\mathrm{r}/\Delta T = -118 \cdot 10^{-6}$) [MHj2] and a tungsten U-shaped wire ($\Delta f_\mathrm{r}/\Delta T = -60 \cdot 10^{-6}$) [MHj4]. For both materials, the effect of the the change of the Young's modulus on the thermally induced change of the resonance frequency is approximately 40 times higher than the effect of thermal expansion.

Material data bases for metals can be found in [213,218–220]. In [221] the Young's modulus of stretched tungsten wires at high temperatures is studied.

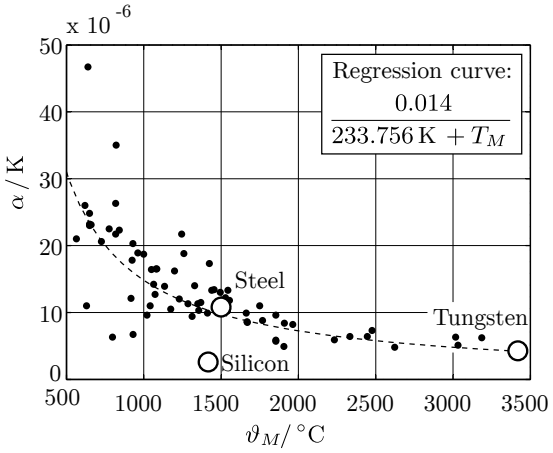

Figure 2.5: Correlation of linear thermal expansion coefficicent α and melting point T_M/K. Here, the thermal expansion coefficients are plotted over ϑ_M which is the melting point on the Celsius scale. The data for pure metals and alloys was taken from [154].

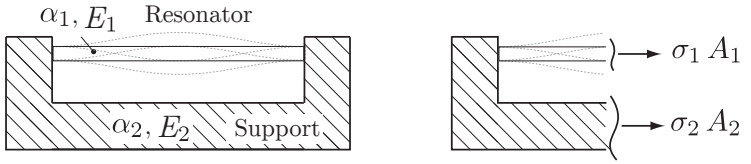

Figure 2.6: A doubly clamped beam with thermal expansion coefficient α_1 and Young's modulus E_1, being clamped in an other material with α_2 and E_2. Equal elongations as well as balanced forces resulting from the inner thermal tensile stresses σ_i are assumed. A_i are the materials effective cross-sections. [MHc19]

2.3.4 Strings

In this section the detuning of doubly clamped resonators due to the change of the ambient temperature is explained. For this, a prismatic beam being clamped with a different material, see Fig. 2.6, is considered. Both materials are assumed to be homogeneous and isotropic. The resonance frequency of a doubly clamped beam (assuming predominant normal stresses σ) is, c.f. Eq. 2.37

$$\omega_{0,i} = \frac{i\,\pi}{L}\sqrt{\frac{\sigma}{\rho}}. \tag{2.71}$$

The main effect of thermal detuning results from the change of normal stresses in the vibrating structure rather than from it's elongation. Thus, in this approach only thermally induced changes of tensile stresses are considered. The strain in one of both materials (denoted by i) is expressed as [222]

$$\varepsilon_i = \frac{\sigma_i}{E_i} + \alpha_i\,\Delta T. \tag{2.72}$$

Under the assumption, that both materials are equally elongated and considering balanced forces i.e. $\sigma_1\,A_1 = -\sigma_2\,A_2$ (σ is the normal stress and A the effective cross-section), the thermally induced tensile stress within the resonator is:

$$\sigma_1 = \frac{\alpha_2 - \alpha_1}{\frac{1}{E_1} + \frac{1}{E_2}\frac{A_1}{A_2}}\Delta T. \tag{2.73}$$

From this simple approach it becomes clear that similar temperature coefficients are favorable to effect low cross-sensitivity to temperature. The resonance frequency's change due to temperature is geometry dependent an thus, can not be given in a general form. However, in general, doubly clamped structures have a significantly higher dependence of their resonance frequency to temperature than singly clamped structures.

2.4 Vibrating structures described by second order systems

The time-dependent deflection $u(x,t)$ at axial position x at time t of a one-dimensional, vibrating structure can be composed by superposition of eigenmodes $\varphi_i(x)$ and time functions $q_i(t)$, i.e., [201]

$$u(x,t) = \sum_{i=0}^{\infty} \varphi_i(x) q_i(t), \tag{2.74}$$

where the index i denotes the particular vibrational mode. For simplicity in the following, one-dimensional models of structures are considered.

The deflection over x and t can also be composed by an infinite sum of solutions of second order systems with effective mass, stiffness, damping and excitation force m_i, k_i, c_i and F_i, respectively. Due to orthogonality of the eigenmodes, individual second order systems for each mode can be set up [200]:

$$m_i\ddot{q}_i(t) + c_i\dot{q}_i(t) + k_i q_i(t) = F_i(t). \tag{2.75}$$

The effective (lumped) parameters are derived by equivalence of energy expressions of kinetic and potential energy and the Rayleigh dissipation function. The approach is shown for beams of density $\rho(x)$, cross-section $A(x)$ and length L.

2.4.1 Effective mass m_i

Substituting $u(x,t)$, Eq. 2.74, into the expression for the instantaneous kinetic energy [201]

$$W_{\text{kin}}(t) = \frac{1}{2}\int_0^L \dot{u}^2(x,t)\rho(x)A(x)\mathrm{d}x, \tag{2.76}$$

where $(\dot{})$ denotes the derivative of a variable in respect to t, yields

$$W_{\text{kin}}(t) = \frac{1}{2}\int_0^L \left(\sum_{i=0}^{\infty}\varphi_i(x)\dot{q}_i(t)\right)^2 \rho(x)A(x)\mathrm{d}x. \tag{2.77}$$

For orthogonal eigenmodes with

$$\int_0^L \varphi_i(x)\varphi_j(x)\rho(x)A(x)\mathrm{d}x = 0 \qquad \text{for} \qquad i \neq j \tag{2.78}$$

it follows

$$W_{\text{kin}}(t) = \frac{1}{2}\sum_{i=0}^{\infty}\int_0^L \varphi_i^2(x)\dot{q}_i^2(t)\rho(x)A(x)\mathrm{d}x. \tag{2.79}$$

Equaling this equation with the expression of the kinetic Energy using a lumped mass m_i

$$W_{\text{kin}}(t) = \frac{1}{2}\sum_{i=0}^{\infty} m_i\dot{q}_i^2(t) \tag{2.80}$$

yields for the lumped mass of mode i:

$$m_i = \int_0^L \varphi_i^2(x)\rho(x)A(x)\mathrm{d}x. \tag{2.81}$$

2.4.2 Effective stiffness k_i

The potential energy of the beam with bending stiffness EI is

$$W_{\text{pot}} = \frac{1}{2}\int_0^L (u''(x,t))^2 EI(x)\mathrm{d}x, \tag{2.82}$$

$$= \frac{1}{2}\int_0^L (\sum_{i=0}^{\infty}\varphi_i''(x)q_i(t))^2 EI(x)\mathrm{d}x, \tag{2.83}$$

$$\tag{2.84}$$

and using again the the orthogonality condition, Eq. 2.78, it follows

$$W_{\text{pot}} = \frac{1}{2}\sum_{i=0}^{\infty}\int_0^L \varphi_i''(x)^2 q_i^2(t)EI(x)\mathrm{d}x \tag{2.85}$$

where $(''')$ denotes a second order derivative of a variable in respect to x. The potential energy can also be expressed using a lumped stiffness k_i

$$W_{\text{pot}} = \frac{1}{2}\sum_{i=0}^{\infty} k_i q_i(t)^2 \tag{2.86}$$

and the effective stiffness therefore can be expressed as

$$k_i = \int_0^L \varphi_i''(x)^2 EI(x) \mathrm{d}x. \tag{2.87}$$

2.4.3 Effective damping c_i

The one-dimensional Rayleigh dissipation function [223]

$$R = \frac{1}{2} \sum_{i=0}^{\infty} c_i \dot{q}_i(t)^2 \tag{2.88}$$

where c_i is a lumped damping parameter, describes the proportionality between velocity and frictional forces. It can also be expressed as

$$R = \frac{1}{2} \int_0^L (\dot{u}(x,t))^2 c_0' \mathrm{d}x \tag{2.89}$$

where c_0' is a damping parameter per unit length. Substituting $u(x,t)$, Eq. 2.74, into the latter yields

$$R = \frac{1}{2} \sum_{i=0}^{\infty} \int_0^L \varphi_i(x)^2 \dot{q}_i(t)^2 c_0' \mathrm{d}x \tag{2.90}$$

and thus it follows for the relation between c_i and c_0'

$$c_i = \int_0^L \varphi_i(x)^2 c_0' \mathrm{d}x. \tag{2.91}$$

2.4.4 Lumped force $F_{\mathrm{ex},i}$

An external force distribution $f(x,t)$ exerts the work

$$W_{\mathrm{ex}} = \int_0^L u(x,t) f(x,t) \mathrm{d}x = \sum_{i=0}^{\infty} \int_0^L \varphi_i(x) q_i(t) f(x,t) \mathrm{d}x. \tag{2.92}$$

Using a lumped force F_{ex} it follows

$$W_{\mathrm{ex}} = \sum_{i=0}^{\infty} F_{\mathrm{ex},i}(t) q_i(t) \tag{2.93}$$

and thus the relation between lumped and distributed forces reads

$$F_{\mathrm{ex},i}(t) = \int_0^L \varphi_i(x) f(x,t) \mathrm{d}x. \tag{2.94}$$

2.4.5 Lumped element oscillator

Introducing an effective deflection $u_i(t) = q_i(t)$ and using the expressions for the effective, i.e. lumped parameters m_i, c_i, k_i a second order equation of motion can be stated for each vibrational mode i by balancing occurring forces. In the following single vibrational modes will be discussed and thus,

for simplicity, the subscript i is not used anymore. The second order equation of motion for a linear, mechanical lumped element resonator as depicted in Fig. 2.7 reads

$$m\,\ddot{u}(t) + c\,\dot{u}(t) + k\,u(t) = F_{\mathrm{ex}}(t). \tag{2.95}$$

For a torsional resonator, the according equation can be expressed as

$$J\,\ddot{\varphi}(t) + c^*\,\dot{\varphi}(t) + k^*\,\varphi(t) = M_{\mathrm{ex}}(t). \tag{2.96}$$

Equivalence to an electrical series resonator

Resonant sensors mostly are operated as electromechanical transducers with an electrical input and an electrical output. Therefore, modeling the device as a purely electrical device might become advantageous in some cases. The most prominent example for such electromechanical transducers are quartz-crystal resonators for which usually, the mechanical oscillation is modeled by an electrical, RLC series resonator, see Fig. 2.7, the so-called motional branch in the Butterworth Van-Dyke circuit, c.f. [97]. Using the capacitors voltage v_{C} as state variable, the motional branch (being excited by the voltage v_{ex}) can be described by

$$L\ddot{v}_{\mathrm{C}}(t) + R\dot{v}_{\mathrm{C}}(t) + \frac{1}{C}\,v_{\mathrm{C}}(t) = \frac{v_{\mathrm{ex}}(t)}{C}. \tag{2.97}$$

Here L, R and C are the series resonator's inductance, resistance and capacity, respectively. For electrodynamic transducers parallel resonant circuit are also commonly used [MHbcc1].

Eqs. 2.95, 2.96 and 2.97 are mathematically identical, i.e. an ordinary second order differential equation with constant coefficients. The equivalence of used coefficients is given in the table in Fig. 2.7. For efficiency and better readability, in the following, only the mechanical case will be discussed. The mechanical results can be related to the electrical case when necessary.

Sinusoidal excitation

Assuming a sinusoidal excitation force $F_{\mathrm{ex}}(t) = \hat{F}_{\mathrm{ex}} \sin(\omega\,t + \varphi_{\mathrm{ex},0})$ in Eq. 2.95 and an underdamped system, i.e.,

$$\frac{c}{2\,m} < \sqrt{\frac{k}{m}} \tag{2.98}$$

yields for the deflection

$$u(t) = C_{\mathrm{u}}\,e^{-\delta t}\,\cos(\omega_{0\delta}\,t + \varphi_0) + \hat{u}(\omega)\,\sin(\omega\,t + \varphi_{\mathrm{ex},0} + \varphi_u(\omega)). \tag{2.99}$$

The first term of this equation is the solution of the homogeneous differential equation and thus describes transient (free) vibrations. The second term considers steady state (forced) vibrations resulting from the sinusoidal excitation. In this equation

$$\delta = \frac{c}{2\,m} \tag{2.100}$$

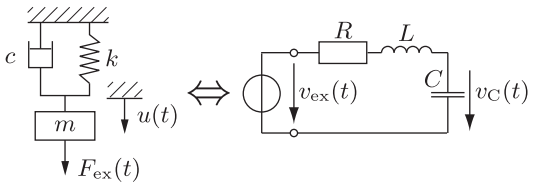

Equivalence table

translat. osc.	m	c	k	F_{ex}
rotat. osc.	J	c^*	k^*	M_{ex}
RLC ser. res.	L	R	$1/C$	v_{ex}/C

Figure 2.7: Equivalence of mechanical and electrical lumped element resonators.

is the damping constant which can also be related to the time constant $\tau = 1/\delta$ and furthermore, in Eq. 2.99

$$\omega_{0\delta} = \sqrt{\omega_0^2 - \delta^2} \qquad \text{where} \qquad \omega_0 = \sqrt{\frac{k}{m}} \tag{2.101}$$

is the angular eigenfrequency of a damped, free oscillation. C_u and φ_0 are constants and have to be determined through the initial conditions considering initial deflection $u(t = 0) = u_0$ and velocity $\left.\frac{du(t)}{dt}\right|_{t=0} = v_0$. $\hat{u}(\omega)$ is the amplitude of the steady state oscillation and $\varphi_u(\omega)$ is the phase angle between excitation force and steady state deflection of the mechanical oscillation. Both quantities can be obtained by evaluating absolute value and phase of the steady state deflection $\underline{u}(\omega)$ in the frequency domain. Using complex notation and assuming a time dependence $e^{j\,\omega\,t}$, the transfer function $G(\omega)$ relating the effective deflection to excitation force reads

$$\underline{G}(\omega) = \frac{\underline{u}(\omega)}{\underline{F}_{\mathrm{ex}}(\omega)} = \frac{1/m}{\omega_0^2 - \omega^2 + \mathrm{j}\,2\,\omega\,\delta}. \tag{2.102}$$

Most electrical transducers allow the determination of quantities corresponding to the oscillation's velocity, e.g., the vibration-induced change of impedance of piezoelectric devices or the motion-induced voltage in case of inductively read-out mechanisms. The transfer function $H(\omega)$ relating steady state velocity of forced vibrations to excitation forces can be given as

$$\underline{H}(\omega) = \frac{\underline{v}(\omega)}{\underline{F}_{\mathrm{ex}}(\omega)} = \frac{1/c}{1 + \mathrm{j}\frac{\omega_0}{2\,\delta}\left(\frac{\omega}{\omega_0} - \frac{\omega_0}{\omega}\right)} = \frac{1}{c + \mathrm{j}\left(m\,\omega - \frac{k}{\omega}\right)}. \tag{2.103}$$

In Sec. 2.5.3 it will be discussed, that in general, evaluating the resonator's velocity (or velocity related quantities) is preferred over deflection (or deflection related quantities).

Eigenfrequency, resonance frequency and quality factor

Defining the angular eigenfrequency $\omega_{0,x}$ as the angular frequency of free oscillation of a quantity x (in this case u or v) and the angular resonance frequency $\omega_{\mathrm{r},x}$ as the angular frequency for which the amplitude of x for forced oscillations become largest, it follows for the angular eigenfrequencies of deflection as well as of velocity oscillation of a damped oscillator

$$\omega_{0,\mathrm{u}} = \omega_{0,\mathrm{v}} = \omega_{0\delta} = \sqrt{\omega_0^2 - \delta^2} \tag{2.104}$$

and for the resonance frequencies

$$\omega_{\mathrm{r,u}} = \sqrt{\omega_0^2 - 2\,\delta^2} \qquad \text{and} \qquad \omega_{\mathrm{r,v}} = \omega_0. \tag{2.105}$$

For weakly damped oscillations $\omega_{\mathrm{r,u}} \approx \omega_0$ is often assumed. This assumption yields a relative deviation lower than 1% for damping ratios $\delta/\omega_0 < 0.1$ i.e., quality factors $Q > 5$.

Examples for publications discussing the definition of the quality factor and its history are given, e.g. in [224–226]. The definition for the quality factor used in this thesis is [227, 228]

$$Q := 2\,\pi\frac{W_{\mathrm{s}}}{W_{\mathrm{d}}/T_{\mathrm{p}}} = \omega_0\frac{W_{\mathrm{s}}}{P_{\mathrm{d}}} \tag{2.106}$$

where W_{s}, W_{d} and P_{d} are the energy stored in the vibration, the dissipative energy per cycle T_{p} and the average dissipated power. For the lumped element oscillator W_{s} and P_{d} can be expressed as

$$W_{\mathrm{s}}(\omega) = k\,\frac{\hat{u}^2(\omega)}{2} \qquad \text{and} \qquad P_{\mathrm{d}}(\omega) = c\,\frac{\hat{v}^2(\omega)}{2} \tag{2.107}$$

and thus, it follows for the quality factor of a second order, lumped element resonator as it is depicted in Fig. 2.7

$$Q = \frac{\sqrt{k\,m}}{c} = \frac{\omega_0}{2\,\delta}. \tag{2.108}$$

With the definitions of the damping constant δ, Eq. 2.100, the eigenfrequency ω_0, Eq. 2.101, and the quality factor Q, Eq. 2.108, and considering Eq. 2.98 , the requirement for an oscillator, can also be expressed as

$$\delta < \omega_0 \qquad \Longleftrightarrow \qquad Q > \frac{1}{2}. \tag{2.109}$$

Substituting the expression for the quality factor from Eq. 2.108 into Eq. 2.103, the transfer function of a second order resonator of a velocity related quantity X (e.g., the admittance of a series resonator or the motion-induced voltage in an inductively read-out resonator) can be expressed as

$$\underline{X}_{2\mathrm{O}}(\omega) = \frac{X_{\max}}{1 + \mathrm{j}\, Q \left(\frac{\omega}{\omega_0} - \frac{\omega_0}{\omega} \right)} \tag{2.110}$$

where $X_{\max}$ is the maximum amplitude of the transfer function.

2.5 Identification of second order systems

2.5.1 Extraction of the second order system

Usually, the recorded frequency response (containing a characteristic resonance) of an electrically driven and read-out resonator consists of the resonator's (intrinsic) spectrum $\underline{X}_{2\mathrm{O}}$ and an additional background spectrum $\underline{X}_{\mathrm{BG}}$. The latter comprises additional signals resulting from electrical cross-talk, impedance related offsets, phase shifts and noise. I.e., the most general form of the recordable signal is:

$$\underline{X} = \underline{X}_{2\mathrm{O}} + \underline{X}_{\mathrm{BG}} \tag{2.111}$$

and thus, in most cases, the resonance spectrum can not be recorded directly but can be determined by subtracting the (identified) background spectrum from the measured frequency response. Offset signals and cross-talk are explained hereafter for two basic cases of Lorentz force driven resonators. A more detailed description will be given in Sec. 3.1. The algorithm presented in [229] separates $\underline{X}_{2\mathrm{O}}$ and $\underline{X}_{\mathrm{BG}}$ by fitting a polynomial function into the recorded frequency response $\underline{X}$ for frequencies where the signals resulting from the mechanical oscillations are negligible.

Offset signals

Lorentz force excitation proved to be a reliable method for resonant sensors' actuation and is mainly used in this work. A resonator consisting of (or carrying) an electrical conductor, is excited by means of Lorentz forces on AC currents in this conductor, placed in an external magnetic field, see Fig. 2.8. The associated movement of the conductor in the magnetic field, in turn, yields a motion-induced voltage on the latter, representing the oscillator's velocity. The measured voltage on the resonating conductor consists of this motion-induced voltage and an additional voltage due to the excitation current and the conductor's impedance. Examples for sensors using this method are described amongst others in, [104], [MHj5], and [MHc13].

Characteristic resonant frequency responses are depicted in Fig. 2.8. There, ω_0, c.f. Eq. 2.101 is marked by a circle and the bandwidth using δ, Eq. 2.100 $[\omega_0 - \delta, \omega_0 + \delta]$ corresponding to the $-3\,\mathrm{dB}$ bandwidth is highlighted by the bold line.

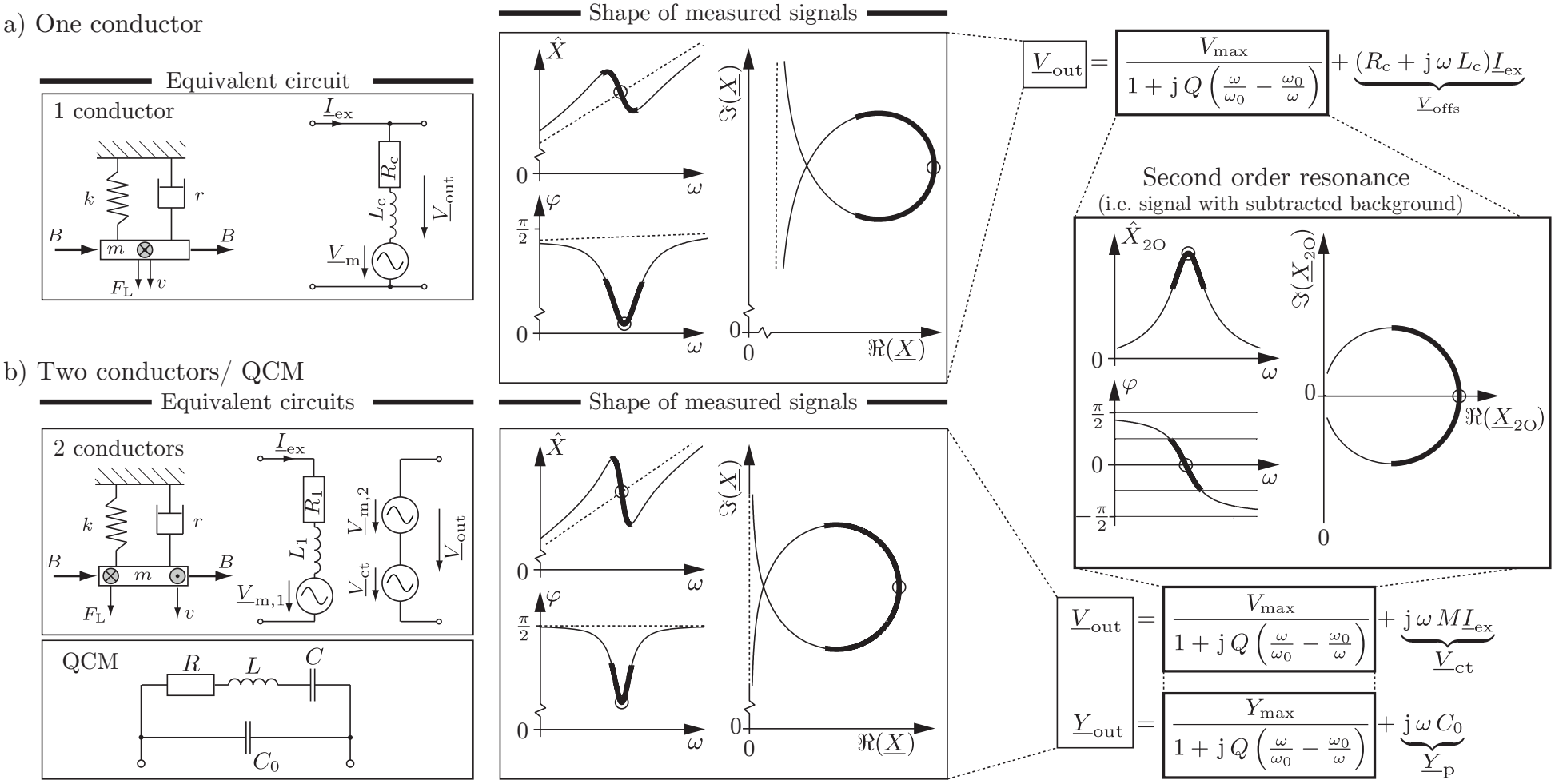

$$\underline{V}_{\mathrm{out}} = \frac{V_{\max}}{1 + \mathrm{j}\,Q\left(\frac{\omega}{\omega_0} - \frac{\omega_0}{\omega}\right)} + \underbrace{(R_\mathrm{c} + \mathrm{j}\,\omega\,L_\mathrm{c})\underline{I}_\mathrm{ex}}_{\underline{V}_\mathrm{offs}}$$

$$\underline{V}_{\mathrm{out}} = \frac{V_{\max}}{1 + \mathrm{j}\,Q\left(\frac{\omega}{\omega_0} - \frac{\omega_0}{\omega}\right)} + \underbrace{\mathrm{j}\,\omega\,M\underline{I}_\mathrm{ex}}_{\underline{V}_\mathrm{ct}}$$

$$\underline{Y}_{\mathrm{out}} = \frac{Y_{\max}}{1 + \mathrm{j}\,Q\left(\frac{\omega}{\omega_0} - \frac{\omega_0}{\omega}\right)} + \underbrace{\mathrm{j}\,\omega\,C_0}_{\underline{Y}_\mathrm{p}}$$

Figure 2.8: Examples for signals of second order resonators being subjected to offset signals and cross-talk. a) Lorentz-Force driven resonator using a single conductor for both, excitation and read-out: V_{out}: measured voltage, $V_{\max}$: maximum amplitude of the motion-induced voltage V_m. V_{offs}: offset voltage R_c, L_c: conductor's resistance and inductance, $\underline{I}_{\mathrm{ex}}$: excitation current. b) Lorentz-Force driven resonator using two separate conductors for excitation and read-out and a Quartz Crystal Microbalance, which is usually read-out performing an impedance (or admittance Y) spectrum analysis. V_{ct}: cross-talk voltage, Y_p: parallel admittance. M is the mutual inductance, describing the electric cross-talk between excitation and read-out coil. The relation for angular resonance frequency and quality factor for the QCM are: $\omega_0 = \frac{1}{\sqrt{L\,C}}$ and $Q = \frac{1}{R}\sqrt{\frac{L}{C}}$.

Cross-talk – Coupling

A further possibility to evaluate a Lorentz-force driven resonator's frequency response is to use a second conductor following the movement of the resonator, see e.g. [MHj6] and [MHj5]. In this case one conductor carrying the AC excitation current I_{ex} is used for excitation and a geometrically separated, second conductor is used for read-out, by measuring the voltage which is induced due to its motion in an external magnetic field. Assuming electrical currents to be zero in the read-out circuit, which is valid if the input resistance of the voltmeter is high, a potential impedance related voltage drop on this conductor is negligible. However, cross-talk has to be considered, if the time variant magnetic field induced by the excitation current in the excitation circuit significantly couples into the read-out circuitry. This coupling can be described by using mutual inductances M. For this type of excitation, i.e., using two separate conductors, the equation for the measurable voltage corresponds to the equation for the measurable admittance Y of a QCM, c.f. [97], i.e. for both cases the shape of measured voltage or measured admittance spectrum is the same.

2.5.2 Evaluation of f_{r} and Q from free oscillations

In the following it is assumed that any signals resulting from the background signals can be ideally subtracted and thus only signal components related to the resonators movement remain. The transient term in Eq. 2.99 describes free oscillations of a resonator. The resonator can be excited to free vibration either by a short force impulse or simply switching off an harmonically excitation force whose excitation frequency is preferentially close to the resonance frequency. A characteristic transient response for the deflection

$$u(t)_{\mathrm{free}} = C_{\mathrm{u}}\, e^{-\delta t}\, \cos(\omega_{0\delta}\, t + \varphi_0) \tag{2.112}$$

is depicted in Fig. 2.9 for an initial normalized deflection $u(0) = 1$ and for the velocity of the oscillation with an initial velocity $v(0) = 1$, respectively. The equation for the velocity of free vibration is of the same kind as Eq. 2.112, however the factors C_{u} and φ_0 become C_{v} and $\varphi_{0,\mathrm{v}} = \varphi_0 + \pi/2$. From both curves, the parameters $\omega_{0\delta}$ and δ can be determined in an equal way by evaluating the time T between two zeros and fitting the envelope function of the free vibration, see Fig. 2.9. δ can also be determined using

$$\delta = \frac{1}{T} \ln \frac{\hat{x}_i}{\hat{x}_{i+1}} \tag{2.113}$$

where x stands either for u or v in this case. With the knowledge of $\omega_{0\delta}$ and δ both, ω_0, and Q can be determined using Eqs. 2.100, 2.101 and 2.108.

The method has been applied for resonator characterization applications e.g. in [105, 230, 231] and is beneficial for high Q resonators, as the entire settling is only recorded once (for one measurement

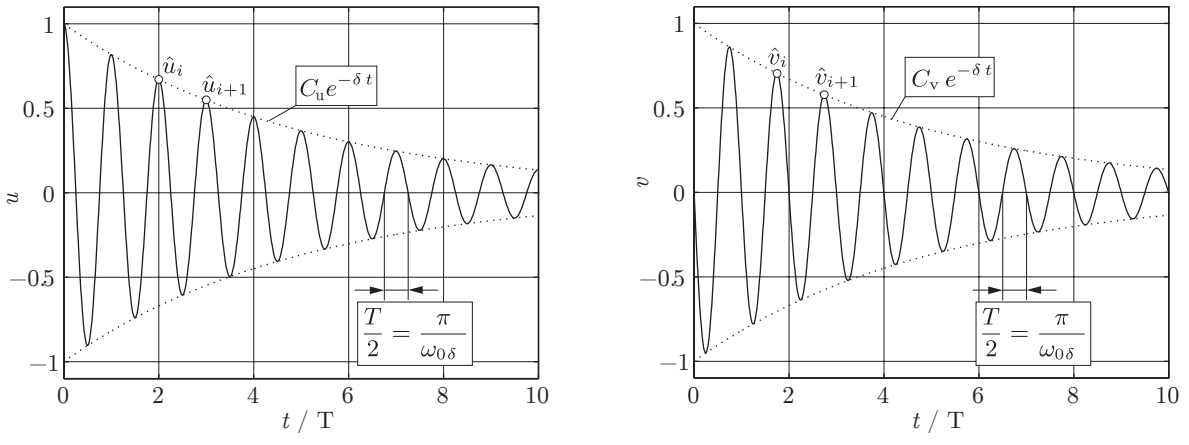

(a) Deflection (b) Velocity

Figure 2.9: Normalized, free vibration for deflection and velocity

cycle). This keeps the required measurement time low compared to recording the frequency response upon forced vibration for which it is necessary to wait for the entire settling time (i.e. at least $5\,\tau$, where τ is the time constant in seconds) for every single frequency, see also Sec. 2.6. However, as for liquid loaded resonators, the quality factor is usually low, the settling time may become critically short for reliably using this method. To give an example: In [88] and [190] liquid loaded resonators with operational frequencies in the order of 10 kHz yielding quality factors down to 1 and lower were reported. For such resonators, the settling time $5\,\tau$ is approximately 150 µs. On the other side, in [MHj2] with a rectangular tuning fork quality factors in liquids $Q = [206.2 \ldots 498.99]$ at resonance frequencies $f_\mathrm{r} = [409.07 \ldots 409.52]\,\mathrm{Hz}$ were obtained and consequently, the settling time for these devices are $5\,\tau = [0.8 \ldots 1.94]\,\mathrm{s}$. For such devices, recording the transient response, e.g. ring up or ring down, might be a considerable alternative.

2.5.3 Evaluation of f_r and Q from the frequency response obtained by spectrum analysis of forced oscillations

The resonant frequency responses of the steady oscillations of displacement and velocity, c.f. Eqs. 2.102 and 2.103, are depicted in Fig. 2.10 for amplitude, phase and locus-plot.

Resonance circle

The velocity's locus plot describes a circle in the complex plane, a fact which can be easily proven by splitting the frequency dependent expression for $\underline{v}(\omega)$ up into its real and imaginary part

$$\underline{v}(\omega) = \frac{\hat{v}_\mathrm{max}}{1 + Q^2\left(\frac{\omega}{\omega_0} - \frac{\omega_0}{\omega}\right)^2} - \mathrm{j}\frac{\hat{v}_\mathrm{max}\,Q\left(\frac{\omega}{\omega_0} - \frac{\omega_0}{\omega}\right)}{1 + Q^2\left(\frac{\omega}{\omega_0} - \frac{\omega_0}{\omega}\right)^2} \tag{2.114}$$

and comparing it with the parametric expression of a circle [232]

$$x = x_\mathrm{M} + r\frac{1-\xi^2}{1+\xi^2} \qquad \text{and} \qquad y = y_\mathrm{M} + r\frac{2\xi}{1+\xi^2} \tag{2.115}$$

where x_M and y_M are the circle's center point in the x,y-plane and $\xi \in [-\infty, \infty]$ is a parameter. Comparison of both equations shows that the velocity's locus plot describes a circle in the complex plane which is symmetric about the real axis, has its center point at $(\frac{\hat{v}_\mathrm{max}}{2}, 0)$ and a radius of $\frac{\hat{v}_\mathrm{max}}{2}$, i.e.

$$r = \frac{\hat{v}_\mathrm{max}}{2}, \qquad \xi = Q\left(\frac{\omega}{\omega_0} - \frac{\omega_0}{\omega}\right), \qquad x_\mathrm{M} = \frac{\hat{v}_\mathrm{max}}{2}, \quad \text{and} \quad y_\mathrm{M} = 0. \tag{2.116}$$

These circumstances are depicted in Fig. 2.10(b). The circular shape is independent of the damping. Damping only changes the circle's diameter (if the excitation force is kept constant). The locus plot for the deflection however, does not describe the shape of a circle as it can be clearly observed in Fig. 2.10(a).

Evaluation of characteristic points

In both plots of Fig. 2.10 the bold lines represent the frequency response for a span of angular frequencies of $[\omega_0 - \delta, \omega_0 + \delta]$. Furthermore, characteristic points from which $\omega_{r,u}$, ω_0 and δ can be evaluated, are indicated and their according relations are given for the particular case. For the frequency response of the deflection, see Fig. 2.10(a), $\omega_{r,u}$ and ω_0 are the angular frequencies for which the amplitude gets largest and the phase angle's value is $-\pi/2$, respectively. The frequency response of the oscillator's velocity offers four possibilities for evaluating ω_0 and δ, see Fig. 2.10(b). ω_0 is the angular frequency where the amplitude has its maximum and for which the phase gets zero. By evaluating the angular frequencies $\omega_{\pm\pi/4}$ for which the phase values are $\pm\pi/4$, δ is obtained by solving the equation $\varphi_\mathrm{v}(\omega_{\pm\pi/4}) = \pm\pi/4$, (i.e, the imaginary term in the denominator of Eq. 2.103 has to become ∓ 1). Similar as for the example of the evaluation of free oscillations of the deflection, with

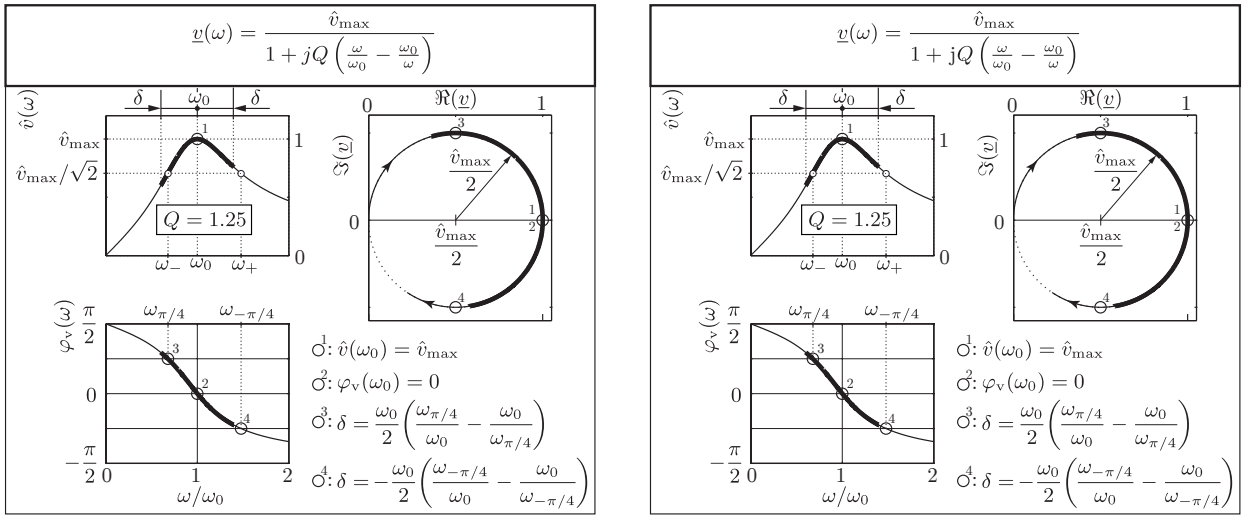

(a) Deflection (b) Velocity

Figure 2.10: Frequency responses for deflection and velocity

the knowledge of at least two of the aforementioned parameters, the parameters ω_0 and Q can be calculated.

The -3 dB method

This method is called "$-3\,\mathrm{dB}$ method" because angular frequencies ω_+ and ω_- satisfying $\hat{x}(\omega_\pm) = \hat{x}_{\max}/\sqrt{2}$ are determined. In other words, for this method, frequencies $\omega_\pm$ are searched for which the power of the oscillation is the half of its maximum value i.e., $-3\,\mathrm{dB}$.

- **Resonance frequency**

  In a first step, the peak value $\hat{x}_{\max}$ and its associated angular frequency $\omega_{\hat{x}_{\max}}$ are determined. It is then assumed that $\omega_{\hat{x}_{\max}} \approx \omega_0$. This assumption is exact in case of the velocity but yields non negligible deviations in case of the the deflection for small quality factors, see Fig. 2.11(a).

- **Bandwidth**

  With the determined peak values $\hat{x}_{\max}$, frequencies ω_+ and ω_- satisfying $\hat{x}(\omega_\pm) = \hat{x}_{\max}/\sqrt{2}$ are evaluated. The bandwidth is then calculated using

  $$\Delta\omega_{3\mathrm{dB}} = \omega_+ - \omega_-, \quad \text{where} \quad \Delta\omega_{3\mathrm{dB,v}} = 2\,\delta, \quad \text{and} \quad \Delta\omega_{3\mathrm{dB,u}} \approx 2\,\delta. \tag{2.117}$$

  In Fig. 2.10 it is clearly observable, that for both cases, analysis of the deflection or velocity spectra, the evaluated frequencies $\omega_- \neq \omega_0 - \delta$ and $\omega_+ \neq \omega_0 + \delta$. However, in case of the velocity the difference between both frequencies is always $\omega_{+,v} - \omega_{-,v} = 2\,\delta$, independent of Q, whereas for the case of evaluated deflection spectrum, the difference of both frequencies $\omega_{+,u} - \omega_{-,u} \approx 2\,\delta$ is only an approximation.

- **Quality factor**

  With the knowledge of $\hat{x}_{\max}$, ω_+ and ω_- is calculated using

  $$Q \approx Q_{3\mathrm{dB}} = \frac{\omega_{\hat{x}_{\max}}}{\omega_+ - \omega_-}. \tag{2.118}$$

  As the determination of ω_0 by evaluating $\hat{u}_{\max}$ and $\omega_{+,v} - \omega_{-,v} = 2\,\delta$ the $-3\,\mathrm{dB}$ method is exact in case of evaluating the velocity's amplitude (independent of the damping) but yields non-negligible deviations for low Q resonances in case of the deflection, see Fig. 2.11(a). As a rule of thumb,

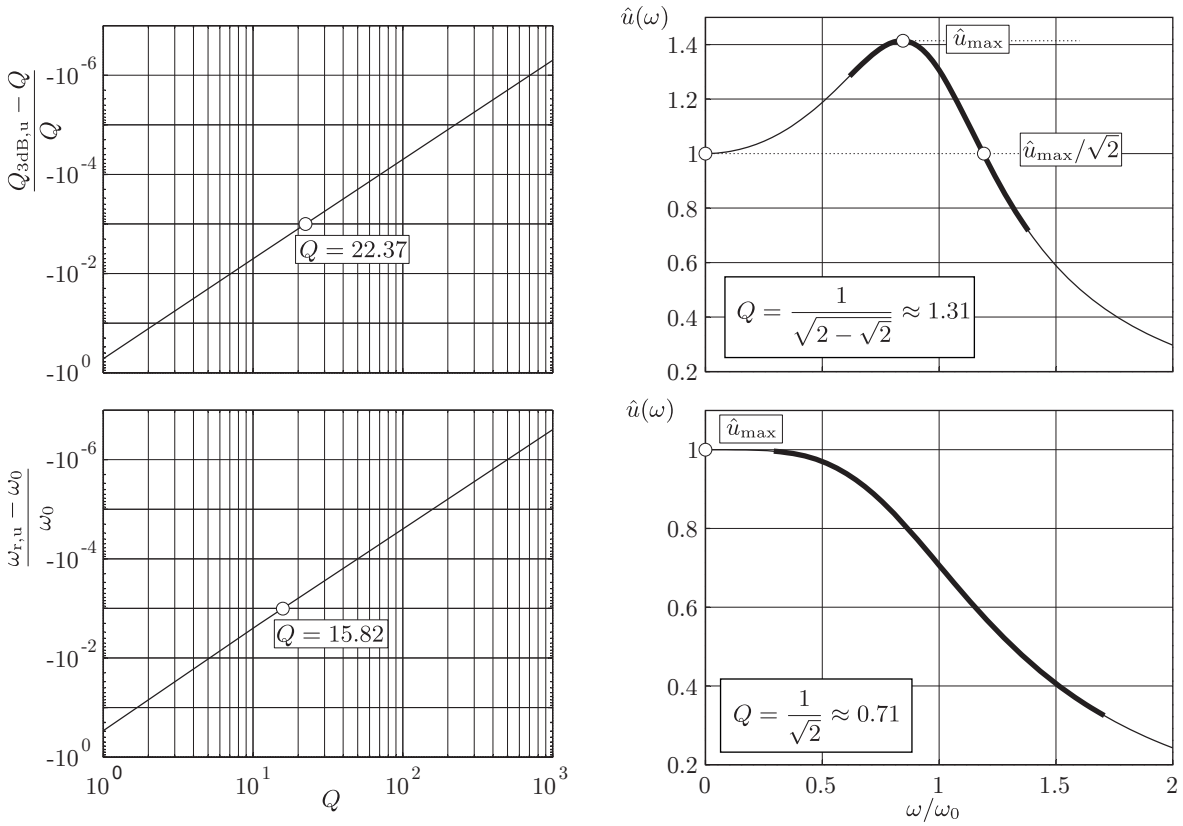

(a) Relative deviations from Q and ω_0

(b) Limiting cases for deflection spectrum

Figure 2.11: Restriction of the -3 dB method in case of recorded deflection: a) Relative deviations of resonance frequency and quality factor determined with the -3 dB method. b) Limits of the - 3 dB Method for recorded deflection: for $Q < 1.31$, the solution for ω_- gets complex valued and for $Q < 0.71$ the resonance peak vanishes completely.

for the accuracy of the $-3\,\mathrm{dB}$ method, quality factors $Q < 20$ yield relative deviations from the exact values of Q and ω_0 higher than 10^{-3} for the case of evaluating the deflection amplitude.

- **Limits**

  Two characteristic limiting cases using the deflection spectrum have to be furthermore mentioned, c.f., Fig. 2.11(b):

  1. for $Q < \frac{1}{\sqrt{2-\sqrt{2}}} \approx 1.31$ the solution for ω_- becomes complex valued, and thus the bandwidth can not be estimated anymore. Such a case, for which ω_- gets complex, is also depicted in Fig. 2.10(a) ($Q = 1.25$).
  2. for $Q < \frac{1}{\sqrt{2}} \approx 0.71$ the frequency response for the deflection does not show a peak any more and thus an approximate solution of ω_0 is not possible anymore.

Linear least-square fit

With this method, ω_0 and Q are determined by performing twice a linear least-square fit with the complex data in the form of Eq. 2.103 and Eq. 2.110, respectively, which describe the shape of a circle with radius r and center point on the real axis at r. For better readability, the notation

$$x = \Re(\underline{X}) \qquad \text{and} \qquad y = \Im(\underline{X}) \tag{2.119}$$

is used in relation to a circle in the x, y-plane. For a given point $\underline{X}_i = x_i + jy_i$ on the circle satisfying $(x_i - r_i)^2 + y_i^2 = r_i^2$ the radius r_i can be calculated by

$$r_i = \frac{x_i^2 + y_i^2}{2x_i}. \tag{2.120}$$

In case of additive complex measurement noise $\underline{\epsilon}_i = \epsilon_{R,i} + \mathrm{j}\epsilon_{I,i}$, the individual estimates of the radii vary. It is therefore necessary to implement an averaging procedure taking into account all data points in $\underline{\boldsymbol{X}}$ to achieve lower uncertainty of the estimated radius r^*. Simple averaging of individual estimates of r_i^* yields significant deviations from the exact value of r, due to large relative estimation errors at small values of x_i. A much better approach is to use a least squares method. For this, the problem can be rearranged into a linear equation system given by

$$\boldsymbol{b} = \boldsymbol{A} \cdot \boldsymbol{x} \quad \text{with} \quad \boldsymbol{b} = [x_i^2 + y_i^2], \quad \boldsymbol{A} = [2x_i] \quad \text{and} \quad \boldsymbol{x} = r. \tag{2.121}$$

The equation system is generally overdetermined and an estimate in the least squares sense can be obtained by [166]

$$r^* = \boldsymbol{x}^* = \left(\boldsymbol{A}^{\mathrm{T}} \cdot \boldsymbol{A}\right)^{-1} \cdot \boldsymbol{A}^{\mathrm{T}} \cdot \boldsymbol{b}\,. \tag{2.122}$$

However, the result is not unbiased and yields slightly too high values for r for non-zero measurement noise. The bias is approximately proportional to the noise variance to radius ratio, and depends on the particular characteristics of the noise. A least squares fitting procedure of circles and ellipses overcoming this problem can be found in [233].

With the knowledge of the circle's radius r, the values of the parameter ξ_i are calculated from the parametric equation of the circle

$$x = \frac{2\,r}{1 + \xi_i^2} \qquad \text{and} \qquad y = -\frac{2\,r\,\xi_i}{1 + \xi_i^2} \tag{2.123}$$

where

$$\xi_i = Q\left(\frac{\omega_i}{\omega_0} - \frac{\omega_0}{\omega_i}\right). \tag{2.124}$$

Using the obtained values for ξ_i and the associated angular frequencies ω_i, ω_0 and Q can be determined by calculating the least-square solution of the system

$$\xi_i = \begin{bmatrix} \omega_i, & -\dfrac{1}{\omega_i} \end{bmatrix} \cdot \begin{bmatrix} \dfrac{Q}{\omega_0} \\ Q\,\omega_0 \end{bmatrix} \tag{2.125}$$

and subsequent determination of ω_0 and Q from the least-square solution for $\boldsymbol{x} = [\frac{Q}{\omega_0} \quad Q\,\omega_0]^{\mathrm{T}}$. The method of a circle fit described here is not unbiased and thus yields errors for signals subjected to noise. In this case, more precise methods should be used see e.g., [229, 233, 234].

Non-linear, iterative least-square fit (Gauss-Newton)

A further possibility for determining a second order resonator's ω_0 and Q is the analysis of the phase spectrum which is fit with non-linear least square algorithms. A common non-linear, iterative least square method is the Gauss-Newton method, which is briefly described here. Starting with the knowledge of the phase of the measured data φ_{M} and initial values for ω_0 and Q (which have been determined e.g. with the -3 dB method) the deviation vector

$$\boldsymbol{\varepsilon}_i = \boldsymbol{\varphi}_i(\boldsymbol{\omega}) - \boldsymbol{\varphi}_{\mathrm{M}} \tag{2.126}$$

is calculated. Here, $\boldsymbol{\varphi}_i(\boldsymbol{\omega})$ is the phase vector of the second order function Eq. 2.103 evaluated for the measured angular frequency vector $\boldsymbol{\omega}$ and reads

$$\boldsymbol{\varphi}_i(\boldsymbol{\omega}) = -\arctan\left(Q_i\left(\frac{\boldsymbol{\omega}}{\omega_{0,i}} - \frac{\omega_{0,i}}{\boldsymbol{\omega}}\right)\right), \tag{2.127}$$

where $\omega_{0,i}$ and Q_i are the iteratively determined values for ω_0 and Q. With the Jacobian

$$\boldsymbol{J}_i = \begin{bmatrix} \dfrac{\partial \boldsymbol{\varphi}_i}{\partial \omega_{0,i}} & \dfrac{\partial \boldsymbol{\varphi}_i}{\partial Q_i} \end{bmatrix} \tag{2.128}$$

the next values for ω_0 and Q are calculated using the expression for the Gauss-Newton method [166]

$$\begin{bmatrix} \omega_{0,i+1} \\ Q_{i+1} \end{bmatrix} = \begin{bmatrix} \omega_{0,i} \\ Q_i \end{bmatrix} - \left(\boldsymbol{J}_i^{\mathrm{T}} \cdot \boldsymbol{J}_i \right)^{-1} \cdot \boldsymbol{J}_i^{\mathrm{T}} \cdot \boldsymbol{\varepsilon}_i. \tag{2.129}$$

2.6 Recording the frequency response

Figure 2.12 shows the basic principle of recording a resonator's frequency response. A harmonic excitation signal forces the resonator to harmonical oscillations at discrete angular frequencies ω_i. After switching to the next frequency, a time span of at least $5\,\tau$ has to be waited until the transient part vanishes and the signal reaches its steady state oscillation. The presence of two frequencies $\omega_{0\delta}$ and ω_i yields ring-up, ring-down and beat phenomenons, respectively, which nicely can be observed in Fig. 2.12. Although only discrete frequencies are excited, in the following the term frequency sweep will be use to express the recording of the frequency response. With the knowledge of steady state amplitudes and phase delay between excitation and read-out signal at the recorded frequencies, the Bode and Nyquist plot, respectively can be determined. Unlike depicted in Fig. 2.12 the frequency sweep preferentially should be performed close to the resonance frequency, to allow accurately investigating the resonance characteristics. Simply speaking, the frequencies should be selected such, that the measured points yield a sufficient distribution on the resonance circle in the Nyquist plot.

2.6.1 Investigated bandwidth

Circle fit algorithms as described in Sec. 2.5.3 are well established methods for determining ω_0 and Q of a second order resonator. As already mentioned above, under real conditions in general, the data points are subjected to additional background signals and noise. For such signals, the accuracy of the fitted parameters ω_0 and Q is dependent on the recorded bandwidth and the distribution of the frequency points as it will be discussed below. In this section, it is discussed in which frequency range $\omega_\mathrm{s} < \omega_0 < \omega_\mathrm{e}$ the frequency response has to be recorded to obtain best fitting results. The optimum starting and ending frequencies ω_s and ω_e respectively, are dependent on ω_0 and Q. For real measurements, after each determination of ω_0 and Q, new values for ω_s and ω_e are calculated for determining the optimum measured bandwidth.

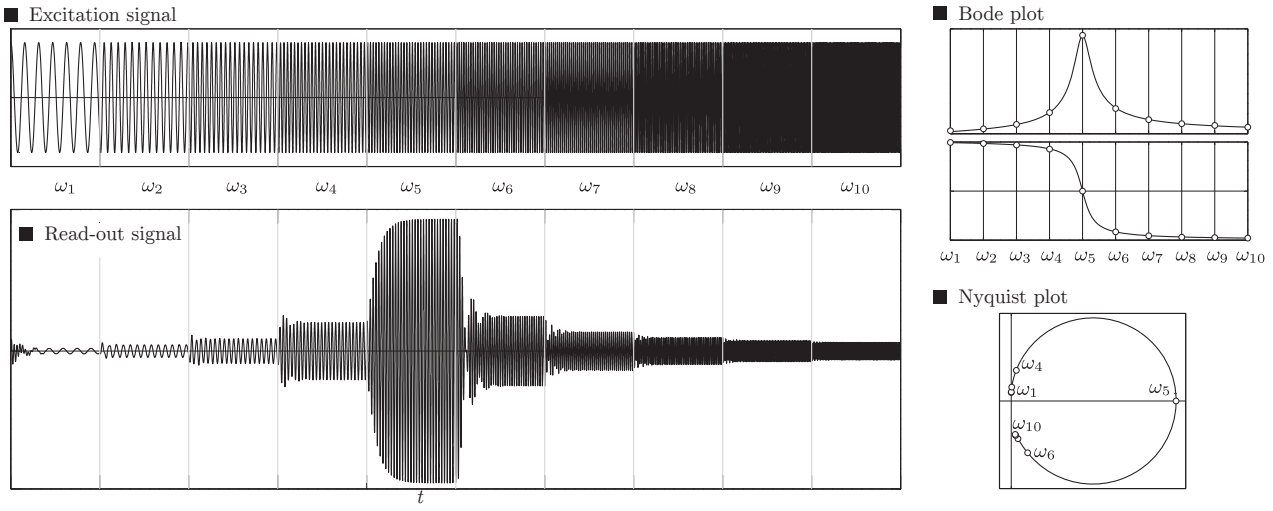

Figure 2.12: Recoding of the frequency response. Left: The resonator is excited to harmonical oscillations at several discrete frequencies. After each frequency step, a time span of at least 5τ is waited before measuring amplitude and phase, with which the Bode as well as the Nyquist plot can be plotted.

Frequency vs. angular symmetry

For testing implemented fitting algorithms based on the principles described in Sec. 2.5.3, data points of a second order resonator in the complex plane using Eq. 2.103 with added noise were generated for different noise levels. The intention of this study was to investigate how the measured points on the Nyquist circle have to be distributed and within which bandwidth the resonance curve should be recorded. For the latter, two quantities have been defined, expressing the bandwidth around the resonance frequency, see also Fig. 2.13:

1. **Covering ratio** r_c

   The covering ratio r_c is a purely geometrical parameter and expresses the ratio of the resonant circle which is covered by the investigated bandwidth. For this, a geometrical symmetry about ω_0 is assumed.

2. **Number of bandwidths** N_δ

   As it was already explained in Sec. 2.5.3 for the $-3\,\mathrm{dB}$ method, the term "the band width" expresses the frequency range $[\omega_0 - \delta, \omega_0 + \delta]$. In relation to that, the parameters

$$N_{\delta,\mathrm{l}} = \frac{\omega_0 - \omega_s}{\delta} \qquad \text{and} \qquad N_{\delta,\mathrm{l}} = \frac{\omega_e - \omega_0}{\delta} \tag{2.130}$$

   express the number of δ gone left or right about the resonance frequency for defining the starting and ending frequencies ω_s and ω_e.

The fitting algorithms were tested for several angular covering ratios r_c of the circle with angular symmetry about $\varphi(\omega_0) = 0$, see Fig. 2.13. This investigation showed that best fitting results are obtained for $r_\mathrm{c} = 0.2 \ldots 0.7$. Independent of this study, for the number of bandwidths it was found

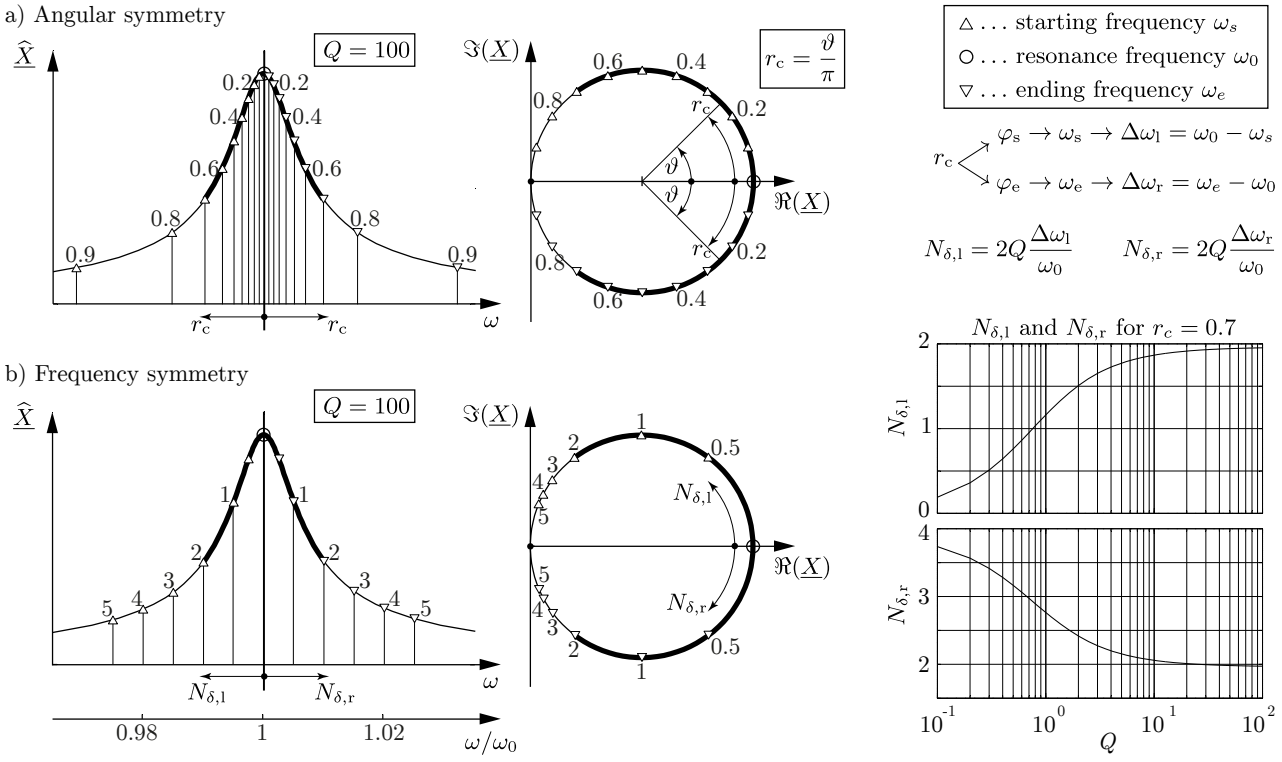

Figure 2.13: Illustration of the covering ratio r_c, the number of bandwidth parameters $N_{\delta,\mathrm{l}}$ and $N_{\delta,\mathrm{r}}$ as well as the difference between frequency points using angular or frequency symmetry, respectively. The figure on the bottom right shows the relation between $N_{\delta,\mathrm{l}}$ and $N_{\delta,\mathrm{r}}$ for a covering ratio of $r_\mathrm{c} = 0.7$. The indices 'l' and 'r' in $N_{\delta,\mathrm{l}}$ and $N_{\delta,\mathrm{r}}$ stand for 'left' and 'right', respectively.

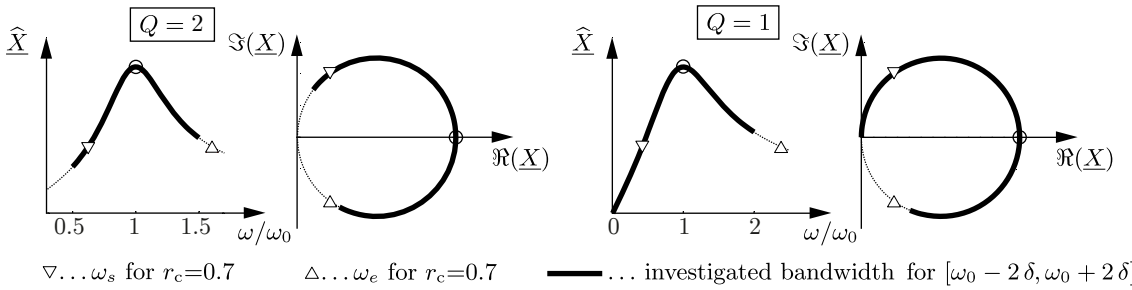

Figure 2.14: Shifting of the investigated bandwidth for low Q. For $Q < 10$, the bandwidth $[\omega_0 - N_{\delta,\mathrm{l}}, \omega_0 + N_{\delta,\mathrm{r}}]$ shifts remarkably counterclockwise on the resonance circle. Thus, the starting frequency $\omega_s = \omega_0 - N_{\delta,\mathrm{l}}$ might become negative. Caused by this shift, the ending frequency ω_e might get high when claiming a certain covering ratio r_c.

that best results are obtained for frequency symmetric bandwidths $\omega_0 \pm (2 \ldots 5)\delta$, see Fig. 2.13. At this point, the investigated bandwidth is determined to be 0.7 r_c and $\omega_0 \pm 2\delta$, respectively which is the intersection of both findings.

For high Q the difference between both methods for determining ω_s and ω_e is negligible, however for very low Q (i.e. $Q < 5$) some minor possible problematic cases, see also Fig. 2.14 have to be prohibited:

1. Calculating the starting frequency ω_s using the frequency symmetric case i.e., $\omega_\mathrm{s} = \omega_0 \left(1 - \frac{N_{\delta,\mathrm{l}}}{2Q}\right)$, the calculated ω_s gets negative for $Q < N_{\delta,\mathrm{l}}/2$.

2. When claiming $r_\mathrm{c} = 0.7$ for calculating the ending frequency ω_e, the latter can get very high for low Q. This finding can be explained as for $Q < 10$ the investigated frequency symmetric bandwidth shifts remarkably counterclockwise on the resonance circle, see Fig. 2.14.

Equidistant vs. equiangular frequency steps

Once ω_s and ω_e are appropriately determined, the frequency points can be distributed in constant frequency steps or in equiangular frequency steps on the circle. It was found in a pilot study that the latter yields slightly better results.

2.6.2 Frequency sweep speed and prevention from non-linear deflections

When the resonant frequency response is recorded by measuring a quantity representing the resonator's deflection or velocity at discrete frequencies, it is necessary to wait at least $5\,\tau$ after each frequency step to ensure that the eigen-oscillation sufficiently decayed. This eigen-oscillation is excited at every frequency step resulting in an oscillation consisting of the eigenfrequency $\omega_{0\delta}$ and the frequency of forced oscillation ω_ex, c.f. Eq. 2.99. For ω_ex close to ω_0 beat becomes significant resulting in an apparent oscillation with (beat) frequency $|\omega_0 - \omega_\mathrm{ex}|$ [235]. Fig. 2.15(a) shows two examples for recorded frequency responses with to fast performed frequency steps for increasing and decreasing frequency sweeps. These results have been obtained with the U-shaped wire sensor [MHj4] which has its fundamental resonant mode at approximately 950 Hz with $Q = 840$ in air, see also Sec. 4.5.

For the present approach of resonator investigation, it is assumed, that the resonance can be characterized by a linear second order oscillator. If the excitation forces become to high, nonlinear deflection resulting in Duffing behavior might occur [236–238]. Figure 2.15(b) shows resonance curves for non linear deflections for the case of the U-shaped wire. These recorded curves where obtained by successively increasing the excitation current from 1 mA to 200 mA. Similar behavior, i.e. deformation of the linear frequency response to lower frequency was also reported in [239]. An example where too high excitation forces deform the resonance curve in the other direction is given in [240]. A recommendable way to prevent from nonlinear deflections is to reduce the excitation force such that nonlinear behavior can not be observed. This can be easily be done by judging the shape in the Nyquist plot. Usually,

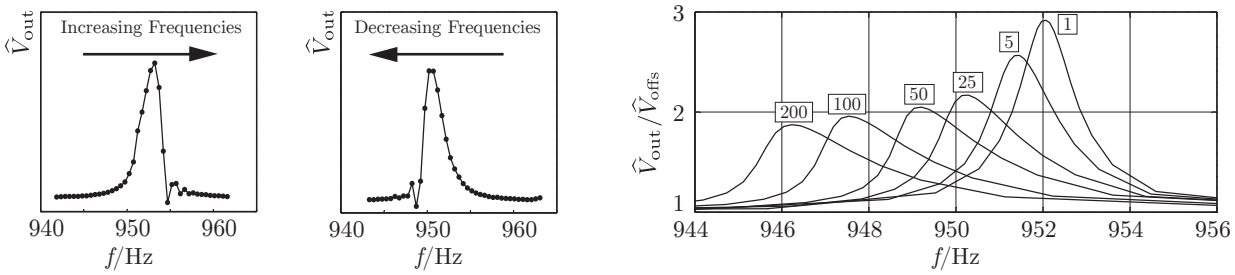

(a) Measuring speed

(b) Nonlinear deflections

Figure 2.15: Results of too fast frequency steps and too high excitation forces. a) Flawed frequency responses obtained for to fast increasing and decreasing frequency sweeps. b) Frequency responses in air obtained with the U-shaped wire resonator for excitation currents from 1 mA to 200 mA. Note that in this figure the ratio of the amplitudes measured voltage V_{out} and offset voltage V_{offs} (see also Fig. 2.8) are depicted.

if the linear second order fit deviates (repeatably) from the measured spectrum, nonlinear effects (too high excitation forces) are the cause. In [231] non-linear deflections are accepted and analyzed to obtain a high signal to noise ratio.

2.7 Liquid loaded resonator (LLR)

2.7.1 Equations for resonance frequency and quality factor

From this point, it is assumed that the resonance is ideally recorded, i.e. any background signals (including noise) can be perfectly subtracted, each measured point gives the steady state value and the measured signal is not subjected to non-linear effects.

As it was already mentioned in Sec. 1.9, a common approach for modeling a liquid loaded resonator is to model the effect of the liquid on the resonance characteristics, i.e. ω_0 and Q by taking an additional fluid related mass m_{f} and damping c_{f} into account. In Sec. 2.1, the equations for m_{f} and c_{f} for the case of an in-plane oscillating plate Eq. 2.7, a transversally oscillating sphere, Eq. 2.18 and an out-of-plane transversally oscillating cylinder, Eq. 2.22 were given. These equations can be summarized in the form [MHj3]

$$\begin{aligned} m_{\mathrm{f}}(\omega,\eta,\rho) &= C_{\mathrm{m}_1}\,\rho + C_{\mathrm{m}_2}\sqrt{\frac{\eta\,\rho}{\omega}} \quad \text{and} \\ c_{\mathrm{f}}(\omega,\eta,\rho) &= C_{\mathrm{c}_1}\,\eta + C_{\mathrm{c}_2}\,\sqrt{\omega\,\eta\,\rho} \end{aligned} \tag{2.131}$$

where the factors C_{ji} are given in Tab. 2.2 for the case of oscillating plate, sphere and cylinder,

	Plate	Sphere	Cylinder
C_{m_1}	0	$\frac{2\,\pi}{3} r_{\mathrm{s}}^3$	$\pi\, r_{\mathrm{c}}^2\, l_{\mathrm{c}}$
C_{m_2}	$\frac{A_{\mathrm{p}}}{\sqrt{2}}$	$\sqrt{2}\,3\,\pi\, r_{\mathrm{s}}^2$	$\sqrt{2}\,2\,\pi\, r_{\mathrm{c}}\, l_{\mathrm{c}}$
C_{c_1}	0	$6\,\pi\, r_{\mathrm{s}}$	$2\,\pi\, l_{\mathrm{c}}$
C_{c_2}	$\frac{A_{\mathrm{p}}}{\sqrt{2}}$	$\sqrt{2}\,3\,\pi\, r_{\mathrm{s}}^2$	$\sqrt{2}\,2\,\pi\, r_{\mathrm{c}}\, l_{\mathrm{c}}$

Table 2.2: Coefficients C_{ji} replacing geometrical dimensions and constants.

respectively. Substituting these equations for $\omega = \omega_0$ in Eq. 1.124 yields [MHj3]

$$\begin{aligned} \frac{1}{\omega_0^2} = \frac{m}{k} &\approx m_{0\mathrm{k}} + m_{\rho\mathrm{k}}\,\rho + m_{\eta\rho\mathrm{k}}\sqrt{\frac{\eta\,\rho}{\omega_0}}, \quad \text{and} \\ \frac{1}{Q} = \frac{c}{\sqrt{k\,m}} &\approx \frac{c_{0\mathrm{k}} + c_{\eta\mathrm{k}}\,\eta + c_{\eta\rho\mathrm{k}}\sqrt{\omega_0\,\eta\,\rho}}{\sqrt{m_{0\mathrm{k}} + m_{\rho\mathrm{k}}\,\rho + m_{\eta\rho\mathrm{k}}\sqrt{\frac{\eta\,\rho}{\omega_0}}}}. \end{aligned} \tag{2.132}$$

As the implicit character of these equations hampers a straightforward solution, the frequency dependence in Eq. 2.131 can be neglected considering that the investigated bandwidth and thus the change of ω are negligibly small. However, Eq. 2.132 can be used for calculating η and ρ for evaluated ω_0 and Q with a LLR as it will be described in Sec. 2.7.2.

Substitution of

$$C_{\mathrm{m}_2} = \sqrt{\omega_0}C^*_{\mathrm{m}_2} \quad \text{and} \quad C_{\mathrm{c}_2} = \frac{C^*_{\mathrm{c}_2}}{\sqrt{\omega_0}} \tag{2.133}$$

in Eq. 2.131 and assuming that the investigated frequency range around the resonance is small (as in case of sufficiently high quality factors) and thus assuming that the influence of ω on m_f and c_f is negligible it follows that

$$\begin{aligned} m_\mathrm{f}(\eta,\rho) &\approx C_{\mathrm{m}_1}\,\rho + C^*_{\mathrm{m}_2}\sqrt{\eta\,\rho} \quad \text{and} \\ c_\mathrm{f}(\eta,\rho) &\approx C_{\mathrm{c}_1}\,\eta + C^*_{\mathrm{c}_2}\,\sqrt{\eta\,\rho}. \end{aligned} \tag{2.134}$$

With these frequency independent solutions for m_f and c_f, ω_0 and Q can be expressed as [MHj3]

$$\begin{aligned} \frac{1}{\omega_0^2} = \frac{m}{k} &\approx m_{0\mathrm{k}} + m_{\rho\mathrm{k}}\,\rho + m^*_{\eta\rho\mathrm{k}}\sqrt{\eta\,\rho}, \quad \text{and} \\ \frac{1}{Q} = \frac{c}{\sqrt{k\,m}} &\approx \frac{c_{0\mathrm{k}} + c_{\eta\mathrm{k}}\,\eta + c^*_{\eta\rho\mathrm{k}}\sqrt{\eta\,\rho}}{\sqrt{m_{0\mathrm{k}} + m_{\rho\mathrm{k}}\,\rho + m^*_{\eta\rho\mathrm{k}}\sqrt{\eta\,\rho}}}. \end{aligned} \tag{2.135}$$

The model parameters $m_{0\mathrm{k}}$, $m_{\rho\mathrm{k}}$, $m^{(*)}_{\eta\rho\mathrm{k}}$, $c_{0\mathrm{k}}$, $c_{\eta\mathrm{k}}$ and $c^{(*)}_{\eta\rho\mathrm{k}}$ are determined applying a linear least square fit procedure using experimentally obtained values for ω_0 and Q in at least three different liquids for known values of η and ρ, see [MHj3].

2.7.2 Inverse model

Eq. 2.132 is used to calculate η and ρ from measured ω_0 and Q as it will be explained in the following. These are implicit equations, however, the simplified and explicit equations 2.135 allow easier analysis for further calculations and investigations such as e.g. the sensitivities of a particular device to η and ρ. As possible way to calculate η and ρ with the knowledge of ω_0 and Q and the identified model parameters from Eq. 2.132, i.e., $m_{0\mathrm{k}}$, $m_{\rho\mathrm{k}}$, $m_{\eta\rho\mathrm{k}}$, $c_{0\mathrm{k}}$, $c_{\eta\mathrm{k}}$ and $c_{\eta\rho\mathrm{k}}$ is

$$\begin{aligned} \rho &= \frac{1}{2}(a_0\,k_1 - b_0 + k_3)\frac{m_{\eta\rho\mathrm{k}}}{\sqrt{\omega_0}m_{\rho\mathrm{k}}\left(1 - \frac{c_{\eta\mathrm{k}}\,m_{\rho\mathrm{k}}}{c_{\eta\rho\mathrm{k}}\,m_{\eta\rho\mathrm{k}}}\right)} \\ \eta &= \frac{1}{2}(b_0\,k_1 - a_0 + k_3)\frac{\sqrt{\omega_0}\,c_3}{c_2\left(1 - \frac{c_{\eta\mathrm{k}}\,m_{\rho\mathrm{k}}}{c_{\eta\rho\mathrm{k}}\,m_{\eta\rho\mathrm{k}}}\right)} \end{aligned} \tag{2.136}$$

where

$$\begin{aligned} a_0 &= \frac{1}{m_{\eta\rho k}\,\omega_0^{3/2}} - \sqrt{\omega_0}\,\frac{m1}{m_{\eta\rho k}} \\ b_0 &= \frac{1}{m_{\eta\rho k}\,\omega_0^{3/2}\,Q} - \frac{1}{\sqrt{\omega_0}\frac{c1}{m_{\eta\rho k}}} \\ k_1 &= 1 - 2\frac{m_{\eta k}\,m_{\rho k}}{m_{\eta\rho k}\,m_{\eta\rho k}} \\ k_2 &= 1 - \frac{m_{\eta k}\,m_{\rho k}}{m_{\eta\rho k}\,m_{\eta\rho k}} \\ k_2 &= \sqrt{(a_0 - b_0)^2 + 4\,a_0\,b_0\frac{m_{\eta k}\,m_{\rho k}}{m_{\eta\rho k}\,m_{\eta\rho k}}} \end{aligned} \tag{2.137}$$

For some resonators it was observed, that the fitted parameters became negative. In this case the given equations for calculating η and ρ can not be used.

The major advantages of such a model are its general applicability to many different resonator principles, (also principles other than in-plane oscillating plates, oscillating spheres and laterally oscillating cylinders), the intuitive descriptiveness of liquid loaded resonators and thus the possibility of comparing different types of viscosity and mass density sensors. Showing the characteristics of such sensors by plotting e.g. Q versus η is not sufficient and might even be misleading as usually not only η but also ρ differ for different liquids. Giving the values in tabulated form does not allow an insightful description of the device, as η and ρ both have significant effects on f_r and Q. Furthermore, giving a number representing the sensitivity of the devices is difficult, as the sensitivities to η and ρ are not constant but strongly η and ρ dependent. With the knowledge of the parameters of this model however, the sensors characteristics are usually very well described. Once the model parameters are determined, a list of further revealing analysis possibilities is disclosed, some of which are discussed in Sec. 2.8.

2.8 Application of the generalized equations

2.8.1 Relative sensitivity

For resonant viscosity and mass density sensors, absolute sensitivities as, e.g., the sensitivity of the resonance frequency to mass density in Hz/(g/cm^3) are often not very descriptive. First of all, by evaluating absolute values, the comparison of sensors operated in a different frequency range is hardly possible. Second, it is difficult to compare the sensitivities to mass density and viscosity, as usually the investigable range of viscosities is much larger than the range of mass densities. For common liquids, the range of mass densities is narrow, hardly exceeding the range between 0.6 to 1.8 g/cm^3, whereas the range of viscosities covers several orders of magnitudes. In [MHj4] for example a viscosity range of 0.2 to 216 mPa·s with an according range of densities from 0.78 g/cm^3 to 1.24 g/cm^3 has been investigated with a single resonant sensor. Due to these reasons, absolute sensitivities are not evaluated. A difficulty in interpretation which arises for absolute as well as for relative sensitivities is, that both types of sensitivities depend on η and ρ.

As already mentioned, it follows from Eqs. 2.132 and 2.135 that f_r and Q are both dependent on η and ρ. This finding was also substantiated by experiments, see, e.g. [MHj4] and[MHj2]. Thus, to completely describe a resonant viscosity and mass density sensor's sensitivity, four sensitivities have to be evaluated. For this, we define the relative sensitivity of a read-out value $X(y_i)$ to one of its variables y_i as

$$S_{X,y_i} := \left|\frac{\partial X}{\partial y_i}\cdot\frac{y_i}{X}\right| \tag{2.138}$$

where in this case X stands either for f_r or Q and y_i for η or ρ. As an example, a comparison of these sensitivities is given in Fig. 2.16 for five different sensors. There, it can be observed for the

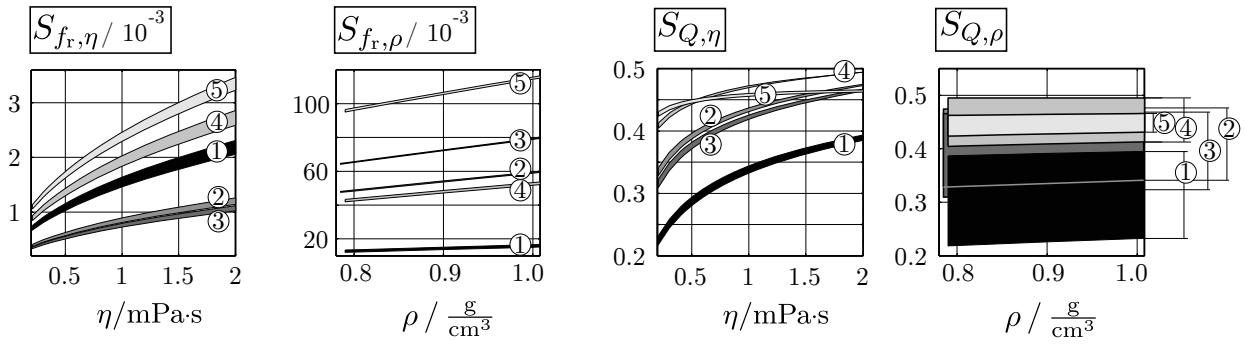

(a) Resonance frequency

(b) Quality factor

Figure 2.16: Sensitivities to viscosity and mass density. 1: torsional cylinder [MHj1], 2: circular tuning fork [MHj2], 3: rectangular tuning fork [MHj2], 4: U-wire [MHj4], 5: quartz tuning fork [230]. The sensitivities of f_r and Q to η and ρ are not constant but dependent both on η and ρ. For this reason the sensitivities are depicted as bands, in the experimentally investigated range of viscosities and mass densities. In the plots for $S_{f_r,\eta}$ and $S_{Q,\eta}$ the upper boundary of the bands are the values for $\rho = 1.01\,\mathrm{g/cm^3}$, the lower boundary for $\rho = 0.79\,\mathrm{g/cm^3}$. In the plots for $S_{f_r,\rho}$ and $S_{Q,\rho}$ the upper and lower boundaries of the bands represent the evaluated values for $\eta = 0.21\,\mathrm{mPa{\cdot}s}$ and $\eta = 2.05\,\mathrm{mPa{\cdot}s}$, respectively.

investigated sensors, that in general the resonance frequency is much more sensitive to mass density than to viscosity. The sensitivity of the quality factor however is similar for both, mass density and viscosity.

2.8.2 Estimation of required accuracies for f_r and Q

Manufacturers of viscosity and mass density meters usually specify the performance of their instruments with absolute accuracy in mass density but relative accuracy in viscosity. For example, the high precision laboratory instrument Anton Paar SVM 3000 features a reproducibility of 0.35 % in viscosity and $0.0005\,\mathrm{g/cm^3}$ for mass density and a repeatability of 0.1 % and $0.0002\,\mathrm{g/cm^3}$, for η and ρ respectively. The reproducibility of the temperature measurement of the SVM 3000 is 0.02 °C and its repeatability is 0.005 °C. To get in the accuracy range of such laboratory instruments, at this point, we target a relative accuracy in viscosity $\Delta\eta/\eta = 10^{-2}$ and absolute accuracy in mass density $\Delta\rho = 1\,\mathrm{mg/cm^3}$ which corresponds to a relative accuracy of $\Delta\rho/\rho = 10^{-3}$ for aqueous liquids. Repeated measurements and long-term stability analyses, see e.g., [MHj4] and [MHj2] and evaluation of f_r and Q showed instabilities (noise) yielding a certain spread for both quantities, which yields an inaccuracy in the η and ρ determination. Using the sensitivities evaluated from Eq. 2.138, the change of f_r and Q upon small changes of η and ρ can be expressed in matrix notation as follows:

$$\begin{bmatrix} \frac{\Delta f_r}{f_r} \\ \frac{\Delta Q}{Q} \end{bmatrix} = \begin{bmatrix} S_{f_r,\eta} & S_{f_r,\rho} \\ S_{Q,\eta} & S_{Q,\rho} \end{bmatrix} \cdot \begin{bmatrix} \frac{\Delta\eta}{\eta} \\ \frac{\Delta\rho}{\rho} \end{bmatrix}. \tag{2.139}$$

With this equation, maximum tolerable variations in the f_r and Q evaluation can be estimated for achieving the desired accuracies in η and ρ. For this estimation it is assumed that η is (exactly) known, if ρ is evaluated from f_r or Q and vice versa, i.e. the estimated allowed variations for f_r and Q are lowest limiting values.

For a rough estimation for the resonance stability it is assumed that ρ is evaluated from f_r and η from Q, respectively. For investigated tuning fork sensors, see [MHj2] and Sec. 4.9, which resonate at 420 Hz with quality factors of some hundreds in the investigated liquids, variances (noise) smaller than 10^{-2} Hz for f_r and 1 for Q have to be obtained to achieve the targeted accuracies of $\Delta\eta/\eta = 1\,\%$ for viscosity and $\Delta\rho = 1\,\mathrm{mg/cm^3}$ for mass density. The accordingly required relative accuracies are in the order of 10^{-5} for the resonance frequency and 10^{-3} for the quality factor.

These values are estimates for the resonance frequency and quality factor stability which are absolutely required. I.e., if the instability is larger than these values, the targeted accuracies can not be achieved on no account. A further source for measurement inaccuracies is the cross-sensitivity of the resonance frequency to temperature, which limits the accuracies in η and ρ as the temperature measurement accuracy is also limited to a certain extent. For instance, a first investigation of the circular tuning fork's temperature behavior was presented in [MHc8] and is also discussed in discussed in Sec. 2.10. There, it was found that the circular tuning fork's cross-sensitivity to temperature is about $-0.049\,\mathrm{Hz/°C}$. In the investigated viscosity and mass density range, the sensitivity of the resonance frequency to mass density is about $-0.024\,\mathrm{Hz/(mg/cm^3)}$. Thus, it follows for the required temperature measurement accuracy to be about $\Delta\vartheta = 0.5\,°\mathrm{C}$ to distinguish mass density variations of $1\,\mathrm{mg/cm^3}$ from temperature variations. This requirement is commonly fulfilled by state of the art thermometers.

2.8.3 Error propagation

The sensitivity parameters S_{X,y_i} which can be obtained using Eq. 2.138 and the simplified model for ω_0 and Q, i.e., Eq. 2.135, depend on density and viscosity. For proper measurements of the resonance characteristics processed with the estimation procedure from [229] it was shown in [234] that there is a relation between the relative standard deviations of f_r and Q which is determined by the signal-to-noise ratio, SNR (which is defined as the ratio of Nyquist circle diameter to standard deviation of noise on the Nyquist circle diameter) of the acquired frequency spectra and the number of frequency points M:

$$\frac{\mathrm{std}\,\{f_\mathrm{r}\}}{f_\mathrm{r}} = \frac{1}{2Q}\frac{\mathrm{std}\,\{Q\}}{Q} \approx \sqrt{\frac{2}{M}}\frac{1}{Q\,\mathrm{SNR}} \tag{2.140}$$

It was furthermore shown, that variations of f_r and Q due to noise are uncorrelated in case of reasonably sampled resonance curves. If deviations from Eq. 2.140 are observed, this is an indicator that unmodeled influences such as parameter drifts persist and that there is still potential for setup improvements. Relative errors on ρ and η for given relative deviations on f_r and Q can be determined by inverting Eq. 2.139, i.e.,

$$\begin{bmatrix} \frac{\Delta\eta}{\eta} \\ \frac{\Delta\rho}{\rho} \end{bmatrix} = \begin{bmatrix} S_{fr,\eta} & S_{fr,\rho} \\ S_{Q,\eta} & S_{Q,\rho} \end{bmatrix}^{-1} \cdot \begin{bmatrix} \frac{\Delta f_\mathrm{r}}{f_\mathrm{r}} \\ \frac{\Delta Q}{Q} \end{bmatrix}. \tag{2.141}$$

The error propagation depends on the invertibility of the matrix in Eq. 2.141. E.g., for pure shear resonators, the matrix gets singular and ρ and η can not be separated. However, this is not the case for manufactured sensors in general.

Fig. 2.17 shows the error propagation for the round and the rectangular tuning fork for the liquids of the viscosity and the mass density series [MHj2]. Errors in f_r and Q cause much higher relative errors

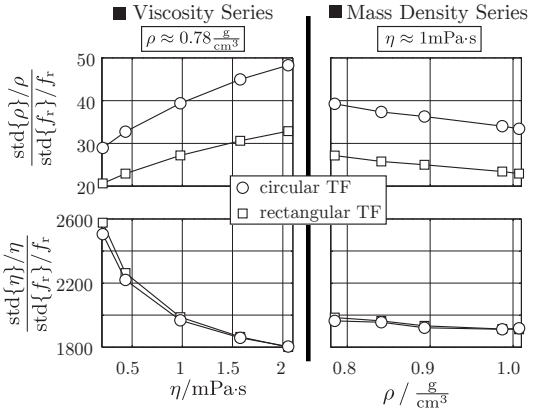

Figure 2.17: The error propagation for rectangular and circular tuning forks evaluated for the viscosity and the density series.

in viscosity than in density. Therefore, the requirements on the frequency accuracy are much stricter when low errors on viscosity shall be achieved. With the recently published tuning fork setups [MHj2] the relative standard deviations in frequency are 10^{-6} approximately, and thus accuracies around $\pm 1\%$ (± 3 standard deviations) are achievable for η and 0.01% (i.e. $0.1\,\mathrm{mg/cm^3}$ for aqueous liquids) for ρ, approximately. These results meet the requirements from Sec. 2.8.2.

2.9 Higher mode excitation

Resonant viscosity and mass density sensors excited at higher modes were presented in [MHc4]. There, measurements with the U-shaped wire sensor [MHj4], Sec. 4.5, the tuning fork [MHj2], Sec. 4.9 and the double membrane sensor [MHj6], Sec. 4.1 were performed in their first and second modes. As the measurements obtained with the double membrane sensor suffered from not sufficiently stable values and as furthermore the applicability of the generalized model to the double membrane sensor is questionable, the discussion of first and second modes for the double membrane sensor is omitted at this point. However, the double membrane sensor was especially designed to show different sensitivities at the first and the second modes. This has been shown and proven, e.g. in [MHj6].

To investigate the differences and potential advantages of recording more than one mode with resonant viscosity and mass density sensors, the frequency responses in four different liquids at the first and the second resonant modes were recorded. From these recorded frequency responses, resonance frequencies $f_{\mathrm{r},ij}$ and quality factors Q_{ij} were evaluated using a resonance circle based fitting algorithm, [229]. The indices i and j stand for the examined liquids and modes respectively. The liquids which have been used for examining the sensors are designated with numbers i in Tab. 2.3. There, their viscosities and mass densities at 25 °C are given.

The evaluated results for the resonance frequencies and quality factors for the first and second modes i.e. $f_{\mathrm{r},i1}$, $f_{\mathrm{r},i2}$ and Q_{i1} and Q_{i2} as well as the according mass densities ρ_i and viscosities η_i were used to identify the parameters of the generalized model Eq. 2.135. With these results the sensitivities using Eq. 2.138 were calculated. The sensitivity bands for the first and the second modes are depicted in Fig. 2.18 for the first and the second modes for the U-shaped wire and the tuning fork sensor. There, it is clearly visible, that both modes yield similar sensitivities, where the second mode tends to be slightly less sensitive. A more detailed and thorough investigation of higher mode excitation for liquid viscosity and mass density sensors however has to be elaborated. Higher mode excitation becomes especially interesting for (e.g. viscoelastic) liquids, which feature a frequency dependent viscosity $\eta(\omega)$.

2.10 Cross-sensitivity to temperature

An experimental investigation of resonant sensors' cross-sensitivities to temperature and an empiric modeling approach has been presented in [MHc8] and [MHc3]. The experiments presented there were repeated and the investigated temperature range was extended from initially 15 to 35 °C to 5 to 45 °C.

Measurements in ethanol, isopropanol, DI-water and a mixture of 61 % glycerol in DI-water were first performed at 25 °C with the circular steel tuning fork setup as it was presented in [MHj2] to determine

	Liquid	η mPa·s	ρ g/cm^3
1.	Ethanol	1.0371	0.7852
2.	Isopropanol	2.0491	0.7803
3.	DI-water	0.85492	0.9969
4.	61 % Glyc/ DI-w.	9.723	1.1545 3

Table 2.3: Values for η and ρ at 25 °C.

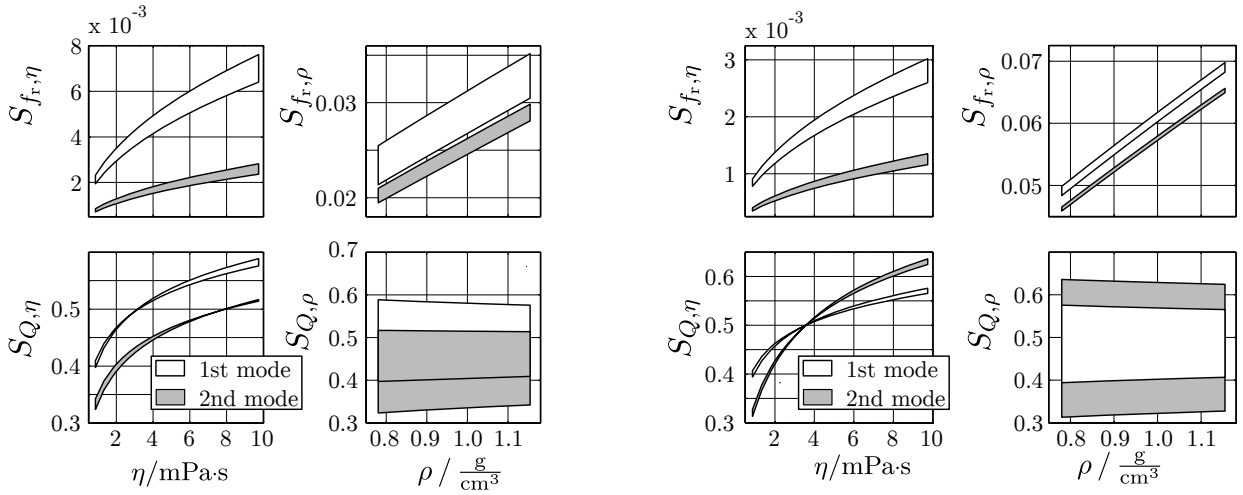

(a) U-shaped wire

(b) Tuning Fork

Figure 2.18: Comparison of sensitivities of the first and the second modes for the U-shaped wire and the tuning fork sensors. The sensitivities for both modes and both sensors are similar, where the sensitivity of the second mode is slightly smaller in general.

the parameters from Eq. 2.135, see also Fig. 2.19. To investigate the tuning fork's intrinsic temperature cross-sensitivity of f_r and Q in a temperature range from 5 to 45 °C the failing of the temperature independent model Eq. 2.135 at temperatures other than 25 °C was evaluated as follows (see also Fig. 2.19): The viscosities $\eta_i(\vartheta_j)$ and mass densities $\rho_i(\vartheta_j)$ of the aforementioned liquids were evaluated with an Anton Paar SVM 3000 viscometer at temperatures ϑ_j from 5 to 45 °C in 5 °C steps. (The subscript i stands for the liquid, the subscript j for the temperature.) With the knowledge of the temperature dependent viscosities $\eta_i(\vartheta_j)$ and mass densities $\rho_i(\vartheta_j)$, resonance frequencies $\omega_{0\mathrm{m},ij}$ and quality factors

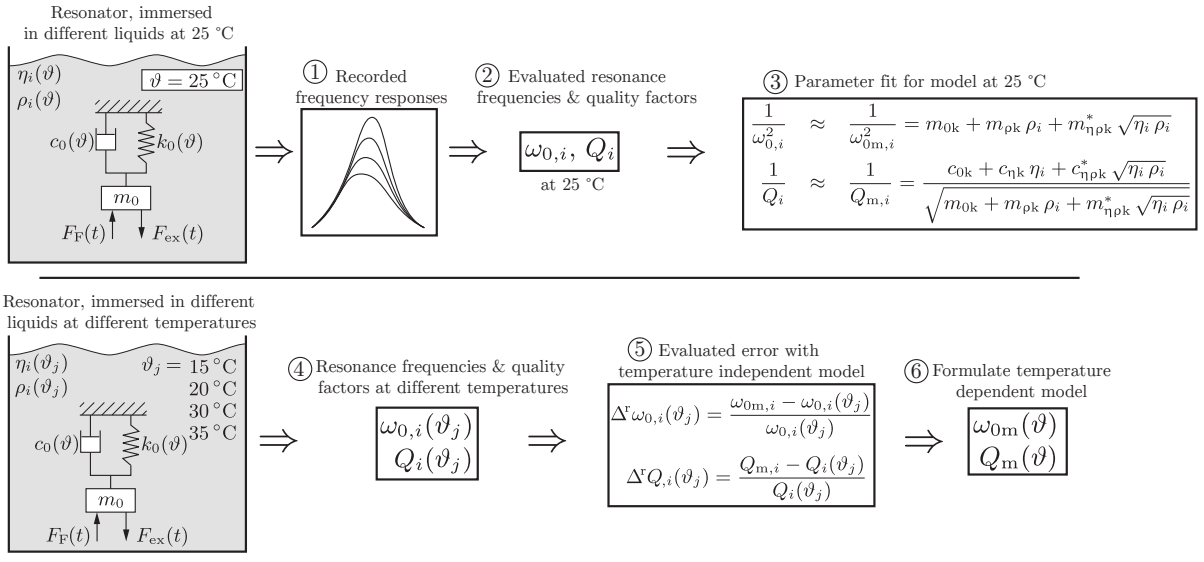

Figure 2.19: Modeling aproach: The frequency responses of a mechanical resonator are recorded upon immersion in liquids (denoted with the index i) with viscosity η_i and mass density ρ_i at 25 °C. The angular resonance frequencies $\omega_{0,i}$ and quality factors Q_i are determined fitting the frequency response of a second order resonator into the recorded frequency response. $\omega_{0,i}$ and Q_i from at least three liquids are necessary to identify the parameters of a temperature-independent model relating ω_0 and Q to η and ρ. The evaluation of relative deviations $\Delta^\mathrm{r}\omega_{0m,i}(\vartheta_j)$ and $\Delta^\mathrm{r}Q_{m,i}(\vartheta_j)$ of the modeled temperature-independent quantities $\omega_{0\mathrm{m},i}$ and $Q_{\mathrm{m},i}$ from measured quantities $\omega_{0,i}(\vartheta_j)$ and $Q_i(\vartheta_j)$ at temperatures ϑ_j reveals the failing of the temperature-independent model. With the knowledge of this deviation, a temperature dependence can be introduced in the existing model.

$Q_{\mathrm{m},ij}$ were calculated using the previously identified temperature independent model, Eq. 2.135. With these calculated values for $\omega_{0\mathrm{m},ij}$ and $Q_{\mathrm{m},ij}$ (resulting from the temperature-independent model) the relative deviations $\Delta^{\mathrm{r}}\omega_{0,i}(\vartheta_j)$ and $\Delta^{\mathrm{r}}Q_i(\vartheta_j)$ from measured resonance frequencies $\omega_{0,i}(\vartheta_j)$ and quality factors $Q_i(\vartheta_j)$ were evaluated for every liquid at each temperature.

The evaluation and interpretation of $\Delta^{\mathrm{r}}\omega_0$ depicted in the upper plots of Fig. 2.20 suggests that the influence of ϑ on $\Delta^{\mathrm{r}}\omega_0$ is (almost) linear and independent of the liquid's viscosity or mass density. Thus an approach such as

$$\Delta^{\mathrm{r}}\omega_0 = \frac{\omega_{0m} - \omega_0(\vartheta)}{\omega_0(\vartheta)} = (\vartheta - 25\,^{\circ}\mathrm{C})\, k_\vartheta \tag{2.142}$$

is used, where k_ϑ is a parameter which is fitted such that the relative deviation $\Delta^{\mathrm{r}}\omega_0$ gets minimal. For the quality factor however not trend following ϑ could be observed so far. The empirically motivated equation for $\omega_0(\vartheta)$ reads:

$$\omega_0(\vartheta) = \frac{1}{(\vartheta - 25\,^{\circ}\mathrm{C})\, k_\vartheta + 1} \cdot \frac{1}{\sqrt{m_{0\mathrm{k}} + m_{\rho\mathrm{k}}\,\rho + m^*_{\eta\rho\mathrm{k}}\,\sqrt{\eta\,\rho}}}. \tag{2.143}$$

The relative deviations of modeled, temperature dependent results from the measured values i.e. $\Delta^{\mathrm{r}}\omega_0(\vartheta)$ are depicted in the lower plots of Fig. 2.20 showing good accordance of modeled and measured results.

For the cross-sensitivity of the resonance frequency to temperature it follows

$$S_{f_{\mathrm{r}},\vartheta} = \frac{\partial\omega_0}{\partial\vartheta}\frac{\vartheta}{\omega_0} = \frac{-k_\vartheta\,\vartheta}{(\vartheta - 25\,^{\circ}\mathrm{C})\, k_\vartheta + 1}. \tag{2.144}$$

For the measurements depicted in Fig. 2.20

$$k_\vartheta = 12.011 \cdot 10^{-3}/^{\circ}\mathrm{C} \qquad \text{and} \qquad k_\vartheta = 12.285 \cdot 10^{-3}/^{\circ}\mathrm{C}$$

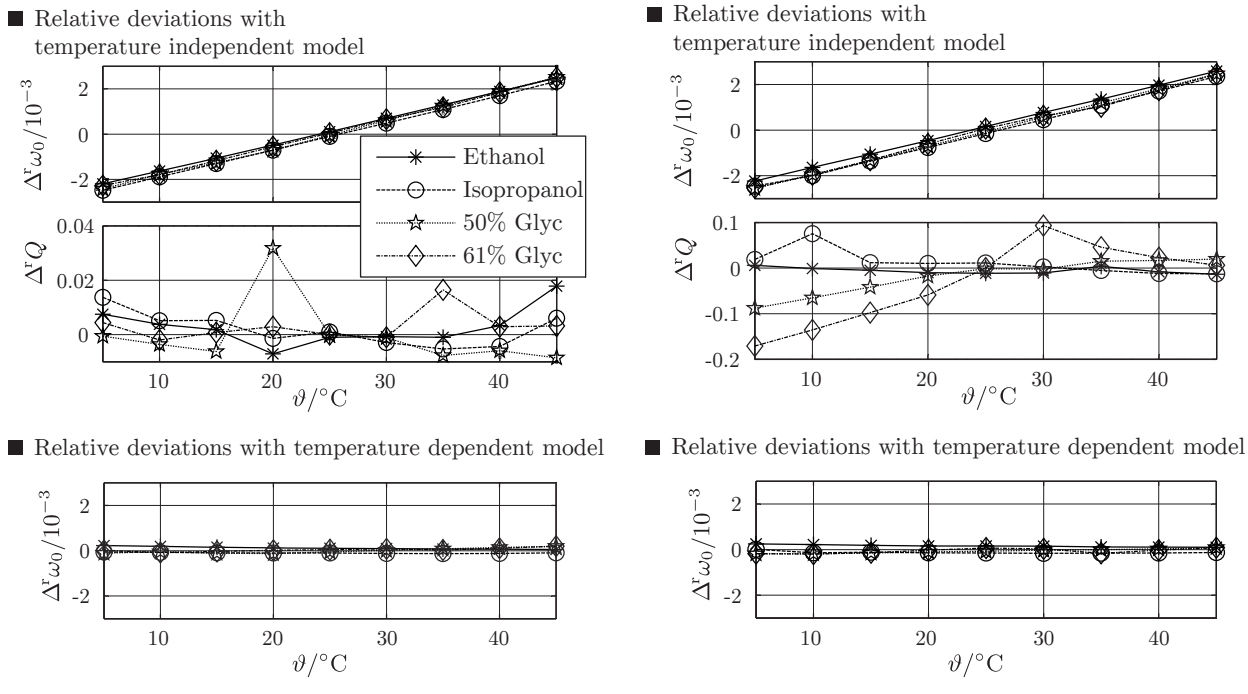

(a) 1st Mode (b) 2nd Mode

Figure 2.20: Relative deviation $\Delta^{\mathrm{r}}Q$ and $\Delta^{\mathrm{r}}\omega_0$ between measured and modeled results.

are obtained for the first and second modes. This finding shows that for beam based resonators, fundamental and higher modes show similar cross-sensitivities to temperature. Equation 2.69 also suggests this statement.

The plots for $\Delta^{\mathrm{r}}Q$ in Fig. 2.20 do not show a clear trend. Thus a temperature dependence of Q was not considered so far in the generalized equations. However, more precise measurements are necessary to further investigate the temperature dependence of f_{r} and Q.

2.11 Theoretical study on the frequency dependence of $m(\omega)$ and $c(\omega)$

2.11.1 Examples of liquid loaded resonators

The model for ω_0 and Q, Eq. 2.135, was successfully applied to liquid loaded resonators which were found in a comprehensive literature review if sufficient data (i.e. f_{r} and Q with associated η and ρ in tabulated form) were provided. The resonators were selected such that operational frequencies in a range from hunderts of Hertz to the Mega Hertz range and quality factors lower than 1 up to over 500 in liquids can be investigated. With the data found in literature and from our own work, the model parameters $m_{0\mathrm{k}}, m_{\rho\mathrm{k}}, m_{\eta\rho\mathrm{k}}$ $c_{0\mathrm{k}}, c_{\eta\mathrm{k}}$ and $c_{\eta\rho\mathrm{k}}$ in the model Eq. 2.135 were determined performing a linear least square fit as it is described in [MHj3]. The selected LLRs are given in Tab. 2.4.

An overview of the characterized LLRs from Tab. 2.4 is shown in Fig. 2.21 on a double logarithmic scale for f_{r} and Q and associated η and ρ. There, the dots indicate the reported values and the solid lines are the results from the fitted model.

2.11.2 Estimation of the change of $m(\omega)$ and $c(\omega)$ in the investigated frequency range

To estimate the change of $m(\omega) = m_0 + m_{\mathrm{f}}(\omega, \eta, \rho)$ and $c(\omega) = c_0 + c_{\mathrm{f}}(\omega, \eta, \rho)$ in the investigated bandwidth $\omega_0 \pm N_{\delta l,r}\delta$ a frequency dependence is re-introduced into the model by substituting $m^*_{\eta\rho\mathrm{k}} \to m^*_{\eta\rho\mathrm{k}}\sqrt{\omega_0}/\sqrt{\omega}$ and $c^*_{\eta\rho\mathrm{k}} \to c^*_{\eta\rho\mathrm{k}}\sqrt{\omega}/\sqrt{\omega_0}$, respectively yielding

$$\begin{aligned} \frac{m(\omega)}{k} &\approx m_{0\mathrm{k}} + m_{\rho\mathrm{k}}\,\rho + \sqrt{\omega_0}\,m^*_{\eta\rho\mathrm{k}}\sqrt{\frac{\eta\,\rho}{\omega}}, \quad \text{and} \\ \frac{c(\omega)}{k} &\approx c_{0\mathrm{k}} + c_{\eta\mathrm{k}}\,\eta + \frac{c^*_{\eta\rho\mathrm{k}}}{\sqrt{\omega_0}}\sqrt{\omega\,\eta\,\rho}. \end{aligned} \tag{2.145}$$

With this result, the relative change of $m_{\mathrm{f}}(\omega)$ and $c_{\mathrm{f}}(\omega)$ can be estimated using

$$\Delta^{\mathrm{r}}m_{\mathrm{l,r}} = \frac{\frac{m(\omega_0 \pm N_{\delta\mathrm{l,r}}\delta)}{k} - \frac{m(\omega_0)}{k}}{\frac{m(\omega_0)}{k}} \quad \text{and} \quad \Delta^{\mathrm{r}}c_{\mathrm{l,r}} = \frac{\frac{c(\omega_0 \pm N_{\delta\mathrm{l,r}}\delta)}{k} - \frac{c(\omega_0)}{k}}{\frac{c(\omega_0)}{k}} \tag{2.146}$$

No.	Device	Year	Reference
1	Si-Cantilever	2002	[88]
2	Si-Platelet	2009	[240]
3	Spiral Spring	2014	[MHc7]
4	Quartz Tuning Fork	2014	[230]
5	AlN Platelet	2014	[230]
6	Circ. Tuning Fork	2015	[MHj2]
7	Rect. Tuning Fork	2015	[MHj2]
8	U-shaped wire	2014	[MHj4]

Table 2.4: Selected liquid loaded resonators. Associated resonance frequencies and quality factors are depicted in Fig. 2.21.

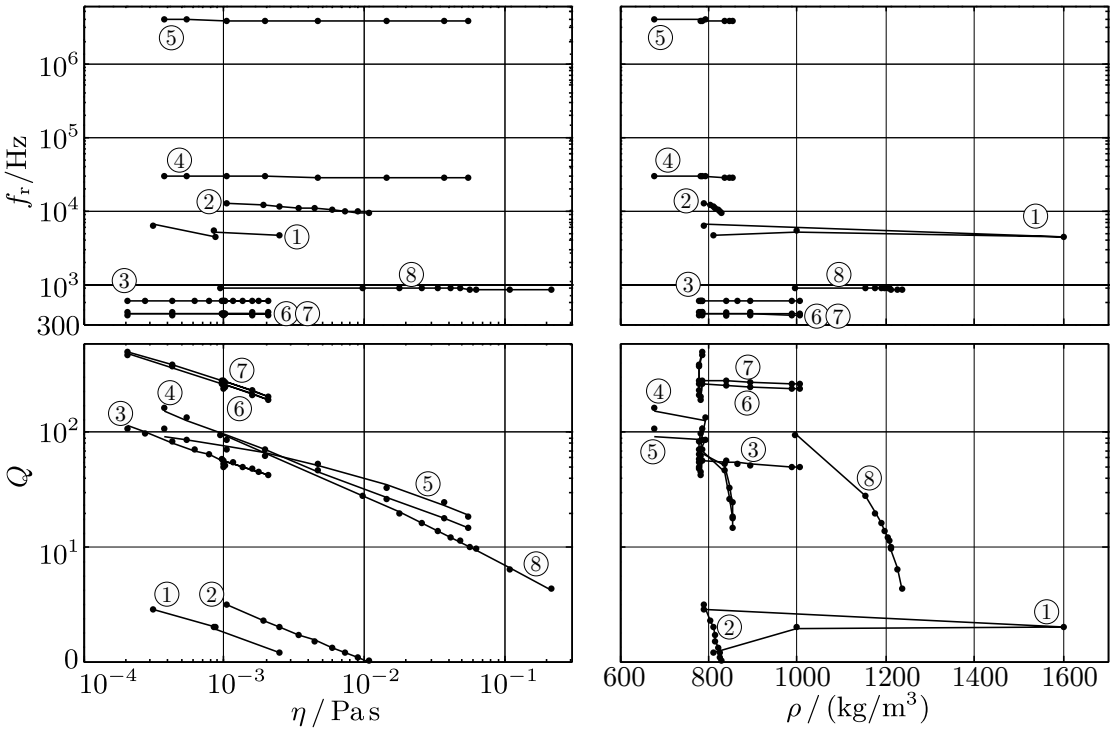

Figure 2.21: Examples of liquid loaded resonators covering a range of hunderts of Hertz to the Mega Hertz range and quality factors lower than 1 up to over 500 with according viscosities from 0.1 mPa·s to 200 mPa·s and mass densities from 0.64 g/cm^3 to 1.6 g/cm^3, approximately. The dots are reported experimental results and the solid lines were obtained using with the fitted model for every reported resonator.

which become dependent on Q only if $\delta = \omega_0/(2Q)$ is substituted in the equations above. The relative changes of the mass parameter $\Delta^{\mathrm{r}} m_{\mathrm{l,r}}$ and the damping parameter $\Delta^{\mathrm{r}} c_{\mathrm{l,r}}$ are depicted for investigated bandwidths claiming a circle covering ratio $r_{\mathrm{c}} = 0.7$ in Fig. 2.22. As a rule of thumb, for $Q > 10$ the relative changes of both parameters are less than 1 %.

2.11.3 Estimation of systematic errors of η and ρ resulting from second order fit

With the frequency dependent parameters $m(\omega)/k$ and $c(\omega)/k$ in Eq. 2.145, the frequency response of a LLR can be calculated for given η and ρ using the relation

$$\underline{H}_{\mathrm{LLR}}(\omega) = \frac{\frac{1}{k}}{\frac{c(\omega)}{k} + j\left(\frac{m(\omega)}{k}\,\omega - \frac{1}{\omega}\right)}. \tag{2.147}$$

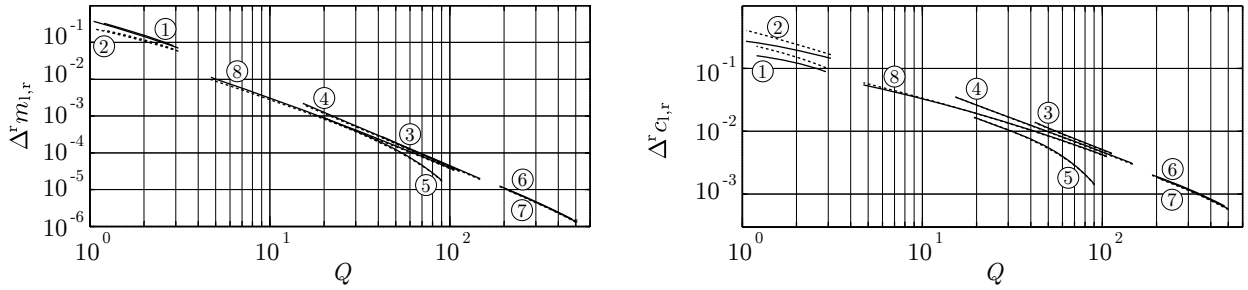

(a) Relative change of mass parameter m

(b) Relative change of damping parameter c

Figure 2.22: Relative changes of $m(\omega)$ and $c(\omega)$ in the investigated frequency range claiming $r_{\mathrm{c}} = 0.7$.

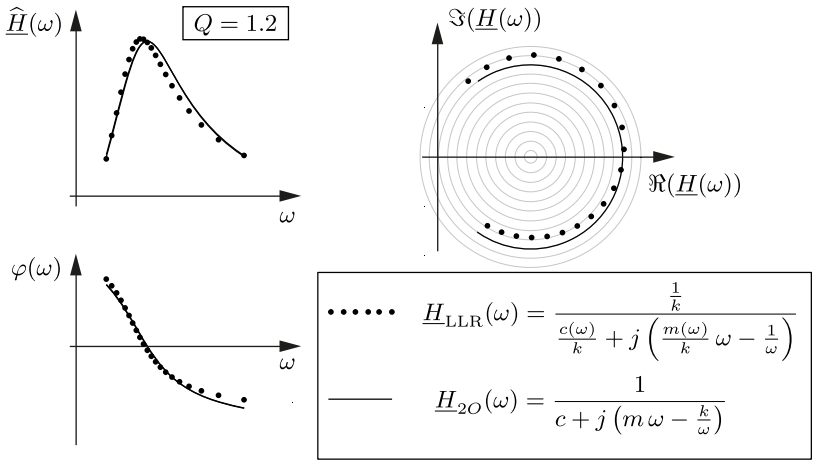

Figure 2.23: Second order fit in LLR data

Through the reintroduction of a frequency dependence, the frequency response $\underline{H}_{\mathrm{LLR}}(\omega)$ does not describe a circle in the complex plane, see Fig. 2.23. This behavior becomes more significant, the smaller Q. Thus, fitting a second order transfer function into the frequency response of a LLR, yields systematic errors in ω_0 and Q and if deduced from the latter, η and ρ. To investigate this systematic error, LLR frequency responses were calculated for the eight cases mentioned above within the reported viscosity and mass density ranges. Then a circle fitting algorithm, c.f. Sec. 2.5.3, is applied to this generated data. Simply speaking, a circle is searched in data which is not a circle and subsequently therefrom resulting errors are calculated. From the resonance frequency $\omega_{0,2O}$ and quality factor Q_{2O} obtained with the second order circle fit algorithm, viscosity η_{2O} and mass density ρ_{2O} are calculated. (The subscript '2O' designates the variables obtained through a second order fit.) To estimate the systematic error which might occur if viscosity and mass density are determined by fitting and evaluating a second order frequency response, the relative deviations

$$\Delta^{\mathrm{r}}\eta = \frac{\eta_{2O} - \eta}{\eta} \qquad \text{and} \qquad \Delta^{\mathrm{r}}\rho = \frac{\rho_{2O} - \rho}{\rho} \tag{2.148}$$

are calculated. The result of this investigation is depicted in Fig. 2.24. The interpretation of this theoretic investigation is that systematic relative errors in η higher than 1 % for $Q < 200$ and relative errors in ρ higher than 1 % for $Q < 20$ result from the linear second order fit. However this result can not be directly related to viscosity and mass density measurements, as real LLRs are calibrated and thus systematic errors are decreased. However, the frequency dependence of the transfer function $\underline{H}_{\mathrm{LLR}}(\omega)$ needs further (experimental) investigation in any case.

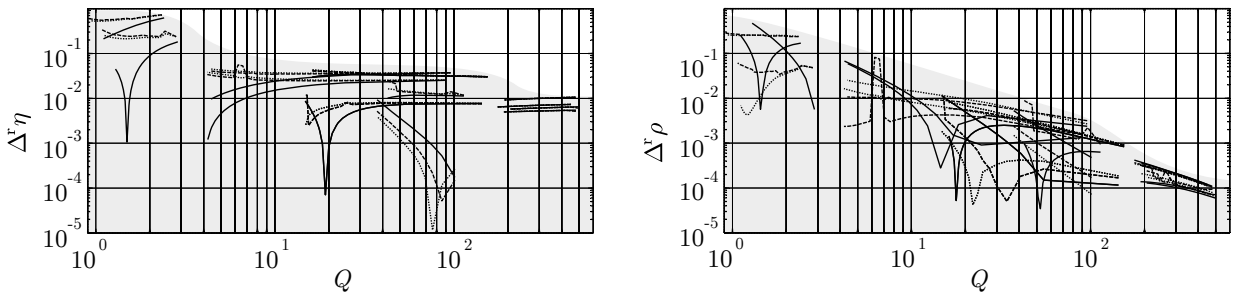

(a) Relative error for viscosity

(b) Relative error for mass density

Figure 2.24: Systematic relative errors $\Delta^{\mathrm{r}}\eta$ and $\Delta^{\mathrm{r}}\rho$ obtained by fitting a linear second order transfer function into the frequency response of a liquid loaded resonator in dependence of Q. Following from a theoretic investigation, the obtained errors which depend on Q, will be in the gray shaded area.

Chapter 3

Device concepts and approaches

3.1 Lorentz force driven resonators (LFDRs)

The Lorentz-force driven sensors discussed here, are mechanical resonators comprising or consisting of electrical conductors carrying electrical currents in the presence of an external magnetic field. The resonator design itself, is manifold but usually consists of singly or doubly clamped beams, torsional bars and membranes. A more detailed overview and explanation of existing resonator designs will be given in Sec. 4. The total Lorentz force which is called excitation force $\boldsymbol{F}_{\mathrm{ex}}$ here, on a conductor following the path $\boldsymbol{s}$ with length l_{c} used for excitation, carrying the current i_{in} in the magnetic field with magnetic flux density $\boldsymbol{B}$ is [241, 242]:

$$\boldsymbol{F}_{\mathrm{ex}} = i_{\mathrm{in}} \int_{l_{\mathrm{c}}} d\boldsymbol{s} \times \boldsymbol{B}(\boldsymbol{s}). \tag{3.1}$$

Using a sinusoidal current $i_{\mathrm{in}}(t) = \hat{I}_{\mathrm{in}} \sin(\omega\, t)$ excites harmonical oscillations of the resonator at angular frequency ω.

For read-out, i.e., for monitoring the motion of the resonator, measuring the motion-induced voltage V_{M} is an elegant way to solve this task. As an electrical conductor is moving in the presence of an external magnetic field, a voltage is induced on the latter. This voltage can be measured on the same conductor which is used for excitation, or on a second conductor which (through mechanical coupling) follows the motion of the oscillating resonator, see Figs. 3.1 and 3.2. From the definition of Lorentz forces and Faraday's law for induction, the motion-induced voltage V_{M} on a conductor moving in an magnetic field is expressed as [241, 242]

$$V_{\mathrm{M}}(t) = -\int_{l_{\mathrm{c}}} \left(\frac{\partial \boldsymbol{u}(\boldsymbol{s})}{\partial t} \times \boldsymbol{B}(\boldsymbol{s}) \right) \cdot \mathrm{d}\boldsymbol{s}. \tag{3.2}$$

where $\boldsymbol{u}$ is the (relative) deflection of the conductor from the points at which the voltage is induced and d$\boldsymbol{s}$ is a vector line element along the conductor. The minus results from the minus in Faraday's law of induction $\nabla \times \boldsymbol{E} = -\frac{\partial \boldsymbol{B}}{\partial t}$ in Maxwell's equations.

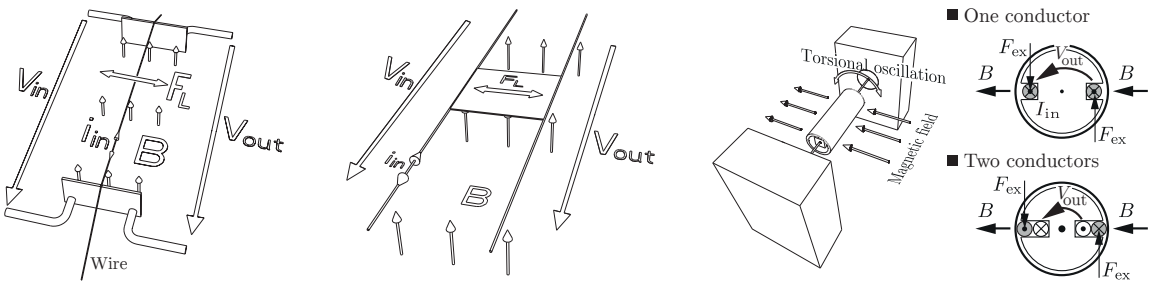

(a) One conductor (b) Two conductors (c) Torsional resonator: both, one and two conductor LFDR possible

Figure 3.1: a) One single conductor is used for both, excitation and read-out. b) one conductor (left) is used for excitation, the other (right), mechanically coupled to the first and thus following the movement of the latter is used for read-out c) Using a torsional resonator allows a comparison of one and two LFDRs with the same geometry.

3.2 Principle of one conductor and two conductors LFDRs

In the following, one conductor and two conductor LFDRs are described and discussed for the example of a transversally vibrating wire [MHj5], an in plane oscillating platelet [MHj5] as well as a torsional resonator [MHj1], c.f. Fig. 3.1. For the torsional resonator, both excitation methods (one and two conductor LFDR) are possible for resonators with the same geometry and the same mechanical characteristics. Using such a torsional resonator as example, the difference and potential advantages as well as drawbacks using one or two conductors will be discussed in Sec. 3.4.3. The mechanical principles for transversal and torsional LFDRs as well as their equivalent circuits are depicted in Fig. 3.2, both for one and two conductors LFDRs.

The simplest design of a one conductor LFDR is a straight wire placed in an external magnetic field. In analogy to the string of a string instrument, the wire is stretched to allow transversal vibrations. The wire is excited by means of Lorentz forces on sinusoidal currents in the wire in the presence of a magnetic field, see Fig. 3.1(a). The motion of the vibrating wire in the external magnetic field in turn, yields a motion-induced voltage V_M on the wire which is proportional to the velocity of the resonator, c.f. Eq. 3.2 and thus, serves as read-out signal. However, this signal can not be measured directly.

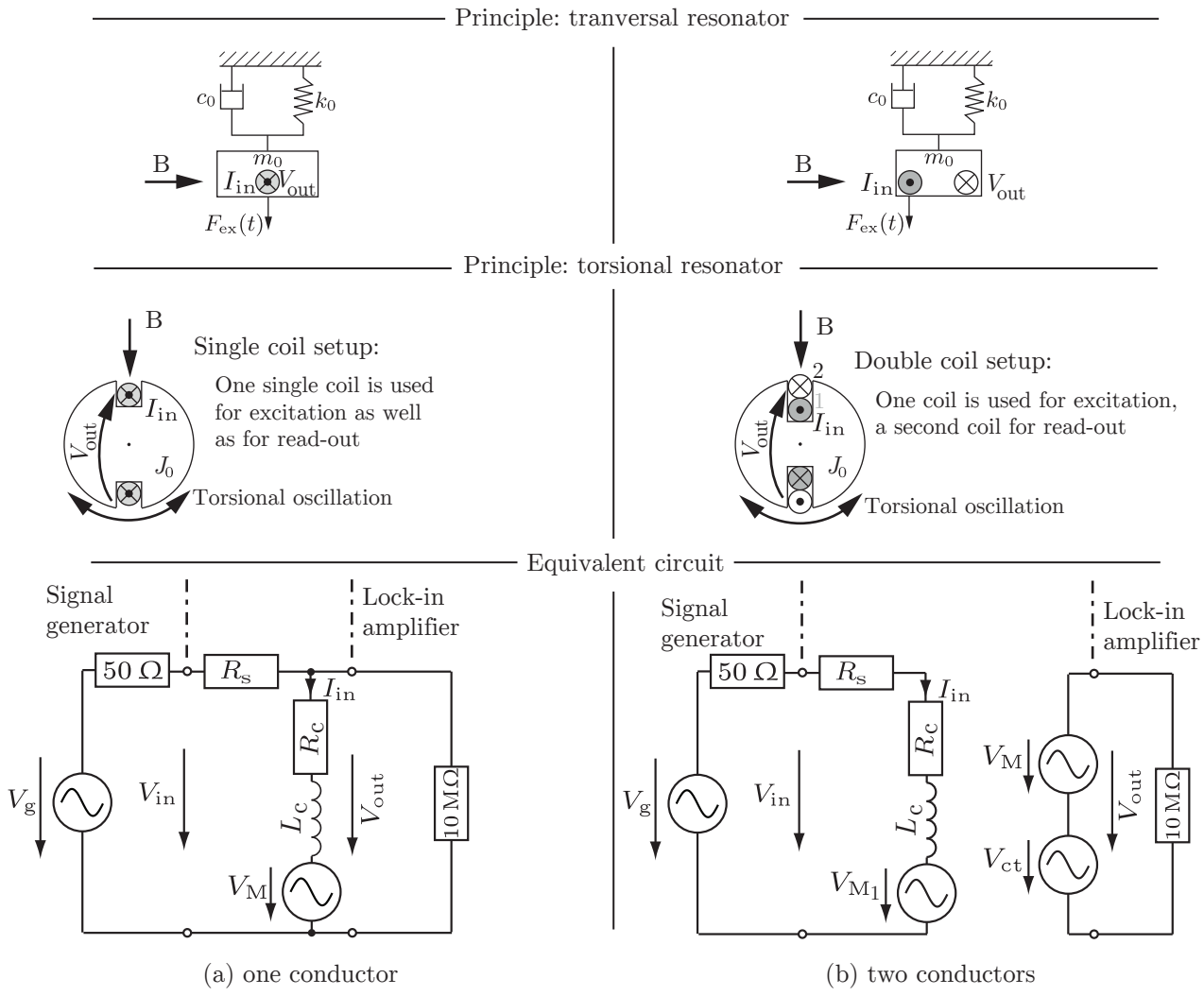

Figure 3.2: a) One conductor LFDR: top: transversal, lumped element oscillator, middle: cross-section of the torsional resonator, bottom: electrical equivalent circuit of a one conductor LFDR. I_in: input (excitation) current, B: external magnetic field, V_g: Voltage of the signal generator, 50 Ω: output resistance of the signal generator, R_s: series resistance, R_c, L_c: conductor's or coil's resistance and inductance, V_M: motion-induced voltage, 10 MΩ: input resistance. b) Two conductors LFDR: One conductor (coil) is used for excitation, the other for read-out, V_ct: induced voltage due to inductive cross-talk.

The measurable output voltage V_{out} contains additional contributions resulting from the impedance of the wire and the excitation currents in it. The impedance of the conductor can be modeled by a serial connection of a (temperature dependent) resistance R_{c} and an inductance L_{c}. The first considers the finite conductivity of the wire, the second the inductivity resulting from the loop which is formed by the vibrating wire and the wiring necessary for electrical connection.

For two conductors LFDRs, excitation and read-out circuits are separated using a second conductor which is galvanically separated from the first. Fig. 3.1(b) shows a two conductors LDFR using two wires which are mechanically coupled by a small platelet. The first conductor, used for excitation, carries the excitation (or input current) I_{in} and the second, used for read-out, follows the movement of the first yielding a motion-induced voltage on it. This motion-induced voltage however, can not be measured directly as the time-variant magnetic field induced by the excitation current couples into the output circuitry which induces a spurious cross-talk voltage V_{ct}. This will be explained in more detail in Sec. 3.4.2. The output voltage V_{out} is measured with a Lock-In amplifier which has a high input resistance of $10\,\mathrm{M}\Omega$, suggesting the assumption that the current in the output circuitry is zero it follows that the impedance of the output circuitry can be neglected.

Similar to a DC-motor, the torsional resonator consists of a winding form carrying an excitation coil. This winding form is affixed to a thin metal rod serving as torsional spring, which in turn is rigidly clamped at both ends. Application of sinusoidal excitation currents and an external magnetic field yields torsional vibrations, see Fig. 3.1(c). As for the case of the transversally oscillating wire, this motion yields an induced voltage which is proportional to the tangential velocity of the excitation coil. In analogy to the straight wire, the motion-induced voltage can not be measured directly but is composed of this motion-induced voltage V_{M} and the impedance related voltage drop. The coil's impedance is modeled using a serial connection of the coil's resistance and its inductance, respectively.

The principle of transversal and torsional one conductor LFDRs is depicted on the left hand side of Fig. 3.2. There, the complete electrical equivalent circuit of one conductor LFDRs is depicted as well. In this electrical equivalent circuit the whole setup including excitation and read-out electronics is considered. For providing the excitation current I_{in}, a signal generator with a $50\,\Omega$ output resistance is used. A series resistance R_{s} can be used to limit the excitation current and to prevent potential, non-linear deflections. The signal from the mechanical oscillator is modeled by a series connection of the conductor's resistance R_{c}, its inductance L_{c} and the motion-induced voltage V_{M}. The effect of the motion-induced voltage could also be interpreted as an additional part of the impedance as the motion of the electrical charges in the conductor due to the applied input voltage is also affected by Lorentz forces if the conductor is set into motion.

The principles of transversal and torsional two conductors LFDRs as well as their electrical equivalent circuit are depicted on the right hand side of Fig. 3.2. For the torsional case, a second coil is wound into the winding form yielding a complete coupling from the magnetic field induced in the excitation coil into the read-out coil.

3.3 Measurable output voltage V_{out}

The LFDRs used for viscosity and mass density sensing are excited at several discrete angular frequencies ω_i to record the resonator's frequency response containing a characteristic resonant mode. The measured voltage $V_{\mathrm{out}}(\omega)$ is composed by three signal components: First, the motion-induced voltage V_{M} which is proportional to the resonator's velocity. The second measured signal component is an offset voltage V_{offs} due to the conductor's impedance or electrical cross-talk. The third signal component is the influence of the measurement setup's total phase shift φ_{m} which results from the phase response of the measurement instruments and transit times affected by the wiring. Thus, the

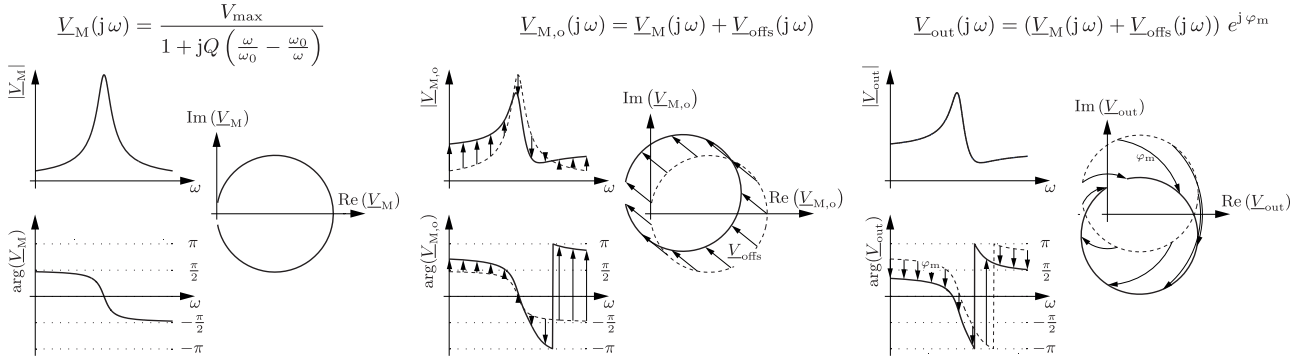

(a) Motion-induced voltage V_{M} (b) V_{M} plus offset voltage V_{offs} (c) $(V_{\mathrm{M}} + V_{\mathrm{offs}})$ phase shifted by φ_{m}

Figure 3.3: Illustration of split signal components: a) shows the motion-induced voltage which is proportional the resonator's velocity. b) illustrates the effect of signals V_{offs} resulting from electrical cross-talk or impedance related voltage drops. c) depicts the total measurable signal including phase shifts resulting from the measuring system and transit times from the wiring [MHj2].

measurable voltage can be written using complex notation as follows

$$\underline{V}_{\mathrm{out}}(\mathrm{j}\,\omega) = (\underline{V}_{\mathrm{M}}(\mathrm{j}\,\omega) + \underline{V}_{\mathrm{offs}}(\mathrm{j}\,\omega))\ e^{\mathrm{j}\,\varphi_{\mathrm{m}}(\omega)}. \tag{3.3}$$

The motion-induced voltage response can be modeled as a second order resonator

$$\underline{V}_{\mathrm{M}}(\mathrm{j}\,\omega) = \frac{V_{\max}}{1 + \mathrm{j}Q\left(\frac{\omega}{\omega_0} - \frac{\omega_0}{\omega}\right)} \tag{3.4}$$

where ω_0 and Q are the resonator's angular resonance frequency and quality factor, respectively. Remember, for the resonator's velocity, the angular eigenfrequency (of undamped vibrations) and the frequency where the amplitude reaches its maximum value are identical. Thus, we may call ω_0 resonance frequency. A characteristic resonance curve of the motion-induced voltage and the effect of an offset voltage as well as the phase shift on the measured signal are qualitatively depicted in Fig. 3.3. These additional offset signals can significantly deform the resonance curve and yield asymmetries in the latter. For highly damped resonators, i.e. $Q < 100$, as it might be the case for resonant viscosity and mass density sensors when examining high viscous liquids, asymmetries in both, the resonator's velocity and deflection frequency response become large. Due to these deformations of the frequency reponse, searching the maximum peak frequency and the frequencies where the amplitude decreased to the $1/\sqrt{2}$ of the peak values or methods based on a Lorentzian fit [243, 244] are not appropriate methods for evaluating resonance frequency f_{r} and Q. For this thesis, an algorithm presented in [229], which was especially developed for highly damped resonators is used. This algorithm separates a second order resonance of the form of Eq. 3.4 from spurious offset signals and determines the resonant parameters f_{r} and Q by fitting the resonance circle in a Nyquist plot of the response function.

3.4 Offset voltage and cross-talk

3.4.1 One conductor LFDR (U-wire)

The modeling of the impedance related offset voltage

$$\underline{V}_{\mathrm{offs}} = (R_{\mathrm{c}} + \mathrm{j}\,\omega\,L_{\mathrm{c}})\underline{I}_{\mathrm{in}} \tag{3.5}$$

i.e. the modeling of R_{c} and L_{c}, in the equivalent circuit in Fig. 3.2 (a), of a one conductor LFDR is explained using the U-shaped wire sensor, see Fig. 3.4, as example. This resonator consists of a tungsten wire, bent to the shape of a 'U' which is placed in an external magnetic field and carrying sinusoidal excitation currents for excitation. This geometry is similar to a cantilever, i.e. a singly clamped beam.

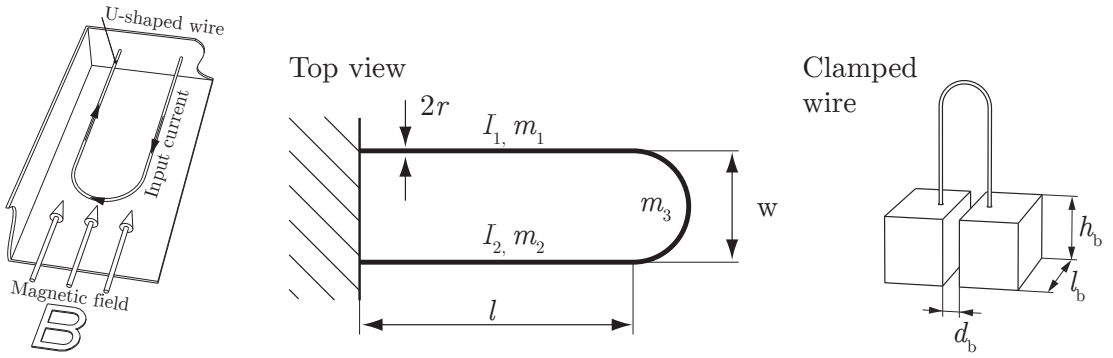

(a) Principle (b) Geometrical dimensions of the U-shaped wire

Figure 3.4: U-shaped wire sensor. a) A 400 µm thick tungsten wire carrying a sinusoidal current is placed in an external magnetic field yielding out of plane oscillations. b) Geometrical dimensions of the U-shaped wire. For clamping, the wire is brazed to two solid brass blocks.

Resistance R_c

The temperature dependent resistance of the wire can be calculated considering its temperature dependent specific electrical resistance ρ_t, the conductor's length l_c and its cross-section A_c

$$R_\mathrm{c}(T) = \rho_\mathrm{t}(T)\frac{l_\mathrm{c}}{A_\mathrm{c}} \approx \rho_t(T)\frac{2\,l + w/2\,\pi}{r_w^2\,\pi} \tag{3.6}$$

with

$$\rho_t(T) \approx \rho_\mathrm{t}(T_0)\,(1 + \alpha_\mathrm{t}\,(T - T_0)) \tag{3.7}$$

where T_0 is a reference temperature, T is the actual temperature and α_t is the linear temperature coefficient of resistivity.

Inductance L_c

The inductivity L of a loop or a coil consists of the internal inductance L_i and the external inductance L_e, [245] i.e.,

$$L = L_\mathrm{i} + L_\mathrm{e}. \tag{3.8}$$

The internal and external inductances are the inductances due to the magnetic fields that are internal and external to the conducting loop, respectively. In the following, the calculation of the inductance of a planar, loop, corresponding to a coil with $N = 1$ turns and a constant electrical current I is discussed. For this, the internal and external inductances are calculated using the defining equation for L_e and the energy stored in the magnetic field of the inductance. For both relations, the magnetic flux density has to be known. In Fig. 3.5 two expressions relating the magnetic flux density with an constant electrical current I are derived. The derivations are intended to be self-explanatory, more detailed explanations can be found in textbooks of fundamental electrodynamics, see e.g. [241, 242].

In general, to relate the magnetic flux density $\boldsymbol{B}$ with its source, an electrical current $I = \int_A \boldsymbol{J} \cdot \mathrm{d}\boldsymbol{A}$ in an electrical conductor with cross-section A and electrical current density J, all four Maxwell's equations have to be considered to describe the electromagnetic field.

(I): $\mathrm{rot}(\boldsymbol{B}) = \mu_0 \boldsymbol{J} + \mu_0 \varepsilon_0 \dfrac{\partial \boldsymbol{E}}{\partial t}$ ... Ampère's circuital law

(II): $\mathrm{rot}(\boldsymbol{E}) = -\dfrac{\partial \mathbf{B}}{\partial t}$ ... Faraday's law of induction

(III): $\mathrm{div}(\boldsymbol{E}) = \dfrac{\rho}{\varepsilon_0}$ ... Gauss's law

(IV): $\boxed{\mathrm{div}(\boldsymbol{B}) = 0}$ ... Gauss's law for magnetism

Magnetostatical case, i.e. $\mathrm{div}(\boldsymbol{J}) = 0$:

(I*): $\boxed{\mathrm{rot}(\boldsymbol{B}) = \mu_0 \boldsymbol{J}}$

(II*): $\boxed{\mathrm{rot}(\boldsymbol{E}) = 0}$

For some simplified cases, analytical solutions directly relating B and I, can be found:

■ Case 1: $\boldsymbol{J} = J\,\boldsymbol{e}_z$, in an infinitely extended, straight, circular conductor

From (I*) and (IV) it follows that $B_z = 0$ and $B_r = 0$, and due to rotational symmetry $B_\varphi(r) = \text{const}$ for constant r.

Applying Kelvin-Stokes theorem to (I*) and considering the above simplifications, it follows $\boxed{B_\varphi = \dfrac{\mu_0 I}{2\,r\,\pi}}$

■ Case 2: Infinitely thin and closed conductor, i.e. $I = \boldsymbol{J} \cdot \mathrm{d}\boldsymbol{A}$.

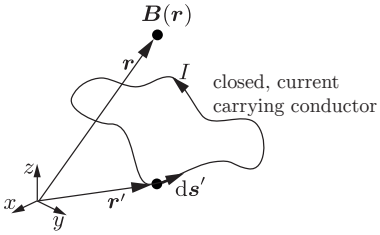

Equations from vector calculus
(1): $\mathrm{div}(\mathrm{rot}(\boldsymbol{F})) = 0$
(2): $\nabla \times (\nabla \times \boldsymbol{F}) = \nabla(\nabla \cdot \boldsymbol{F}) - \nabla \cdot \nabla \boldsymbol{F} = \mathrm{grad}(\mathrm{div}(\boldsymbol{F})) - \Delta \boldsymbol{F}$
(3): $\mathrm{rot}(f\,\boldsymbol{F}) = f\,\mathrm{rot}(\boldsymbol{F}) + \mathrm{grad}(f) \times \boldsymbol{F}$

(IV) and (1) suggest the ansatz $\boxed{\boldsymbol{B} = \mathrm{rot}(\boldsymbol{A})}$ (4) $\quad \boldsymbol{A}$ ... vector potential

(4) → (I*): $\mathrm{rot}(\mathrm{rot}(\boldsymbol{A})) \overset{(2)}{=} \mathrm{grad}(\mathrm{div}(\boldsymbol{A})) - \Delta \boldsymbol{A} = \mu_0 \boldsymbol{J}$

The ansatz only defined $\mathrm{rot}(\boldsymbol{A}) = \boldsymbol{B}$, $\mathrm{div}(\boldsymbol{A})$ is arbitrary and thus $\mathrm{div}(\boldsymbol{A}) = 0$ is assumed.

Poisson's equation

$\Rightarrow \boxed{-\Delta \boldsymbol{A} = \mu_0 \boldsymbol{J}}$

$\Rightarrow \boxed{\boldsymbol{A}(\boldsymbol{r}) = \dfrac{\mu_0}{4\,\pi} \int \dfrac{\boldsymbol{J}(\boldsymbol{r}')}{|\boldsymbol{r} - \boldsymbol{r}'|} \mathrm{d}V'}$ (5)

Solution of Poisson's equation (satisfies $\mathrm{div}(\boldsymbol{A}) = 0$)

(5) → (4):

$$\boldsymbol{B}(\boldsymbol{r}) = \frac{\mu_0}{4\,\pi} \int \nabla \times \frac{\boldsymbol{J}(\boldsymbol{r}')}{|\boldsymbol{r} - \boldsymbol{r}'|} \mathrm{d}V' \overset{(3)}{=} \frac{\mu_0}{4\,\pi} \int \frac{1}{|\boldsymbol{r} - \boldsymbol{r}'|} \underbrace{\nabla \times \boldsymbol{J}}_{=0\ (\mathrm{II}^*)} + \nabla \frac{1}{|\boldsymbol{r} - \boldsymbol{r}'|} \times \boldsymbol{J}(\boldsymbol{r}') \mathrm{d}V' = -\frac{\mu_0}{4\,\pi} \int \frac{\boldsymbol{r} - \boldsymbol{r}'}{|\boldsymbol{r} - \boldsymbol{r}'|^3} \times \underbrace{\boldsymbol{J}(\boldsymbol{r}') \mathrm{d}V'}_{=I\,\mathrm{d}\boldsymbol{s}'}$$

for an infinitely thin conductor

$$\boxed{\boldsymbol{B}(\boldsymbol{r}) = -\frac{\mu_0 I}{4\,\pi} \int \frac{\boldsymbol{r} - \boldsymbol{r}'}{|\boldsymbol{r} - \boldsymbol{r}'|^3} \times \mathrm{d}\boldsymbol{s}'}$$

Biot-Savart law

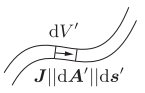

$\boldsymbol{J}(\boldsymbol{r}')\,\mathrm{d}V' = \boldsymbol{J}(\boldsymbol{r}')\,\mathrm{d}\boldsymbol{A}' \cdot \mathrm{d}\boldsymbol{s}'$
$= \boldsymbol{J}(\boldsymbol{r}')\,|\mathrm{d}\boldsymbol{A}'|\,|\mathrm{d}\boldsymbol{s}'|$
$= \underbrace{|\boldsymbol{J}(\boldsymbol{r}')|\,|\mathrm{d}\boldsymbol{A}'|}_{=I}\,\mathrm{d}\boldsymbol{s}'$

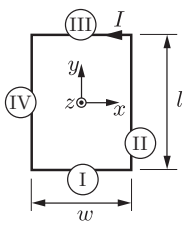

$\boldsymbol{r} = \begin{bmatrix} p_x \\ p_y \\ 0 \end{bmatrix}$

(I) $\boldsymbol{r}' = \begin{bmatrix} x \\ -l/2 \\ 0 \end{bmatrix}$ $\mathrm{d}\boldsymbol{s}' = \begin{bmatrix} \mathrm{d}x \\ 0 \\ 0 \end{bmatrix}$ $x = [-\frac{w}{2}, \frac{w}{2}]$

(II) $\boldsymbol{r}' = \begin{bmatrix} w/2 \\ y \\ 0 \end{bmatrix}$ $\mathrm{d}\boldsymbol{s}' = \begin{bmatrix} 0 \\ \mathrm{d}y \\ 0 \end{bmatrix}$ $y = [-\frac{l}{2}, \frac{l}{2}]$

(III) $\boldsymbol{r}' = \begin{bmatrix} x \\ l/2 \\ 0 \end{bmatrix}$ $\mathrm{d}\boldsymbol{s}' = \begin{bmatrix} \mathrm{d}x \\ 0 \\ 0 \end{bmatrix}$ $x = [\frac{w}{2}, -\frac{w}{2}]$

(IV) $\boldsymbol{r}' = \begin{bmatrix} -w/2 \\ y \\ 0 \end{bmatrix}$ $\mathrm{d}\boldsymbol{s}' = \begin{bmatrix} 0 \\ \mathrm{d}y \\ 0 \end{bmatrix}$ $y = [\frac{l}{2}, -\frac{l}{2}]$

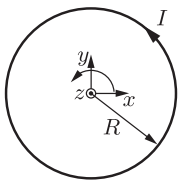

$\boldsymbol{r}' = R \begin{bmatrix} \cos\varphi \\ \sin\varphi \\ 0 \end{bmatrix}$

$\mathrm{d}\boldsymbol{s}' = \dfrac{\partial \boldsymbol{r}'}{\partial \varphi} \mathrm{d}\varphi = R \begin{bmatrix} -\sin\varphi \\ \cos\varphi \\ 0 \end{bmatrix} \mathrm{d}\varphi$

$\varphi = [0, 2\,\pi]$

Figure 3.5: Top: Derivation of analytical expresssions relating magnetic flux density and electrical current for the magnetostatic case. Bottom: vectors, necessary to calculate the magnetic flux density in the x, y-plane for a rectangular and a circular loop using the Biot-Savart law.

The first derived relation in Fig. 3.5

$$B_\varphi(r) = \frac{\mu_0\, I(r)}{2\, r\, \pi} \qquad \text{where} \quad I(r) = I\frac{r^2}{r_\mathrm{w}^2} \quad \text{for} \quad r < r_\mathrm{w} \qquad \text{and} \quad I(r) = I \quad \text{for} \quad r \geq r_\mathrm{w} \tag{3.9}$$

is the magnetic flux density of an infinitely extended, straight conductor, with rotational symmetric, time constant electrical current density. The second derrived term

$$\boldsymbol{B}(\boldsymbol{r}) = -\frac{\mu_0\, I}{4\,\pi} \int \frac{\boldsymbol{r} - \boldsymbol{r}'}{|\boldsymbol{r} - \boldsymbol{r}'|^3} \times \mathrm{d}\boldsymbol{s}' \tag{3.10}$$

is the Biot-Savart law and in this notation, it is valid for an infinitely thin, closed, current carrying conductor of arbitrary shape. In Fig. 3.5 the vectors necessary to calculate the magnetic flux density in the x, y-plane for a flat rectangular and a circular loops are given as well. For the rectangular loop, the integral is split up into four integrals I–IV and the solution for $\boldsymbol{B}(\boldsymbol{r})$ is obtained adding the results of the single integrals. Note, that this is not a superposition of single (real) magnetic flux densities rather than just the sum of partial solutions.

L_e is defined as the proportionality factor between linked magnetic flux ψ_e, and electrical current I, i.e.,

$$\psi_\mathrm{e} = L_\mathrm{e}\, I \qquad \text{where} \qquad \psi_\mathrm{e} = N\phi_\mathrm{e} \qquad \text{and} \qquad \phi_\mathrm{e} = \int_{A_\mathrm{e}} \boldsymbol{B} \cdot \mathrm{d}\boldsymbol{A}. \tag{3.11}$$

ϕ_e is the magnetic flux through the area A_e spanned and confined by the conductive loop, see Fig. 3.6. That is, for current carrying loops for which an expression for $\boldsymbol{B}$ can be found, for which the integral in Eq. 3.11 can be solved L_e can be expressed analytically. L_e can be calculated e.g., using Biot-Savart's law, integrating over the external surface A_e and dividing by the current I, i.e.

$$L_\mathrm{e} = -\frac{\mu_0}{4\,\pi} \int_{A_\mathrm{e}} \int_{s'} \frac{\boldsymbol{r} - \boldsymbol{r}'}{|\boldsymbol{r} - \boldsymbol{r}'|^3} \times \mathrm{d}\boldsymbol{s}' \cdot \mathrm{d}\boldsymbol{A}. \tag{3.12}$$

For a rectangular loop with length l, width w and wire radius r_w, c.f. Fig. 3.5 , it follows

$$\begin{aligned} L_\mathrm{e,rect} \;\approx\; & \frac{\mu_0}{\pi}\left[l\,\mathrm{asinh}\!\left(\frac{l}{r_\mathrm{w}}\right) + w\,\mathrm{asinh}\!\left(\frac{w}{r_\mathrm{w}}\right) \right. \\ & \left. -l\,\mathrm{asinh}\!\left(\frac{l}{w}\right) - w\,\mathrm{asinh}\!\left(\frac{w}{l}\right) + 2\sqrt{l^2+w^2} - 2\,(l+w) \right]. \end{aligned} \tag{3.13}$$

For the internal inductance, the magnetic flux density within the conductor has to be known, which can not be calculated using this representation of Biot-Savart's law. In this case the solution of a straight, infinitely extended conductor can be used, as this solution yields acceptable results close or within the conductor even if the conductor is nor straight, nor infinitely extended. To calculate the internal

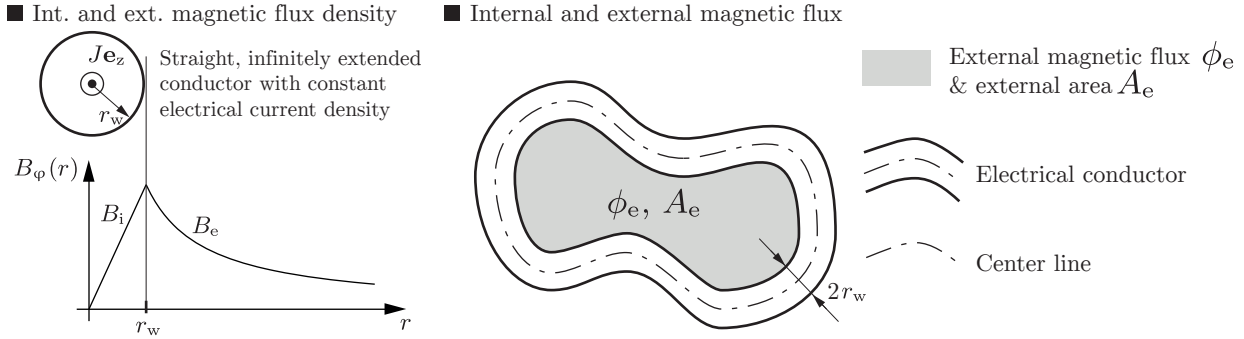

Figure 3.6: External and internal magnetic flux

inductance, the relation between the stored energy in the magnetic field W_{mag} of an inductance can be used. The energy stored in the magnetic field of the inductance $L = L_{\mathrm{i}} + L_{\mathrm{e}}$ is

$$W_{\mathrm{mag}} = \int_{\mathbb{R}^3} \frac{\boldsymbol{B} \cdot \boldsymbol{H}}{2} \mathrm{d}V = \frac{L\, I^2}{2}, \tag{3.14}$$

where $\mathbb{R}^3$ denotes the volume of total space. For calculating the internal inductance only, the volume integral over the conductors volume has to be calculated. Using the above assumption for calculating $\boldsymbol{B}$ inside the conductor it follows:

$$W = \frac{\mu_0\, I^2}{8\, r_{\mathrm{w}}^4\, \pi^2} \int_{V_{\mathrm{c}}} r^2 \mathrm{d}V = \frac{\mu_0\, I^2 l_{\mathrm{c}}}{16\, \pi^2} = \frac{L_{\mathrm{i}}\, I^2}{2}, \tag{3.15}$$

where l_{c} is the total length of the conductor and thus it follows for the internal inductance

$$L_{\mathrm{i}} = \frac{\mu_0}{8\, \pi}\, l_{\mathrm{c}}. \tag{3.16}$$

Considering $l_{\mathrm{c}} = 2(l + w)$ for a rectangular loop, it follows

$$\begin{aligned} L_{\mathrm{rect}} \approx \frac{\mu_0}{\pi} \Bigg[& l \operatorname{asinh}\left(\frac{l}{r_{\mathrm{w}}}\right) + w \operatorname{asinh}\left(\frac{w}{r_{\mathrm{w}}}\right) \\ & - l \operatorname{asinh}\left(\frac{l}{w}\right) - w \operatorname{asinh}\left(\frac{w}{l}\right) + 2\sqrt{l^2 + w^2} - 1.75\,(l + w) \Bigg]. \end{aligned} \tag{3.17}$$

Similar results can be found in [246, 247]. For this result it was assumed that the permeability of the surrounding medium is equal to the permeability of free space. Furthermore, (e.g., thermally induced) geometrical changes of the conductor are not considered and thus the inductivity is assumed to be constant.

Comparison of theoretical and experimental results

The values of the specific resistance $\rho_{\mathrm{t}}(T_0)$ and the linear temperature coefficient of tungsten are $\rho_{\mathrm{t}}(T_0 = 20\,^{\circ}\mathrm{C}) = 5.28 \cdot 10^{-8}\,\Omega{\cdot}\mathrm{m}$ and $\alpha_{\mathrm{t}} = 4.1 \cdot 10^{-3}\mathrm{K}^{-1}$. Thus, for the resistances of the U-shaped wire ($l = 16\,\mathrm{mm}$, $w = 6\,\mathrm{mm}$, $r_{\mathrm{w}} = 200\,\mu\mathrm{m}$) at 25 °C and 50 °C it follows that:

- $R_{\mathrm{c},25} \approx 17.8\,\mathrm{m}\Omega$
- $R_{\mathrm{c},50} \approx 19.5\,\mathrm{m}\Omega$

and using Eq. 3.17 for an estimation of the U's inductance yields

- $L_{\mathrm{c}} \approx 28.8\,\mathrm{nH}$.

To verify these theoretical results, measurements were made in a frequency range from 100 Hz to 100 kHz at 25 °C and 50 °C. These measurements were performed in air, in isopropanol as well as in a 90 g DI water and 10 g NaCl solution (which is close to saturation) to investigate potential effects resulting from differing surrounding physical conditions such as electrical conductivities. The conductivity of this used salt-water mixture is $\sigma_{\mathrm{l}} \approx 14\,\mathrm{S/m}$.

Figure 3.7 shows amplitude and phase spectra obtained with the U-shaped wire sensor. In Fig. 3.7(a) the first two resonant modes can be observed and in Fig. 3.7(b) the measured voltage V_{out} of all measurements (i.e., in all investigated liquids) is shown in a single plot. From there, it is already clearly visible that only the temperature yields significant changes of the offset voltage which result from the thermal dependence of the tungsten wire's resistance, c.f. Eqs. 3.6 and 3.7. The different physical parameters of air, isopropanol and the closely saturated salt-water mixture however, do not yield measurable changes. The peaks in the measured frequency responses are due to electrical resonances which are not further discussed. The model parameters in Eqs. 3.3 – 3.5 were fitted into the measured frequency response and are:

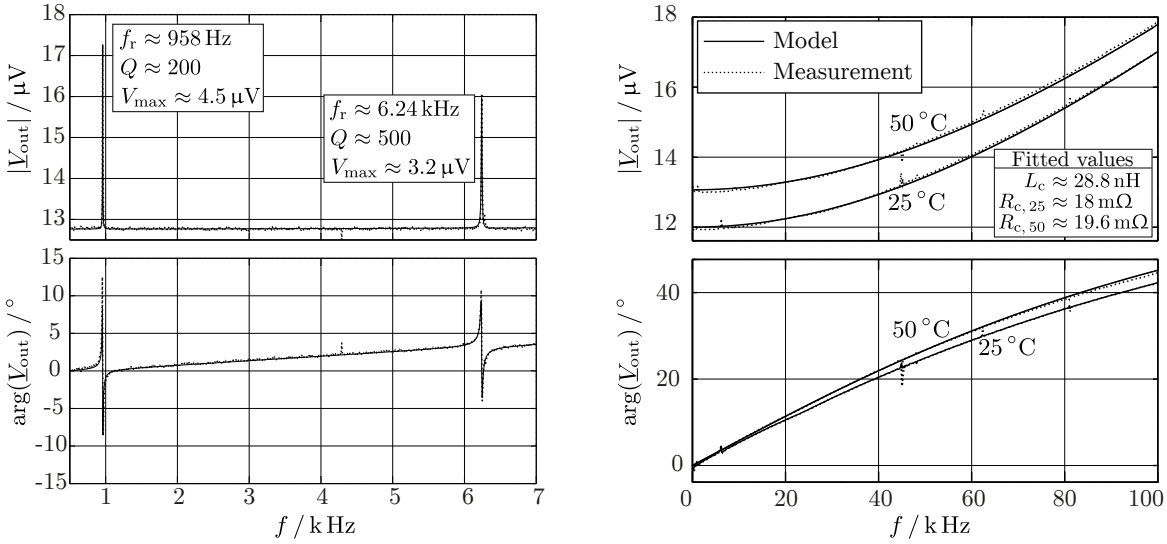

(a) Spectrum from 100 Hz to 7 kHz

(b) Spectra from 100 Hz to 100 kHz

Figure 3.7: a) Recorded spectra obtained with the U-shaped wire in air. Two mechanical resonances can be observed. b) Effect of the conductor's temperature dependent impedance and experimental verification of theoretical findings. Only the wire's thermally dependent resistance affects significant variations of the offset voltage. This comparison of experimental with theoretical results shows the validity of the used equivalent circuit.

- $R_{\mathrm{w},\,25,\,\mathrm{fit}} \approx 18\,\mathrm{m\Omega}$
- $R_{\mathrm{w},\,50,\,\mathrm{fit}} \approx 19.6\,\mathrm{m\Omega}$
- $L_{\mathrm{w,\,fit}} \approx 28.8\,\mathrm{nH}$

These values are in surprisingly good accordance with the values calculated from Eqs. 3.6 and 3.17 ($R_{\mathrm{w},25} = 17.8\,\mathrm{m\Omega}$, $R_{\mathrm{w},50} = 19.5\,\mathrm{m\Omega}$ and $L_{\mathrm{w}} = 28.8\,\mathrm{nH}$).

Additional impedances

Although the applicability of the equivalent circuit in Fig. 3.2 (a) is already sufficiently demonstrated, the order of magnitude of potential, additional impedance contributions is investigated for the case of the U-shaped wire the setup. For clamping, the U-shaped tungsten wire was brazed into two solid brass blocks. For estimation of additional impedances, the resistance and the capacitance between these brass blocks is calculated. That is, for this estimation the influence of the wire is neglected. In fact, the capacitance between both brass blocks is short-circuited by the U-shaped wire and thus would (ideally) be zero. The block's dimensions are, c.f. Fig. 3.4(b),: $h_{\mathrm{b}} = 7\,\mathrm{mm}$, $l_{\mathrm{b}} = 14\,\mathrm{mm}$ and $d_{\mathrm{b}} = 2\,\mathrm{mm}$. The resistance and capacitance between the brass blocks are:

$$R_{\mathrm{b}} = \frac{d_{\mathrm{b}}}{\sigma_l\, h_{\mathrm{b}}\, l_{\mathrm{b}}} \quad \text{and} \quad C_{\mathrm{b}} = \varepsilon_0 \varepsilon_l \frac{h_{\mathrm{b}}\, l_{\mathrm{b}}}{d_{\mathrm{b}}}. \tag{3.18}$$

(σ_l: electrical conductivity of the liquid, ε_0: electric field constant, ε_{l}: relative permittivity of the liquid). To estimate the capacity, a relative permittivity of the liquid $\varepsilon_l < 100$ is assumed. Inserting the associated values in Eq. 3.18 gives:

- $R_{\mathrm{b}} > 1.28\,\Omega$
- $C_{\mathrm{b}} < 49\,\mathrm{pF}$.

As the resistance between the blocks is large compared to the wire's resistance even for the case of the highly concentrated salt-water solution and as the capacitance for high relative permittivities is small, it is assumed that additional resistances and capacitances are negligible.

With these insights, the measured output-voltage can be calculated in the frequency domain assuming time-dependence $e^{\mathrm{j}\,\omega\,t}$as follows:

$$\underline{V}_{\mathrm{out}} = \underline{V}_{\mathrm{M}} + (R_{\mathrm{c}} + \mathrm{j}\,\omega\,L_{\mathrm{c}})\,\underline{I}_{\mathrm{in}} \tag{3.19}$$

where

$$\underline{I}_{\mathrm{in}} = \frac{\underline{V}_{\mathrm{g}} - \underline{V}_{\mathrm{M}}}{50\Omega + R_{\mathrm{s}} + R_{\mathrm{c}} + \mathrm{j}\,\omega\,L_{\mathrm{c}}}. \tag{3.20}$$

Conclusion

The comparison of the model and associated calculated parameters with the experimental results shows good accordance. Thus it follows, that the electrical equivalent circuit depicted in Fig. 3.2 (a) sufficiently accounts for the offset voltage. The conductivity of the liquid does not significantly influence the offset voltage, as the liquid's resistance is large compared with the wire's resistance.

3.4.2 Two conductors LFDRs

Two conductors LFDRs consist of two galvanically isolated excitation and read-out circuits. The sinusoidal excitation current in the excitation path induces a time variant magnetic field which couples into the read-out circuit which in turn induces a cross-talk voltage

$$V_{\mathrm{ct}}(t) = \frac{\mathrm{d}\psi_{12}(t)}{\mathrm{d}t} \qquad \text{where} \qquad \psi_{12}(t) = M\,i_{in}(t). \tag{3.21}$$

Here, ψ_{12} is the linked magnetic flux induced from the input circuit (denoted by the index '1') which intersects the output circuit (denoted by the index '2'). This coupling can be described using the mutual inductance M and thus, the measurable output voltage in frequency domain for the case of two conductors LFDRs can be expressed as:

$$\underline{V}_{\mathrm{out}} = \underline{V}_{\mathrm{M}} + \mathrm{j}\,\omega\,M\,\underline{I}_{\mathrm{in}} \tag{3.22}$$

In the following, this cross-talk is investigated for the case of the double membrane sensor [MHj6] and the suspended platelet sensor [MHj5].

Double membrane sensor

The double membrane sensor consists of two vibrating polymer membranes carrying copper paths for excitation and read-out. The principle design of such a membrane and the magnetic flux density induced by the excitation currents are depicted in Fig. 3.8.

In [MHj6] an estimate for the order of magnitude of the mutual inductance was calculated using Ampère's law Eq. 3.9 for calculating the magnetic flux density. The mutual inductance for a single membrane, c.f. Fig. 3.8(a) and (b) was estimated estimated from

$$M_{\mathrm{A.L.}} \approx \frac{\psi_{21}}{I} = \frac{l\,\mu_0}{\pi} \int_{x_1}^{x_2} \left(\frac{1}{x} + \frac{1}{b-x} \right) \mathrm{d}x \approx 17\,\mathrm{nH}. \tag{3.23}$$

Figure 3.8(b) shows a comparison of results for the magnetic flux density using Ampère's law Eq. 3.9 and Biot-Savart's law Eq. 3.10. There, the solutions for $B(x)$ are shown for different y-positions. The further the distance of the conductors tip (conductor in x-direction), the more both solutions coincide. In Fig. 3.8(c) a three-dimensional illustration of the magnetic flux density is shown. In [189] the mutual inductance was calculated using the solution obtained using Biot-Savart's law and the result was

$$M_{\mathrm{B.S.}} \approx 13.2\,\mathrm{nH}. \tag{3.24}$$

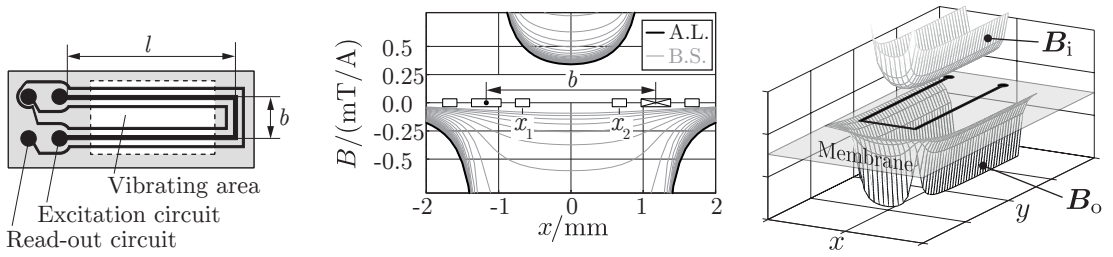

(a) Top view (b) Front view (c) 3D-view

Figure 3.8: Double membrane sensor: a) Top view of one of two membranes used for the double membrane sensor: A polymer membrane carries two copper paths, where one is used for excitation, the other is used for read-out. b) Front view including several solutions of the magnetic flux density at different y-positions using Biot-Savart's law (B.S.) and Ampère law (A.L.). Note that the scale of this figure is given in mT per 1 A excitation current. For this sensor the excitation currents were in the order of 100 mA. c) Three dimensional illustration of the magnetic flux density calculated using Biot-Savart's law and assuming that the conductive path is infinitely extended in y-direction.

Suspended platelet sensor

For the suspended platelet sensor, two mechanically stretched wires are used, where one is used for excitation, the other is used for read-out. These wires and the wiring for power supply and read-out, form two loops (single-turn coils) with a certain cross-sectional area. The magnetic flux affected by the current in the first loop penetrating the second loop induces a voltage in this second loop, see Fig. 3.9(a). Displacing the wires changes the cross-sectional areas of the loops, resulting in a different cross-talk voltage V_{ct}, making reliable measuring difficult. To reduce the effect of electrical cross-talk, rigid conductors and BNC-connectors were used, first, to minimize the effective cross-sectional area of the single-turn loops and second, to keep this cross-sectional area constant, see Fig. 3.9(b).

Experimental verification

The cross-talk was analyzed for both sensors by recording and investigating the frequency responses of both sensors, see Fig. 3.10. The amplitude and phase spectra were recorded for a single membrane and is depicted in Fig. 3.10(a). As the time variant magnetic field from the excitation path directly couples into the read-out path, the cross-talk signals become dominant. Fitting the model parameters from Eqs. 3.4 and 3.22 into the recorded frequency response yielded the model parameters as they are given in Fig. 3.10(a). For the mutual inductance M, the calculated values $M_{\mathrm{A.L.}} \approx 17\,\mathrm{nH}$, $M_{\mathrm{B.S.}} \approx 13.2\,\mathrm{nH}$ and the fitted value $M_{\mathrm{fit}} = 15.10\,\mathrm{nH}$ are in good accordance.

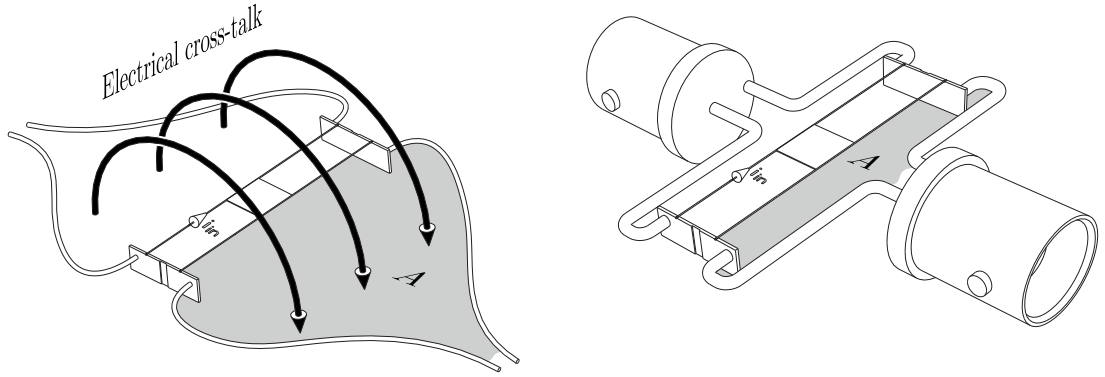

(a) Cross-talk (b) Reduced cross-talk

Figure 3.9: Cross-talk for two galvanically isolated circuits: Reducing the area of the output circuitry reduces the effect of cross-talk signals. To keep the electric cross-talk constant, a rigid connection of the read-out wire and BNC connectors are advantageous.

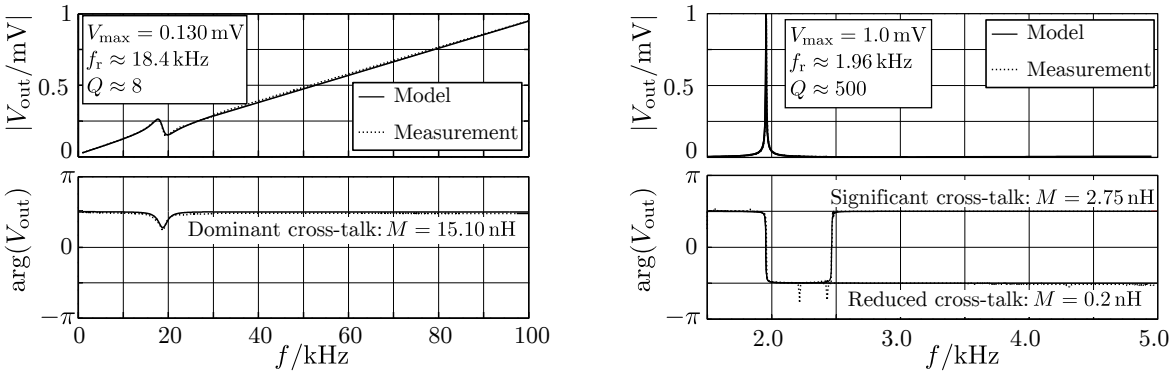

(a) Double membrane sensor

(b) Suspended platelet

Figure 3.10: Recorded spectra showing dominant, significant and reduced cross-talk using the membrane sensor and the suspended platelet sensor as example. Forth both cases, the measurements were made in air. In each figure the fitted values for the model of the output voltage V_{out} using Eqs. 3.4 and 3.22 are given.

For the suspended plate sensor, the cross-talk is significantly smaller, see Fig. 3.10(b). There, the effect of both wiring techniques as depicted in Fig. 3.9 are shown. The first case yields significant cross-talk with a mutual inductance $M = 2.75\,nH$. Compared with the double membrane sensor the effect of the offset voltage is much smaller and is mainly visible in the phase spectrum. As the signal components of V_M become small for frequencies higher than $\approx 3\,kHz$ the part of the cross-talk voltage $\underline{V}_{ct} = j\,\omega\,M\,\underline{I}_{in}$ becomes dominant which shifts the phase back to $\frac{\pi}{2}$. Reducing the area formed by the excitation and read-out circuitry reduced the mutual inductance by a factor of 10, approximately ($M = 0.2\,nH$). In the recorded frequency band the signals of the reduced cross-talk do not become significant and thus, the phase remains at $-\frac{\pi}{2}$ but will shift back to $\frac{\pi}{2}$ at higher frequencies, as the electrical cross-talk can not be completely eliminated.

Figure 3.11 shows electric equivalent circuits for both cases of LFDRs with which the offset voltages can be compensated. There a reference voltage obtained by using, e.g., the second channel of the signal generator and a reference resistance is used to compensate the offset. Instead of the reference resistance the same setup as it is used for the resonator but without the external magnetic field or prohibiting movements of the resonator, i.e. ensuring that $V_M = 0\,V$ for the reference device could be used as well.

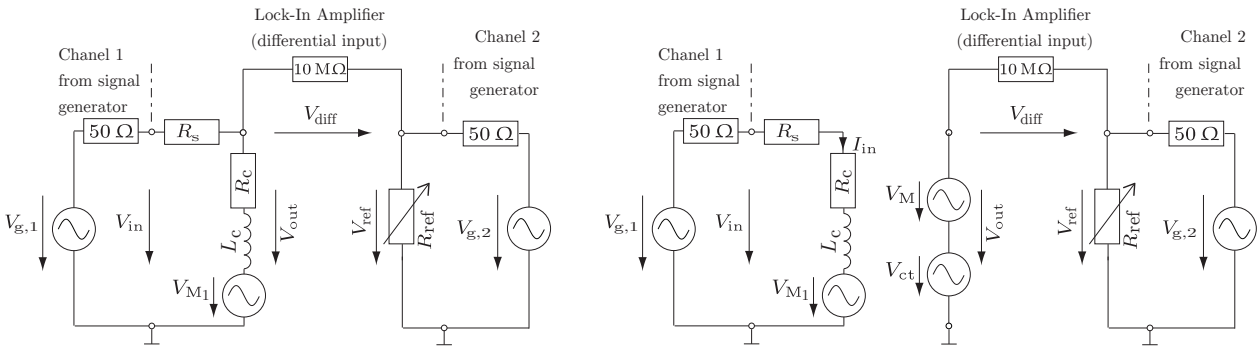

(a) Compensated circuit for one conductor LFDRs

(b) Compensated circuit for two conductors LFDRs

Figure 3.11: Equivalent circuits for compensating offset voltages.

3.4.3 Single versus double coil setup (torsional resonator)

The benefits and disadvantages of using single or double coil setups were experimentally investigated for the case of the torsional resonator [MHj1]. Schematic drawings of the rotors' cross-sections were already depicted in Fig. 3.2. For the first case of the single conductor LFDR, a single coil with 100 turns is used for both, excitation and read-out and for the second case, two coils with 50 turns each are separately used for these purposes. The voltage of the signal generator V_g was 0.1 V and the series resistance R_s was 100 Ω. For the manufactured rotor of the single coil setup, $R_\mathrm{c} = 21.3\,\Omega$ and $L_\mathrm{c} = 215\,\mu\mathrm{H}$ and for the rotor of the double coil setup $M = 480\,\mu\mathrm{H}$ were obtained.

Both types of rotors have been manufactured and mounted on a tungsten rod with 0.58 mm diameter and 5 cm length for each torsional spring. The recorded frequency responses covering a frequency range of 100 Hz to 10 kHz as well as detailed plots of the fundamental resonance are shown in Fig. 3.12 for both cases. The resonance peak is more than twice as high in case of the single coil setup compared with the double coil setup. (11.6 mV in contrast to 4.5 mV for the double coil setup.) This results from the fact that for the single coil setup, the number of coil turns is twice as high which yields a higher effective driving force in the rotor and a proportional to the coil turns higher induced voltage. Due to the large offset voltage for the single coil (≈ 12 mV) the change of phase at resonance is significantly smaller as for the double coil (39° in comparison to 178°). The reason of the phase shift of 178° instead of supposedly 180° is that the output voltage is subjected to a slight cross-talk voltage at these frequencies. This cross-talk voltage increases proportionally to the excitation frequency as it can be observed in Fig. 3.12(b) which is also considered in Eq. 3.22.

3.5 Magnetic circuitry

Equations 3.1 and 3.2 indicate that the influence of the magnetic field on the motion-induced voltage is quadratic. Thus the external magnetic field should preferentially be large to obtain high output signals. In the following, the dependence of the magnetic field on the motion-induced voltage as well as permanent magnet assemblies for achieving high magnetic flux densities are presented.

3.5.1 Effect of magnetic flux density on the motion-induced voltage

To investigate the effect of the magnetic flux density on the motion-induced voltage, three different magnetic circuits using Neodymium (NdFeB) magnets were manufactured. In Fig. 3.13 the influence of the external magnetic field on the motion-induced voltage for the case of the straight, stretched wire LFDR, see Fig. 3.1(a) is illustrated, for measured and modeled data, see also [MHc21]. There, Fig. 3.13(a) shows the magnitude over the excitation current's frequency and Fig. 3.13(b) shows the Nyquist plots. Both, amplitude spectrum as well as Nyquist plot were evaluated from the same

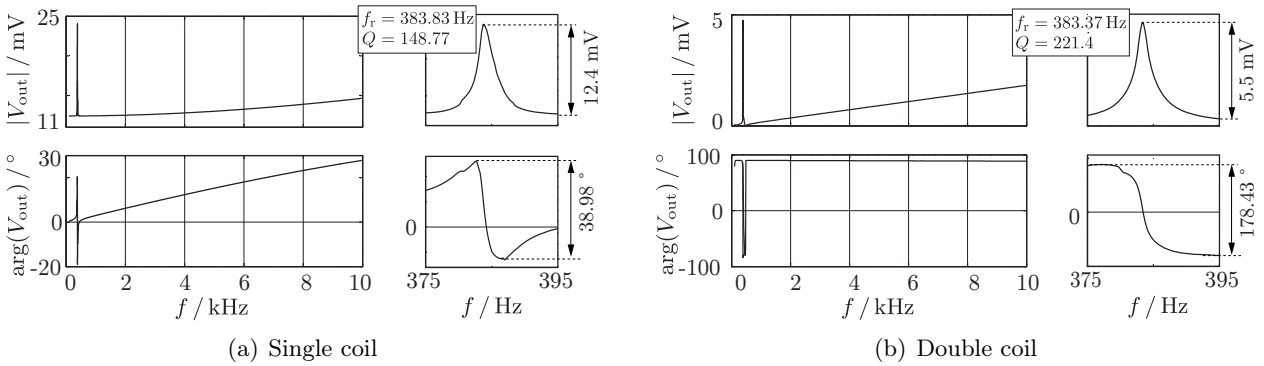

(a) Single coil (b) Double coil

Figure 3.12: Frequency responses measured with the single coil (a) and the double coil (b) setup using the torsional resonator. The recorded spectra between 100 Hz and 10 kHz as well as detailed plots of the resonance are shown for both setups.

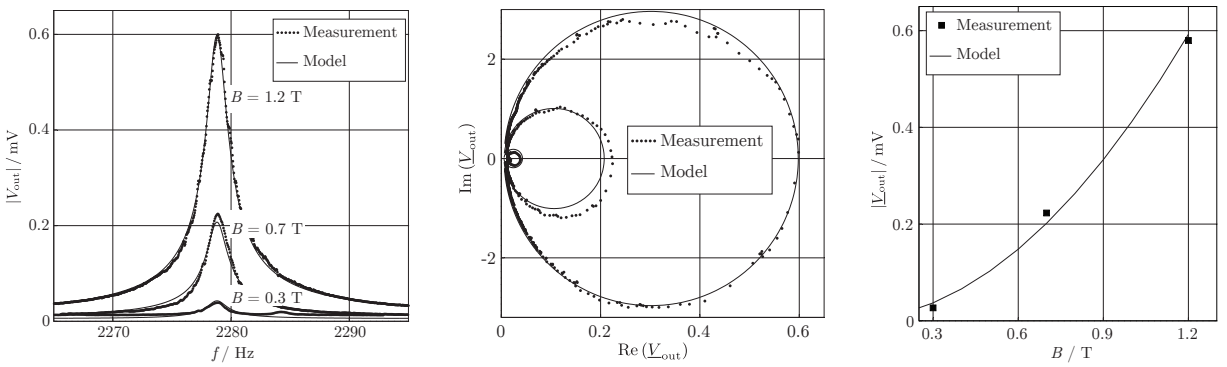

(a) Magnitude (b) Nyquist (c) Response to magnetic flux density

Figure 3.13: Response to magnetic flux density.

measurements containing the fundamental harmonic of the wire. In Fig. 3.13(c) the maximum value of the measured voltage $\max(V_{\text{out}})$ over the magnetic flux density is depicted. There, the quadratic influence of the external magnetic flux density on the motion-induced voltage is observable. The measurements were made in air for a 3 cm long, 47 µm thick tungsten wire with an excitation current of 6.25 µA and a load of 60.6 g tensioning the wire. For better visibility, in the plot of the magnitude, the resonance peaks were centered in respect to the resonance peak of the 1.2 T frequency response. This was necessary due to shifts of the resonance frequency which were in the order of ± 5 Hz for these measurements.

3.5.2 Halbach array for straight structures

Annular Halbach magnets (also know as circular Halbach arrays) can be used to induce strong and homogeneous magnetic fields and are easily applicable for straight LFDRs such as the straight vibrating wire. The benefits of such Halbach arrays are, amongst others, strongest field per magnet mass, high homogeneity and weak stray-fields [248], just to name some of them. In [249] a Halbach magnet assembly is presented which yields flux densities exceeding 5 T for an air-gap length of 2 mm. However, the outer dimensions of the Halbach array presented there were 570x570x490 mm with a total weight of 900 kg (including the supporting structure). The direction of the magnetic flux density of an ideal Halbach array is depicted in Fig. 3.14(a).

For implementing a miniaturized Halbach ring with an inner diameter of 4 mm, 36 NdFeB cylindric magnets with a flattened face, which is necessary for the alignment, see Fee. 3.14(b), were used. For fabrication, this pattern was CNC-milled into a fibre glass block allowing the alignment of the magnets. The dimensions of this miniaturized Halbach array were $L = 25\,\text{mm}$ in length, $D_{\text{o}} = 29\,\text{mm}$ outer diameter and , $D_{\text{i}} = 4\,\text{mm}$ inner diameter. The total weight was about 80 g and the measured magnetic flux density initially was 1.4 T and decreased to 1.2 T, supposably due to small realignments of the discrete magnets. The simulated flux density was 1.6 T, see Fig. 3.14(c).

3.5.3 Magnet assemblies for non-straight structures (U-shaped wire)

For non-straight LFDRs such as the U-shaped wire resonator, Halbach arrays are difficult to be implemented. Thus, other permanent magnet assemblies are used to yield high magnetic flux densities at the tip of the U-shaped wire. For the latter, the magnetic field, has to be aligned from the front of the U-shaped structure, see also Fig. 3.4(a). Three possible designs for the magnetic circuits yielding high magnetic flux densities and the solution of finite elements simulations are depicted in Fig. 3.15. For the experiments performed for this thesis, all these three types of magnetic circuits were used. In Fig. 3.15(a) only one cubic NdFeB magnet is used where higher magnetic flux densities can be used if the 'U' is placed to one of the magnet's side such that the 'U' is in parallel with the magnetization

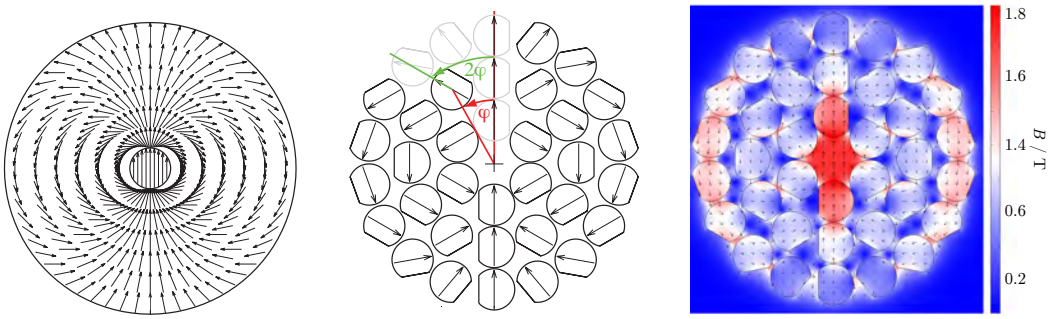

(a) Ideal Halbach magnet (b) Discretized Halbach magnet (c) FE-Simulation

Figure 3.14: In (a) an ideal annular Halbach magnet is depicted. In the air-gap, inside of the Halbach ring, a very strong homogenous flux density is obtained, whereas outside of the ring the flux density is low. (b) shows a sketch of the implementation of an discretized annular Halbach magnet. There, the contours and the orientations of magnetization of the 36 NdFeB magnets with a remanent flux density of 1.42 T are depicted. (L=25 mm, D =3.9 mm; "flattened diameter": 3.4 mm; the magnetization is in parallel to the flattened face.) For symmetry reasons the magnets for $\varphi \geq 180°$, were turned upside down. (c) shows the results of an 2D FE-simulation obtained with COMSOL Multiphysics 3.5. The flux density inside of the ring (airgap diameter of $\sim$ 4mm) obtained by this 2D FE-anaylsis is 1.6 T. [MHc22]

direction. In Fig. 3.15(b) a second magnet is used yielding higher magnetic flux densities. For this assembly however high repelling forces of the magnets require solid clamping of the latter. Figure 3.15(c) shows an assembly of two permanent magnets where a cylindrical permanent magnet is placed inside of a ring magnet. This assembly yielded the highest magnetic flux densities and was used for the setup presented in [MHj4].

3.6 Reluctance actuation and electromagnetic pickups

As an alternative to LFDRs, reluctance actuation and the use of electromagnetic pickups for read-out were also investigated using steel tuning forks with circular and rectangular cross-sections as resonators, see [MHj2] . Figure 3.16 shows a basic sketch of a reluctance acutated tuning fork. The used steel tuning forks were welded to a solid stainless steel stand. One of the ferromagnetic tuning fork's prongs was placed close to an electromagnet, used for excitation. At the end of the opposed prong, an electrodynamic pick-up is placed, consisting of a permanent magnet in the center of a copper coil. A sinusoidal Voltage $V_{\text{in}} = \hat{V}_{\text{in}} \sin(\omega\, t) + V_{\text{in,offs}}$ with a DC offset $V_{\text{in,offs}} \geq \hat{V}_{\text{in}}/2$ is used as input signal,

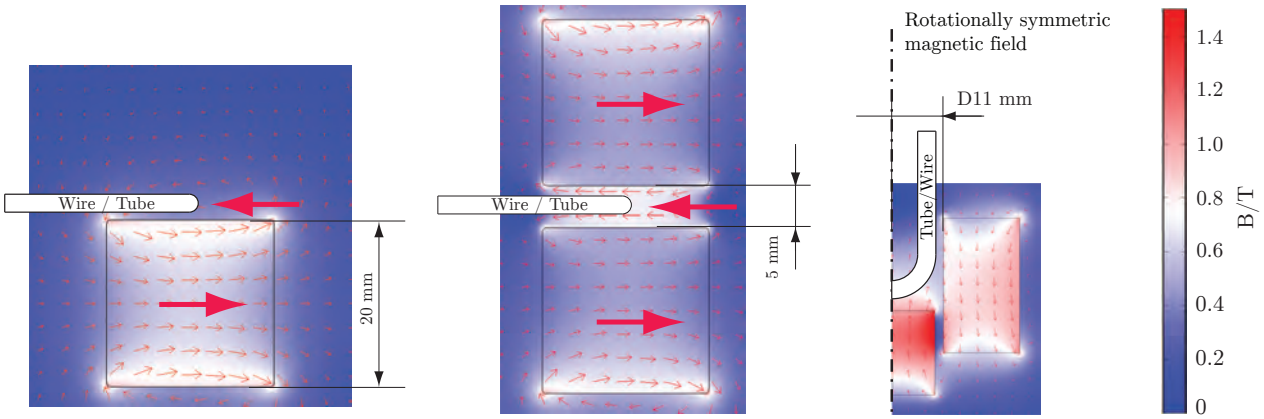

(a) One magnet (2x2 cm), side view (b) Two magnets (2x2 cm), side view (c) Ring (12 - 30x4mm), cylinder (10x10 mm), front view

Figure 3.15: Magnet assemblies. The simulated results for the magnetic flux density are obtained for Neodymium magnets. All three types of magnet circuits were used for the experiments for this thesis.

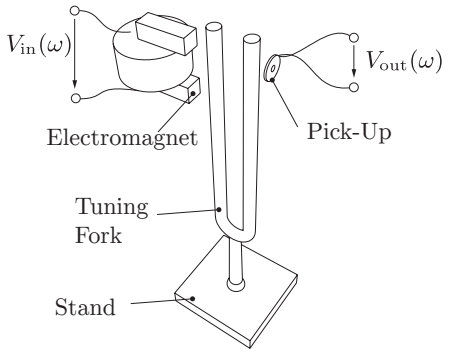

Figure 3.16: Sensor principle: a) A ferromagnetic steel tuning fork is actuated and read-out with an electromagnet and an electromagnetic pick-up, respectively.

exciting harmonic oscillations of the tuning fork. These oscillations effect an induced voltage in the pick-up serving as read-out signal. By sweeping the excitation current's frequency (containing the frequency of the fundamental mode), the frequency response of the tuning fork is recorded.

Chapter 4

Sensors

In chapter 3 the principles of one and two conductor Lorentz force driven resonators (LFDRs) and a ferromagnetic resonator-concept using reluctance actuation and an electromagnetic pickup were discussed. The concepts and their types of resonators which were investigated in the course of this thesis are listed in Tab. 4.1 in chronological order and are briefly explained in the following. In Tab. 4.1 the according sections, the year of publication as well as the references for first authorships in journals and conference proceedings are given as well. For further information for a particular device these publications can be consulted. Devices and according publications which were examined by colleagues of the Institute of Microelectronics and Microsensors are [94, 250–254], [MHjc4], [MHjc5], [MHcc17], [MHcc19], [MHcc20], for the double membrane sensor and [255], [MHjc1], [MHjc2], [MHcc1], [MHcc3], [MHcc4],[MHcc5], [MHcc7], [MHcc9], [MHcc10], [MHcc11], [MHcc12], [MHcc13], [MHcc14], [MHcc16], [MHcc18] for the single plate sensor, respectively.

The elaborated sensor concepts were designed to show measurable resonances in the range from 100 Hz to 100 kHz. This frequency range is especially interesting from a rheological point of view as it closes the examinable frequency gap between commercially available rheometers which cover frequencies below 100 Hz and well established shear oscillating quartz devices which are usually operated in the MHz range.

Device	Type	Sec.	Year	Journal	Conference
Double membrane sensor	2CLFDR	4.1	2011	[MHj6]	[MHc4], [MHc20], [MHc27], [MHc29], [MHc30]
Suspended platelet	2CLFDR	4.2	2012	[MHj5]	[MHc19], [MHc20], [MHc23], [MHc24], [MHc25], [MHc26], [MHc27]
Single plate resonator	1.5CLFDR	4.3	2012	—	[MHc12], [MHc19]
Wire viscometer	1CLFDR	4.4	2012	[MHj5]	[MHc17], [MHc20], [MHc21], [MHc22], [MHc23], [MHc25], [MHc27]
U-shaped wire	1CLFDR	4.5	2014	[MHj4]	[MHc4], [MHc11], [MHc12], [MHc13], [MHc14], [MHc15], [MHc16], [MHc17], [MHc18], [MHc20], [MHc26]
U-tube densimeter	1CLFDR	4.6	2013	—	[MHc12], [MHc13], [MHc16], [MHc18]
Spiral spring	1CLFDR	4.7	2014	—	[MHc7]
Torsional resonator	1CLFDR	4.8	2015	[MHj1]	[MHc5] [MHc10]
Ferromagnetic tuning fork	FMDR	4.9	2015	[MHj2]	[MHc6], [MHc4], [MHc12]

Table 4.1: Overview of investigated sensors

4.1 Double membrane sensor

In previous works by Reichel et al. the idea of the double membrane sensor was already introduced, see e.g. [250]. This sensor consists of two vibrating polymer membranes between which the sample liquid is contained. The motivation for such sensors using polymer membranes were low cost fabrication and the capability of disposable devices e.g., for application in medical analysis, or the monitoring of crystallization and polymerization processes [84, 251]. In [99] a first prototype and measurement results were presented. A model of the double membrane sensor was presented in [94] and in [253], a semi-numerical modeling approach in the spectral domain was performed. The insights obtained by the experimental results of first prototypes demanded redesigning the sensor assembly to achieve several improvements. First, there was a need to increase the repeatability and the sensor's sensitivity. Second, a design avoiding the formation of air bubbles within the test liquid, which moreover does not suffer from leakage had to be found. Third, measurement series obtained with the new devices had to be compared with theoretical findings from, e.g., [253] and confirm the latter. The works performed in this thesis with the focus to realize these requirements were [MHj6], [MHc29], [MHc30] and [MHjc5].

4.1.1 Sensor principle

Figure 4.1 shows exploded, schematic drawings of the double membrane sensor concepts. Two polymer membranes are bonded to supporting frames which ensures that only one side of the membrane gets wetted upon immersion. Depending on the used spacer which separates both membranes, open and closed setups can be manufactured. In Fig. 4.1(a) the concept of an open, fork-like assembly which can be immersed into the sample liquid is shown. Compared to closed setups as it is depicted in 4.1(b), this open, immersion principle reduces the probability of air bubble formation when filling the sensor. Furthermore, sensor designs based on an immersion principle are better suited for in-line sensing capabilities. However, a closed design benefits from the advantages that it requires less sample liquid volume and handling is more convenient if a large amount of different liquids has to be investigated.

Depending on the particular membrane design, see Fig. 4.1(c), the (1,1) and (2,1)-eigenmodes of the membranes can be excited, see Fig. 4.2(a), by means of Lorentz forces on the sinusoidal excitation currents in the excitation paths. The membranes are deflected either symmetrically or antisymmetrically depending on opposite or equal direction of the electric current through the excitation paths of both membranes, see Fig. 4.2(b). Thus, two different deformation fields can be applied, each leading to different resonance frequencies and responses to viscosity and mass density. Using the excitation

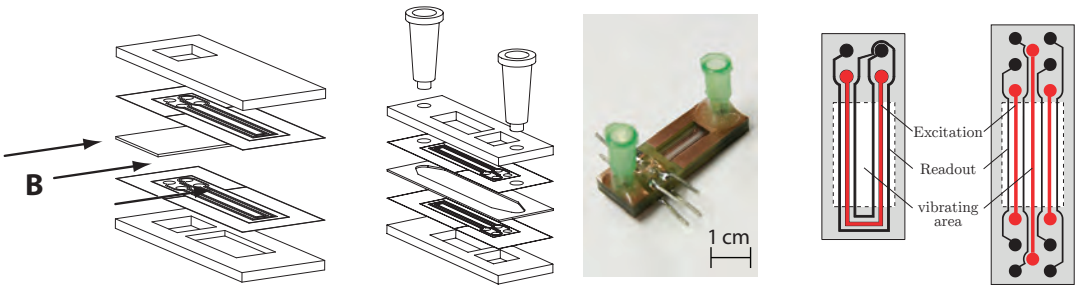

(a) Open sensor (b) Closed sensor (c) Membrane designs

Figure 4.1: In (a) the exploded view of the double membrane rheometer is illustrated. Two polymer membranes carrying conductive paths for excitation and read-out are bonded to rigid platelets. The bonding, also acting as sealing, ensures that the membranes' sides carrying the conductive paths do not get wetted with the liquid to be examined. I.e., only the liquid in the space between both membranes will be examined. The distance of both membranes is determined by the height of the spacer between both sensor parts. The arrows on the left side indicate the direction of the external magnetic field provided by two NdFeB magnets on each side of the sensor. The characteristic difference of the closed type (b) is that the spacer seals and encircles the measuring zone from the surrounding and thus requires inlet and outlet for charging the sensor cell. In (c) single membranes and their excitation paths (red) and read-out paths are illustrated in detail.

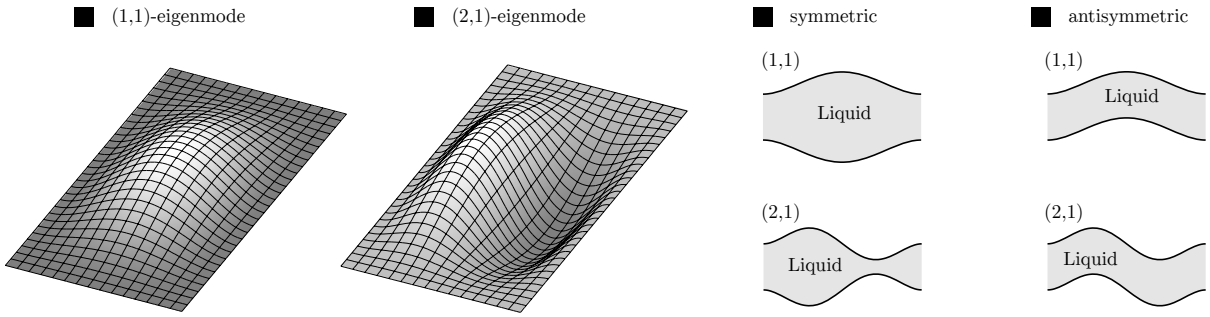

(a) Eigenmodes (b) Excitation modes

Figure 4.2: In (a) the deflection of single membranes in the (1,1)- and the (2,1)-eigenmode is depicted. (b) Depending on the direction of the electric current in the particular excitation path, the deflection can either be symmetric (opposite direction) or antisymmetric (same direction).

and read-out technique as it was described in Sec. 3.2 for two conductors LFDRs, an excitation signal of about $V_{\text{in}} = 1.3\,\text{V}$ yields read-out signals on the order of $V_{\text{out}} = 0.1\,\mu\text{V}$.

In principle, it would also be possible to use one membrane only to measure both, viscosity and mass density. However, the key feature of this sensor is the usage of two polymer membranes where the main advantage of the usage of a second membrane is the possibility of switching between two different modes of operation which allows changing the device's sensitivity to viscosity and mass density without changing the sensor's geometry.

4.1.2 Fabrication

The membranes carrying the conductive paths are realized by photolithography and wet etching of a 100 µm thick polyester based (PET) sheet coated with a 2 µm copper layer. The dimensions of the membranes are $30 \times 11.8\,\text{mm}^2$, with a vibrating area of $12 \times 5.6\,\text{mm}^2$. As polyester based polymers are highly solvent-proof, reaction adhesives (e.g., epoxy resin) are normally used for bonding or gluing [256]. However, epoxy resin showed to be hardly suitable for an easy manufacturing process to ensure uniform and reproducible bonding of the PET sheets. To account for an uniform adherend, pressure sensitive adhesive (PSA) foils are used to bond the membranes with the rigid top and bottom plate and the spacer which determines the gap between both membranes. The membranes and the foils are cut with a digital craft cutter [257] with a mechanical resolution of 50 µm. The external magnetic field was provided by two cubic NdFeB magnets with 2 cm in length yielding a magnetic flux density of $B = 0.6\,\text{T}$, which was measured with a Gauss meter (GM05, Hirst Magnetic Instrument LTD).

4.1.3 Results

In the investigated frequency range (500 Hz to 100 kHz) two dominant mechanical resonance frequencies at 2.5 kHz and 13 kHz approximately, could be observed using the membrane design on the left hand side of Fig. 4.1(c). The investigation of the double membrane sensors showed that in the (anti)symmetric mode only one mechanical resonance is excited. According to theoretical findings in [253], symmetric actuation, which is more sensitive to viscosity, excites the resonances at $f_{\text{r}} \approx 2.5\text{kHz}$, whereas in antisymmetric mode, which is more sensitive to mass density $f_{\text{r}} \approx 13\,\text{kHz}$ are observed. Furthermore, in [253] it was found that the resonance frequencies in symmetric mode shift to higher and those in antisymmetric excitation to lower frequencies for larger gaps between both membranes. These findings were experimentally validated in [MHj6] and are shown in Figs. 4.3 and 4.4.

In Fig. 4.3 relative Q-factors and resonance frequencies are depicted with respect to the dynamic viscosity and mass density respectively, for four test liquids. The values for Q_{rel} and $f_{\text{r,rel}}$ are given with

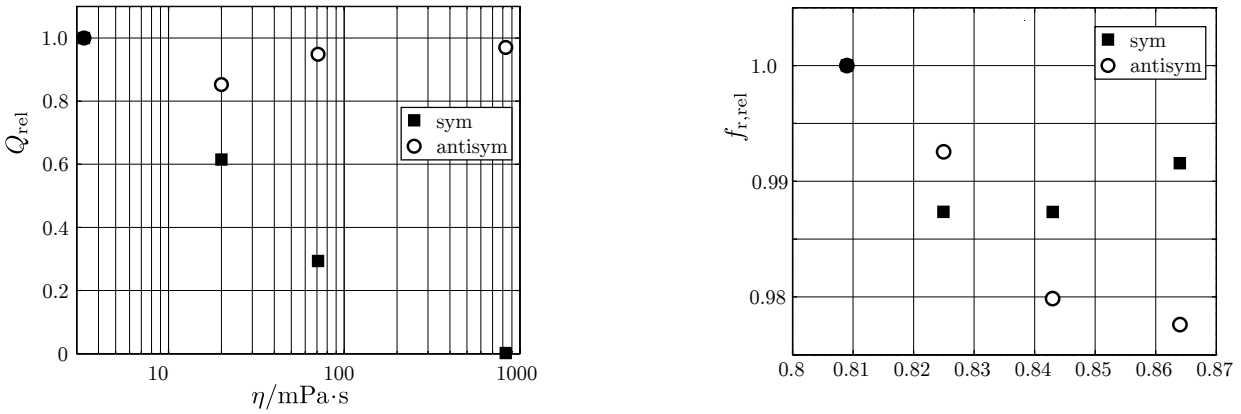

(a) Relative Q-factor over viscosity

(b) Relative Eigenfrequency over mass density

Figure 4.3: In (a) relative Q-factors and in (b) relative eigenfrequencies are illustrated for symmetric and antisymmetric excitation for four different viscosity standards (s3, n14, n44, n415, Cannon Instrument Company®) @ 25°C.

respect to the highest viscosity or mass density value, respectively. Figure 4.3 shows that the symmetric mode is more sensitive to viscosity while the antisymmetric mode is more sensitive to mass density. In symmetric mode, there was no more resonant behavior for the highest viscous examined liquid (viscosity standard N415, 830 mPa s at 25°C) due to overdamping while in antisymmetric mode the resonance was hardly damped. The influence of the gap on the resonance frequencies was investigated by varying the distance between both membranes using a micrometer positioning unit. With this experiment it was possible to prove the findings presented in [253] and [MHcc17]: Higher gaps yield a shift to higher frequencies in symmetric and a shift to lower frequencies in antisymmetric mode, respectively. This behavior could be observed for gaps from 100 µm to 400 µm, see Fig. 4.4(a).

The concept of the double membrane sensor was theoretically and experimentally monitored and proven. However, it was not further investigated as aging of the membrane yielded severe instabilities of measurement result, see [MHjc5] and due to their mechanical structure and clamping, membranes and plates are highly cross sensitive to temperature variations.

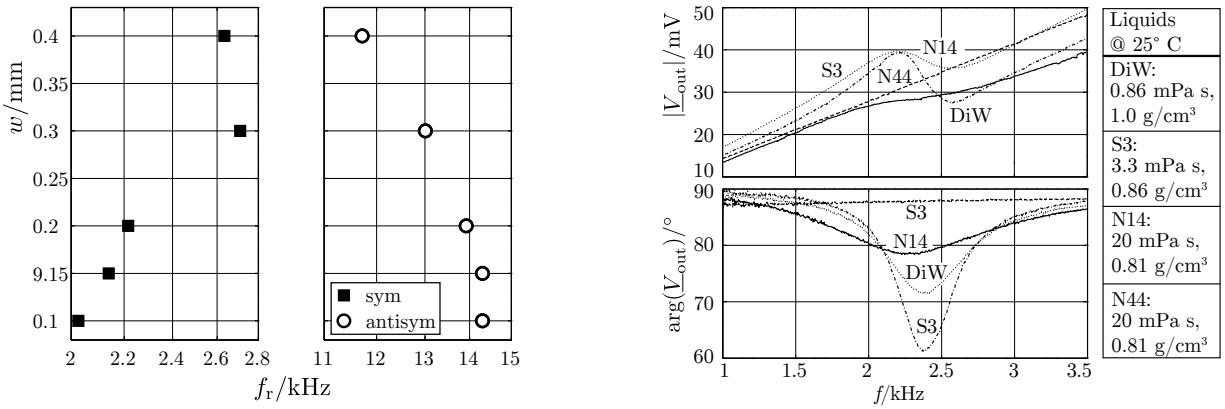

(a) Influence of gap w

(b) Frequency responses

Figure 4.4: a) Influence of the gap w between both membranes on the resonance frequencies f_r. Higher gaps generally yield a shift to higher frequencies in symmetric and a shift to lower frequencies in antisymmetric mode. b) shows recorded frequency responses. The associated liquids are indicated on the right hand side.

4.2 Suspended platelet

In Fig. 4.5(a) a schematic drawing of the suspended platelet viscosity and mass density sensor is depicted and in Fig. 4.5(b) measurements achieved with this device are shown. The sensor, surrounded by an experimental well containing the sample liquid, consists of a small platelet and two parallel wires which are placed in an external magnetic field. In Fig. 4.5(a), the left wire is used for exciting lateral vibrations by means of Lorentz forces. The second wire on the right, used for pick-up, is mechanically coupled to the excitation wire with a platelet, thus following the movement of the left wire, which effects an induced voltage which is used as read-out. By changing the tensile stresses in the wires, the device's resonance frequency can be changed. In first experiments a frequency range of about 800Hz to 4 kHz for 100 µm thick and 3 cm long tungsten wires and a 3x3 mm^2, 100 µm thick PET platelet was achieved.

The suspended platelet sensor has two galvanically isolated excitation and read-out paths as it is the case for the double membrane sensor. However, in this case the inductive cross-talk between excitation and read-out path is much weaker as it is for the double membrane sensor, see also [MHc26]. Considering the fluid-structure interaction for the modeling, the oscillating platelet sensor requires a less complex model than the double membrane sensor.

For the measurements obtained with this sensor, unstable and shifting resonance frequencies were observed. These resonance frequency shifts are not caused by the different liquids' physical properties but by detuning of the sensor which results e.g., from thermal stresses, slacking of the entire setup, etc. As these unstable resonance frequencies did not allow reliable and repeatable measurements, this concept was not further investigated.

4.3 Single plate resonator

The core of the single plate sensor which was already introduced by Reichel et al. in [96], is a wet-etched new-silver sheet which consists of a rectangular area (platelet) being supported by four, either straight or meander-shaped springs, see Fig. 4.6. Besides supporting purposes, these springs furthermore serve as electrical paths for actuation and read-out. The device is excited to in-plane oscillations due to Lorentz forces on sinusoidal currents over the structure which is placed in an external magnetic field as it is depicted in Fig. 4.6(a). The device consists of a single electric conductor, however excitation

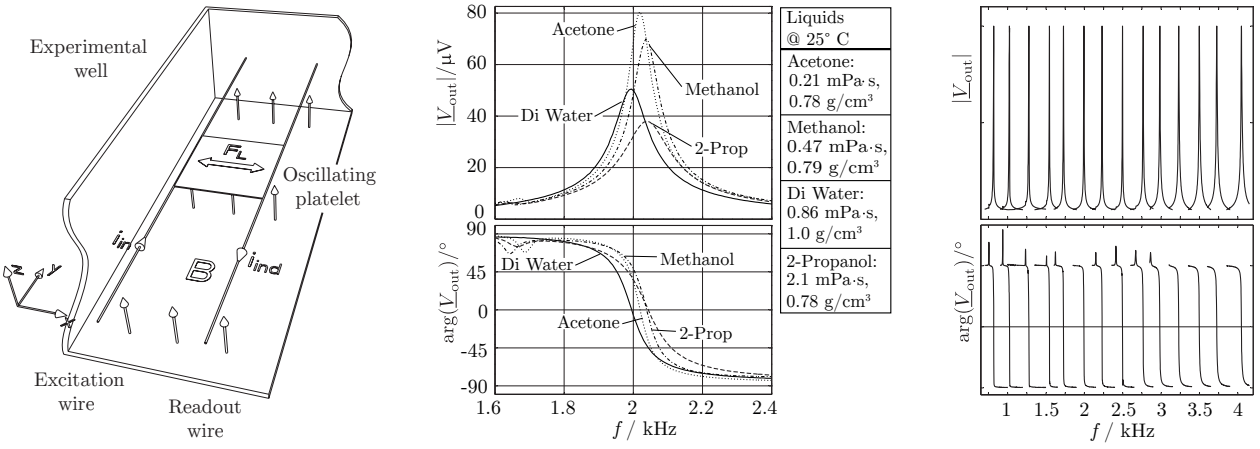

(a) Suspended platelet (b) Measurements (c) Tuning

Figure 4.5: Suspended platelet sensor. a) shows the principle of the sensor. b) measured frequency responses including the fundamental harmonic in four different liquids (Excitation Voltage $V_{in} \approx 0.5\,V$). It is clearly visible that higher viscosities yield higher damping. c) Measured frequency responses showing the detuning of the resonance frequency. In this experiment, resonance frequencies in a frequency range of about 800Hz to 4 kHz were achieved.

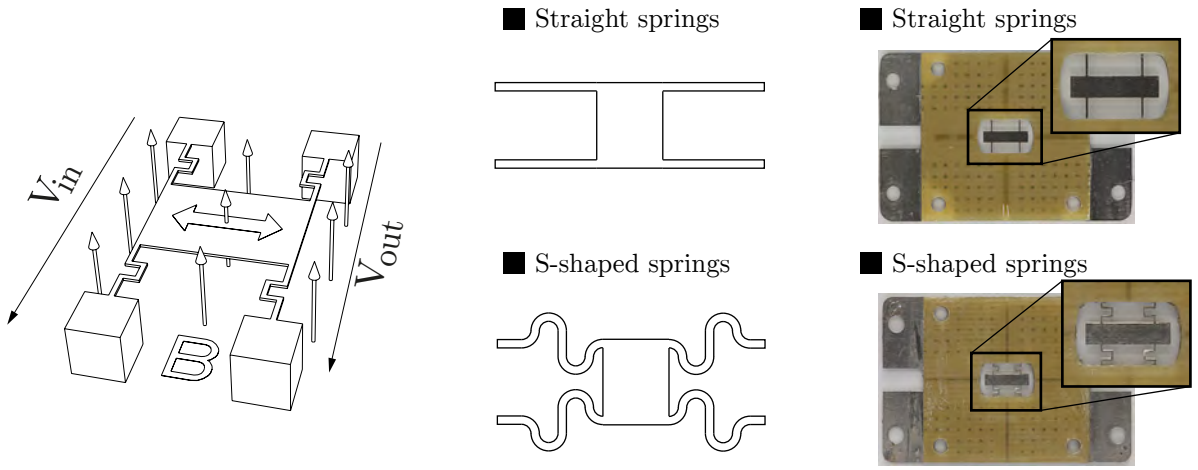

(a) Sketch

(b) Straight beams vs. S-shaped beams

(c) Photographs

Figure 4.6: Single plate viscosity and mass density sensor. a) shows a sketch of the sensor, which is manufactured using a wet etched Niclkel-Brass sheet to obtain the sensor's geometry consisting of a center platelet which is supported by four springs also serving for electrical contacts for excitation and read-out. The device is similar to the suspended platelet, however consists of a homogenous material. b) sketch of the basic difference between straight and S-shaped springs. c) shows two photographs of the resonator cards with the single plate sensors in their center. In both pictures a detailed view of the single plate resonator with straight and S-shaped springs is given.

and read-out electrodes are geometrically separated which does not allow assigning the device neither to '1CLFDR' nor to a '2CLFDR'. For this reason the term '1.5CLFDR' was used in Tab. 4.1.

The work performed in the course of this thesis for the single plate sensor concerned the investigation of possible advantages and disadvantages of straight beams versus S-shaped beams, see Figs. 4.6(b) and 4.6(c) as well as a long-term measurement for investigating f_r and Q variations. Further developments of this device were presented in [MHjc2], [MHcc1] and [MHjc1]. It was found [MHc19], that S-shaped springs yield lower cross-sensitivities to temperature and more stable resonance frequencies. The stability of the resonance frequencies was investigated in [MHc12] in respect to the U-shaped wire and the tuning fork sensors which were already briefly introduced in Chapter 3 and will be explained more in detail in Secs. 4.5 and 4.9. Figure 4.7 shows the evaluation of this study. All three sensors were filled with ethanol and put into a Weiss WKL 100 climate chamber controlling the temperature to 25 °C for providing constant physical conditions. The sensors' frequency responses were continuously recorded during 39, 90 and 162 hours for the single plate, the U-shaped wire and the round tuning fork sensor, respectively, yielding 2755, 4193 and 4232 values for f_r and Q. Figure 4.7 shows the relative changes $\Delta^\mathrm{r} f_\mathrm{r}$ and $\Delta^\mathrm{r} Q$ for f_r and Q with respect to their starting values $f_{\mathrm{r},0i}$ and Q_{0i}.

Figure 4.7 shows that the variations of the single plate sensor in f_r and Q were the highest and that all three investigated sensors showed clear trends in f_r and Q. It was found e.g. in [MHj2] that these trends resulted from changing viscosities and mass densities of the examined liquids themselves. In case of the experiments performed for the results shown in Fig. 4.7 ethanol dissolved plastics and glues in the setup yielding a continuous change in viscosity and mass density. For the experimental results depicted in Fig. 4.7(c) the viscosity and mass density were determined with an Anton Paar SVM 3000 before and after the measurements. The relative changes in viscosity and mass density were $\Delta^\mathrm{r}\eta = 53.15 \cdot 10^{-3}$ and $\Delta^\mathrm{r}\rho = 4.97 \cdot 10^{-3}$ and the relative changes in resonance frequency and quality factor were $\Delta^\mathrm{r} f_\mathrm{r} = -0.17 \cdot 10^{-3}$ and $\Delta^\mathrm{r} Q = -27.91 \cdot 10^{-3}$.

The shape of the trend of f_r and Q in Fig. 4.7(a) might result from changing and varying tensile stresses in the resonator, a problem which was already observed and addressed for doubly clamped structures in [MHj6]. Judging the results shown in Fig. 4.7 suggests a complete revision of all three setups, which are also stable against solvents such as ethanol. However, as the trends in Fig. 4.7(c) could be assigned

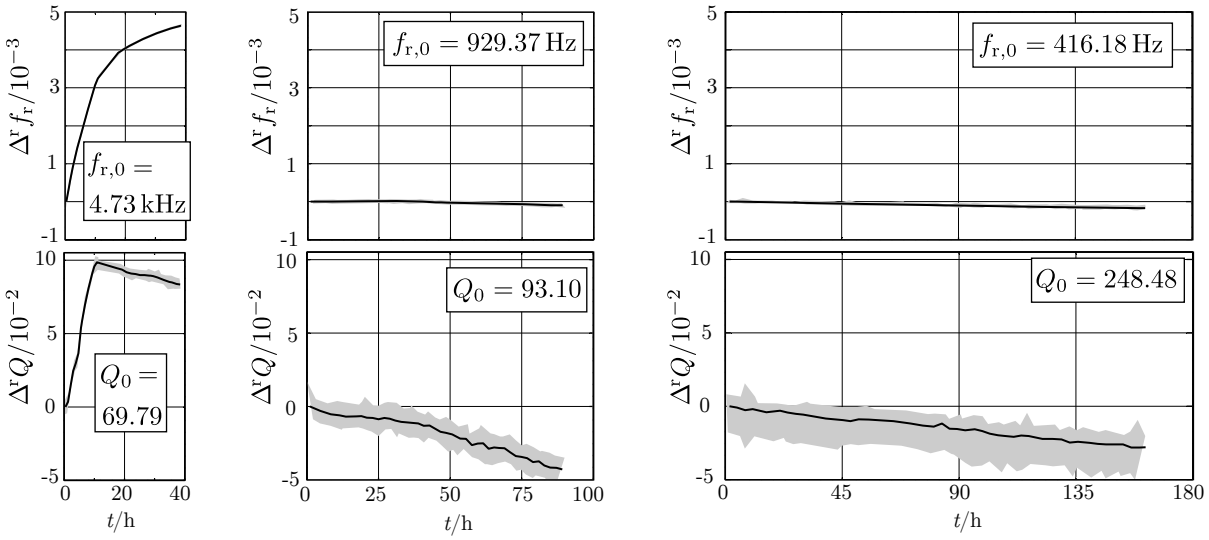

(a) Single plate (b) U-shaped wire (c) Tuning fork

Figure 4.7: Long-term measurements and evaluated resonance frequencies and quality factors.

to small η and ρ variations, this results shows the great capabilities of resonant viscosity and mass density sensors. The revision of these setups and more precise long-term measurements will be subject of future research.

4.4 Wire viscometer

Resonating viscometers using a single wire only, are known as wire viscometers in literature [104, 231, 258]. These viscometers were designed to be operated at one fixed resonance frequency only. The motivation for the wire viscometers investigated within this thesis however, was the investigation of tuning the resonance frequencies online within a preferentially large frequency range and with focus on miniaturized devices [MHj5]. Furthermore, the wire viscometer benefits from a very simple design allowing closed form modeling.

Figure 4.8(a) shows a schematic sketch of the wire viscometer. A tungsten wire is stretched over two electrical conductive blades. For first (test) setups, these blades, determining the vibrating length and assuring for electrical contact, were made of PCB (copper coated fiberglass) which were later replaced by machined metal blades. The series resistor limits the excitation current to avoid non linear deflection yielding Duffing behavior, see [231]. For measurements in air about 10 kΩ and in liquids, resistors between 50 Ω and 1 kΩ were used. The external magnetic field was generated with different NdFeB magnet assemblies yielding magnetic flux densities from 0.3 T up to 1.4 T, see [MHc22].

In figure 4.8(b) recorded frequency responses in four different liquids are shown. There the resonance frequency obtained for measurements in DI-water shifted to unexpected lower resonance frequencies compared to those of the solvents. This finding can only be explained by slacking of the tensioned wire which is a major issue concerning resonance stability and thus measurement accuracy. Due to these instabilities which only can be overcome with relatively highly sophisticated tensioning mechanisms, see [MHj5], this concept was not further investigated. Similar to the measurements for the suspended platelet sensor presented in Sec. 4.2, the bandwidth of achievable resonance frequencies by changing the tensile stresses in the wire was investigated, see Fig. 4.8(c). There, frequency responses yielding resonance frequencies in the range of 1000 Hz to 4250 Hz for a 3 cm long and 100 µm thick tungsten wire are shown.

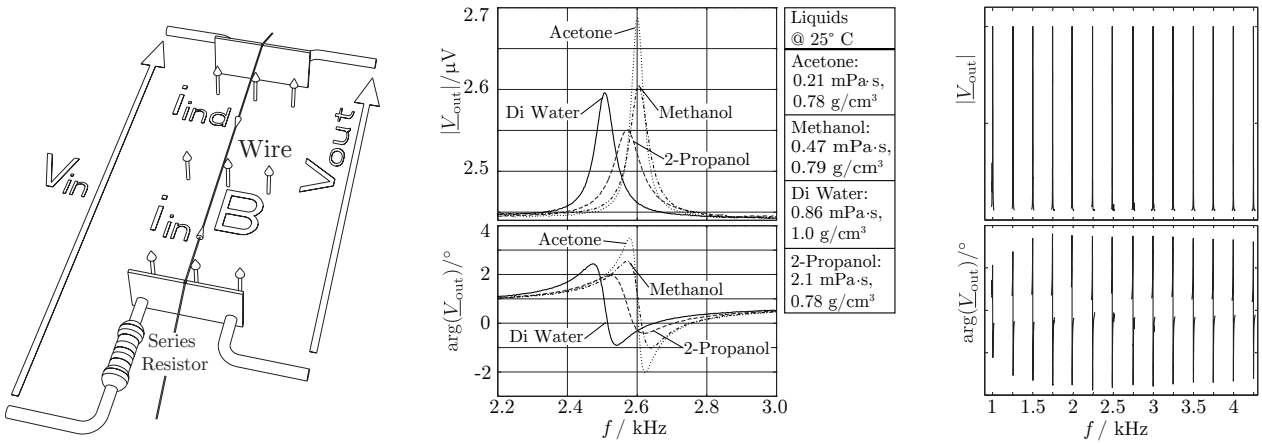

(a) Wire Viscometer (b) Measurements (c) Tuning

Figure 4.8: In (a) a schematic drawing of the wire viscometer is depicted. The experimental well for investigating sample liquids is not shown in this sketch. A 100 µm thick tungsten wire carrying sinusoidal currents is placed in an external magnetic field and thus transversally oscillating. A series resistors is used to limit the excitation current. The resonance frequency can be changed by (mechanically) changing the tensile stresses in the wire. (b) shows recorded frequency responses in liquids and in (c) the band width of achievable resonance frequencies (in air) using a 3 cm long and 100 µm thick tungsten wire is illustrated. The obtained resonance frequency range is 1000 Hz to 4250 Hz.

4.5 U-shaped wire sensor

First prototypes of the U-shaped wire sensor were presented in [MHc18]. A similar silicon-based device for magnetic field measurements was presented in [259] and in [87], a U-shaped cantilever device for the characterization of DNA solutions was presented. For the setup investigated in this thesis, a tungsten wire, bent to the shape of a 'U', rigidly clamped and immersed in a sample liquid, carries sinusoidal currents in the presence of an external magnetic field, as depicted in Fig. 4.9(a). Due to the resulting Lorentz forces, the latter deflects in an out-of-plane oscillation yielding a motion-induced voltage corresponding to the wire's tip velocity and thus serves as a quantity for read-out.

The U-shaped wire resonator was designed aiming at operational frequencies in the low kilohertz range, circular cross-sections of the resonator, electrodynamic actuation and read-out by means of Lorentz forces and last but not least, low cross-sensitivity of the sensor's resonance frequency to temperature. Circular cross-sections are beneficial for closed form modeling of the fluid-structure interaction, as the well known analytical expressions for a laterally oscillating cylinder [191] can be easily applied. The modeling of the fluid-structure interaction of resonators with rectangular cross-sections (as it is the case for the classical micro-cantilever), is e.g. based on considering an infinitely thin structure [260] or introducing a correction function to the well known equations for the circular case [193]. Both approaches yield relatively complex expressions for the fluid-structure interaction.

The cross-sensitivities of the resonance frequency to temperature of resonant viscosity and mass density sensors have to be small, as the temperature measurement is limited to a certain accuracy. In comparison to doubly clamped structures, for which high cross-sensitivities of the resonance frequency to temperature have been observed [MHj5], singly clamped approaches yield lower dependencies of the resonance frequency to temperature in general. The U-shaped design might be interpreted as such a singly clamped beam, or in other words, two singly clamped beams, which are connected at their ends. Tungsten was used as resonator material as it features a low thermal expansion coefficient and thus, keeps the thermal dependence of the resonance frequency low. In [MHj4] it was experimentally shown, that the U-shaped tungsten wire resonator yielded lower relative cross-sensitivity of the resonance frequency to temperature than similar devices implemented in silicon.

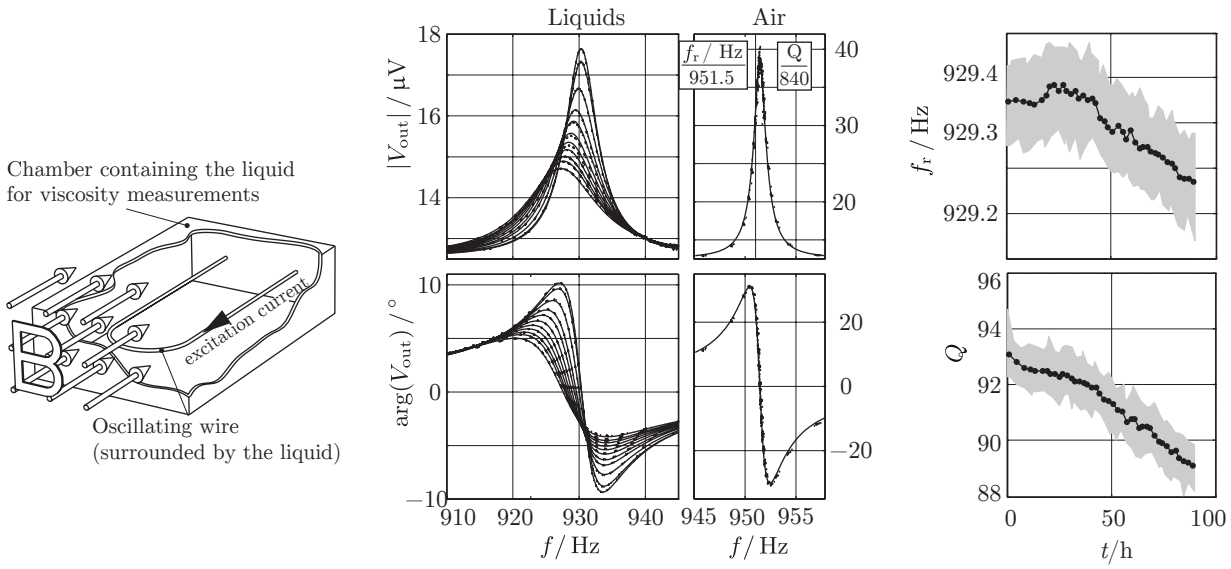

(a) U-shaped wire (b) Measurements in liquids (c) Long-term measurements

Figure 4.9: (a) Schematic sketch of the U-shaped wire viscosity and mass density sensor. (b) Comparison of measured and modeled results for acetone-isopropanol solutions. (c) Long-term measurements in ethanol yielding a drift of resonance frequency and quality factor. The black line indicates averaged values of 100 measurements where the gray surface represents all measured values.

Setup and Measurements

Several prototypes of the U-shaped wire sensor were fabricated. Photographs of the latest and most reliable setup are shown in Fig. 4.10. To prevent from evaporation and associated thermal changes of the liquid due to evaporation heat losses, the U-shaped wire was integrated in a sealed aluminum housing, see Fig. 4.10(a). An assembly of cylindrical and ring permanent magnets, c.f. Fig. 4.10(b), provides magnetic flux densities of $B \approx 0.5\,\mathrm{T}$ [MHc18]. A 400 µm thick tungsten wire was bent to the shape of a 'U' with a radius of 3 mm and 12 mm in length. To achieve a stable and reliable clamping, the wire was brazed into two brass blocks, see Fig. 4.10(c). For clamping, two screws for each block were used, which furthermore served to provide a stable electrical connection between the U-shaped wire and a PCB carrying BNC connectors. For measuring and controlling the liquid's temperature, a Pt-100 temperature sensor was placed close to the U-shaped wire.

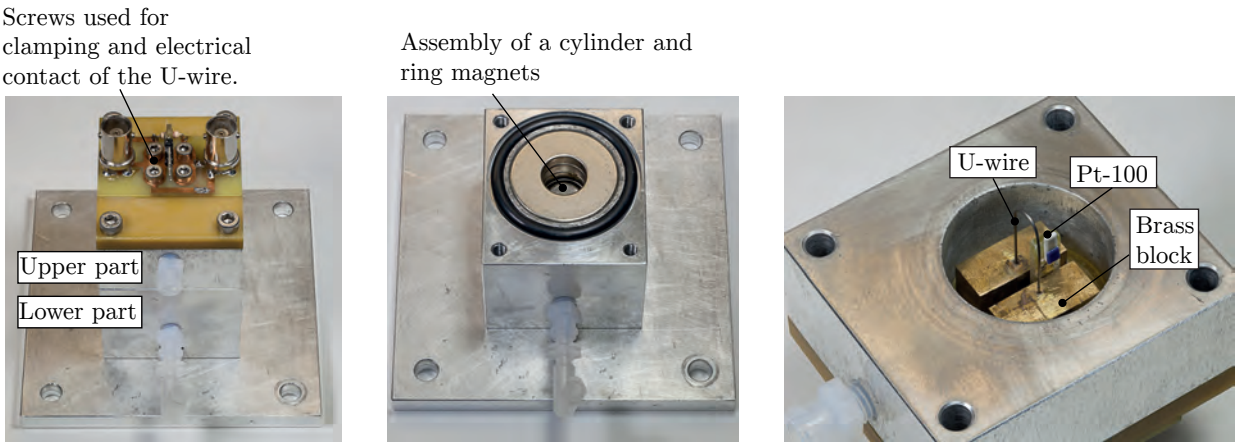

(a) Closed aluminium setup (b) Lower part (c) Upper part

Figure 4.10: Photographs of the measurement setup

The setup has been extensively tested in several measurement series. For these measurements, the setup was placed in a Weiss WKL 100 climate chamber to provide stable measuring conditions by controlling the temperature at 25 °C. The voltage of the signal generator was $V_g = 0.1\,\mathrm{V}$ and a series resistance $R_s = 100\,\Omega$ was used, c.f. electrical equivalent circuit in Fig. 3.2 for a 1CLFDR. In Fig. 4.9(b), a comparison between recorded and modeled results is shown. The experimental results were obtained with the 11 acetone-isopropanol solutions depicted in Fig. 1.2 in Chapter 1. For modeling a complete, closed form model has been devised and was presented in [MHj4]. The setup has furthermore been tested in liquids recording f_r and Q over several days in the climate chamber at 25 °C. In comparison to previously investigated doubly clamped devices [MHj5], the long-term stability improved significantly. However, in some cases, minor but clear trends of both f_r and Q could be observed, see e.g., Fig. 4.9(c). There, the evaluated results for f_r and Q of 4193 measurements which were recored during 90 hours in ethanol are depicted. In this case, the shift to lower f_r and Q is related to the change of the liquid properties itself. It was found that O-ring seals were slightly dissolved by the ethanol leading to a slight increase in viscosity and mass density of the liquid which was detected by the sensor.

In other experiments, electrolytical solutions were investigated, which yielded corrosion within the setup. To overcome this, a complete redesign using other materials, will be necessary. However, the principle of the U-shaped wire yielded already very promising results. The principle ability for long-term stability can be explained by its singly clamped approach and by its low cross-sensitivity to temperature. These circumstances can also be observed in case of string instruments, which have to be frequently tuned, compared to reed-based instruments (like accordions) and tuning forks which are based on singly clamped oscillating objects for which re-tuning is not necessary.

4.6 U-tube density sensor

Inspired by the commercially available, vibrating U-tube principle [261, 262] for precise mass density measurements, a feasibility study for a miniaturized U-tube mass density sensor was elaborated [MHc18]. Although it is possible to determine both, viscosity and mass density with resonant viscosity and mass density sensors, the motivation for such a device yielding mass density values only is to increase the measuring accuracy for both quantities with a second reference measurement. The idea behind the concept, which is depicted in Fig. 4.11(a), was to have a second device of (approximately)

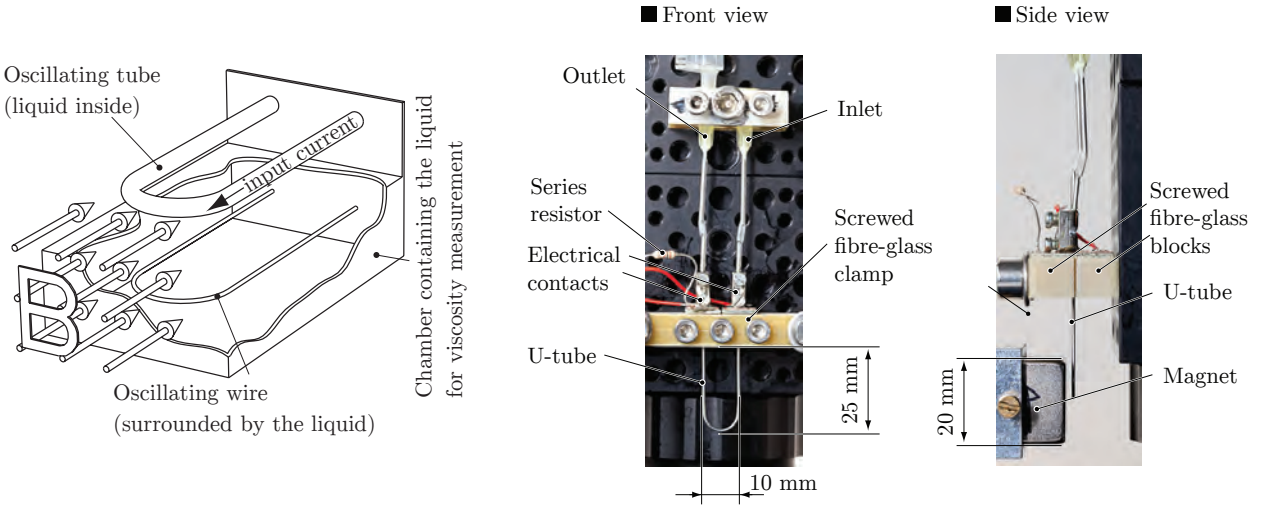

(a) Measuring cell

(b) Photographs of the mass density sensor

Figure 4.11: Sketch of the measuring cell and photographs of the mass density sensor. (a) Principle of the measuring cell consisting of a density sensor (top) and a viscosity sensor (bottom). The density sensor consists of a stainless steel tube (0.5 – 0.8 mm) with the sample liquid inside. The viscosity sensor consists of a 0.4 mm thick, bent tungsten wire being immersed in the sample liquid. (b) shows photographs of the setup used for a first feasibility study.

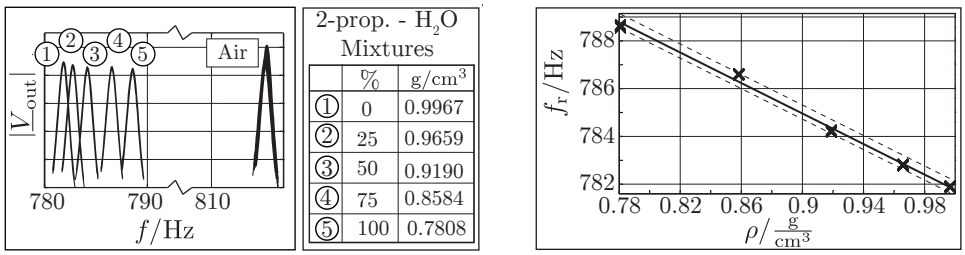

(a) Measurements (b) Evaluation

Figure 4.12: Mass density measurements and evaluation: (a) shows the amplitude of measured frequency responses in five different liquids given in the table aside. For every liquid 100 measurements have been performed. (b) shows the evaluated resonance frequencies of the recorded frequency responses. The solid line is the result from a fitted model. The dashed lines indicate the margins of maximum negative and positive deviations of recorded values from the fitted model.

the same size and the same excitation and read-out principles as the U-shaped wire sensor. Photographs of a first feasibility study are depicted in Fig. 4.11(b). A stainless steel capillary with inner and outer diameter of 0.5 mm and 0.8 mm, respectively was used as tube. The U-tube was clamped with two fibre-glass blocks and three screws. For electrical contact, the free ends of the tube were contacted with electrical clamps and additional soldering. For enabling filling of the tube, the latter was connected to cannulas with heat shrink tubes, which furthermore acted as stress reliefs.

The experimental results obtained with this prototype at 25 °C are shown in Fig. 4.12(a). Five isopropanol–water mixtures have been used for investigating the sensor's sensitivity to mass density. With every mixture, 100 measurements have been performed. After the cleaning of the tube, 100 resonance curves have been recorded in air before filling the sensor with a new sample liquid to certify the cleaning procedure. For this mass density sensor, the resonance frequency can be directly related to the liquid's mass density. The (fitted) solid line in Fig. 4.12(b) for the resonance frequency f_r as function of mass density ρ in g / cm^3 is $f_r(\rho) = 813.70 - 31.93 \cdot \rho$ Hz and the dashed lines indicate the maximum positive and negative deviations of recorded values from these fitted values. All recorded measurements for this mass density sensor lie within an (accuracy) margin of -0.0073 to 0.0112 g/cm^3. Note that these values were achieved for a very first, relatively simple prototype which was developed in the course of a feasibility study. Commercially available mass density measurement hand-held devices feature an accuracy of $\Delta\rho = \pm 0.001\,\mathrm{g/cm^3}$. To be able to achieve this accuracy with such a mass density sensor which features a sensitivity of $\Delta f_r/\Delta\rho = -31.93\,\mathrm{Hz\,/\,g/cm^3}$ and assuming an accuracy of the temperature measurement of $\Delta T = \pm 0.1\,°\mathrm{C}$, the maximum allowable dependency of the sensor's resonance frequency on temperature is given by $\Delta f_r/\Delta T \leq \pm$ 0.32 Hz/°C.

4.7 Spring viscometer

The principle of the spring viscosimeter as well as a photograph of the latter are depicted in Fig. 4.13, [MHc7]. A spiral spring, placed in an external magnetic field and carrying sinusoidal currents, is immersed into a sample liquid. Due to Lorentz forces on the AC currents in the spring, the latter oscillates transversally, which in turn induces a voltage on the spring. For this first prototype, a spiral spring was mounted and stretched on two brass screws which in turn were fixed with two brass screws which furthermore allowed for electrically contacting the spring, see Fig. 4.13(b). This clamping method is sufficient for principle investigations, and a first estimation of side effects such as cross-sensitivity to temperature. However, when aiming at using the device as an accurate viscosity and mass density sensor, a more reliable clamping technique has to be developed. As a first attempt, to overcome this drawback, the spring was braced on small brass cylinders. However, due to the high temperatures, the spring's elasticity significantly suffered from the brazing procedure and thus this approach was not further refined.

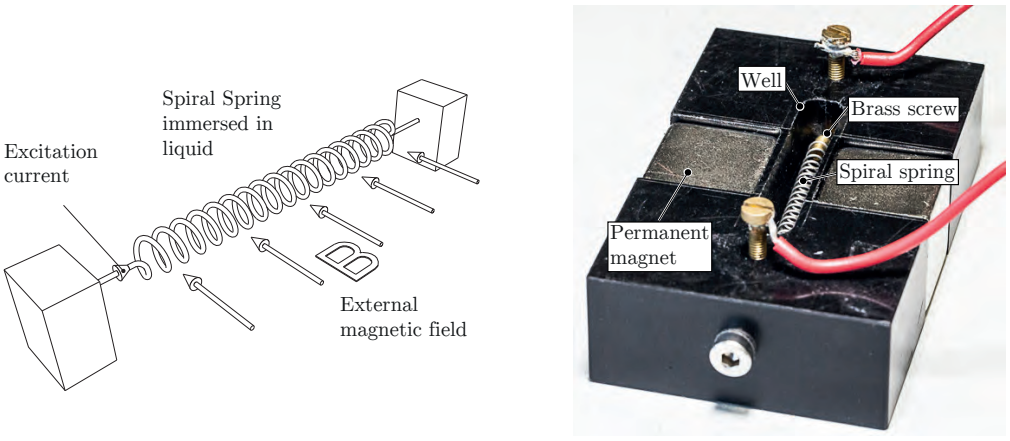

(a) Sensor Principle (b) Photograph

Figure 4.13: (a) An electrical conductive, streched spiral spring, immersed in a sample liquid, carries sinusoidal currents in the presence of an external magnetic field and thus oscillates transversally. (b) photograph of a first prototype: the spring was mounted on brass screws and stretched in a machined well.

Recorded frequency responses with the acetone–isopropanol mixtures and evaluated quality factors and resonance frequencies over viscosity are depicted in Fig. 4.14. Figure 4.14(a) shows a characteristic frequency response in air with a quality factor $Q = 3028.6$ and resonance frequency $f_\mathrm{r} = 643.75\,\mathrm{Hz}$ as well as 100 recorded frequency responses for every liquid at 25 °C. After the examination of a liquid, the sensor was cleaned and then a measurement in air was performed. Due to the provisional clamping method mechanical cleaning might have changed the resonance frequency of the device. The span of variations of the evaluated resonance frequencies in air (after every measurement in a liquid) was 0.6958 Hz, which is a justifiable stability for a very first feasibility study of the sensor's principle but not for an accurate sensor. Contrary to expectations, the resonance frequency in the second liquid is higher than for the first liquid see Fig. 4.14(b). This effect was also observed for tuning forks and an oscillating U-shaped wire for the acetone–isopropanol mixtures. This behavior is due to the fact that the second liquid's mass density is $0.0034\mathrm{g/cm^3}$ lower than the first, see Fig. 1.2. The generalized

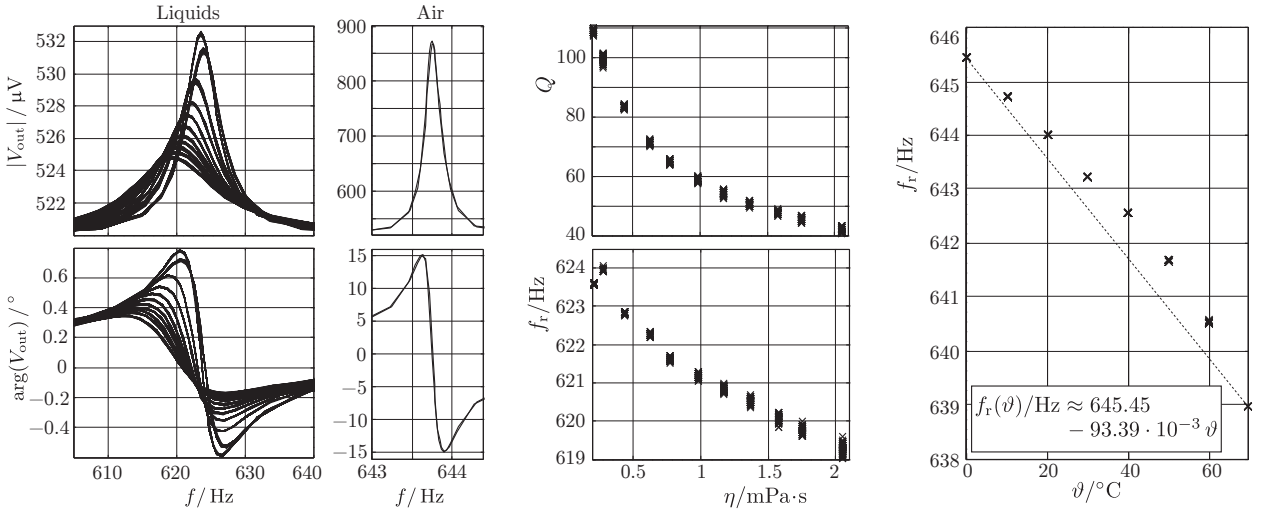

(a) Frequency responses (b) Evaluated f_r and Q (c) Cross-sensitivity to temperature

Figure 4.14: Experimental results obtained with the spring viscometer: (a) Recorded frequency responses in air (right) and in the acetone-isopropanol mixtures. (b) evaluated quality factors and resonance frequencies. (c) cross-sensitivity of the resonance frequency to temperature. Note, that the straight line just represents an estimate for the cross-sensitivity of the resonance. The deviation of measured values might be influences of the non-ideal clamping technique.

model Eq. 2.132 also considers this behavior. This experimental result very nicely shows that first, resonant sensors are sensitive to both, viscosity and mass density and second, that due to their high (but different) sensitiviteis to both quantities, accurate measurements can be achieved.

The purpose of using a spiral spring as resonator for viscosity and mass density sensing was first, to benefit from the design related advantages of doubly clamped structures but second, to reduce thermally induced (normal) stresses in such doubly clamped structures. Using a spiral spring instead of a straight wire drastically reduces the cross-sensitivity to temperature. In first experiments $\Delta f_\mathrm{r}/\Delta T = -0.983\,\mathrm{Hz/K}$ was achieved which divided by the devices resonance frequency of 640 Hz, approximately, gives a temperature coefficient of $\Delta^\mathrm{r} f_\mathrm{r}/\Delta T = -145 \cdot 10^{-6}\ 1/\mathrm{K}$, see Fig. 4.14(c). Regarding future work, a more reliable setup has to be designed, the sensitivities to viscosity and mass density as well as the device's cross-sensitivity to temperature have to be further investigated.

4.8 Torsional resonator

The motivation for the torsional resonator sensor, which is depicted in Fig. 4.15, was first, to manufacture a resonator, which according to theoretical results from Sec. 2.1.3 yields only shear wave propagation in the liquid and second, to have a resonator with which single and double conductor excitation can be compared. The latter was already discussed in Sec. 3.4.3. There, it was shown that the use of a second coil did not show a major advantage in the obtained signals compared to the setup where only one coil is used for excitation and read-out. However, using only one coil has a significant advantage for electrical connection. In this case, the electrical conductive torsional springs can be used for this task [MHj1].

One hundred turns of a copper wire with a diameter of 80 µm were wound on a 3D-printed bobbin. Two tungsten rods with a diameter of 0.58 mm serve as torsional springs with a spring length of 14 mm each. Both rods are brazed to brass cylinders with 10 mm diameter and 10 mm height. Each tungsten rod carries a brazed brass platelet and is put into the bobbin ensuring no contact between both torsional springs. Each end of the coil is glued with electrical conductive glue to one of these brass platelets which are furthermore used for a form-fitted connection with epoxy resin poured into both sides of the bobbin which in turn is put into a POM-C (polyacetal) plastics jacket with an outer diameter of 10 mm and 25 mm length. It is essential that the tungsten rods do not get in contact in order not to shortcut the coil. The torsional resonator is put into a milled POM-C plastics frame with a well for containing the sample liquids. The brass cylinders are clamped with brass screws, which in

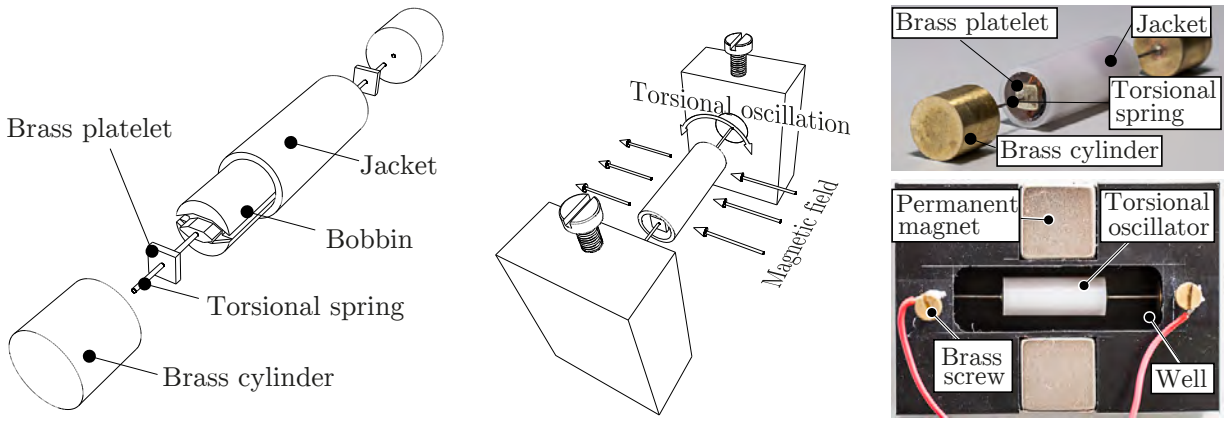

(a) Exploded illustration (b) Assembled, clamped illustration (c) Photographs

Figure 4.15: (a) Exploded view of the torsional resonator. (b) Illustration of the assembled, clamped setup. (c) The upper photograph shows the manufactured torsional oscillator. The lower photograph shows the complete setup including both permanent magnets and the torsional oscillator placed in the experimental well which was filled with the sample liquids.

turn are used for further electrical connection for power supply and read-out. Two neodymium magnets are used for providing a magnetic field necessary for excitation and read-out based on Lorentz-forces.

Measured amplitudes as well as evaluated quality factors and resonance frequencies obtained with the viscosity and mass density series are depicted in Fig. 4.16. The viscosity series consist of acetone – isopropanol mixtures which were depicted in Fig. 1.2. The intention of these mixtures was to obtain a liquid series with varying viscosities but constant mass densities and thus is called viscosity series. For the mass density series, five solutions using acetone, isopropanol, ethanol, DI-water and glycerol were prepared. The liquids were mixed to obtain constant viscosities of $1\,\mathrm{mPa{\cdot}s}$ but mass densities between $0.78\,\mathrm{g/cm^3}$ and $1\,\mathrm{g/cm^3}$. These liquid series have been mixed to allow separate experimental investigation of the effect of viscosity and mass density on the resonators' frequency responses. The viscosity and mass density values for the viscosity and the mass density series will be given in Tab. 4.3 in Sec. 4.9. Figure 4.16 shows the results of fitted models for f_r and Q. The curves depicted there were obtained by fitting the model parameters aside using all experimentally obtained values for f_r and Q and the values for η and ρ measured with the SVM 3000. With the identified model parameters, f_r and Q were than recalculated using again the same values for η and ρ. Relatively large deviations of the measured from the modeled values for f_r can be observed. The third value for the quality factor obtained with the viscosity series is considered to be an outlier. These deviations originate from imperfections in the prototype setup. These imperfections include, first, detuning of the sensor during cleaning, second, evaporation of the liquid during the measurements, and third, geometrical imperfections such as, e.g., surface roughnesses and a not perfect alignment of the oscillating cylinder with the torsional springs. For Q, both models, i.e. the model considering shear waves only and the generalized model yield similar results. For f_r, the generalized model clearly yields better results but still shows significant deviations. This finding can be explained by surface roughness, which yields so-called liquid trapping [90, 263] and thus a higher sensitivity to mass density. This effect may even be beneficial, as the effect of η and ρ on f_r and Q can not be separated for devices yielding pure one-dimensional shear waves without liquid trapping.

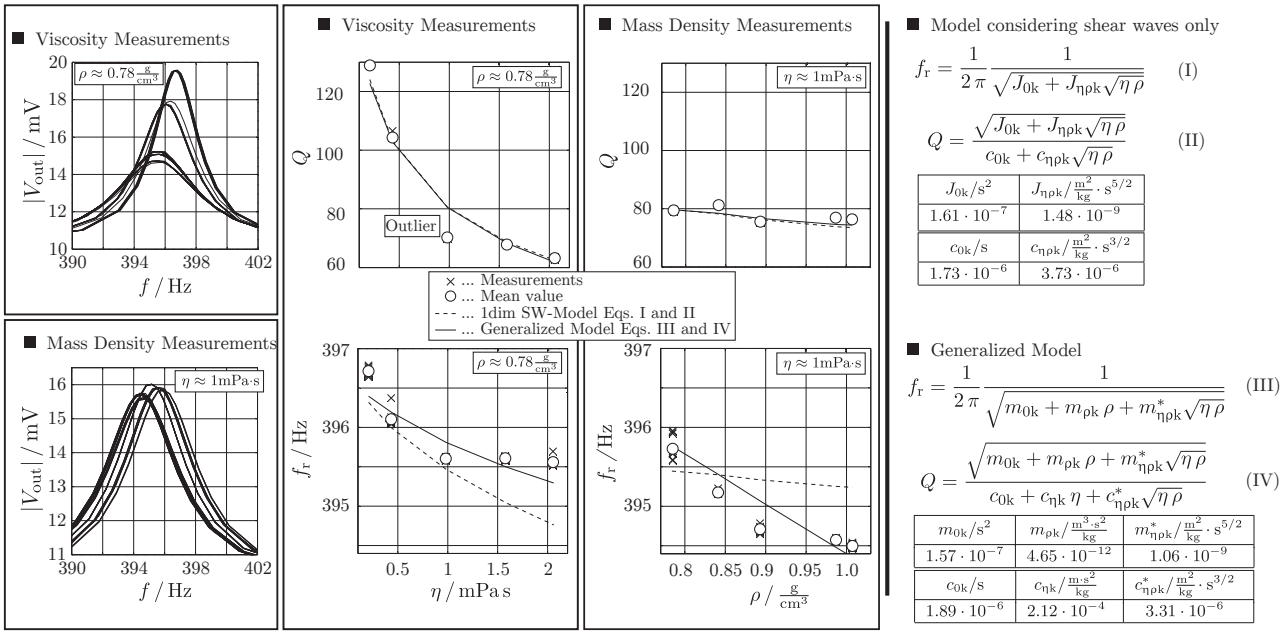

Figure 4.16: Measured amplitudes as well as evaluated resonance frequencies and quality factors for two liquid series. The one dimensional shear wave model as well as the generalized model are fit to the measured data. The model parameters are given on the right hand side.

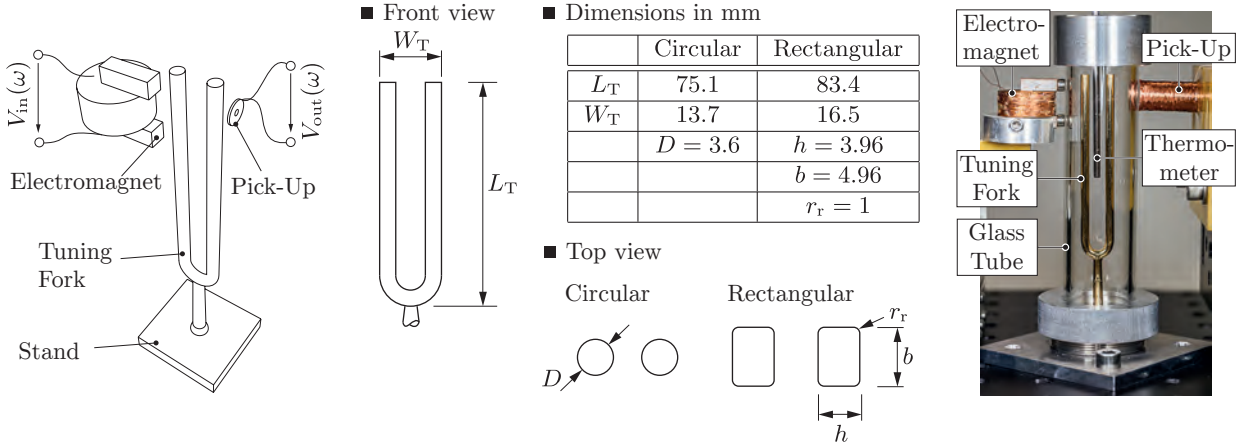

	Circular	Rectangular
L_{T}	75.1	83.4
W_{T}	13.7	16.5
	$D = 3.6$	$h = 3.96$
		$b = 4.96$
		$r_{\text{r}} = 1$

(a) Sensor principle (b) Geometries of investigated tuning forks (c) Photograph

Figure 4.17: Sensor principle: (a) A ferromagnetic steel tuning fork is actuated and read-out with an electromagnet and an electromagnetic pick-up, respectively. (b) in the table above, the geometrical dimensions of the circular and rectangular tuning fork are given. c) photograph of the measurement setup with a gold coated circular cross-sectioned tuning fork.

4.9 Tuning fork

In contrast to the Lorentz force driven resonators discussed in the previous sections, reluctance actuation and read-out using an electromagnetic pickup has been investigated using ferromagnetic tuning forks. Figure 4.17(a) shows a basic sketch of the setup for viscosity and mass density measurements using commercially available steel tuning forks and in Fig. 4.17(b) the geometries of the used tuning forks with circular and rectangular cross-sections, both resonating at nominally 440 Hz in air in their fundamental mode, are given [MHj2]. Figure 4.17(c) shows a photograph of the circular tuning fork setup.

The steel tuning forks were welded to a solid stainless steel stand and put into a glass tube (not depicted in Fig. 4.17(a)) which was sealed at both sides. To avoid corrosion, the tuning forks were gold-coated by electro-plating. An electromagnet, used for excitation, is placed (outside of the tube) close to the end of one of the ferromagnetic tuning fork's prongs. At the end of the opposed prong, an electrodynamic pick-up is placed, consisting of a permanent magnet in the center of a copper coil. A sinusoidal voltage $V_{\text{in}} = \hat{V}_{\text{in}} \sin(\omega\, t) + V_{\text{in,offs}}$ with a DC offset $V_{\text{in,offs}} \geq \hat{V}_{\text{in}}/2$ is used as input signal, exciting harmonic oscillations of the tuning fork. These oscillations effect an induced voltage in the pick-up serving as read-out signal. By sweeping the excitation current's frequency (containing a resonant mode), the frequency response of the fully immersed tuning fork is recorded.

4.9.1 Measurements

To experimentally investigate the effects of viscosity and mass density separately on both tuning forks' resonant behaviors, both tuning forks have been examined using the 'viscosity series' with (almost) constant mass densities, and the 'mass density series' with (almost) constant viscosities. Recorded frequency responses as well as evaluated resonance frequencies and quality factors obtained with both

	$m_{0\text{k}}/\text{s}^2$	$m_{\rho\text{k}}/\frac{\text{m}^3\cdot\text{s}^2}{\text{kg}}$	$m_{\eta\rho\text{k}}/\frac{\text{m}^2\,\text{s}^2}{\text{kg}}$	$c_{0\text{k}}/\text{s}$	$c_{\eta\text{k}}/\frac{\text{m}\cdot\text{s}^2}{\text{kg}}$	$c_{\eta\rho\text{k}}/\frac{\text{m}^2\,\text{s}^2}{\text{kg}}$
Circular	$1.31 \cdot 10^{-7}$	$1.74 \cdot 10^{-11}$	$2.71 \cdot 10^{-8}$	$2.79 \cdot 10^{-7}$	$7.82 \cdot 10^{-5}$	$2.41 \cdot 10^{-8}$
Rectangular	$1.32 \cdot 10^{-7}$	$2.45 \cdot 10^{-11}$	$2.50 \cdot 10^{-8}$	$2.97 \cdot 10^{-7}$	$7.16 \cdot 10^{-5}$	$2.24 \cdot 10^{-8}$

Table 4.2: Fitted model parameters for the circular and the rectangular tuning fork

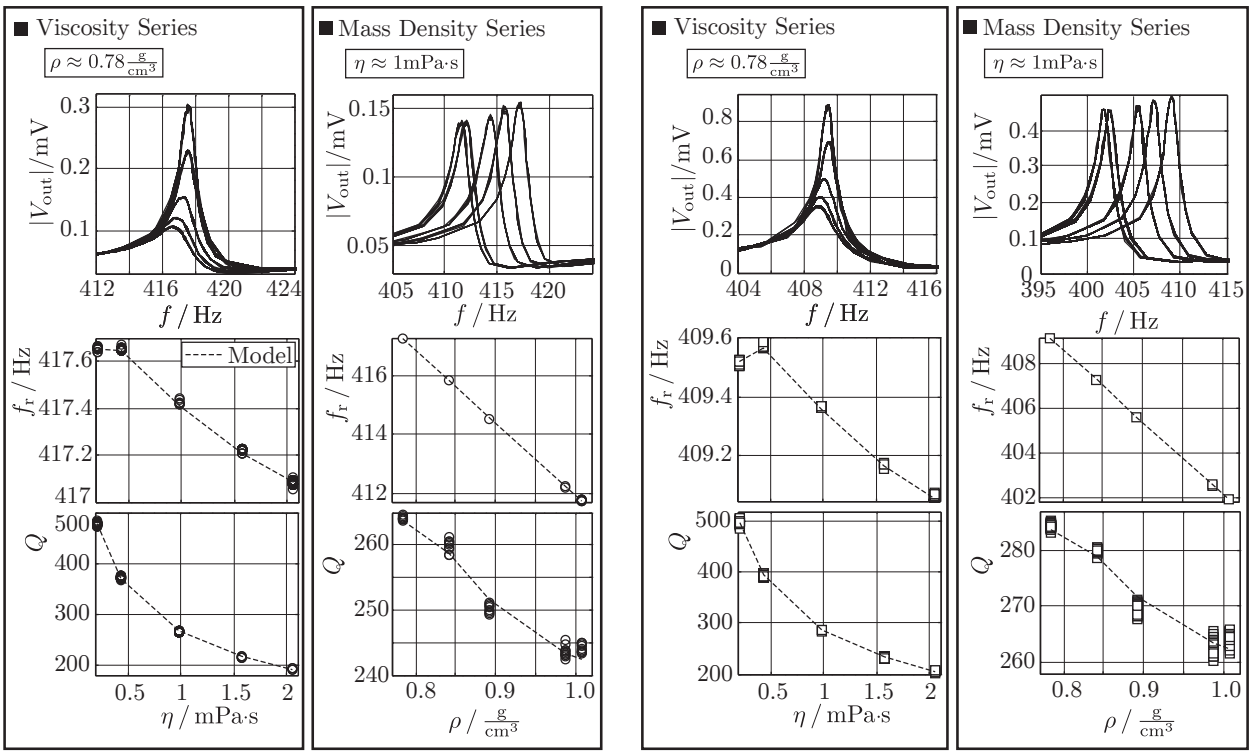

(a) Circular (b) Rectangular

Figure 4.18: Recorded frequency responses and therefrom evaluated resonance frequencies and quality factors for the circular and rectangular tuning fork.

tuning forks using the viscosity and the mass density series are depicted in Fig. 4.18. These measurement results have been used to fit the parameters of the generalized model Eq. 2.132 in Sec. 2.7 and are given in Tab. 4.2 for the circular and the rectangular tuning fork, respectively.

The viscosity and mass density values of the used liquids at 25 C°, determined with an Anton Paar SVM300 which features a reproducibility of 0.35 % for viscosity and 0.000 5 g/cm^3 for mass density are given in Tabs. 4.3 and 4.4. There, the evaluated resonance frequencies, quality factors and their single standard deviations as well as calculated viscosity and mass density values and their absolute

Viscosity Series – Circular Tuning Fork – $T = 25°\mathrm{C}$									
$\frac{\eta}{\mathrm{mPa{\cdot}s}}$	$\frac{\rho}{\mathrm{g/cm^3}}$	$f_{\mathrm{r}}/\mathrm{Hz}$	Q	$\frac{\eta_{\mathrm{c}}}{\mathrm{mPa{\cdot}s}}$	$\frac{\Delta\,\eta}{\mathrm{mPa{\cdot}s}}$	$\Delta^{\mathrm{r}}\,\eta$	$\frac{\rho_{\mathrm{c}}}{\mathrm{g/cm^3}}$	$\frac{\Delta\,\rho}{\mathrm{g/cm^3}}$	$\Delta^{\mathrm{r}}\,\rho$
0.207	0.7841	$417.65 \pm 2.9 \cdot 10^{-3}$	477.38 ± 1.88	0.211	0.0045	0.0216	0.7841	-0.000 014	$0.018{\cdot}10^{-3}$
0.433	0.7790	$417.65 \pm 2.9 \cdot 10^{-3}$	371.81 ± 1.44	0.427	-0.0060	-0.0139	0.7791	0.000 067	$0.086{\cdot}10^{-3}$
0.980	0.7793	$417.42 \pm 3.5 \cdot 10^{-3}$	265.16 ± 0.34	0.986	-0.0053	-0.0054	0.7792	-0.000 101	$-0.130{\cdot}10^{-3}$
1.576	0.7803	$417.22 \pm 3.1 \cdot 10^{-3}$	214.52 ± 0.33	1.591	0.015	0.0094	0.7798	-0.000 542	$-0.694{\cdot}10^{-3}$
2.054	0.7804	$417.08 \pm 7.1 \cdot 10^{-3}$	190.83 ± 0.52	2.048	-0.0065	-0.0032	0.7808	0.000 409	$0.523{\cdot}10^{-3}$
Density Series – Circular Tuning Fork – $T = 25°\mathrm{C}$									
$\frac{\eta}{\mathrm{mPa{\cdot}s}}$	$\frac{\rho}{\mathrm{g/cm^3}}$	$f_{\mathrm{r}}/\mathrm{Hz}$	Q	$\frac{\eta_{\mathrm{c}}}{\mathrm{mPa{\cdot}s}}$	$\frac{\Delta\,\eta}{\mathrm{mPa{\cdot}s}}$	$\Delta^{\mathrm{r}}\,\eta$	$\frac{\rho_{\mathrm{c}}}{\mathrm{g/cm^3}}$	$\frac{\Delta\,\rho}{\mathrm{g/cm^3}}$	$\Delta^{\mathrm{r}}\,\rho$
1.006	0.7849	$417.28 \pm 1.5 \cdot 10^{-3}$	264.15 ± 0.26	0.989	-0.016	-0.021	0.7847	-0.000 220	$-0.281{\cdot}10^{-3}$
0.994	0.8411	$415.85 \pm 8.4 \cdot 10^{-3}$	259.70 ± 1.0	0.979	-0.015	-0.015	0.8413	0.000 179	$0.212{\cdot}10^{-3}$
1.010	0.8931	$414.52 \pm 0.9 \cdot 10^{-3}$	250.03 ± 0.68	1.023	0.014	0.013	0.8932	0.000 610	$0.684{\cdot}10^{-3}$
1.006	0.9870	$412.21 \pm 7.2 \cdot 10^{-3}$	243.58 ± 0.88	1.013	0.007	0.007	0.9872	0.000 177	$0.179{\cdot}10^{-3}$
0.998	1.0073	$411.75 \pm 8.0 \cdot 10^{-3}$	244.08 ± 0.62	0.995	-0.033	-0.003	1.0067	-0.000 597	$-0.592{\cdot}10^{-3}$

Table 4.3: Measurement results for the circular tuning fork. The values on the left hand side are viscosity and mass density values measured with the SMV3000. The plus-minus values for f_{r} and Q are evaluated typical errors (single standard deviations). x_{c} are the calculated values for viscosity and mass density using the generalized equations and evaluated mean values for f_{r} and Q. $\Delta\,x = x_{\mathrm{c}} - x$ and $\Delta^{\mathrm{r}}\,x = \Delta\,x/x$ are absolute and relative deviations from the values for viscosity and mass density, respectively.

Viscosity Series – Rectangular Tuning Fork – $T = 25°C$									
$\frac{\eta}{\text{mPa·s}}$	$\frac{\rho}{\text{g/cm}^3}$	f_r/Hz	Q	$\frac{\eta_c}{\text{mPa·s}}$	$\frac{\Delta\eta}{\text{mPa·s}}$	$\Delta^r\eta$	$\frac{\rho_c}{\text{g/cm}^3}$	$\frac{\Delta\rho}{\text{g/cm}^3}$	$\Delta^r\rho$
0.207	0.7841	$409.52 \pm 3.8 \cdot 10^{-3}$	499.00 ± 3.03	0.214	0.0069	0.0334	0.7841	-0.000 006	$-0.008{\cdot}10^{-3}$
0.433	0.7790	$409.58 \pm 6.3 \cdot 10^{-3}$	394.58 ± 1.91	0.427	-0.0060	-0.0139	0.7789	-0.000 055	$-0.070{\cdot}10^{-3}$
0.980	0.7793	$409.36 \pm 0.9 \cdot 10^{-3}$	285.74 ± 0.29	0.977	-0.0031	-0.0031	0.7794	0.000 054	$0.069{\cdot}10^{-3}$
1.576	0.7803	$409.17 \pm 1.8 \cdot 10^{-3}$	232.25 ± 0.39	1.582	0.0053	0.0034	0.7803	0.000 039	$0.050{\cdot}10^{-3}$
2.054	0.7804	$409.07 \pm 3.1 \cdot 10^{-3}$	206.20 ± 0.74	2.059	0.0043	-0.0021	0.7804	-0.000 020	$-0.026{\cdot}10^{-3}$
Density Series – Rectangular Tuning Fork – $T = 25°C$									
$\frac{\eta}{\text{mPa·s}}$	$\frac{\rho}{\text{g/cm}^3}$	f_r/Hz	Q	$\frac{\eta_c}{\text{mPa·s}}$	$\frac{\Delta\eta}{\text{mPa·s}}$	$\Delta^r\eta$	$\frac{\rho_c}{\text{g/cm}^3}$	$\frac{\Delta\rho}{\text{g/cm}^3}$	$\Delta^r\rho$
1.006	0.7849	$409.18 \pm 1.8 \cdot 10^{-3}$	284.34 ± 0.31	0.984	-0.021	-0.021	0.7849	0.000 016	$0.020{\cdot}10^{-3}$
0.994	0.8411	$407.30 \pm 1.0 \cdot 10^{-3}$	279.90 ± 0.29	0.976	-0.017	-0.018	0.8412	0.000 125	$0.149{\cdot}10^{-3}$
1.010	0.8931	$405.58 \pm 0.9 \cdot 10^{-3}$	269.94 ± 0.65	1.023	0.013	0.012	0.8932	0.000 066	$0.074{\cdot}10^{-3}$
1.006	0.9870	$402.55 \pm 2.6 \cdot 10^{-3}$	262.74 ± 0.93	1.023	0.018	0.017	0.9868	-0.000 151	$-0.152{\cdot}10^{-3}$
0.998	1.0073	$401.91 \pm 3.4 \cdot 10^{-3}$	264.43 ± 0.75	0.995	-0.030	-0.003	1.0072	-0.000 076	$-0.076{\cdot}10^{-3}$

Table 4.4: Measurement results for the rectangular tuning fork.

and relative deviations from the measured values are listed for both tuning forks.

Measurement accuracy

The evaluation of absolute and relative deviations given in Tabs. 4.3, 4.4 and plotted in Fig. 4.19(a) gives the range of absolute and relative deviations of values determined with the tuning forks from the values obtained with the SVM 3000, see also Tab. 4.5. For the investigated viscosities a range of $[|\Delta\eta|_{\min}, |\Delta\eta|_{\max}] = [0.003, 0.021]$ mPa·s and $[|\Delta^r\eta|_{\min}, |\Delta^r\eta|_{\max}] = [0.003, 0.033]$ and for the determined mass densities $[|\Delta\rho|_{\min}, |\Delta\rho|_{\max}] = [0.000\,006, 0.000\,610]$ g/cm^3 and $[|\Delta^r\rho|_{\min}, |\Delta^r\rho|_{\max}] = \left[0.008 \cdot 10^{-3}, 0.694 \cdot 10^{-3}\right]$ was obtained. In Fig. 4.19(a) the relative deviations between values obtained with the tuning forks and the SVM 3000 are depicted. The evaluation shows that there is a clear correlation between the relative deviations for viscosity but not for mass density. This suggests the consideration that the values for viscosity which were determined with the SVM 3000 are subjected to significant errors or in other words that in this viscosity range, achievable accuracies similar

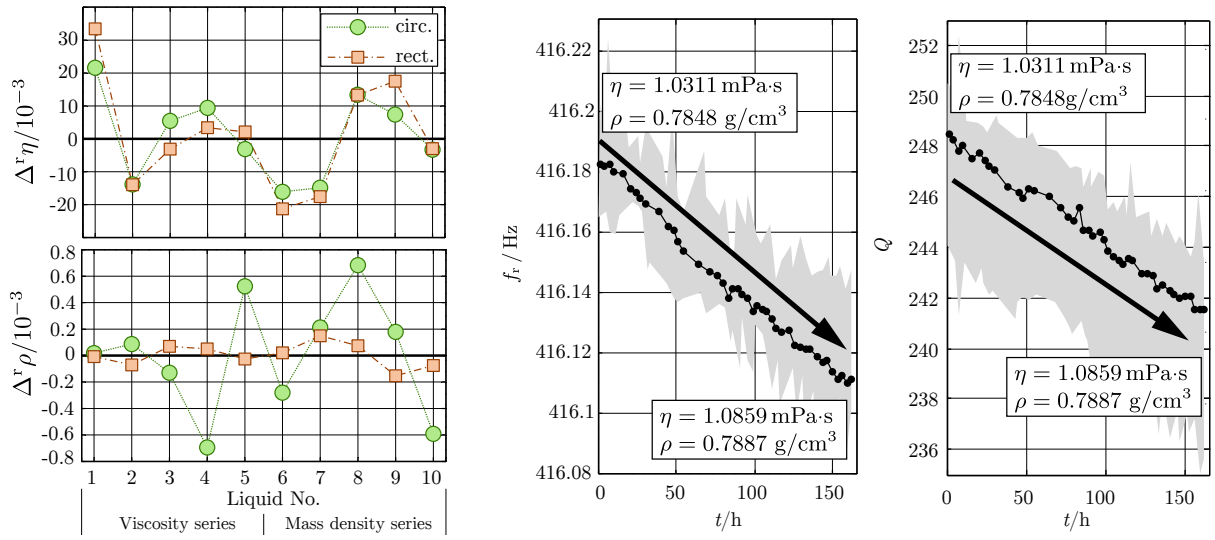

(a) Relative deviations (b) Long term measurements

Figure 4.19: (a) Relative deviations between values determined with the tuning forks and the SVM 3000. (b) Long-term measurements for dissolving rubber in ethanol. The changes of the liquid properties are 5.3 % in viscosity and 0.5 % in mass density, respectively. The grey shaded areas indicate the span of recorded resonance frequencies and quality factors. The black dots indicate the values averaged over 100 measurements.

	$\frac{\Delta\eta_{\min}}{\text{mPa·s}}$	$\frac{\Delta\eta_{\max}}{\text{mPa·s}}$	$\Delta^{\text{r}}\eta_{\min}$	$\Delta^{\text{r}}\eta_{\max}$	$\frac{\Delta\rho_{\min}}{\text{g/cm}^3}$	$\frac{\Delta\rho_{\max}}{\text{g/cm}^3}$	$\Delta^{\text{r}}\rho_{\min}$	$\Delta^{\text{r}}\rho_{\max}$
Circular	0.0033	0.0162	0.0032	0.0216	0.000 014	0.000 610	$0.017 \cdot 10^{-3}$	$0.694 \cdot 10^{-3}$
Rectangular	0.0030	0.0214	0.0021	0.0334	0.000 006	0.000 150	$0.008 \cdot 10^{-3}$	$0.152 \cdot 10^{-3}$

Table 4.5: Absolute and relative deviations from viscosity values determined with the SVM 3000 and with the circular and rectangular tuning fork, respectively.

as with the SVM3000 can be obtained with such tuning fork setups. This assumption is furthermore supported by the fact that the SVM 3000 yields errors higher than given in its specifications for liquids with viscosities lower than 0.5 mPa·s and for aqueous liquids. In Fig. 4.19(a) Liquid No. 1 features a viscosity in the order of 0.2 mPa·s and Liquids No. 6 to 9 contain water. An interesting fact is, that these liquids yield the highest deviations. Fig. 4.19(a) furthermore shows that relative deviations for viscosity are similar but are significantly higher for the mass density in case of the circular tuning fork. This finding can be explained (as it was already shown in Fig. 2.16) that the sensitivities of both tuning forks to viscosity are similar but is higher to mass density in case of the rectangular tuning fork.

These insights reveal the high potential of resonant viscosity and mass density sensors. For an estimation of achievable accuracies, with the present tuning fork setups, accuracies in the order of 1 % in viscosity and and 0.01 % in mass density can be obtained.

To further investigate the accuracy and the resolution of such viscosity and mass density measurement setups experimentally, the dissolving of rubber in ethanol was recorded during 150 hours, see Fig. 4.19(b). The viscosity and mass density have been determined with a SVM 3000 before and after the experiment. The change of the liquid's viscosity and mass density was 0.05 mPa·s (i.e. 5.3 %) and 0.0039 g/cm^3 (i.e. 0.5 %) respectively, which could be clearly detected by the change of f_{r} and Q. With an appropriate data analysis similar accuracies as they are achieved with high precision laboratory instruments may be obtainable with such comparatively low-cost tuning fork-based sensors.

4.10 Examples of resonant sensors for fluid properties from literature

So far in this manuscript, only the concepts and the underlying theory investigated during this thesis have been presented. The large amount of resonant viscosity and mass density sensors from other research groups is difficult to be summed up or to be described in a general manner. Thus, in the following, a short overview of resonant viscosity and mass density sensors, which can be found in literature, is presented, see also [MHbcc1].

The amount of devices reported for fluid property sensing is exceptionally large and thus only some characteristic examples of their types can be presented and discussed at this point. Selected works are shown, which are considered to be representative in their field without claiming completeness. From a mechanical point of view, three major resonator principles are considered: Singly clamped, doubly (or multiply) clamped, and membrane based devices. These different types may be operated in in-plane, out-of-plane or torsional modes.

In the following, the discussed sensor concepts for liquid property sensing include conventional cantilevers (which seems to be the mostly investigated device), U-shaped cantilevers, tuning forks, doubly clamped beams, shear vibrating devices, membranes, discs, and other principles. For the actuation of the vibration, piezoelectric, electromagnetic, thermal, and external vibrational actuation are used. Concerning the read-out of the sensor's mechanical oscillation, piezoresistive, capacitive, inductive, and optical methods are mainly reported.

4.10.1 Microacoustic devices

These devices emerged from the utilization of piezoelectric media in electronic components where, by means of the piezoelectric effect, vibrations in the utilized crystal are excited. If these vibrating structures get in contact with a fluid, the vibration characteristics are affected by the fluid properties as discussed above. The associated sensor principles can similarly be realized using alternative actuation mechanisms (i.e. other than the piezoelectric effect). Many of the issues and aspects that are encountered with microacoustic devices hold in a similar manner for MEMS resonators.

A very common technique for sensing viscosity and mass density with microacoustic devices is that of bringing a shear-vibrating surface in contact with the liquid, e.g., by using a thickness shear mode (TSM) quartz resonator and related devices [98,264–270] acoustic plate mode devices [271] or Love wave sensors [272–274]. For resonant sensors in highly viscous liquids, read-out can become difficult since due to overdaming the sensor can not be used as the frequency-determining element in an oscillator circuit. To overcome this, dedicated read-out circuits and algorithms for damped resonators have been investigated recently [229, 275–281].

For high frequencies the penetration depth becomes critically short. For instance, at 5 MHz the penetration depth for water would be in the order of 0.25 microns, which means that only a thin layer of liquid is examined. For liquids featuring a microstructure with characteristic dimensions above such penetration depths, the measured viscosity will be different from that obtained by laboratory instruments, see, e.g., the cases of emulsions, microemulsions and zeolite synthesis solutions discussed, e.g., in [106, 282, 283].

The devices discussed above use in-plane motion of the surface being in contact with the liquid. Out-of-plane vibrations generally lead to radiation of pressure waves which leads to spurious damping. This is the reason why classical surface acoustic wave (SAW) devices [284] are scarcely used as fluid sensors. An exception is when the slowness of the guided wave prevents pressure wave radiation into the adjacent fluid, such as, e.g., in the Lamb wave devices discussed in [285].

Pressure waves can be utilized, however, to sense the so-called longitudinal viscosity (which is associated with the second coefficient of viscosity or the bulk viscosity) as the latter determines the attenuation of pressure waves propagating in the fluid. In [286–288] setups utilizing piezoceramic transducers are discussed for this purpose considering also the acoustic pressure wave impedance as well as the sound velocity of the liquid.

4.10.2 MEMS devices

In the following, selected MEMS devices for mass density and viscosity sensing are discussed. Photographs of associated devices are shown in Fig. 4.20 and an overview is given in Tab. 4.6.

Cantilever devices

The micro-cantilever is the most reported resonant device for mass density and viscosity sensing applications, see, e.g., [291–293] and references cited there. The read-out mechanisms involve piezoresistive, impedance spectroscopic and optical principles. In general, optical read-out mechanisms are very commonly used as they allow very precise amplitude measurements which are moreover convenient and straight-forward to implement. However, when it comes to measurements in liquids, optical mechanisms might involve serious drawbacks. Optical read-out allows measurements in transparent liquids only and furthermore, the complete setup has to be mounted on a vibration compensated setup, which makes the application as a sensor difficult.

Figure 4.20 (a) shows a pair of two identical silicon micro-machined cantilevers. The structure on the right hand side, completely released from the bulk material acts as cantilever and is operated in an out-of-plane mode. The other device on the left hand side serves for reference measurements accounting

for the influence of cross-sensitivities on the measured signal. The device was designed to be actuated electromagnetically and read-out using piezoresistors. In [91] three different geometries of cantilevers are investigated, where the released cantilever yields resonance frequencies of about 5 kHz in liquids, See. Tab. 4.6. There, L, W, T denote the cantilevers' lengths, widths and thicknesses, respectively. In [294] and [295] the operation of cantilevers at higher vibration modes is discussed.

U-shaped cantilevers

A special class of cantilevers are so called U-shaped cantilevers, which have been reported e.g., in [195] and [87]. Fig. 4.20 (b) shows the tip of a U-shaped cantilever carrying a gold path for electromagnetic actuation. For read-out, optical, piezoresistive and inductive methods by means of a motion-induced voltage can be implemented. In Tab. 4.6 the overall sizes are given. W and T denote the width and the thickness of the cross-sectional dimensions.

Tuning forks

Commercially available quartz tuning forks have successfully been applied for viscosity and mass density sensing in liquids, see e.g., [93, 230, 296]. As it is the case for microacoustic TSM resonators, viscosity and mass density are measured by evaluating the immersed tuning fork's impedance spectrum, see also [263].

Doubly-clamped beam devices

Similar to vibrating cantilevers, straight doubly clamped vibrating beams (also termed clamped-clamped beams, bridges or wires) are used for viscosity sensing [231, 297, 298]. An example for the latter is depicted in Fig. 4.20 (c). The bridges can be excited using Lorentz-forces and the read-out can be performed inductively. The modeling of such devices is presented, e.g., in [193, 260, 299].

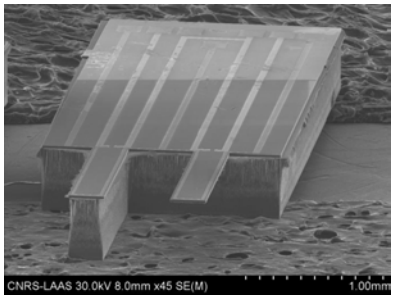

(a) [91]

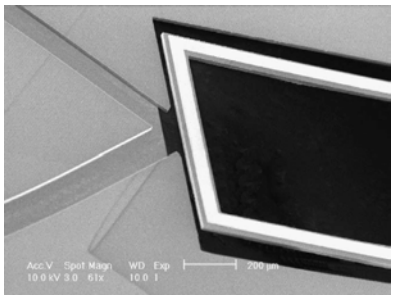

(b) [195]

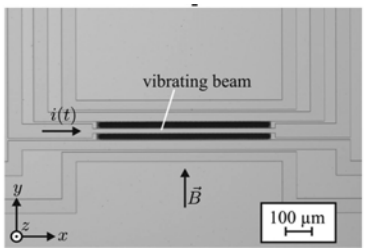

(c) [89]

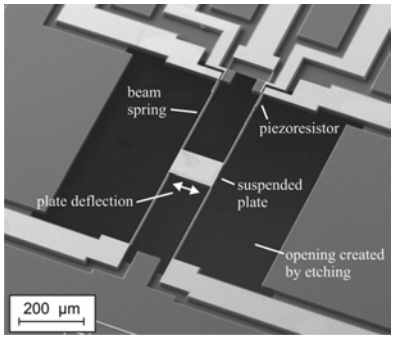

(d) [240]

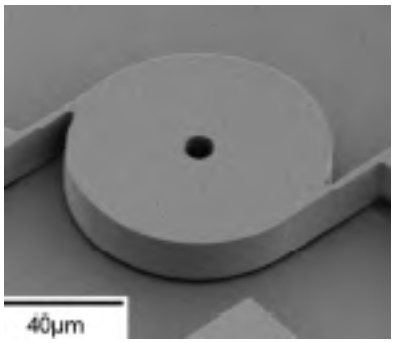

(e) [289]

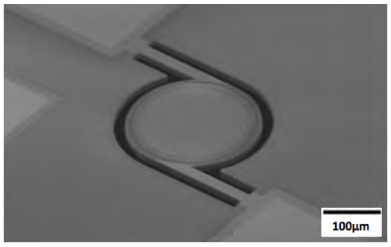

(f) [290]

Figure 4.20: Examples for resonant MEMS mass density and viscosity sensors

In-plane resonators

Examples for in-plane oscillating resonators, designed to preferentially excite shear waves in the liquid, are suspended platelets [240, 300], see Fig. 4.20 (d), mid-point suspended plates [301], thermally actuated [289, 302, 303] and piezoelectric [290] disks see Figs. 4.20 (e) and (f) as well as semicircular disks [304]. Fig. 4.20 (d) shows a scanning electron microscopy image of the aforementioned suspended silicon based plate which is actuated by means of Lorentz-forces on AC-currents in an external magnetic field and read-out with two piezoresistors implemented in the supporting beams. In the overview in Tab. 4.6, D denotes the diameter of the disk-based devices.

Membrane devices

The work presented in [237] discusses a Lorentz force actuated silicon membrane.

Other principles

Other devices which are not assigned to a general principle are a suspended micro-channel [305] which is a miniaturized version of a commercially available concept for mass density sensing, see [261, 262] and a vibrating diaphragm with capacitive read-out [306].
A thermally actuated disc, see Fig. 4.20 (e), which is operated in a rotational mode, was presented in [289] and successfully modeled in [303]. In [307], a sensor utilizing the excitation of a rubber-like magnetoelastic sheet, embedded in the liquid under test is described, where the sensor features a resonance frequency in the range of 50 kHz. In [308], a longitudinally vibrating tip is immersed in the liquid also vibrating in the lower frequency regime around 50 kHz. The vibration is driven by a PZT element whose impedance can be used to deduce the viscosity (and the density) of the liquid. A pole mounted on a vibrating membrane, whose tip interacts with the liquid under test is discussed in [95].

Device	Material(s)	Operational Mode	f_r (air) kHz	f_r (liquid) kHz	Q (air) —	Q (liquid) —	Actuation	Read-out	η mPas	Dimensions µm	Year	Ref.
Cantilever	Si/ Metall	o-o-p	206.5	93.4 (water)	900	17 (water)	L-F	Stress sensitive PMOS Transistors	0.9 (water)	L 200 W 50 . . . 186 T 8.2	2007	[309]
	Si with conductive paths	o-o-p	—	5 (CL 2.) (water)	—	—	L-F	Piezores./ Optical	0.9 . . . 20	1.: 2810x100x20 2.: 1440x285x20 3.: 500x100x20	2012	[91]
	Silicon	o-o-p (fundamental)	17.31	5.39 (water)	55.5	2 (water)	Thermal	Thermal noise spectrum	0.3 . . . 2.5	397x29x2	2002	[88]
	Si with Au paths	6 Modes	—	2 . . . 55	—	—	Photothermal	Optical	1 . . . 20	500x100x4	2013	[294]
	—	8 Modes	6.23 . . . 988.83	1.08 . . . 283.83 (water)	16 . . . 455.2	1.5 . . . 21.4 (water)	None (Noise)	Optical	0.9 (water)	519.6x47.1x1.17	2005	[295]
	Si/Au	i-p	50 . . . 2200	—	4200	67	Thermal	Piezores.	0.9 (water)	L 200 . . . 1000 W 45 . . . 90 T 12	2010	[310]
U-Shaped CL	Si with Au paths	o-o-p	8	3	—	—	L-F	Optical	05 . . . 400	1500x1100 W 100 T 15	2005	[195]
	Si with Au paths	o-o-p	20	12.5 (water)	—	25 . . . 30	L-F	Inductive (Motion ind. Voltage)	1 . . . 1.3	1600x1600 W 200 T 70	2013	[87]
Tuning Fork	Quartz Crystal	Fundamental (antiphase, in-plane)	32.7	29.8 (Hep.) 28.25 (N35)	—	163.76 (Hep.) 14.75 (N35)	Piezoel.	Impedance Spectroscopy	0.38 . . . 55.2	1000	2014	[230]
Bridge	Si with Al paths	o-o-p	5.8 . . . 68.7	2.5 . . . 57	210 . . . 881	0.4 . . . 10	L-F	Inductive, Optical	0.2 . . . 103.9	L 1500 . . . 5000 W 30, 50 T 20	2007	[297]
	Si with Au paths	o-o-p	96.7	31 (Toluene) 24 (Octanol)	—	3.5 (Tol.) 1 (Oct.)	L-F	Optical	0.57 . . . 7.37	350x50x1.3	2007	[92]
Suspended Plate	Si with Al paths	i-p	19.47	13.29 (water)	330	3.47 (water)	L-F	Piezores.	0.89 . . . 81.5	plate: 100x100 overall: 1000 T 20	2012	[300]
Mid-point Supported Plate	AlN (extensional)	i-p	3700	3700	3000	100 (water) 18 (51.15 mPas)	Piezoel.	Impedance Spectroscopy	0.9 . . . 51.15	1000x125x1	2012	[301]
Rotational Disk	Si (rotational)	i-p	1770 . . . 8410	1770 . . . 8410	600 . . . 11700	50 . . . 304 (heptane)	Thermal	Impedance Spectroscopy	0.38	D 100 . . . 200 T 5 . . . 20	2010	[289]
Semicircular Disks	Si (parylene coated)	i-p (rotational)	300 . . . 1000	585 (water)	1200, 5000	100 (water)	Thermal	Piezores.	0.9 (water)	D 240 . . . 300 T 8	2008	[304]
Suspended Microchannel	SiN	o-o-p	143	130.4	—	10400 (ethanol)	External (piez. act.)	Optical	0.8 . . . 10	20x200 cross-sec: 4x3	2013	[305]
Vibrating Diaphragm	Parylene (on Si)	o-o-p	—	1200	—	—	Electromag.	Capacitive	(glucose solutions)	400x400	2009	[306]

Table 4.6: Resonant MEMS devices for viscosity and mass density sensing. o-o-p: out-of-plane, L-F: Lorentz force, L: length, W: width, T: thickness, CL: cantilever, i-p: in-plane, D: diameter

Chapter 5

Summary, conclusions and outlook

In this thesis, the interaction of electrically actuated and read-out, mechanical resonators with viscous liquids was investigated with respect to viscosity and mass density measuring applications. Such mechanical, resonant sensors can furthermore be used for in-line, in-situ and hand-held devices at operational frequencies from approximately 100 Hz to 100 kHz. This frequency range is not yet covered by state of the art instruments, but represents an interesting frequency range from a rheological point of view. An extensive literature review showed that many different device designs and approaches for such sensors have already been published in literature prior to this work. Questions which arose from this review included the possibility of measuring viscosity and mass density with a single device, optimum device designs and materials for high measurement accuracies, required stabilities of the resonance frequency and quality factor and an estimate for achievable accuracies for viscosity and mass density measurements. To address these requirements, the frequency responses of immersed, mechanical resonators interacting with sample liquids were investigated.

The applied examination methods were dominated by experimental approaches. However, a broad study and elaboration of the underlying theory of structural and fluid mechanics as well as electrodynamics was undertaken to consolidate these disciplines in order to allow closed form modeling of observed effects and findings. A generalized model relating resonance frequency and quality factor of an immersed mechanical resonator with the liquid's viscosity and mass density could be formulated. This model was extended to consider the mechanical resonator's intrinsic cross-sensitivity to temperature. Nine resonators were manufactured and successively investigated, improving not only handling but even more important, measurement accuracy. The major conclusions and insights gained by the above mentioned approaches and investigation methods were:

1. The **separability of viscosity and mass density** was shown for several resonator designs, see Sec. 2.8.2. If the sensitivity matrix in Eq. 2.139 is invertible, or in other words, if the sensitivities of f_r and Q to η and ρ are different, both, viscosity and mass density can be determined with a single device. In general, this is the case for resonators whose fluid-structure interactions do not yield pure shear waves only.

2. An important issue for measurement stability and accuracy is **clamping**. It was shown that singly clamped devices yield much higher stability of their resonance frequency than doubly clamped devices. This can be exemplified by considering the difference between e.g. reed based or string instruments. The latter have to be frequently tuned, where the resonance frequency of the first does not significantly change. Furthermore, doubly clamped devices are prone to varying mechanical stresses, which are induced, e.g., by thermal changes or strains due to simply touching the resonator's housing while handling with the latter.

3. It was shown that tuning forks are well suited **types of resonators** for viscosity and mass density sensing. Due to their balanced resonator design, their dependency of resonance characteristics to (varying) clamping conditions is low. This becomes especially important when aiming for handheld devices.

4. The investigation of different **resonator materials** showed that the usage of tungsten yielded the best results for Lorentz-force driven resonators. In case of U-shaped tungsten wire resonators, the lowest cross-sensitivities to temperature, see also Tab. 5.1, were obtained. If lower cross-sensitivities become important, temperature compensated resonators represent an interesting

and considerable alternative, see e.g., [311,312]. Furthermore, the high mass density of tungsten ($19.3\,\mathrm{g/cm^3}$, [214]) is beneficial for distinct resonances in liquids.

5. Aiming for an accuracy of 1 % in viscosity and $1\,\mathrm{mg/cm^3}$ for mass density implies **required relative stabilities** in the order of 10^{-5} for resonance frequency and 10^{-3} for the quality factor, see Sec. 2.8.2.

6. Claiming the above mentioned accuracies for viscosity and mass density requires an **a temperature measurement accuracy** of at least $0.5\,^{\circ}\mathrm{C}$ for the investigated steel tuning forks.

7. The usage steel tuning forks showed that with mechanical resonators for viscosity and mass density sensing **accuracies** in the order of 1 % in viscosity and 0.01 % in mass density (i.e. an accuracy of $0.1\,\mathrm{mg/cm^3}$ for aqueous liquids) can be obtained. This lies within in the accuracy range of commercially available laboratory instruments.

5.1 Theoretical approach and insights

Assuming that volumetric forces, the hydrostatic pressure gradient as well as the convective term in the Navier-Stokes equation 1.94 are negligible, i.e., $\boldsymbol{f} = 0$, $\nabla p_0 = 0$, $(\boldsymbol{v} \cdot \nabla)\boldsymbol{v} = 0$, the equation of motion of liquids obtains the same form as the equation of motion for acoustic waves in solids, i.e.,

$$-\rho\,\omega^2 \underline{\boldsymbol{u}} = \nabla \cdot (\boldsymbol{c} : \nabla_{\mathrm{s}}\, \underline{\boldsymbol{u}}) \tag{1.109}$$

in complex notation [179]. Using this notation for the equation of motion, the elasticity tensor $\boldsymbol{c}$ can be formulated for linear elastic solids as well as for liquids. For incompressible liquids which were considered in this thesis, the elasticity tensor reads $\boldsymbol{c} = \mathrm{j}\,\omega\,\mathrm{diag}(2\,\eta,\, 2\,\eta,\, 2\,\eta,\, \eta,\, \eta,\, \eta)$, where diag(.) designates a diagonal matrix [MHbcc1].

Describing the immersed resonator's frequency response of a characteristic resonating mode using a mechanical, lumped element oscillator and considering the fluid forces on transversally oscillating plates, spheres and cylinders, generalized equations for the immersed resonators' resonance frequency and quality factor could be formulated. These equations read

$$\frac{1}{\omega_0^2} \approx m_{0\mathrm{k}} + m_{\rho\mathrm{k}}\,\rho + m_{\eta\rho\mathrm{k}} \sqrt{\frac{\eta\,\rho}{\omega_0}}, \qquad \text{as well as} \tag{2.135}$$

$$\frac{1}{Q} \approx \frac{c_{0\mathrm{k}} + c_{\eta\mathrm{k}}\,\eta + c_{\eta\rho\mathrm{k}} \sqrt{\omega_0\,\eta\,\rho}}{\sqrt{m_{0\mathrm{k}} + m_{\rho\mathrm{k}}\,\rho + m_{\eta\rho\mathrm{k}} \sqrt{\frac{\eta\rho}{\omega_0}}}}$$

and have been successively applied to a variety of different resonator designs. The parameters $m_{0\mathrm{k}}$, $m_{\rho\mathrm{k}}$, $m_{\eta\rho\mathrm{k}}$, $c_{0\mathrm{k}}$, $c_{\eta\mathrm{k}}$, $c_{\eta\rho\mathrm{k}}$ can be determined, evaluating ω_0 and Q from measurements in at least three liquids with known viscosity and mass density values.

This model was extended by a temperature dependence of the resonance frequency, introducing a temperature parameter k_ϑ. This temperature dependent equation reads:

$$\omega_0(\vartheta) = \frac{1}{(\vartheta - 25\,^{\circ}\mathrm{C})\,k_\vartheta + 1} \cdot \frac{1}{\sqrt{m_{0\mathrm{k}} + m_{\rho\mathrm{k}}\,\rho + m_{\eta\rho\mathrm{k}} \sqrt{\frac{\eta\rho}{\omega_0}}}}. \tag{2.143}$$

For the quality factor, a clear temperature dependence could not be shown experimentally so far , and thus the temperature was not considered in the quality factor equation yet but will be investigated in future research.

A big advantage of using the generalized equations is that the sensor's sensitivities

$$S_{X,y_i} := \left| \frac{\partial X}{\partial y_i} \cdot \frac{y_i}{X} \right| \tag{2.138}$$

(X stands either for f_r or Q and y_i for η or ρ) easily can be evaluated allowing a further comparison of different sensor designs. A comparison of sensitivities of five different sensors given in Fig. 2.16 showed that the resonance frequency is much more sensitive to mass density than to viscosity whereas the sensitivity of the quality factor is similar for both, mass density and viscosity.

5.2 Experimental approach and insights

In this thesis, nine different mechanical resonator concepts were manufactured and examined. For some of these devices, only the basic operation principles were investigated but for more promising sensor designs, extensive measurement series have been performed. These experimental studies include the investigation of the resonators' responses to viscosity and mass density, the determination of their cross-sensitivities to temperature as well as the determination of the resonator's long-term stability.

An important achievement yielding revealing insights, was the usage of so-called viscosity and mass density series, allowing to separately investigate the effect of η and ρ on f_r and Q. For the acetone-isopropanol mixture used in this thesis as viscosity series, the variation of mass densities is to large ($\Delta\rho = 5.3\,\mathrm{mg/cm^3}$), to consider these mixtures as a liquid series with constant mass densities. However, as such liquid series are highly desirable, a study on modeling the temperature dependent viscosity and mass density of binary and ternary liquid mixtures was performed. Using theses models, the amount of each liquid, necessary to obtain a certain viscosity and mass density at a given temperature can be calculated.

The sensor concepts examined within this thesis were mainly actuated and read-out by means of Lorentz forces, as with this approach high excitation forces and read-out signals can be achieved. Furthermore, the performance of this actuation and read-out principle is not affected by the investigated liquid as it is e.g., the case for optical read-out for which transparent liquids are a fundamental requirement. Reluctance actuation in combination with electromagnetic pickups for read-out also yielded excellent results, however this method requires more complex measurement setups.

Experimental results showed that singly clamped devices yielded best results judging measuring accuracy and long-term stability. At the present stage of our research, the most promising designs are the U-shaped wire as well as the tuning fork sensors. These devices yielded good measurement accuracy and long-term stability as well as low cross-sensitivity to temperature.

Mechanical resonators can show a significant dependence of their resonance frequency to temperature. This dependence is mainly due to the thermal expansion of the resonator and the temperature dependence of the resonator's Young's modulus. For doubly clamped structures such as e.g. bridges [190,297] and straight wire resonators [6, 104], the cross-sensitivity of the resonance frequency to temperature becomes large, if significant thermal tensile stresses are induced into the vibrating part. The sensitivity of mechanical resonators can even become large enough, to be used as accurate temperature sensor, see e.g. [313] which is not desired for resonant viscosity and mass density sensors. The cross-sensitivity to temperature directly limits the sensor's accuracy and thus should be kept as low as possible. In Tab. 5.1 a comparison of the resonance frequency's dependence to temperature is given for different resonators. The first five sensors, i.e the U-shaped tungsten wire sensor, U (W), a U-shaped gold coated silicon resonator, U(Si, Au), a steel tuning fork, TF (steel), a silicon cantilever, CL (Si) and a gold coated silicon cantilever, CL (Si, Au) are singly clamped structures and thus show a relatively small dependence of the resonance frequency to temperature. The last four sensors i.e., the spiral spring sensor SS, the single plate sensor SP, the torsional resonator, TR, and a straight tungsten wire sensor, SW (W), are doubly clamped structures and thus, show a much higher dependence of the resonance frequency to temperature.

Sensor	f_0 kHz	$\Delta f_\mathrm{r}/\Delta T$ (Hz/K)	$\Delta^\mathrm{r} f_\mathrm{r}/\Delta T$ (1/K)	Ref.
U (W)	0.95	-0.048	$-60 \cdot 10^{-6}$	[MHj4]
U (Si, Au)	5.96	-0.441	$-69 \cdot 10^{-6}$	[314]
TF (Steel)	0.44	-0.0519	$-118 \cdot 10^{-6}$	[MHj2]
CL (Si)	43.83	-1.3	$-29.7 \cdot 10^{-6}$	[315]
CL (Si, Au)	18.33	-1.83	$-100 \cdot 10^{-6}$	[316]
SS	0.64	-0.093	$-145 \cdot 10^{-6}$	[MHc7]
SP	5.6	-1.2	$-214.29 \cdot 10^{-6}$	[MHc19]
TR	0.39	-0.15	$-385.58 \cdot 10^{-6}$	[MHj1]
SW (W)	2.98	30	0.01	[MHj5]

Table 5.1: Cross sensitivities of the resonance frequency (fundamental mode) to temperature. f_0: nominal resonance frequency, $\Delta f_\mathrm{r} = f_\mathrm{r}(T_0) - f_\mathrm{r}(T_1)$: resonance frequency shift, $\Delta T = T_0 - T_1$ difference of temperatures T_0 and T_1, $\Delta^\mathrm{r} f_\mathrm{r} = \Delta f_\mathrm{r}/f_0$: relative resonance frequency shift.

A literature review showed that the variety of resonant viscosity and mass density sensors is huge. These devices involve different resonator designs, the usage of different materials as well as different actuation and read-out methods. These diversities make the comparison of different sensors difficult and thus the following experimental investigation procedure is suggested:

1. Determination of f_r and Q in (at least) three different liquids and subsequent determination of the parameters of the generalized equations. The values for f_r and Q in air as well as the procedure how f_r and Q have been evaluated are also of high interest. The ambient temperature and associated viscosity and mass density values have to be given in any case. Using viscosity and mass density series are beneficial to experimentally show the sensors' dependencies to viscosity and mass density, respectively.

2. Determination of the resonator's f_r- and Q-cross-sensitivity to temperature.

3. Long-term measurements, i.e. continuous determination of f_r and Q under as stable as possible conditions over a long period of time (e.g., for 24 hours or longer). These measurements show the spread or noise of obtained values for f_r and Q and furthermore reveal the stability of the device. Especially doubly clamped devices might be subjected to internal stresses, which might relax over time which detunes the sensor's resonance frequency and thus limiting its accuracy.

Such a characterization process based on these three (or similar) experimental investigations gives a good insight of the particular sensor's characteristics and allows the comparison of different sensors.

The literature review of resonant MEMS devices for viscosity and mass density showed that, in most cases, the devices' cross-sensitivities of f_r and Q (e.g. to temperature) are not investigated. However, this investigation is extremely important, particularly if the sensor's resolution or accuracy is of interest. This statement is explained by the following example: In [305] a suspended silicon based microchannel resonator is reported. The device features a mass density resolution of $0.01\,\mathrm{kg/cm^3}$ with a sensitivity of $16\,\mathrm{Hz/(kg/m^3)}$, and operational frequencies of about 130 kHz. Taking the cross-sensitivity of the resonance frequencies to temperature of a bare silicon cantilever and a gold coated cantilever into account which are $\Delta f_\mathrm{r}/(f_\mathrm{r}\,\Delta T) \approx -30 \cdot 10^{-6}/\mathrm{K}$ [315] and $-100 \cdot 10^{-6}/\mathrm{K}$ [316] respectively, allows estimating the devices cross-sensitivity to temperature. In this particular case this would be $\Delta f_\mathrm{r}/\Delta T = -(3.9 \ldots 13)\,\mathrm{Hz/K}$. To achieve the aforementioned resolution for mass density, the accuracy of the temperature would have to be in the order of $(0.01 \ldots 0.04)\,\mathrm{K}$. This example substantiates the addressed need for precise temperature measurements and the characterization of the sensor's temperature dependence.

5.3 Outlook

5.3.1 Works in progress

The investigations performed in this thesis raised many questions. Some of these problems could already be answered but were not published yet. In the following, ongoing studies as well as topics which might be interesting for future research are listed and briefly discussed.

1. **Variants of the U-shaped wire**

   The U-shaped wire sensor presented in [MHj4] features a round tip. Three variants of this U-shaped wire sensor including a straight tip, a tip carrying a small platelet and a tip carrying a sphere have been fabricated, see Fig. 5.1. Measurement series in different liquids and temperatures have been performed [MHc2] and a theoretical investigation of these variants was already presented in [MHc16]. At present, these theoretical and experimental findings are compared and further investigated [MHwp7].

Figure 5.1: Variants of the U-shaped wire sensor

The tuning fork setups presented in [MHj2], allowed very precise measurements but suffered from an O-ring sealing that was dissolved by solvents such as ethanol. A possible way to overcome this drawback would be to replace the used O-ring by a chemically resistive O-ring. Two new measurement setups containing circular and rectangular tuning forks have been designed. These setups include an experimental well containing five steel tuning forks with circular cross-sections with the same diameter but different lengths and thus yielding different resonance frequencies. The setup with the rectangular tuning forks contains eight tuning forks with different aspect ratios but all resonating at 440 Hz in air at their fundamental mode. The tuning forks for both setups were already fabricated and Nickel-coated, see Fig. 5.2. The setups will be used to run, amongst others, measurements in viscosity and mass density series, temperature measurements in Viscosity standards from Cannon Instruments and long-term measurements. The results of these measurements and already developed models will provide the data for the following topics:

2. **Modeling of cross-senstivity to temperature** [MHwp6]

   In Sec. 2.10 the generalized equations have been extended to describe the resonance frequency's cross-sensitivity to temperature, see also Eq. 2.143. More precise measurements have to be performed to substantiate this equation and to investigate the quality factor's cross-sensitivity to temperature. The experiments should be performed using a precise temperature-controlled bath together with an precise thermometer for temperature control. Instruments, available at the Institut for Microelectronics and Microsensors which can be used for this task are the Julabo F32 temperature controlled bath and the Anton Paar MKT 50 thermometer. The accuracy of these instruments are $\pm 0.01\,^{\circ}\mathrm{C}$ for the water bath and $0.001\,^{\circ}\mathrm{C}$ for the thermometer. Furthermore, for these experiments, viscosity standards from Cannon Instruments should be used to eliminate any inaccuracies of the viscosity and mass density values which have to be known for investigating the resonator's intrinsic cross-sensitivity to temperature.

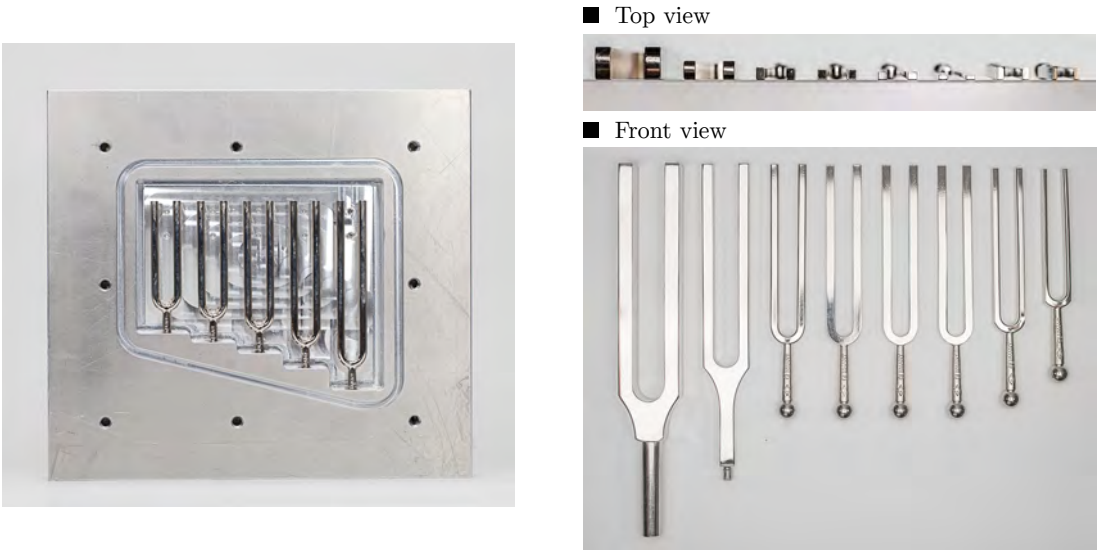

(a) Circular tuning forks (b) Rectangular tuning forks

Figure 5.2: Circular and rectangular tuning fork setups

3. **Higher mode excitation** [MHwp5]

   In Sec. 2.9 higher mode excitation has already been discussed. Findings, which were already presented in [MHc4] have to be substantiated and approved. For this, measurements at higher modes obtained with the circular and rectangular tuning fork setups and the U-shaped wire and its variants have to be evaluated and compared with elaborated models.

4. **Scaling and miniaturization** [MHwp4]

   Scaling the resonators' dimensions, changes their sensitivity to viscosity and mass density. Experimental results for scaling the U-shaped wire sensor have already been presented in [MHc15]. As the new tuning fork setups provide 13 tuning forks with different geometries, the measurements obtained with these devices will give insights concerning the dependence of the sensors' sensitivities on their aspect ratios and sizes.

5. **Aspect ratio of rectangular resonators and error propagation** [MHwp3]

   Different aspect ratios of the mechanical resonators interacting with the sample liquids yield different sensitivities to viscosity and mass density. If viscosity and mass density are to be measured with a single device these sensitivities to viscosity and mass density have to be different to be able to separate both quantities. For example, for an ideal shear oscillating plate yielding shear wave propagation in the liquid only, viscosity and mass density can not be separated from a single measurement. However, as it was already shown for resonators with finite thicknesses, viscosity and mass density can be separated. The ability of separating these two quantities and the accuracy of determined viscosities and mass densities will depend on the aspect ratio of the resonator's cross-section. Furthermore, the effect of error propagation, i.e. the effect of inaccurate f_r and Q measurements on the accuracy of η and ρ has to be investigated. To study these problems, the setup containing eight rectangular tuning forks with different aspect ratios will provide sufficient data.

6. **Experimental investigation of the validity of existing models** [MHwp2]

   In [193] the hydrodynamic function for a transversally oscillating cylinder has been extended by a correction function to model the hydrodynamic function of a transversally oscillating prism with rectangular cross-section. It is claimed that the obtained expression is accurate to within

0.1 % over the range of Reynold's numbers of Re $\in [10^{-6}, 10^{4}]$. Using the setup with the eight rectangular tuning forks Reynold's numbers in the range of Re $\in [10^{6}, 10^{8}]$ will be obtained. These measurement results will give a good basis for comparing theoretical with experimental results as well as extending the Reynolds number range for the hydrodynamic function.

In the course of this thesis, studies about other principles for mass density and viscosity measurements have been started. These concepts comprise:

7. **Glass-U-tube with evaporated metal for excitation, read-out and temperature measurements** [MHwp1]

   In [MHc18] a stainless steel U-shaped tube was used as mass density sensor. To reduce the cross-sensitivity to temperature of such U-shaped tube devices, glass tubes can be used, see Fig. 5.3. These glass tubes will be coated with conductive layers to be excited and read-out by means of Lorentz forces which will be an alternative of existing U-tube mass density sensor principles [317]. Analogous to the idea of the measurement cell presented in [MHc18] the advantage of using an additional mass density sensor to increase the accuracy of viscosity measurements should be investigated.

Figure 5.3: Glass U-tubes

8. **Falling ball viscometer with differential transformers for read-out** [MHwp8]

   Falling ball viscometers are still frequently used in laboratories. However, handling with these instruments is time consuming and usually, the time required for the ball to fall a certain length is measured at two positions along the tube. As an alternative to such instruments, a falling ball viscometer has been manufactured using differential transformers along the entire falling length for measuring the ball's speed. The design of the device is intended for automated use e.g. in a by-pass of a production line. The ball is lifted automatically after each descent.

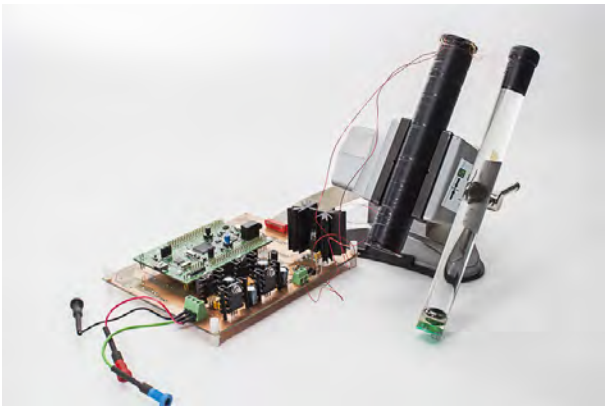

Figure 5.4: Falling ball viscometer

9. **Syringe viscometer** [MHwp9]

   A new concept for hand-held viscosimetry is the syringe viscometer. This viscometer consists of a syringe whose piston carries a pressure sensor, see Fig. 5.5. During filling or discharging the syringe, the piston's velocity and the pressure in the syringe are recorded. These recorded values are related to the liquid's viscosity.

Figure 5.5: Syringe viscometer

5.3.2 Future research

The investigation of the above topics are currently in progress. Ideas for theoretical and experimental studies which could be elaborated in future research are:

1. **Spurious negative coefficients in the generalized model**

   Fitting the model parameters of the generalized model with measurement data of our own work or data found in literature yielded negative coefficients in some cases. From a physical point of view, negative modeling coefficients are not possible, c.f. Tab. 2.2. It was found, that negative coefficients can result from resonators featuring unstable resonance frequencies. However, these spurious, negative coefficients have to be further investigated.

2. **Limits of describing a liquid loaded resonator with a second order system**

   A short discussion of the limits of describing a liquid loaded resonator's frequency response using a linear, second order resonator was given in Sec. 2.11.3. These theoretical findings have to be further investigated and approved by experimental results.

3. **Cross-sensitivity to ambient pressure**

   Viscosity is not only temperature but also pressure dependent [81]. Compared to conventional devices, a large benefit of liquid loaded resonators used for viscosity and mass density sensing might be their relatively good applicability for measurements at elevated pressures. However, for this task, the cross sensitivities to the ambient pressure of mechanical resonators have to be analyzed first.

4. **Examination of viscoelastic liquids**

   One of the many arguments for resonant viscosity and mass density sensors is to extend the frequency range of conventional rheometers for the characterization of viscoelastic liquids. The applicability of these devices for the characterization of viscoelasticity should be investigated in future research.

5. **Investigation of mixing laws for gasses**

   Based on the insights obtained by the research done in the course of this thesis for liquid mixtures, the accuracy of the mixing laws for gasses can be investigated. As resonant sensors are also used to measure the mass density and the viscosity of gasses, these devices can be used to investigate possible limits of the mixing laws for gases.

6. **Comparison of steel tuning forks with tuning forks made of tungsten and silicon**

   The investigation of steel tuning forks for viscosity and mass density measurements showed very promising results, [MHj2]. However, using tungsten or silicon as material for such tuning forks would reduce the cross-sensitivity to temperature and thus, such devices would be highly desirable. Using these materials however, would not allow reluctance actuation and read-out. Thus appropriate actuation and read-out principles for non-ferromagnetic tuning forks have to be elaborated.

7. **Lorentz-Force driven tungsten tuning fork**

   Similar to the U-shaped wire resonator, two U-shaped wires could be used to build tuning fork-similar devices yielding mechanically balanced resonators. The advantage of such balanced resonators is that they do not require high counterweights for stable resonance frequencies.

8. **Semi exposed tungsten-tuning fork**

   It was shown that liquid loaded resonators are strongly damped by the sample liquid and thus, could only be used for liquids with viscosities lower than 100 mPa·s approximately. A possible approach allowing the investigation of higher viscosities would be the usage of a tuning fork, of which only one of both prongs is exposed to the sample liquid, e.g. by putting one of both prongs in a tube. This approach would furthermore allow optical read-out, independent of the transparency of the sample liquid as one prong is not exposed to the latter.

9. **Spiral spring resonator using a Halbach array for the external magnetic field**

   The spiral spring sensor presented in [MHc7] suffered from unreliable clamping, yielding unstable resonance frequencies. However such a device is especially interesting as it shows low cross-sensitivites to temperature. A more reliable setup using a Halbach array yielding high output signals would be an interesting device.

10. **Long-term measurements for single plate resonator, U-shaped wire, and tuning fork in single measurement cell**

    The single plate resonator, the U-shaped wire sensor as well as tuning fork setups were the most investigated sensors during the last years on the Institute for Microelectronics and Microsensors. However the benefits and disadvantages of each device compared with the others are not exactly known yet. For this purpose, a measuring cell containing all three types of sensors would be desirable for investigating these devices under the same physical conditions. Such a setup would allow reliable comparison of these devices.

11. **Droplet on a tuning fork's tip**

    The single plate resonator was used not only upon complete immersion but also only putting a

droplet on the plate, see e.g. [MHcc7]. As tuning fork setups can be used for providing stable resonators, it might be beneficial to replace the single plate resonator by a tuning fork with a platelet put at a prong's end on which the droplet could be placed. A further advantage of using tuning fork instead of single plate resonators is that the sensitivity easily can be set by using tuning forks with different cross-sections.

12. **Droplet between two tuning forks' tips**

    Another very interesting application of single plate resonators is using two platelets placed on top of each other but with a certain distance between both plates [MHcc3]. A droplet is put between both plates, such that both plates get wetted. The lower plate is excited to lateral vibrations and due to the hydrodynamical coupling, these vibrations excite vibration of the upper plate which is used for read-out. This technique is especially beneficial for high viscous liquids. Similar to the previous idea, an investigation of replacing the single platelet resonators by tuning forks is an interesting topic.

Bibliography

[1] E. K. Reichel, M. Heinisch, B. Jakoby, Chapter 17, fluid property sensors in, resonant mems: Principles, modeling, implementation, and applications, Wiley, Editors: O. Brand, I. Dufour, S. Heinrich, F. Josse, J.G. Korvnik and O. Tabata (2015) 427–446.

[2] M. Heinisch, T. Voglhuber-Brunnmaier, E. Reichel, I. Dufour, B. Jakoby, Electromagnetically driven torsional resonators for viscosity and mass density sensing applications, Sensors and Actuators A: Physical.

[3] M. Heinisch, T. Voglhuber-Brunnmaier, E. Reichel, I. Dufour, B. Jakoby, Application of resonant steel tuning forks with circular and rectangular cross sections for precise mass density and viscosity measurements, Sensors and Actuators A: Physical 226 (2015) 163–174.

[4] M. Heinisch, T. Voglhuber-Brunnmaier, E. K. Reichel, I. Dufour, B. Jakoby, Reduced order models for resonant viscosity and mass density sensors, Sens. Actuators A: Physical 220 (2014) 76–84.

[5] M. Heinisch, E. K. Reichel, I. Dufour, B. Jakoby, A u-shaped wire for viscosity and mass density sensing, Sens. Actuators A: Phys. 214 (2014) 245–251.

[6] M. Heinisch, E. K. Reichel, I. Dufour, B. Jakoby, Tunable resonators in the low khz range for viscosity sensing, Sensors and Actuators A: Physical 186 (2012) 111–117. doi:http://dx.doi.org/10.1016/j.sna.2012.03.009.

[7] M. Heinisch, E. K. Reichel, I. Dufour, B. Jakoby, A resonating rheometer using two polymer membranes for measuring liquid viscosity and mass density, Sensors and Actuators A: Physical 172 (1) (2011) 82–87. doi:10.1016/j.sna.2011.02.031.

[8] A. Abdallah, E. K. Reichel, T. Voglhuber-Brunmaier, M. Heinisch, S. Clara, B. Jakoby, Symmetric mechanical plate resonators for fluid sensing, Sensors and Actuators A: Physical.

[9] A. Abdallah, M. Heinisch, B. Jakoby, Measurement error estimation and quality factor improvement of an electrodynamic-acoustic resonator sensor for viscosity measurement, Sensors and Actuators A: Physical 199 (2013) 318–324.

[10] E. Lemaire, M. Heinisch, B. Caillard, B. Jakoby, I. Dufour, Comparison and experimental validation of two potential resonant viscosity sensors in the kilohertz range, Measurement Science and Technology 24 (8) (2013) 084005.

[11] T. Voglhuber-Brunnmaier, M. Heinisch, E. K. Reichel, B. Weiss, B. Jakoby, Derivation of reduced order models from complex flow fields determined by semi-numeric spectral domain models, Sensors and Actuators A: Physical 202 (2013) 44–51.

[12] B. Weiss, M. Heinisch, E. Reichel, B. Jakoby, Driving modes and material stability of a double membrane rheometer and density sensor, J. Sens. Sens. Syst. 2 (2013) 19–26.

[13] T. Lederer, Thomas, M. Heinisch, W. Hilber, B. Jakoby, Electromagnetically actuated membrane-based micropumps with integrated magnetic yoke, Journal of microelectronics and electronic packaging 6 (4) (2009) 205–210.

[14] M. Heinisch, T. Voglhuber-Brunnmaier, E. K. Reichel, I. Dufour, B. Jakoby, Separate experimental investigation of the influence of liquids' mass densities and viscosities on the frequency response of resonant sensors using designated liquid series, Proc. IEEE Sensors 2015, Accepted Manuscript.

[15] M. Heinisch, T. Voglhuber-Brunnmaier, E. K. Reichel, A. Abdallah, S. Clara, I. Dufour, B. Jakoby, U-shaped wire based resonators for mass density and viscosity sensing, Proc. IEEE Sensors 2015, Accepted Manuscript.

[16] M. Heinisch, T. Voglhuber-Brunnmaier, E. Reichel, I. Dufour, B. Jakoby, Introduction of a general model for the resonance parameters of fluid sensors and validation with recent sensor setups, in: IEEE Sensors 2014, 2014, pp. 4–pages.

[17] M. Heinisch, E. Reichel, T. Voglhuber-Brunnmaier, I. Dufour, B. Jakoby, Investigation of higher mode excitation of resonant mass density and viscosity sensors, in: IEEE Sensors 2014, 2014, pp. 4–pages.

[18] M. Heinisch, A. O. Niedermayer, I. Dufour, B. Jakoby, Concept studies of torsional resonators for viscosity and mass density sensing applications, Procedia Engineering 87 (2014) 1198–1201.

[19] M. Heinisch, A. Abdallah, I. Dufour, B. Jakoby, Resonant steel tuning forks for precise inline viscosity and mass density measurements in harsh environments, Procedia Engineering 87 (2014) 1139–1142.

[20] M. Heinisch, S. Clara, I. Dufour, B. Jakoby, A spiral spring resonator for mass density and viscosity measurements, Procedia Engineering 87 (2014) 1143–1146.

[21] M. Heinisch, E. K. Reichel, I. Dufour, B. Jakoby, Modeling and experimental investigation of resonant viscosity and mass density sensors considering their cross-sensitivity to temperature, Procedia Engineering 87 (2014) 472–475.

[22] M. Heinisch, T. Voglhuber-Brunnmaier, I. Dufour, B. Jakoby, Validity of describing resonant viscosity and mass density sensors by linear 2nd order resonators, Proc. Eurosensors XXVIII (2014).

[23] M. Heinisch, T. Voglhuber-Brunnmaier, E. K. Reichel, S. Clara, A. Abdallah, B. Jakoby, Concept study on an electrodynamically driven and read-out torsional oscillator, Proceedings Microelectronic Systems Symposium (2014).

[24] M. Heinisch, T. Voglhuber-Brunnmaier, E. K. Reichel, B. Jakoby, Modeling approaches for electrodynamically driven viscosity and mass density sensors operated in the khz range and experimental verifications, in: SENSORS, 2013 IEEE, IEEE, 2013, pp. 1–4.

[25] M. Heinisch, T. Voglhuber-Brunnmaier, E. K. Reichel, B. Jakoby, Experimental and theoretical evaluation of the achievable accuracies of resonating viscosity and mass density sensors, in: SENSORS, 2013 IEEE, IEEE, 2013, pp. 1–4.

[26] M. Heinisch, E. K. Reichel, T. Voglhuber-Brunnmaier, B. Jakoby, Characterization and calibration of u-shaped mass density and viscosity sensors by an analytical modeling approach, The 17th International Conference on Solid-State Sensors, Actuators and Microsystems (2013) 1448 –1 1451.

[27] M. Heinisch, E. K. Reichel, T. Voglhuber-Brunnmaier, B. Jakoby, U-shaped, wire-based oscillators for rheological applications bridging the gap between 100 hz and 100 khz, The 17th International Conference on Solid-State Sensors, Actuators and Microsystems.

[28] M. Heinisch, E. Reichel, T. Voglhuber-Brunnmaier, W. Hortschitz, M. Stifter, J. Schalko, E. Lemaire, I. Dufour, B. Jakoby, Wire based and micromachined u-shaped cantilever devices for viscosity and mass density sensing for measurements in a frequency range of 100 hz to 100 khz, in: 10th International Workshop on Nanomechanical Cantilever Sensors, 2013, pp. 2–pages.

[29] M. Heinisch, E. K. Reichel, B. Jakoby, U-shaped wire based resonators for viscosity and mass density sensing, Proc. of. SENSOR 2013 OPTO 2013 IRS2 2013.

[30] M. Heinisch, E. Lemaire, B. Caillard, I. Dufour, B. Jakoby, A study of wire-based resonators for viscosity sensing, Proceedings Microfluidics 2012.

[31] M. Heinisch, E. K. Reichel, T. Voglhuber-Brunnmaier, B. Jakoby, Miniaturized viscosity and mass density sensors combined in a measuring cell for handheld applications, in: Proceedings of the IEEE Sensors conference 2012, 2012.

[32] M. Heinisch, A. Abdallah, B. Jakoby, The effect of temperature on resonant viscosity sensors, Procedia Engineering 47 (2012) 786–790.

[33] M. Heinisch, A. Abdallah, E. K. Reichel, B. Weiss, B. Jakoby, Concepts for lorentz force driven resonators for inline and handheld viscosimetry, Proceedings of the 13th Mechatronics Forum International Conference (2012) 632 – 638.

[34] M. Heinisch, T. Voglhuber-Brunnmaier, A. Abdallah, B. Jakoby, Application of resonant sensors for magnetic flux density measurements, Proceedings I2MTC conference.

[35] M. Heinisch, E. K. Reichel, I. Dufour, B. Jakoby, Tunable miniaturized viscosity sensors operating in the khz-range, in: Proceedings of the IEEE Sensors conference 2011, 2011.

[36] M. Heinisch, E. K. Reichel, I. Dufour, B. Jakoby, Miniaturized resonating viscometers facilitating measurements at tunable frequencies in the low khz-range, in: Proc. Eurosensors, 2011.

[37] M. Heinisch, E. K. Reichel, B. Jakoby, A suspended plate in-plane resonator for rheological measurements at tunable frequencies, in: Proc. Sensor + Test, 2011, pp. 61– 66.

[38] M. Heinisch, E. K. Reichel, B. Jakoby, A study on tunable resonators for rheological measurements, in: Proc. SPIE, Vol. 8066, 2011. doi:10.1117/12.887103.

[39] M. Heinisch, E. K. Reichel, B. Jakoby, A feasibility study on tunable resonators for rheological measurements, in: Proceedings GMe Forum, 2011, pp. 85–89.

[40] M. Heinisch, E. K. Reichel, B. Jakoby, On the modelling of resonant fluid sensors, Springer LNCS (2011) 25–32.

[41] M. Heinisch, E. K. Reichel, B. Jakoby, A comprehensive study and optimization of nozzle-diffuser valves for reciprocating micropumps, Proceedings of the 2nd European Conference on Microfluidics.

[42] M. Heinisch, T. Voglhuber-Brunnmaier, A. Niedermayer, B. Jakoby, E. K. Reichel, Double membrane sensors for liquid viscosity and mass density facilitating measurements in a large frequency range, in: Sensors, 2010 IEEE, IEEE, 2010, pp. 1750–1753.

[43] M. Heinisch, E. Reichel, T. Voglhuber-Brunnmaier, B. Jakoby, A double membrane sensor for liquid viscosity facilitating measurements in a large frequency range, Procedia Engineering 5 (2010) 1458–1461.

[44] M. Heinisch, E. K. Reichel, B. Jakoby, Electromagnetically actuated valveless micropump in polymer-technology, The 12th Mechatronics Forum Biennial International Conference Proceedings Book 2/2 (2010) 360 – 367.

[45] A. Abdallah, E. Reichel, S. Clara, M. Heinisch, B. Jakoby, Tuning fork based electrodynamically actuated resonating-plate viscosity sensor, in: Proceedings Microelectronics System Symposium, Vienna, 2014.

[46] A. Abdallah, E. Reichel, M. Heinisch, S. Clara, B. Jakoby, Symmetric plate resonators for viscosity and density measurement, Procedia Engineering 87 (2014) 36–39.

[47] A. Abdallah, E. K. Reichel, M. Heinisch, B. Jakoby, T. Voglhuber-Brunnmaier, Parallel plates shear-wave transducers for the characterization of viscous and viscoelastic fluids, SENSORS, 2014 IEEE (2014) 245–248.

[48] E. Reichel, A. Abdallah, T. Voglhuber-Brunnmaier, M. Heinisch, B. Jakoby, Parallel plate resonators for shear-wave rheometry of viscoelastic fluids, German Rheological Society (Eds.): AERC.

[49] E. K. Reichel, M. Heinisch, B. Jakoby, T. Voglhuber-Brunnmaier, Efficient numerical modeling of oscillatory fluid-structure interaction, sensors 9 10.

[50] T. Voglhuber-Brunnmaier, M. Heinisch, A. O. Niedermayer, A. Abdallah, R. Beigelbeck, B. Jakoby, Optimal parameter estimation method for different types of resonant liquid sensors, Procedia Engineering 87 (2014) 1581–1584.

[51] E. K. Reichel, M. Heinisch, B. Jakoby, Droplet mixing and liquid property tracking using an electrodynamic plate resonator, in: SENSORS, 2013 IEEE, IEEE, 2013, pp. 1–4.

[52] E. K. Reichel, M. Heinisch, B. Jakoby, Resonator sensors for rheological properties-theory and devices.

[53] E. K. Reichel, M. Heinisch, A. Vananroye, J. Vermant, B. Jakoby, Rheometry using shear-wave resonators, Belgian Group of Rheology (Eds.): AERC 2013, Series Annual European Rheology Conference (2013) 73.

[54] E. K. Reichel, M. Heinisch, J. Vermant, C. E. A. Kirschhock, B. Jakoby, Acoustic streaming in sessile droplets driven by in-plane actuation, Proc. of the Nanomechanical Sensing Workshop (2013) 2.

[55] A. Abdallah, M. Heinisch, B. Jakoby, Viscosity measurement cell utilizing electrodynamic-acoustic resonator sensors: Design considerations and issues, Procedia Engineering 47 (2012) 160–164.

[56] A. Abdallah, M. Heinisch, F. Lucklum, A. O. Niedermayer, B. Jakoby, A viscosity sensor utilizing electrodynamic-acoustic resonators, Informationstagung Mikroelektronik12 OVE (64) (2012) 103.

[57] A. Abdallah, M. Heinisch, F. Lucklum, A. O. Niedermayer, B. Jakoby, A viscosity measurement unit utilizing an electrodynamic-acoustic resonator, The 13th Mechatronics Forum International Conference Proceedings 2 (2012) 621.

[58] A. Abdallah, F. Lucklum, M. Heinisch, A. Niedermayer, B. Jakoby, Viscosity measurement cell utilizing electrodynamic-acoustic resonator sensors: Issues and improvements, Proceedings I2MTC conference 2012.

[59] E. Lemaire, M. Heinisch, B. Caillard, B. Jakoby, I. Dufour, Fluid characterization using a vibrating microstructure - the future (micro)rheology?, The 13th Mechatronics Forum International Conference Proceedings.

[60] E. K. Reichel, M. Heinisch, B. Jakoby, J. Vermant, C. Kirschhock, Modeling and data analysis of a multimode resonator sensor loaded with viscous and viscoelastic fluids, in: Sensors, 2012 IEEE, IEEE, 2012, pp. 1–4.

[61] T. Voglhuber-Brunnmaier, M. Heinisch, E. Reichel, B. Weiss, B. Jakoby, Complete semi-numeric model of a double membrane liquid sensor for density and viscosity measurements, Procedia Engineering 47 (2012) 598–602.

[62] E. K. Reichel, M. Heinisch, B. Jakoby, J. Vermant, C. E. Kirschhock, Viscoelasticity sensor with resonance tuning and low-cost interface, Procedia Engineering 25 (2011) 623–626.

[63] B. Weiss, M. Heinisch, B. Jakoby, E. K. Reichel, Density sensitive driving mode of a double membrane viscometer, in: Sensors, 2011 IEEE, IEEE, 2011, pp. 1538–1541.

[64] B. Weiss, M. Heinisch, E. Reichel, B. Jakoby, Driving modes and material stability of a vibrating polyethylene membrane viscosity sensor, Procedia Engineering 25 (2011) 176–179.

[65] T. Lederer, M. Heinisch, W. Hilber, B. Jakoby, Electromagnetic membrane-pump with an integrated magnetic yoke, in: Sensors, 2009 IEEE, IEEE, 2009, pp. 532–537.

[66] L. Lederer, M. Heinisch, W. Hilber, B. Jakoby, Electromagnetic membrane-pumps with integrated mangetic yoke, Proc. Internationales Forum für Mechatronik.

[67] M. Heinisch, Lorentz force driven and read out glass tubes for mass density measurements, Work in Progress.

[68] M. Heinisch, Experimental investigation of the validity of existing models for viscously damped mechanical resonators with rectangular cross-sections, Work in Progress.

[69] M. Heinisch, Optimal aspect ratios of mechanical resonators with rectangular cross-sections for precise viscosity and mass density measurements, Work in Progress.

[70] M. Heinisch, Scaling of resonant viscosity and mass density sensors using resonant tuning forks as example, Work in Progress.

[71] M. Heinisch, Higher mode excitation of resonant viscosity and mass density sensors, Work in Progress.

[72] M. Heinisch, Cross-sensitivity of resonant viscosity and mass density sensors to temperature, Work in Progress.

[73] M. Heinisch, Theoretical and experimental investigation of u-shaped wire based resonators for mass density and viscosity sensing, Work in Progress.

[74] M. Heinisch, A falling ball viscosimeter using differential transformers for precise position measurements, Work in progress.

[75] M. Heinisch, A handheld capillary viscosimeter using pressure – velocity measurements in a convential syringe, Work in progress.

[76] M. Heinisch, Investigation of temperature models for the viscosity and mass densitity of liquids, Work in Progress.

[77] M. Heinisch, Modeling of the viscosity and mass densitity of binary liquid mixtures, considering their temperature dependence, Work in Progress.

[78] M. Heinisch, Modeling of the viscosity and mass densitity of ternary liquid mixtures, considering their temperature dependence, Work in Progress.

[79] M. Heinisch, Viscosity and mass densitity of the ternary liquid mixture acetone – ethanol – isopropanol in a temperature range from 5°C to 45°C, Work in Progress.

[80] M. Heinisch, Viscosity and mass densitity of the ternary liquid mixture ethanol – glycerol – water in a temperature range from 5°C to 45°C, Work in Progress.

[81] C. W. Macosko, Rheology, Principles, Measurements and Applications, Wiley- VCH, 1994.

[82] S. V. Gupta, Viscometry for Liquids, Calibration of Viscometers, Springer, 2014.

[83] D. S. Viswanath, T. K. Ghosh, D. H. L. Prasad, N. V. K. Dutt, K. Y. Rani, Viscosity of Liquids. Theory, Estimation, Experiment and Data, Springer, 2007.

[84] E. K. Reichel, Dynamic methods for viscosity and mass-density sensing, Trauner, 2012.

[85] A. Agoston, C. Ötsch, B. Jakoby, Viscosity sensors for engine oil condition monitoring – application and interpretation of results, Sensors and Actuators A 121 (2005) 327–332.

[86] R. Haskell, J. Taku, J. Steichen, B. Witham, Calibration of in-line acoustic wave viscosity sensors for measurement of printing inks, Proceedings SENSOR 2013 (2013) 592–597.

[87] P. Rust, D. Cereghetti, J. Dual, A micro-liter viscosity and density sensor for the rheological characterization of dna solutions in the kilo-hertz range, Lab Chip 13 (24) (2013) 4794–4799. doi:10.1039/C3LC50857A.

[88] S. Boskovic, J. W. M. Chon, P. Mulvaney, J. E. Sader, Rheological measurements using microcantilevers, Journal of Rheology 46 (4) (2002) 891–899.

[89] B. Jakoby, R. Beigelbeck, F. Keplinger, F. Lucklum, A. Niedermayer, E. K. Reichel, C. Riesch, T. Voglhuber-Brunnmaier, B. Weiss, Miniaturized sensors for the viscosity and density of liquids – performance and issues, IEEE transactions on ultrasonics, ferroelectrics, and frequency control 57 (1) (2010) 111–120. doi:10.1109/TUFFC.2010.1386.

[90] B. Jakoby, M. Vellekoop, Physical sensors for liquid properties, IEEE sensors journal 11 (12) (2011) 3076–3085.

[91] I. Dufour, A. Maali, Y. Amarouchene, et al., The microcantilever: A versatile tool for measuring the rheological properties of complex fluids, Journal of Sensors 2012. doi:10.1155/2012/719898.

[92] C. Riesch, A. Jachimowicz, F. Keplinger, E. K. Reichel, B. Jakoby, A novel sensor system for liquid properties based on a micromachined beam and a low-cost optical readout, Proceedings IEEE Sensors (2007) 872–875.

[93] L. Matsiev, J. Bennett, O. Kolosov, High precision tuning fork sensor for liquid property measurements, IEEE Ultrasonics Symposium (2005) 1492–1495.

[94] E. K. Reichel, C. Riesch, F. Keplinger, B. Jakoby, Modeling of the fluid-structure interaction in a fluidic sensor cell, Sensors and Actuators A: Physical 156 (1) (2009) 222–228.

[95] P. Peiker, E. Oesterschulze, Impact of the miniaturization on the response of a hybrid diaphragm resonator considering its finite support, Proc. of the Nanomechanical Sensing Workshop (2013) pp. 127–128.

[96] E. K. Reichel, C. Riesch, F. Keplinger, C. E. A. Kirschhock, B. Jakoby, Analysis and experimental verification of a metallic suspended plate resonator for viscosity sensing, Sensors and Actuators A: Physical 162 (2010) 418–424. doi:10.1016/j.sna.2010.02.017.

[97] S. J. Martin, V. E. Granstaff, G. C. Frye, Characterization of a quartz crystal microbalance with simultaneous mass and liquid loading, Anal. Chem. 63 (1991) 2272–2281.

[98] R. Thalhammer, S. Braun, B. Devcic-Kuhar, M. Gröschl, F. Trampler, E. Benes, H. Nowotny, M. Kostal, Viscosity sensor utilizing a piezoelectric thickness shear sandwich resonator, IEEE Trans. Ultrasonics Ferroel. Frequ. Contr. 45 (5) (1998) 1331–1340.

[99] E. K. Reichel, C. Riesch, B. Weiss, B. Jakoby, A vibrating membrane rheometer utilizing electromagnetic excitation, Sensors and Actuators A: Physical 145 (2008) 349–353.

[100] C. Castille, I. Dufour, C. Lucat, Longitudinal vibration mode of piezoelectric thick-film cantilever-based sensors in liquid media, Applied Physics Letters 96 (15) (2010) 154102. doi:10.1063/1.3387753.

[101] J. M. Goodwin, A vibrating wire viscometer for measurements at elevated pressures, Journal of Physics E: Scientific Instruments 6 (5) (1973) 452.

[102] M. J. Assael, C. P. Oliveira, M. Papadaki, W. A. Wakeham, Vibrating-wire viscometer for liquids at high pressures, International Journal of Thermophysics 13 (4) (1992) 593 –615.

[103] F. J. P. Caetano, J. M. N. A. Fareleira, C. M. B. P. Oliveira, W. A. Wakeham, Validation of a vibrating-wire viscometer: Measurements in the range of 0.5 to 135 mpa s, Journal of Chemical & Engineering Data 50 (1) (2005) 201–205.

[104] D. Seibt, Schwingdrahtviskosimeter mit integriertem ein-senkkörper-dichtemessverfahren für untersuchungen an gasen in größeren temperatur- und druckbereichen, Ph.D. thesis, Universität Rostock (2007).

[105] G. Dehestru, M. Leman, J. Jundt, P. Dryden, M. Sullivan, C. Harrison, A microfluidic vibrating wire viscometer for operation at high pressure and high temperature, Review of Scientific Instruments 82 (3) (2011) 035113.

[106] B. Jakoby, M. Vellekoop, Physical sensors for water-in-oil emulsions, Sensors and Actuators A: Physical 110 (1) (2004) 28–32.

[107] https://www.cannoninstrument.com/.

[108] M. Dizechi, E. Marschall, Viscosity of some binary and ternary liquid mixtures, Journal of Chemical and Engineering Data 27 (3) (358–363) 1982.

[109] M. Contreras S, Densities and viscosities of binary mixtures of 1, 4-dioxane with 1-propanol and 2-propanol at (25, 30, 35, and 40) c, Journal of Chemical & Engineering Data 46 (5) (2001) 1149–1152.

[110] D. Gómez-Díaz, J. C. Mejuto, J. M. Navaza, Physicochemical properties of liquid mixtures. 1. viscosity, density, surface tension and refractive index of cyclohexane+ 2, 2, 4-trimethylpentane binary liquid systems from 25 c to 50 c, Journal of Chemical & Engineering Data 46 (3) (2001) 720–724.

[111] J. George, N. V. Sastry, Densities, dynamic viscosities, speeds of sound, and relative permittivities for water+ alkanediols (propane-1, 2-and-1, 3-diol and butane-1, 2-,-1, 3-,-1, 4-, and-2, 3-diol) at different temperatures, Journal of Chemical & Engineering Data 48 (6) (2003) 1529–1539.

[112] J. George, N. V. Sastry, Densities, viscosities, speeds of sound, and relative permittivities for water+ cyclic amides (2-pyrrolidinone, 1-methyl-2-pyrrolidinone, and 1-vinyl-2-pyrrolidinone) at different temperatures, Journal of Chemical & Engineering Data 49 (2) (2004) 235–242.

[113] P. S. Nikam, S. J. Kharat, Densities, viscosities, and thermodynamic properties of (n, n-dimethylformamide+ benzene+ chlorobenzene) ternary mixtures at (298.15, 303.15, 308.15, and 313.15) k, Journal of Chemical & Engineering Data 48 (5) (2003) 1202–1207.

[114] P. S. Nikam, S. J. Kharat, Densities and viscosities of binary mixtures of n, n-dimethylformamide with benzyl alcohol and acetophenone at (298.15, 303.15, 308.15, and 313.15) k, Journal of Chemical & Engineering Data 48 (5) (2003) 1291–1295.

[115] V. Rattan, S. Kapoor, K. Tochigi, Viscosities and densities of binary mixtures of toluene with acetic acid and propionic acid at (293.15, 303.15, 313.15, and 323.15) k, Journal of Chemical & Engineering Data 47 (5) (2002) 1182–1184.

[116] U. Kapadi, D. Hundiwale, N. Patil, M. Lande, Viscosities, excess molar volume of binary mixtures of ethanolamine with water at 303.15, 308.15, 313.15 and 318.15 k, Fluid phase equilibria 201 (2) (2002) 335–341.

[117] U. Kapadi, D. Hundiwale, N. Patil, M. Lande, Effect of temperature on excess molar volumes and viscosities of binary mixtures of ethylenediamine and water, Fluid phase equilibria 205 (2) (2003) 267–274.

[118] C. Yang, P. Ma, F. Jing, D. Tang, Excess molar volumes, viscosities, and heat capacities for the mixtures of ethylene glycol+ water from 273.15 k to 353.15 k, Journal of Chemical & Engineering Data 48 (4) (2003) 836–840.

[119] E. Gómez, B. González, Á. Domínguez, E. Tojo, J. Tojo, Dynamic viscosities of a series of 1-alkyl-3-methylimidazolium chloride ionic liquids and their binary mixtures with water at several temperatures, Journal of Chemical & Engineering Data 51 (2) (2006) 696–701.

[120] H.-W. Chen, C.-C. Wen, C.-H. Tu, Excess molar volumes, viscosities, and refractive indexes for binary mixtures of 1-chlorobutane with four alcohols at t=(288.15, 298.15, and 308.15) k, Journal of Chemical & Engineering Data 49 (2) (2004) 347–351.

[121] N. Indraswati, Mudjijati, F. Wicaksana, H. Hindarso, S. Ismadji, Density and viscosity for a binary mixture of ethyl valerate and hexyl acetate with 1-pentanol and 1-hexanol at 293.15 k, 303.15 k, and 313.15 k, Journal of Chemical & Engineering Data 46 (1) (2001) 134–137.

[122] C. M. Kinart, W. J. Kinart, A. Cwiklinska, Density and viscosity at various temperatures for 2-methoxyethanol+ acetone mixtures, Journal of Chemical & Engineering Data 47 (1) (2002) 76–78.

[123] J. N. Nayak, M. I. Aralaguppi, T. M. Aminabhavi, Density, viscosity, refractive index, and speed of sound for the binary mixtures of ethyl chloroacetate with n-alkanes (c6 to c12) at (298.15, 303.15, and 308.15) k, Journal of Chemical & Engineering Data 46 (4) (2001) 891–896.

[124] J. N. Nayak, M. I. Aralaguppi, T. M. Aminabhavi, Density, viscosity, refractive index, and speed of sound in the binary mixtures of 1, 4-dioxane+ ethanediol,+ hexane,+ tributylamine, or+ triethylamine at (298.15, 303.15, and 308.15) k, Journal of Chemical & Engineering Data 48 (5) (2003) 1152–1156.

[125] J. N. Nayak, M. I. Aralaguppi, U. S. Toti, T. M. Aminabhavi, Density, viscosity, refractive index, and speed of sound in the binary mixtures of tri-n-butylamine+ triethylamine,+ tetrahydrofuran,+ tetradecane,+ tetrachloroethylene,+ pyridine, or+ trichloroethylene at (298.15, 303.15, and 308.15) k, Journal of Chemical & Engineering Data 48 (6) (2003) 1483–1488.

[126] J. N. Nayak, M. I. Aralaguppi, T. M. Aminabhavi, Density, viscosity, refractive index, and speed of sound in the binary mixtures of 1, 4-dioxane+ ethyl acetoacetate,+ diethyl oxalate,+ diethyl phthalate, or+ dioctyl phthalate at 298.15, 303.15, and 308.15 k, Journal of Chemical & Engineering Data 48 (6) (2003) 1489–1494.

[127] P. S. Nikam, T. R. Mahale, M. Hasan, Densities and viscosities for ethyl acetate+ pentan-1-ol,+ hexan-1-ol,+ 3, 5, 5-trimethylhexan-1-ol,+ heptan-1-ol,+ octan-1-ol, and+ decan-1-ol at (298.15, 303.15, and 308.15) k, Journal of Chemical & Engineering Data 43 (3) (1998) 436–440.

[128] A. Pal, R. K. Bhardwaj, Excess molar volumes and viscosities for binary mixtures of 2-propoxyethanol and of 2-isopropoxyethanol with propylamine and dipropylamine at (298.15, 308.15, and 318.15) k, Journal of Chemical & Engineering Data 46 (4) (2001) 933–938.

[129] U. Kapadi, D. Hundiwale, N. Patil, Thermodynamic interactions of 2, 3-butanediol with water, Fluid phase equilibria 208 (1) (2003) 91–98.

[130] B. González, A. Domínguez, J. Tojo, Dynamic viscosities, densities, and speed of sound and derived properties of the binary systems acetic acid with water, methanol, ethanol, ethyl acetate and methyl acetate at t=(293.15, 298.15, and 303.15) k at atmospheric pressure, Journal of Chemical & Engineering Data 49 (6) (2004) 1590–1596.

[131] B. Gonzalez, A. Domınguez, J. Tojo, Dynamic viscosities of 2-butanol with alkanes (c 8, c 10, and c 12) at several temperatures, The Journal of Chemical Thermodynamics 36 (4) (2004) 267–275.

[132] R. Rosal, I. Medina, E. Forster, J. MacInnes, Viscosities and densities for binary mixtures of cresols, Fluid phase equilibria 211 (2) (2003) 143–150.

[133] C.-H. Tu, H.-C. Ku, W.-F. Wang, Y.-T. Chou, Volumetric and viscometric properties of methanol, ethanol, propan-2-ol, and 2-methylpropan-2-ol with a synthetic c6+ mixture from 298.15 k to 318.15 k, Journal of Chemical & Engineering Data 46 (2) (2001) 317–321.

[134] E. Gómez, B. González, N. Calvar, E. Tojo, Á. Domínguez, Physical properties of pure 1-ethyl-3-methylimidazolium ethylsulfate and its binary mixtures with ethanol and water at several temperatures, Journal of Chemical & Engineering Data 51 (6) (2006) 2096–2102.

[135] B. Gonzalez, A. Dominguez, J. Tojo, Viscosities, densities and speeds of sound of the binary systems: 2-propanol with octane, or decane, or dodecane at t=(293.15, 298.15, and 303.15) k, The Journal of Chemical Thermodynamics 35 (6) (2003) 939–953.

[136] E. J. González, L. Alonso, Á. Domínguez, Physical properties of binary mixtures of the ionic liquid 1-methyl-3-octylimidazolium chloride with methanol, ethanol, and 1-propanol at t=(298.15, 313.15, and 328.15) k and at p= 0.1 mpa, Journal of Chemical & Engineering Data 51 (4) (2006) 1446–1452.

[137] B. González, N. Calvar, E. Gómez, Á. Domínguez, Density, dynamic viscosity, and derived properties of binary mixtures of methanol or ethanol with water, ethyl acetate, and methyl acetate at t=(293.15, 298.15, and 303.15) k, The Journal of Chemical Thermodynamics 39 (12) (2007) 1578–1588.

[138] E. J. González, B. González, N. Calvar, Á. Domínguez, Physical properties of binary mixtures of the ionic liquid 1-ethyl-3-methylimidazolium ethyl sulfate with several alcohols at t=(298.15, 313.15, and 328.15) k and atmospheric pressure, Journal of Chemical & Engineering Data 52 (5) (2007) 1641–1648.

[139] B. González, N. Calvar, Á. Domínguez, J. Tojo, Dynamic viscosities of binary mixtures of cycloalkanes with primary alcohols at t=(293.15, 298.15, and 303.15) k: New unifac-visco interaction parameters, The Journal of Chemical Thermodynamics 39 (2) (2007) 322–334.

[140] K. J. Laidler, The development of the arrhenius equation, Journal of Chemical Education 61 (6) (1984) 494.

[141] A. Brancker, Viscosity-temperature dependence., Nature 166 (4230) (1950) 905–906.

[142] J. De Guzman, Relation between fluidity and heat of fusion, Anales Soc. Espan. Fis. Y. Quim 11 (1913) 353–362.

[143] C. Duhne, Viscosity-temperature correlations for liquids, chemical engineering 86 (15) (1979) 83–91.

[144] D. S. Viswanath, G. Natavajan, Data book on the viscosity of liquids.

[145] I. Williamson, Viscosity-temperature dependence, Nature 167 (1951) 316–317.

[146] Z. Wang, L. Fu, H. Xu, Y. Shang, L. Zhang, J. Zhang, Density, viscosity, and conductivity for the binary systems of water+ dual amino-functionalized ionic liquids, Journal of Chemical & Engineering Data 57 (4) (2012) 1057–1063.

[147] U. Domańska, M. Zawadzki, A. Lewandrowska, Effect of temperature and composition on the density, viscosity, surface tension, and thermodynamic properties of binary mixtures of n-octylisoquinolinium bis {(trifluoromethyl) sulfonyl} imide with alcohols, The Journal of Chemical Thermodynamics 48 (2012) 101–111.

[148] L. Girifalco, Temperature dependence of viscosity and its relation to vapor pressure for associated liquids, The Journal of Chemical Physics 23 (12) (1955) 2446–2447.

[149] T. E. Thorpe, J. Rodger, R. Barnett, On the relations between the viscosity (internal friction) of liquids and their chemical nature. part ii, Philosophical Transactions of the Royal Society of London. Series A, Containing Papers of a Mathematical or Physical Character (1897) 71–107.

[150] R. C. Reid, J. M. Prausnitz, B. E. Poling, The properties of gases and liquids.

[151] C. L. Yaws, X. Lin, L. Bu, Calculate viscosities for 355 liquids, Chemical Engineering (New York);(United States) 101 (4).

[152] D. J. Kingham, W. Adams, M. McGuire, Viscosity measurements of water in region of its maximum density, Journal of Chemical and Engineering Data 19 (1) (1974) 1–3.

[153] G. S. Kell, Density, thermal expansivity, and compressibility of liquid water from 0. deg. to 150. deg.. correlations and tables for atmospheric pressure and saturation reviewed and expressed on 1968 temperature scale, Journal of Chemical and Engineering Data 20 (1) (1975) 97–105.

[154] D. Lide, W. Haynes, CRC handbook of chemistry and physics: a ready-reference book of chemical and physical data-/editor-in-chief, David R. Lide; ass. ed. WM" Mickey" Haunes, Boca Raton, Fla: CRC, 2009.

[155] J. Sengers, J. T. R. Watson, Improved international formulations for the viscosity and thermal conductivity of water substance, American Chemical Society and the American Institute of Physics for the National Bureau of Standards, 1986.

[156] S. Arrhenius, Über die Dissociation der in Wasser gelösten Stoffe, Verlag von Wilhelm Engelmann, 1887.

[157] L. Grunberg, A. H. Nissan, Mixture law for viscosity, Nature 164 (1949) 799–800.

[158] N.-S. Cheng, Formula for the viscosity of a glycerol-water mixture, Industrial & engineering chemistry research 47 (9) (2008) 3285–3288.

[159] A. Jouyban, A. Fathi-Azarbayjani, M. Khoubnasabjafari, Mathematical representation of the density of liquid mixtures at various temperatures using jouyban-acree model, INDIAN JOURNAL OF CHEMISTRY SECTION A 44 (8) (2005) 1553.

[160] A. Jouyban, J. Soleymani, F. Jafari, M. Khoubnasabjafari, W. E. Acree, Mathematical representation of viscosity of ionic liquid+ molecular solvent mixtures at various temperatures using the jouyban–acree model, Journal of Chemical & Engineering Data 58 (6) (2013) 1523–1528.

[161] S. Oswal, H. Desai, Studies of viscosity and excess molar volume of binary mixtures.: 1. propylamine+ 1-alkanol mixtures at 303.15 and 313.15 k, Fluid phase equilibria 149 (1) (1998) 359–376.

[162] S. Oswal, H. Desai, Studies of viscosity and excess molar volume of binary mixtures: 2. butylamine+ 1-alkanol mixtures at 303.15 and 313.15 k, Fluid phase equilibria 161 (1) (1999) 191–204.

[163] S. Oswal, H. Desai, Studies of viscosity and excess molar volume of binary mixtures: 3. 1-alkanol+ di-n-propylamine, and+ di-n-butylamine mixtures at 303.15 and 313.15 k, Fluid phase equilibria 186 (1) (2001) 81–102.

[164] W. E. Acree, Mathematical representation of thermodynamic properties: Part 2. derivation of the combined nearly ideal binary solvent (nibs)/redlich-kister mathematical representation from a two-body and three-body interactional mixing model, Thermochimica Acta 198 (1) (1992) 71–79.

[165] A. Jouyban, M. Khoubnasabjafari, Z. Vaez-Gharamaleki, Z. Fekari, W. E. J. Acree, Calculation of the viscosity of binary liquids at various temperatures using jouyban-acree model, Chemical and pharmaceutical bulletin 53 (5) (2005) 519–523.

[166] E. K. Chong, S. H. Zak, An introduction to optimization, 2nd Edition, John Wiley & Sons, 2001.

[167] J.-W. Lee, S.-B. Park, H. Lee, Densities, surface tensions, and refractive indices of the water+ 1, 3-propanediol system, Journal of Chemical & Engineering Data 45 (2) (2000) 166–168.

[168] E. Jimenez, M. Cabanas, L. Segade, S. Garcı a Garabal, H. Casas, Excess volume, changes of refractive index and surface tension of binary 1, 2-ethanediol+ 1-propanol or 1-butanol mixtures at several temperatures, Fluid phase equilibria 180 (1) (2001) 151–164.

[169] C. Tovar, E. Carballo, C. Cerdeiriña, J. Legido, L. Romaní, Effect of temperature on w-shaped excess molar heat capacities and volumetric properties: oxaalkane-nonane systems, International journal of thermophysics 18 (3) (1997) 761–777.

[170] O. Redlich, A. Kister, Algebraic representation of thermodynamic properties and the classification of solutions, Industrial & Engineering Chemistry 40 (2) (1948) 345–348.

[171] J. Tomiska, Mathematical conversions of the thermodynamic excess functions represented by the redlich-kister expansion, and by the chebyshev polynomial series to power series representations and vice-versa., Calphad 8 (4) (1984) 283–294.

[172] R. Kalidas, G. Laddha, Viscosity of ternary liquid mixtures., Journal of Chemical & Engineering Data.

[173] J. Pandey, S. Pandey, S. Gupta, A. Shukla, Viscosity of ternary liquid mixtures, Journal of solution chemistry 23 (9) (1994) 1049–1059.

[174] H.-C. Ku, C.-H. Tu, Densities and viscosities of binary and ternary mixtures of ethanol, 2-butanone, and 2, 2, 4-trimethylpentane at t=(298.15, 308.15, and 318.15) k, Journal of Chemical & Engineering Data 50 (2) (2005) 608–615.

[175] F. M. White, I. Corfield, Viscous fluid flow, Vol. 3, McGraw-Hill New York, 2006.

[176] D. J. Acheson, Elementary fluid dynamics, Oxford University Press, 1990.

[177] G. K. Batchelor, An introduction to fluid dynamics, Cambridge university press, 2000.

[178] L. D. Landau, E. M. Lifshitz, Fluid Mechanics, Butterworth-Heinemann, 1987.

[179] B. A. Auld, Acoustic fields and waves in solids, Vol. I, Wiley, 1973.

[180] R. Beigelbeck, B. Jakoby, A two-dimensional analysis of spurious compressional wave excitation by thickness-shear-mode resonators, Journal of applied physics 95 (9) (2004) 4989–4995.

[181] J. N. Reddy, An introduction to continuum mechanics, Cambridge University Press, 2013.

[182] P. C. Y. Lee, R. Huang, Effects of a liquid layer on thickness-shear vibrations of rectangular at-cut quartz plates, Ultrasonics, Ferroelectrics and Frequency Control, IEEE Transactions on 49 (5) (2002) 604–611.

[183] T. Lindenbauer, Seminumerische analyse von piezoelektrischen tsm quarz resonatoren in viskosen flüssigkeiten, Master's thesis, Vienna University of Technology (2005).

[184] T. Lindenbauer, B. Jakoby, Fully three-dimensional analysis of tsm quartz sensors immersed in viscous liquids, in: Sensors, 2005 IEEE, IEEE, 2005, pp. 1249–1252.

[185] B. Weiss, Modellierung eines in einem kompressiblen fluid vibrierenden biegebalkens zur viskositäts– und dichtemessung, Master's thesis, Johannes Kepler University Linz, Austria (2006).

[186] J. D. Anderson, J. Wendt, Computational fluid dynamics, Vol. 206, Springer, 1995.

[187] L. D. Landau, E. Lifshitz, Theory of elasticity, vol. 7, Course of Theoretical Physics 3 (1986) 109.

[188] W. M. Lai, D. H. Rubin, D. Rubin, E. Krempl, Introduction to continuum mechanics, Butterworth-Heinemann, 2009.

[189] T. Voglhuber-Brunnmaier, The modeling of acoustic fluidic sensors using spectral methods, Trauner, 2013.

[190] C. Riesch, Micromachined Viscosity Sensors, Shaker Verlag, 2009.

[191] L. Rosenhead, Laminar Boundary Layers: Fluid Motion Memoirs, Clarendon, Oxford, 1963.

[192] E. O. Tuck, Calculation of unsteady flows due to small motions of cylinders in a viscous fluid, Journal of Engineering Mathematics 3 (1) (1969) 29–44.

[193] J. E. Sader, Frequency response of cantilever beams immersed in viscous fluids with applications to the atomic force microscope, Journal of Applied Physics 84 (1998) 64–76.

[194] B. Weiss, E. K. Reichel, B. Jakoby, Modeling of a clamped–clamped beam vibrating in a fluid for viscosity and density sensing regarding compressibility, Sensors and Actuators A: Physical 143 (2) (2008) 293–301.

[195] A. Agoston, F. Keplinger, B. Jakoby, Evaluation of a vibrating micromachined cantilever sensor for measuring the viscosity of complex organic liquids, Sensors and Actuators: A (2005) 82–86.

[196] T. D. Rossing, D. A. Russell, D. E. Brown, On the acoustics of tuning forks, Am. J. Phys 60 (7) (1992) 620–626.

[197] R. Blaauwgeers, M. Blazkova, M. Človečko, V. Eltsov, R. De Graaf, J. Hosio, M. Krusius, D. Schmoranzer, W. Schoepe, L. Skrbek, Quartz tuning fork: thermometer, pressure-and viscometer for helium liquids, Journal of Low Temperature Physics 146 (5-6) (2007) 537–562.

[198] D. Gross, W. Hauger, J. Schröder, W. Wall, Technische Mechanik 1, Springer-Verlag, 2013.

[199] D. Gross, W. Hauger, J. Schröder, W. Wall, Technische Mechanik 2: Elastostatik, Springer-Verlag, 2014.

[200] D. Gross, W. Hauger, J. Schröder, W. Wall, Technische Mechanik 3: Kinetik, Springer-Verlag, 2012.

[201] D. Gross, W. Hauger, P. Wriggers, Technische Mechanik 4 Hydromechanik, Elemente Der Hoheren Mechanik, Numerische Methoden, Springer-Verlag, 2014.

[202] J. A. Schultz, Lateral-mode vibration of microcantilever-based sensors in viscous fluids using timoshenko beam theory, Ph.D. thesis, Marquette University (2012).

[203] J. A. Schultz, S. M. Heinrich, F. Josse, I. Dufour, N. J. Nigro, L. A. Beardslee, O. Brand, Lateral-mode vibration of microcantilever-based sensors in viscous fluids using timoshenko beam theory.

[204] W. W. Weaver, S. P. Timoshenko, D. H. Young, Vibration Problems in Engineering, 5th Edition, Wiley, 1990.

[205] X. Zhang, E. Myers, J. Sader, M. Roukes, Nanomechanical torsional resonators for frequency-shift infrared thermal sensing, Nano letters 13 (4) (2013) 1528–1534.

[206] S. Timoshenko, S. Woinowsky-Krieger, S. Woinowsky, Theory of plates and shells, Vol. 2, McGraw-hill New York, 1959.

[207] R. D. Belvins, Formulas for natural frequency and mode shape, Krieger Publishing Company, 2001.

[208] A. F. Bower, Applied mechanics of solids, CRC, 2009.

[209] S. M. Dickinson, The buckling and frequency of flexural vibration of rectangular isotropic and orthotropic plates using rayleigh's method, Journal of Sound and Vibration 61 (1) (1978) 1–8.

[210] M. Baù, V. Ferrari, D. Marioli, E. Sardini, M. Serpelloni, A. Taroni, Contactless excitation and readout of passive sensing elements made by miniaturized mechanical resonators, Sensors, 2007 IEEE (2007) 36–39.

[211] M. Baù, V. Ferrari, D. Marioli, E. Sardini, M. Serpelloni, A. Taroni, Contactless electromagnetic excitation of resonant sensors made of conductive miniaturized structures, Sensors and Actuators A: Physical 148 (1) (2008) 44–50.

[212] A. M. Howatson, J. D. Todd, P. G. Lund, Engineering tables and data.

[213] E. Lassner, W.-D. Schubert, Tungsten: properties, chemistry, technology of the elements, alloys, and chemical compounds, Springer Science & Business Media, 1999.

[214] Plansee, Tungsten, material properties and applications, www.plansee.com.

[215] A. International, J. R. Davis, A. I. H. Committee, et al., Properties and selection: irons, steels and high-performance alloys, ASM International, 2005.

[216] G. F. Vander Voort, Atlas of time-temperature diagrams for irons and steels, ASM international, 1991.

[217] J. Rösler, H. Harders, M. Bäker, Mechanisches verhalten der werkstoffe, Springer-Verlag, 2006.

[218] W. Martienssen, H. Warlimont, Springer handbook of condensed matter and materials data, Springer Science & Business Media, 2006.

[219] J. Pelleg, Mechanical properties of materials, Vol. 190, Springer Science & Business Media, 2012.

[220] C. Rollins, The chemistry of chromium, molybdenum, and tungsten (1973).

[221] G. P. Skoro, J. R. J. Bennett, T. R. Edgecock, S. A. Gray, A. J. McFarland, C. N. Booth, K. J. Rodgers, J. J. Back, Dynamic young's moduli of tungsten and tantalum at high temperature and stress, Journal of Nuclear Materials (2011) 40 – 46.

[222] J. F. Nye, Physical Properties of Crystals. Their Representation by Tensors and Matrices, Oxford Science Publications, 1985.

[223] H. Goldstein, Classical mechanics, Pearson Education India, 1965.

[224] L. J. Chu, Physical limitations of omni-directional antennas, Journal of applied physics 19 (12) (1948) 1163–1175.

[225] E. I. Green, The story of q, American Scientist (1955) 584–594.

[226] A. D. Yaghjian, S. R. Best, Impedance, bandwidth, and q of antennas, Antennas and Propagation, IEEE Transactions on 53 (4) (2005) 1298–1324.

[227] M. Elwenspoek, R. Wiegerink, Mechanical Microsensors, Springer-Verlag, 2001.

[228] K. Y. Yasumura, T. D. Stowe, E. M. Chow, T. Pfafman, T. W. Kenny, B. C. Stipe, D. Rugar, Quality factors in micron-and submicron-thick cantilevers, Microelectromechanical Systems, Journal of 9 (1) (2000) 117–125.

[229] A. O. Niedermayer, T. Voglhuber-Brunnmaier, J. Sell, B. Jakoby, Methods for the robust measurement of the resonant frequency and quality factor of significantly damped resonating devices, Measurement Science and Technology 23 (8) (2012) 085107.

[230] J. Toledo, T. Manzaneque, J. Hernando-García, J. Vázquez, A. Ababneh, H. Seidel, M. Lapuerta, J. Sánchez-Rojas, Application of quartz tuning forks and extensional microresonators for viscosity and density measurements in oil/fuel mixtures, Microsystem Technologies (2014) 1–9.

[231] M. Sullivan, C. Harrison, A. R. H. Goodwin, K. Hsu, S. Godefroy, On the nonlinear interpretation of a vibrating wire viscometer operated at large amplitude, Fluid Phase Equilibria 276 (2009) 99—107. doi:10.1016/j.fluid.2008.10.017.

[232] H.-J. Bartsch, Taschenbuch mathematischer Formeln für Ingenieure und Naturwissenschaftler, Carl Hanser Verlag GmbH Co KG, 2014.

[233] K. Kanatani, P. Rangarajan, Hyper least squares fitting of circles and ellipses, Computational Statistics & Data Analysis 55 (6) (2011) 2197–2208.

[234] T. Voglhuber-Brunnmaier, A. Niedermayer, R. Beigelbeck, B. Jakoby, Resonance parameter estimation from spectral data: Cramér–rao lower bound and stable algorithms with application to liquid sensors, Measurement Science and Technology 25 (10) (2014) 105303–105313.

[235] C. Gerthsen, D. Meschede, Gerthsen Physik, Springer-Verlag, 2013.

[236] H. A. C. Tilmans, M. Elwenspoek, J. H. J. Fluitman, Micro resonant force gauges, Sensors and Actuators A: Physical 30 (1) (1992) 35–53.

[237] S. J. Martin, M. A. Butler, J. J. Spates, M. A. Mitchell, W. K. Schubert, Flexural plate wave resonator excited with lorentz forces, Journal of Applied Physics 83 (9) (1998) 4589–4601.

[238] L. Villanueva, R. Karabalin, M. Matheny, D. Chi, J. Sader, M. Roukes, Nonlinearity in nanomechanical cantilevers, Physical Review B 87 (2) (2013) 024304.

[239] M. Baù, V. Ferrari, D. Marioli, A. Taroni, Cost-effective system for the characterization of microstructures vibrating in out-of-plane modes, Sensors and Actuators A: Physical 142 (1) (2008) 270–275.

[240] C. Riesch, E. K. Reichel, A. Jachimowicz, J. Schalko, P. Hudek, B. Jakoby, F. Keplinger, A suspended plate viscosity sensor featuring in-plane vibration and piezoresistive readout, J. Micromech. Microeng. 19 (2009) 075010. doi:10.1088/0960-1317/19/7/075010.

[241] D. J. Griffiths, Introduction to Electrodynamics, Pearson, 2013.

[242] J. D. Jackson, R. F. Fox, Classical electrodynamics, 3rd Edition, American Association of Physics Teachers, 1999.

[243] P. J. Petersan, S. M. Anlage, Measurement of resonant frequency and quality factor of microwave resonators: Comparison of methods, J. Appl. Phys.

[244] M. C. Sanchez, E. Martin, J. M. Zamarro, Unified and simplified treatment of techniques for characterising transmission, reflection or absorption resonators, Microwaves, Antennas and Propagation, IEE Proceedings H 137 (1990) 209 – 212.

[245] C. R. Paul, Inductance: loop and partial, John Wiley & Sons, 2011.

[246] E. B. Rosa, The self and mutual inductances of linear conductors, US Department of Commerce and Labor, Bureau of Standards, 1908.

[247] F. W. Grover, Inductance Calculations, Dover, 2009.

[248] H. Soltner, P. Blümler, Dipolar halbach magnet stacks made from identically shaped permanent magnets for magnetic resonance, Concepts in Magnetic Resonance Part A 36 (4) (2010) 211–222.

[249] M. Kumada, E. I. Antokhin, Y. Iwashita, M. Aoki, E. Sugiyama, Super strong permanent dipole magnet, Applied Superconductivity, IEEE Transactions on 14 (2) (2004) 1287–1289.

[250] E. K. Reichel, B. Jakoby, C. Riesch, A novel combined rheometer and density meter suitable for integration in microfluidic systems, in: Sensors, 2007 IEEE, IEEE, 2007, pp. 908–911.

[251] E. Reichel, C. Riesch, F. Keplinger, B. Jakoby, Resonant measurement of liquid properties in a fluidic sensor cell, Proc. Eurosensor XXII (2008) 540–543.

[252] E. K. Reichel, B. Jakoby, Microsensors based on mechanically vibrating structures, in: Advanced Dynamics and Model-Based Control of Structures and Machines, Springer, 2012, pp. 183–193.

[253] T. Voglhuber-Brunnmaier, E. K. Reichel, B. Jakoby, Characterization of a novel membrane-rheometer utilizing a semi-numerical modelling approach in the spectral domain, Sens. Actuators A: Phys. 162-2 (2010) 310–315.

[254] T. Voglhuber-Brunnmaier, E. K. Reichel, B. Jakoby, A1. 4-semi-numerical simulation of a miniaturized vibrating membrane-rheometer, Proceedings SENSOR 2009, Volume I (2009) 41–46.

[255] E. K. Reichel, C. Riesch, F. Keplinger, B. Jakoby, A novel oscillating shear viscosity sensor for complex liquids, Procedia Chemistry 1 (1) (2009) 895–898.

[256] G. Habenicht, Kleben, Grundlagen and Technologien, Anwendungen, Springer-Verlag Berlin Heidelberg, 2009.

[257] P. K. Yuen, V. N. Goral, Low-cost rapid prototyping of flexible microfluidic devices using a desktop digital craft cutter, Lab on a Chip 10 (3) (2010) 384–387.

[258] T. Retsina, S. M. Richardson, W. A. Wakeham, The theory of a vibrating-rod viscometer, Applied Scientific Research 4 (1986) 325–346. doi:10.1007/BF00540567.

[259] F. Keplinger, R. Beigelbeck, F. Kohl, S. Kvasnica, A. Jachimowicz, B. Jakoby, Frequency and transient analysis of micromachined u-shaped cantilever devices for magnetic field measurement, Solid-State Sensors, Actuators and Microsystems 1 (2005) 630 – 635.

[260] B. Weiss, E. K. Reichel, B. Jakoby, Modeling of a clamped–clamped beam vibrating in a fluid for viscosity and density sensing regarding compressibility, Sensors and Actuators A: Physical 143 (2) (2008) 293–301.

[261] O. Kratky, H. Leopold, H. H. Stabinger, Dichtemessungen an flüssigkeiten und gasen auf 10^{-6} g/cm^3 bei 0.6 cm^3 präparatvolumen, Zeitschrift für angewandte Physik 27 (4) (1969) 273–277.

[262] O. Kratky, H. Leopold, H. Stabinger, Apparatus for density determination, uS Patent 4,170,128 (Oct. 9 1979).

[263] S. J. Martin, R. W. Cernosek, J. J. Spates, Sensing liquid properties with shear-mode resonator sensors, Transducers, Eurosensors IX (1995) 712–715.

[264] S. Martin, G. Frye, K. Wessendorf, Sensing liquid properties with thickness-shear mode resonators, Sensors and Actuators A: Physical 44 (3) (1994) 209–218.

[265] C. E. Reed, K. K. Kanazawa, J. H. Kaufman, Physical description of a viscoelastically loaded at-cut quartz resonator, Journal of Applied Physics 68 (5) (1990) 1993–2001.

[266] F. Josse, Z. A. Shana, D. E. Radtke, D. T. Haworth, Analysis of piezoelectric bulk-acoustic-wave resonators as detectors in viscous conductive liquids, Ultrasonics, Ferroelectrics, and Frequency Control, IEEE Transactions on 37 (5) (1990) 359–368.

[267] R. Lucklum, C. Behling, R. W. Cernosek, S. J. Martin, Determination of complex shear modulus with thickness shear mode resonators, Journal of Physics D: Applied Physics 30 (3) (1997) 346.

[268] D. Johannsmann, K. Mathauer, G. Wegner, W. Knoll, Viscoelastic properties of thin films probed with a quartz-crystal resonator, Physical Review B 46 (12) (1992) 7808.

[269] Y. Hu, J. LA French, K. Radecsky, M. Pereira da Cunha, P. Millard, J. F. Vetelino, A lateral field excited liquid acoustic wave sensor, Ultrasonics, Ferroelectrics, and Frequency Control, IEEE Transactions on 51 (11) (2004) 1373–1380.

[270] B. Jakoby, F. P. Klinger, P. Svasek, A novel microacoustic viscosity sensor providing integrated sample temperature control, Sensors and Actuators A: Physical 123 (2005) 274–280.

[271] A. J. Ricco, S. J. Martin, Acoustic wave viscosity sensor, Applied physics letters 50 (21) (1987) 1474–1476.

[272] B. Jakoby, M. J. Vellekoop, Viscosity sensing using a love-wave device, Sensors and Actuators A: Physical 68 (1) (1998) 275–281.

[273] F. Herrmann, D. Hahn, S. Büttgenbach, Separate determination of liquid density and viscosity with sagittally corrugated love-mode sensors, Sensors and Actuators A: Physical 78 (2) (1999) 99–107.

[274] A. Turton, D. Bhattacharyya, D. Wood, High sensitivity love-mode liquid density sensors, Sensors and Actuators A: Physical 123 (2005) 267–273.

[275] F. Eichelbaum, R. Borngräber, J. Schröder, R. Lucklum, P. Hauptmann, Interface circuits for quartz-crystal-microbalance sensors, Review of scientific instruments 70 (5) (1999) 2537–2545.

[276] J. Schröder, R. Borngräber, R. Lucklum, P. Hauptmann, Network analysis based interface electronics for quartz crystal microbalance, Review of Scientific Instruments 72 (6) (2001) 2750–2755.

[277] C. Riesch, B. Jakoby, Novel readout electronics for thickness shear-mode liquid sensors compensating for spurious conductivity and capacitances, Sensors Journal, IEEE 7 (3) (2007) 464–469.

[278] M. Ferrari, V. Ferrari, K. Kanazawa, Dual-harmonic oscillator for quartz crystal resonator sensors, Sensors and Actuators A: Physical 145 (2008) 131–138.

[279] R. Schnitzer, C. Reiter, K.-C. Harms, E. Benes, M. Groschl, A general-purpose online measurement system for resonant baw sensors, Sensors Journal, IEEE 6 (5) (2006) 1314–1322.

[280] A. O. Niedermayer, E. K. Reichel, B. Jakoby, Yet another precision impedance analyzer (yapia) readout electronics for resonating sensors, Sensors and Actuators A: Physical 156 (1) (2009) 245–250.

[281] B. Jakoby, G. Art, J. Bastemeijer, Novel analog readout electronics for microacoustic thickness shear-mode sensors, Sensors Journal, IEEE 5 (5) (2005) 1106–1111.

[282] B. Jakoby, A. Ecker, M. J. Vellekoop, Monitoring macro-and microemulsions using physical chemosensors, Sensors and Actuators A: Physical 115 (2) (2004) 209–214.

[283] L. R. A. Follens, E. K. Reichel, C. Riesch, J. Vermant, J. A. Martens, C. E. A. Kirschhock, B. Jakoby, Viscosity sensing in heated alkaline zeolite synthesis media, Physical Chemistry Chemical Physics 11 (16) (2009) 2854–2857.

[284] A. D'amico, E. Verona, Saw sensors, Sensors and Actuators 17 (1) (1989) 55–66.

[285] M. Vellekoop, G. Lubking, P. Sarro, A. Venema, Evaluation of liquid properties using a silicon lamb wave sensor, Sensors and Actuators A: Physical 43 (1) (1994) 175–180.

[286] H. Antlinger, S. Clara, R. Beigelbeck, S. Cerimovic, F. Keplinger, B. Jakoby, Sensing the characteristic acoustic impedance of a fluid utilizing acoustic pressure waves, Sensors and Actuators A: Physical 186 (2012) 94–99.

[287] H. Antlinger, S. Clara, R. Beigelbeck, S. Cerimovic, F. Keplinger, B. Jakoby, An acoustic transmission sensor for the characterization of fluids in terms of their longitudinal viscosity, Procedia Engineering 47 (2012) 248–252.

[288] R. Beigelbeck, H. Antlinger, S. Cerimovic, S. Clara, F. Keplinger, B. Jakoby, Resonant pressure wave setup for simultaneous sensing of longitudinal viscosity and sound velocity of liquids, Measurement Science and Technology 24 (12) (2013) 125101.

[289] A. Rahafrooz, S. Pourkamali, Rotational mode disk resonators for high-q operation in liquid, in: Sensors, 2010 IEEE, IEEE, 2010, pp. 1071–1074.

[290] E. Mehdizadeh, J. Gonzales, A. Rahafrooz, R. Abdolvand, S. Pourkamali, Piezoelectric rotational mode disk resonators for liquid viscosity monitoring, in: Tech. Dig. Hilton Head Workshop, Vol. 35, 2012, pp. 359–362.

[291] M. Youssry, N. Belmiloud, B. Caillard, C. Ayela, C. Pellet, I. Dufour, A straightforward determination of fluid viscosity and density using microcantilevers: from experimental data to analytical expressions, Sensors and Actuators A: Physical 172 (1) (2011) 40–46.

[292] M. Youssry, E. Lemaire, B. Caillard, A. Colin, I. Dufour, On-chip characterization of the viscoelasticity of complex fluids using microcantilevers, Measurement Science and Technology 23 (12) (2012) 125306.

[293] E. Lemaire, B. Caillard, M. Youssry, I. Dufour, High-frequency viscoelastic measurements of fluids based on microcantilever sensing: New modeling and experimental issues, Sensors and Actuators A: Physical 201 (2013) 230–240.

[294] B. A. Bircher, L. Duempelmann, K. Renggli, H. P. Lang, C. Gerber, N. Bruns, T. Braun, Real-time viscosity and mass density sensors requiring microliter sample volume based on nanomechanical resonators, Analytical chemistry 85 (18) (2013) 8676–8683.

[295] A. Maali, C. Hurth, R. Boisgard, C. Jai, T. Cohen-Bouhacina, J. P. Aimé, Hydrodynamics of oscillating atomic force microscopy cantilevers in viscous fluids, Journal of Applied Physics 97 (7) (2005) 074907–074907.

[296] J. Zhang, C. Dai, X. Su, S. J. O'Shea, Determination of liquid density with a low frequency mechanical sensor based on quartz tuning fork, Sensors and Actuators B: Chemical 84 (2) (2002) 123–128.

[297] I. Etchart, H. Chen, P. Dryden, J. Jundt, C. Harrison, K. Hsu, F. Marty, B. Mercier, Mems sensors for density–viscosity sensing in a low-flow microfluidic environment, Sensors and Actuators A: Physical 141 (2) (2008) 266–275.

[298] C. Riesch, E. K. Reichel, F. Keplinger, B. Jakoby, Characterizing vibrating cantilevers for liquid viscosity and density sensing, Journal of Sensors 2008 (Article ID 697062) (2008) 9 pages.

[299] E. K. Reichel, C. Riesch, B. Weiss, B. Jakoby, A vibrating membrane rheometer utilizing electromagnetic excitation, Sensors and Actuators A: Physical 145 (2008) 349–353.

[300] S. Cerimovic, R. Beigelbeck, H. Antlinger, J. Schalko, B. Jakoby, F. Keplinger, Sensing viscosity and density of glycerol–water mixtures utilizing a suspended plate mems resonator, Microsystem technologies 18 (7-8) (2012) 1045–1056.

[301] T. Manzaneque, V. Ruiz, J. Hernando-García, A. Ababneh, H. Seidel, J. Sánchez-Rojas, Characterization and simulation of the first extensional mode of rectangular micro-plates in liquid media, Applied Physics Letters 101 (15) (2012) 151904.

[302] A. Rahafrooz, S. Pourkamali, Characterization of rotational mode disk resonator quality factors in liquid, Frequency Control and the European Frequency and Time Forum (FCS), 2011 Joint Conference of the IEEE International (2011) 5 pages.

[303] M. S. Sotoudegan, S. M. Heinrich, F. Josse, N. J. Nigro, I. Dufour, O. Brand, Analytical modeling of a novel high-disk resonator for liquid-phase applications, Microelectromechanical Systems, Journal of 24 (1) (2015) 38–49.

[304] J. H. Seo, O. Brand, High q-factor in-plane-mode resonant microsensor platform for gaseous/liquid environment, Journal of Microelectromechanical Systems 17 (2) (2008) 483–493.

[305] M. F. Khan, S. Schmid, P. E. Larsen, Z. J. Davis, W. Yan, E. H. Stenby, A. Boisen, Online measurement of mass density and viscosity of pl fluid samples with suspended microchannel resonator, Sensors and Actuators B: Chemical 185 (2013) 456–461.

[306] X. Huang, S. Li, J. Schultz, Q. Wang, Q. Lin, A capacitive mems viscometric sensor for affinity detection of glucose, Journal of Microelectromechanical Systems 18 (6) (2009) 1246–1254.

[307] K. T. Loiselle, C. A. Grimes, Viscosity measurements of viscous liquids using magnetoelastic thick-film sensors, Review of scientific instruments 71 (3) (2000) 1441–1446.

[308] G. Leveque, J. Ferrandis, J. Van Est, B. Cros, An acoustic sensor for simultaneous density and viscosity measurements in liquids, Review of Scientific Instruments 71 (3) (2000) 1433–1440.

[309] C. Vančura, I. Dufour, S. M. Heinrich, F. Josse, A. Hierlemann, Analysis of resonating microcantilevers operating in a viscous liquid environment, Sensors and Actuators A: Physical 141 (1) (2008) 43–51.

[310] L. A. Beardslee, A. M. Addous, S. Heinrich, F. Josse, I. Dufour, O. Brand, Thermal excitation and piezoresistive detection of cantilever in-plane resonance modes for sensing applications, Journal of Microelectromechanical Systems 19 (4) (2010) 1015–1017.

[311] H. Jianqiang, Z. Changchun, L. Junhua, L. Peng, A novel temperature-compensating structure for micromechanical bridge resonator, Journal of Micromechanics and Microengineering 15 (4) (2005) 702.

[312] A. K. Samarao, F. Ayazi, Temperature compensation of silicon micromechanical resonators via degenerate doping, in: Electron Devices Meeting (IEDM), 2009 IEEE International, IEEE, 2009, pp. 789–792.

[313] T. Larsen, S. Schmid, L. Grönberg, A. O. Niskanen, J. Hassel, S. Dohn, A. Boisen, Ultrasensitive string-based temperature sensors, Applied Physics Letters 98 (12) (2011) 121901.

[314] M. Stifter, T. Sauter, W. Hortschitz, F. Keplinger, H. Steiner, Mems heterodyne amf detection with capacitive sensing, Proceedings IEEE Sensors 2012 (2012) 1–4doi:10.1109/ICSENS.2012.6411171.

[315] H. S. Wasisto, S. Merzsch, A. Waag, E. Uhde, T. Salthammer, E. Peiner, Airborne engineered nanoparticle mass sensor based on a silicon resonant cantilever, Sensors and Actuators B: Chemical 180 (2013) 77–89.

[316] R. Sandberg, W. Svendsen, K. Mølhave, A. Boisen, Temperature and pressure dependence of resonance in multi-layer microcantilevers, Journal of Micromechanics and Microengineering 15 (8) (2005) 1454.

[317] A. Goodwin, K. Marsh, W. Wakeham, Measurement of the thermodynamic properties of single phases, Elsevier, 2003.

Journal Publications

Sensors and Actuators A 172 (2011) 82–87

Contents lists available at ScienceDirect

Sensors and Actuators A: Physical

journal homepage: www.elsevier.com/locate/sna

A resonating rheometer using two polymer membranes for measuring liquid viscosity and mass density

M. Heinisch[a,*], E.K. Reichel[b], I. Dufour[c], B. Jakoby[a]

[a] Institute for Microelectronics and Microsensors, Johannes Kepler University, Linz, Austria
[b] Center for Surface Science and Catalysis, Katholieke Universiteit Leuven, Belgium
[c] Universitéde Bordeaux, Laboratoire de l'Intégration du Matériau au Systéme, France

ARTICLE INFO

Article history:
Available online 26 February 2011

Keywords:
Viscosity
Mass
Density
Sensor
Frequency
Vibrating membrane
Lorentz forces
Cross talk

ABSTRACT

A resonating sensor for mechanical liquid properties facilitating measurements at two different modes of operation is presented. One mode is more sensitive to liquid viscosity the other to mass density. A sample liquid is subjected to time-harmonic shear stress induced by two opposed vibrating polymer membranes. These membranes, placed in an external static magnetic field, carry two conductive paths each. The first path is used to actuate the membranes by means of Lorentz forces while the second acts as a pick-up coil providing an induced voltage representing the movement of the membrane. From the resulting frequency response the liquid's viscosity and mass density can be deduced. This double membrane based setup allows examining the test liquid at adjustable frequencies in the low kilohertz range from 500 Hz to 20 kHz by varying the gap between both membranes. The sensor is suitable, e.g., for low cost handheld devices with inline capabilities and disposable sensor elements for measuring Newtonian liquids such as, e.g., oils and aqueous solutions.

© 2011 Elsevier B.V. All rights reserved.

1. Introduction

As it is an extremely important property for many technological and scientific applications, viscosity has been subject of an enormous effort of measurement, correlation, and interpretation. The viscosity of a fluid is a measure of its tendency to dissipate energy when it is disturbed from equilibrium by a velocity field. In most cases the term viscosity is associated to shear viscosity only and volume viscosity is not taken into account or expected to be zero which is valid for incompressible liquids. In theory, the analysis of any fluid motion could be suitable to determine the viscosity of the examined fluid. However, only relatively simple designs of viscometers yielding fluid motion for which analytical closed form models can be defined have been preferably considered for viscosity sensing.

Methods for which working equations relating the viscosity to measured parameters are available but where the values of some of these parameters must be obtained by an independent calibration with known standards, are called quasi-primary [1]. (So far, no primary method requiring no calibration of the sensor could be found). Nieto de Castro [1] consider as quasi primary: oscillating body (disk, cup, cylinder or sphere), vibrating wire, torsionally oscillating quartz crystal and surface light scattering spectroscopy. However, based on the definition above the list of quasi primary methods can be extended by: capillary flow, falling body [2], acoustic methods [3] (e.g., thickness shear mode (TSM)), microacoustic quartz resonator [4] and vibration tubes [5].

In previous works the idea of a double membrane based rheometer was introduced [6]. The main advantages of this sensor concept are that it allows inline sensing and second, due to low cost fabrication, these sensors can be used as disposable elements for application in medical analysis, or the monitoring of crystallization or polymerization processes [7]. In an earlier work [8] a first prototype and measurement results were presented. The modeling of the sensor utilizing a semi-numerical modeling approach in the spectral domain was presented in [9]. The insights obtained by the experimental results of first prototypes demanded redesigning the sensor assembly to achieve several improvements enabling accurate as well as reliable sensing, which moreover is a prerequisite to get proper data for a meaningful comparison with theoretical considerations and results. First, there was a need to increase the repeatability and the sensor's sensitivity. Second, a design avoiding the formation of air bubbles within the test liquid, which moreover does not suffer from leakage had to be found. Third, measurement series obtained with the new devices had to be compared with theoretical findings from, e.g., [9] and confirm the latter. Additionally, the focus was set on an appropriate closed-form model

* Corresponding author. Tel.: +43 73224686266.
E-mail address: martin.heinisch@jku.at (M. Heinisch).

0924-4247/$ – see front matter © 2011 Elsevier B.V. All rights reserved.
doi:10.1016/j.sna.2011.02.031

representing the sensor's frequency behavior and thus relating to the liquid's viscosity and mass density.

For all liquids, viscosity decreases with increasing temperature [10]. Thus, it has to be pointed out that it is always necessary to indicate the temperature prevailing during the measurement of viscosity. E.g., a change in temperature of the standard N415 (which was used for measurements in this contribution) from 10 °C to 20 °C leads to a decrease in viscosity from 2385.3 mPa s to 1157.5 mPa s which corresponds to a change of more than 50%. For this liquid, a measurement error in temperature of about ±0.16 °C results in an error in viscosity of ±1%. An overview of models describing the temperature depending decrease in viscosity is given in [11]. At the same time the intrinsic temperature dependence of the device characteristics may become relevant and need to be calibrated (which goes beyond the scope of this contribution, see, e.g., related discussion [12]).

2. Sensor principle

In Fig. 1(a) a schematic of the redesigned sensor is depicted. The major change compared to first prototypes is the open, fork-like assembly which is immersed into the test liquid. Due to this principle of immersion the formation of air bubbles is not a subject anymore when filling the sensor. The sensor is well suited for inline sensing which can be useful, e.g., to observe a lubricant's conditions and aging. However, a closed design benefits from the advantages that it requires less of the test liquid and handling is more convenient if a variety of different liquids has to be investigated.

The sensor width was reduced thus resulting in a smaller air gap within the magnetic circuit. This smaller gap and a complete revision of the magnetic circuit yield an enhancement of the magnetic flux density from 150 mT to approximately 0.6 T which was measured with a Gauss meter (GM05, Hirst Magnetic Instrument Ltd.). A higher magnetic flux density quadratically improves the sensor's sensitivity [13].

A sinusoidal electrical current through the membranes' excitation paths being placed in an external static magnetic field provided by a neodymium permanent magnet assembly is used as input i.e., excitation signal driving the sensor. By means of Lorentz forces, the (2,1)-eigenmode of the membranes is excited, see Fig. 1(c). The membranes are deflected either symmetrically or antisymmetrically depending on opposite or equal direction of the electric current through the membranes' excitation loops. In both cases the excitation loops (and also the pick-up loops) are electrically connected in series. Thus, two different deformation fields can be applied, each leading to different resonance frequencies and response to viscosity and mass density. This viscosity- and mass-density-dependent oscillation of the membranes is represented via the induced voltage in a second conductive path (pick-up coil) close to the excitation loop. This induced voltage is measured with a lock-in amplifier setup allowing the analysis of both amplitude and phase relation between the excitation and readout signals. An excitation signal of about 1.3 V (corresponding to about 250 mA for an excitation loop with about 5 Ω) yields read out signals in the order of 0.1 V. The frequency response is recorded by sweeping the frequency of the excitation signal in the range of interest, in this case 500–20 kHz. The measured frequency response is used to identify the parameters of a closed-form model with which the resonance frequency ω_r and the Q-factor Q are determined. With the knowledge of these parameters the liquid's properties viscosity and mass density can be determined. Before every single measurement it has to be ensured that the sensor is clean (e.g., with a reference measurement) as for all resonant sensors contaminations or coatings, e.g., resulting from fouling of the surface result in a tremendous measuring error.

The key feature of this sensor is the usage of two polymer membranes instead of using only one. The main advantage of the second membrane is the possibility of switching between two different modes of operation which allows determining the liquid's viscosity and mass density with a single device. The frequency response of a device with only one vibrating membrane is depicted in Fig. 2(a) for DI-water as sample liquid. In the investigated frequency range (500–20 MHz) of the single membrane device two dominant mechanical resonance frequencies (≈2.5 kHz and 13 kHz) could be observed. The investigation of the double membrane sensors showed that in the (anti)symmetric mode only one mechanical resonance is excited. According to theoretical findings in [9], symmetric actuation, which is more sensitive to viscosity, excites resonances at the lower frequencies (≈2.5 kHz), whereas in antisymmetric mode, which is more sensitive to mass density, only the resonances at higher frequencies (≈13 kHz) are observed. Another advantage is that using two membranes instead of one increases the sensitivity of the sensor.

Furthermore, Voglhuber-Brunnmaier et al. [9] found that the resonance frequencies in symmetric mode shift to higher and those in antisymmetric excitation to lower frequencies for larger gaps between both membranes. This shows that the resonance frequencies can be adjusted by varying the gap between both membranes.

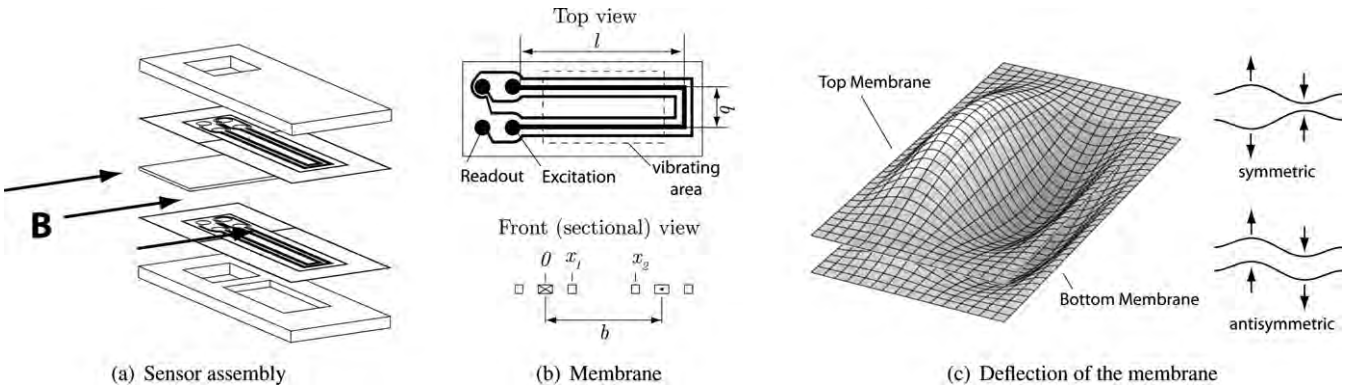

Fig. 1. In (a) the exploded view of the double membrane rheometer is illustrated. Two polymer membranes carrying conductive paths for excitation and readout are bonded to rigid platelets. The bonding, also acting as sealing, ensures that the membranes' sides carrying the conductive paths do not get wetted with the liquid to be examined. I.e., only the liquid in the space between both membranes will be examined. The distance of both membranes is determined by the height of the spacer between both senor parts. The arrows on the left side indicate the direction of the external magnetic field provided by two NdFeB magnets on each side of the sensor. In (b) one membrane is illustrated in detail. In (c) the deflection of the membranes in the (2,1)-eigenmode is depicted. Depending on the direction of the electric current in the particular excitation path, the deflection can either be symmetric (opposite direction) or antisymmetric (same direction).

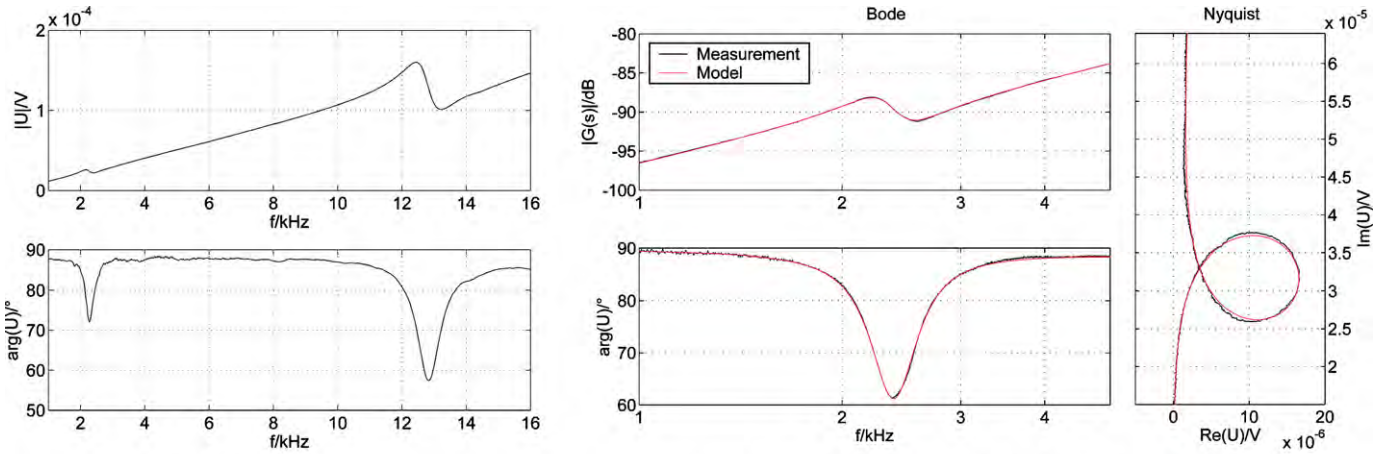

(a) Single membrane excitation

(b) Bode and Nyquist Plot in symmetric mode for viscosity standard S3

Fig. 2. In (a) the frequency response of one membrane being excited (the other remaining unactivated) is depicted for the case of DI water. Both membranes yield virtually the same response. When both membranes are activated, lower resonance frequencies (2.2 kHz) remain in the case of symmetric mode, where higher frequencies (13 kHz) remain for antisymmetric mode. In (b) a comparison of the measured data with the identified model Eq. (1) for the viscosity standard S3 (3.3 mPa s® @ 25 °C) in the symmetric mode is depicted.

3. Fabrication

The membranes carrying the conductive paths are realized by photolithography and wet etching of a 100 m thick polyester based (PET) sheet coated with a 2 m copper layer. The dimensions of the membranes are 30 mm × 11.8 mm, with a vibrating area of 12 mm × 5.6 mm. As polyester based plastics are highly solvent-proof, reaction adhesives (e.g., epoxy resin) are normally used for bonding or gluing [14]. However, epoxy resin showed to be hardly suitable for an easy manufacturing process to ensure uniform and reproducible bonding of the PET sheets. To account for an uniform adherend, pressure sensitive adhesive (PSA) foils are used to bond the membranes with the rigid top and bottom plate and the spacer which determines the gap between both membranes. The membranes and the foils are cut with a digital craft cutter [15] with a mechanical resolution of 50 m. To replace the PSA foils by a more reliable means of bonding, a special process for reaction adhesive bonding or ultrasonic welding has to be developed.

4. Modeling

A purely numerical approach to model the fluid structure interaction, using finite element analysis, turned out to be inappropriate as the vibration amplitudes of the membranes (several micrometers [7]) and thus the penetration depth of shear waves emerging from the vibrating membranes is much smaller than the membrane's planar dimensions. Thus, a very fine discretization is required resulting in a tremendous number of finite elements for discretizing the vibrating area. A modeling approach based on the Fourier method which greatly improves the numerical efficiency was presented in [16]. There, the two different modes of operation (symmetrical and antisymmetrical) and the response to viscosity and mass density are outlined. A drawback of the application of the Fourier method is that it causes problems to correctly incorporate the required clamped boundary conditions for the diaphragm [7]. As an alternative, an empirical closed-form model was found describing the sensor's frequency response in terms of the ratio of output voltage V_{out} to input voltage V_{in} at either symmetric or antisymmetric excitation, see Fig. 2(b):

$$G(s) = \frac{V_{\text{out}}}{V_{\text{in}}} = A\frac{s^2/\omega_2^2 + 2d_2(s/\omega_2) + 1}{s^2/\omega_1^2 + 2d_1(s/\omega_1) + 1} s e^{a s}, \tag{1}$$

where s denotes the complex frequency ($s = j\omega$ for time-harmonic excitation with angular frequency ω). A, ω_1, d_1, ω_2, d_2 and a are the identified parameters. A is an amplification factor. The denominator of the fraction implements the resonance peak, while the numerator models the dip right after the peak. The multiplication by s yields an additional $+20dB/dec$ slope. The last term considers spurious phase shifts and delays. This model is in good agreement with the result of measurement. However, it does not relate physical effects to the measured data.

For this purpose, a different approach was devised by decomposing the measured voltage into two parts: A motion-induced voltage in the readout path due to the movement of the membrane, which, in term, is modeled by a lumped mechanical oscillator, and another induced voltage due to electrical cross talk from the excitation path to the readout path. The simplified electrical equivalent circuit and the mechanical model of the double membrane sensor are depicted in Fig. 3. The resonant movement of the membrane is approximated by a linear (mass–spring–dashpot) oscillator described by the transfer function (which is the quotient of deflection u_z and Lorentz forces $F_L = I_{\text{in}} B\, l^*$)

$$G_m(s) = \frac{u_z(s)}{F_L(s)} = \frac{G_0}{s^2/\omega_0^2 + 2d(s/\omega_0) + 1}, \tag{2}$$

where I_{in} is the electrical current in the excitation path, B is the magnetic flux density, l^* the effective length of the excitation loop effecting the membrane's deflection. In the following it is assumed that $l^* \approx l^*_{in} \approx l^*_{out}$, where the latter are the effective lengths of the excitation and readout path respectively. G_0 is the mechanical amplification, $d = d_M + d_L$ is the total damping accounting for intrinsic damping of the membrane, d_M, and damping due to the liquid loading, d_L. Furthermore, d is related to the quantities used in the equivalent circuit by $d = r/2\sqrt{mk}$.

$$\omega_0 = \sqrt{\frac{k}{m}} \quad \text{and} \quad \omega_r = \omega_0\sqrt{1 - 2d^2} \tag{3}$$

is the mechanical eigenfrequency and resonance frequency respectively, where k is the spring constant of the oscillator (represents stiffness of the membrane) and $m = m_M + m_L$ is the total effective mass considering the intrinsic effective mass of the membrane, m_Z and the inertial component of the liquid loading, m_L. The Q-factor

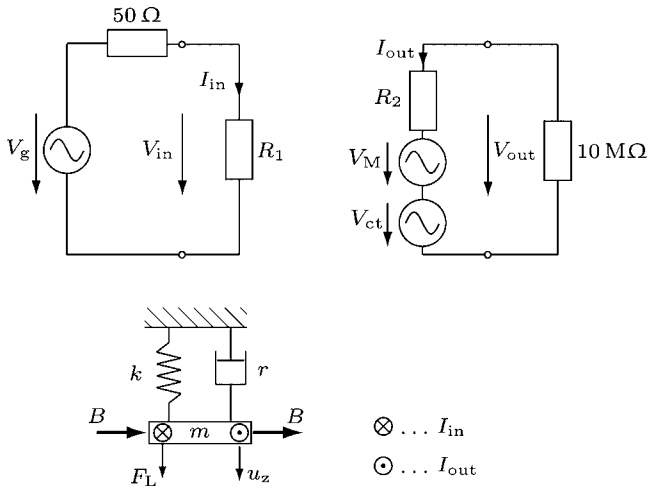

V_g, 50 Ω ... signal generator

R_1, R_2 ... resistance of the excitation and readout path

V_{in}, V_{out} ... actuating and measured voltage

I_{in}, I_{out} ... electrical current in the excitation and readout path

V_M ... induced voltage in the readout path representing the movement of the membrane

V_{ct} ... induced voltage in the readout path by electrical cross talking

10 MΩ ... input resistance of the lock-input amplifier

k, r, m ... spring stiffness, damping parameter, mass of the mechanical oscillator

B, F_L, u_z ... magnetic flux density, Lorentz force, membrane's effective z-deflection

Fig. 3. Electrical equivalent circuit and mechanical model of the double membrane sensor.

was calculated with the relation

$$Q = \frac{\omega_0}{\omega_+ - \omega_-} = \frac{\sqrt{1-2d^2}}{\sqrt{1-2d^2+2d\sqrt{1-d^2}} - \sqrt{1-2d^2-2d\sqrt{1-d^2}}} \quad (4)$$

where ω_- and ω_+ are the angular frequencies at −3 dB of the maximum amplitude.

The induced voltage in the readout path effected by the movement of the latter in an external magnetic field (assuming that the occurring terms are in perpendicular) can be written as:

$$V_M = N v_z B l^* \quad (5)$$

where N is the number of turns and l^* the effective length of the readout paths and

$$v_z = s\,u_z = s\,G_m\,F_L \quad (6)$$

is the mean velocity of the vibrating readout paths. Substituting F_L in Eq. (6), replacing I_{in} by the quotient of input voltage V_{in} and input resistance R_1 and some further manipulations lead to the transfer function of the motion induced voltage

$$G_M = \frac{V_M}{V_{in}} = s\,\frac{NB^2 l^{*2}}{R_1} G_m. \quad (7)$$

To account for the electrical cross talk, the sensor can be modeled as a transformer consisting of the electrical resistance R_1 and the inductance L_1 of the excitation path, the electrical resistance R_2 and the inductance L_2 of the excitation path as well as the mutual inductance

$$M = k_c\sqrt{L_1 L_2} \quad (8)$$

representing the inductive coupling between excitation and readout path, where $k_c = 0 \ldots 1$ is the coupling factor.

Under the assumptions that $\{\omega L_1, \omega L_2, \omega M\} \ll \{R_1, R_2\}$ and $I_{in} \gg I_{out} \approx 0$ the excitation path can be modeled by its electrical resistance R_1 only. The readout path can be modeled as a voltage source $V_{ct} = s\,M\,I_{in}$ and its electrical resistance R_2, where $I_{in} = V_{in}/R_1$. Thus, the transfer function relating the cross talk induced voltage in the readout path to the input voltage is

$$G_{ct} = \frac{V_{ct}}{V_{in}} = \frac{s\,M}{R_1} \quad (9)$$

The complete transfer function of the double membrane sensor which is the quotient of output and input voltage (note that $V_{out} \approx V_M + V_{ct}$) is the sum of G_M and G_{ct}:

$$G(s) = \frac{V_{out}}{V_{in}} = G_M + G_{ct} = s\frac{NB^2 l^{*2}}{R_1}\,\frac{G_0}{s^2/\omega_0^2 + 2d(s/\omega_0) + 1} + \frac{sM}{R_1}. \quad (10)$$

This transfer functions can be transformed into Eq. (1) (and vice versa) except for the empirical term e^{as} which does not have an influence on the quantities to be measured. The viscosity and mass density of the analyzed liquid are only related to the parameters ω_0 and d (corresponding to ω_1 and d_1 in Eq. (1)) in these modeling approaches.

To check the feasibility of our model, an estimate for the order of magnitude of the mutual inductance, which can be compared to the value for M obtained from fitting the model to the measurement data, is calculated as follows. The mutual inductance for a single membrane (Fig. 1(b)) can be estimated from

$$M_s = \frac{\Psi_{21}}{I_{in}} = \frac{l\mu_0}{\pi}\int_{x_1}^{x_2}\left(\frac{1}{x} + \frac{1}{b-x}\right)dx \approx 17\,\text{nH}. \quad (11)$$

Here, Ψ_{21} denotes the flux linkage of output and input circuit and μ_0 is the permeability in air. For the total mutual inductance, as a very rude approximation $M \approx 2M_s$ can be assumed, however, the wiring (antisymmetric or symmetric) has a significant influence since the magnetic flux from our membrane partially intersects the other (which is not considered in Eq. (11)). The inductances of the excitation and readout path of a single membrane were measured with an impedance analyzer, where $L_1 \approx 47$ nH and $L_2 \approx 96$ nH. Thus, the coupling factor could be calculated with Eq. (8), yielding $k_c \approx 0.25$ which is a realistic value. The cross talk was analyzed by investigating the frequency response of the sensor without and external magnetic field. The insights gained by this method showed that the simplified model Eq. (9) is a good approximation of the electrical cross talk. In case of the evaluation of the cross talk in a single membrane, the order of magnitudes of the calculated value $M_s \approx 17$ nH and the identified parameter $M = 8.5$ nH are in good agreement.

5. Results

The model described in Eq. (10) was used to fit the data of experimental measurement results and Q-factors and Eigenfrequencies were evaluated. With the results obtained by this measurements, it was shown that a frequency response with two mechanical resonances is obtained if only one of both membranes is actuated

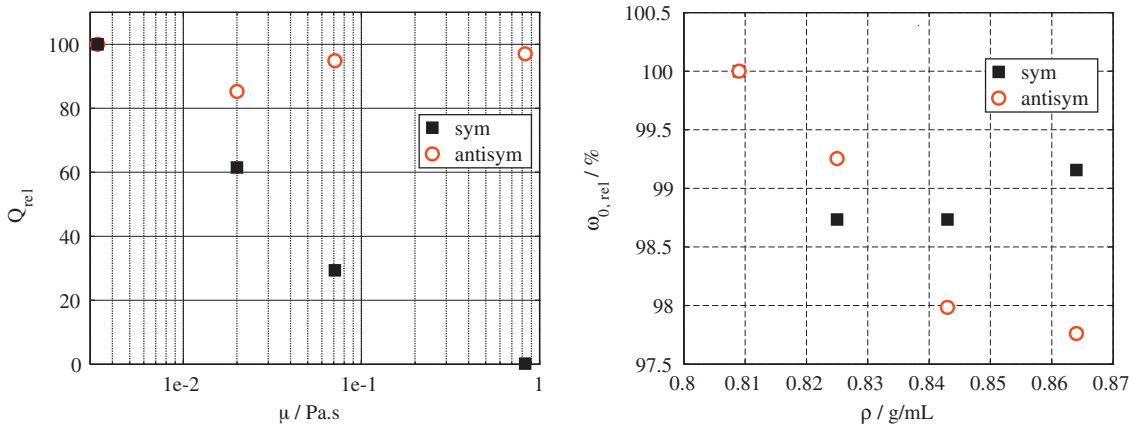

(a) Relative Q-factor over viscosity (b) Relative Eigen frequency over mass density

Fig. 4. In (a) relative *Q*-factors and in (b) relative eigenfrequencies are illustrated for symmetric and antisymmetric excitation for four different viscosity standards (s3, n14, n44, n415, Cannon Instrument Company®) @ 25 °C.

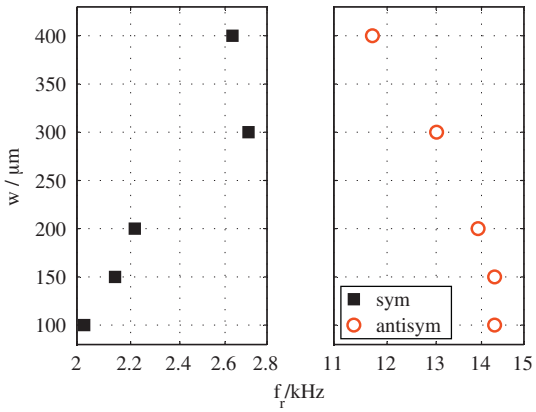

Fig. 5. Influence of the gap *w* between both membranes on the resonance frequencies f_r. Higher gaps generally yield a shift to higher frequencies in symmetric and a shift to lower frequencies in antisymmetric mode.

(Fig. 2(a)) and if both membranes being excited, one of these resonances remains and the other vanishes. Symmetric excitation maintains the lower, antisymmetric excitation the higher resonance frequencies. The influence of the gap on the resonance frequencies was investigated by varying the distance between two membranes using a micrometer positioning unit. With this experiment it was possible to prove the findings presented in [9]. Higher gaps yield a shift to higher frequencies in symmetric and a shift to lower frequencies in antisymmetric mode. This behavior could be observed for gaps from 100 m to 400 m, see Fig. 5. In Fig. 4 *Q*-factors and Eigenfrequencies are depicted in respect to the dynamic viscosity and mass density respectively for four test liquids. There, it can be observed that the symmetric mode is more sensitive to viscosity while the antisymmetric mode is more sensitive to mass density. In symmetric mode, there was no more resonant behavior for the highest viscous examined liquid (viscosity standard N415, 830 mPa s at 25 °C) while in antisymmetric mode the resonance was hardly damped.

The detailed character of the relation between the parameters viscosity/density and *Q*-factor/resonance frequency is crucially determined by the oscillating flow-field excited by the membranes. This analysis has yet to be performed, such that at this moment we can not provide a simple relation between these parameters. Of course it would also be possible to fit generic mathematical models to the measurement data but the amount of existing data is not sufficient to ensure the establishment of a reliable model.

6. Conclusion

By redesigning the first prototype of the double membrane based rheometer presented in [8] to an open fork-like assembly, the formation of air bubbles is avoided. The sensor's sensitivity is increased by a magnetic circuit yielding an air gap flux density of 0.6 T. The open fork-like assembly is well suited for inline sensing, whereas closed types facilitate more convenient handling when examining different liquids. The results of new measurement series were compared with theoretical findings and affirm the latter. A linear second order closed-form model representing the sensor's frequency behavior is used to relate to the liquid's properties viscosity and mass density. Regarding future work, it is desirable to find an appropriate bonding technique for fabricating accurate sensors with high repeatability. Furthermore, extensive measurement series using a large amount of different test liquids (e.g., viscosity standards) characterizing the sensor's properties have to be done.

References

[1] C.A. Nieto de Castro, Metrology of viscosity: have we learned enough? J. Chem. Eng. Data 54 (2009) 171–178.
[2] C. Tropea, et al., Springer Handbook of Experimental Fluid Mechanics, Springer-Verlag, Berlin Heidelberg, 2007.
[3] B. Jakoby, M. Scherer, M. Buskies, H. Eisenschmid, Microacoustic viscosity sensor for automotive applications, in: Tech. Digest 2002 IEEE Intl. Conf. on Sensors, Orlando, FL, June, 2002, pp. 1587–1590.
[4] A. Agoston, C. Ötsch, B. Jakoby, Viscosity sensors for engine oil condition monitoring—application and interpretation of results, Sens. Actuators A 121 (2005) 327–332.
[5] D. Sparks, R. Smith, V. Cruz, N. Tran, A. Chimbayo, D. Riley, N. Najafi, Dynamic and kinematic viscosity measurements with a resonating microtube, Sens. Actuators A 149 (2009) 38–41.
[6] E.K. Reichel, et al., A novel combined rheometer and density meter suitable for integration in microfluidic systems, in: IEEE Sensors 2007 Proceedings, 2007, pp. 903–906.
[7] E.K. Reichel, Dynamic Methods for Viscosity and Mass-Density Sensing, Insitute for Microelectronics and Microsensors, Johannes Kepler University, Linz, Austria, 2009.
[8] E.K. Reichel, et al., Resonant measurement of liquid properties in a fluidic sensor cell, in: Eurosensors XXII Proceedings, 2008, pp. 540–543.
[9] T. Voglhuber-Brunnmaier, et al., Characterization of a novel membrane-rheometer utilizing a semi-numerical modelling approach in the spectral domain, Sens. Actuators A: Phys. (2010), doi:10.1016/j.sna.2009.12.037.
[10] C.W. Macosko, Rheology, Principles, Measurements and Applications, Wiley-VCH, 1994.
[11] C.J. Seeton, Viscosity–temperature correlation for liquids, Tribol. Lett. 22 (April (1)) (2006).
[12] F. Lucklum, E.K. Reichel, B. Jakoby, Miniature Density-Viscosity Measurement Cell Utilizing Electrodynamic-Acoustic Resonator Sensors, Sensors Actuators A (2011), doi:10.1016/j.sna.2011.01.028.
[13] E.K. Reichel, et al., Modeling of the fluid-structure interaction in a fluidic sensor cell, Sens. Actuators A 156 (2009) 222–228, doi:10.1016/j.sna.2009.03.002.

[14] G. Habenicht, Kleben, Grundlagen, Technologien, Anwendungen 6, Auflage, Springer-Verlag, Berlin/Heidelberg, 2009.
[15] P.K. Yuen et al., Low-cost rapid prototyping of flexible microfluidic devices using a desktop digital craft cutter, Lab on a Chip, doi:10.1039/b918089c (technical note, www.rsc.org/loc).
[16] T. Voglhuber, et al., Semi-numerical simulation of a miniaturized vibrating membrane rheometer, in: Proc. Sensor 2009 Conference, vol. 1, Nuremberg, Germany, May 26–28, 2009, pp. 41–46.

Biographies

Martin Heinisch obtained his Dipl.-Ing. (M.Sc.) in mechatronics from Johannes Kepler University Linz, Austria, in 2009. After his master studies he went to the University of California, Los Angeles (U.C.L.A.) as a Marshall Plan Scholarship grantee, where he did research in the field of microfluidic applications and self assembling systems. In 2010 he started a Ph.D. program at the Institute of Microelectronics and Microsensors of the Johannes Kepler University Linz, Austria where he is currently working on resonating liquid sensors.

Erwin K. Reichel was born in Linz, Austria, in 1979. He received the Dipl.-Ing. (M.Sc.) degree in mechatronics from Johannes Kepler University, Linz, Austria, in 2006. From 2006 to 2009 he was working on the Ph.D. thesis at the Institute for Microelectronics and Microsensors of the Johannes Kepler University, Linz. In 2009 he obtained his doctoral (Ph.D.) degree and now holds a Post-Doctoral position at the Centre for Surface Chemistry and Catalysis, KU Leuven, Belgium. The main research fields are the modeling, design, and implementation of sensors for liquid properties, and monitoring of phase transition in complex solutions.

Isabelle Dufour graduated from Ecole Normale Supérieure de Cachan in 1990 and received the Ph.D. and H.D.R. degrees in engineering science from the University of Paris-Sud, Orsay, France, in 1993 and 2000, respectively. She was a CNRS research fellow from 1994 to 2007, first in Cachan working on the modeling of electrostatic actuators (micromotors, micropumps) and then after 2000 in Bordeaux working on microcantilever-based chemical sensors. She is currently Professor of electrical engineering at the University of Bordeaux and her research interests are in the areas of microcantilever-based sensors for chemical detection, rheological measurements and materials characterisation.

Bernhard Jakoby obtained his Dipl.-Ing. (M.Sc.) in communication engineering and his doctoral (Ph.D.) degree in electrical engineering from the Vienna University of Technology (VUT), Austria, in 1991 and 1994, respectively. In 2001 he obtained a venia legendi for theoretical electrical engineering from the VUT. From 1991 to 1994 he worked as a Research Assistant at the Institute of General Electrical Engineering and Electronics of the VUT. Subsequently he stayed as an Erwin SchrÃdinger Fellow at the University of Ghent, Belgium, performing research on the electrodynamics of complex media. From 1996 to 1999 he held the position of a Research Associate and later Assistant Professor at the Delft University of Technology, The Netherlands, working in the field of microacoustic sensors. From 1999 to 2001 he was with the Automotive Electronics Division of the Robert Bosch GmbH, Germany, where he conducted development projects in the field of automotive liquid sensors. In 2001 he joined the newly formed Industrial Sensor Systems group of the VUT as an Associate Professor. In 2005 he was appointed Full Professor of microelectronics at the Johannes Kepler University Linz, Austria. He is currently working in the field of liquid sensors and monitoring systems.

Sensors and Actuators A 186 (2012) 111–117

Contents lists available at SciVerse ScienceDirect

Sensors and Actuators A: Physical

journal homepage: www.elsevier.com/locate/sna

Tunable resonators in the low kHz range for viscosity sensing

M. Heinisch[a], E.K. Reichel[b], I. Dufour[c], B. Jakoby[a]

[a] Institute for Microelectronics and Microsensors, Johannes Kepler University, Linz, Austria
[b] Center for Surface Science and Catalysis, Katholieke Universiteit Leuven, Belgium
[c] Université de Bordeaux, Laboratoire de l'Intégration du Matériau au Système, France

ARTICLE INFO

Article history:
Received 26 October 2011
Received in revised form 4 March 2012
Accepted 5 March 2012
Available online 28 March 2012

Keywords:
Viscosity
Mass density
Sensor
Frequency
Lorentz forces

ABSTRACT

This contribution gives an overview of the design and development of miniaturized, tunable resonating viscosity sensors in the low kHz range incorporating first modeling approaches as well as experimental results. The effect of different designs, potential improvements in the setups as well as the effect of cross sensitivities are discussed and outlined.

© 2012 Elsevier B.V. All rights reserved.

1. Introduction

Miniaturized viscosity sensors are attractive devices for condition monitoring applications involving fluid media. Most recently introduced devices utilize vibrating resonant mechanical structures interacting with the fluid where the resonant behavior i.e., resonance frequency and quality factor, is affected by the fluid's mass density and viscosity [1,2]. So far, the ability of tuning the resonance frequency of such devices in a larger frequency range has hardly been reported. However, such a feature is highly desirable particularly when investigating complex liquids showing viscoelastic behavior. We devised two different types of resonating viscosity sensors with tunable resonance frequencies in a range of over two octaves for a fixed geometry. Analytical models relating measured data to the viscosity of the examined liquid have been presented earlier together with first measurement data where we briefly discussed the benefits of different geometries in terms of high tunability and their sensitivity to viscosity [3–5].

Complex fluids often show viscoelastic behavior which means that they exhibit a significant frequency dependence in their shear modulus (whose imaginary part is related to the shear viscosity) when using oscillatory rheometers. Laboratory rheometers work in a limited frequency range not exceeding typically 100 Hz and commonly, they are not suitable for online monitoring applications as they are expensive and maintenance intensive e.g., due to macroscopically moving parts involving bearings etc. Miniaturized devices sensing viscosity in the MHz range have been discussed extensively in the past, e.g. thickness shear mode resonators [6]. Between these devices, providing a "high-frequency viscosity" and the aforementioned laboratory viscometers is a gap, which we are aiming to bridge with devices as presented in this contribution. Recently, we proposed a design for a tunable in-plane resonating sensor for viscosity [3]. As an alternative, a single wire device has been investigated [4]. Both types of these resonating sensors provide a large range of achievable resonance frequencies of over two octaves up to ~4 kHz for our first devices with a fixed vibrating length of ~3 cm. The tuning of the resonance frequency is achieved by the variation of tensile stresses in the wires by an appropriate tensioning mechanism.

These and previously reported sensors (e.g., [7]) underlie the same principles of actuation and read out, namely actuation by means of Lorentz forces F_L and read out via the motion induced voltage V_M, where

$$dF_L = I_{in}\, B\, dl_a \tag{1}$$

(A preceeding d indicates the differential of a quantity, I_{in}: sinusoidal input (driving) current, B: magnetic flux density provided by a permanent magnet (assembly), l_a: length of the electrical conductive path used for actuation) and

$$dV_M = v\, B\, dl_{ro} \tag{2}$$

(v: velocity of the electrical conductive path used for read out, l_{ro}: length of the readout path). Here, orthogonality of the direction of the current flow, B and v was assumed.

The motion induced voltage is the quantity representing the resonator's movement in the fluid-structure interaction which is thus related to the fluid's dynamic viscosity for a known mass density (and vice versa).

0924-4247/$ – see front matter © 2012 Elsevier B.V. All rights reserved.
doi:10.1016/j.sna.2012.03.009

This contribution explains the principles and the physical relations by means of closed form models of the suspended plate and the wire viscometer in Sections 2 and 3, respectively. Section 4 briefly shows experimental results revealing both sensors' response and sensitivity to viscosity. The following section focuses on the tunability of the resonance frequencies of both resonators, see Section 5. Based on these first feasibility concepts discussed in the aforementioned sections, this work is extended by several (indispensable) improvement strategies effecting higher readout signals and more reliable setups allowing for more accurate sensing, see Section 6.

2. Suspended plate viscometer

2.1. Setup

The principle of the suspended plate viscometer which is fully surrounded by the sample liquid is depicted in Fig. 1(a). A small platelet which is suspended by two wires is forced to lateral vibrations by means of Lorentz forces on AC-currents in the excitation wire. This in-plane fluid-structure interaction of the platelet with the surrounding liquid is recorded via the motion induced voltage in the second wire which follows the movement of the platelet (and the excitation wire). Note that there are a lot of other modes of vibrations featuring out of plane displacements. As the magnetic field is not perfectly aligned and not perfectly uniform, these spurious modes will also be excited to a certain extent. The minor ripple at around 1.6 kHz in Fig. 1(c) is supposedly related to such a spurious out of plane vibration.

Varying the tensile stresses within both wires by tensioning with micrometer screws, see Section 5 allows for setting the desired resonance frequency.

In first setups, 3 cm long and 100 μm thick wires were used. The used material was tungsten which features a high ultimate strength exceeding 1.5 GPa. For the 3 × 3 mm platelets, glass or PET was used which yielded both good results and mainly differed in the fabrication technique, see [3]. The results shown in Section 4 were obtained with the aforementioned dimensions using PET for the platelet.

Regarding large scale production and easy manufacturing, similar designs have also been fabricated using 100 μm thick nickel brass metal sheets and wet etching. Their tunability was briefly investigated but has not been published yet. Types of these resonating platelets are reported e.g., in [8,9].

2.2. Semi lumped element model

As the platelet's lateral dimensions are much larger than its thickness and as its surface A is much larger than the wire's surfaces, boundary effects emerging from displacement of the liquid at the platelets front sides as well as the flow around the wires are not taken into account here. The equation of motion for the mechanical oscillator as it is depicted in Fig. 1(b) is

$$m\frac{\mathrm{d}^2 u_\mathrm{x}(t)}{\mathrm{d}t^2} = F_\mathrm{L} - F_\mathrm{F} - r_0\frac{\mathrm{d}u_\mathrm{x}(t)}{\mathrm{d}t} - k_0 u_\mathrm{x}(t) \tag{3}$$

which then is transformed to the frequency domain.

The fluid forces F_F acting on the platelet which can be given in terms of the shear stress T

$$F_\mathrm{F} = -2\,T(z=0)A \tag{4}$$

are modeled by one-dimensional shear wave propagation, where the shear stress is (using complex notation assuming time dependence $e^{j\omega t}$) [3,6]

$$T(z=0) = u_\mathrm{x}(\omega)(1-j)\sqrt{\frac{\mu\,\rho\,\omega^3}{2}} \tag{5}$$

With this, the transfer function of the mechanical oscillator, which is the quotient of displacement in x-direction u_x and Lorentz forces can be written as (see also Fig. 1(b) and Eq. 1)

$$G_\mathrm{m}(\omega) = \frac{u_\mathrm{x}(\omega)}{F_\mathrm{L}(\omega)} \tag{6}$$

$$= \frac{1}{-\omega^2\left(m + A\sqrt{\frac{\mu\rho}{2\omega}}\right) + j\,\omega\left(r_0 + A\sqrt{\frac{\mu\rho\omega}{2}}\right) + k_0} \tag{6}$$

Finally, the motion-induced voltage (see Eq. 2) in the pickup wire can be written as follows

$$V_\mathrm{M} = j\,\omega\,G_\mathrm{m}\frac{B^2\,l_\mathrm{a}^* l_\mathrm{ro}^*}{R_1}\,V_\mathrm{in} \tag{7}$$

here l_a^* and l_ro^* are the wire's effective lengths (which depend on the mode shape but are in the order of the actual length).

It may be necessary to consider the effect of electrical cross-talk in the measured voltage as well, see [10], which can be easily taken into account with

$$V_\mathrm{ct} = \frac{j\,\omega\,M}{R_1}\,V_\mathrm{in} \tag{8}$$

where M is the mutual inductance describing the inductive coupling between excitation and read-out circuit. As the input resistance of the lock-in amplifier is 10 MΩ, it is assumed that $I_\mathrm{out} \approx 0$ and thus the total amount of output voltage is given by

$$V_\mathrm{out} = V_\mathrm{M} + V_\mathrm{ct} \tag{9}$$

A comparison between this simple (fitted) model and measured data for isopropanol is shown in Fig. 1(c). In this fit procedure, the reference values of the liquid's ρ and μ have been used and the model-parameters r_0, k_0 and m have been fitted.

3. Wire viscometer

Resonating viscometers using a single wire only, are known as wire viscometers in literature [11–13]. These viscometers were designed to be operated at one fixed resonance frequency only. In our work, we focus on the investigation of tuning the resonance frequencies of the vibrating sensors within a preferentially large range and focus on miniaturized devices.

3.1. Setup

Fig. 2(a) shows a schematic sketch of the wire viscometer. A tungsten wire is stretched over two electrical conductive blades. For first (test) setups, these blades, determining the vibrating length and assuring for electrical contact, were made of PCB (copper coated fiberglass) which were later replaced by machined metal blades, see Section 6. The series resistor limits the excitation current to avoid non linear effects such as e.g., Duffing behavior, see [13]. For measurements in air about 10 kΩ and in liquids, resistors between 50 Ω and 1 kΩ were used. The external magnetic field was generated with different NdFeB magnet assemblies yielding magnetic flux densities from 0.3 T up to 1.4 T, see [14].

3.2. Modeling

For the modeling of the wire viscometer, the transversal movements $w(x,t)$ of the wire subjected to an axial force N, driving

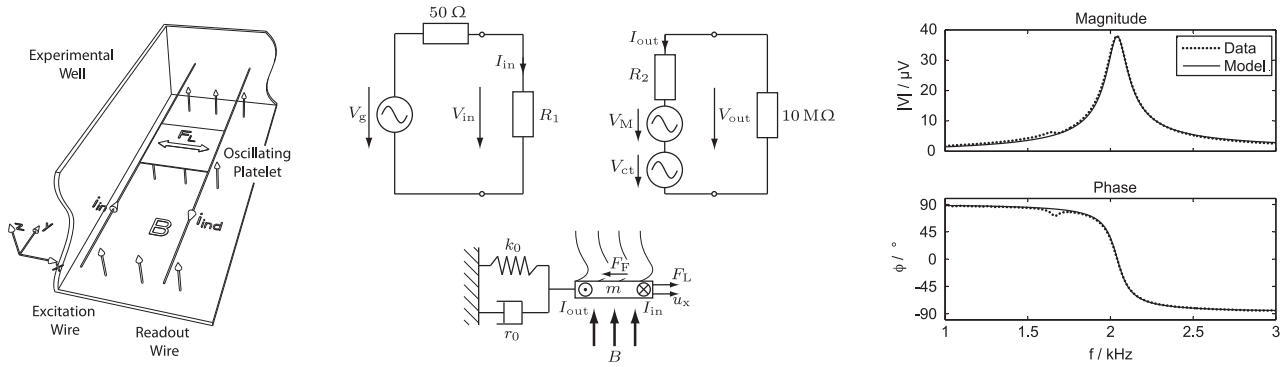

(a) Suspended Plate Viscometer (b) Semi lumped element model (c) Frequency response

Fig. 1. In (a) a schematic drawing of the suspended plate rheometer is depicted. The sensor, surrounded by an experimental well, consists of two parallel wires (placed in external field **B**) and a small platelet. In this figure, the left wire is used for exciting lateral vibrations by means of Lorentz forces. The second wire on the right used for pick-up, is coupled to the excitation wire with a rigid plate, thus following the movement of the left wire which effects an induced voltage which is used as read-out. By changing the tensile stresses in the wires, the resonance frequency can be changed. In (b) the scheme of the modeling approach is depicted. The upper figure shows the electrical equivalent circuit consisting of two galvanically isolated circuits representing the excitation and read-out circuits. (V_g: voltage of the function generator, 50 Ω: Internal resistance of the function generator, R_1: resistance of the excitation wire, R_2: resistance of the pick-up wire, V_M: motion induced voltage, V_{ct}: induced voltage trough electrical cross-talk, 10 MΩ: input resistance of the lock-in amplifier, I_{in}, I_{out}, V_{in}, V_{out}: input and output currents/voltages). The lower figure shows the mechanical lumped-element model. (k_0: intrinsic spring constant, r_0: intrinsic damping parameter, F_F: fluid forces, F_L: Lorentz forces, u_x: displacement in x-direction, B: external magnetic field). In (c) a comparison between measured data (in this case for isopropanol) and the model obtained by fitting the parameters from Eq. 7 is shown. (a) Suspended plate viscometer. (b) Semi lumped element model. (c) Frequency response.

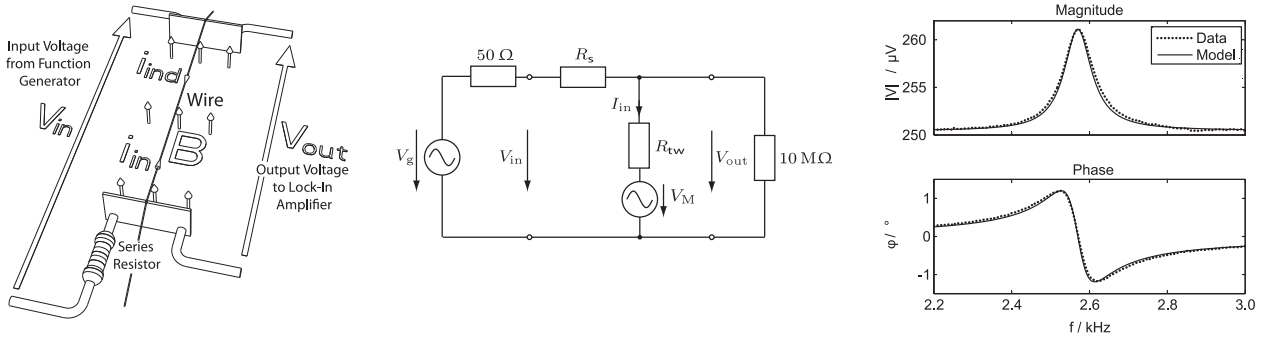

(a) Wire Viscometer (b) Model (c) Frequency response

Fig. 2. In (a) the schematic drawing of the wire viscometer is depicted. The experimental well for investigating sample liquids is not shown in this sketch. A 100 µm thick tungsten wire carrying sinusoidal currents is placed in an external magnetic field and thus oscillating due to Lorentz forces. For excitation, a function generator is used for the input signal. A series resistors is used to limit the excitation current. The motion induced voltage (i.e., the read-out signal) is measured with a lock-in amplifier. The resonance frequency can be changed by (mechanically) changing the tensile stresses in the wire. In (b) the electrical equivalent circuit of the wire viscometer is illustrated. (R_s: series resistor to limit the excitation current, R_{tw}: resistance of the tungsten wire). In (c) a comparison between measured data (in this case for isopropanol) and the model obtained by fitting the parameters from Eq. 14 is shown. (a) Wire viscometer. (b) Model. (c) Frequency response.

Lorentz forces F_L and the loading of the fluid forces F_F can be described by the following linear, inhomogenous, partial differential equation in time domain [15,16]:

$$E I \frac{\partial^4 w(x,t)}{\partial x^4} - N \frac{\partial^2 w(x,t)}{\partial x^2} + m' \frac{\partial^2 w(x,t)}{\partial t^2} \tag{10}$$

$$= F'_L(x,t) + F'_F(x,t) \tag{10}$$

(E: Young's modulus, I: second moment of area, m: wire's mass, $'$: quantity in respect of unit length)

Eq. 10 is transformed to the frequency domain again assuming a time dependence $e^{j\omega t}$ and the forces per unit length on the right hand side of Eq. 10 acting on the wire are substituted by the following expressions

$$F'_L = I_{in}(\omega) B \tag{11}$$

(I_{in}: input current, B: flux density of the external magnetic field which is provided by a permanent magnet)

From [17–19] the fluid forces acting on a circular cylinder are calculated as follows:

$$F'_F(x,\omega) = \tag{12}$$

$$\pi \rho_f \omega^2 r^2 \left(1 - \frac{4 j K_1\left(j\sqrt{-j Re}\right)}{\sqrt{-j Re}\, K_0\left(j\sqrt{-j Re}\right)} \right) w(x,\omega) \tag{12}$$

$$\text{where} \qquad Re = \frac{\rho \omega r^2}{\mu} \tag{13}$$

(r: wire radius, K_0, K_1: modified Bessel functions, μ: dynamic viscosity)

After the analytical calculation of the deflection of the wire $w(x,\omega)$, the induced voltage is calculated as follows:

$$V_{out} = j \omega B \int_0^l w(x,\omega)\, dx + R_{tw} I_{in}(\omega) \tag{14}$$

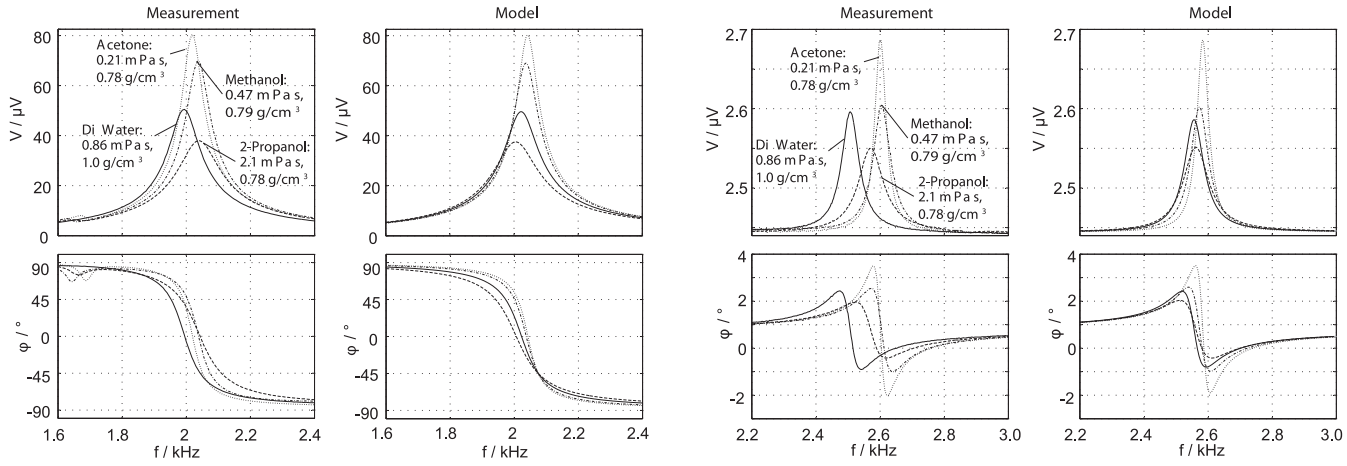

(a) Suspended Plate:3 cm x 100 µm tungsten wires, 3x3 mm PET platelet

(b) Wire Viscometer: 3 cm x 100 µm tungsten wire

Fig. 3. In both figures the sensors measured and theoretical frequency responses including the fundamental harmonic in four different liquids are illustrated (Excitation voltage V_g=0.5 V). For both sensors, clearly, it is visible that higher viscosities yield higher damping. The effect of the viscosity and the mass density on the resonance frequency shift can be observed in the according theoretical frequency responses. The deviation in the resonance frequencies between model and experiment are mainly caused by undesired de-tuning of the sensor. (a) Suspended plate: 3 cm × 100 µm tungsten wires, 3 × 3 mm PET platelet. (b) Wire viscometer: 3 cm × 100 µm tungsten wire.

(l: wire length, R_{tw}: wire ohmic resistance). The first term corresponds to the motion induced voltage Eq. 7. Fig. 2(c) shows a comparison of measurement data and a fit of this model.

4. Response to viscosity

From the resonant behavior which is monitored by the motion induced voltage in the wire the viscosity of a sample liquid is determined (knowing the liquid's mass density).

The effect of different viscosities on the resonant behavior was examined by recording the frequency response including the fundamental mode in four different liquids. The selected liquids have only small differences in their viscosity, ranging from 0.21 mPa s to 2.1 mPa s to investigate the sensitivity to viscosity. The used liquids were acetone, methanol, isopropanol and DI-water, see Fig. 3. The indicated reference values for viscosity and mass-density were measured with a Stabinger Viscometer (SVM 3000) at 25 °C.

For the measurements in this study, we observed shifts in the resonance frequencies, see Fig. 3, which are mainly not caused by the different physical properties of the liquids but by de-tuning of the sensor (e.g., from thermal stresses, slacking of the entire setup, etc.). However the liquid's physical properties (theoretically) have a significant effect on the shift of the resonance frequency which can nicely be observed in the theoretical frequency responses in Fig. 3. From these theoretical frequency responses it can also be seen, that the wire viscometer is more sensitive to mass density than the suspended plate sensor. (Compare the theoretical frequency responses of water, which has a higher mass density than the examined solvents.)

For obtaining these theoretical frequency responses, the models described in Sections 2.2 and 3.2 were compared to the four measured frequency responses. In the theoretical evaluation of the wire viscometer and the suspended plate sensor the normal stresses and the intrinsic spring constant, respectively, were kept constant to show the effect of the physical properties on the frequency shift.

Based on the insights gained with these measurements, we aim at setups yielding stable resonance frequencies, see discussion in Section 6, for accurate and reliable sensing.

4.1. Discussion and comparison

For a rough estimate, to compare the sensors' sensitivity to viscosity, we evaluated the Q-factors detecting the maximum (at $f=f_r$) and −3 dB values (at $f=f_-$ and $f=f_+$, respectively) in the magnitude

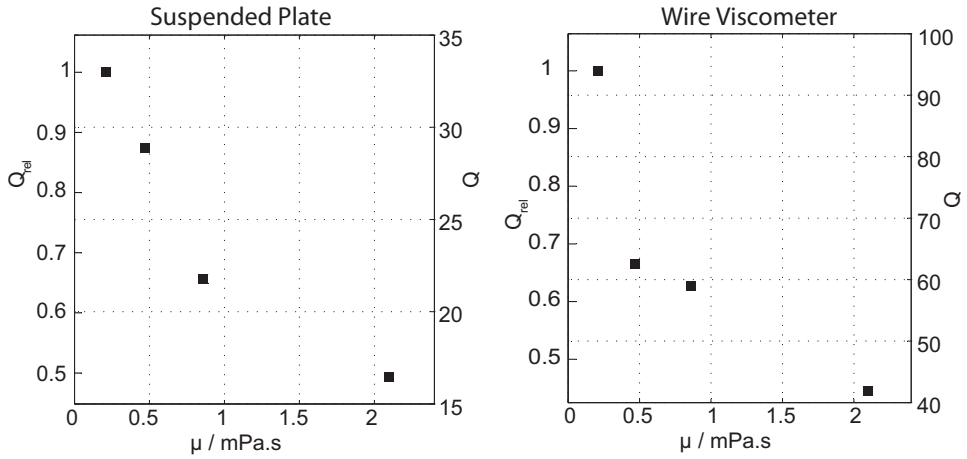

Fig. 4. Comparison of the Q-factor. For both sensors, the relative and the absolute values are indicated. The relative values are in respect to the highest value of the according measurement. In the investigated range, both sensors show a similar sensitivity to viscosity.

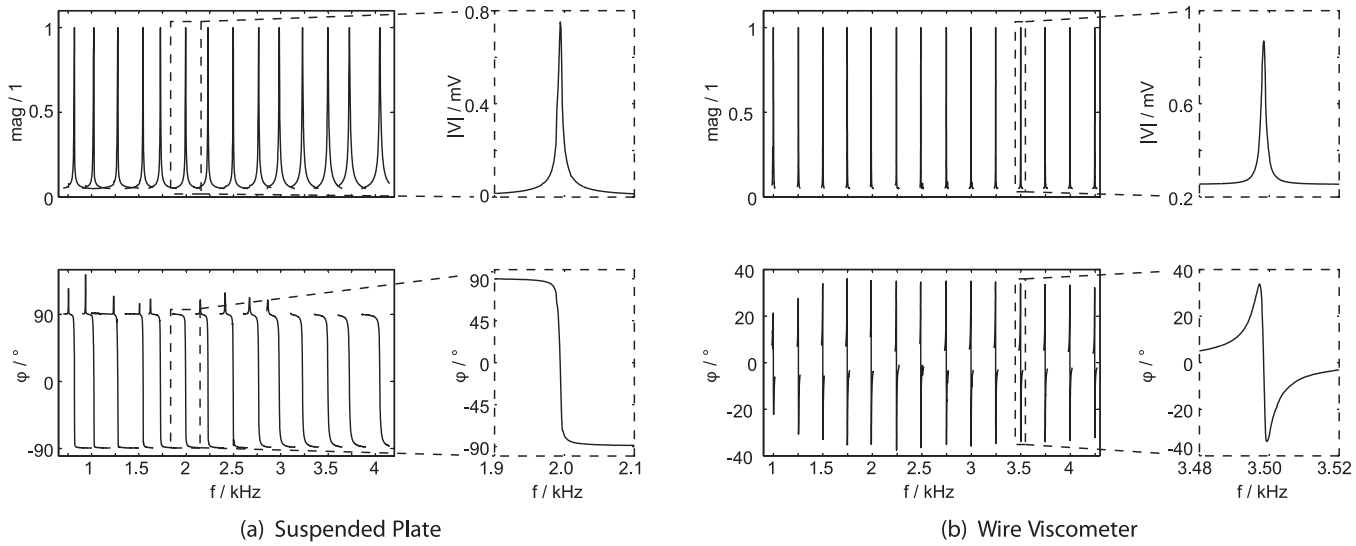

Fig. 5. In both figures the band width of achievable resonance frequencies (in air) using 3 cm long and 100 μm thick tungsten wires are illustrated. In each case a detailed view of one characteristic resonance is depicted as well. In case (b) (wire viscometer) higher quality factors are obtained. (Note that the bandwidths in the detailed views are 40 Hz for the wire viscometer and 200 Hz for the suspended plate rheometer.) The obtained resonances in first measurements go from 1000 Hz to 4250 Hz in case of the wire viscometer and from 820 Hz to 4040 Hz for the suspended plate rheometer. In both cases, for changing the resonance frequencies for these measurements, the normal stresses in the wires were varied by tensioning the wires with micro-stages with micrometer screws. These figures serve to illustrate the basic mechanism. The detailed characteristic resonance frequency versus tensile stresses are shown in Fig. 6(b). (a) Suspended Plate. (b) Wire viscometer.

of the frequency response when the sensors were immersed in the different sample liquids yielding $Q = f_r/(f_+ - f_-)$. Both sensors show a similar sensitivity to viscosity when evaluating their quality factors in the examined range of viscosity, see Fig. 4. We note that with the wire viscometer, in principle, it is possible to measure both, mass density and viscosity with a single measurement only, however, with restricted accuracy [12]. The sensitivity of the wire viscometer to mass density can be observed in the theoretical frequency response in Fig. 3(b). There, the shift of the resonance frequency is mainly affected by the mass density which is nicely visible for the case of water which has a higher mass density than the other examined liquids.

5. Tunability of the resonance frequency

To show the capability of the tuning of the resonance frequency the normal stresses in the wires were changed by tensioning the wires with micro-stages with micrometer screws. With this method it is difficult to set a prescribed tension. We instead applied a certain tension by adjusting the micrometer screw and determined the resulting resonance frequency in the measurement. Like stringed instruments, the setup is subject to detunig effects. This disadvantage can be overcome by presetting a mechanical tension, see below for the case of the vibrating wire. In first experiments in air resonances between 1000 Hz and 4250 Hz in case of the wire viscometer and 820 Hz and 4040 Hz in case of the suspended plate rheometer were achieved, see Fig. 5, [4]. The intention of these experiments was to monitor the frequency range of measurable resonances. The integration of the tensioning mechanism in the microsensor as well as the investigation of the applicability to characterize frequency dependent liquid behavior will be subject of our future research.

With a second experiment, see Fig. 6(a), we wanted to further investigate the achievable tunable range with known normal stresses for the case of an oscillating wire. For presetting the normal stresses in the wire we attached several weights to the wire, see e.g., Fig. 6(a). Fig. 6(b) shows the results of experiments for a 47 μm thick tungsten wire with a constant length $l = 30$ mm for different normal stresses in the wire. There, the results of two different types of wire clamping are compared. 'Pinned' corresponds to the setup as it is depicted in Figs. 6(a) and 7(b), where 'clamped' corresponds to Fig. 7(c). The solid black line in Fig. 6(b) was obtained by the equation for the resonance frequency of a string with radius r, length l, preset normal stresses T_N and mass density ρ [15]

$$f_r = \frac{1}{2l}\sqrt{\frac{T_N}{\rho}}. \tag{15}$$

Note that for obtaining good accordance of the measured resonance frequencies with the theoretical values, the wire's nominal diameter of 47 μm was changed to 49 μm in our calculations.

These results show the same range of resonance frequencies as in the first experiment, c.f., Fig. 5(b). Fig. 6(c) shows the (theoretically) total achievable range of resonance frequencies when changing the normal stresses as well as the wire's vibrating length for a 100 μm thick tungsten wire with the limiting factors $L = 10 \ldots 30$ mm and $T_N = 0 \ldots 1.4$ GPa. This range has been verified experimentally and good accordance was observed.

6. Improved setups using the wire viscometer as example

6.1. Reducing cross sensitivities

The previous sections showed a proof of concept of both types of sensors. They are well applicable for viscosity sensing and can be detuned in a range of over one decade. However, from the first experiments, it became clear that several improvements have to be achieved, which we want to discuss for the example of the wire viscometer. In this contribution we focus on the discussion on improving the stability of the resonance frequency (once it is set to a desired value). In [14] a discrete permanent magnet assembly is presented yielding a flux density of 1.2 T in a 4 mm airgap, which drastically improves the magnitude of the read-out signal.

6.2. Reducing instabilities in the resonance frequency

We investigated three different types of wire clamping, see Fig. 7, in the laboratory during 25 h recording the ambient

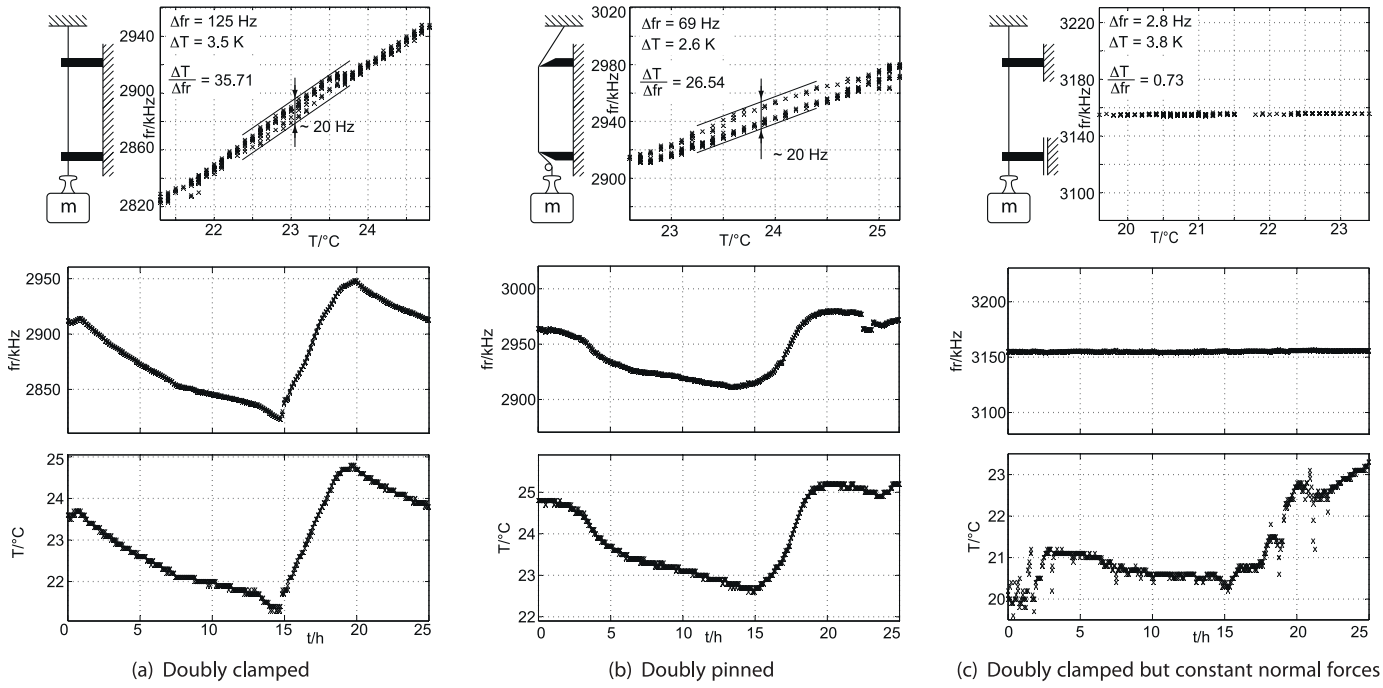

Fig. 6. In (a) a setup of the wire viscometer allowing for changing both, the normal stresses in the wire as well as its length is depicted. A tungsten wire is placed in an external magnetic field (not depicted; perpendicular to the wire). The conductive blades allow for electrical contact and for changing the wire's vibrating length. One end of the wire is rigidly affixed. The other is attached to a weight, which is varied for changing the normal stresses in the wire but keeping the normal stresses constant when changing the vibrating length. (b) Comparison of measured and theoretic resonance frequencies for different normal stresses N. The solid line shows the theoretic results obtained by using the given material parameters. In (c) the results from a theoretical estimation of achievable resonance frequencies, when changing the normal stresses as well as the wire's vibrating length for a 100 μm thick tungsten wire with $L = 10 \ldots 30$ mm and $T_N = 0 \ldots 1.4$ GPa is depicted. (Tungsten has a yield stress of 1.5 GPa, approximately.) (a) Setup. (b) Resonance frequencies. (c) Theoretic achievable range.

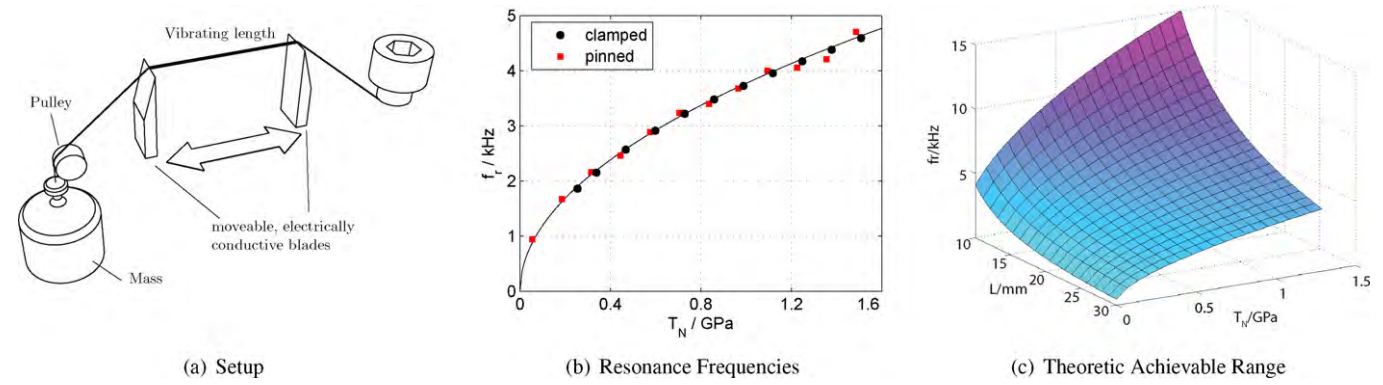

Fig. 7. Effect of three different types of wire clamping on the resonance frequency. For each case the resonance frequency over temperature as well as resonance frequency and temperature over time is plotted. (a) Doubly clamped. (b) Doubly pinned. (c) Doubly clamped but constant normal forces.

temperature to study the range of resonance frequency changes under (randomly) varying conditions in a non-air-conditioned room.

For the first case (Fig. 7(a)) in which the wire was rigidly and doubly clamped, we expected high shifts of the resonance frequency due to thermal stresses resulting from the different thermal expansion coefficients of the used materials. The problematic characteristic of setup (a) is not only this high temperature dependency but that for a given temperature there is a spurious variation of resonance frequencies of about 20 Hz for one and the same device. Thus, the idea was to keep the normal stresses constant by pinning the wire instead of clamping, see Fig. 7(b). However, in this case, there is still a relatively large temperature dependency which can only be explained with friction forces between the blades and the wire, c.f. discussion in Section 5. Here, also a significant hysteresis can be observed within a temperature cycle. In the third setup, see Fig. 7(c) an almost frictionless linear stage was used to keep the normal stresses in the clamped wire as constant as possible. With this setup the variation of the resonance frequency is less than 3 Hz and mainly not dependent on the ambient temperature.

7. Conclusion

This work shows the feasibility of measuring viscosity with both presented sensors at tunable resonance frequencies. For the case of the wire viscometer an improved setup has been found allowing for stable resonance frequencies. Furthermore, first closed-form models have been developed which can be fitted into the measured data with high accuracy. Regarding future work, the stability of both sensors has to be investigated and most likely,

improved with more sophisticated setups. For this investigation large measurement series with multiple test liquids over a long period of time have to be carried out.

Acknowledgement

We are indebted to the Austrian Center of Competence in Mechatronics (ACCM) for the financial support.

References

[1] B. Jakoby, R. Beigelbeck, F. Keplinger, F. Lucklum, A. Niedermayer, E. Reichel, C. Riesch, T. Voglhuber-Brunnmaier, B. Weiss, Miniaturized sensors for the viscosity and density of liquids-performance and issues, ITUCER 57 (1) (2010), doi:10.1109/TUFFC.2010.1386.
[2] C. Riesch, E. Reichel, A. Jachimowicz, J. Schalko, P. Hudek, B. Jakoby, F. Keplinger, A suspended plate viscosity sensor featuring in-plane vibration and piezoresistive readout, Journal of Micromechanics and Microengineering 19 (2009), doi:10.1088/0960-1317/19/7/075010.
[3] M. Heinisch, E. Reichel, B. Jakoby, A suspended plate in-plane resonator for rheological measurements at tunable frequencies, in: Proceedings of Sensor +Test, 2011, pp. 61–66.
[4] M. Heinisch, E. Reichel, B. Jakoby, A study on tunable resonators for rheological measurements, in: Proceedings of SPIE, Vol. 8066, 2011, doi:10.1117/12.887103.
[5] M. Heinisch, E. Reichel, I. Dufour, B. Jakoby, Miniaturized resonating viscometers facilitating measurements at tunable frequencies in the low khz-range, in: Proceedings of Eurosensors, 2011.
[6] S. Martin, V.E. Granstaff, G.C. Frye, Characterization of a quartz crystal microbalance with simultaneous mass and liquid loading, Analytical Chemistry 63 (1991) 2272–2281.
[7] M. Heinisch, E. Reichel, I. Dufour, B. Jakoby, A resonating rheometer using two polymer membranes for measuring liquid viscosity and mass density, Sensors and Actuators A: Physical (2011), doi:10.1016/j.sna.2011.02.031.
[8] E. Reichel, C. Riesch, F. Keplinger, C. Kirschhock, B. Jakoby, Analysis and experimental verification of a metallic suspended plate resonator for viscosity sensing, Sensors and Actuators A: Physical 162 (2010) 418–424, doi:10.1016/j.sna.2010.02.017.
[9] E. Reichel, J. Vermant, B. Jakoby, C. Kirschhock, Shear wave sensors for viscoelastic properties, in: Procedia Engineering, Vol. 5, 2010, pp. 1316–1319, doi:10.1016/j.proeng.2010.09.356.
[10] M. Heinisch, E. Reichel, B. Jakoby, A feasibility study on tunable resonators for rheological measurements, in: Proceedings of GMe Forum, 2011, pp. 85–89.
[11] T. Retsina, S.M. Richardson, W.A. Wakeham, The theory of a vibrating-rod viscometer, Applied Scientific Research 4 (1986) 325–346, doi:10.1007/BF00540567.
[12] D. Seibt, Schwingdrahtviskosimeter mit integriertem ein-senkkörper-dichtemessverfahren für untersuchungen an gasen in größeren temperatur- und druckbereichen, Ph.D. thesis, Universität Rostock (2007).
[13] M. Sullivan, C. Harrison, A. Goodwin, K. Hsu, S. Godefroy, On the nonlinear interpretation of a vibrating wire viscometer operated at large amplitude, Fluid Phase Equilibria 276 (2009) 99–107, doi:10.1016/j.fluid.2008.10.017.
[14] M. Heinisch, E. Reichel, I. Dufour, B. Jakoby, Tunable miniaturized viscosity sensors operating in the kHz-range, in: Proceedings of IEEE Sensors, 2011.
[15] W. Weaver, S. Timoshenko, D. Young, Vibaration Problems in Engineering, 5th ed., Wiley, 1990.
[16] M. Elwenspoek, R. Wiegerink, Mechanical Microsensors, Springer-Verlag, 2001.
[17] L. Landau, E. Lifshitz, Fluid Mechanics, Butterworth-Heinemann, 1987.
[18] L. Rosenhead, Laminar Boundary Layers, Clarendon, Oxford, 1963.
[19] J. Sader, Frequency response of cantilever beams immersed inviscous fluids with applications to the atomic force microscope, Journal of Applied Physics 84 (1998) 64–76.

Biographies

Martin Heinisch obtained his Dipl.-Ing. (M.Sc.) in Mechatronics from Johannes Kepler University Linz, Austria, in 2009. After his Master studies he went to the University of California, Los Angeles (U.C.L.A.) as a Marshall Plan Scholarship grantee, where he did research in the field of microfluidic applications and self assembling systems. In 2010 he started a Ph.D. program at the Institute for Microelectronics and Microsensors of the Johannes Kepler University Linz, Austria where he is currently working on resonating liquid sensors.

Erwin K. Reichel was born in Linz, Austria, in 1979. He received the Dipl.-Ing. (M.Sc.) degree in mechatronics from Johannes Kepler University, Linz, Austria, in 2006. From 2006 to 2009 he was working on the Ph.D. thesis at the Institute for Microelectronics and Microsensors of the Johannes Kepler University, Linz. In 2009 he obtained his doctoral (Ph.D.) degree and now holds a post-doctoral position at the Centre for Surface Chemistry and Catalysis, KU Leuven, Belgium. The main research fields are the modeling, design, and implementation of sensors for liquid properties, and monitoring of phase transition in complex solutions.

Isabelle Dufour graduated from Ecole Normale Supérieure de Cachan in 1990 and received the Ph.D. and H.D.R. degrees in engineering science from the University of Paris-Sud, Orsay, France, in 1993 and 2000, respectively. She was a CNRS research fellow from 1994 to 2007, first in Cachan working on the modelling of electrostatic actuators (micromotors, micropumps) and then after 2000 in Bordeaux working on microcantilever-based chemical sensors. She is currently Professor of electrical engineering at the University of Bordeaux and her research interests are in the areas of microcantilever-based sensors for chemical detection, rheological measurements and materials characterisation.

Bernhard Jakoby obtained his Dipl.-Ing. (M.Sc.) in Communication Engineering and his doctoral (Ph.D.) degree in electrical engineering from the Vienna University of Technology (VUT), Austria, in 1991 and 1994, respectively. In 2001 he obtained a venia legendi for Theoretical Electrical Engineering from the VUT. From 1991 to 1994 he worked as a Research Assistant at the Institute of General Electrical Engineering and Electronics of the VUT. Subsequently he stayed as an Erwin Schrödinger Fellow at the University of Ghent, Belgium, performing research on the electrodynamics of complex media. From 1996 to 1999 he held the position of a Research Associate and later Assistant Professor at the Delft University of Technology, The Netherlands, working in the field of microacoustic sensors. From 1999 to 2001 he was with the Automotive Electronics Division of the Robert Bosch GmbH, Germany, where he conducted development projects in the field of automotive liquid sensors. In 2001 he joined the newly formed Industrial Sensor Systems group of the VUT as an Associate Professor. In 2005 he was appointed Full Professor of Microelectronics at the Johannes Kepler University Linz, Austria. He is currently working in the field of liquid sensors and monitoring systems.

Sensors and Actuators A 220 (2014) 76–84

Contents lists available at ScienceDirect

Sensors and Actuators A: Physical

journal homepage: www.elsevier.com/locate/sna

Reduced order models for resonant viscosity and mass density sensors

M. Heinisch[a,*], T. Voglhuber-Brunnmaier[a,b], E.K. Reichel[a], I. Dufour[c], B. Jakoby[a]

[a] Institute for Microelectronics and Microsensors, Johannes Kepler University, Linz, Austria
[b] Center for Integrated Sensors Systems, Danube University, Krems, Austria
[c] Université de Bordeaux, Laboratoire de l'Intégration du Matériau au Système, France

ARTICLE INFO

Article history:
Received 28 March 2014
Received in revised form 8 August 2014
Accepted 8 September 2014
Available online 2 October 2014

Keywords:
Lumped element model
Resonant sensor
Plate
Sphere
Cylinder
Tuning fork

ABSTRACT

A generalized reduced order model for resonant viscosity and mass density sensors is presented and experimentally verified. The reduced expressions for the resonance frequency and quality factor, respectively, are mathematically valid for in-plane oscillating plates, oscillating spheres and laterally oscillating cylinders. However, as shown for measurements obtained with a tuning fork resonator with rectangular cross-section, the model can also be applied for resonating structures, for which closed form solutions of the fluid structure interaction are not available. Benefits of the presented model are amongst others first, its simplicity, which requires no more than three calibration measurements for parameter identification and second, its general applicability for resonant mass density and viscosity sensors which furthermore facilitates the comparison of different resonant mass density and viscosity sensors in terms of sensitivity and measurement noise propagation.

© 2014 Elsevier B.V. All rights reserved.

1. Introduction

During the last two decades, there has been a remarkable interest in resonant viscosity and mass density sensors. As a matter of fact, this interest is still increasing which is substantiated by the large amount of publications associated with this field. Some of the incentives for resonant viscosity and mass density sensors are, amongst others, their reduced size compared to conventional instruments (down to the micrometer range), their relatively straightforward integrability in a process line or potentially low manufacturing costs [1]. Furthermore, from a rheological point of view, these devices allow measurements in a frequency range higher than conventional rheometers (about 100 Hz) up to the MHz range, which becomes especially interesting when investigating linear viscoelastic liquids for which measurements in the mentioned frequency range are scarcely available yet. Finally, for many resonant principles, miniaturized devices can be fabricated, and thus these sensors allow characterizing liquid samples for which only very few amounts (lower than 1 nL) are available [2].

The variety of reported designs and fabrication technologies is extremely diverse. Common principles include thickness shear mode oscillating quartz crystals, [3,4], quartz tuning forks [5] and singly [6] or doubly clamped beams [7] in silicon technology. Similar devices were also fabricated using wet-etched copper coated polymer sheets [8] or longitudinally vibrating PZT screen-printed cantilevers [9]. For frequencies between 100 Hz and 100 kHz and similar to doubly clamped beams, wire based sensors [10,11] were reported. Other principles also operating in the aforementioned frequency range include U-shaped cantilevers [12,13], membrane based devices [14,15] and in-plane oscillating platelets [16–18].

Concerning excitation and readout, the previously reported concepts cover most established principles used in MEMS technology. Recording the frequency responses of piezoelectric or piezoresistive devices [6,9,19], is a very common technique. In [20] a capacitive readout principle was reported. Electromagnetic principles allow high driving forces and large deflections [21] as well as measuring the frequency response by recording a motion induced voltage [14] at the same time. In [22–24] thermally actuated devices are discussed which allow an in-plane oscillation of the particular device. Optical readout using e.g. a laser vibrometer [25] is a further very common technique, though hardly suitable for integration in a sensor device used in the industrial field and only applicable for transparent liquids. Due to their high accuracy in deflection measurements, laser vibrometers are often used for the readout of miniaturized cantilever based setups e.g. in biosensing applications [26] in a laboratory environment. In [7] an optical readout using a DVD-pickup was implemented and in [27] a setup with a closed fluid cell using optical readout is presented. For all types of

* Corresponding author. Tel.: +43 73224686266.
E-mail address: martin.heinisch@jku.at (M. Heinisch).

http://dx.doi.org/10.1016/j.sna.2014.09.006
0924-4247/© 2014 Elsevier B.V. All rights reserved.

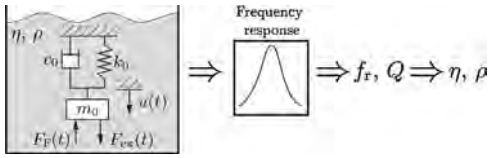

Fig. 1. Mechanical, lumped elements oscillator, immersed into a liquid. m_0: lumped mass, c_0: damping coefficient, k_0: spring constant, $u(t)$: displacement, $F_{ex}(t)$: excitation force, $F_F(t)$: fluid force, f_r: resonance frequency, Q: Quality factor, η: fluid's dynamic viscosity, ρ: fluid's mass density.

liquid sensors, closed setups are a basic requirement when aiming at accurate measurement results. Open setups usually involve evaporation of the liquid, which in turn is one of the sources for non-stable measuring conditions as the liquid's temperature varies due to evaporative cooling. This variation of temperature during the measurement involves mostly unknown changes of the resonator's mechanical parameters but also changes of the liquid's mass density and viscosity.

The principles which were discussed in the previous paragraphs have in common, that the devices' frequency responses, including a characteristic resonant mode, are recorded from which the sample liquid's mass density ρ and viscosity η are deduced. In many cases, resonance frequency f_r and quality factor Q are first evaluated, which are then related to the liquid's viscosity and mass density by an appropriate model, see Fig. 1. Depending on the particular resonator design, closed form models considering structural and fluid mechanics may become relatively complex demanding high modeling effort and computational power. Furthermore, the parameters in these models have to be identified with an appropriate parameter fit or the model might have to be completed by calibration functions which require additional calibration measurements, see e.g. [12]. In addition to this high modeling and calibration effort, there is a lack of a generalized model for resonant mass density and viscosity sensors which can be used as figure of merit and allowing for comparison of different sensor principles.

In this paper, a generalized reduced order model is presented, relating resonance frequency f_r and quality factor Q to mass density ρ and viscosity η. The equations for the latter have the form

$$f_r \approx \frac{1/(2\pi)}{\sqrt{m_{0k} + m_{\rho k}\,\rho + m^*_{\eta\rho k}\sqrt{\eta\,\rho}}} \quad \text{and}$$

$$Q \approx \frac{\sqrt{m_{0k} + m_{\rho k}\,\rho + m^*_{\eta\rho k}\sqrt{\eta\,\rho}}}{c_{0k} + c_{\eta k}\,\eta + c^*_{\eta\rho k}\sqrt{\eta\,\rho}}$$

which will be derived in the following. (m_{0k}, $m_{\rho k}$, $m^*_{\eta\rho k}$, c_{0k}, $c_{\eta k}$, $c^*_{\eta\rho k}$ are coefficients which can be determined with a parameter fit.) These generic equations can be derived for resonators where an infinitely thin, in-plane oscillating plate, an oscillating sphere or a laterally oscillating cylinder interact with the fluid. However, as it will be shown for measurements obtained with sensors e.g. with rectangular cross-section, this reduced order model can also be applied for geometries other than the aforementioned, for which analytical expression are not available or hardly accessible.

Assuming linearity for the mechanical oscillation, and thus small deflection amplitudes of the resonator [28], the investigated resonant mode is represented by a mechanical, lumped element oscillator, assuming validity of eigenmode decomposition. In the presented model, the fluid structure interactions are described in a reduced generalized expression, considering the well known equations for an in-plane oscillating plate, an oscillating sphere and a laterally oscillating cylinder. In this generalized model, any material or geometrical related parameters as well as any other factors are not explicitly considered but contained in single factors. Thereby, only the dependencies to mass density and viscosity remain in the derived expressions for the resonance frequency and the quality or damping factor. This basically allows the applicability of the model for any convexly shaped resonator, regardless of the implemented designs, materials or fabrication technologies as well as actuation and readout mechanisms.

Besides the simplicity of the model and its general applicability, a further big advantage is that only measurements in three calibration liquids are necessary to identify the model's coefficients. From every measurement f_r and Q are evaluated which then allows evaluating the six coefficients in the equations above. For resonant sensors whose identified model slightly deviates from the measurements, the model still can be used to approximately describe the sensor's characteristics and allows comparison with other principles which were identified with this generalized, reduced order model.

2. Lumped element approach

We consider a linear, mechanical oscillator, see Fig. 1, with lumped mass m_0, damping coefficient c_0 and spring constant k_0, being immersed in a liquid. The time dependent equation of motion with time variable t for the displacement u upon forced actuation with an excitation force F_{ex} and accounting for the influence of the liquid on the oscillation with a fluid related force F_F is

$$m_0 \frac{d^2u(t)}{dt^2} + c_0 \frac{du(t)}{dt} + k_0\,u(t) = F_{ex}(t) - F_F(t). \tag{1}$$

A harmonic excitation force with angular frequency ω and time dependence $e^{j\omega t}$ where $j = \sqrt{-1}$ is furthermore assumed. Thus, the equation of motion using the steady state velocity of the oscillation in the frequency domain $\underline{v}(\omega) = j\,\omega\,\underline{u}(\omega)$ reads

$$\left(c_0 + j\left(\omega\,m_0 - \frac{k_0}{\omega}\right)\right)\underline{v}(\omega) = \underline{F}_{ex}(\omega) - \underline{F}_F(\omega). \tag{2}$$

The force $\underline{F}_F$ induced by the fluid can be represented by a complex valued function of ω in the frequency domain. As the interaction will have a linear character for small vibration amplitudes it will be proportional to the velocity such that we can write

$$\underline{F}_F(\omega) = \underline{Z}_F(\omega)\,\underline{v}(\omega) \tag{3}$$

where we used the symbol $\underline{Z}_F$ for the proportionality factor as it resembles an acoustic impedance. $\underline{Z}_F(\omega)$ can be split in a real and imaginary part, $Z_{F,\Re}$ and $Z_{F,\Im}$, respectively. Intuitively, the interaction with the fluid will lead to an added mass (due to fluid mass moved in unison with the vibration) and to a damping due to viscous losses and radiated acoustic waves. The latter effect will lead to a real part of $\underline{Z}_F(\omega)$ while the mass entrainment corresponds to the imaginary part. This motivates to write the real part as

$$Z_{F,\Re} = c_f \tag{4}$$

and the imaginary part as

$$Z_{F,\Im} = \omega\,m_f, \tag{5}$$

where c_f represents the additional damping and m_f represents the added mass. If additional lumped mass were actually added to the lumped mass m_0 of the mechanical oscillator, m_f would represent this added mass. However, as it represents the fluid interaction of a distributed resonator, the terms m_f and c_f will, in general, be frequency dependent. Thus the fluid forces in the frequency domain can be written as

$$\underline{F}_F(\omega) = (c_f(\omega) + j\,\omega\,m_f(\omega))\,\underline{v}(\omega). \tag{6}$$

Just as the parameters of the lumped mass model (m_0, c_0, k_0), the frequency dependence of $m_f(\omega)$ and $c_f(\omega)$ can be moderate, though,

such that, if ω is close to the resonance frequencies, the values can be approximated by their values at the resonance frequency.

Introducing the above relation Eq. (6) in Eq. (2) we obtain the following spectral transfer function

$$\frac{\underline{v}}{\underline{F}_{ex}} = \frac{1}{c_0 + c_f(\omega) + j(\omega(m_0 + m_f(\omega)) - (k_0/\omega))}. \tag{7}$$

This frequency response can be compared to the standardized response of a second order system

$$\underline{H}_2(\omega) = \frac{A}{1 + jQ((\omega/\omega_0) - (\omega_0/\omega))} \tag{8}$$

where ω_0 represents the resonance frequency and Q the quality factor. Neglecting the frequency dependence of $\underline{Z}_F$ near resonance, the resonance frequency and the Q-factor of our model system can be readily identified. The resonance frequency is defined as the frequency where the above transfer function Eq. (7) becomes real-valued which yields an implicit equation for ω_0:

$$\omega_0(m_0 + m_f(\omega)) = \frac{k_0}{\omega_0}. \tag{9}$$

This equation could, e.g. be solved iteratively using the approximation $m_f(\omega) \approx m_f(\omega_{00})$ as a starting value for $m_f(\omega)$ where $\omega_{00} = \sqrt{k_0/m_0}$ is the resonance eigenfrequency for the unloaded resonator. For weak frequency dependence of $m_f(\omega)$ or small resonance frequency shifts, this first approximation may already be considered as sufficiently accurate (see also the discussion below for specific cases). With this simple approximation we find

$$\omega_0 \approx \omega_{01} = \sqrt{\frac{k_0}{m_0 + m_f(\omega_{00})}} \tag{10}$$

which represents the decrease of resonance frequency associated with the added mass as expected. ω_{01} is the approximated value for ω_0 after the first iteration. Similarly, for Q we find

$$Q \approx Q_1 = \frac{1}{\omega_0} \cdot \frac{k_0}{c_0 + c_f(\omega_{00})}. \tag{11}$$

The exact values for ω_0 and Q are

$$\omega_0 = \sqrt{\frac{k_0}{m_0 + m_f(\omega_0)}} \quad \text{and} \quad Q = \frac{1}{\omega_0} \cdot \frac{k_0}{c_0 + c_f(\omega_0)} \tag{12}$$

yielding an implicit equation for ω_0.

3. Fluid forces

3.1. In-plane oscillating plate

The shear stress $\underline{T}_p$ resulting from the in-plane oscillation of an infinitely extended plate in a viscous liquid with dynamic viscosity η and mass density ρ at the liquid–solid interface in the frequency domain reads [3,29]

$$\underline{T}_p = -(1 + j)\sqrt{\frac{\eta\rho\omega}{2}}\underline{v}. \tag{13}$$

The fluid forces acting on the plate with effective surface A_p are $\underline{F}_F = -\underline{T}_p A_p$. We call A_p effective surface, as this coefficient which might be determined by a data fit, considers not only the surface of wetted parts of a plane plate, but it might also consider geometrical imperfections such as slight surface roughnesses and plates with a finite thickness. Comparison of coefficients of the latter and Eq. (6) yields for the additional effective fluid mass and damping parameter in case of the in-plane oscillating plate

$$m_{f,p}(\omega) = \sqrt{\frac{\eta\rho}{2\omega}}A_p \quad \text{and} \quad c_{f,p}(\omega) = \sqrt{\frac{\eta\rho\omega}{2}}A_p \tag{14}$$

Introducing coefficients $m_{\eta\rho,p} = c_{\eta\rho,p} = A_p/\sqrt{2}$ used in the expressions for the added mass and damping parameters in case of the plate, Eq. (14) gives

$$m_{f,p}(\omega) = m_{\eta\rho,p}\sqrt{\frac{\eta\rho}{\omega}} \quad \text{and} \quad c_{f,p}(\omega) = c_{\eta\rho,p}\sqrt{\omega\eta\rho} \tag{15}$$

3.2. Oscillating sphere

The fluid forces acting on a sphere with radius r_s, oscillating with velocity $v(t)$ is [30]

$$F_{F,s} = 6\pi\eta r_s\left(1 + \frac{r_s}{\delta}\right)v(t) + 3\pi r_s^2\sqrt{\frac{2\eta\rho}{\omega}}\left(1 + \frac{2r_s}{9\delta}\right)\frac{\partial v(t)}{\partial t} \tag{16}$$

where

$$\delta = \sqrt{\frac{2\eta}{\omega\rho}} \tag{17}$$

is the so-called penetration depth.

Substituting Eq. (17) in Eq. (16), transformation to the frequency domain and comparison of coefficients with Eq. (6) yields

$$m_{f,s}(\omega) = 3\pi r_s^2\left(\sqrt{\frac{2\eta\rho}{\omega}} + \frac{2r_s}{9}\rho\right) \quad \text{and}$$

$$c_{f,s}(\omega) = 6\pi r_s\left(\eta + r_s\sqrt{\frac{\omega\eta\rho}{2}}\right). \tag{18}$$

Considering all coefficients and r_s in factors $m_{x,s}$ and $c_{x,s}$ used in the expressions for the fluid loading related additive mass and damping parameter in case of the sphere, Eq. (18) can be brought into the form

$$m_{f,s}(\omega) = m_{\rho,s}\rho + m_{\eta\rho,s}\sqrt{\frac{\eta\rho}{\omega}} \quad \text{and}$$

$$c_{f,s}(\omega) = c_{\eta,s}\eta + c_{\eta\rho,s}\sqrt{\omega\eta\rho}. \tag{19}$$

3.3. Oscillating cylinder

The fluid force per unit length $\underline{F}'_{F,c}$ on an oscillating cylinder with radius r_c, also given in [31–33], reads:

$$\underline{F}'_{F,c}(\omega) = -\pi\rho\omega^2 r_c^2\,\underline{\Gamma}_{cyl}\,\underline{u}(\omega) \tag{20}$$

with

$$\underline{\Gamma}_{cyl} = 1 + \frac{4K_1\left(\sqrt{jRe}\right)}{\sqrt{jRe}\,K_0\left(\sqrt{jRe}\right)} \tag{21}$$

where

$$Re = \frac{\rho\omega r_c^2}{\eta} \tag{22}$$

is the Reynold's number, K_0 and K_1 are modified Bessel functions of second kind and $\underline{\Gamma}_{cyl}$ is the so-called hydrodynamic function. To allow evaluating the real and imaginary part of Eq. (20), necessary for calculating added mass $m_{f,c}$ and damping parameter $c_{f,c}$ for the oscillating cylinder, a second order series expansion of $\underline{\Gamma}_{cyl}$ at $jRe \to \infty$ is performed, yielding

$$\underline{\Gamma}_{cyl} \approx \underline{\Gamma}_{cyl,T} = 1 + \frac{4}{\sqrt{2Re}} - j\left(\frac{4}{\sqrt{2Re}} + \frac{2}{Re}\right) \tag{23}$$

where the subscript T denotes the Taylor series developed expression. The relative deviations of real and imaginary parts $\delta\underline{\Gamma}_{cyl,R}$ and

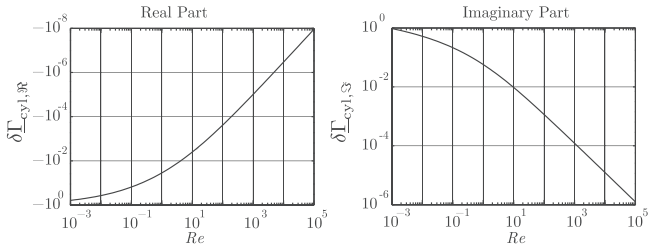

Fig. 2. Relative deviations of the real and imaginary parts of the approximated hydrodynamic function Eq. (23) from the exact solution Eq. (21).

$\delta\underline{\Gamma}_{\mathrm{cyl},\Im}$ of the approximated hydrodynamic function Eq. (23) and the exact solution Eq. (21) is depicted in Fig. 2. This comparison shows that for Reynolds numbers larger than 10, the deviation of the Taylor series approximated solution is less than 1 %.

Substituting the approximated solution of the hydrodynamic function in Eq. (20) and comparison of coefficients with Eq. (6) yields

$$m_{\mathrm{f,c}}(\omega) \approx \pi\, r_{\mathrm{c}}^2 \left(\rho + \frac{4}{\sqrt{2}\, r_{\mathrm{c}}}\sqrt{\frac{\eta\,\rho}{\omega}}\right) l_{\mathrm{c}} \quad \text{and}$$
$$c_{\mathrm{f,c}}(\omega) \approx \left(2\,\pi\,\eta + \frac{4\,\pi}{\sqrt{2}}\, r_{\mathrm{c}}\sqrt{\omega\,\eta\,\rho}\right) l_{\mathrm{c}} \tag{24}$$

for the added mass and damping parameters in case of the oscillating cylinder, where l_{c} is the effective length of the cylinder. By reducing all coefficients and r_{c} in factors $m_{\mathrm{x,c}}$ and $c_{\mathrm{x,c}}$,

$$m_{\mathrm{f,\,c}}(\omega) = m_{\rho,\mathrm{c}}\,\rho + m_{\eta\rho,\mathrm{c}}\sqrt{\frac{\eta\,\rho}{\omega}} \quad \text{and}$$
$$c_{\mathrm{f,\,c}}(\omega) = c_{\eta,\mathrm{c}}\,\eta + c_{\eta\rho,\mathrm{c}}\,\sqrt{\omega\,\eta\,\rho} \tag{25}$$

is obtained for the oscillating cylinder which is the same form as Eq. (19) for the oscillating sphere.

3.4. Generalized equations for added mass and damping

Comparison of the Eqs. (15), (19) and (25) shows that the frequency dependent expressions for the fluid related added mass and damping can be given in a generalized form as follows

$$m_{\mathrm{f}}(\omega) = m_{\rho}\,\rho + m_{\eta\rho}\sqrt{\frac{\eta\,\rho}{\omega}} \quad \text{and} \quad c_{\mathrm{f}}(\omega) = c_{\eta}\,\eta + c_{\eta\rho}\,\sqrt{\omega\,\eta\,\rho} \tag{26}$$

where the factors for m_{x} and c_{x} are given in Tab. 1 for the case of an in-plane oscillating plate, an oscillating sphere and a laterally oscillating cylinder.

Table 1
Coefficients.

	Plate	Sphere	Cylinder
m_{ρ}	0	$\frac{2\pi}{3} r_{\mathrm{s}}^3$	$\pi\, r_{\mathrm{c}}^2\, l_{\mathrm{c}}$
$m_{\eta\rho}$	$\frac{A_{\mathrm{p}}}{\sqrt{2}}$	$\sqrt{2}\,3\,\pi\, r_{\mathrm{s}}^2$	$\sqrt{2}\,2\,\pi\, r_{\mathrm{c}}\, l_{\mathrm{c}}$
c_{η}	0	$6\,\pi\, r_{\mathrm{s}}$	$2\,\pi\, l_{\mathrm{c}}$
$c_{\eta\rho}$	$\frac{A_{\mathrm{p}}}{\sqrt{2}}$	$\sqrt{2}\,3\,\pi\, r_{\mathrm{s}}^2$	$\sqrt{2}\,2\,\pi\, r_{\mathrm{c}}\, l_{\mathrm{c}}$

4. Generalized equations for resonance frequency and damping factor for a liquid loaded oscillator

4.1. Resonance frequency

Considering the three solutions for the fluid-loading related mass parameter, a generalized expression for the angular resonance frequency

$$\omega_0 = \frac{1}{\sqrt{m_{0\mathrm{k}} + m_{\rho\mathrm{k}}\,\rho + m_{\eta\rho\mathrm{k}}\sqrt{\eta\,\rho/\omega_0}}} \tag{27}$$

is obtained by substituting the mass parameter from Eq. (26) in Eq. (12) and dividing the such obtained equation by k_0. $m_{x\mathrm{k}}$ are coefficients which can be determined by a parameter fit for measurement results for $f_{\mathrm{r}} = \omega_0/(2\,\pi)$ obtained with at least three different liquids with known mass densities and viscosities. In case of one-dimensional plane shear waves, the factor $m_{\rho\mathrm{k}}$ is zero.

4.2. Quality factor

Similar to the generalized equation for the resonance frequency, the quality factor is calculated by substituting the damping coefficient from Eq. (26) in Eq. (12). It follows

$$Q = \frac{1}{\omega_0} \cdot \frac{1}{c_{0\mathrm{k}} + c_{\eta\mathrm{k}}\,\eta + c_{\eta\rho\mathrm{k}}\sqrt{\omega_0\,\eta\,\rho}}, \tag{28}$$

where $c_{x\mathrm{k}}$ are coefficients and $c_{\eta\mathrm{k}}$ is zero in case of one-dimensional shear waves.

5. Simplified equation for the resonance frequency and damping factor

5.1. Resonance frequency

The implicit nature of Eq. (27) might be troublesome in some cases, e.g. when an estimation for ω_0 for given η and ρ has to be calculated. For this purpose, the equation is simplified by neglecting the frequency dependence of the added mass $m_{\mathrm{f}}(\omega)$ in Eq. (26). Thus, it follows for the angular resonance frequency

$$\omega_0 = \frac{1}{\sqrt{m_{0\mathrm{k}} + m_{\rho\mathrm{k}}\,\rho + m^*_{\eta\rho\mathrm{k}}\sqrt{\eta\,\rho}}}. \tag{29}$$

5.2. Quality factor

Similar to the simplification of ω_0, the expression for Q can be simplified by neglecting the frequency dependence of the damping parameter $c_{\mathrm{f}}(\omega)$ in Eq. (26). Using Eq. (29) for ω_0 in Eq. (28), it follows

$$Q = \frac{\sqrt{m_{0\mathrm{k}} + m_{\rho\mathrm{k}}\,\rho + m^*_{\eta\rho\mathrm{k}}\sqrt{\eta\,\rho}}}{c_{0\mathrm{k}} + c_{\eta\mathrm{k}}\,\eta + c^*_{\eta\rho\mathrm{k}}\sqrt{\eta\,\rho}}. \tag{30}$$

As already mentioned above, the simplification of the equations for ω_0 and Q by neglecting the frequency dependence of the parameters $m_{\mathrm{f}}(\omega)$ and $c_{\mathrm{f}}(\omega)$ is valid for small investigated bandwidths and high quality factors. In a first theoretical investigation which will be published elsewhere it was found, that for an investigated bandwidth of $[\omega_0 - \omega_0/Q \ldots \omega_0 + \omega_0/Q]$ the relative changes of $m_{\mathrm{f}}(\omega)$ and $c_{\mathrm{f}}(\omega)$ are less than 1 % for quality factors higher than 5 in case of m_{f} and 50 in case of c_{f}, respectively. A comparison of the generalized model and simplified model for fitted parameters is given in Section 6 and in Appendix B.

The procedure how to fit the model parameters in Eqs. (27)–(30) using a linear least squares fit, is explained in Appendix A.

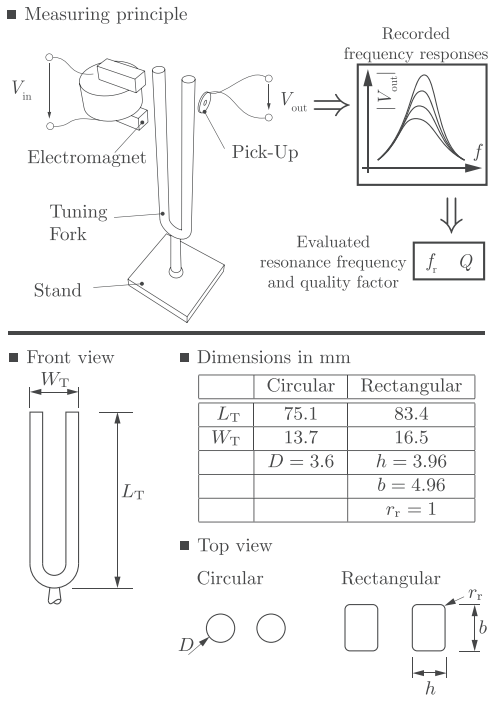

	Circular	Rectangular
L_T	75.1	83.4
W_T	13.7	16.5
	$D = 3.6$	$h = 3.96$
		$b = 4.96$
		$r_r = 1$

Fig. 3. Measuring principle and geometries of the circular and rectangular cross-sectioned tuning fork. The frequency response of a fully immersed, ferromagnetic tuning fork is recorded by electromagnetic excitation and readout. From these frequency responses, resonance frequencies and quality factor are evaluated.

6. Model verification

For investigating its validity, the model has been applied to experimental results obtained with steel tuning forks and to data of recently published sensors. The deviations of measured and modeled results for each sensor are depicted in Fig. B1 in Appendix B.

The intention of the experiments performed for this work was to experimentally examine the effect of mass density and viscosity to resonance frequency and quality factor separately. This was achieved by investigating the resonance characteristics of tuning forks in liquid mixture series with varying viscosities but constant mass densities and vice versa. This procedure is explained in detail in the following subsection.

6.1. Experimental investigation using steel tuning forks

The validity and applicability of the equations for resonance frequency and quality factor discussed in Sections 4 and 5 is demonstrated by an experimental investigation using conventional steel tuning forks with circular and rectangular cross sections but with the same nominal resonance frequency (440 Hz) in air. The usage of tuning forks was motivated by their simple and well defined geometry as well as their stability of resonance frequency and low cross-sensitivity to temperature. Due to these conditions, the results obtained with the tuning forks are expected to yield good accordance with the model. The circular tuning fork was chosen to meet the requirements for the oscillating cylinder, Section 3.3 whereas the rectangular tuning fork was selected to demonstrate the applicability of the model for oscillating structures other than plates, cylinders and spheres. The model has furthermore been tested for other sensor types (not only from our own work) described in Section 6.2.

The measuring principle as well as the dimensions of the used steel tuning forks are shown in Fig. 3. Each tuning fork was put in a glass tube (not depicted) which was sealed at both sides of the tube after filling it with the sample liquid. For excitation, an electromagnet was placed (outside of the tube) at the end of one of the ferromagnetic tuning fork's prongs. For measuring the oscillation of the tuning fork, an electrodynamic pick-up consisting of a coil carrying a permanent magnet in its center was placed at the other prong's end. By sweeping the excitation current's frequency, the tuning forks' frequency responses containing the tuning forks' fundamental mode were recorded upon immersion in various sample liquids at controlled temperatures of $25 \pm 0.1\,^{\circ}\mathrm{C}$. From these frequency responses, resonance frequencies and quality factors were evaluated with a fitting procedure presented in [34].

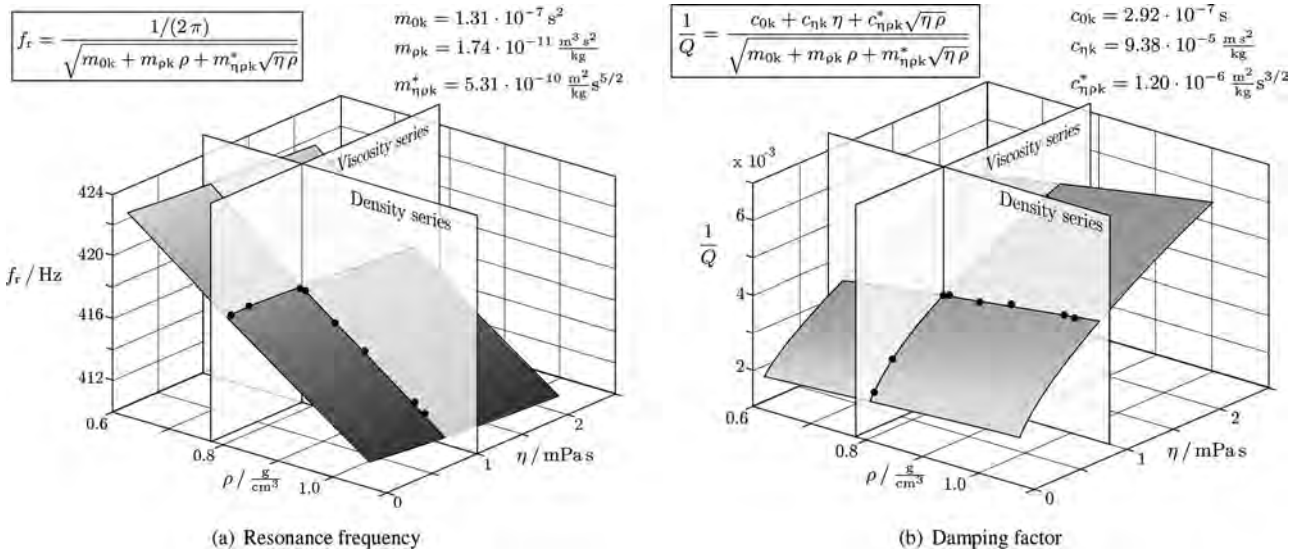

(a) Resonance frequency (b) Damping factor

Fig. 4. Modeled and measured values for resonance frequency and quality factor. The shaded surfaces for f_r and Q were obtained by evaluating Eqs. (29) and (30) for f_r and Q for identified parameters for the circular tuning fork. The intersection lines on the shaded surfaces with the planes entitled density and viscosity series indicate the values which would be obtained for f_r and Q for constant ρ and η, respectively. In this case, the viscosity series consist of five acetone–isopropanol solutions with mass densities of roughly 0.78 mg/cm^3 and covering a viscosity range of 0.2 to 2 mPa s. The density series consist of five solutions with a viscosity of 1 mPa s and mass densities of 0.78 to 1 mg/cm^3. The measured points are indicated by the black dots on the shaded surfaces. A more detailed illustration of measured values for f_r and D obtained with the viscosity and mass density series is given in Fig. 5. Note that here, $1/Q$ (instead of Q) is plotted for better visibility of the surface plot.

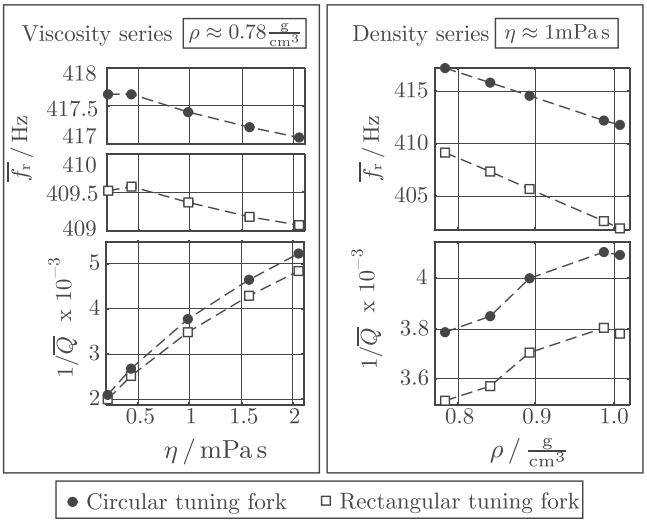

Fig. 5. Measured, averaged damping and resonance frequency for a circular and a rectangular tuning fork versus viscosity and mass density.

The dependence of the resonance frequency as well as the quality factor on both, the liquid's viscosity and mass density was already shown in the equations for the models discussed in Sections 4 and 5 (generalized and simplified model). To easier distinguish the tuning forks' responses to mass density and viscosity and to allow plotting $f_r(\eta)$, $Q(\eta)$, $f_r(\rho)$ and $Q(\rho)$ in a two dimensional plot, two series of liquids have been prepared. The mass density series with a nominal viscosity of 1 mPa s and the viscosity series with a nominal mass density of 0.78 mg/cm^3. An illustration of $f_r(\eta, \rho)$ and $1/Q(\eta, \rho)$ in the investigated range of viscosities and mass densities is shown Fig. 4.

The response to viscosity was investigated by evaluating both tuning forks' quality factors and resonance frequencies in five acetone–isopropanol solutions covering a viscosity range from 0.2 to 2 mPa s for mass densities of roughly 0.78 mg/cm^3 at 25 °C. After mixing, the viscosity and mass density of these solutions were measured with an Anton Paar SVM 3000 viscometer.

For investigating the response to mass density, five solutions using acetone, isopropanol, ethanol, DI-water and glycerol were prepared. The liquids were mixed to obtain almost constant viscosities of 1 mPa s but mass densities between 0.78 and 1 mg/cm^3 at 25 °C. The values for viscosity and mass density of these solutions were again determined with the SVM 3000 viscometer.

The values for the inverse of the quality factor $1/\bar{Q}$ and the resonance frequency $\bar{f}_r$, averaged over 100 repeated measurements for every liquid from the viscosity and mass density series are depicted in Fig. 5 for the circular and rectangular tuning fork, respectively. This illustration of $f_r(\eta)$, $1/Q(\eta)$, $f_r(\rho)$ and $Q(\rho)$ correspond to the measurements in the viscosity series and mass density series planes in Fig. 4.

6.2. Application to results from literature

To investigate the applicability of the model not only for tuning forks but furthermore to the work of other groups, the model was tested for other sensors where sufficient data for f_r, Q, η and ρ, was provided in tabulated form. There, the liquids' viscosities and mass densities were not split up in viscosity and mass density series as for the investigation of the tuning forks in this work. In [2] a single-crystal silicon cantilever operated at 5 kHz approximately, with a length of 397 μm, a width of 29 μm, and a thickness of 2 μm was investigated in gaseous and liquid environments. An in-plane vibrating silicon platelet [16] supported by four silicon beams, featuring an overall size of 1.3 mm in length, 100 μm in width and 20 μm in height was examined in 9 different liquids at operational frequencies of roughly 10 kHz. In [35] a millimeter-sized quartz tuning fork resonating at 30 kHz as well as a 1 mm long, 250 μm wide AlN platelet actuated in an extensional mode at roughly 4 MHz was presented.

From our own work, we further investigated the applicability of the model to a U-shaped wire sensor and a spiral spring sensor. The U-shaped wire sensor [36], consisting of a tungsten wire with a diameter of 400 μm which is bent to the shape of a 'U', features an overall size of 12 mm in length and 6 mm in width and is operated at 930 Hz in liquids. The frequency responses were recorded in eleven DI–water–glycerol mixtures. The spiral spring sensor, see [37], with a length of 35 mm was tested in 17 liquids at operational frequencies of 630 Hz in liquids.

6.3. Comparison of modeled and experimental results

The relative deviations δf_r and δQ of the modeled values for f_r and Q with respect to the measured values f_r^M and Q^M are used to show the deviation of the modeled result from the measured value. In case of the circular and rectangular tuning fork, as well as for the U-shaped wire and the spiral spring sensor, which are all from our own work, the mean values for 100 repeated measurements for f_r^M and Q^M have been used. For the other sensors, the reported values have been taken. The relative root mean square (rms) deviations $\delta f_{r,rms}$ and δQ_{rms} are used as a figure of merit to judge the applicability of the particular model for resonance frequency and quality factor. The relative deviations and the relative rms deviations were evaluated as follows:

$$\delta X = \frac{X - X^M}{X^M} \quad \text{and} \quad \delta X_{rms} = \sqrt{\frac{1}{N}\sum_{i=1}^{N}\left(\frac{X_i - X_i^M}{X_i^M}\right)^2}, \tag{31}$$

where X stands either for f_r or Q and N is the number of investigated liquids. The such evaluated results are depicted in Appendix B in Fig. B1 for eight different sensors.

In total, 77 values for the relative deviations for f_r and Q for both models were evaluated, for the eight investigated sensors. By this investigation, ranges of $\eta = 0.21 \ldots 215.7$ mPa s, $\rho = 0.68 \ldots 1.6$ g/cm^3, $f_r \approx 400 \ldots 3.85 \times 10^6$ Hz and $Q = 1.02 \ldots 498.99$ in liquids, have been covered.

The comparison of the relative rms deviations of the models for the resonance frequency Eq. (27) (generalized model) and Eq. (29) (simplified model) shows, that the generalized model in general yields slightly better results than the simplified model. The total rms deviation (for the 77 values) for the resonance frequency is 1.01×10^{-3} for the generalized model and 1.66×10^{-3} for the simplified model. In some cases, (circular tuning fork, rectangular tuning fork, U-shaped wire) the simplified model yields negligibly better results. The best fitting results and the highest deviations were obtained in case of the rectangular tuning fork (8.94×10^{-6} and 8.91×10^{-6}) and the U-shaped wire (2.05×10^{-3}) as well as the silicon cantilever (4.65×10^{-3}), respectively.

Concerning the relative deviations of the values of modeled and measured results for the quality factor, the simplified model Eq. (30) yields in general better results than the generalized model Eq. (28). The total relative rms deviations for the quality factors are 32.44×10^{-3} for the generalized model and 31.45×10^{-3} for the simplified model, respectively. The lowest relative deviations are obtained with the silicon platelet (2.50×10^{-3} and 4.08×10^{-3}) whereas the AlN platelet yields the highest relative deviations in case of both models (79.20×10^{-3} and 78.93×10^{-3}).

7. Conclusion

Based on the representation of a mass density and viscosity sensor's characteristic resonant mode by a lumped element oscillator and considering the fluid forces of oscillating plates, spheres and cylinders on the mechanical resonator, generalized reduced order equations for resonance frequency and damping factor were obtained. As the generalized model yielded implicit equations, which might be troublesome in some cases, a simplified model has been formulated, neglecting the frequency dependence of the

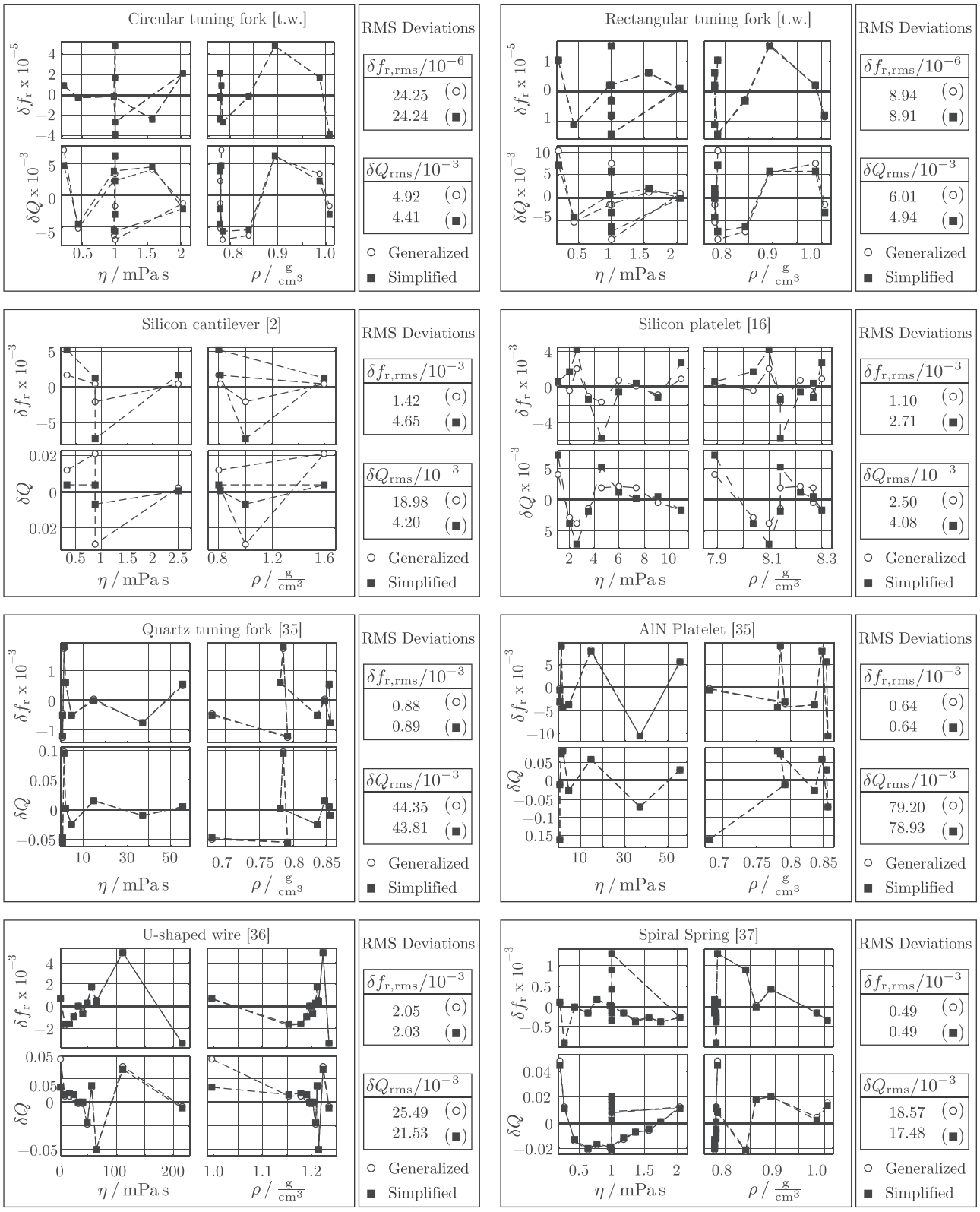

Fig. B1. Relative deviations of modeled from measured results. ■ designates the generalized model whereas ○ represents the simplified model. In some cases, only one of both markers is visible, as both models yield similar results.

fluid forces acting on the resonator. For the resonance frequency the difference between both approaches is negligible, whereas in case of the quality factor, the simplified model in general yielded better results. This finding, which needs further investigation, might have different reasons. Measurement errors, resulting e.g., from varying temperatures, not perfectly cleaned sensors, unstable measurement setups and outliers as well as errors resulting from the evaluation of f_r and Q from the frequency response are just a few examples for potential reasons. A first investigation of the applicability of the model using the experimental results of conventional steel tuning forks with circular and rectangular cross-sections and six further recently published sensors showed first, that the model can be also applied for resonant sensors not exactly meeting the geometrical requirements (plate, sphere, cylinder) considered in the presented model. Second, the experimental results showed good accordance with the fitted model. The achieved values for the relative rms deviations over 77 investigated measurements are better than 1.7×10^{-3} for $\delta f_{r,\mathrm{rms}}$ and 3.3×10^{-2} for δQ_{rms}.

Thus, the presented equations appear suitable for a general description of a resonant mass density and viscosity sensor's performance even if slight deviations of experimental results might be observed. This furthermore allows comparison of sensors of different types, geometries, fabrication technologies as well as actuation and readout principles.

Acknowledgments

This work has been partially supported by the Linz Center of Mechatronics (LCM) in the framework of the Austrian COMET-K2 program. We also want to thank Bernhard Mayrhofer and Johann Katzenmayer for their help and excellent assistance.

Appendix A. Parameter fit

Assuming that resonance frequencies $f_{r,i}$ and quality factors Q_i from at least three measurements in liquids with viscosities η_i and ρ_i are available, all parameters in Eqs. (27)–(30) can be determined by a linear least squares fit as follows. All four equations can be brought into the form

$$\mathbf{b} = \mathbf{A} \cdot \mathbf{x} \tag{A.1}$$

where $\mathbf{x}$ is a vector with the unknown parameters for which the least squares solution reads [38]:

$$\mathbf{x} = (\mathbf{A}^{\mathrm{T}} \cdot \mathbf{A})^{-1} \cdot \mathbf{A}^{\mathrm{T}} \cdot \mathbf{b} \tag{A.2}$$

A.1. Generalized model

The vectors of unknowns $[m_{0k}, m_{\rho k}, m_{\eta\rho k}]^{\mathrm{T}}$ and $[c_{0k}, c_{\eta k}, c_{\eta\rho k}]^{\mathrm{T}}$ of the generalized model can be determined independently with known values for $\omega_{0,i} = 2\pi f_{r,i}$, Q_i, η_i and ρ_i. The equations for ω_0 and Q are rearranged to allow formulating matrix equations of the form of Eq. (A.1) as follows:

- Eq. (27) is rearranged to

$$\frac{1}{\omega_0^2} = m_{0k} + m_{\rho k}\,\rho + m_{\eta\rho k}\sqrt{\frac{\eta\,\rho}{\omega_0}} \tag{A.3}$$

and thus, the least squares solutions for the parameters in $\mathbf{x} = [m_{0k}, m_{\rho k}, m_{\eta\rho k}]^{\mathrm{T}}$ can be found using Eq. (A.2) with

$$\mathbf{b} = \left[\frac{1}{\omega_{0,i}^2}\right], \quad \mathbf{A} = \left[1,\ \rho_i,\ \sqrt{\frac{\eta_i\,\rho_i}{\omega_{0,i}}}\right] \tag{A.4}$$

- Eq. (28) brought into the form

$$\frac{1}{Q} = \omega_0 \cdot (c_{0k} + c_{\eta k}\,\eta + c_{\eta\rho k}\sqrt{\omega_0\,\eta\,\rho}) \tag{A.5}$$

shows that the least squares solutions for the parameters of the vector of unknowns $\mathbf{x} = [c_{0k}, c_{\eta k}, c_{\eta\rho k}]^{\mathrm{T}}$ can be found using

$$\mathbf{b} = \left[\frac{1}{Q_i}\right], \quad \mathbf{A} = [\omega_{0,i},\ \omega_{0,i}\eta_i,\ \omega_{0,i}\sqrt{\omega_{0,i}\,\eta_i\,\rho_i}] \tag{A.6}$$

and Eq. (A.2)

A.2. Simplified model

Similar to the procedure above, the parameters of the simplified model can be determined by a linear least squares fit, whereas in this case, for calculating $[c_{0k}, c_{\eta k}, c^*_{\eta\rho k}]^{\mathrm{T}}$, the parameters for the resonance frequency $[m_{0k}, m_{\rho k}, m^*_{\eta\rho k}]^{\mathrm{T}}$ have to be known, i.e., determined first.

- The parameters of Eq. (29) are fitted using Eq. (A.2), where $\mathbf{x} = [m_{0k}, m_{\rho k}, m^*_{\eta\rho k}]^{\mathrm{T}}$ and

$$\mathbf{b} = \left[\frac{1}{\omega_{0,i}^2}\right], \quad \mathbf{A} = [1,\ \rho_i,\ \sqrt{\eta_i\,\rho_i}]. \tag{A.7}$$

- To determine the least squares values of $\mathbf{x} = [c_{0k}, c_{\eta k}, c^*_{\eta\rho k}]^{\mathrm{T}}$

$$\mathbf{b} = \left[\frac{1}{Q_i}\right], \quad \mathbf{A} = [\omega_{0f,i},\ \omega_{0f,i}\,\eta_i,\ \omega_{0f,i}\sqrt{\eta_i\,\rho_i}] \tag{A.8}$$

with

$$\omega_{0f,i} = \frac{1}{\sqrt{m_{0k} + m_{\rho k}\,\rho_i + m^*_{\eta\rho k}\sqrt{\eta_i\,\rho_i}}}. \tag{A.9}$$

are used and substituted in Eq. (A.2).

Appendix B. Model evaluation using experimental results

Fig. B1 shows the relative deviations δf_r and δQ of modeled from measured values for resonance frequency and quality factor for eight different sensors versus η and ρ. The references are given in each plot. The marker ■ indicates the values for the generalized model whereas the marker ○ designates the values for the simplified model. Furthermore, the relative rms deviations $\delta f_{r,\mathrm{rms}}$ and δQ_{rms} are given for each sensor for the generalized and the simplified model.

References

[1] B. Jakoby, R. Beigelbeck, F. Keplinger, F. Lucklum, A. Niedermayer, E.K. Reichel, C. Riesch, T. Voglhuber-Brunnmaier, B. Weiss, Miniaturized sensors for the viscosity and density of liquids – performance and issues, IEEE Trans. Ultrason. Ferroelectr. Freq. Control 57 (1) (2010) 111–120, http://dx.doi.org/10.1109/TUFFC.2010.1386.
[2] S. Boskovic, J.W.M. Chon, P. Mulvaney, J.E. Sader, Rheological measurements using microcantilevers, J. Rheol. 46 (4) (2002) 891–899.
[3] S.J. Martin, V.E. Granstaff, G.C. Frye, Characterization of a quartz crystal microbalance with simultaneous mass and liquid loading, Anal. Chem. 63 (1991) 2272–2281.
[4] R. Thalhammer, S. Braun, B. Devcic-Kuhar, M. Gröschl, F. Trampler, E. Benes, H. Nowotny, M. Kostal, Viscosity sensor utilizing a piezoelectric thickness shear sandwich resonator, IEEE Trans. Ultrason. Ferroelectr. Freq. Control 45 (5) (1998) 1331–1340.
[5] L. Matsiev, J. Bennett, O. Kolosov, High precision tuning fork sensor for liquid property measurements, in: IEEE Ultrasonics Symposium, 2005, pp. 1492–1495.
[6] I. Dufour, A. Maali, Y. Amarouchene, et al., The microcantilever: a versatile tool for measuring the rheological properties of complex fluids, J. Sens. (2012), http://dx.doi.org/10.1155/2012/719898.
[7] C. Riesch, A. Jachimowicz, F. Keplinger, E.K. Reichel, B. Jakoby, A novel sensor system for liquid properties based on a micromachined beam and a low-cost optical readout, in: Proceedings IEEE Sensors, 2007, pp. 872–875.

[8] E.K. Reichel, C. Riesch, B. Weiss, B. Jakoby, A vibrating membrane rheometer utilizing electromagnetic excitation, Sens. Actuators A: Phys. 145 (2008) 349–353.
[9] C. Castille, I. Dufour, C. Lucat, Longitudinal vibration mode of piezoelectric thick-film cantilever-based sensors in liquid media, Appl. Phys. Lett. 96 (15) (2010) 154102, http://dx.doi.org/10.1063/1.3387753.
[10] F.J.P. Caetano, J.M.N.A. Fareleira, C.M.B.P. Oliveira, W.A. Wakeham, Validation of a vibrating-wire viscometer: measurements in the range of 0.5 to 135 mPa s, J. Chem. Eng. Data 50 (1) (2005) 201–205.
[11] M. Heinisch, E.K. Reichel, I. Dufour, B. Jakoby, Tunable resonators in the low kHz range for viscosity sensing, Sens. Actuators A: Phys. 186 (2012) 111–117, http://dx.doi.org/10.1016/j.sna.2012.03.009.
[12] P. Rust, D. Cereghetti, J. Dual, A micro-liter viscosity and density sensor for the rheological characterization of DNA solutions in the kilo-hertz range, Lab Chip 13 (24) (2013) 4794–4799, 10.1039/C3LC50857A.
[13] M. Heinisch, E.K. Reichel, B. Jakoby, U-shaped wire based resonators for viscosity and mass density sensing, in: Proceedings of the SENSOR 2013, OPTO 2013, IRS2, 2013.
[14] M. Heinisch, E.K. Reichel, I. Dufour, B. Jakoby, A resonating rheometer using two polymer membranes for measuring liquid viscosity and mass density, Sens. Actuators A: Phys. 172 (1) (2011) 82–87, http://dx.doi.org/10.1016/j.sna.2011.02.031.
[15] P. Peiker, E. Oesterschulze, Impact of the miniaturization on the response of a hybrid diaphragm resonator considering its finite support, Proceedings of the Nanomechanical Sensing Workshop (2013) 127–128.
[16] C. Riesch, E.K. Reichel, A. Jachimowicz, J. Schalko, P. Hudek, B. Jakoby, F. Keplinger, A suspended plate viscosity sensor featuring in-plane vibration and piezoresistive readout, J. Micromech. Microeng. 19 (2009) 075010, http://dx.doi.org/10.1088/0960-1317/19/7/075010.
[17] E.K. Reichel, C. Riesch, F. Keplinger, C.E.A. Kirschhock, B. Jakoby, Analysis and experimental verification of a metallic suspended plate resonator for viscosity sensing, Sens. Actuators A: Phys. 162 (2010) 418–424, http://dx.doi.org/10.1016/j.sna.2010.02.017.
[18] A. Abdallah, M. Heinisch, B. Jakoby, Measurement error estimation and quality factor improvement of an electrodynamic-acoustic resonator sensor for viscosity measurement, Sens. Actuators A: Phys. 199 (2013) 318–324.
[19] G. Wingqvist, J. Bjurstrom, L. Liljeholm, I. Katardjiev, A.L. Spetz, Shear mode ALN thin film electroacoustic resonator for biosensor applications, in: Proceedings IEEE Sensors, 2005, pp. 492–495.
[20] X. Huang, S. Li, J. Schultz, Q. Wang, Q. Lin, A capacitive MEMS viscometric sensor for affinity detection of glucose, J. Microelectromech. Syst. 18 (6) (2009) 1246–1254.
[21] C. Vančura, J. Lichtenberg, A. Hierlemann, F. Josse, Characterization of magnetically actuated resonant cantilevers in viscous fluids, Appl. Phys. Lett. 87 (16) (2005) 162510.
[22] J.H. Seo, O. Brand, High q-factor in-plane-mode resonant microsensor platform for gaseous/liquid environment, J. Microelectromech. Syst. 17 (2) (2008) 483–493.
[23] L.A. Beardslee, A.M. Addous, S. Heinrich, F. Josse, I. Dufour, O. Brand, Thermal excitation and piezoresistive detection of cantilever in-plane resonance modes for sensing applications, J. Microelectromech. Syst. 19 (4) (2010) 1015–1017.
[24] A. Rahafrooz, S. Pourkamali, Characterization of rotational mode disk resonator quality factors in liquid. Frequency Control and the European Frequency and Time Forum (FCS), in: 2011 Joint Conference of the IEEE International, 2011, p. 5.
[25] C. Riesch, E.K. Reichel, F. Keplinger, B. Jakoby, Characterizing vibrating cantilevers for liquid viscosity and density sensing, J. Sens (2008), 9 pp. (Article ID 697062).
[26] B.N. Johnson, R. Mutharasan, Biosensing using dynamic-mode cantilever sensors: a review, Biosens. Bioelectron. 32 (1) (2012) 1–18.
[27] B.A. Bircher, L. Duempelmann, K. Renggli, H.P. Lang, C. Gerber, N. Bruns, T. Braun, Real-time viscosity and mass density sensors requiring microliter sample volume based on nanomechanical resonators, Anal. Chem. 85 (18) (2013) 8676–8683.
[28] W.W. Weaver, S.P. Timoshenko, D.H. Young, Vibration Problems in Engineering, 5th ed., Wiley, New York, 1990.
[29] M. Heinisch, E.K. Reichel, B. Jakoby, A suspended plate in-plane resonator for rheological measurements at tunable frequencies, in: Proceedings Sensor + Test, 2011, pp. 61–66.
[30] L.D. Landau, E.M. Lifshitz, Fluid Mechanics, Butterworth-Heinemann, Oxford, 1987.
[31] L. Rosenhead, Laminar Boundary Layers: Fluid Motion Memoirs, Clarendon, Oxford, 1963.
[32] E.O. Tuck, Calculation of unsteady flows due to small motions of cylinders in a viscous fluid, J. Eng. Math. 3 (1) (1969) 29–44.
[33] J.E. Sader, Frequency response of cantilever beams immersed in viscous fluids with applications to the atomic force microscope, J. Appl. Phys. 84 (1998) 64–76.
[34] A.O. Niedermayer, T. Voglhuber-Brunnmaier, J. Sell, B. Jakoby, Methods for the robust measurement of the resonant frequency and quality factor of significantly damped resonating devices, Meas. Sci. Technol. 23 (8) (2012) 085107.
[35] J. Toledo, T. Manzaneque, J. Hernando-García, J. Vázquez, A. Ababneh, H. Seidel, M. Lapuerta, J. Sánchez-Rojas, Application of quartz tuning forks and extensional microresonators for viscosity and density measurements in oil/fuel mixtures, Microsyst. Technol. (2014) 1–9.
[36] M. Heinisch, E.K. Reichel, I. Dufour, B. Jakoby, A U-shaped wire for viscosity and mass density sensing, Sens. Actuators A: Phys. 214 (2014) 245–251.
[37] M. Heinisch, S. Clara, I. Dufour, B. Jakoby, A spiral spring resonator for mass density and viscosity measurements, in: Proceedings of the Eurosensors XXVIII, 2014.
[38] E.K. Chong, S.H. Zak, An Introduction to Optimization, 2nd ed., John Wiley & Sons, New York, 2001.

Biographies

Martin Heinisch obtained his Dipl.-Ing. (M.Sc.) in mechatronics from Johannes Kepler University Linz, Austria, in 2009. After his Master studies he went to the University of California, Los Angeles (U.C.L.A.) as a Marshall Plan Scholarship grantee, where he did research in the field of microfluidic applications and self assembling systems. In 2010 he started a Ph.D. program at the Institute for Microelectronics and Microsensors of the Johannes Kepler University Linz, Austria where he is currently working on resonating liquid sensors.

Thomas Voglhuber-Brunnmaier received the Dipl.-Ing. (M.Sc.) degree in Mechatronics in 2007 and the Dr. Techn. (Ph.D.) in May 2013 at the Institute for Microelectronics and Microsensors (IME) at the Johannes Kepler University (JKU) in Linz, Austria. From May 2013 he holds a Post-Doc position at the Center for Integrated Sensor Systems (CISS) at the Danube University Krems (DUK), where he works in close cooperation with IME on fluid sensors. His fields of interest are the modeling of micro-sensors, statistical signal processing, numerical methods and analog electronics.

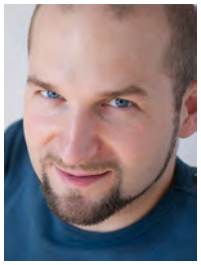

Erwin K. Reichel was born in Linz, Austria, in 1979. He received the Dipl.-Ing. (M.Sc.) degree in mechatronics from Johannes Kepler University, Linz, Austria, in 2006. From 2006 to 2009 he was working on the Ph.D. thesis at the Institute for Microelectronics and Microsensors of the Johannes Kepler University, Linz and graduated in October 2009. Afterwards he held a post-doctoral position at the Centre for Surface Chemistry and Catalysis as well as at the Department for Chemical Engineering, KU Leuven, Belgium until June 2012. Since then he holds a position as university assistant at the Johannes Kepler University Linz. The main research fields are the modeling, design, and implementation of sensors for liquid properties, and monitoring of phase transition in complex solutions.

Isabelle Dufour graduated from Ecole Normale Supérieure de Cachan in 1990 and received the Ph.D. and H.D.R. degrees in engineering science from the University of Paris-Sud, Orsay, France, in 1993 and 2000, respectively. She was a CNRS research fellow from 1994 to 2007, first in Cachan working on the modelling of electrostatic actuators (micromotors, micropumps) and then after 2000 in Bordeaux working on microcantilever-based chemical sensors. She is currently Professor of electrical engineering at the University of Bordeaux and her research interests are in the areas of microcantilever-based sensors for chemical detection, rheological measurements and materials characterization.

Bernhard Jakoby obtained his Dipl.-Ing. (M.Sc.) in Communication Engineering and his doctoral (Ph.D.) degree in electrical engineering from the Vienna University of Technology (VUT), Austria, in 1991 and 1994, respectively. In 2001 he obtained a venia legendi for Theoretical Electrical Engineering from the VUT. From 1991 to 1994 he worked as a Research Assistant at the Institute of General Electrical Engineering and Electronics of the VUT. Subsequently he stayed as an Erwin Schrödinger Fellow at the University of Ghent, Belgium, performing research on the electrodynamics of complex media. From 1996 to 1999 he held the position of a Research Associate and later Assistant Professor at the Delft University of Technology, The Netherlands, working in the field of microacoustic sensors. From 1999 to 2001 he was with the Automotive Electronics Division of the Robert Bosch GmbH, Germany, where he conducted development projects in the field of automotive liquid sensors. In 2001 he joined the newly formed Industrial Sensor Systems group of the VUT as an Associate Professor. In 2005 he was appointed Full Professor of Microelectronics at the Johannes Kepler University Linz, Austria. He is currently working in the field of liquid sensors and monitoring systems.

Provided for non-commercial research and education use.
Not for reproduction, distribution or commercial use.

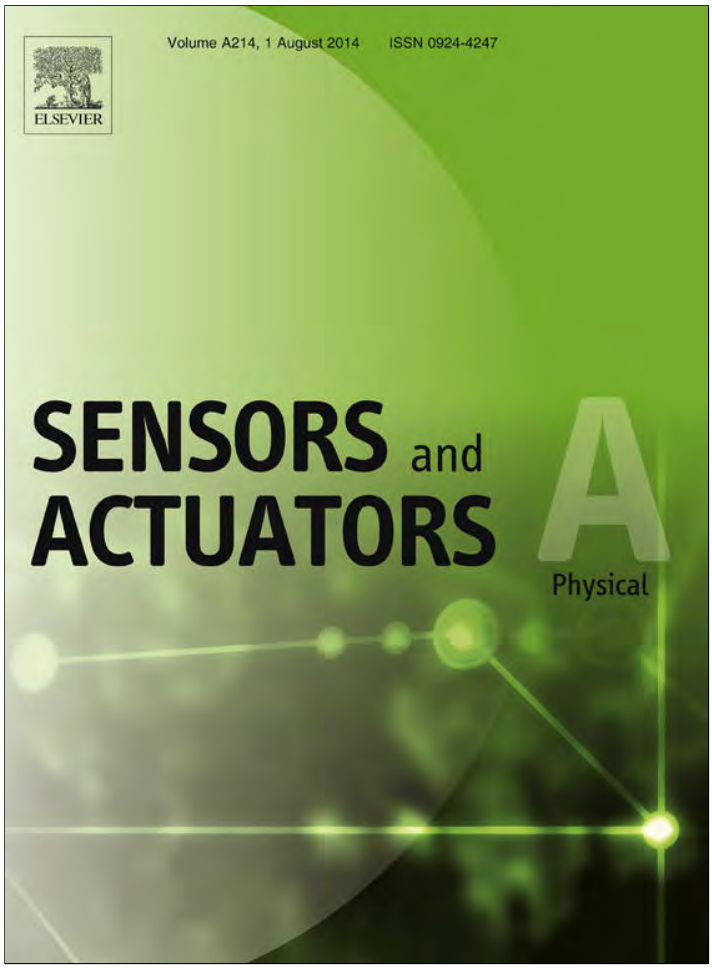

This article appeared in a journal published by Elsevier. The attached copy is furnished to the author for internal non-commercial research and education use, including for instruction at the authors institution and sharing with colleagues.

Other uses, including reproduction and distribution, or selling or licensing copies, or posting to personal, institutional or third party websites are prohibited.

In most cases authors are permitted to post their version of the article (e.g. in Word or Tex form) to their personal website or institutional repository. Authors requiring further information regarding Elsevier's archiving and manuscript policies are encouraged to visit:

http://www.elsevier.com/authorsrights

Author's personal copy

Sensors and Actuators A 214 (2014) 245–251

Contents lists available at ScienceDirect

Sensors and Actuators A: Physical

journal homepage: www.elsevier.com/locate/sna

A U-shaped wire for viscosity and mass density sensing

M. Heinisch[a,*], E.K. Reichel[a], I. Dufour[b], B. Jakoby[a]

[a] Institute for Microelectronics and Microsensors, Johannes Kepler University, Linz, Austria
[b] Université de Bordeaux, Laboratoire de l'Intégration du Matériau au Système, France

ARTICLE INFO

Article history:
Received 20 January 2014
Received in revised form 9 April 2014
Accepted 11 April 2014
Available online 1 May 2014

Keywords:
Viscosity
Mass density
Sensor
U-shaped
Resonator

ABSTRACT

A resonant sensor for a fluid's viscosity and mass density, employing an out-of-plane vibrating U-shaped tungsten wire is presented. The motivation for such a design is based on four major aspects, which are: operation in the low kilohertz range, circular cross-section of the resonator, electrodynamic actuation and read-out by means of Lorentz forces and low cross-sensitivity of the device's resonance frequency to temperature. The setup is described in detail, an analytical model is presented and results from experiments using acetone–isopropanol and DI-water–glycerol solutions are discussed to show the sensor's performance.

© 2014 Elsevier B.V. All rights reserved.

1. Introduction

Viscosity and mass density are important quantities describing the physical behavior of a liquid. Once determined, these quantities can be used to draw conclusions about the condition of the examined liquid. Examples for the latter are the monitoring of a lubricant's quality and aging [1], the condition of printing inks [2] or the characterization of DNA solutions [3]. The need for using viscosity and mass density sensors instead of conventional laboratory instruments may have many reasons. For example, they are applied if only very low amounts of the sample liquid are available [4], or the measurement has to be performed inline in a closed reservoir or a production line. When aiming at handheld devices, the capability for miniaturized devices becomes especially advantageous. Furthermore, from a rheological point of view, these resonating devices have been introduced to allow measurements for frequencies higher than 100 Hz, which is usually the limit for conventional rheometers.

During the last two decades, a large amount of different principles was reported [5,6]. The variety of different approaches can, for example, be distinguished by their fundamental mechanical structure, the manufacturing technology, the used materials as well as actuation and read-out principles. The mechanical structures comprise amongst others, singly clamped beams [7], doubly clamped beams [8], tuning forks [9], vibrating membranes [10,11], and oscillating platelets [12,13]. Concerning technology and materials, silicon and quartz crystal [14,15] based devices but also concepts using copper coated polymer sheets [16], screen printed PZT cantilevers [17] or tungsten wires [18] were also reported, just to name some examples.

Some of the concepts discussed above feature high operational frequencies in case of shear oscillating quartz crystals, complex fluid-structure interactions, which might be difficult to describe in a closed form model and high cross-sensitivities, e.g., to temperature in the case of doubly clamped resonators, in general.

In contrast to such devices, the U-shaped wire resonator was designed aiming at operational frequencies in the low kilohertz range, circular cross-sections of the resonator, electrodynamic actuation and read-out by means of Lorentz forces and last but not least, low cross-sensitivity of the sensor's resonance frequency to temperature. In comparison with well established shear oscillating quartz crystals which are usually operated in the megahertz range, lower operational frequencies might become important when investigating complex liquids such as emulsions, see Ref. [19]. Circular cross-sections are beneficial for closed form modeling of the fluid-structure interaction, as the well known analytical expressions for a laterally oscillating cylinder can be easily applied. The modeling of the fluid–structure interaction of resonators with rectangular cross-sections (as it is the case for the classical microcantilever), is e.g. based on considering an infinitely thin structure [20] or introducing a correction function to the well known equations for the circular case [21]. Both approaches yield relatively complex expressions for the fluid-structure interaction. The aforementioned frequency range implies device dimensions in the

* Corresponding author. Tel.: +43 73224686266.
E-mail address: martin.heinisch@jku.at (M. Heinisch).

http://dx.doi.org/10.1016/j.sna.2014.04.020
0924-4247/© 2014 Elsevier B.V. All rights reserved.

Author's personal copy

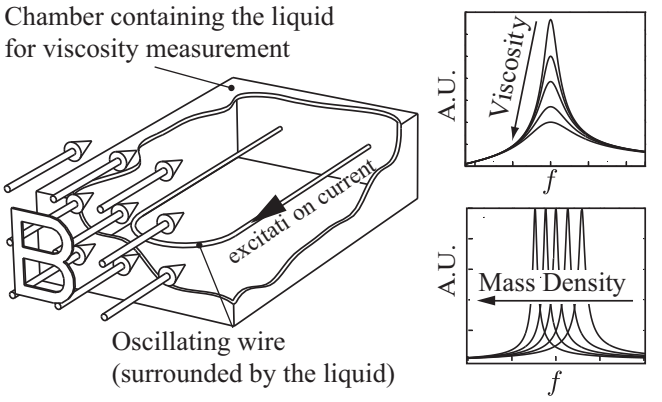

Fig. 1. Principle of the U-shaped viscosity and mass density sensor: the frequency response containing the fundamental (out-of-plane) mode is inductively recorded. The effect of the liquid's viscosity and mass density on the resonance curve is qualitatively shown for the amplitudes of calculated frequency responses of the wire's tip velocity.

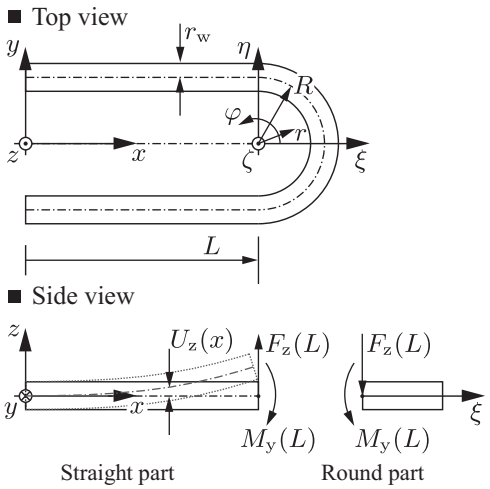

Fig. 2. Geometry used for modeling.

millimeter range. For such structures, electrodynamic actuation and read-out by means of Lorentz forces is a good choice, as high excitation forces and read-out signals can be achieved. Furthermore, the performance of this actuation and read-out principle is not affected by the investigated liquid as it is e.g., the case for optical read-out [8] for which transparent liquids are a fundamental requirement. Basically, the working principle of resonant viscosity and mass density sensors is based on determining the change of the frequency response of a specific resonant mode upon immersion in a test liquid. Thus, cross-sensitivities of the resonance frequency to temperature have to be preferentially small, as the temperature measurement (which is necessary for reliably measuring a fluid's viscosity and mass density in any case) is limited to a certain accuracy. In comparison to doubly clamped structures, for which high cross-sensitivities of the resonance frequency to temperature have been observed [16], singly clamped approaches yield lower dependencies of the resonance frequency to temperature in general. The U-shaped design might be interpreted as such a singly clamped beam, or in other words, two singly clamped beams, which are connected at their ends. In this contribution, tungsten was used as resonator material as it features a low thermal expansion coefficient and thus, keeps the thermal dependence of the resonance frequency additionally low. As it will be shown in this contribution experimentally, the U-shaped tungsten wire resonator yielded lower relative cross-sensitivity of the resonance frequency to temperature than a similar device implemented in silicon.

First prototypes of the U-shaped wire sensor were presented e.g., in Ref. [22]. A similar silicon-based device for magnetic filed measurements was presented in [23]. In this paper an overall revised sensor setup, a complete analytical model, as well as measurement series demonstrating the sensor's performance and allowing a validation of the devised model are presented and discussed.

2. Sensor principle

A tungsten wire, bent to the shape of a U, clamped to a rigid wall and immersed in a sample liquid, carries sinusoidal currents in the presence of an external magnetic field, as depicted in Fig. 1. Due to the resulting Lorentz forces on the round tip of the wire, the latter deflects in an out-of-plane oscillation. This oscillation in turn yields a motion-induced voltage corresponding to the wire's tip velocity and thus serves as a quantity for read-out. By sweeping the excitation current's frequency in a range containing the structure's (fundamental) resonance, the frequency response of the resonator is recorded. In general, higher viscosities of the surrounding liquid yield higher damping, i.e., lower quality factors, and higher mass densities yield lower resonance frequencies.

3. Mechanical model

3.1. Oscillating beam

The U-shaped wire viscosity and mass density sensor is symmetric with respect to its x-axis, see Fig. 2. Therefore, the U-shaped structure can be approximately modeled as a single, straight, circular and singly clamped beam. As the external magnetic field is assumed to primarily have components in (negative) x-direction, only excitation forces along the round end become significant in z-direction. Due to these circumstances it is possible to describe the U's deflection $u_z(x,t)$ in z-direction by the homogeneous differential equation for a single, elastic, singly clamped beam, subjected to dissipative and inertial forces, see [24]. The effect of the round end on the oscillation is considered in the boundary conditions. Assuming a sinusoidal excitation force and furthermore a time dependence $e^{j\omega t}$, the steady state, time harmonic deflection in the frequency domain $U_z(x,\omega)$ can be expressed considering Euler–Bernoulli beam theory [24] by the following harmonic differential equation:

$$E\,I\,\frac{\partial^4 U_z(x,\omega)}{\partial x^4} + (-\omega^2\,m' + j\,\omega\,d')\,U_z(x,\omega) = 0. \tag{1}$$

Here E is the Young's modulus, $I = r_w^4\,\pi/4$ is the second moment of area in respect to the y-axis, r_w is the wire's radius, m' and d' are the effective mass and damping parameter per unit length and are both split up into intrinsic and fluid loading related components

$$m' = m'_0 + m'_f \quad \text{and} \quad d' = d'_0 + d'_f. \tag{2}$$

For ρ_w being the wire's mass density, it follows for the wire's intrinsic mass per unit length $m'_0 = \rho_w\,r^2\pi$. The intrinsic damping parameter d'_0 has to be determined in a parameter fit. The parameters m'_f and d'_f resulting from the liquid loading are calculated in Section 3.2.

The general solution of Eq. (1) is

$$U_z(x,\,\omega) = C_1\,e^{\lambda x} + C_2\,e^{-\lambda x} + C_3\,e^{j\lambda x} + C_4\,e^{-j\lambda x} \tag{3}$$

with

$$\lambda = \left(\frac{\omega^2\,m' - j\,\omega\,d'}{E\,I}\right)^{\frac{1}{4}} \tag{4}$$

Author's personal copy

and C_i being determined by imposing the boundary conditions

$$U_z(0,\omega)=0 \qquad \frac{\partial U_z(0,\omega)}{\partial x}=0$$
$$\frac{\partial^2 U_z(L,\omega)}{\partial x^2}=-\frac{M_y(L)}{EI} \qquad \frac{\partial^3 U_z(L,\omega)}{\partial x^3}=-\frac{F_z(L)}{EI} \tag{5}$$

where $F_z(L)$ are all forces in z-direction and $M_y(L)$ are all mechanical moments in y-direction acting on the beam at its tip i.e, at $x=L$.

3.2. Fluid forces

To be able to consider for the fluid–structure interaction by additive terms in the inertial and dissipative coefficients as in Eq. (2), a solution for the fluid forces F'_f per unit length in the form

$$F'_f(x,\ \omega)=(-\omega^2\, m'_f(\omega)+j\,\omega\, d'_f(\omega))\, U_z(x,\ \omega) \tag{6}$$

has to be found. Considering a circular cylinder oscillating in a liquid with dynamic viscosity η_f and mass density ρ_f it follows [25,26,21]:

$$F'_f(x,\omega)= \tag{7}$$

$$\pi\,\rho_f\,\omega^2\, r_w^2\left(1-\frac{4\,j\,K_1(j\sqrt{-j\,Re})}{\sqrt{-j\,Re}\,K_0(j\sqrt{-j\,Re})}\right)U_z(x,\omega)$$

$$\text{with}\qquad Re=\frac{\rho_f\,\omega\, r_w^2}{\eta_f} \tag{8}$$

where Re is the Reynold's number, and K_0 and K_1 are modified Bessel functions.With this, the terms m'_f and d'_f in Eq. (2) can be expressed in closed form by means of a Taylor series expansion of Eq. (7) which yields

$$m'_f\approx\pi\,\rho_f\, r_w^2\left(1+\frac{4}{\sqrt{2\,Re}}\right)\quad\text{and}$$
$$d'_f\approx\pi\,\rho_f\,\omega\, r_w^2\left(\frac{4}{\sqrt{2\,Re}}+\frac{2}{Re}\right). \tag{9}$$

3.3. Third and fourth boundary condition

The round end of the U is considered to be stiff and thus deflections of the latter i.e., deflection of the U for $L<x\le L+R$ can be expressed as follows using a coordinate system with position vector $\boldsymbol{\xi}$, see Fig. 2

$$U_z(L+\xi)=U_z(L)+\left.\frac{\partial U_z(x)}{\partial x}\right|_{x=L}\xi. \tag{10}$$

The moment $M_y(L)$ and the force $F_z(L)$ in Eq. (5) are expressed as

$$M_y(L)=-M_{ex}+M_{i,f}\quad\text{and}\quad F_z(L)=F_{ex}-F_{i,f} \tag{11}$$

where the subscripts 'ex' and 'i, f' denote excitation as well as intrinsic and fluid moments and forces. For the Lorentz forces on the excitation current I_{ex} along the space variable $\mathbf{s}$ in the magnetic field with magnetic flux density $\mathbf{B}$ it follows (bold variables denote vectors and $\mathbf{e}_x$ is a unity vector in x-direction)

$$\mathbf{F}_{ex}=I_{ex}\int_{\boldsymbol{\xi}=(R,0,0)}^{\boldsymbol{\xi}=(R,\pi/2,0)} d\mathbf{s}(r,\varphi,\zeta)\times\mathbf{B}(r,\varphi,\zeta)=I_{ex}\,R\,B\,\mathbf{e}_z \tag{12}$$

assuming $\mathbf{B}(r,\varphi,\zeta)=-B\,\mathbf{e}_\xi$ being constant at the U's tip. Note, that only half of the excitation force is calculated here, due to the structure's symmetry. I.e., the U is interpreted as two singly clamped beams connected in parallel which allows considering only one half of the latter to calculate it's deflection.

The moment resulting from the excitation at $x=L$ is

$$M_{ex}=F_{ex}\,\xi_c \tag{13}$$

where $\xi_c\,\mathbf{e}_\xi$ is the center of excitation forces which can be calculated assuming $\partial U_z(x=L)/\partial x$ to be negligibly small and solving the integral equation

$$\int_0^{\xi_c} f_{ex}(\xi)\,d\xi=\int_{\xi_c}^{R} f_{ex}(\xi)\,d\xi \tag{14}$$

for ξ_c with

$$f_{ex}(\xi)=I_{ex}\,B\,\frac{\xi}{\sqrt{R^2-\xi^2}} \tag{15}$$

being the excitation force per unit length transformed to the ξ-axis. Substituting Eq. (15) in (14) and solving the obtained equation yields $\xi_c=\sqrt{3}/2\,R$ and thus

$$M_{ex}=\frac{\sqrt{3}}{2}I_{ex}\,R^2\,B. \tag{16}$$

The intrinsic and fluid forces for the U's round end are

$$F_{i,f}=\int_0^R f_{i,f}(\xi)\,d\xi \tag{17}$$

with

$$f_{i,f}(\xi)=(-\omega^2\,m'+j\,\omega\,d'_f)\frac{R}{\sqrt{R^2-\xi^2}}\,U_z(\xi). \tag{18}$$

Note as the round end is considered to be stiff, the intrinsic damping parameter d_0 is not taken into account here. Assuming $\partial U_z(x=L)/\partial x$ to be negligibly small again, it follows for the moment

$$M_{i,f}=F_{i,f}\xi_{c,fi} \tag{19}$$

with the center of intrinsic and fluid forces $\xi_{c,fi}=R/\sqrt{2}$ in this case.

3.4. Correction functions

In the calculation of the fluid forces above, ideal conditions are assumed. However as in practice, the setup suffers e.g., from material and production related geometrical imperfections, the real fluid forces may deviate from the calculated values. For this reason, the terms in Eq. (9) have to be corrected. As both quantities, mass density and viscosity affect both, inertial and dissipative terms, four additional terms are introduced into the model.

In this case, the inertial and dissipative terms in Eq. (9) are extended by four correction functions $C_{i,j}$ as follows

$$m'_f(\rho_f,\ \eta_f)\to m'_f(C_{\rho,m}(\rho)\cdot\rho_f,\ C_{\eta,m}(\eta)\cdot\eta_f)$$
$$d'_f(\rho_f,\ \eta_f)\to d'_f(C_{\rho,d}(\rho)\cdot\rho_f,\ C_{\eta,d}(\eta)\cdot\eta_f). \tag{20}$$

In this work, for the correction functions, constants as well as linear and quadratic Bézier functions were used.

3.5. Cross-sensitivity to temperature

The effect of temperature T on the oscillation of the oscillating U-shaped wire is considered in the mechanical model by taking thermal expansion and the change of the Young's modulus into account. As in this work, the sensor's operating temperature range is around room temperature (25 °C), linear relations sufficiently describe the cross-sensitivity to temperature. It follows that

$$L(T)=L_{T_0}(1+\alpha_w\,(T-T_0))\quad\text{and}\quad E(T)=E(T_0)+C_E\,T \tag{21}$$

where T_0 is a reference Temperature, α_w is the linear thermal expansion coefficient and C_E is the linear coefficient for the Young's modulus.

Author's personal copy

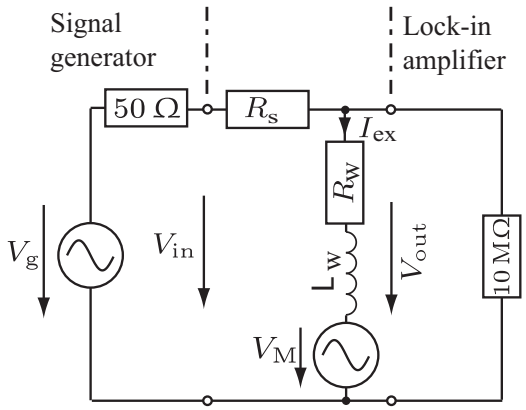

Fig. 3. Electrical equivalent model: the U-shaped wire viscosity and mass density sensor is modeled by its electrical impedance and a motion induced voltage. V_g: voltage of the signal generator, 50 Ω output resistance of the signal generator, R_s: series resistance (100 Ω), R_w: resistance of the tungsten wire, L_w: inductance of the U-shaped tungsten wire, V_M: motion induced voltage.

4. Read-out

The voltage V_{out} on the oscillating U-shaped wire consists of a motion induced voltage V_M which is proportional to the oscillator's velocity and an additional offset voltage V_{offs} due to the wire's impedance, i.e.,

$$V_{out}(\omega) = V_M(\omega) + V_{offs}(\omega) \tag{22}$$

as it is depicted in the equivalent circuit in Fig. 3.

From the definition of Lorentz forces and Faraday's law for induction, the motion induced voltage v_M in a conductor of length l_c moving in an magnetic field is expressed as

$$v_M(t) = -\int_0^{l_c} \left(\frac{\partial \mathbf{u}}{\partial t} \times \mathbf{B}\right) \cdot \mathrm{d}\mathbf{s}. \tag{23}$$

where **u** is the (relative) deflection of the conductor with respect to the points at which the voltage is induced and d**s** is a vector line element along the conductor. In this case, assuming the magnetic field to be constant at the U's tip, it follows for the motion induced voltage in the frequency domain

$$V_M(\omega) = 2\,B\,R\,j\,\omega\,U_z(L) + \frac{\pi}{2}R^2\,B\,j\,\omega\,\left.\frac{\partial U_z(x)}{\partial x}\right|_{x=L}. \tag{24}$$

As depicted in Fig. 3, a signal generator (with 50 Ω output resistance) serves as voltage source and a lock-in amplifier (with a 10 MΩ input resistance) as voltmeter. A series resistance R_s is used to limit the excitation current to prevent significant non-linear oscillations. Furthermore, the U-shaped wire shows a non-negligible resistance R_w and inductance L_w which are calculated as follows:

$$R_w = \rho_r \frac{l}{A} \approx \rho_r \frac{2L + R\pi}{r_w^2\,\pi}. \tag{25}$$

To find an approximate value for the inductance of the U-shaped wire, the equation for the inductance of a rectangular loop is used [27]:

$$L_w \approx \frac{\mu}{\pi}\left[L \ln\left(\frac{2L}{r_w}\right) + 2R \ln\left(\frac{4R}{r_w}\right) + 2\sqrt{L^2 + (2R)^2} - 1.75\,(L + 2R) - L\,\mathrm{a\,sin\,h}\left(\frac{L}{2R}\right) - 2R\,\mathrm{a\,sin\,h}\left(\frac{2R}{L}\right)\right] \tag{26}$$

where μ is the permeability of the surrounding medium. With this, it follows for the measured voltage

$$V_{out}(\omega) = V_M + I_{ex}\,(R_w + j\,\omega\,L_w) \tag{27}$$

where

$$I_{ex} = \frac{V_g - V_M}{50\Omega + R_s + R_w + j\,\omega\,L_w}. \tag{28}$$

5. Sensor setup

Several prototypes of the U-shaped wire sensor were fabricated. For the prototype presented in this paper, photographs are shown in Fig. 4. To prevent from evaporation and associated thermal changes of the liquid due to evaporation heat losses, the U-shaped wire was integrated in a sealed aluminum housing. An assembly of cylindrical and ring permanent magnets provides magnetic flux densities of $B \approx 0.5$ T [22]. A tungsten wire ($\rho_w = 19.3 \cdot 10^3$ kg/m^3, $E \approx 410$ GPa) with $r_w = 200$ µm, $R = 3$ mm and $L = 12$ mm, c.f. Fig. 2, was used. To achieve a stable and reliable clamping, the wire was brazed into two brass blocks. For rigidly clamping these blocks to the housing, two screws for each block were used, which furthermore serve to provide a stable electrical connection between the U-shaped wire and a PCB carrying BNC connectors. For measuring and controlling the liquid's temperature, a Pt-100 temperature sensor was placed close to the U-shaped wire.

For the measurements shown in Section 6, the setup was placed in a climate chamber to provide stable measuring conditions by controlling the temperature at 25 °C. The voltage of the signal generator was $V_g = 0.1$ V and the series resistance $R_s = 100$ Ω.

6. Measurements

6.1. Response to viscosity

For evaluating the sensor's response to viscosity, 11 acetone–isopropanol solutions were prepared and then characterized with a high precision viscosity and mass density laboratory instrument (SVM 3000) featuring an accuracy of 0.35% for viscosity and 500 µg/cm^3 for density. The ratios of each liquid were chosen to obtain almost constant viscosity steps between each solution. The obtained viscosity values ranged from 0.21 mPa s to 2.05 mPa s at 25 °C for hardly varying densities in a range from 0.7789 g/cm^3 to 0.7848 g/cm^3 which however do not correlate with the change of viscosity. The relatively small range of investigated viscosities in this experiment was chosen to examine the resolution of the viscosity sensor. A further experiment in liquids covering a higher viscosity and mass density range will be discussed in Section 6.2. The resonance frequency and quality factor in air for the fundamental mode were 951.5 Hz and 840, respectively. Using the same excitation and read-out principle and for the same direction of the magnetic field, a higher mode was observed at 6234.3 Hz with a quality factor of 759 in air. However, this higher mode was not further investigated in this contribution. Fig. 5(a) shows the recorded frequency responses with respect to the modeled results. In Fig. 5(a) the dots indicate the measured points and the solid lines are results obtained with the fitted model. For every liquid, 100 frequency responses have been recorded during 30 min approximately. Between the examination of two samples, the sensor was cleaned and a measurement in air was performed for evaluating the properly cleaned condition of the sensor. In Figs. 5(b) and (c), the evaluated Q and f_r are plotted versus η_f. The range of quality factors of the recorded frequency responses is $Q \approx 170 \ldots 72$ for low to high viscous samples.

For the fitting procedure in this work, first the length L and the intrinsic damping d_0 have been adjusted to fit the model for V_{out} to

Author's personal copy

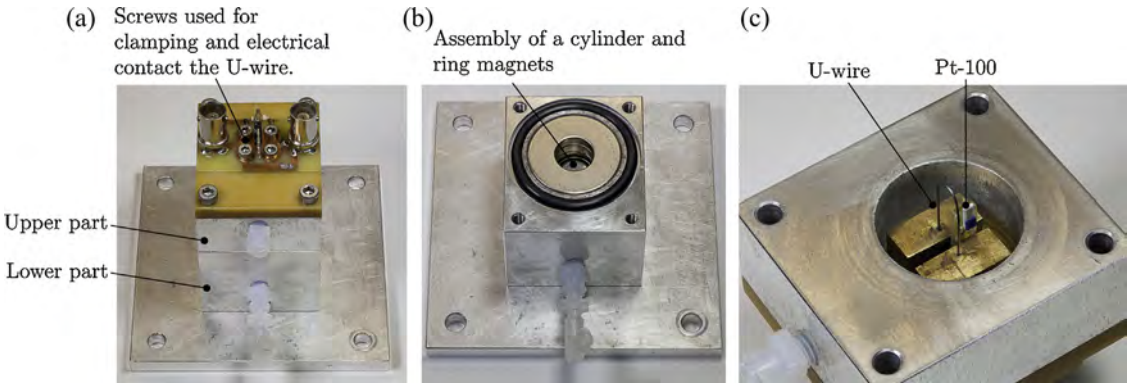

Fig. 4. Photographs of the measurement setup.

the measured data in air considering the mass density and viscosity of air at 25 °C, see right hand side of Fig. 5(a) (the fitted value for L was 12.04 mm for nominally 12 mm and $d_0 = 16.5 \cdot 10^{-3}$ kg/(m s)). To improve the accordance between model and measurements in liquids, empiric corrections functions have been introduced into the model as described in Section 3.4. A comparison of corrected and non-corrected modeling results for liquids is illustrated in Fig. 5(b) and (c).

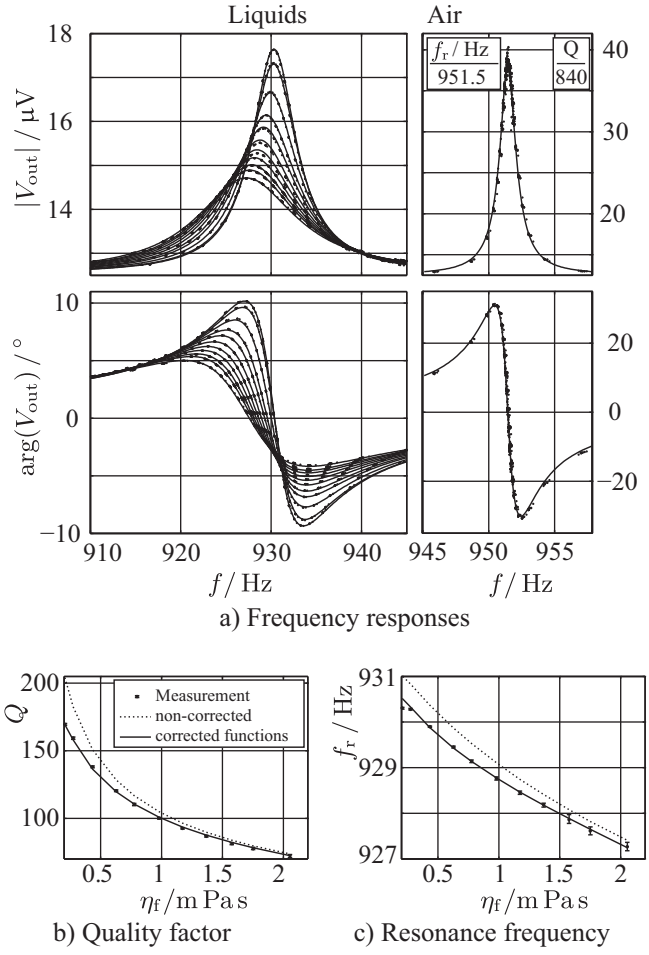

Fig. 5. Comparison of measured and modeled results for acetone–isopropanol solutions. In (a) amplitude and phase of the frequency responses are depicted. (b) and (c) show a comparison of evaluated quality factors and resonance frequencies for measured frequency responses (dots), and modeled frequency responses, Eq. (27), considering the non-corrected model (dashed lines) and the model using correction functions (solid lines) introduced in Section 3.4.

Table 1
Sensitivities.

η_f (mPa s)	ρ_f (g/cm^3)	$S_{f_r,\eta}$ (10^{-3})	$S_{f_r,\rho}$ (10^{-3})	$S_{Q,\eta}$ (10^{-3})	$S_{Q,\rho}$ (10^{-3})
0.21	0.7841	3.80	682.07	422.00	427.72
215.73	1.2359	33.65	106.43	673.16	318.18

6.2. Measured range and sensitivity

In contrast to the measurements depicted in Fig. 5 for which liquids of almost constant mass densities but varying viscosities were used, 11 DI-water–glycerol mixtures were prepared yielding a viscosity range of 0.93 mPa s to 215.73 mPa s and mass densities in a range from 0.9966 g/cm^3 to 1.2359 g/cm^3 at 25 °C. The highest viscous liquid (η_f = 215.73 mPa s, ρ_f = 1.2359 g/cm^3) yielded a quality factor of 4.31 and a resonance frequency of 871.09 Hz, see Table 2. As f_r and Q depend on both, η_f and ρ_f, plotting the measurement results as in Fig. 5(b) and (c) would be misleading as in this case, not only the liquid's viscosity but also it is mass density change significantly. Thus the obtained values are given in Table 2.

It is also to this η_f and ρ_f dependency of f_r and Q, that a general sensitivity value cannot be given. Furthermore the change of f_r and Q in respect to η_f and ρ_f depends on the geometrical dimensions of the particular resonator. However, to give an idea of the order of magnitude of sensitivities S_{X,y_i} of the presented device, with

$$S_{X,y_i} = \left| \frac{\partial X}{\partial y_i} \cdot \frac{y_i}{X} \right| \tag{29}$$

where X stands either for f_r or Q and y_i for η_f or ρ_f, these sensitivities are evaluated for the lowest and highest viscous liquids and listed in Table 1. Note, when aiming at a characterization of high viscous liquids, the sensitivity of the particular resonant devices has to be even low, as otherwise the considered resonant mode would be completely damped preventing accurate readout.

6.3. Cross-sensitivity to temperature

For previously introduced setups, high cross-sensitivities of the resonance frequency to temperature were observed cf., [28]. To overcome this drawback, the U-shaped wire was devised. The advantage of this structure compared to straight doubly clamped setups is the approach similar to singly clamped structures such as cantilevers. The singly clamped approach eliminates temperature related variations of normal stresses in the structure and thus significantly reduces the thermally induced change of resonance

Author's personal copy

Table 2
Measurement results for DI-water–glycerol mixtures. The values for η_f and ρ_f were determined with a SVM 3000 viscometer.

	η_f (mPa s)	ρ_f (g/cm^3)	f_r (Hz)	Q
1	0.93	0.9966	926.67	95.77
2	9.78	1.1545	915.79	27.83
3	17.65	1.1770	910.54	19.92
4	25.46	1.1880	906.07	16.15
5	33.37	1.1966	902.87	13.88
6	41.16	1.2025	900.00	12.25
7	48.46	1.2062	897.00	11.35
8	56.13	1.2098	893.49	9.68
9	63.71	1.2126	892.72	9.89
10	110.62	1.2242	879.03	6.41
11	215.73	1.2359	871.09	4.31

frequency. Furthermore, the choice of tungsten as resonator material, which features a low thermal expansion coefficient, keeps this cross-sensitivity additionally low. The resonance frequencies of the U-shaped tungsten wire sensor were evaluated in a temperature range from 25 °C to 50 °C in air. The resonance frequencies for a 400 μm thick tungsten wire, $R = 3$ mm and $L = 12$ mm at 25 °C was $fr = 952.96$ Hz. The evaluated dependencies of resonance frequencies on temperature were $\Delta f_r/\Delta T = -0.0479$ Hz/K. This temperature dependence was modeled using Eq. (21) with $\alpha_w = 5.25 \cdot 10^{-6}$ 1/K, $E(T_0) = 409.08$ GPa and $C_E \approx 0.03$ GPa/K. These values for α_w and C_E, necessary for accurately accounting for the dependence of resonance frequency to temperature are higher than values given in the literature, cf., [29,30]. There, e.g. the thermal expansion coefficient for tungsten usually is $\alpha_w = 4.5 \cdot 10^{-6}$ 1/K. This deviation is one of the reasons revealing the need for further investigation of resonators' temperature dependencies in general.

The dependence of the U-shaped tungsten wire's fundamental resonance frequency to temperature was compared to other singly clamped resonators, see Table 3. There, the U-shaped tungsten wire sensor (U(W)) is compared to the following devices: A U-shaped silicon cantilever (U (Si, Au)) carrying a gold path on a thin silicon nitride layer, see [31], a steel tuning fork (TF (Steel)), a bare silicon cantilever (CL (Si)) [32] and a gold-coated cantilever (CL (Si, Au)) [33]. The comparison of the relative resonance frequency shifts in respect to temperature shows, that only the bare silicon cantilever features a lower cross-sensitivity to temperature. However, bare silicon is not adaptable in this case to meet the requirements for the sensor discussed in Section 1.

6.4. Long-term measurements

The setup as it is depicted in Fig. 4 has been tested in several liquids recording f_r and Q over several days in a climate chamber at 25 °C. In comparison to previously investigated doubly clamped devices [18], the long-term stability improved significantly. However, in some cases, minor but clear trends of both f_r and Q could be observed, see e.g., Fig. 6. There, the evaluated results for f_r and Q of 4193 measurements which were recorded during 90 h in ethanol are depicted. In this case, the shift to lower f_r and Q is related to the

Table 3
Cross-sensitivities of the resonance frequency (fundamental mode) to temperature. f_0: nominal frequency, $\Delta f_r = f_r(T_0) - f_r(T_1)$: resonance frequency shift, $\Delta T = T_0 - T_1$ difference of temperatures T_0 and T_1, $\Delta f_{r,rel} = \Delta f_r/f_0$: relative resonance frequency shift, 't.w.' designates this work.

Sensor	f_0 (kHz)	$\Delta f_r/\Delta T$ (Hz/K)	$\Delta f_{r,rel}/\Delta T$ (1/K)	Refs.
U (W)	0.95	−0.048	$-60 \cdot 10^{-6}$	t.w.
U (Si, Au)	5.96	−0.441	$-69 \cdot 10^{-6}$	t.w., [31]
TF (Steel)	0.44	−0.0519	$-118 \cdot 10^{-6}$	t.w.
CL (Si)	43.83	−1.3	$-29.7 \cdot 10^{-6}$	[32]
CL (Si, Au)	18.33	−1.83	$-100 \cdot 10^{-6}$	[33]

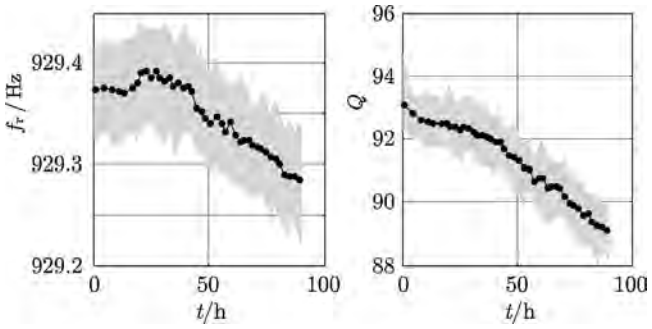

Fig. 6. Long-term measurements in ethanol, yielding a drift of resonance frequency and quality factor. The black line indicates averaged values of 100 measurements where the gray surface represents all measured values.

change of the liquid properties itself. It was found that O-ring seals were slightly dissolved by the ethanol leading to a slight increase in viscosity and mass density of the liquid which was detected by the sensor.

In another experiment, electrolytical solutions were investigated, which yielded corrosion within the setup. It is due to such instabilities of the setup itself that the long-term stability cannot be reliably quantified at the present stage of our research. For this, a complete redesign aiming at a more stable setup using other materials, will be necessary.

However, the principle of the U-shaped wire yielded already acceptable and promising results for the long-term stability. The principle ability for long-term stability can be explained by its singly clamped approach and by its low cross-sensitivity to temperature. These circumstances can also be observed in case of string instruments, which have to be frequently tuned, compared to reed-based instruments (like accordions) and tuning forks which are based on singly clamped oscillating objects.

7. Conclusion and outlook

The U-shaped wire mass density and viscosity sensor is a candidate promising improvements in terms of low cross-sensitivity to temperature and stability of resonance frequency compared to previously introduced principles. A closed form model was developed relating the driving voltage to the measured sensor's output voltage. This model was experimentally verified for acetone–isopropanol and DI-water–glycerol solutions, showing good accordance of measured and theoretical values. However, when aiming at high accuracies, this comparison revealed the need for an appropriate calibration process.

For the setup used in this work, aluminum and chromium get wetted by the sample liquid which causes corrosion of the latter when investigating electrolytic solutions. Regarding future work, a new setup has to be designed avoiding corrosion. Furthermore, comprehensive measurement series have to be performed allowing for evaluating the device's accuracy, repeatability and long-term stability. As for the modeling of the cross-sensitivity to temperature, material parameters deviating from values reported in literature were used, a thorough study on the dependence of oscillators' resonance frequencies on temperature has to be elaborated.

Acknowledgements

We are indebted to the Austrian COMET program (Austrian Centre of Competence in Mechatronics, ACCM) for the financial support. We also want to thank Bernhard Mayrhofer and Johann Katzenmayer for their help and excellent assistance.

Author's personal copy

References

[1] A. Agoston, C. Ötsch, B. Jakoby, Viscosity sensors for engine oil condition monitoring – application and interpretation of results, Sens. Actuators A 121 (2005) 327–332.
[2] R. Haskell, J. Taku, J. Steichen, B. Witham, Calibration of in-line acoustic wave viscosity sensors for measurement of printing inks, in: Proceedings SENSOR 2013, 2013, pp. 592–597.
[3] P. Rust, D. Cereghetti, J. Dual, A micro-liter viscosity and density sensor for the rheological characterization of dna solutions in the kilo-hertz range, Lab Chip 13 (24) (2013) 4794–4799, http://dx.doi.org/10.1039/C3LC50857A.
[4] S. Boskovic, J. Chon, P. Mulvaney, J. Sader, Rheological measurements using microcantilevers, J. Rheol. 46 (4) (2002) 891–899.
[5] B. Jakoby, R. Beigelbeck, F. Keplinger, F. Lucklum, A. Niedermayer, E.K. Reichel, C. Riesch, T. Voglhuber-Brunnmaier, B. Weiss, Miniaturized sensors for the viscosity and density of liquids – performance and issues, ITUCER 57 (1) (2010), http://dx.doi.org/10.1109/TUFFC.2010.1386.
[6] B. Jakoby, M. Vellekoop, Physical sensors for liquid properties, IEEE Sens. J. 11 (12) (2011) 3076–3085.
[7] I. Dufour, A. Maali, Y. Amarouchene, et al., The microcantilever: a versatile tool for measuring the rheological properties of complex fluids, J. Sens. (2012), http://dx.doi.org/10.1155/2012/719898.
[8] C. Riesch, A. Jachimowicz, F. Keplinger, E.K. Reichel, B. Jakoby, A novel sensor system for liquid properties based on a micromachined beam and a low-cost optical readout, in: Proceedings IEEE Sensors, 2007, pp. 872–875.
[9] L. Matsiev, J. Bennett, O. Kolosov, High precision tuning fork sensor for liquid property measurements, in: IEEE Ultrasonics Symposium, 2005, pp. 1492–1495.
[10] E.K. Reichel, C. Riesch, F. Keplinger, B. Jakoby, Modeling of the fluid–structure interaction in a fluidic sensor cell, Sens. Actuators A: Phys. 156 (1) (2009) 222–228.
[11] P. Peiker, E. Oesterschulze, Impact of the miniaturization on the response of a hybrid diaphragm resonator considering its finite support, in: Proceedings of the Nanomechanical Sensing Workshop, 2013, pp. 127–128.
[12] E.K. Reichel, C. Riesch, F. Keplinger, C.E.A. Kirschhock, B. Jakoby, Analysis and experimental verification of a metallic suspended plate resonator for viscosity sensing, Sens. Actuators A: Phys. 162 (2010) 418–424, http://dx.doi.org/10.1016/j.sna.2010.02.017.
[13] A. Abdallah, M. Heinisch, B. Jakoby, Measurement error estimation and quality factor improvement of an electrodynamic-acoustic resonator sensor for viscosity measurement, Sens. Actuators A: Phys. 199 (2013) 318–324.
[14] S. Martin, V.E. Granstaff, G.C. Frye, Characterization of a quartz crystal microbalance with simultaneous mass and liquid loading, Anal. Chem. 63 (1991) 2272–2281.
[15] R. Thalhammer, S. Braun, B. Devcic-Kuhar, M. Gröschl, F. Trampler, E. Benes, H. Nowotny, M. Kostal, Viscosity sensor utilizing a piezoelectric thickness shear sandwich resonator, IEEE Trans. Ultrason. Ferroelectr. Freq. Control 45 (5) (1998) 1331–1340.
[16] M. Heinisch, E.K. Reichel, I. Dufour, B. Jakoby, A resonating rheometer using two polymer membranes for measuring liquid viscosity and mass density, Sens. Actuators A: Phys. 172 (1) (2011) 82–87, http://dx.doi.org/10.1016/j.sna.2011.02.031.
[17] C. Castille, I. Dufour, C. Lucat, Longitudinal vibration mode of piezoelectric thick-film cantilever-based sensors in liquid media, Appl. Phys. Lett. 96 (15) (2010) 154102, http://dx.doi.org/10.1063/1.3387753.
[18] M. Heinisch, E.K. Reichel, I. Dufour, B. Jakoby, Tunable resonators in the low kHz range for viscosity sensing, Sens. Actuators A: Phys. (2012), http://dx.doi.org/10.1016/j.sna.2012.03.009.
[19] B. Jakoby, M. Vellekoop, Physical sensors for water-in-oil emulsions, Sens. Actuators A: Phys. 110 (1) (2004) 28–32.
[20] B. Weiss, E.K. Reichel, B. Jakoby, Modeling of a clamped–clamped beam vibrating in a fluid for viscosity and density sensing regarding compressibility, Sens. Actuators A: Phys. 143 (2) (2008) 293–301.
[21] J. Sader, Frequency response of cantilever beams immersed in viscous fluids with applications to the atomic force microscope, J. Appl. Phys. 84 (1998) 64–76.
[22] M. Heinisch, E.K. Reichel, T. Voglhuber-Brunnmaier, B. Jakoby, Miniaturized viscosity and mass density sensors combined in a measuring cell for handheld applications, in: Proceedings of the IEEE Sensors Conference, 2012.
[23] F. Keplinger, R. Beigelbeck, F. Kohl, S. Kvasnica, A. Jachimowicz, B. Jakoby, Frequency and transient analysis of micromachined U-shaped cantilever devices for magnetic field measurement, Solid-State Sens. Actuators Microsyst. 1 (2005) 630–635.
[24] W. Weaver, S. Timoshenko, D. Young, Vibration Problems in Engineering, 5th ed., Wiley, Toronto, 1990.
[25] L. Landau, E. Lifshitz, Fluid Mechanics, Butterworth-Heinemann, Oxford, 1987.
[26] L. Rosenhead, Laminar Boundary Layers: Fluid Motion Memoirs, Clarendon, Oxford, 1963.
[27] F.W. Grover, Inductance Calculations, Dover, New York, 2009.
[28] M. Heinisch, E. Lemaire, B. Caillard, I. Dufour, B. Jakoby, A study of wire-based resonators for viscosity sensing, in: Proceedings of the conference on Microfluidics, 2012.
[29] R.H. Knibbs, The measurement of thermal expansion coefficient of tungsten at elevated temperatures, J. Phys. E: Sci. Instrum. (1969) 515–517.
[30] G. Skoro, J. Bennett, T. Edgecock, S. Gray, A. McFarland, C. Booth, K. Rodgers, J. Back, Dynamic Young's moduli of tungsten and tantalum at high temperature and stress, J. Nucl. Mater. (2011) 40–46.
[31] M. Stifter, T. Sauter, W. Hortschitz, F. Keplinger, H. Steiner, MEMS heterodyne AMF detection with capacitive sensing, in: Proceedings of the IEEE Sensors 2012, 2012, pp. 1–4, http://dx.doi.org/10.1109/ICSENS.2012.6411171.
[32] H. Wasisto, S. Merzsch, A. Waag, E. Uhde, T. Salthammer, E. Peiner, Airborne engineered nanoparticle mass sensor based on a silicon resonant cantilever, Sens. Actuators B: Chem. 180 (2013) 77–89.
[33] R. Sandberg, W. Svendsen, K. Mølhave, A. Boisen, Temperature and pressure dependence of resonance in multi-layer microcantilevers, J. Micromech. Microeng. 15 (8) (2005) 1454.

Biographies

Martin Heinisch obtained his Dipl.-Ing. (M.Sc.) in Mechatronics from Johannes Kepler University Linz, Austria, in 2009. After his Master studies he went to the University of California, Los Angeles (U.C.L.A.) as a Marshall Plan Scholarship grantee, where he did research in the field of microfluidic applications and self assembling systems. In 2010 he started a Ph.D. program at the Institute for Microelectronics and Microsensors of the Johannes Kepler University Linz, Austria where he is currently working on resonating liquid sensors.

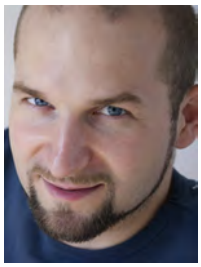

Erwin K. Reichel was born in Linz, Austria, in 1979. He received the Dipl.-Ing. (M.Sc.) degree in Mechatronics from Johannes Kepler University, Linz, Austria, in 2006. From 2006 to 2009 he was working on the Ph.D. thesis at the Institute for Microelectronics and Microsensors of the Johannes Kepler University, Linz and graduated in October 2009. Afterwards he held a post-doctoral position at the Centre for Surface Chemistry and Catalysis as well as at the Department for Chemical Engineering, KU Leuven, Belgium until June 2012. Since then he holds a position as university assistant at the Johannes Kepler University Linz. The main research fields are the modeling, design, and implementation of sensors for liquid properties, and monitoring of phase transition in complex solutions.

Isabelle Dufour graduated from Ecole Normale Supérieure de Cachan in 1990 and received the Ph.D. and H.D.R. degrees in engineering science from the University of Paris-Sud, Orsay, France, in 1993 and 2000, respectively. She was a CNRS research fellow from 1994 to 2007, first in Cachan working on the modelling of electrostatic actuators (micromotors, micropumps) and then after 2000 in Bordeaux working on microcantilever-based chemical sensors. She is currently Professor of electrical engineering at the University of Bordeaux and her research interests are in the areas of microcantilever-based sensors for chemical detection, rheological measurements and materials characterisation.

Bernhard Jakoby obtained his Dipl.-Ing. (M.Sc.) in Communication Engineering and his doctoral (Ph.D.) degree in electrical engineering from the Vienna University of Technology (VUT), Austria, in 1991 and 1994, respectively. In 2001 he obtained a venia legendi for Theoretical Electrical Engineering from the VUT. From 1991 to 1994 he worked as a Research Assistant at the Institute of General Electrical Engineering and Electronics of the VUT. Subsequently he stayed as an Erwin Schrödinger Fellow at the University of Ghent, Belgium, performing research on the electrodynamics of complex media. From 1996 to 1999 he held the position of a Research Associate and later Assistant Professor at the Delft University of Technology, The Netherlands, working in the field of microacoustic sensors. From 1999 to 2001 he was with the Automotive Electronics Division of the Robert Bosch GmbH, Germany, where he conducted development projects in the field of automotive liquid sensors. In 2001 he joined the newly formed Industrial Sensor Systems group of the VUT as an Associate Professor. In 2005 he was appointed Full Professor of Microelectronics at the Johannes Kepler University Linz, Austria. He is currently working in the field of liquid sensors and monitoring systems.

Sensors and Actuators A xxx (2015) xxx–xxx

Contents lists available at ScienceDirect

Sensors and Actuators A: Physical

journal homepage: www.elsevier.com/locate/sna

Application of resonant steel tuning forks with circular and rectangular cross sections for precise mass density and viscosity measurements☆

M. Heinisch[a,*], T. Voglhuber-Brunnmaier[a,b], E.K. Reichel[a], I. Dufour[c], B. Jakoby[a]

[a] Institute for Microelectronics and Microsensors, Johannes Kepler University, Linz, Austria
[b] Center for Integrated Sensors Systems, Danube University, Krems, Austria
[c] Université de Bordeaux, Laboratoire de l'Intégration du Matériau au Système, Pessac, France

ARTICLE INFO

Article history:
Received 20 October 2014
Received in revised form 16 January 2015
Accepted 9 February 2015
Available online xxx

Keywords:
Tuning fork
Sensor
Viscosity
Mass density
Circular
Rectangular

ABSTRACT

The feasibility of using commercially available steel tuning forks for viscosity and mass density sensing is investigated. For this task, the tuning forks are electromagnetically driven and read out to record their frequency responses containing the fundamental resonant mode upon immersion in a sample liquid. Evaluated resonance frequencies and quality factors are then related to the liquids' mass density and viscosity. The used electromagnetic actuation and readout principle allows that only the tuning fork which is placed in the center of a glass tube gets wetted with the liquid to be examined. All excitation and read out related structures and electronics are placed outside the glass tube and thus, are not affected or influenced by the liquid. A generalized model relating evaluated quality factors and resonance frequencies to viscosity and mass density is used to describe the tuning forks' sensitivities and furthermore to estimate required stabilities of apparent quality factors and resonance frequencies to achieve measurement accuracies similar to those of laboratory instruments. It is shown that relative accuracies in the order of 1% in viscosity and 0.1 mg/cm^3 in mass density are achievable.

© 2015 Elsevier B.V. All rights reserved.

1. Introduction

Lately, we examined the applicability of mechanical resonators for sensing a liquid's (complex) viscosity and mass density, see [1]. A very promising approach for this task is the use of electrodynamically driven and read out mechanical oscillators. The investigated principles featuring fundamental resonance frequencies in the range from some hundreds of hertz to several kilohertz include, amongst others, oscillating membranes [2,3], in-plane oscillating platelets [4,5], straight wires [6] and U-shaped wires [7,8]. Similar miniaturized devices are silicon cantilevers [9,10], quartz crystal tuning forks [11], doubly clamped silicon beams [12] and vibrating diaphragms [13] just to name a few examples of the relatively large variety of principles reported in literature.

The resonant principles mentioned above are all potential candidates for mass density and viscosity sensors. In some cases they were especially designed for specific applications, such as, e.g., the use of miniaturized devices for liquids where only tiny amounts of sample volumes are available [14]. As an alternative to these devices usually aiming at low viscosity measurements and furthermore serving as reference devices, conventional steel tuning forks showing a fundamental resonance frequency at nominally 440 Hz have been investigated in this contribution. A first investigation of such tuning fork based setups has already been presented in [15]. The motivation for such steel tuning fork setups is based on several arguments. First, due to the momentum balanced motion in the fundamental mode, the resonant behavior of tuning forks is less sensitive to clamping issues as it is the case e.g. for singly or doubly clamped beams and membranes. Second, the relatively large and solid structure is less prone to deteriorations, such as not perfectly cleaned surfaces, air bubbles, etc. Third, in comparison to doubly clamped structures in general, the cross sensitivity of their resonance frequency to temperature is small. Such cross sensitivities of the resonance frequency to temperature can be characterized, determined and modeled on the one hand but on the other hand, they limit the sensor's accuracy and thus, should be kept as low as possible.

☆ Selected papers presented at EUROSENSORS 2014, the XXVIII edition of the conference series, Brescia, Italy, September 7–10, 2014.

* Corresponding author. Tel.: +43 73224686266.
E-mail address: martin.heinisch@jku.at (M. Heinisch).

http://dx.doi.org/10.1016/j.sna.2015.02.007
0924-4247/© 2015 Elsevier B.V. All rights reserved.

Please cite this article in press as: M. Heinisch, et al., Application of resonant steel tuning forks with circular and rectangular cross sections for precise mass density and viscosity measurements, Sens. Actuators A: Phys. (2015), http://dx.doi.org/10.1016/j.sna.2015.02.007

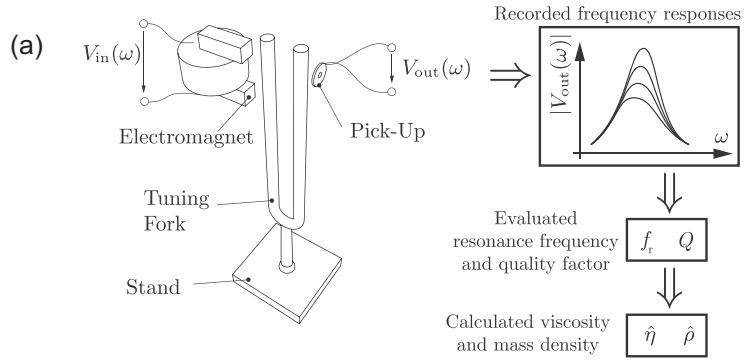

(b)

■ Front view

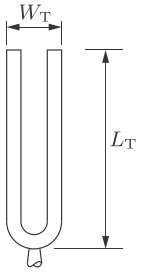

■ Dimensions in mm

	Circular	Rectangular
L_T	75.1	83.4
W_T	13.7	16.5
	$D = 3.6$	$h = 3.96$
		$b = 4.96$
		$r_r = 1$

■ Top view

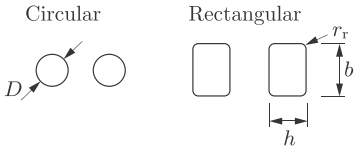

Fig. 1. Sensor principle: (a) A ferromagnetic steel tuning fork is actuated and read out with an electromagnet and an electromagnetic pick-up, respectively. Frequency responses are recorded for the completely immersed tuning fork and evaluated resonance frequencies and quality factors are related to the sample liquid's viscosity and mass density. (b) In the table above, the geometrical dimensions of the circular and rectangular tuning fork are given.

In this contribution, the basic setup for ferromagnetic tuning forks used for viscosity and mass density sensing is explained. Furthermore, measurements showing the response to viscosity and mass density for circular and rectangular cross-sectioned tuning forks are presented. The sensitivities of both tuning forks are discussed in detail and required stabilities for the resonance frequency and quality factor to achieve measurement accuracies of 1% for viscosity and 1 mg/cm^3 for mass density are estimated. It is furthermore shown, that with the investigated steel tuning forks accuracies in the order of 1% in viscosity and 0.1 mg/cm^3 in mass density are achievable.

2. Measurement setup

Fig. 1 shows a basic sketch of the setup for viscosity and mass density measurements using commercially available tuning forks with circular and rectangular cross sections. The measurement procedure is depicted in Fig. 1(a) and the geometries of the used steel tuning forks, both resonating at nominally 440 Hz in air in their fundamental mode are given in Fig. 1(b). Fig. 2 shows a photograph of the circular tuning fork setup.

The steel tuning forks were welded to a solid stainless steel stand and put into a glass tube (not depicted in Fig. 1(a)) which was sealed at both sides. To avoid corrosion, the tuning forks were gold-coated by electro-plating. An electromagnet, used for excitation, is placed (outside of the tube) close to the end of one of the ferromagnetic tuning fork's prongs. At the end of the opposed prong, an electrodynamic pick-up is placed, consisting of a permanent magnet in the center of a copper coil. A sinusoidal Voltage $V_{in} = \hat{V}_{in} \sin(\omega t) + V_{in,offs}$ with a DC offset $V_{in,offs} \geq \hat{V}_{in}/2$ is used as input signal, exciting harmonic oscillations of the tuning fork (ω is the angular frequency and t is the time). These oscillations effect an induced voltage in the pick-up serving as the read out signal. By sweeping the excitation current's frequency (containing the frequency of a resonant mode), the frequency response of the tuning fork is recorded.

The measured frequency response $V_{out}(\omega)$ is composed of three effects. First, a motion-induced voltage V_M in the pick-up coil resulting from the movement of the tuning fork's ferromagnetic prong. This voltage is proportional to the prong's velocity. The second measured signal component is an induced offset voltage V_{offs} due

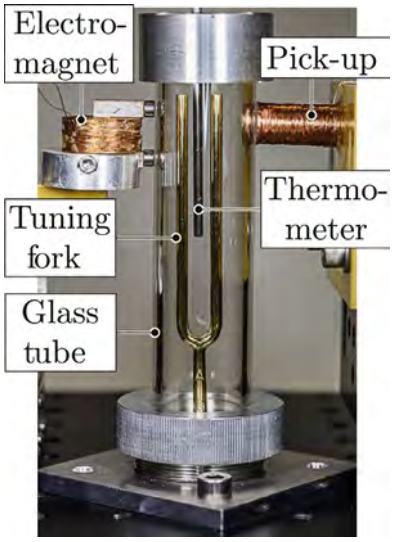

Fig. 2. Photograph of the measurement setup with a gold coated circular cross-sectioned tuning fork.

Please cite this article in press as: M. Heinisch, et al., Application of resonant steel tuning forks with circular and rectangular cross sections for precise mass density and viscosity measurements, Sens. Actuators A: Phys. (2015), http://dx.doi.org/10.1016/j.sna.2015.02.007

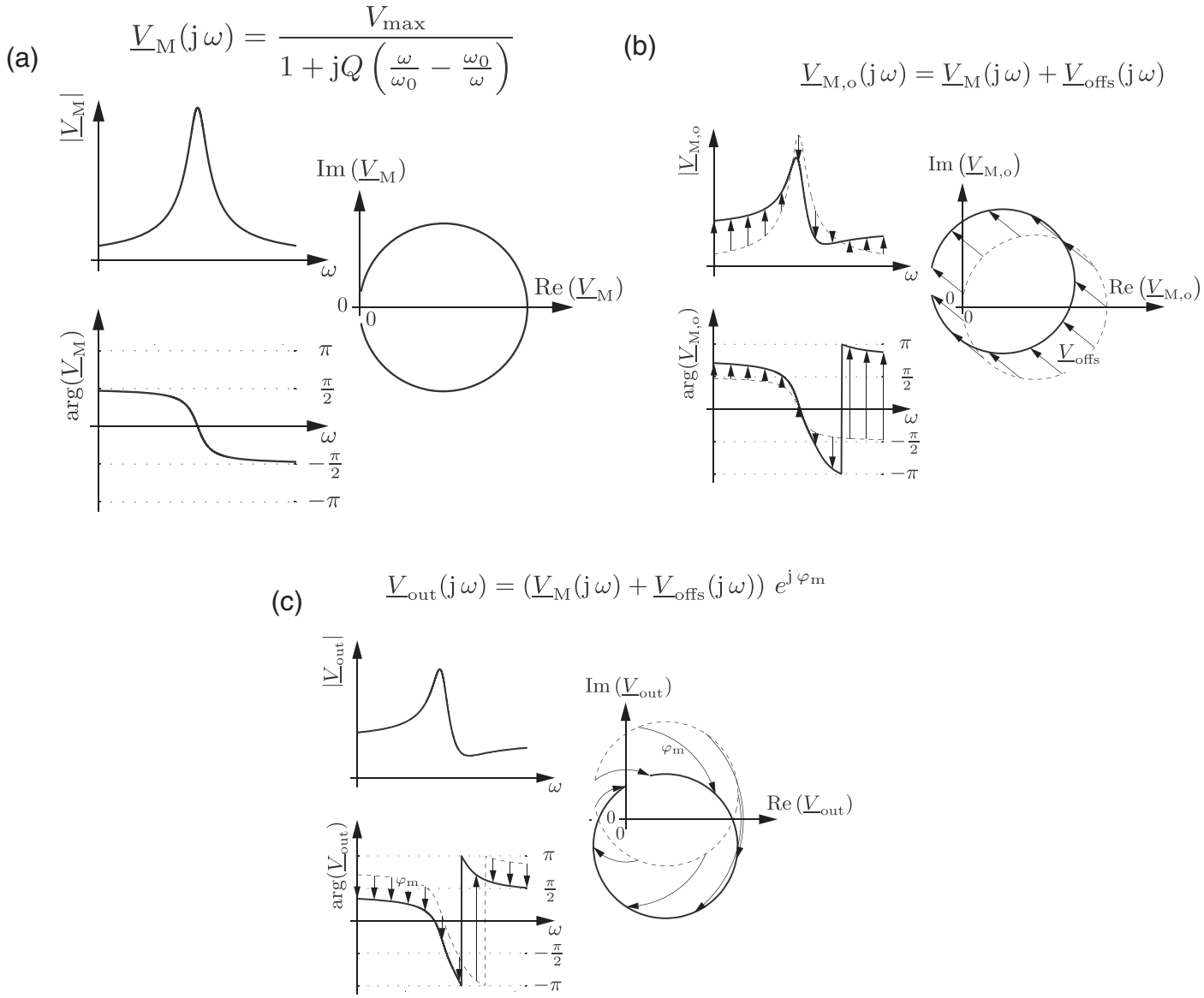

Fig. 3. Illustration of split signal components: (a) shows the motion induced voltage which is proportional the resonator's velocity. (b) illustrates the effect of signals V_{offs} resulting from electrical cross talk. (c) depicts the total measurable signal including phase shifts resulting from the measuring system and transit times from the wiring.

to electrical cross talk from the excitation into the read out coil. And third, the influence of the measurement setup's total phase shift φ_{m} which results from the phase response of the measurement instruments and transit times affected by the wiring. Thus, the measurable voltage can be written using complex notation as follows

$$\underline{V}_{\mathrm{out}}(\mathrm{j}\,\omega) = (\underline{V}_{\mathrm{M}}(\mathrm{j}\,\omega) + \underline{V}_{\mathrm{offs}}(\mathrm{j}\,\omega))\ e^{\mathrm{j}\,\varphi_{\mathrm{m}}(\omega)} \tag{1}$$

where the motion induced voltage response can be described as a second order resonator

$$\underline{V}_{\mathrm{M}}(\mathrm{j}\,\omega) = \frac{V_{\max}}{1 + \mathrm{j}Q\left(\frac{\omega}{\omega_0} - \frac{\omega_0}{\omega}\right)} \tag{2}$$

where ω_0 and Q are the resonator's angular resonance frequency and quality factor, respectively. For the resonator's velocity, the angular eigenfrequency (of undamped vibrations) and the frequency where the amplitude reaches its maximum value are identical. Thus, we may call ω_0 resonance frequency. For the resonator's deflection, the frequency of the peak is smaller than the eigenfrequency. A characteristic resonance curve of the motion induced voltage and the effect of an offset voltage as well as the phase shift on the measured signal are qualitatively depicted in Fig. 3. These additional offset signals can significantly deform the resonance curve and yield asymmetries in the latter. For highly damped resonators, i.e. $Q < 100$, as it might be the case for resonant viscosity and mass density sensors when examining high viscous liquids, asymmetries in both, the resonator's velocity and deflection frequency response become large. Due to these deformations, searching the maximum peak frequency and the frequencies where the amplitude decreased to the $1/\sqrt{2}$ of the peak values or methods based on a Lorentzian fit [16,17] are not appropriate methods for evaluating resonance frequency f_{r} and Q. In this work, an algorithm presented in [18], which was especially developed for highly damped resonators is used. This algorithm separates a second order resonance of the form of Eq. (2) from spurious offset signals and determines the resonant parameters f_{r} and Q by fitting the resonance circle in a Nyquist plot of the response function.

Fig. 4 shows the circular tuning fork's frequency response in air from 100 Hz to 3.5 kHz. There, amplitude and phase responses as well as the Nyquist plots are illustrated. In the recorded frequency

Please cite this article in press as: M. Heinisch, et al., Application of resonant steel tuning forks with circular and rectangular cross sections for precise mass density and viscosity measurements, Sens. Actuators A: Phys. (2015), http://dx.doi.org/10.1016/j.sna.2015.02.007

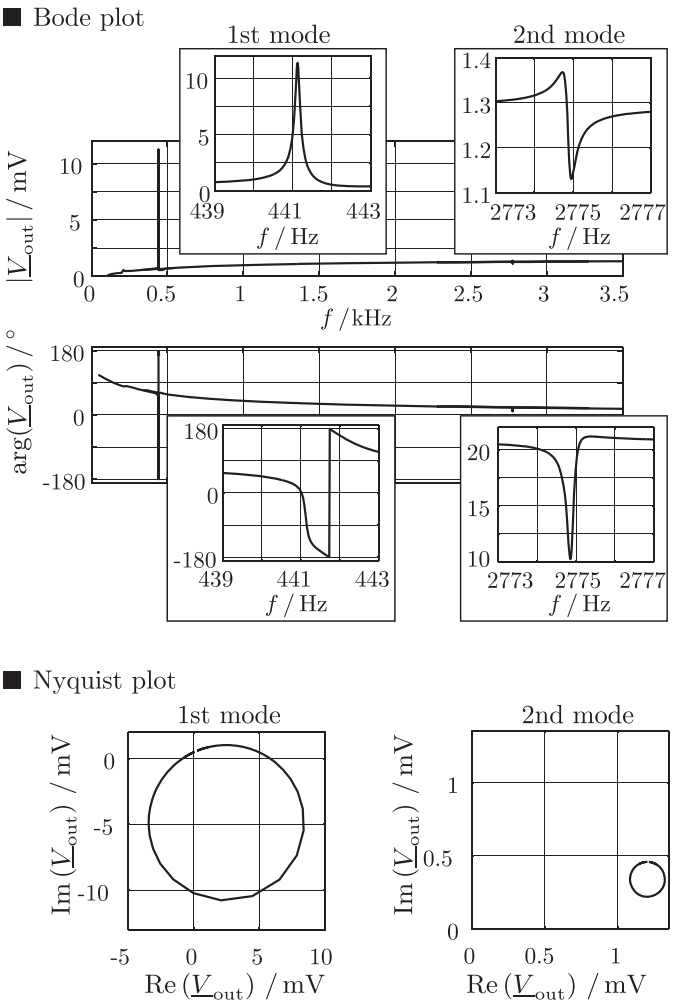

Fig. 4. Frequency response of the circular tuning fork in air containing the first and the second mode.

range the first and second mode at 441 Hz and 2775 Hz, respectively, are measurable and depicted in detail. For both resonances, the effect of electrical cross talk and phase shifts from the measurement system is significant. The parameters necessary for reproducing the measured resonances using Eqs. (1) and (2) are given on the bottom of Fig. 4. In this case, the offset and phase shift spectra, i.e., $\underline{V}_{offs}(j\omega)$ and $\varphi(\omega)$ are approximated by their mean values.

For investigating the effect of the liquid's viscosity and mass density on the resonant behavior, i.e., resonance frequency and quality factor, the tuning fork is completely immersed into the sample liquid. As a rule of thumb, higher viscosities yield higher damping and higher mass densities yield lower resonance frequencies. However, as it will be experimentally shown in Section 3 and discussed in Section 4.1, viscosity and mass density affect both quantities, resonance frequency and quality factor. In this contribution, the examination of the first resonant mode and achievable accuracies using the latter are discussed for a circular and rectangular cross-sectioned steel tuning fork. In [19] the second mode was investigated in liquids for the circular tuning fork. Similar sensitivities of the first and second mode were achieved and thus examining the second mode instead of the first or recording both modes at once for η and ρ measurements did not show a significant advantage. As spurious offset signals and the motion induced voltage are significantly lower and larger respectively, for the first mode, higher measurement accuracies can be obtained examining and evaluating the latter.

3. Measurements in liquids

3.1. Viscosity measurements

The response to viscosity was investigated by recording both tuning forks' frequency responses in five acetone–isopropanol solutions covering a viscosity range of 0.2 mPa s to 2 mPa s for mass densities of roughly 0.78 g/cm^3 at 25 °C. After mixing, the viscosity and mass density of these solutions were measured with an Anton Paar SVM 3000 for reference purposes. In every liquid, 100 frequency responses have been recorded for both tuning forks in a Weiss WKL 100 climate chamber at temperatures of 25 ± 0.1 °C. 100 measurements appeared to be a reasonable number of measurement points particularly when considering the measuring time. For determining the liquids's temperature more accurately than it is possible with the climate chamber's internal thermometer, a Dostmann electronic GmbH P795 thermometer with an accuracy of 0.01 °C was used. The probe head was put inside of the glass tube and is visible in Fig. 2.

The upper parts in Fig. 5(a) and (b) show the recorded frequency responses of measurements in the viscosity series as well as the evaluated resonance frequencies and quality factors for the circular and rectangular tuning fork, respectively. Resonance frequency and quality factor have been evaluated using the fitting algorithm presented in [18]. In Table 4, the measured values for viscosity and mass density, as well as evaluated resonance frequencies and quality factors are given.

3.2. Mass density measurements

For investigating the response to mass density, five solutions using acetone, isopropanol, ethanol, DI-water and glycerol were prepared. The liquids were mixed to obtain constant viscosities of 1 mPa s but mass densities between 0.78 g/cm^3 and 1 g/cm^3. The values for viscosity and mass density of these solutions measured with a SVM 3000 at 25 °C are given in Table 5.

The recorded frequency responses as well as evaluated quality factors and resonance frequencies versus mass density are shown in the lower parts of Fig. 5(a) and (b). The values for viscosity and mass density measured with a SVM 3000 as well as evaluated resonance frequencies and quality factors are given in Table 5.

4. Data interpretation

For both, the circular and the rectangular cross-sectioned tuning fork, clearly, higher viscosities yield higher damping and lower resonance frequencies. The evaluation of the resonance frequency versus viscosity, see Fig. 5, shows an (almost) equal resonance frequency for the first and second liquid in case of the round tuning fork and an even higher resonance frequency in case of the rectangular tuning fork. This behavior can be explained by the fact that the mass density of the second liquid is about 5.1 mg/cm^3 lower than of the first liquid, which shifts the resonance frequency upwards. The quality factor, however, significantly decreases for both tuning forks, as the viscosity of the second liquid is more than twice as high as the viscosity of the first liquid (The first liquid is acetone

Please cite this article in press as: M. Heinisch, et al., Application of resonant steel tuning forks with circular and rectangular cross sections for precise mass density and viscosity measurements, Sens. Actuators A: Phys. (2015), http://dx.doi.org/10.1016/j.sna.2015.02.007

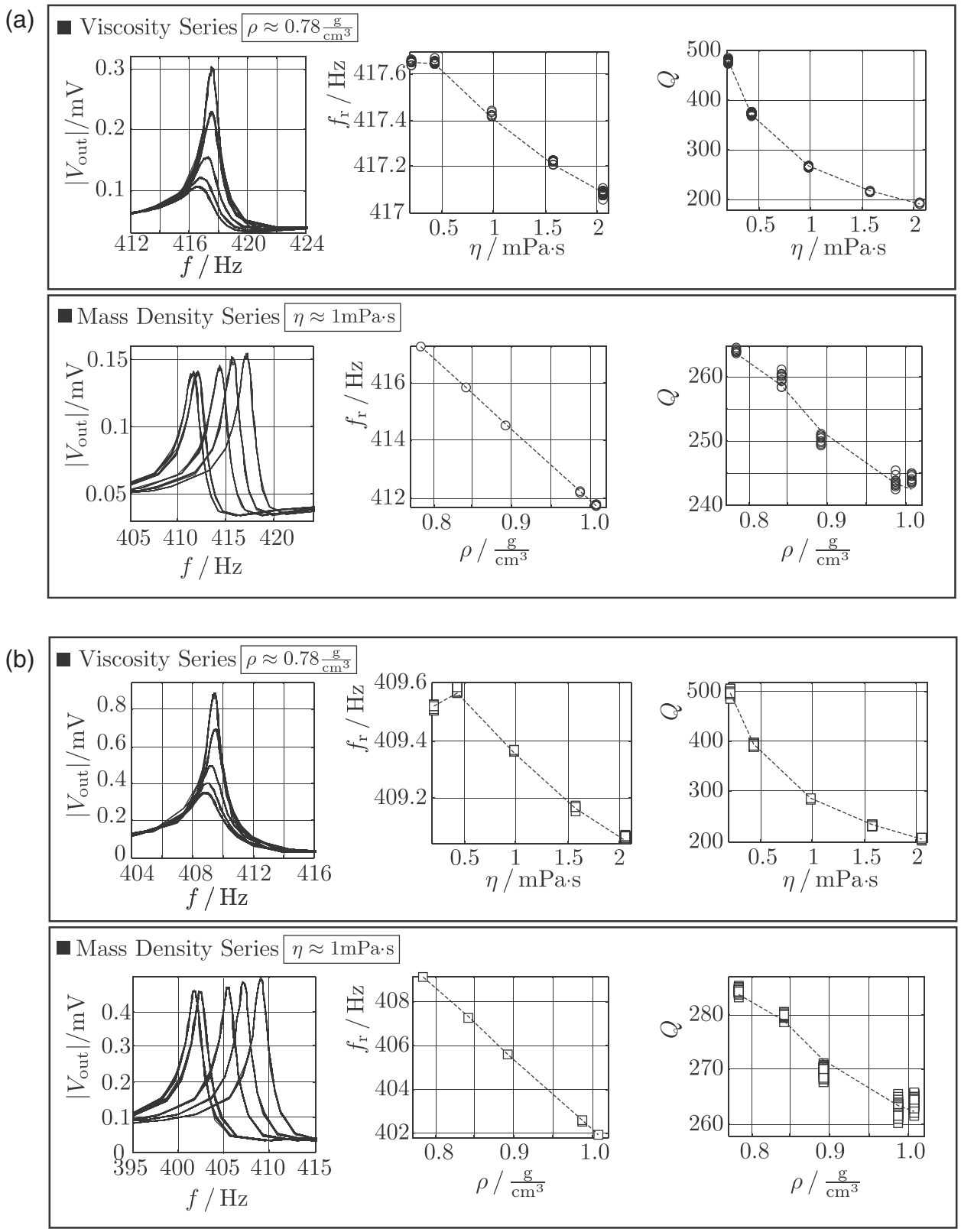

Fig. 5. Recorded frequency responses and therefrom evaluated resonance frequencies and quality factors for the circular and rectangular tuning fork.

and the second is a solution of 51% mass isopropanol in acetone.). This behavior is more distinct for the rectangular tuning fork, as the latter shows a higher sensitivity to mass density than the circular cross-sectioned tuning fork. This finding is also substantiated by the results obtained with the mass density measurements.

4.1. Generalized model

In [20], Sauerbrey introduced an equation for the resonance frequency shift of a thickness shear mode quartz resonator which is induced by the rigid attachment of a film of mass on the quartz's

Please cite this article in press as: M. Heinisch, et al., Application of resonant steel tuning forks with circular and rectangular cross sections for precise mass density and viscosity measurements, Sens. Actuators A: Phys. (2015), http://dx.doi.org/10.1016/j.sna.2015.02.007

Table 1
Fitted model parameters for the generalized model, Eqs. (3) and (4) for the circular and the rectangular tuning fork.

	$m_{0k}(s^2)$	$m_{\rho k}(m^3\,s^2/kg)$	$m_{\eta\rho k}((m^2/kg)\,s^2)$	$c_{0k}(s)$	$c_{\eta k}(m\,s^2/kg)$	$c_{\eta\rho k}((m^2/kg)\,s^2)$
Circular	$1.31\cdot10^{-7}$	$1.74\cdot10^{-11}$	$2.71\cdot10^{-8}$	$2.79\cdot10^{-7}$	$7.82\cdot10^{-5}$	$2.41\cdot10^{-8}$
Rectangular	$1.32\cdot10^{-7}$	$2.45\cdot10^{-11}$	$2.50\cdot10^{-8}$	$2.97\cdot10^{-7}$	$7.16\cdot10^{-5}$	$2.24\cdot10^{-8}$

Table 2
Fitted model parameters for the simplified model Eqs. (5) and (6) for the circular and the rectangular tuning fork.

	$m_{0k}(s^2)$	$m_{\rho k}(m^3\,s^2/kg)$	$m^*_{\eta\rho k}((m^2/kg)\,s^{5/2})$	$c_{0k}(s)$	$c_{\eta k}(m\,s^2/kg)$	$c^*_{\eta\rho k}((m^2/kg)\,s^{3/2})$
Circular	$1.31\cdot10^{-7}$	$1.74\cdot10^{-11}$	$5.31\cdot10^{-10}$	$2.92\cdot10^{-7}$	$9.38\cdot10^{-5}$	$1.20\cdot10^{-6}$
Rectangular	$1.31\cdot10^{-7}$	$2.45\cdot10^{-11}$	$4.94\cdot10^{-10}$	$3.13\cdot10^{-7}$	$9.09\cdot10^{-5}$	$1.10\cdot10^{-6}$

surface. This equation was further developed in [21] by Kanazawa and Gordon for such a quartz crystal microbalance (QCM) interacting with a liquid, considering its mass density and viscosity. In [22], Martin et al. extended the Butterworth–Van Dyke equivalent circuit, see also [23,24], to describe the impedance of a liquid loaded QCM. This equivalent circuit enabled evaluating not only the resonance frequency but also the quality factor of a liquid loaded QCM. However, these models consider only one-dimensional shear-wave propagation in the fluid, which is valid for an infinitely extended in-plane oscillating plate. The obtained equations (which consider one-dimensional shear waves only) do not allow separating the effect of η and ρ on the resonator's f_r and Q. On the one hand, due to non-uniform shear displacement of the QCM, spurious compressional waves are also excited, see [25]. Such spurious effects which are not considered in the models mentioned above, however, allow separating the effect of η and ρ on the resonator's f_r and Q.

For this purpose and furthermore to provide simple equations for f_r and Q, a recently developed model was introduced in [26] which is generally applicable to resonant viscosity and mass density sensors relating η and ρ to $f_r = \omega_0/(2\pi)$ and Q. The model reads

$$\omega_0 = \frac{1}{\sqrt{m_{0k} + m_{\rho k}\,\rho + m_{\eta\rho k}\sqrt{\frac{\eta\rho}{\omega_0}}}} \tag{3}$$

and

$$Q = \frac{1}{\omega_0}\cdot\frac{1}{c_{0k} + c_{\eta k}\,\eta + c_{\eta\rho k}\sqrt{\omega_0\,\eta\,\rho}}, \tag{4}$$

where m_{xk} and c_{xk} are coefficients and $m_{\rho k}$ as well as $c_{\eta k}$ are zero in case of pure one-dimensional shear waves. Similar approaches and expressions have been found in [27–29].

4.1.1. Simplified generalized equations

Eq. (3) is an implicit equation for ω_0, which makes an exact evaluation of ω_0 for given η and ρ difficult. Therefore, the equations are simplified by considering that the frequency dependence of certain parameters occurring in the analysis is negligible as they are virtually constant within the bandwidth of the resonant system. Doing so, we obtain the following expressions for the angular resonance frequency

$$\omega_0 = \frac{1}{\sqrt{m_{0k} + m_{\rho k}\,\rho + m^*_{\eta\,\rho k}\sqrt{\eta\,\rho}}} \tag{5}$$

and the quality factor

$$Q = \frac{\sqrt{m_{0k} + m_{\rho k}\,\rho + m^*_{\eta\rho k}\sqrt{\eta\,\rho}}}{c_{0k} + c_{\eta k}\,\eta + c^*_{\eta\rho k}\sqrt{\eta\,\rho}}. \tag{6}$$

Thus, if ω_0 and Q for given η and ρ using Eqs. (3) and (4) have to be calculated, numerical (e.g., iterative) methods can be used. Alternatively, the above simplified expressions give remedy. Conversely, if η and ρ have to be determined from measured $f_r = \omega_0/(2\pi)$ and Q, Eqs. (3) and (4) can be used directly.

The parameters m_{0k}, $m_{\rho k}$, $m_{\eta\rho k}$, $m^*_{\eta\rho k}$, c_{0k}, $c_{\eta k}$, $c_{\eta\rho k}$ and $c^*_{\eta\rho k}$ are determined by a parameter fit using the values for η, ρ, f_r and Q given in Tables 4 and 5. The fitted model parameters for the circular and rectangular tuning fork are given in Tables 1 and 2. The derivation of the equations for the generalized and the simplified model is based on the equations for resonance frequency and quality factor of a lumped element mechanical oscillator, considering the interaction with in-plane oscillating platelets [22,30], oscillating spheres [31] and laterally oscillating cylinders [32,33]. If only one-dimensional shear wave propagation should be considered, Eqs. (3)–(6) can be simplified by neglecting the terms multiplied by η and ρ, i.e. substituting $m_{\rho k} = 0$ and $c_{\eta k} = 0$.

The complete derivation of Eqs. (3)–(6) is presented in [26]. There, the model has been applied to the measurements obtained by eight different sensor setups showing good performance for all investigated sensors including tuning forks, silicon cantilevers [34], silicon platelets [35], U-shaped wires [36], and spiral spring sensors [37]. The investigation of the applicability of the model evaluating the relative root mean square deviations of modeled and measured resonance frequencies and quality factors yielded results better than $1.7\cdot10^{-3}$ for the resonance frequency and $3.3\cdot10^{-2}$ for the quality factor, respectively.

With the identified model for f_r and Q it is now possible to evaluate the sensors' sensitivities to viscosity and mass density. Furthermore, different sensors (in this case a circular and rectangular cross-sectioned tuning fork) can be compared and an estimation for required accuracies and stabilities of resonance frequency and quality factor to achieve a certain accuracy for viscosity and mass density measurements can be made.

4.2. Measurement accuracy

Eqs. (3) and (4) can be used to calculate η and ρ for evaluated f_r and Q. The fitted model parameters using a linear fitting procedure described in [26,38] are given in Table 1. The mean values for f_r and Q given in Tables 4 and 5 are used to calculate the values for viscosity and mass density for both liquid series. The evaluation of absolute and relative errors given in Tables 4 and 5 shows that with the present setup, absolute and relative accuracies for viscosity and mass density as given in Table 3 can be achieved.

Table 3
Achieved accuracies with the circular and rectangular tuning fork.

	Circular	Rectangular
$[\lvert\Delta\eta\rvert_{min},\ \lvert\Delta\eta\rvert_{max}]$ (μPa s)	[3.34, 16.22]	[3.02, 21.44]
$[\lvert\Delta\eta_{rel}\rvert_{min},\ \lvert\Delta\eta_{rel}\rvert_{max}]$ (10^{-3})	[3.16, 21.57]	[2.10, 33.44]
$[\lvert\Delta\rho\rvert_{min},\ \lvert\Delta\rho\rvert_{max}]$ (mg/(cm^3))	[14.06, 610.50]	[6.08, 150.51]
$[\lvert\Delta\rho_{rel}\rvert_{min},\ \lvert\Delta\rho_{rel}\rvert_{max}]$ (10^{-6})	[17.93, 694.43]	[7.76, 152.49]

Please cite this article in press as: M. Heinisch, et al., Application of resonant steel tuning forks with circular and rectangular cross sections for precise mass density and viscosity measurements, Sens. Actuators A: Phys. (2015), http://dx.doi.org/10.1016/j.sna.2015.02.007

Table 4
Results for viscosity measurements. The plus–minus values are evaluated typical errors (single standard deviations). $\hat{x}$ are the calculated values for viscosity and mass density using Eqs. (3) and (4) and evaluated mean values for f_r and Q. $\Delta x = \hat{x} - x$ and $\Delta x_{rel} = \Delta x/x$ are absolute and relative deviations from the values for viscosity and mass density, respectively.

Viscosity Series $T = 25\,^{\circ}C$									
η (mPa s)	ρ (g/cm^3)	f_r (Hz)	Q	$\hat{\eta}$ (mPa s)	$\Delta\eta$ (μPa s)	$\Delta\eta_{rel}$ (10^{-3})	$\hat{\rho}$ (g/cm^3)	$\Delta\rho$ (mg/cm^3)	$\Delta\rho_{rel}$ (10^{-6})
Circular tuning fork									
0.207	0.7841	$417.653 \pm 2.89 \cdot 10^{-3}$	477.4 ± 1.88	0.211	4.46	21.57	0.7841	0.014	17.93
0.433	0.7790	$417.650 \pm 2.92 \cdot 10^{-3}$	371.8 ± 1.44	0.427	−6.02	−13.90	0.7791	0.067	86.41
0.980	0.7793	$417.418 \pm 3.47 \cdot 10^{-3}$	265.2 ± 0.34	0.986	5.31	5.41	0.7792	−0.101	−129.90
1.576	0.7803	$417.224 \pm 3.08 \cdot 10^{-3}$	214.5 ± 0.33	1.591	14.76	9.36	0.7798	−0.541	−694.43
2.054	0.7804	$417.083 \pm 7.08 \cdot 10^{-3}$	190.8 ± 0.52	2.048	−6.50	−3.16	0.7808	0.409	523.50
Rectangular tuning fork									
0.207	0.7841	$409.517 \pm 3.82 \cdot 10^{-3}$	499.0 ± 3.03	0.214	6.92	33.44	0.7841	−0.006	−7.76
0.433	0.7790	$409.576 \pm 6.27 \cdot 10^{-3}$	394.6 ± 1.91	0.427	−6.05	−13.95	0.7789	−0.055	−70.32
0.980	0.7793	$409.365 \pm 0.93 \cdot 10^{-3}$	285.7 ± 0.29	0.977	−3.08	−3.14	0.7794	0.054	69.26
1.576	0.7803	$409.173 \pm 1.80 \cdot 10^{-3}$	232.2 ± 0.39	1.582	5.30	3.36	0.7803	0.039	49.68
2.054	0.7804	$409.067 \pm 3.09 \cdot 10^{-3}$	206.2 ± 0.74	2.059	4.32	2.10	0.7804	−0.020	−25.79

4.3. Relative sensitivity

For resonant viscosity and mass density sensors, absolute sensitivities as, e.g., the sensitivity of the resonance frequency to mass density in Hz/(g/cm^3) are in general not very descriptive. First of all, by evaluating absolute values, the comparison of sensors operated in a different frequency range is hardly possible. Second, it is difficult to compare the sensitivities to mass density and viscosity, as usually the investigable range of viscosities is much larger than the range of mass densities. For common liquids, the range of mass densities is narrow, hardly exceeding the range between 0.6 and 1.8 g/cm^3, whereas the range of viscosities covers several orders of magnitudes, e.g., in [36] a viscosity range of 0.2–216 mPa s has been investigated with a single resonant sensor. Due to these reasons we refrain from evaluating absolute rather than relative sensitivities. A difficulty in interpretation which arises for absolute as well as for relative sensitivities is, that both types of sensitivities depend on η and ρ.

As it can be observed in the measured results as well as in Eqs. (3)–(6), f_r and Q are both dependent on η and ρ. Thus, to completely describe a resonant viscosity and mass density sensor's sensitivity, four sensitivities have to be evaluated. For this, we define the relative sensitivity of a quantity $X(y_i)$ to one of its variables y_i as

$$S_{X,y_i} = \left| \frac{\partial X}{\partial y_i} \cdot \frac{y_i}{X} \right| \tag{7}$$

where in this case X stands either for f_r or Q and y_i for η and ρ.

The evaluation of relative sensitivities, Eq. (7) (i.e. relative change of f_r or Q versus relative change of η or ρ) is shown in Fig. 6 for the circular and rectangular case for the experimentally investigated viscosity and mass density range. Both, sensitivity to viscosity and mass density increase for higher viscosities and mass densities, respectively. The relative sensitivity of the quality factor to viscosity is only slightly higher than that to mass density. In case of the sensitivity of the resonance frequency, the dependence on viscosity is significantly smaller than the sensitivity to mass density. The comparison of both tuning forks (i.e. the comparison of Fig. 6(a) and (b)) shows, that they show similar sensitivities except for the relative sensitivity of the resonance frequency to mass density. In this case, the sensitivity of the rectangular tuning fork is higher. In other words, both tuning forks show similar sensitivities to viscosity, in case of sensitivity to mass density, the rectangular tuning fork is more sensitive.

4.4. Estimation of required accuracies for f_r and Q

Manufacturers of viscosity and mass density meters usually specify the performance of their instruments with absolute accuracy in mass density and relative accuracy in viscosity. For example, the high precision laboratory instrument Anton Paar SVM 3000 features a reproducibility of 0.35% in viscosity and 0.0005 g/cm^3 for mass density and a repeatability of 0.1% and 0.0002 g/cm^3, for η and ρ respectively. The reproducibility in temperature of the SVM 3000 is 0.02 °C and its repeatability is 0.005 °C. To get in the accuracy range of such laboratory instruments, at this point, we target a relative accuracy in viscosity $\Delta\eta/\eta = 10^{-2}$ and absolute accuracy in mass density $\Delta\rho = 1$ mg/cm^3 which corresponds to a relative accuracy of $\Delta\rho/\rho = 10^{-3}$ for aqueous liquids. Repeated measurements and evaluation of f_r and Q showed instabilities yielding a certain

Table 5
Results for mass density measurements. The same notation as in Table 4 is used.

Density Series $T = 25\,^{\circ}C$									
η (mPa s)	ρ (g/cm^3)	f_r (Hz)	Q	$\hat{\eta}$ (mPa s)	$\Delta\eta$ (μPa s)	$\Delta\eta_{rel}$ (10^{-3})	$\hat{\rho}$ (g/cm^3)	$\Delta\rho$ (mg/cm^3)	$\Delta\rho_{rel}$ (10^{-6})
Circular tuning fork									
1.006	0.7849	$417.278 \pm 1.53 \cdot 10^{-3}$	264.1 ± 0.26	0.989	−16.22	−16.13	0.7847	−0.220	−280.53
0.994	0.8411	$415.851 \pm 8.36 \cdot 10^{-3}$	259.7 ± 1.00	0.979	−14.79	−14.88	0.8413	0.179	212.31
1.010	0.8931	$414.523 \pm 0.92 \cdot 10^{-3}$	250.0 ± 0.68	1.023	13.51	13.38	0.8937	0.611	683.57
1.006	0.9870	$412.220 \pm 7.24 \cdot 10^{-3}$	243.6 ± 0.88	1.013	7.40	7.36	0.9872	0.177	179.33
0.998	1.0073	$411.750 \pm 8.03 \cdot 10^{-3}$	244.1 ± 0.62	0.995	−3.34	−3.34	1.0067	−0.597	−592.31
Rectangular tuning fork									
1.006	0.7849	$409.176 \pm 1.78 \cdot 10^{-3}$	284.3 ± 0.31	0.984	−21.44	−21.32	0.7849	0.016	20.41
0.994	0.8411	$407.301 \pm 1.04 \cdot 10^{-3}$	279.9 ± 0.29	0.976	−17.46	−17.57	0.8412	0.125	148.90
1.010	0.8931	$405.578 \pm 0.87 \cdot 10^{-3}$	269.9 ± 0.65	1.023	13.39	13.26	0.8932	0.067	74.42
1.006	0.9870	$402.551 \pm 2.62 \cdot 10^{-3}$	262.7 ± 0.93	1.023	17.58	17.48	0.9868	−0.151	−152.49
0.998	1.0073	$401.911 \pm 3.41 \cdot 10^{-3}$	264.4 ± 0.75	0.995	−3.02	−3.03	1.0072	−0.761	−75.51

Please cite this article in press as: M. Heinisch, et al., Application of resonant steel tuning forks with circular and rectangular cross sections for precise mass density and viscosity measurements, Sens. Actuators A: Phys. (2015), http://dx.doi.org/10.1016/j.sna.2015.02.007

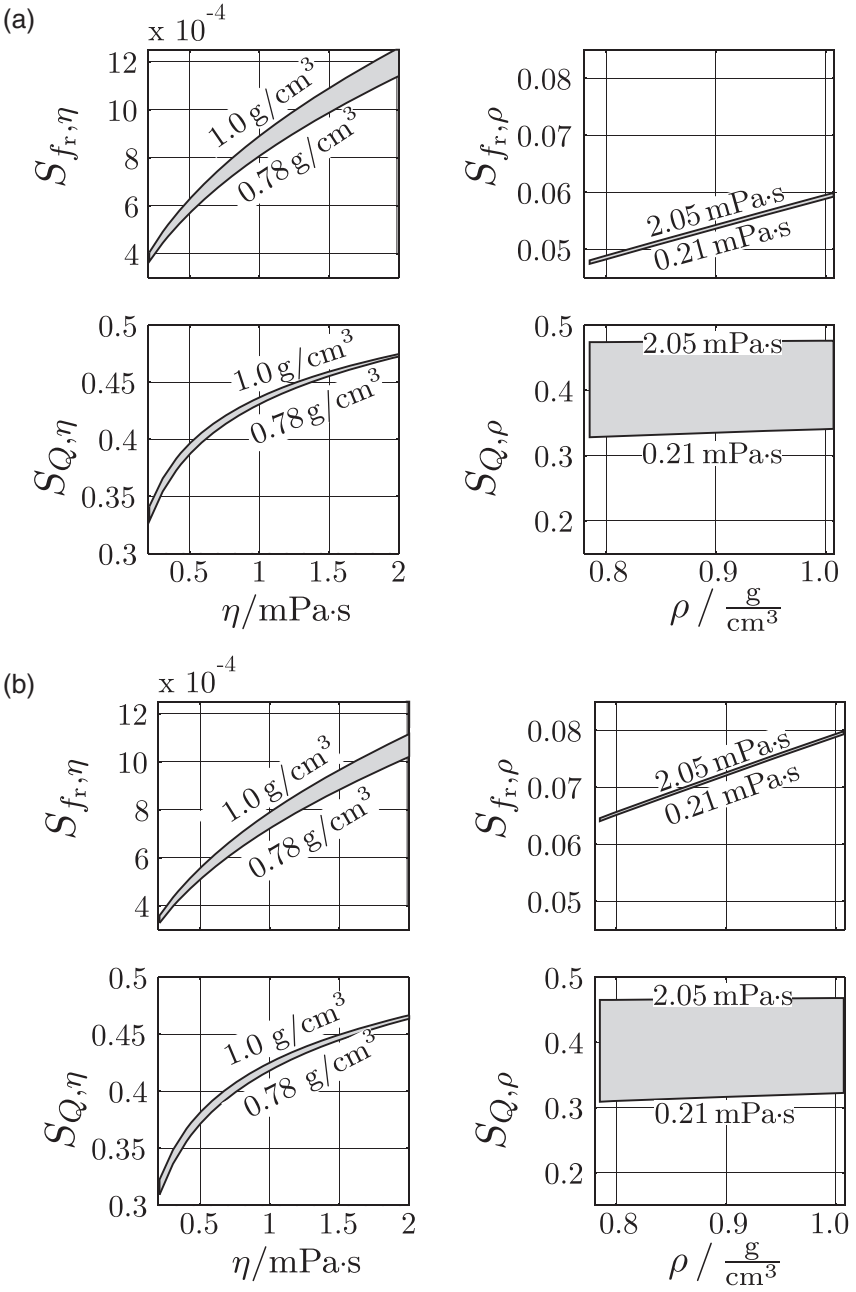

Fig. 6. Sensitivities to viscosity and mass density: the sensitivities of f_r and Q to η and ρ are not constant but both dependent on η and ρ. For this reason the sensitivities are depicted as bands, where the given values at each band indicate the boundary of evaluated values.

spread for both quantities, which yields an inaccuracy in the η and ρ determination.

Using the sensitivities evaluated from Eq. (7), the change of f_r and Q upon change of η and ρ can be expressed in matrix notation as follows:

$$\begin{bmatrix} \frac{\Delta f_r}{f_r} \\ \frac{\Delta Q}{Q} \end{bmatrix} = \begin{bmatrix} S_{f_r,\eta} & S_{f_r,\rho} \\ S_{Q,\eta} & S_{Q,\rho} \end{bmatrix} \cdot \begin{bmatrix} \frac{\Delta \eta}{\eta} \\ \frac{\Delta \rho}{\rho} \end{bmatrix}. \quad (8)$$

With this equation, maximum tolerable variations in the f_r and Q evaluation can be estimated for achieving the desired accuracies in η and ρ. For this estimation it is assumed that η is (exactly) known, if ρ is evaluated from f_r or Q and vice versa. The evaluated relative and absolute changes for f_r and Q are depicted in Fig. 7.

For a rough estimation for the resonance stability it is assumed that ρ is evaluated from f_r and η from Q, respectively. It follows for the case of the presented tuning forks that variances smaller than 10^{-2} Hz and 1 for f_r and Q have to be obtained to achieve the claimed accuracies of $\Delta\eta/\eta = 1\%$ for viscosity and $\Delta\rho = 1$ mg/cm^3 for mass density. The accordingly required relative accuracies are in the order of 10^{-5} for the resonance frequency and 10^{-3} for the quality factor.

These values are estimations for the resonance frequency and quality factor stability which are required in any case, i.e., if the instability is larger than these values, the addressed accuracies cannot be achieved on no account. A further source for measurement

Please cite this article in press as: M. Heinisch, et al., Application of resonant steel tuning forks with circular and rectangular cross sections for precise mass density and viscosity measurements, Sens. Actuators A: Phys. (2015), http://dx.doi.org/10.1016/j.sna.2015.02.007

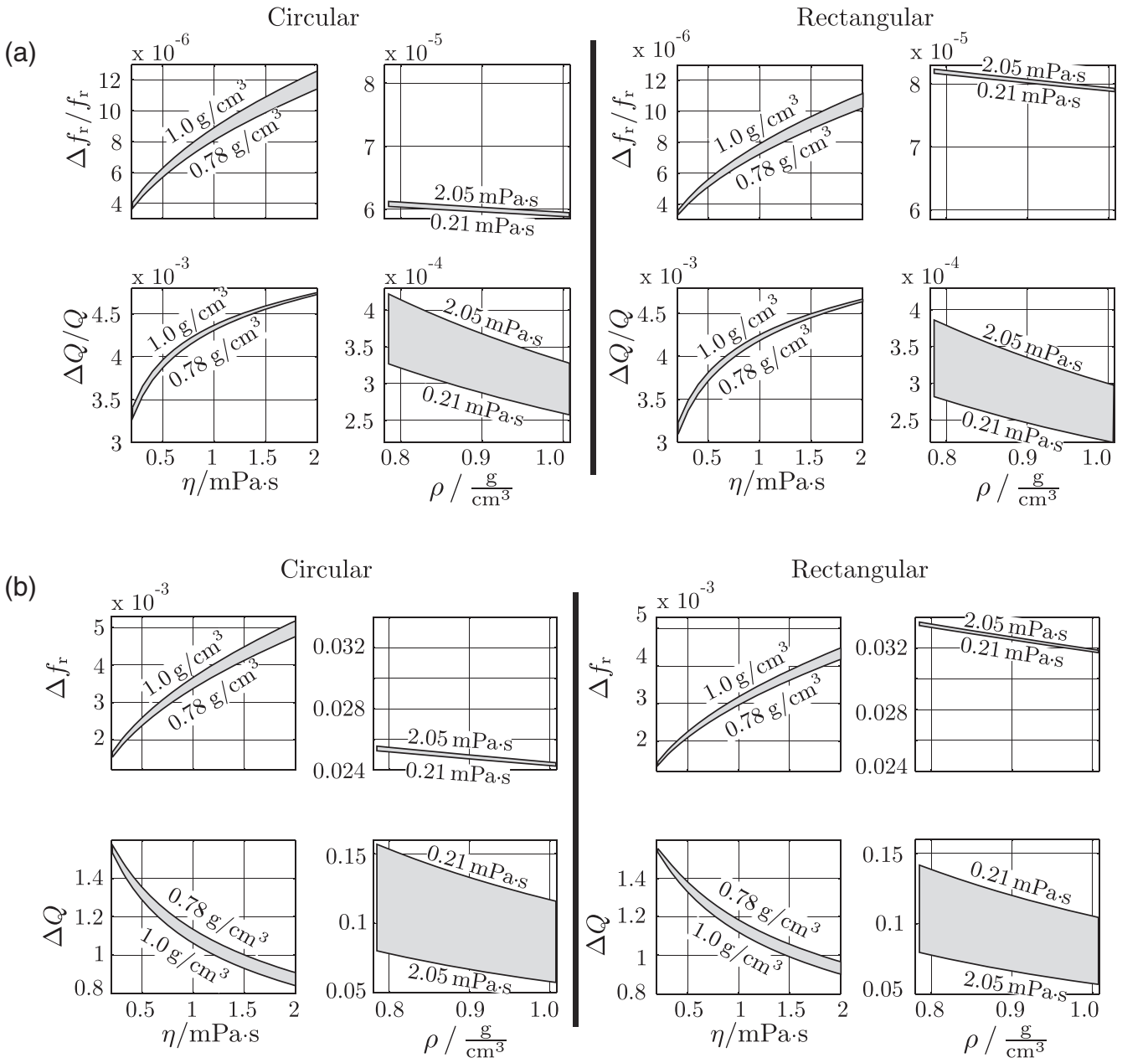

Fig. 7. Required accuracies for f_r and Q to achieve a relative accuracy of $\Delta\eta/\eta = 10^{-2}$ and an absolute accuracy $\Delta\rho = 1$ mg/cm³.

inaccuracies is the cross-sensitivity of the resonance frequency to temperature, which limits the accuracies in η and ρ as the temperature measurement accuracy is also limited to a certain extent. For measurements presented in this contribution, the fluids' temperatures were controlled at 25 °C and thus, the tuning forks' cross-sensitivities were not considered for these accuracy estimations. The validity of this approximation is substantiated by a first investigation of the circular tuning fork's temperature behavior presented in [39]. There, it was found that the circular tuning fork's cross sensitivity to temperature is about −0.049 Hz/°C. In the investigated viscosity and mass density range, the sensitivity of the resonance frequency to mass density is about −0.024 Hz/(mg/cm³). Thus, it follows for the required temperature measurement accuracy to be about $\Delta T = 0.5$ °C to distinguish mass density variations of 1 mg/cm³ from temperature variations. This guideline is fulfilled by the used climate chamber and the thermometer which directly measures the liquid's temperature.

4.5. Error propagation

As it was already mentioned and as it can be observed in Fig. 6, the sensitivity parameters S_{X,y_i} (which have been calculated using Eq. (7) and the simplified model for f_r and Q, i.e., Eqs. (5) and (6)) depend on density and viscosity. For proper measurements of the resonance characteristics processed with the estimation procedure from [18] it was shown in [40] that there is a relation between the relative standard deviations of f_r and Q which is determined by the signal-to-noise ratio[1] (SNR) of the acquired frequency spectra and the number of frequency points M:

[1] It is defined as the ratio of Nyquist circle diameter to standard deviation of noise on the Nyquist circle diameter.

Please cite this article in press as: M. Heinisch, et al., Application of resonant steel tuning forks with circular and rectangular cross sections for precise mass density and viscosity measurements, Sens. Actuators A: Phys. (2015), http://dx.doi.org/10.1016/j.sna.2015.02.007

$$\frac{\mathrm{std}\{f_r\}}{f_r} = \frac{1}{2Q}\frac{\mathrm{std}\{Q\}}{Q} \approx \sqrt{\frac{2}{M}}\frac{1}{Q\,\mathrm{SNR}} \tag{9}$$

It was furthermore shown, that f_r and Q are uncorrelated in case of reasonably sampled resonance curves e.g., as shown in Fig. 5. If deviations from Eq. 9 are observed, this is an indicator that unmodeled influences such as parameter drifts persist and that there is still potential for setup improvements. Relative errors on ρ and η for given relative deviations on f_r and Q can be determined by inverting Eq. (8), i.e.,

$$\begin{bmatrix} \frac{\Delta\eta}{\eta} \\ \frac{\Delta\rho}{\rho} \end{bmatrix} = \begin{bmatrix} S_{fr,\eta} & S_{fr,\rho} \\ S_{Q,\eta} & S_{Q,\rho} \end{bmatrix}^{-1} \cdot \begin{bmatrix} \frac{\Delta f_r}{f_r} \\ \frac{\Delta Q}{Q} \end{bmatrix}. \tag{10}$$

The error propagation depends on the invertibility of the matrix in Eq. 10, e.g., for pure shear resonators, the matrix is singular and ρ and η can not be separated. However, this is not the case for the presented tuning fork sensors.

Fig. 8 shows the error propagation for the round and rectangular tuning fork for the liquids of the viscosity and the density series. Errors in f_r and Q cause much higher relative deviations in viscosity than in density. Therefore, the requirements on the frequency accuracy are much stricter when low errors on viscosity shall be achieved. With the current setups the relative standard deviations in frequency are 10^{-6} approximately, and thus accuracies around ±1% (±3 standard deviations) are achievable for η and 0.01% (i.e. 0.1 mg/cm^3 for aqueous liquids) for ρ, approximately. These results meet the requirements from Section 4.4.

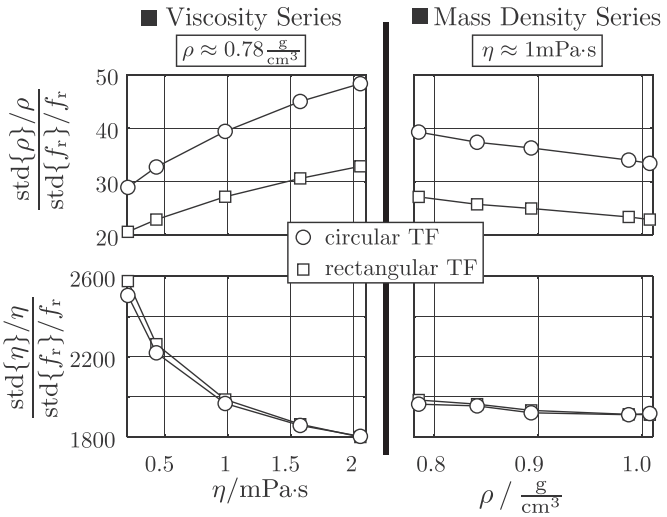

Fig. 8. The error propagation for rectangular and circular tuning forks evaluated for the viscosity and the density series.

4.6. Experimental estimation of achievable accuracies with the present setup

To furthermore investigate experimentally the accuracy and the resolution of this viscosity and mass density measurement setup, the dissolving of rubber in ethanol was recorded during 150 h, see Fig. 9. The viscosity and mass density have been determined with a SVM 3000 before and after the experiment. The change of the liquid's viscosity and mass density was 0.05 mPa s (i.e. 5.3%) and 0.0039 g/cm^3 (i.e. 0.5%) respectively, which can be clearly detected. With an appropriate data analysis similar accuracies as they are achieved with high precision laboratory instruments might be obtainable with such comparatively tuning fork-based sensors.

5. Conclusion

Viscosity and mass density show a clear and significant influence on the frequency responses of electromagnetically driven and read out steel tuning forks with circular and rectangular cross-sections. The application and the discussion of a fitted model for f_r and Q revealed that both tuning forks have a similar sensitivity to viscosity. However, in case of sensitivity to mass density, the rectangular

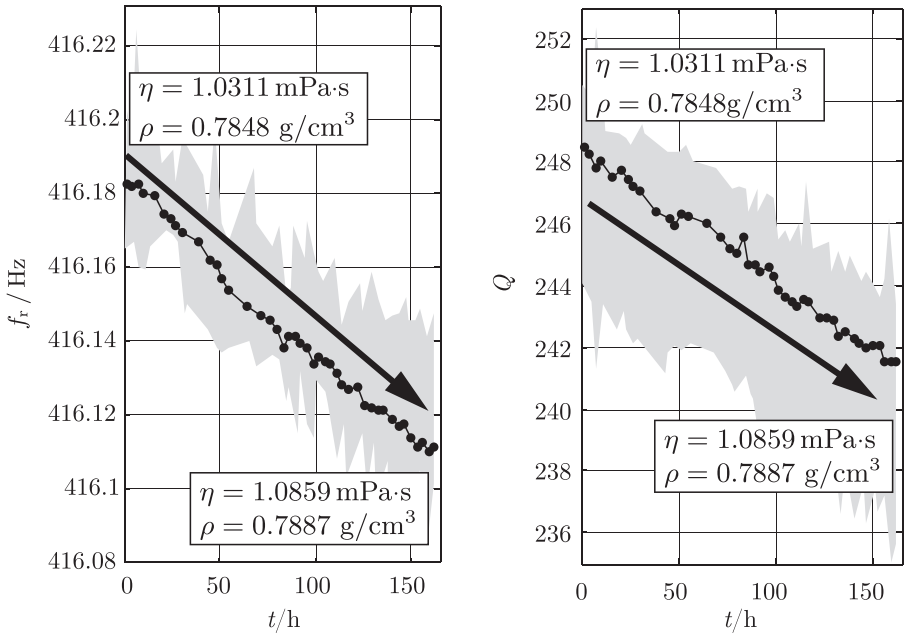

Fig. 9. Long term measurements for dissolving rubber in ethanol. The changes of the liquid properties are 5.3% in viscosity and 0.5% in mass density, respectively. The gray shaded areas indicate the span of recorded resonance frequencies and quality factors. The black dots indicate the values averaged over 100 measurements.

Please cite this article in press as: M. Heinisch, et al., Application of resonant steel tuning forks with circular and rectangular cross sections for precise mass density and viscosity measurements, Sens. Actuators A: Phys. (2015), http://dx.doi.org/10.1016/j.sna.2015.02.007

cross-sectioned tuning fork shows a higher sensitivity. An estimation of the required stabilities of the sensors' resonance frequencies and quality factors to achieve accuracies for viscosity and mass density in the order of commercially available measurement instruments showed that the accuracy of the resonance frequency has to be in the order of 10^{-2} Hz (i.e. 10^{-5} relative stability) and for the quality factor roughly 1 (i.e. 10^{-3} relative stability).

With the present setups, accuracies in the order of 1% in viscosity and 0.01% in mass density are achievable.

Acknowledgments

This work has been partially supported by the Linz Center of Mechatronics (LCM) in the framework of the Austrian COMET-K2 program. We also want to thank Bernhard Mayrhofer and Johann Katzenmayer for their help and excellent assistance.

References

[1] B. Jakoby, M. Vellekoop, Physical sensors for liquid properties, IEEE Sens. J. 11 (12) (2011) 3076–3085.
[2] T. Voglhuber-Brunnmaier, M. Heinisch, E.K. Reichel, B. Weiss, B. Jakoby, Derivation of reduced order models from complex flow fields determined by semi-numeric spectral domain models, Sens. Actuators A: Phys. 202 (2013) 44–51.
[3] M. Heinisch, E.K. Reichel, I. Dufour, B. Jakoby, A resonating rheometer using two polymer membranes for measuring liquid viscosity and mass density, Sens. Actuators A: Phys. 172 (1) (2011) 82–87, http://dx.doi.org/10.1016/j.sna.2011.02.031.
[4] E.K. Reichel, C. Riesch, F. Keplinger, C.E.A. Kirschhock, B. Jakoby, Analysis and experimental verification of a metallic suspended plate resonator for viscosity sensing, Sens. Actuators A: Phys. 162 (2010) 418–424, http://dx.doi.org/10.1016/j.sna.2010.02.017.
[5] A. Abdallah, M. Heinisch, B. Jakoby, Measurement error estimation and quality factor improvement of an electrodynamic-acoustic resonator sensor for viscosity measurement, Sens. Actuators A: Phys. 199 (2013) 318–324.
[6] M. Heinisch, E.K. Reichel, I. Dufour, B. Jakoby, Tunable resonators in the low kHz range for viscosity sensing, Sens. Actuators A: Phys. 186 (2012) 111–117, http://dx.doi.org/10.1016/j.sna.2012.03.009.
[7] M. Heinisch, E.K. Reichel, B. Jakoby, U-shaped wire based resonators for viscosity and mass density sensing, in: Proc. of. SENSOR 2013, OPTO 2013 IRS2, 2013.
[8] E. Lemaire, M. Heinisch, B. Caillard, B. Jakoby, I. Dufour, Comparison and experimental validation of two potential resonant viscosity sensors in the kilohertz range, Meas. Sci. Technol. 24 (8) (2013) 084005.
[9] I. Dufour, A. Maali, Y. Amarouchene, et al., The microcantilever: a versatile tool for measuring the rheological properties of complex fluids, J. Sens. (2012), http://dx.doi.org/10.1155/2012/719898.
[10] A. Maali, C. Hurth, R. Boisgard, C. Jai, T. Cohen-Bouhacina, J.P. Aimé, Hydrodynamics of oscillating atomic force microscopy cantilevers in viscous fluids, J. Appl. Phys. 97 (7) (2005) 074907.
[11] J. Toledo, T. Manzaneque, J. Hernando-García, J. Vázquez, A. Ababneh, H. Seidel, M. Lapuerta, J. Sánchez-Rojas, Application of quartz tuning forks and extensional microresonators for viscosity and density measurements in oil/fuel mixtures, Microsyst. Technol. (2014) 1–9.
[12] I. Etchart, H. Chen, P. Dryden, J. Jundt, C. Harrison, K. Hsu, F. Marty, B. Mercier, MEMS sensors for density–viscosity sensing in a low-flow microfluidic environment, Sens. Actuators A: Phys. 141 (2) (2008) 266–275.
[13] X. Huang, S. Li, J. Schultz, Q. Wang, Q. Lin, A capacitive MEMS viscometric sensor for affinity detection of glucose, J. Microelectromech. Syst. 18 (6) (2009) 1246–1254.
[14] B.A. Bircher, L. Duempelmann, K. Renggli, H.P. Lang, C. Gerber, N. Bruns, T. Braun, Real-time viscosity and mass density sensors requiring microliter sample volume based on nanomechanical resonators, Anal. Chem. 85 (18) (2013) 8676–8683.
[15] M. Heinisch, A. Abdallah, I. Dufour, B. Jakoby, Resonant steel tuning forks for precise inline viscosity and mass density measurements in harsh environments, Procedia Eng. 87 (2014) 1139–1142.
[16] P.J. Petersan, S.M. Anlage, Measurement of resonant frequency and quality factor of microwave resonators: comparison of methods, J. Appl. Phys. 84 (1998) 3392–3402.
[17] M.C. Sanchez, E. Martin, J.M. Zamarro, Unified and simplified treatment of techniques for characterising transmission, reflection or absorption resonators, IEEE Proc. Microw. Antennas Propag. H 137 (1990) 209–212.
[18] A.O. Niedermayer, T. Voglhuber-Brunnmaier, J. Sell, B. Jakoby, Methods for the robust measurement of the resonant frequency and quality factor of significantly damped resonating devices, Meas. Sci. Technol. 23 (8) (2012) 085107.
[19] M. Heinisch, T. Voglhuber-Brunnmaier, E.K. Reichel, I. Dufour, B. Jakoby, Investigation of higher mode excitation of resonant mass density and viscosity sensors, in: Proceedings IEEE Sensor, 2014.
[20] G. Sauerbrey, Verwendung von schwingquarzen zur wägung dünner schichten und zur mikrowägung, Z. Phys. 155 (1959) 206–222.
[21] K.K. Kanazawa, J.G. Gordon, Frequency of a quartz microbalance in contact with liquid, Anal. Chem. 57 (8) (1985) 1770–1771.
[22] S.J. Martin, V.E. Granstaff, G.C. Frye, Characterization of a quartz crystal microbalance with simultaneous mass and liquid loading, Anal. Chem. 63 (1991) 2272–2281.
[23] S. Butterworth, On electrically-maintained vibrations, Proc. Phys. Soc. Lond. 27 (1) (1914) 410.
[24] K. Van Dyke, The piezo-electric resonator and its equivalent network, Proc. Inst. Radio Eng. 16 (6) (1928) 742–764.
[25] R. Beigelbeck, B. Jakoby, A two-dimensional analysis of spurious compressional wave excitation by thickness-shear-mode resonators, J. Appl. Phys. 95 (9) (2004) 4989–4995.
[26] M. Heinisch, T. Voglhuber-Brunnmaier, E.K. Reichel, I. Dufour, B. Jakoby, Reduced order models for resonant viscosity and mass density sensors, Sens. Actuators A: Phys. 220 (2014) 76–84.
[27] W.Y. Shih, X. Li, H. Gu, W.-H. Shih, I.A. Aksay, Simultaneous liquid viscosity and density determination with piezoelectric unimorph cantilevers, J. Appl. Phys. 89 (2) (2001) 1497–1505.
[28] C. Riesch, E.K. Reichel, F. Keplinger, B. Jakoby, Characterizing vibrating cantilevers for liquid viscosity and density sensing, J. Sens. 9 (2008) (Article ID 697062).
[29] T. Manzaneque, V. Ruiz-Díez, J. Hernando-García, E. Wistrela, M. Kucera, U. Schmid, J.L. Sánchez-Rojas, Piezoelectric MEMS resonator-based oscillator for density and viscosity sensing, Sens. Actuators A: Phys. 220 (2014) 305–315.
[30] M. Heinisch, E.K. Reichel, B. Jakoby, A suspended plate in-plane resonator for rheological measurements at tunable frequencies, in: Proc. Sensor + Test, 2011, pp. 61–66.
[31] L. Rosenhead, Laminar Boundary Layers: Fluid Motion Memoirs, Clarendon, Oxford, 1963.
[32] E.O. Tuck, Calculation of unsteady flows due to small motions of cylinders in a viscous fluid, J. Eng. Math. 3 (1) (1969) 29–44.
[33] J.E. Sader, Frequency response of cantilever beams immersed in viscous fluids with applications to the atomic force microscope, J. Appl. Phys. 84 (1998) 64–76.
[34] S. Boskovic, J.W.M. Chon, P. Mulvaney, J.E. Sader, Rheological measurements using microcantilevers, J. Rheol. 46 (4) (2002) 891–899.
[35] C. Riesch, E.K. Reichel, A. Jachimowicz, J. Schalko, P. Hudek, B. Jakoby, F. Keplinger, A suspended plate viscosity sensor featuring in-plane vibration and piezoresistive readout, J. Micromech. Microeng. 19 (2009) 075010, http://dx.doi.org/10.1088/0960-1317/19/7/075010.
[36] M. Heinisch, E.K. Reichel, I. Dufour, B. Jakoby, A U-shaped wire for viscosity and mass density sensing, Sens. Actuators A: Phys. 214 (2014) 245–251.
[37] M. Heinisch, S. Clara, I. Dufour, B. Jakoby, A spiral spring resonator for mass density and viscosity measurements, in: Proc. Eurosensors XXVIII, 2014.
[38] E.K. Chong, S.H. Zak, An Introduction to Optimization, 2nd ed., John Wiley & Sons, 2001.
[39] M. Heinisch, E.K. Reichel, I. Dufour, B. Jakoby, Modeling and experimental investigation of resonant viscosity and mass density sensors considering their cross-sensitivity to temperature, in: Proc. Eurosensors XXVIII, 2014.
[40] T. Voglhuber-Brunnmaier, A. Niedermayer, R. Beigelbeck, B. Jakoby, Resonance parameter estimation from spectral data: Cramér-rao lower bound and stable algorithms with application to liquid sensors, Meas. Sci. Technol. 25 (10) (2014) 105303–105313.

Biographies

Martin Heinisch obtained his Dipl.-Ing. (M.Sc.) in Mechatronics from Johannes Kepler University Linz, Austria, in 2009. After his Master studies he went to the University of California, Los Angeles (U.C.L.A.) as a Marshall Plan Scholarship grantee, where he did research in the field of microfluidic applications and self assembling systems. In 2010 he started a Ph.D. program at the Institute for Microelectronics and Microsensors of the Johannes Kepler University Linz, Austria where he is currently working on resonating liquid sensors.

Thomas Voglhuber-Brunnmaier received the Dipl.-Ing. (M.Sc.) degree in Mechatronics in 2007 and the Dr.techn. (Ph.D.) in May 2013 at the Institute for Microelectronics and Microsensors (IME) at the Johannes Kepler University (JKU) in Linz, Austria. From May 2013 he holds a Post-Doc position at the Center for Integrated Sensor Systems (CISS) at the Danube University Krems (DUK), where he works in close cooperation with IME on fluid sensors. His fields of interest are the modeling of micro-sensors, statistical signal processing, numerical methods and analog electronics.

Please cite this article in press as: M. Heinisch, et al., Application of resonant steel tuning forks with circular and rectangular cross sections for precise mass density and viscosity measurements, Sens. Actuators A: Phys. (2015), http://dx.doi.org/10.1016/j.sna.2015.02.007

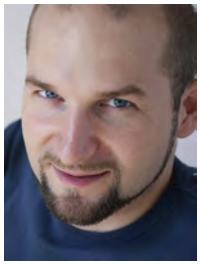

Erwin K. Reichel was born in Linz, Austria, in 1979. He received the Dipl.-Ing. (M.Sc.) degree in Mechatronics from Johannes Kepler University, Linz, Austria, in 2006. From 2006 to 2009 he was working on the Ph.D. thesis at the Institute for Microelectronics and Microsensors of the Johannes Kepler University, Linz and graduated in October 2009. Afterwards he held a post-doctoral position at the Centre for Surface Chemistry and Catalysis as well as at the Department for Chemical Engineering, KU Leuven, Belgium until June 2012. Since then he holds a position as university assistant at the Johannes Kepler University Linz. The main research fields are the modeling, design, and implementation of sensors for liquid properties, and monitoring of phase transition in complex solutions.

Isabelle Dufour graduated from Ecole Normale Supérieure de Cachan in 1990 and received the Ph.D. and H.D.R. degrees in Engineering Science from the University of Paris-Sud, Orsay, France, in 1993 and 2000, respectively. She was a CNRS research fellow from 1994 to 2007, first in Cachan working on the modeling of electrostatic actuators (micromotors, micropumps) and then after 2000 in Bordeaux working on microcantilever-based chemical sensors. She is currently Professor of electrical engineering at the University of Bordeaux and her research interests are in the areas of microcantilever-based sensors for chemical detection, rheological measurements and materials characterization.

Bernhard Jakoby obtained his Dipl.-Ing. (M.Sc.) in Communication Engineering and his doctoral (Ph.D.) degree in electrical engineering from the Vienna University of Technology (VUT), Austria, in 1991 and 1994, respectively. In 2001 he obtained a venia legendi for Theoretical Electrical Engineering from the VUT. From 1991 to 1994 he worked as a Research Assistant at the Institute of General Electrical Engineering and Electronics of the VUT. Subsequently he stayed as an Erwin Schrödinger Fellow at the University of Ghent, Belgium, performing research on the electrodynamics of complex media. From 1996 to 1999 he held the position of a Research Associate and later Assistant Professor at the Delft University of Technology, The Netherlands, working in the field of microacoustic sensors. From 1999 to 2001 he was with the Automotive Electronics Division of the Robert Bosch GmbH, Germany, where he conducted development projects in the field of automotive liquid sensors. In 2001 he joined the newly formed Industrial Sensor Systems group of the VUT as an Associate Professor. In 2005 he was appointed Full Professor of Microelectronics at the Johannes Kepler University Linz, Austria. He is currently working in the field of liquid sensors and monitoring systems.

Please cite this article in press as: M. Heinisch, et al., Application of resonant steel tuning forks with circular and rectangular cross sections for precise mass density and viscosity measurements, Sens. Actuators A: Phys. (2015), http://dx.doi.org/10.1016/j.sna.2015.02.007

Sensors and Actuators A xxx (2015) xxx–xxx

Contents lists available at ScienceDirect

Sensors and Actuators A: Physical

journal homepage: www.elsevier.com/locate/sna

Electromagnetically driven torsional resonators for viscosity and mass density sensing applications☆

M. Heinisch[a,*], T. Voglhuber-Brunnmaier[a,b], E.K. Reichel[a], I. Dufour[c], B. Jakoby[a]

[a] Institute for Microelectronics and Microsensors, Johannes Kepler University, Linz, Austria
[b] Center for Integrated Sensors Systems, Danube University, Krems, Austria
[c] Université de Bordeaux, Laboratoire de l'Intégration du Matériau au Système, Pessac, France

ARTICLE INFO

Article history:
Received 8 October 2014
Received in revised form 6 March 2015
Accepted 26 March 2015
Available online xxx

Keywords:
Torsional
Resonator
Cylinder
Shear wave
Viscosity
Mass density

ABSTRACT

In this contribution a conceptual study for torsional oscillators, which are electromagnetically driven and read out, is presented. The aim is to experimentally investigate the basic feasibility of a torsional resonator with application to viscosity and mass density sensing in liquids. Such a device is particularly interesting as cylindrical, torsional resonators for fluid sensing applications are hardly reported but unlike many other devices, yield pure shear wave excitation in the liquid. The design of first conceptual demonstrators for measurements in air as well as in liquids and their benefits and disadvantages is discussed in detail. A closed form as well as a reduced order model and measurement results obtained with first demonstrators are presented.

© 2015 Elsevier B.V. All rights reserved.

1. Introduction

Recently, we investigated various resonant sensors for liquid viscosity and mass density, see e.g., [1], which were particularly designed to be operated in the low kilohertz range. Amongst these devices, in-plane oscillating platelets, emitting mainly shear waves into the sample liquids, were investigated e.g., in [2,3] where millimeter sized metal platelets were used. In [4,5] similar miniaturized devices have been implemented in silicon technology. Generally used shear oscillating resonators, such as shear oscillating quartz crystals [6] and the aforementioned in-plane oscillating platelets, have in common that, besides the desired shear waves, compressional waves are also radiated into the liquid. These pressure waves result e.g., from non-uniform shear displacement [7,8], the resonators' finite thicknesses, and spurious out-of-plane modes e.g. from the plate itself or of supporting beams. Potential candidates for resonators which only emit shear waves into the test fluid are cylindrical torsional oscillators. First, such pure shear wave emitting devices are of special interest from a rheological point of view, when it comes to the analysis of complex liquids such as viscoelastic liquids. For pure shear wave deformation, the liquid can be described by a complex-valued shear modulus or a complex valued viscosity, which, in general, are frequency dependent quantities [9]. With oscillatory measurements, the values obtained at a number of discrete frequencies can be used to obtain a rheological spectrum. A second merit for cylindrical, torsional resonators is that, due to their geometry, they resemble concentric cylinder rheometers. Thus, they yield comparable measurements but extend the measurable frequency range of conventional rheometers which is usually limited at approximately 100 Hz. Third, cylindrical, torsional oscillators allow experimental comparison of measurement results obtained with the above mentioned in-plane oscillating resonators, which excite spurious compressional waves. Thus, by means of such a comparison the impact of these compressional waves could be experimentally estimated.

In-plane oscillating devices, oscillating rotational disks [10] and other resonators for viscosity and mass density sensors such as cantilevers [11,12], quartz tuning forks [13] and vibrating bridges [14,15] are based on a similar operational principle. Usually, the devices' frequency responses, containing a characteristic resonant mode, are recorded upon immersion in a sample liquid. The change of evaluated resonance frequencies and quality factors are then related to the liquid's mass density and viscosity.

In this work a feasibility study for electromagnetically driven and read out torsional oscillators for operation in liquids is presented. Two concepts for actuation and readout discussed in

☆ Selected papers presented at EUROSENSORS 2014, the XXVIII edition of the conference series, Brescia, Italy, September 7–10, 2014.

* Corresponding author. Tel.: +43 73224686266.
E-mail address: martin.heinisch@jku.at (M. Heinisch).

http://dx.doi.org/10.1016/j.sna.2015.03.033
0924-4247/© 2015 Elsevier B.V. All rights reserved.

Please cite this article in press as: M. Heinisch, et al., Electromagnetically driven torsional resonators for viscosity and mass density sensing applications, Sens. Actuators A: Phys. (2015), http://dx.doi.org/10.1016/j.sna.2015.03.033

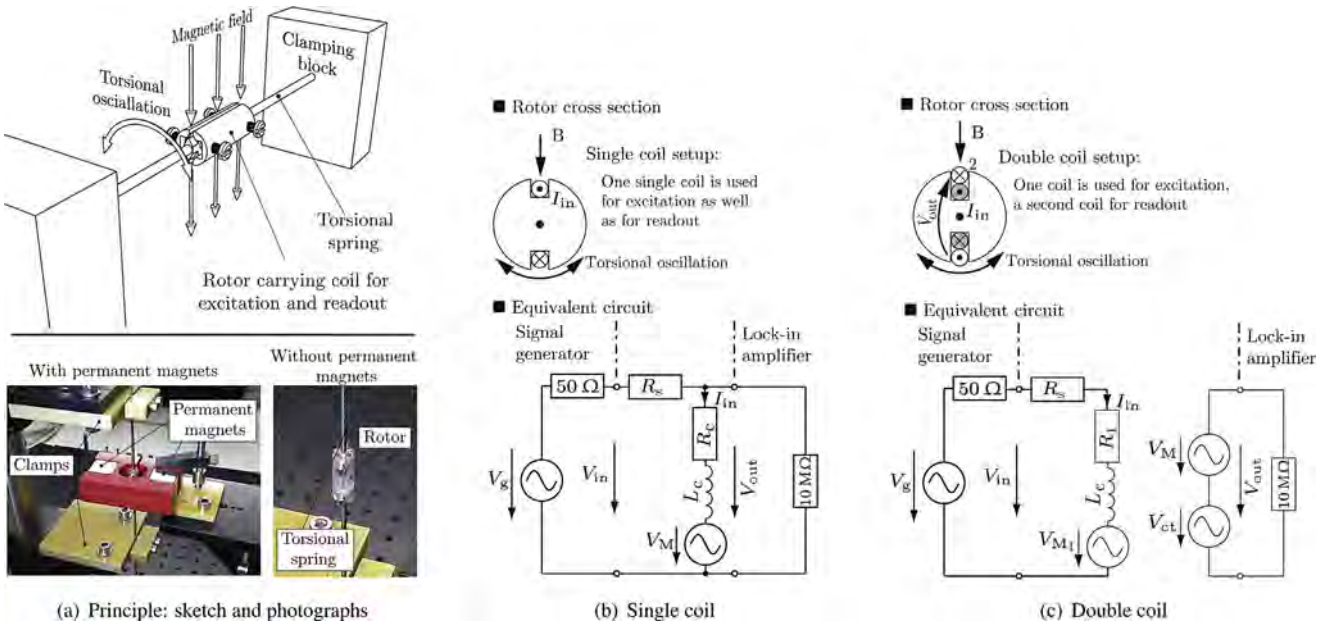

Fig. 1. (a) Principle and photographs of first demonstrators allowing to record frequency responses in air, (b) cross section and electrical equivalent circuit of the demonstrator with a rotor carrying a single coil for excitation and readout by means of Lorentz-forces. I_{in}: input (excitation) current, B: external magnetic field, V_g: voltage of the signal generator, 50 Ω: output resistance of the signal generator, R_s: series resistance, R_c, L_c: coil's resistance and inductance, V_M: motion induced voltage, 10 MΩ: input resistance, (c) cross section and electrical equivalent circuit of the rotor carrying two coils. One coil is used for excitation, the other for read out, V_{ct}: induced voltage due to inductive crosstalk.

Section 2 were manufactured and the experimental analysis in air allowed investigating the benefits and disadvantages of both approaches. The analysis of measurements obtained with three different torsional spring diameters and various spring lengths allowed designing a demonstrator for measurements in liquids, which is explained in detail in Section 3. A closed form model for the resonator, relating the input to the output voltage, is derived in Section 4. In Section 5 evaluated results of measurements obtained with the cylindrical torsional resonator in ten different liquids are shown. Furthermore, the sensor's sensitivity and cross sensitivity to temperature are evaluated and compared to other sensor concepts.

2. Torsional resonator

2.1. Concept

The basic idea of the torsional resonator is to excite a cylinder to torsional vibrations by means of Lorentz forces acting on sinusoidal currents in a constant external magnetic field. For recording the device's frequency response, the excitation current's frequency is swept over a frequency range containing the resonant fundamental mode and simultaneously measuring the motion induced voltage on an electrical conductor, following the torsional oscillation. To implement this idea, a rotor (bobbin) is mounted on torsional springs, where two different principles were realized and compared. In the first approach, the bobbin carries one single coil which is used for both, excitation and read out, where in the second approach, two separate coils are used for these tasks.

2.2. Conceptual investigation in air

To investigate the functional principle of the electromagnetic torsional oscillator and to estimate the achievable range of resonance frequencies and signal strengths, a single coil type bobbin has been mounted and investigated on three torsional springs at various spring lengths. For this, a setup as depicted in Fig. 1(a) and (b) has been used. There, one hundred turns of a 80 μm thick copper wire were wound on a 3D printed bobbin with 8 mm in diameter and 22 mm in length, which was attached to tungsten rods with diameters of 0.58 mm, 1.6 mm and 2 mm serving as torsional springs. For each torsional spring, the same rotor was used so that only the effect of different torsional spring lengths and diameters could be examined. For attaching, the rotor was affixed with screws to the torsional springs, which were rigidly clamped at their ends with fiber-glass blocks through which the torsional spring lengths could be adjusted. The bobbin was placed in a magnetic field (denoted with B) provided by neodymium permanent magnets and set to torsional oscillations by means of Lorentz forces on sinusoidal currents (I_{in}) in the coil which was connected to a signal generator (V_g and 50 Ω output resistance) and a series resistance R_s = 100 Ω which was used to limit the excitation current, to prevent from non-linear deflections. By sweeping the excitation current's frequency, the oscillator's frequency response can be recorded. In this case, for the sake of straight forward manufacturing, the coil's ends of the 80 μm thick copper wire were kept long enough for direct connection with the excitation and readout electronics. However, for a stable resonator, this wiring approach is not adequate. In the demonstrator used for measurements in liquids which will be presented in Section 3 this drawback has been overcome by connecting the coil's ends to the torsional springs for electrical connection of the resonator.

Fig. 2 shows the results of recorded frequency responses and evaluated resonance frequencies in air for tungsten rods with diameters of 0.58 mm and 1.6 mm for various spring lengths in comparison with theoretical results also presented in [16]. These results proved the basic feasibility of the concept and allowed designing a torsional resonator in the desired frequency range.

2.3. Single versus double coil setup

The benefits and disadvantages of using single or double coil setups were experimentally investigated. The cross sections of the rotors as well as the electrical equivalent circuits for both cases are depicted in Fig. 1(c) and (d). For the first case, a single coil with

Please cite this article in press as: M. Heinisch, et al., Electromagnetically driven torsional resonators for viscosity and mass density sensing applications, Sens. Actuators A: Phys. (2015), http://dx.doi.org/10.1016/j.sna.2015.03.033

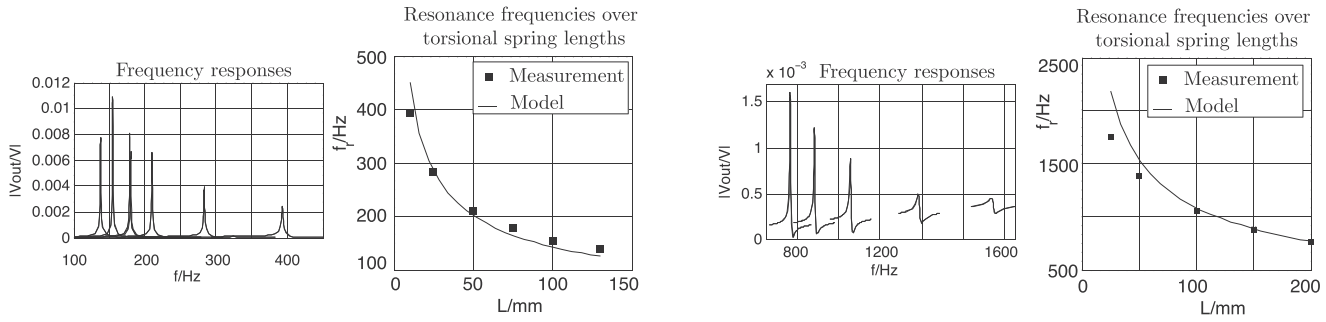

(a) Spring diameter 0.58 mm (b) Spring diameter 1.6 mm

Fig. 2. Examples for recorded frequency responses in air using a single coil for excitation and read-out. These experiments were performed to estimate achievable signal strengths and resonance frequencies for different spring diameters and spring lengths.

100 turns, a length of 20 mm and a width of 8 mm is used for both, excitation and read out and for the second case, two coils with 50 turns each are used separately for these purposes. The voltage of the signal generator V_g was 0.1 V and the series resistance R_s was 100 Ω.

For the single coil setup, the rotor is excited to torsional vibrations by means of Lorentz forces on sinusoidal currents I_{in}. The oscillation of the coil in the presence of the external magnetic field causes a motion induced voltage V_M on the excitation coil itself. This motion induced voltage is proportional to the velocity of the oscillation and thus an appropriate quantity for measuring the oscillation. However, the measurable output voltage V_{out} consists of an additional voltage resulting from the coil's impedance related voltage drop. The coil's impedance is modeled as a serial connection of a resistance R_c and an inductance L_c. For the manufactured rotor $R_c = 21.3\ \Omega$ and $L_c = 215\ \mu$H were obtained by fitting the parameters in the recorded frequency response from 100 Hz to 100 kHz. The output voltage was measured with a lock-in amplifier (with an input resistance of 10 MΩ) and reads

$$\underline{V}_{out}(\omega) = \underline{V}_M(\omega) + (R_c + j\,\omega L_c)\underline{I}_{in} \quad (1)$$

in complex notation where $j = \sqrt{-1}$, ω is the angular frequency and the time dependence $e^{j\omega t}$ is suppressed.

To reduce this impedance-related offset voltage, a second coil is used in the double coil setup for readout. This second coil follows the motion of the oscillating cylinder and thus, as in the single coil setup, a voltage is induced. However, in this case due to electrical crosstalk resulting from the current I_{in} in the excitation coil, an additional voltage V_{ct} is induced in the measuring coil. Assuming that the output current I_{out} is negligible, the output voltage reads

$$\underline{V}_{out}(\omega) = \underline{V}_M(\omega) + j\,\omega M\,\underline{I}_{in} \quad (2)$$

where M is the mutual inductance describing the inductive coupling from the excitation to the readout coil. For the rotor used in this experiment $M = 480\ \mu$H was obtained.

Both types of rotors have been manufactured and mounted on a tungsten rod with 0.58 mm diameter and 5 cm length for each torsional spring. The recorded frequency responses covering a frequency range of 100 Hz to 10 kHz as well as detailed plots of the fundamental resonance are shown in Fig. 3 for both cases. The resonance peak is more than twice as high in case of the single coil setup compared with the double coil setup (12.4 mV in contrast to 5.5 mV for the double coil setup.) This results from the fact that for the single coil setup, the number of coil turns is twice as high which yields a higher effective driving force in the rotor and a proportional to the coil turns higher induced voltage. Thus, assuming the same mechanical conditions for both setups, the voltage peak of the single coil setup should be four times as high as the double coil setup. However, in the performed experiments, this is not the case, as the quality factor of the single coil setup ($Q = 148.77$) is significantly smaller than in case of the double coil setup ($Q = 221.4$). Due to the large offset voltage for the single coil (≈12 mV) the change of phase at resonance is significantly smaller as for the double coil (38.98° in comparison to 178.43°). The reason of the phase shift of 178.43° instead of supposedly 180° is that the output voltage is subjected to a slight crosstalk voltage at these frequencies. This crosstalk voltage increases proportionally to the excitation frequency as it can be observed in Fig. 3(b) which is also considered in Eq. (2).

3. Demonstrator for measurements in liquids

The use of a second coil did not show a major advantage in the obtained signals compared to the setup where only one coil is used for excitation and readout. However, using only one coil has a

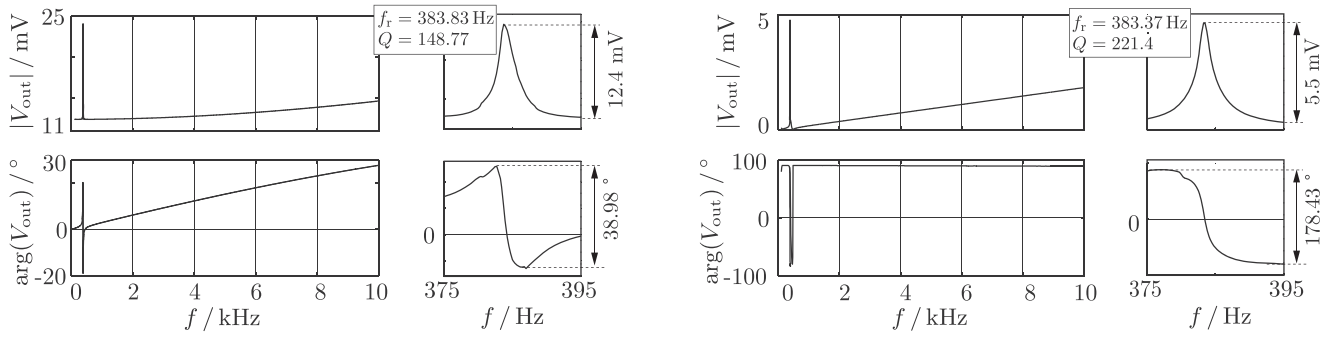

(a) Single coil (b) Double coil

Fig. 3. Frequency responses measured with the single coil (a) and the double coil (b) setup. The recorded spectra between 100 Hz and 10 kHz as well as detailed plots of the resonance are shown for both setups.

Please cite this article in press as: M. Heinisch, et al., Electromagnetically driven torsional resonators for viscosity and mass density sensing applications, Sens. Actuators A: Phys. (2015), http://dx.doi.org/10.1016/j.sna.2015.03.033

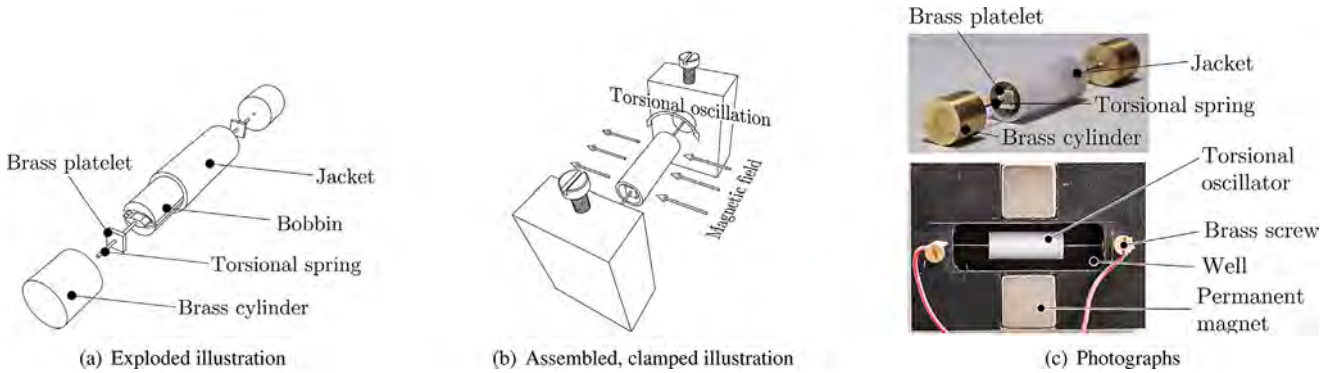

Fig. 4. (a) Exploded view of the torsional resonator used for measurements in liquids. The coil is electrically connected via the torsional springs and the brazed brass cylinders, which are clamped with brass screws to which connecting wires are soldered. (b) shows an illustration of the assembled, clamped setup, the direction of the external magnetic field as well as the torsional oscillation. (c) The upper photograph shows the manufactured torsional oscillator. The lower photograph shows the complete setup including both permanent magnets and the torsional oscillator placed in the experimental well which was filled with the sample liquids.

significant advantage for electrical connection. In this case, the electrical conductive torsional springs can be used for this task. For the double coil setup which requires the connection of four wires, the usage of tubes would be necessary (serving as torsional springs) through which the coils' wires have to be threaded which might be a rather tedious manufacturing process. Fig. 4 shows drawings and photographs of the torsional resonator with which first measurements in ten different liquids were obtained.

As for the single coil type rotor, which was investigated in air, one hundred turns of a copper wire with a diameter of 80 μm were wound on a 3D printed bobbin. Two tungsten rods with a diameter of 0.58 mm serve as torsional springs with a spring length of 14 mm each. Each rod is brazed to a brass cylinder with 10 mm diameter and 10 mm height. Both tungsten rods carry a brazed brass platelet and are put into the bobbin on both sides ensuring no contact of both torsional springs. Each end of the coil is glued with electrical conductive glue to one of these brass platelets which are furthermore used for a form-fitted connection with epoxy resin poured into both sides of the bobbin which in turn is put into a POM-C (polyacetal) plastics jacket with an outer diameter of 10 mm and 25 mm length. As mentioned before, it is essential that the tungsten rods do not get in contact in order not to shortcut the coil. The torsional resonator is put into a milled POM-C plastics frame with a well for containing the sample liquids. The brass cylinders are clamped with brass screws, which in turn are used for further electrical connection for power supply and read-out. Two neodymium magnets are used for providing a magnetic field necessary for excitation and read-out based on Lorentz-forces.

4. Modeling

4.1. Mechanical model

4.1.1. Structural mechanics

Considering the rotor's moment of inertia J_0, the torque resulting from the tungsten rods' torsional stiffnesses M_T, the excitation torque M_{ex}, a torque M_c, representing the intrinsic dissipative losses of the resonator and a torque M_F accounting for the torque due to the liquid loading, the principle of momentum equilibrium yields, cf. Fig. 5

$$J_0 \frac{d^2\varphi(t)}{dt^2} + 2M_T + M_c + M_F = M_{ex} \tag{3}$$

where φ is the twisting angle of the rotor.

For a cylindrical rod with shear modulus G, radius r_s, length l_s and twisting angle φ the torsional torque reads [17]

$$M_T = k_T^* \varphi. \tag{4}$$

where

$$k_T^* = G \frac{\pi}{2} \frac{r_s^4}{l_s}. \tag{5}$$

is the torsional spring constant of one torsional spring and $k_T = 2\,k_T^*$ is the spring constant of both torsional springs in our case.

Dissipative losses are considered by a loss coefficient c_0 and the associated loss torque is

$$M_c = c_0 \frac{d\varphi}{dt}. \tag{6}$$

4.1.2. Fluid dynamics

As we are facing a rotational problem, the solution of the fluid forces acting on the oscillating cylinder contains Hankel functions which make the obtained equations difficult to interpret. For this reason, the fluid forces acting on the cylinder are approximated by one dimensional shear waves of an in-plane oscillating plate which yields a negligible error if the cylinder's radius r_c is significantly larger than the penetration depth [18], also termed decay length [6]

$$\delta = \sqrt{\frac{2\eta}{\rho\,\omega}} \tag{7}$$

where η and ρ are the liquid's viscosity and mass density, respectively and ω is the angular frequency of the oscillation.

A comparison of the relative deviations ε of the solutions for the cylindrical and the planar case over the ratio r_c/δ are depicted in Fig. 6. The complete derivation for the fluid forces is only given for the planar case in this contribution. For aqueous liquids at 1 kHz the penetration depth is 18 μm approximately. Considering the cylinder's radius of the manufactured demonstrator r_c = 5 mm it follows

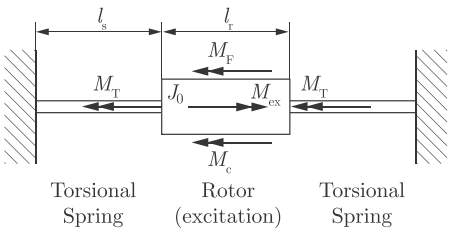

Fig. 5. Torques considered in the principle of moment equilibrium. A double arrow illustrates an acting torque.

Please cite this article in press as: M. Heinisch, et al., Electromagnetically driven torsional resonators for viscosity and mass density sensing applications, Sens. Actuators A: Phys. (2015), http://dx.doi.org/10.1016/j.sna.2015.03.033

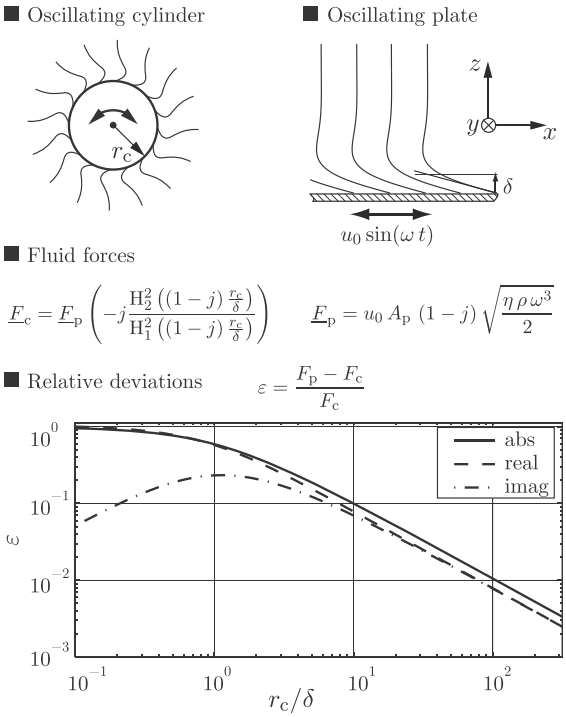

Fig. 6. Comparison of the solutions for the fluid forces F_c and F_p acting on an oscillating cylinder and an in-plane oscillating plate, respectively. For both cases, the same surface interacting with the liquid is considered. In case of the solution for the cylinder, Hankel functions are obtained which make an intuitive interpretation of the obtained equations difficult. For high ratios of the cylinder's radius r_c and the penetration depth δ, the difference between both solutions is negligibly small.

$r_c/\delta = 280$ and thus $\varepsilon = 3.8 \cdot 10^{-3}$ which substantiates the applicability and the validity of the approximated solution.

Under the assumptions of an infinitely extended plate oscillating only in x-direction (thus imposing only shear stress in x-direction), that gravitational forces are negligible, and that the liquid is incompressible, the equation of motion and the shear stress T_{xz} in liquids can be expressed as a one dimensional problem and reads [6,19]:

$$\rho \frac{\partial^2 u_x}{\partial t^2} = \frac{\partial T_{xz}}{\partial z} \qquad \text{with} \qquad T_{xz} = \eta \frac{\partial^2 u_x}{\partial z \, \partial t}. \tag{8}$$

Here, ρ is the mass density of the liquid, u_x is the displacement of the liquid in x-direction, t is the time variable.

Substituting T_{xz} in the equation of motion, transforming the problem to the frequency domain assuming a time dependence $e^{j\omega t}$ and solving the linear differential equation of second order yields the solution for the x-displacement propagating in z-direction

$$\underline{u}_x(z,t) = u_0 \, e^{-\frac{z}{\delta}} \, e^{-j\left(\frac{z}{\delta} - \omega t\right)} \tag{9}$$

where u_0 is the amplitude of the oscillation. With this solution for $\underline{u}_x$, the shear stress at the liquid–solid interface (i.e., $z = 0$) in the frequency domain reads

$$\underline{T}_{xz}(z=0) = \underline{u}_x (1-j) \sqrt{\frac{\eta \rho \omega^3}{2}}. \tag{10}$$

Expressing the planar deflection in rotational form, i.e. $u_x \rightarrow \varphi \, r_c$ and assuming $M_F = -r_c \, T A_c$, where A_c is the cylinder's surface, the torque acting on the oscillating cylinder can be expressed as

$$\underline{M}_F = \left[-\omega^2 \sqrt{\frac{\eta \rho}{2\omega}} \, r_c^2 A_c + j\omega \sqrt{\frac{\eta \rho \omega}{2}} \, r_c^2 A_c \right] \underline{\varphi}(\omega). \tag{11}$$

Eqs. (4) and (6) are substituted in Eq. (3) and after transformation of the obtained expression to the frequency domain, Eq. (11) can be considered in the equation of the moment equilibrium

$$\left[-\omega^2 J + k_T + j\omega c \right] \underline{\varphi}(\omega) = \underline{M}_{ex} \tag{12}$$

where J and c have been introduced and read

$$J = J_0 + \sqrt{\frac{\eta \rho}{2\omega}} \, r_c^2 A_c \quad \text{and} \quad c = c_0 + \sqrt{\frac{\eta \rho \omega}{2}} \, r_c^2 A_c. \tag{13}$$

As the torsional resonator is operated close to its (fundamental) angular resonance frequency ω_0, these expressions can be approximated by

$$J \approx J_0 + \sqrt{\frac{\eta \rho}{2\omega_0}} \, r_c^2 A_c \quad \text{and} \quad c \approx c_0 + \sqrt{\frac{\eta \rho \omega_0}{2}} \, r_c^2 A_c. \tag{14}$$

Substituting these relations into Eq. (12) yields a closed form model of the oscillating cylinder in liquids and is beneficial for design purposes. However, as the model consists of a relatively large amount of variables, which are usually not exactly known, constants and variables are combined in single factors where possible to reduce the amount of variables which have to be determined in a parameter fit.

4.2. Reduced order models

4.2.1. One dimensional shear waves

Combining factors and variables in Eq. (14) in single factors and neglecting the ω_0 dependence allows writing J and c in reduced form as follows

$$J \approx J_0 + J^*_{\eta\rho} \sqrt{\eta \rho} \quad \text{and} \quad c \approx c_0 + c^*_{\eta\rho} \sqrt{\eta \rho}. \tag{15}$$

With this, the angular speed $\underline{\Omega}(\omega) = j\omega\underline{\varphi}(\omega)$ can be expressed as

$$\underline{\Omega}(\omega) = \frac{\underline{M}_{ex}/c}{1 + jQ\left(\frac{\omega}{\omega_0} - \frac{\omega_0}{\omega}\right)} \tag{16}$$

with angular resonance frequency

$$\omega_0 = \sqrt{\frac{k_T}{J}} = \frac{1}{\sqrt{J_{0k} + J^*_{\eta\rho k}\sqrt{\eta\rho}}} \tag{17}$$

and quality factor

$$Q = \frac{\sqrt{J\,k_T}}{c} = \frac{1}{\omega_0}\frac{k_T}{c} = \frac{\sqrt{J_{0k} + J^*_{\eta\rho k}\sqrt{\eta\rho}}}{c_{0k} + c^*_{\eta\rho k}\sqrt{\eta\rho}}. \tag{18}$$

where the subscript k denotes that the factors in Eq. (15) have been divided by k_T to obtain these solutions for ω_0 and Q.

For resonators, which are readout via a motion induced voltage (which is proportional to the oscillator's velocity, see Section 4.3.2) the maximum peak frequency and the frequency of free, undamped oscillations (usually termed ω_0) are identical. For this reason, we may call ω_0 resonance frequency. For read-out principles evaluating the resonator's deflection using e.g. optical methods [20], the frequency of free, undamped oscillations and the maximum peak frequency of deflection amplitude are not identical.

4.2.2. Generalized model

In [21] a similar reduced order model was presented which considers not only one dimensional shear waves but convexly shaped, oscillating objects in general and reads

$$\omega_0 = \frac{1}{\sqrt{m_{0k} + m_{\rho k}\,\rho + m_{\eta\rho k}\sqrt{\frac{\eta\rho}{\omega_0}}}} \tag{19}$$

Please cite this article in press as: M. Heinisch, et al., Electromagnetically driven torsional resonators for viscosity and mass density sensing applications, Sens. Actuators A: Phys. (2015), http://dx.doi.org/10.1016/j.sna.2015.03.033

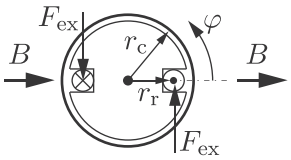

Fig. 7. Rotor cross section.

and

$$Q = \frac{1}{\omega_0} \cdot \frac{1}{c_{0k} + c_{\eta k}\,\eta + c_{\eta\rho k}\sqrt{\omega_0\,\eta\,\rho}}, \tag{20}$$

where m_{xk} and c_{xk} are coefficients and $m_{\rho k}$ as well as $c_{\eta k}$ are zero in case of pure one-dimensional shear waves.

4.2.3. Simplified generalized equations

Eq. (19) is an implicit equation for ω_0, which makes an exact evaluation of ω_0 for given η and ρ difficult. Therefore, the equations are simplified by considering that the frequency dependence of certain parameters occurring in the analysis is negligible as they are virtually constant within the bandwidth of the resonant system. Doing so, we obtain the following expressions for the angular resonance frequency

$$\omega_0 = \frac{1}{\sqrt{m_{0k} + m_{\rho k}\,\rho + m^*_{\eta\rho k}\sqrt{\eta\,\rho}}} \tag{21}$$

and the quality factor

$$Q = \frac{\sqrt{m_{0k} + m_{\rho k}\,\rho + m^*_{\eta\rho k}\sqrt{\eta\,\rho}}}{c_{0k} + c_{\eta k}\,\eta + c^*_{\eta\rho k}\sqrt{\eta\,\rho}}. \tag{22}$$

Thus if ω_0 and Q for given η and ρ using Eqs. (19) and (20) have to be calculated, numerical (e.g., iterative) methods can be used. Alternatively, the above simplified expressions give remedy. Conversely, if η and ρ have to be determined from measured $f_r = \omega_0/(2\pi)$ and Q, Eqs. (19) and (20) can be used directly.

The advantage of such reduced order models is that in comparison with completely closed form models, only a few variables have to be determined by means of a parameter fit.

In Section 5 these models are fit to experimental results. By means of a comparison of the fitted models it will be shown that the generalized models fit the measured data better than the model considering shear waves only. This supposedly is due to the fact that in addition to one dimensional shear waves, spurious effects such as liquid trapping [22,23] may be present.

4.3. Electrical model

4.3.1. Excitation torque

The Lorentz force on a charge q moving with velocity $\mathbf{v}$ in the presence of a magnetic field with magnetic flux density $\mathbf{B}$ and an electric field $\mathbf{E}$ is (bold variables denote vectors) [24]

$$\mathbf{F}_L = q\,(\mathbf{v} \times \mathbf{B} + \mathbf{E}). \tag{23}$$

Assuming perpendicular conditions between the excitation current I_{ex}, i.e. the charges moving in a wire of length l_r, and the external magnetic field, it follows that the force acting on the wire is given by

$$\underline{F}_{ex} = B\,l_r\,\underline{I}_{ex}. \tag{24}$$

With this, the excitation torque can be expressed as

$$\underline{M}_{ex} \approx 2\,N\,B\,r_r\,l_r\,\underline{I}_{ex} \tag{25}$$

where N is the number of turns of the excitation coil and r_r is the radius of the coil, see Fig. 7.

4.3.2. Motion induced voltage

Using Faraday's law of induction and the equation for Lorentz forces, the motion induced voltage on the coil can be expressed as:

$$V_M(t) = -\int_{coil} (\mathbf{v} \times \mathbf{B}) \cdot \mathrm{d}\mathbf{s}. \tag{26}$$

Assuming the magnetic flux density to be symmetric in the air gap, constant along the coil's length and aligned in parallel with the coil for $\varphi = 0$, see Fig. 7, it follows

$$V_M(t) = 2\,N\,r_r \cos\varphi\,\frac{\mathrm{d}\varphi}{\mathrm{d}t}\,B\,l_r. \tag{27}$$

For small twisting angles, the motion induced voltage in the frequency domain using the angular speed Eq. (16) reads

$$\underline{V}_M(\omega) \approx 2\,N\,r_r\,B\,l_r\,\underline{\Omega}(\omega). \tag{28}$$

This equation for the motion induced voltage is used for modeling the measurable output voltage V_{out} for the single as well as for the double coil setup in Eqs. (1) and (2).

5. Experimental investigation

5.1. Measurements in liquids

The demonstrator discussed in Section 3 has been used to experimentally test the principle operation of such a torsional resonator in liquids and to investigate the effect of different mass densities and viscosities on recorded frequency responses. Amplitudes as well as evaluated quality factors and resonance frequencies for two different sets of liquid series are depicted in Fig. 8. There, the results of the fitted models performing a linear fitting procedure, see [25], for $f_r = \omega_0/(2\pi)$ and Q using Eqs. (17), (18), (21) and (22) are depicted as well. The values for the examined liquids' viscosities η and mass densities ρ (which were determined with an Anton Paar SVM 3000) as well as the mean values of the associated, evaluated resonance frequencies f_r and quality factors Q are given in Table 1. The SVM 3000 features a reproducibility of 0.35% for viscosity and 0.0005 g/cm^3 for mass density. The measurements were performed at 25 °C. The values for f_r and Q were evaluated from the recorded frequency responses using a fitting algorithm described in [26]. The used liquid series are the so-called viscosity series and mass density series in the following. The first is a mixture of isopropanol and acetone covering a viscosity range of 0.21 mPa s to 2.05 mPa s for mass densities of roughly 0.78 g/cm^3. The percentage of mass isopropanol m_I and mass acetone m_A is given in the left column of Table 1. The mass density series cover a range of mass densities of 0.79 g/cm^3 to 1.01 g/cm^3 for viscosities of roughly 1 mPa s and were prepared using acetone, isopropanol, ethanol, DI-water and glycerol. After mixing, the liquids were investigated with the SVM 3000. These two liquid series are used to separately investigate experimentally the effect of varying viscosities or mass densities on f_r and Q.

The results obtained with both liquid series clearly show the effect of mass density and viscosity on the experimentally obtained values for f_r and Q. Deviations of the measured from the modeled values as well as slight variations in f_r and Q can be observed. These supposedly originate from imperfections in the prototype setup. These imperfections are associated with the fact that first, during cleaning and refilling of the sensor, the resonator may have been detuned due to an insufficiently stable clamping, second, the open experimental well, which allows evaporation of the liquid during the measurements, and third, geometrical imperfections such as e.g., surface roughnesses and a not perfect alignment of the oscillating cylinder with the torsional springs. For Q, both models yield approximately the same results, where for f_r, the generalized model

Please cite this article in press as: M. Heinisch, et al., Electromagnetically driven torsional resonators for viscosity and mass density sensing applications, Sens. Actuators A: Phys. (2015), http://dx.doi.org/10.1016/j.sna.2015.03.033

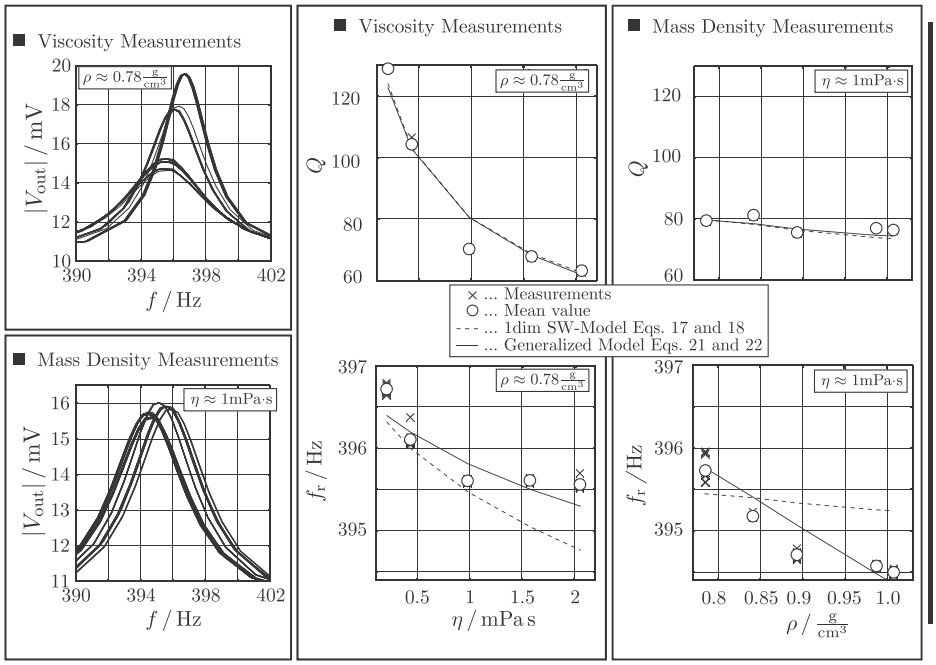

$$f_r = \frac{1}{2\pi}\frac{1}{\sqrt{J_{0k} + J_{\eta\rho k}\sqrt{\eta\rho}}}$$

$$Q = \frac{\sqrt{J_{0k} + J_{\eta\rho k}\sqrt{\eta\rho}}}{c_{0k} + c_{\eta\rho k}\sqrt{\eta\rho}}$$

J_{0k}/s^2	$J_{\eta\rho k}/\frac{\mathrm{m}^2}{\mathrm{kg}}\cdot\mathrm{s}^{5/2}$
$1.61\cdot10^{-7}$	$1.48\cdot10^{-9}$
c_{0k}/s	$c_{\eta\rho k}/\frac{\mathrm{m}^2}{\mathrm{kg}}\cdot\mathrm{s}^{3/2}$
$1.73\cdot10^{-6}$	$3.73\cdot10^{-6}$

$$f_r = \frac{1}{2\pi}\frac{1}{\sqrt{m_{0k} + m_{\rho k}\rho + m^*_{\eta\rho k}\sqrt{\eta\rho}}}$$

$$Q = \frac{\sqrt{m_{0k} + m_{\rho k}\rho + m^*_{\eta\rho k}\sqrt{\eta\rho}}}{c_{0k} + c_{\eta k}\eta + c^*_{\eta\rho k}\sqrt{\eta\rho}}$$

m_{0k}/s^2	$m_{\rho k}/\frac{\mathrm{m}^3\cdot\mathrm{s}^2}{\mathrm{kg}}$	$m^*_{\eta\rho k}/\frac{\mathrm{m}^2}{\mathrm{kg}}\cdot\mathrm{s}^{5/2}$
$1.57\cdot10^{-7}$	$4.65\cdot10^{-12}$	$1.06\cdot10^{-9}$
c_{0k}/s	$c_{\eta k}/\frac{\mathrm{m}\cdot\mathrm{s}^2}{\mathrm{kg}}$	$c^*_{\eta\rho k}/\frac{\mathrm{m}^2}{\mathrm{kg}}\cdot\mathrm{s}^{3/2}$
$1.89\cdot10^{-6}$	$2.12\cdot10^{-4}$	$3.31\cdot10^{-6}$

Fig. 8. Measured amplitudes as well as evaluated resonance frequencies and quality factors for two liquid series. The one dimensional shear wave model as well as the generalized model are fit to the measured data. The model parameters are given on the right hand side.

clearly yields better results. This finding can be explained by surface roughness, which yields so-called liquid trapping [22,23] and thus a higher sensitivity to mass density. This effect might be beneficial, as the effect of η and ρ on f_r and Q cannot be separated with devices yielding pure one-dimensional shear waves without liquid trapping.

Despite the discussed drawbacks in the presented setup, a rough estimation of the device's sensitivity can be made. We define the relative sensitivity of a quantity $X(y_i)$ to an independent variable y_i as

$$S_{X,y_i} = \left|\frac{\partial X}{\partial y_i}\cdot\frac{y_i}{X}\right| \tag{29}$$

where X either stands for f_r or Q and y_i for η and ρ, yielding four different sensitivities which are evaluated from the fitted generalized model Eqs. (21) and (22). The four sensitivities $S_{f_r,\eta}$, $S_{f_r,\rho}$, $S_{Q,\eta}$ and $S_{Q,\rho}$ are not constant but depend on η as well as on ρ and thus are depicted as bands in Fig. 9 for the experimentally evaluated range of viscosities and mass densities. The upper boundary of the bands in the plots on the left hand side (i.e., $S_{f_r,\eta}$ and $S_{Q,\eta}$) are the values for $\rho = 1.01\ \mathrm{g/cm^3}$, the lower boundary for $\rho = 0.79\ \mathrm{g/cm^3}$. On the right hand side (i.e., $S_{f_r,\rho}$ and $S_{Q,\rho}$) the upper and lower boundaries of the bands represent the evaluated values for $\eta = 0.21$ mPa s and $\eta = 2.05$ mPa s, respectively. In Fig. 9 the sensitivities obtained with the torsional resonator are depicted in comparison with the sensitivities achieved with circular and rectangular cross sectioned steel tuning forks oscillating at 400 Hz in liquids approximately, a U-shaped wire sensor ($f_r \approx 930$ Hz) [27], and a quartz tuning fork ($f_r \approx 32.7$ kHz) [13].

5.2. Measurement accuracy

Equations (19) and (20) were used to calculate η and ρ for evaluated f_r and Q. The fitted model parameters using a linear fitting procedure described in [21,25] are given in Table 2. Despite their limited accuracy, the mean values for f_r and Q

Table 1
Upper part: acetone–isopropanol solutions for viscosity measurements. Lower part: solutions for mass density measurements. The plus–minus values are evaluated typical errors (single standard deviations). $\hat{x}$ are the calculated values for viscosity and mass density using Eqs. (19) and (20) and evaluated mean values for f_r and Q. $\Delta x = \hat{x} - x$ and $\Delta x_{rel} = \Delta x/x$ are absolute and relative deviations from the values for viscosity and mass density, respectively.

Viscosity series $T = 25\,^\circ$C										
$\frac{m_I}{m_A+m_I}$/%	η/(mPa s)	ρ/(g/cm³)	f_r/Hz	Q	$\hat{\eta}$/(mPa s)	$\Delta\eta$/(mPa s)	$\Delta\eta_{rel}$	$\hat{\rho}$/(g/cm³)	$\Delta\rho$/(g/cm³)	$\Delta\rho_{rel}$
0	0.207	0.7841	$396.710 \pm 1.4\cdot10^{-3}$	129.0 ± 0.44	0.173	−0.034	−0.164	0.7394	−0.0447	−0.057
51	0.433	0.7790	$396.103 \pm 3.3\cdot10^{-3}$	104.4 ± 0.04	0.399	−0.034	−0.079	0.7985	0.0195	0.025
83	0.980	0.7793	$395.599 \pm 0.3\cdot10^{-3}$	70.3 ± 0.16	1.464	0.484	0.493	0.7730	−0.0063	−0.008
95	1.576	0.7803	$395.605 \pm 3.5\cdot10^{-3}$	67.8 ± 0.03	1.636	0.059	0.038	0.7602	−0.0201	−0.026
100	2.054	0.7804	$395.56 \pm 4.8\cdot10^{-3}$	63.3 ± 0.36	2.006	−0.049	−0.024	0.7444	−0.0360	−0.046

Density series $T = 25\,^\circ$C									
η/(mPa s)	ρ/(g/cm³)	f_r/Hz	Q	$\hat{\eta}$/(mPa s)	$\Delta\eta$/(mPa s)	$\Delta\eta_{rel}$	$\hat{\rho}$/(g/cm³)	$\Delta\rho$/(g/cm³)	$\Delta\rho_{rel}$
1.006	0.7849	$395.729 \pm 0.8\cdot10^{-3}$	79.4 ± 0.15	1.009	0.003	0.003	0.7894	0.0045	0.006
0.994	0.8411	$395.177 \pm 1.4\cdot10^{-3}$	81.2 ± 0.31	0.850	−0.144	−0.145	0.8918	0.0507	0.060
1.010	0.8931	$394.706 \pm 10.5\cdot10^{-3}$	76 ± 2.2	0.999	−0.011	−0.011	0.9513	0.0582	0.065
1.006	0.9870	$394.574 \pm 8.6\cdot10^{-3}$	77 ± 2.4	0.925	−0.080	−0.080	0.9798	−0.0072	−0.007
0.998	1.0073	$394.500 \pm 5.5\cdot10^{-3}$	76 ± 1.3	0.937	−0.061	−0.061	0.9904	−0.0169	−0.017

Please cite this article in press as: M. Heinisch, et al., Electromagnetically driven torsional resonators for viscosity and mass density sensing applications, Sens. Actuators A: Phys. (2015), http://dx.doi.org/10.1016/j.sna.2015.03.033

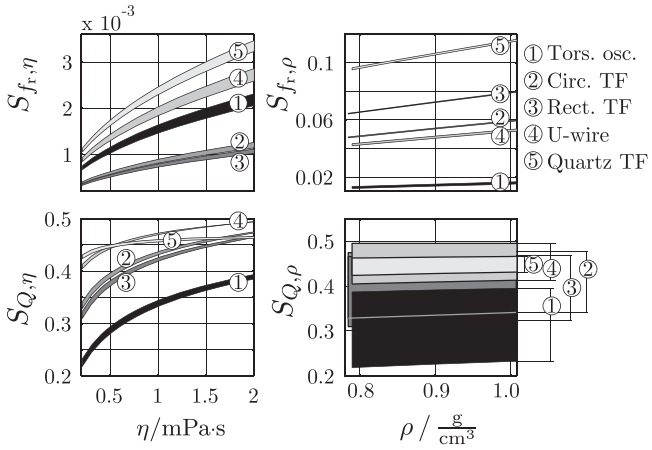

Fig. 9. Sensitivities to viscosity and mass density: the sensitivities of f_r and Q to η and ρ are not constant but dependent both on η and ρ. For this reason the sensitivities are depicted as bands, in the experimentally investigated range of viscosities and mass densities. In the plots for $S_{f_r,\eta}$ and $S_{Q,\eta}$ the upper boundary of the bands are the values for $\rho = 1.01$ g/cm^3, the lower boundary for $\rho = 0.79$ g/cm^3. In the plots for $S_{f_r,\rho}$ and $S_{Q,\rho}$ the upper and lower boundaries of the bands represent the evaluated values for $\eta = 0.21$ mPa s and $\eta = 2.05$ mPa s, respectively.

Table 2
Fitted model parameters using Eqs. (19) and (20).

m_{0k}/s^2	$m_{\rho k}/\frac{m^3 \cdot s^2}{kg}$	$m_{\eta\rho k}/\frac{m^2}{kg} \cdot s^2$
$1.57 \cdot 10^{-7}$	$4.64 \cdot 10^{-12}$	$5.29 \cdot 10^{-8}$
c_{0k}/s	$c_{\eta k}/\frac{m \cdot s^2}{kg}$	$c_{\eta\rho k}/\frac{m^2}{kg} \cdot s^2$
$1.88 \cdot 10^{-6}$	$1.93 \cdot 10^{-4}$	$6.73 \cdot 0^{-8}$

given in Table 1 are used to calculate the values for viscosity and mass density for both liquid series. The evaluation of absolute and relative errors given in Table 1 shows that with the present setup, absolute and relative accuracies for viscosity in the range of $[|\Delta\eta|_{min}, |\Delta\eta|_{max}] = [0.003, 0.484]$ mPa s and $[|\Delta\eta_{rel}|_{min}, |\Delta\eta_{rel}|_{max}] = [0.003, 0.493]$, respectively are obtained. For the calculated mass densities the obtained accuracies are $[|\Delta\rho|_{min}, |\Delta\rho|_{max}] = [0.0045, 0.0058]$ g/cm^3 and $[|\Delta\rho_{rel}|_{min}, |\Delta\rho_{rel}|_{max}] = [0.005, 0.065]$. This evaluation substantiates the need for setup improvement, especially to obtain more accurate measurement results for viscosity. However, the purpose of this work was a feasibility study of torsional, resonant viscosity and mass density sensors, their modeling and first designs of promising demonstrators. In [28] the advantages and capability of resonant viscosity and mass density sensors using conventional steel tuning forks with circular and rectangular cross sections was demonstrated.

5.3. Cross sensitivity to temperature

Mechanical resonators can show a significant dependence of their resonance frequency to temperature. This dependence is mainly due to the thermal expansion of the resonator and the temperature dependence of the resonator's Young's modulus. For doubly clamped structures such e.g. bridges [15,29] and straight wire resonators [30,31], the cross sensitivity of the resonance frequency to temperature becomes large if significant thermal prestresses are induced. The dependence of the resonance frequency to temperature can be positive as well as negative. In [32], micromachined vibrating strings are used as ultrasensitive temperature sensors. For the case of resonant viscosity sensors, this cross sensitivity directly limits the sensor's accuracy and thus should be kept as low as possible. The dependence of the torsional resonator's resonance frequency has been evaluated in a temperature range from

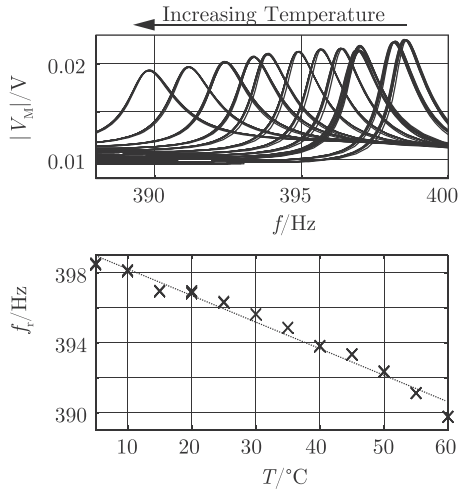

Fig. 10. Cross sensitivity of the resonance frequency to temperature. The upper figure shows the magnitudes of recorded frequency responses, the lower figure evaluated resonance frequencies versus temperature.

Table 3
Cross sensitivities of the resonance frequency (fundamental mode) to temperature. f_0: nominal resonance frequency, $\Delta f_r = f_r(T_0) - f_r(T_1)$: resonance frequency shift, $\Delta T = T_0 - T_1$ difference of temperatures T_0 and T_1, $\Delta f_{r,rel} = \Delta f_r/f_0$: relative resonance frequency shift, 't.w.' designates this work.

Sensor	f_0 kHz	$\Delta f_r/\Delta T$ (Hz/K)	$\Delta f_{r,rel}/\Delta T$ (1/K)	Ref.
U (W)	0.95	−0.048	$-60 \cdot 10^{-6}$	[27]
U (Si, Au)	5.96	−0.441	$-69 \cdot 10^{-6}$	[33]
TF (Steel)	0.44	−0.0519	$-118 \cdot 10^{-6}$	t.w.
CL (Si)	43.83	-1.3	$-29.7 \cdot 10^{-6}$	[34]
CL (Si, Au)	18.33	-1.83	$-100 \cdot 10^{-6}$	[35]
TR	0.4	−0.15	$-385.58 \cdot 10^{-6}$	t.w.
SW (W)	2.98	30	0.01	[31]

5 °C to 60 °C in 5 °C temperature steps. Fig. 10 shows the magnitude of measured frequency responses as well as evaluated resonance frequencies at these temperatures. In Table 3 a comparison of the resonance frequency's dependence to temperature is given for different resonators. The first five sensors, i.e. a U-shaped tungsten wire sensor, U (W), [27], a U-shaped gold coated silicon resonator, U(Si, Au), [33], a steel tuning fork, TF (steel), a silicon cantilever, CL (Si), [34] and a gold coated silicon cantilever, CL (Si, Au), [35] are singly clamped structures and thus show a relatively small dependence of the resonance frequency to temperature. The last two sensors i.e., the torsional resonator, TR, and a straight tungsten wire sensor, SW (W), [31] are doubly clamped structures and thus, show a much higher dependence of the resonance frequency to temperature. However, this dependence is much lower for the torsional resonator compared to the straight wire sensor. To reduce this cross sensitivity, using only one torsional spring instead of two may be a possible approach.

6. Conclusion and outlook

A first study of the electromagnetically driven and read out torsional oscillator in air showed the advantages of using one single coil for both, excitation and readout. The advantages are mainly based on the manufactural benefit that in case of using one coil (instead of two) only two wires have to be electrically connected for power supply and readout which in this case is implemented by contacting the torsional springs. The feasibility of such a torsional resonator for viscosity and mass density sensing applications has

Please cite this article in press as: M. Heinisch, et al., Electromagnetically driven torsional resonators for viscosity and mass density sensing applications, Sens. Actuators A: Phys. (2015), http://dx.doi.org/10.1016/j.sna.2015.03.033

been shown by measurements in ten different liquids. For design purposes, a complete analytical model comprising the structural and fluid mechanics and relating output to input signals has been elaborated. Therefrom, reduced order models have been derived which relate resonance frequency and quality factor to viscosity and mass density, respectively. The advantage of such models is that only four to six factors have to be determined to describe the sensors characteristics. The comparison of both fitted model results shows that the generalized model yields significantly better results for f_r which can be explained by liquid trapping due to surface roughnesses of the cylinder shell. A first estimation of the device's sensitivity and its cross sensitivity of its resonance frequency has been made and compared to other resonant viscosity and mass density sensors.

Regarding future work, a more reliable clamping and housing has to be designed and manufactured aiming to obtain more stable and accurate results. By means of further experiments, the maximum measurable viscosities and resolution have to be investigated.

Acknowledgments

This work has been partially supported by the Linz Center of Mechatronics (LCM) in the framework of the Austrian COMET-K2 program. We also want to thank Bernhard Mayrhofer and Johann Katzenmayer for their help and excellent assistance.

References

[1] B. Jakoby, R. Beigelbeck, F. Keplinger, F. Lucklum, A. Niedermayer, E.K. Reichel, C. Riesch, T. Voglhuber-Brunnmaier, B. Weiss, Miniaturized sensors for the viscosity and density of liquids – performance and issues, IEEE Trans. Ultrason. Ferroelectr. Freq. Control 57 (1) (2010) 111–120, http://dx.doi.org/10.1109/TUFFC.2010.1386
[2] E.K. Reichel, C. Riesch, F. Keplinger, C.E.A. Kirschhock, B. Jakoby, Analysis and experimental verification of a metallic suspended plate resonator for viscosity sensing, Sens. Actuators A: Phys. 162 (2010) 418–424, http://dx.doi.org/10.1016/j.sna.2010.02.017
[3] A. Abdallah, M. Heinisch, B. Jakoby, Measurement error estimation and quality factor improvement of an electrodynamic-acoustic resonator sensor for viscosity measurement, Sens. Actuators A: Phys. 199 (2013) 318–324.
[4] C. Riesch, E.K. Reichel, A. Jachimowicz, J. Schalko, P. Hudek, B. Jakoby, F. Keplinger, A suspended plate viscosity sensor featuring in-plane vibration and piezoresistive readout, J. Micromech. Microeng. 19 (2009) 075010, http://dx.doi.org/10.1088/0960-1317/19/7/075010
[5] S. Cerimovic, R. Beigelbeck, H. Antlinger, J. Schalko, B. Jakoby, F. Keplinger, Sensing viscosity and density of glycerol–water mixtures utilizing a suspended plate MEMS resonator, Microsyst. Technol. 18 (7–8) (2012) 1045–1056.
[6] S.J. Martin, V.E. Granstaff, G.C. Frye, Characterization of a quartz crystal microbalance with simultaneous mass and liquid loading, Anal. Chem. 63 (1991) 2272–2281.
[7] R. Beigelbeck, B. Jakoby, A two-dimensional analysis of spurious compressional wave excitation by thickness-shear-mode resonators, J. Appl. Phys. 95 (9) (2004) 4989–4995.
[8] T. Voglhuber-Brunnmaier, B. Jakoby, Efficient spectral domain formulation of loading effects in acoustic sensors, Sens. Actuators A: Phys. 186 (2012) 38–47.
[9] C.W. Macosko, Rheology, Principles, Measurements and Applications, Wiley-VCH, 1994.
[10] A. Rahafrooz, S. Pourkamali, Characterization of rotational mode disk resonator quality factors in liquid, in: Frequency Control and the European Frequency and Time Forum (FCS), 2011 Joint Conference of the IEEE International, 2011, p. 5.
[11] I. Dufour, A. Maali, Y. Amarouchene, et al., The microcantilever: a versatile tool for measuring the rheological properties of complex fluids, J. Sens. (2012), http://dx.doi.org/10.1155/2012/719898
[12] C. Vančura, I. Dufour, S.M. Heinrich, F. Josse, A. Hierlemann, Analysis of resonating microcantilevers operating in a viscous liquid environment, Sens. Actuators A: Phys. 141 (1) (2008) 43–51.
[13] J. Toledo, T. Manzaneque, J. Hernando-Garc’í, J. Vázquez, A. Ababneh, H. Seidel, M. Lapuerta, J. Sánchez-Rojas, Application of quartz tuning forks and extensional microresonators for viscosity and density measurements in oil/fuel mixtures, Microsyst. Technol. (2014) 1–9.
[14] C. Riesch, A. Jachimowicz, F. Keplinger, E.K. Reichel, B. Jakoby, A novel sensor system for liquid properties based on a micromachined beam and a low-cost optical readout, in: Proceedings IEEE Sensors, 2007, pp. 872–875.
[15] I. Etchart, H. Chen, P. Dryden, J. Jundt, C. Harrison, K. Hsu, F. Marty, B. Mercier, MEMS sensors for density–viscosity sensing in a low-flow microfluidic environment, Sens. Actuators A: Phys. 141 (2) (2008) 266–275.
[16] M. Heinisch, T. Voglhuber-Brunnmaier, E.K. Reichel, S. Clara, A. Abdallah, B. Jakoby, Concept study on an electrodynamically driven and read-out torsional oscillator, in: Proceedings Microelectronic Systems Symposium, 2014.
[17] W.W. Weaver, S.P. Timoshenko, D.H. Young, Vibration Problems in Engineering, 5th ed., Wiley, 1990.
[18] L.D. Landau, E.M. Lifshitz, Fluid Mechanics, Butterworth-Heinemann, 1987.
[19] M. Heinisch, E.K. Reichel, B. Jakoby, A suspended plate in-plane resonator for rheological measurements at tunable frequencies, in: Proc. Sensor + Test, 2011, pp. 61–66.
[20] M. Baù, V. Ferrari, D. Marioli, A. Taroni, Cost-effective system for the characterization of microstructures vibrating in out-of-plane modes, Sens. Actuators A: Phys. 142 (1) (2008) 270–275.
[21] M. Heinisch, T. Voglhuber-Brunnmaier, E.K. Reichel, I. Dufour, B. Jakoby, Reduced order models for resonant viscosity and mass density sensors, Sens. Actuators A: Phys. 220 (2014) 76–84.
[22] S.J. Martin, R.W. Cernosek, J.J. Spates, Sensing liquid properties with shear-mode resonator sensors, in: Transducers, Eurosensors IX, 1995, pp. 712–715.
[23] B. Jakoby, M. Vellekoop, Physical sensors for liquid properties, IEEE Sens. J. 11 (12) (2011) 3076–3085.
[24] D.J. Griffiths, Introduction to Electrodynamics, Pearson, 2013.
[25] E.K. Chong, S.H. Zak, An Introduction to Optimization, 2nd ed., John Wiley & Sons, 2001.
[26] A.O. Niedermayer, T. Voglhuber-Brunnmaier, J. Sell, B. Jakoby, Methods for the robust measurement of the resonant frequency and quality factor of significantly damped resonating devices, Meas. Sci. Technol. 23 (8) (2012) 085107.
[27] M. Heinisch, E.K. Reichel, I. Dufour, B. Jakoby, A u-shaped wire for viscosity and mass density sensing, Sens. Actuators A: Phys. 214 (2014) 245–251.
[28] M. Heinisch, T. Voglhuber-Brunnmaier, E.K. Reichel, I. Dufour, B. Jakoby, Application of resonant steel tuning forks with circular and rectangular cross sections for precise mass density and viscosity measurements, Sens. Actuators A: Phys. (2015).
[29] C. Riesch, Micromachined Viscosity Sensors, Shaker Verlag, 2009.
[30] D. Seibt, Schwingdrahtviskosimeter mit integriertem ein-senkkörper-dichtemessverfahren für untersuchungen an gasen in größeren temperatur- und druckbereichen, Ph.D. thesis, Universität Rostock, 2007.
[31] M. Heinisch, E.K. Reichel, I. Dufour, B. Jakoby, Tunable resonators in the low kHz range for viscosity sensing, Sens. Actuators A: Phys. 186 (2012) 111–117, http://dx.doi.org/10.1016/j.sna.2012.03.009
[32] T. Larsen, S. Schmid, L. Grönberg, A.O. Niskanen, J. Hassel, S. Dohn, A. Boisen, Ultrasensitive string-based temperature sensors, Appl. Phys. Lett. 98 (12) (2011) 121901.
[33] M. Stifter, T. Sauter, W. Hortschitz, F. Keplinger, H. Steiner, MEMS heterodyne AMF detection with capacitive sensing, Proc. IEEE Sens. 2012 (2012) 1–4, http://dx.doi.org/10.1109/ICSENS.2012.6411171
[34] H.S. Wasisto, S. Merzsch, A. Waag, E. Uhde, T. Salthammer, E. Peiner, Airborne engineered nanoparticle mass sensor based on a silicon resonant cantilever, Sens. Actuators B: Chem. 180 (2013) 77–89.
[35] R. Sandberg, W. Svendsen, K. Mølhave, A. Boisen, Temperature and pressure dependence of resonance in multi-layer microcantilevers, J. Micromech. Microeng. 15 (8) (2005) 1454.

Biographies

Martin Heinisch obtained his Dipl.-Ing. (M.Sc.) in Mechatronics from Johannes Kepler University Linz, Austria, in 2009. After his Master studies he went to the University of California, Los Angeles (U.C.L.A.) as a Marshall Plan Scholarship grantee, where he did research in the field of microfluidic applications and self assembling systems. In 2010 he started a Ph.D. program at the Institute for Microelectronics and Microsensors of the Johannes Kepler University Linz, Austria where he is currently working on resonating liquid sensors.

Thomas Voglhuber-Brunnmaier received the Dipl.-Ing. (M.Sc.) degree in Mechatronics in 2007 and the Dr.techn. (Ph.D.) in May 2013 at the Institute for Microelectronics and Microsensors (IME) at the Johannes Kepler University (JKU) in Linz, Austria. From May 2013 he holds a Post-Doc position at the Center for Integrated Sensor Systems (CISS) at the Danube University Krems (DUK), where he works in close cooperation with IME on fluid sensors. His fields of interest are the modeling of micro-sensors, statistical signal processing, numerical methods and analog electronics.

Please cite this article in press as: M. Heinisch, et al., Electromagnetically driven torsional resonators for viscosity and mass density sensing applications, Sens. Actuators A: Phys. (2015), http://dx.doi.org/10.1016/j.sna.2015.03.033

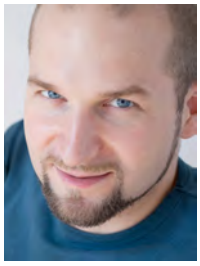

Erwin K. Reichel was born in Linz, Austria, in 1979. He received the Dipl.-Ing. (M.Sc.) degree in mechatronics from Johannes Kepler University, Linz, Austria, in 2006. From 2006 to 2009 he was working on the Ph.D. thesis at the Institute for Microelectronics and Microsensors of the Johannes Kepler University, Linz and graduated in October 2009. Afterwards he held a post-doctoral position at the Centre for Surface Chemistry and Catalysis as well as at the Department for Chemical Engineering, KU Leuven, Belgium until June 2012. Since then he holds a position as university assistant at the Johannes Kepler University Linz. The main research fields are the modeling, design, and implementation of sensors for liquid properties, and monitoring of phase transition in complex solutions.

Isabelle Dufour graduated from Ecole Normale Supérieure de Cachan in 1990 and received the Ph.D. and H.D.R. degrees in engineering science from the University of Paris-Sud, Orsay, France, in 1993 and 2000, respectively. She was a CNRS research fellow from 1994 to 2007, first in Cachan working on the modelling of electrostatic actuators (micromotors, micropumps) and then after 2000 in Bordeaux working on microcantilever-based chemical sensors. She is currently Professor of electrical engineering at the University of Bordeaux and her research interests are in the areas of microcantilever-based sensors for chemical detection, rheological measurements and materials characterisation.

Bernhard Jakoby obtained his Dipl.-Ing. (M.Sc.) in Communication Engineering and his doctoral (Ph.D.) degree in electrical engineering from the Vienna University of Technology (VUT), Austria, in 1991 and 1994, respectively. In 2001 he obtained a venia legendi for Theoretical Electrical Engineering from the VUT. From 1991 to 1994 he worked as a Research Assistant at the Institute of General Electrical Engineering and Electronics of the VUT. Subsequently he stayed as an Erwin Schrödinger Fellow at the University of Ghent, Belgium, performing research on the electrodynamics of complex media. From 1996 to 1999 he held the position of a Research Associate and later Assistant Professor at the Delft University of Technology, The Netherlands, working in the field of microacoustic sensors. From 1999 to 2001 he was with the Automotive Electronics Division of the Robert Bosch GmbH, Germany, where he conducted development projects in the field of automotive liquid sensors. In 2001 he joined the newly formed Industrial Sensor Systems group of the VUT as an Associate Professor. In 2005 he was appointed Full Professor of Microelectronics at the Johannes Kepler University Linz, Austria. He is currently working in the field of liquid sensors and monitoring systems.

Please cite this article in press as: M. Heinisch, et al., Electromagnetically driven torsional resonators for viscosity and mass density sensing applications, Sens. Actuators A: Phys. (2015), http://dx.doi.org/10.1016/j.sna.2015.03.033

Curriculum Vitae

Name and Address

Name	Martin Heinisch
Academic Degree	Diplom-Ingenieur (equivalent to M.Sc.)
Date and Place of Birth	September 25, 1982 in Wels, Austria

Education

Oct. 2011 - present	Joint Doctorate at Johannes Kepler University Linz, Austria and University of Bordeaux, France. Topic: Mechanical resonators for liquid sensing
2002 – 2009	Studies of Mechatronics at the Johannes Kepler University of Linz Graduation with distinction
1999 - 2000	École secondaire de La Magdeleine, La Prairie, Québec, Canada Formation Générale
1993 – 2001	Humanistic Highschool of Kremsmünster, Austria General qualification for university entrance

Professional and Research Experience

Dec. 2009 - present	Graduate scientist (“university assistant”) at the institute for Microelectronics and Microsensors, Johannes Kepler University Linz Research fields: Resonators, Microfluidics, Rheology
Jun. 2009 – Dez. 2009	Visiting student at the University of California, Los Angeles (UCLA) Research fields: Artificial cells, self-assembling systems and emerging properties. Microfluidics
Sept. 2008 – Feb. 2009	Undergraduate scientist at the Institute for Microelectronics and Microsensors, Johannes Kepler University Linz Tutor for the courses "Introduction to mechatronics" and "Practical training of electrical engineering"
Jun. 2008 – Jun. 2009	Diploma thesis at the Institute for Microelectronics and Microsensors, Johannes Kepler University Linz Title of the thesis: Electromagnetically Actuated Valveless Micropump in Polymer-Technology for Sensor Applications
Jul. 2007 – Sept. 2007	Visiting student at the University of California, Los Angeles (UCLA) Development of a transparent temperature controlled cooler for a microfluidic chip
Mar. 2007 – Jun. 2007	Undergraduate scientist at the Institute for Measurement Technology Johannes Kepler University of Linz Tutor for the course "Exercises in electrical measurements and senor systems"

Languages

German	Native language
English	Fluent in writing and speaking
French	Fluent in writing and speaking

Awards

MEC 2009	Mechatronic Price 2009 in the category: Best Austrian Diploma Thesis
OVE 2010	Award for the diploma thesis from the Austrian association for electrical engineering

Eidesstattliche Erklärung

Ich erkläre an Eides statt, dass ich die vorliegende Dissertation selbstständig und ohne fremde Hilfe verfasst, andere als die angegebenen Quellen und Hilfsmittel nicht benutzt bzw. die wörtlich oder sinngemäß entnommenen Stellen als solche kenntlich gemacht habe. Die vorliegende Dissertation ist mit dem elektronisch übermittelten Textdokument identisch.

Martin Heinisch, Linz, August 31, 2015